# Solar Cells

## Silicon Wafer-Based Technologies

*Edited by Leonid A. Kosyachenko*

# SOLAR CELLS –
# SILICON WAFER-BASED TECHNOLOGIES

Edited by **Leonid A. Kosyachenko**

**Solar Cells - Silicon Wafer-Based Technologies**
http://dx.doi.org/10.5772/1758
Edited by Leonid A. Kosyachenko

**Contributors**

Javier Navas, Rodrigo Alcántara, Concha Fernández-Lorenzo, Joaquín Martín-Calleja, Ching-Hsi Lin, Shih-Peng Hsu, Wei-Chih Hsu, Purnomo Sidi Priambodo, Nji Raden Poespawati, Djoko Hartanto, Michael Levy, Tetyana Nychyporuk, Mustapha Lemiti, Fengxiang Chen, Lisheng Wang, Mohsen Taherbaneh, Karim Rahmani, Gholamreza Farahani, Jiri Vanek, Kristyna Jandova, Vasiliki Perraki, Anis Sellami, Mongi Bouaicha, Leonid Bruc, Alexei Simaschevici, Dormidont Serban, Predrag Osmokrovic, Aleksandra Vasic, Milos Vujisic, Koviljka Stankovic, Filippo Spertino, Paolo Di Leo, Fabio Corona, B. Erik Ydstie, Juan Du, Yahia Chergui, Asmiet Ramizy, Yarub Al-Douri, Khalid Omar, Zainuriah Hassan

**Notice**

Statements and opinions expressed in the chapters are these of the individual contributors and not necessarily those of the editors or publisher. No responsibility is accepted for the accuracy of information contained in the published chapters. The publisher assumes no responsibility for any damage or injury to persons or property arising out of the use of any materials, instructions, methods or ideas contained in the book.

# We are IntechOpen,
# the world's leading publisher of Open Access books
# Built by scientists, for scientists

## 4,100+
Open access books available

## 116,000+
International authors and editors

## 120M+
Downloads

## 151
Countries delivered to

Our authors are among the

## Top 1%
most cited scientists

## 12.2%
Contributors from top 500 universities

Interested in publishing with us?
Contact book.department@intechopen.com

Numbers displayed above are based on latest data collected.
For more information visit www.intechopen.com

# Meet the editor

Dr. Leonid A. Kosyachenko is professor of National University of Chernivtsi, Ukraine. After receiving his Doctor of Sciences Degree in Physics and Mathematics in 1983, he founded and became a head of Optoelectronics Department – the first department of this kind at Ukrainian universities. About twenty of his pupils have performed work to obtain the degrees of Candidate (Ph.D.) and Doctor of Sciences. His research interests have been in physics and technology of solar cells, semiconductor X-ray and $\gamma$-ray detectors, light-emitting and photosensitive devices. He is author (co-author) of several books and numerous scientific articles; presented reports at international scientific conferences and meetings in Germany, Italy, England, Japan, China, Greece, Spain, Belgium, Russia. He was the leader of several collaborative projects with the institutions of Russia, Belorussia and is one of the leaders of the long-term projects of the European Commission. Prof. L.A. Kosyachenko is a member of the Ukrainian Physical Society and the guest editor of journal "Solar Energy Materials and Solar Cells".

# Contents

# Preface

The third book of four-volume edition of "Solar Cells" is devoted to solar cells based on silicon wafers, i.e., the main material used in today's photovoltaics. Single-crystalline Si (c-Si) modules are among the most efficient but at the same time the most expensive since they require the highest purity silicon and involve a lot of stages of complicated processes in their manufacture. Polycrystalline silicon (mc-Si) cells are less expensive to produce solar cells but are less efficient. As a result, cost per unit of generated electric power for c-Si and mc-Si modules is practically equal. Nevertheless, wafer silicon technology provides a fairly high rate of development of solar energy. Photovoltaics of all types on silicon wafers (ribbons), representatives of the so-called first generation photovoltaics, will retain their market position in the future. In hundreds of companies around the world, one can always invest with minimal risk and implement the silicon technology developed for microelectronics with some minor modifications.

For decades, an intensive search for cheaper production technology of silicon wafer-based solar cells is underway. The results of research and development, carried out for this purpose, lead to positive results although too slowly. This book includes the chapters that present new results of research aimed to improve efficiency, to reduce consumption of materials and to lower the cost of wafer-based silicon solar cells as well as new methods of research and testing of the devices contributing to the achievement of this goal. Light trapping design in c-Si and mc-Si solar cells, solar-energy conversion as a function of the geometric-concentration factor, design criteria for spacecraft solar arrays are considered in several chapters. A system for extracting the physical parameters from I-V curves of solar cells and PV solar generators, the micrometric characterization of solar cells, LBIC method for characterization of solar cells, and a new model for non-idealities in the I-V characteristic of the PV generators are discussed in other chapters of the volume.

It is hoped that this volume of "Solar Cells" will be of interest for many readers.

The editor addresses special thanks to the contributors for their initiative and high quality work, and to the technical editors that conveyed the text into a qualitative and pleasant presentation.

**Professor, Doctor of Sciences, Leonid A. Kosyachenko**
National University of Chernivtsi
Ukraine

**1**

# Solar Cell

Purnomo Sidi Priambodo, Nji Raden Poespawati and Djoko Hartanto
*Universitas Indonesia*
*Indonesia*

## 1. Introduction

Solar cell is the most potential energy source for the future, due to its characteristics of renewable and pollution free. However, the recent technology still does not achieve high Watt/m$^2$ and cost efficiency. Solar cell technology still needs to be developed and improved further to obtain optimal efficiency and cost. Moreover, in order to analyze and develop the solar cell technologies, it is required the understanding of solar cell fundamental concepts. The fundamentals how the solar works include 2 phenomena, i.e.: (1) Photonics electron excitation effect to generate electron-hole pairs in materials and (2) diode rectifying.

The phenomenon of photonics electron excitation is general nature evidence in any materials which absorbs photonic energy, where the photonic wavelength corresponds to energy that sufficient to excite the external orbit electrons in the bulk material. The excitation process generates electron-hole pairs which each own quantum momentum corresponds to the absorbed energy. Naturally, the separated electron and hole will be recombined with other electron-holes in the bulk material. When the recombination is occurred, it means there is no conversion energy from photonics energy to electrical energy, because there is no external electrical load can utilize this natural recombination energy.

To utilize the energy conversion from photonic to electric, the energy conversion process should not be conducted in a bulk material, however, it must be conducted in a device which has rectifying function. The device with rectifying function in electronics is called diode. Inside diode device, which is illuminated and excited by incoming light, the electron-hole pairs are generated in *p* and *n*-parts of the *p-n* diode. The generated pairs are not instantly recombined in the surrounding exciting local area. However, due to rectifying function, holes will flow through *p*-part to the external electrical load, while the excited electron will flow through *n*-part to the external electrical load. Recombination process of generated electron-hole pairs ideally occurs after the generated electrons-holes experience energy degradation after passing through the external load outside of the diode device, such as shown in illustration on Figure-1.

The conventional structure of p-n diode is made by crystalline semiconductor materials of Group IV consists of silicon (Si) and germanium (Ge). As an illustration in this discussion, Si diode is used, as shown in Figure-1 above, the sun light impinges on the Si p-n diode, wavelengths shorter than the wavelength of Si bandgap energy, will be absorbed by the Si material of the diode, and exciting the external orbit electrons of the Si atoms. The electron excitation process causes the generation of electron-hole pair. The wavelengths longer than the wavelength of Si bandgap energy, will not be absorbed and not cause excitation process

to generate electron-hole pair. The excitation and electron-hole pair generation processes are engineered such that to be a useful photon to electric conversion. The fact that electron excitation occurs on $\lambda < \lambda_{bandgap-Si}$, shows the maximum limit possibility of energy conversion from sun-light to electricity, for solar cell made based on Si.
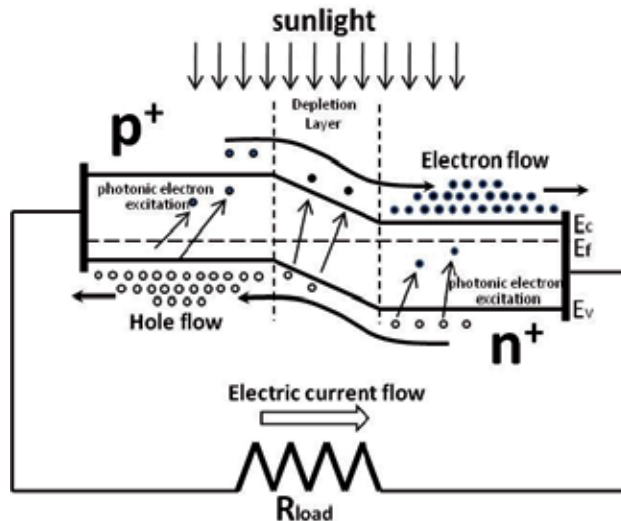


Fig. 1. Illustration of solar cell device structure in the form of p-n diode with external load. The holes flow to the left through the valanche band of diode p-part and the electrons flow through the conduction band of diode n-part.

The fundamental structure of solar cell diode does not change. The researchers have made abundance engineering experiment to improve efficiency by involving many different materials and alloys and also restructuring the solar cell fundamental structure for the following reasons:
1. Energy conversion efficiency Watt/m2 improvement from photon to electricity.
2. Utilization of lower cost material that large availability in nature
3. Utilization of recyclable materials
4. The simplification of fabrication process and less waste materials
5. Longer solar cell life time

In this Chapter, we will discuss several topics, such as: (1) Solar cell device in an ideal diode perspective; (2) Engineering methods to improve conversion energy efficiency per unit area by involving device-structure engineering and material alloys; (3) Standar solar cell fabrications and (4) Dye-sensitized solar cell (DSSC) as an alternative for inexpenssive technology.

## 2. Solar cell device in an ideal diode perspective

In order to be able to analyze further the solar cell performance, we need to understand the concepts of an ideal diode, as discussed in the following explanation. In general, an ideal diode with no illumination of light, will have a dark *I-V* equation as following [1]:

$$I = I_0 \left( e^{qV/k_B T} - 1 \right) \tag{1}$$

where $I$ is current through the diode at forward or reverse bias condition. While, $I_0$ is a well known diode saturation current at reverse bias condition. $T$ is an absolute temperature $^oK$, $k_B$ is Boltzmann constant, $q$ (> 0) is an electron charge and $V$ is the voltage between two terminals of $p$-$n$ ideal diode. The current capacity of the diode can be controlled by designing the diode saturation current $I_0$ parameter, which is governed by the following equation [1]:

$$I_0 = qA \left( \frac{D_e}{L_e} \frac{n_i^2}{N_A} + \frac{D_h}{L_h} \frac{n_i^2}{N_D} \right) \tag{2}$$

where $A$ is cross-section area of the diode, $n_i$ is concentration or number of intrinsic electron-hole pair /cm³, $D_e$ is the diffusion coefficient of negative (electron) charge, $D_h$ is the diffusion coefficient of positive (hole) charge, $L_e$ and $L_h$ are minority carrier diffusion lengths, $N_A$ is the extrinsic acceptor concentration at $p$-diode side and $N_D$ is the extrinsic donor concentration at $n$-diode side [1].

$$L_e = \sqrt{D_e \tau_e} \quad dan \quad L_h = \sqrt{D_h \tau_h} \tag{3}$$

where $\tau_e$ and $\tau_h$ are minority carrier lifetime constants, which depend on the material types used. From Equations (2) & (3) above, it is clearly shown that the diode saturation current $I_0$ is very depended on the structure and materials of the diode. The I-V relationship of a dark condition is shown on Figure-2.
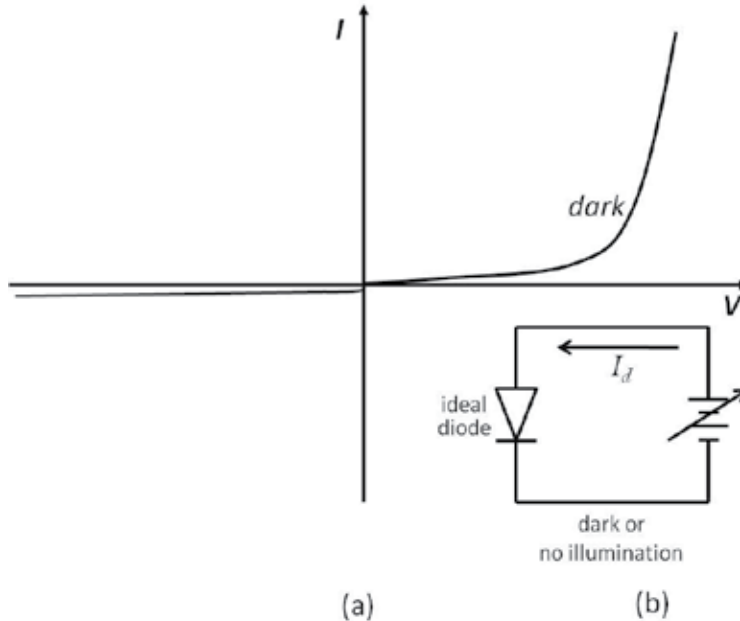


Fig. 2. I-V relationship of ideal diode for dark or no illumination. (a) I-V graph and (b) the equivalent ideal diode circuit.

Furthermore, if an ideal diode is designed as a solar cell, when illuminated by sun-light, there will be an energy conversion from photon to electricity as illustrated by a circuit model shown on Figure-3. As already explained on Figure-1 that the electron excitation caused by photon energy from the sun, will corresponds to generation of electron-hole pair, which electron and hole are flowing through their own bands. The excited electron flow will be recombined with the hole flow after the energy reduced due to absortion by the external load.

The circuit model of Figure-3, shows a condition when an ideal diode illuminated, the ideal diode becomes a current source with an external load having a voltage drop *V*. The total output current, which is a form of energy conversion from illumination photon to electricity, is represented in the form of superposition of currents, which are resulted due to photon illumination and forward current bias caused by positive voltage across *p* and *n* terminals. The corresponding *I-V* characteristic of an ideal diode solar cell is described by the Shockley solar cell equation as follows [3]:

$$I = I_{photon} - I_0\left(e^{qV/k_BT} - 1\right) \tag{4}$$

$I_{photon}$ is the photogenerated current, closely related to the photon flux incident to the solar cell. In general, $I_{photon}$ can be written in the following formula [2]

$$I_{photon} = qAG\left(L_e + W + L_h\right) \tag{5}$$

where *G* is the electron-hole pair generation rate of the diode, *W* is depletion region width of the solar cell diode. The *G* value absolutely depends on material types used for the device and the illumination spectrum and intensity (see Eq 14a & b), while *W* value depends on the device structure, A is the cross-section of illuminated area. The *I-V* characteristic of an ideal diode solar cell is illustrated in Figure-4.
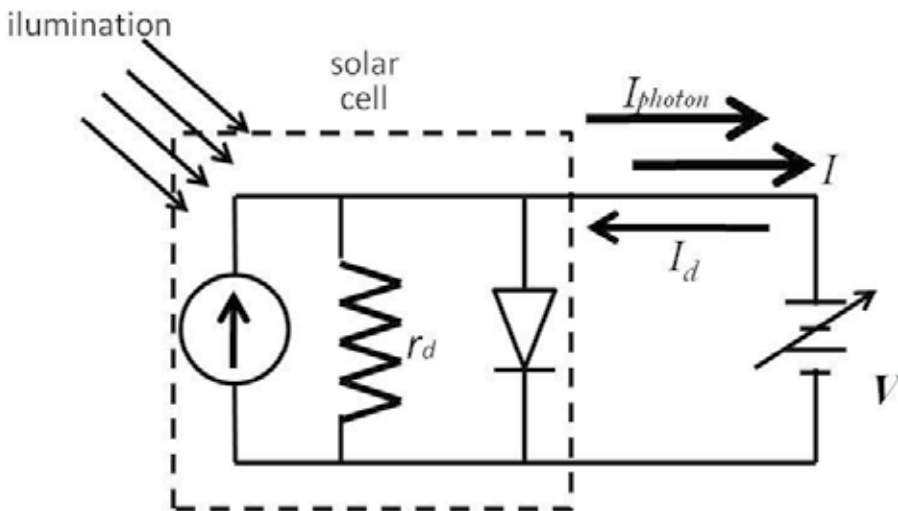


Fig. 3. The equivalent circuit model of an ideal diode solar cell.
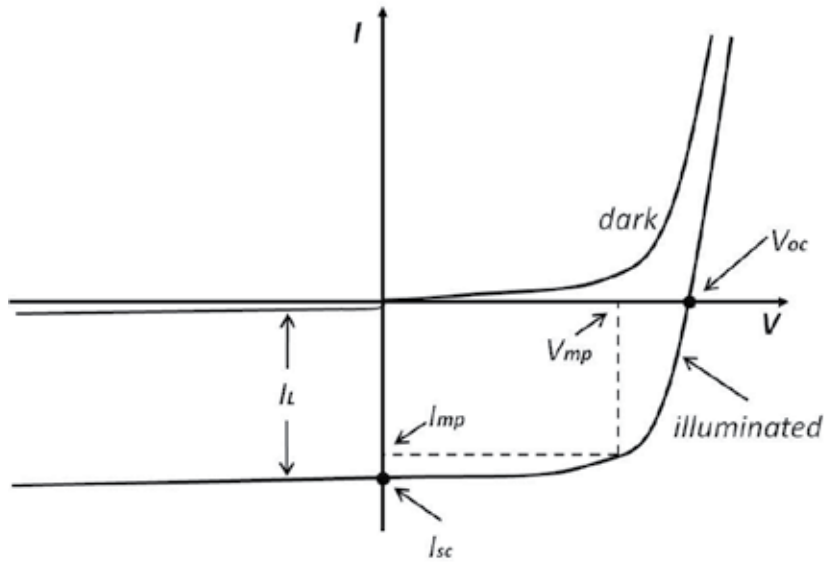
Fig. 4. The Graph of the I-V characteristics of an ideal diode solar cell when non-illuminated (dark) and illuminated.

**Solar cell output parameters**

From Figure-4, it is shown that there are 4 output parameters, which have to be considered in solar cell. The first parameter is $I_{SC}$ that is short circuit current output of solar cell, which is measured when the output terminal is shorted or $V$ is equal to 0. The value of output current $I = I_{SC} = I_{photon}$ represents the current delivery capacity of solar cell at a certain illumination level and is represented by Equation (4). The second parameter is $V_{OC}$ that is the open circuit output voltage of solar cell, which is measured when the output terminal is opened or $I$ is equal to 0. The value of output voltage $V_{OC}$ represents the maximum output voltage of solar cell at a certain illumination level and can be derived from Equation (4) with output current value setting at $I = 0$, as follows:

$$V_{OC} = \frac{k_B T}{q} \ln\left( \frac{I_{photon}}{I_0} + 1 \right) \qquad (6)$$

In general, $V_{OC}$ is determined by $I_{photon}$, $I_0$ and temperature, where $I_0$ absolutely depends on the structure design and the choice of materials for solar cell diode, while $I_{photon}$ besides depending on the structure design and the choice of materials, depends on the illumination intensity as well.

The maximum delivery output power is represented by the area of product $V_{MP}$ by $I_{MP}$ as the maximum possible area at fourth quadrant of Figure-4.

$$P_{MP} = V_{MP} \cdot I_{MP} \qquad (7)$$

The third parameter is fill factor $FF$ that represents the ratio PMP to the product $V_{OC}$ and $I_{SC}$. This parameter gives an insight about how "square" is the output characteristic.

$$FF = \frac{P_{MP}}{V_{OC} \cdot I_{SC}} = \frac{V_{MP} \cdot I_{MP}}{V_{OC} \cdot I_{SC}} \qquad (8)$$

In the case of solar cell with sufficient efficiency, in general, it has FF between 0.7 and 0.85. The energy –conversion efficiency, η as the fourth parameter can be written as [2]

$$\eta = \frac{V_{MP} \cdot I_{MP}}{P_{in}} = \frac{V_{OC} \cdot I_{SC} \cdot FF}{P_{in}} \qquad (9)$$

where $P_{in}$ is the total power of light illumination on the cell. Energy-conversion efficiency of commercial solar cells typically lies between 12 and 14 % [2]. In designing a good solar cell, we have to consider and put any effort to make those four parameters $I_{SC}$, $V_{OC}$, FF and η as optimum as possible. We like to use term optimum than maximum, since the effort to obtain one parameter maximum in designing solar cell, will degrade other parameters. Hence the best is considering the optimum efficiency of solar cell.

## 3. Improvement of solar cell performance

In the process to improve solar cell output performance that is energy conversion efficiency from photon to electricity, which is typically lies between 12 to 14 % [2], the researchers have been conducting many efforts which can be categorized and focused on:

1.  Diode device structure engineering to improve current output $I_{sc}$, by reducing $I_0$ and increasing photon illumination conversion to $I_{photon}$ in the form of improving $G$ parameter, electron-hole pair generation constant. The diode structure engineering, at the same time also improving output voltage in the form of $V_{OC}$, and improving FF and finally improving the energy conversion efficiency from photon to electricity.
2.  Material engineering, especially to obtain improvement on $G$ parameter, electron-hole pair generation.
3.  Device structure engineering to improve quantum efficiency and lowering top-surface lateral current flow to reduce internal resistance.
4.  Solar cell structure engineering includes concentrating photon energy to the solar cell device.

### 3.1 Solar cell diode structure engineering

In general, sun-light illuminates solar cell with the direction as shown on Figure-5.

The light illumination with $\lambda > \lambda_{bandgap}$ will pass through without absorbed by solar cell. While the light with $\lambda < \lambda_{bandgap}$ will be absorbed. Whatever spectrum, basically, incident light with $\lambda < \lambda_{bandgap}$ will be absorbed as a function of exponential decay with respect to distance parameter as $e^{-\alpha(\lambda)z}$ from the top surface, where $a(\lambda)$ is absorption coefficient and $z$ is the depth distance in the solar cell diode. Absorption occurs at any absorbed wavelength are shown on Figure-6.

As shown on Figure-6, red light will be absorbed exponentially slower than the blue light. The photons with different wavelengths will be absorbed in different speed. This discrepancy can be explained and derived by using the probability of state occupancies in material, which is illustrated by Fermi function as follows [1]:

$$f(E) = \frac{1}{\exp\left[\left(E - E_f\right)/k_B T\right] + 1} \qquad (10)$$
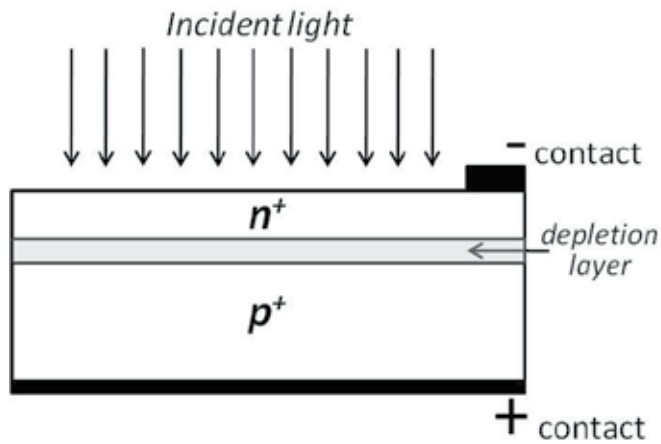
Fig. 5. A generic solar cell diode structure and the incidence light direction
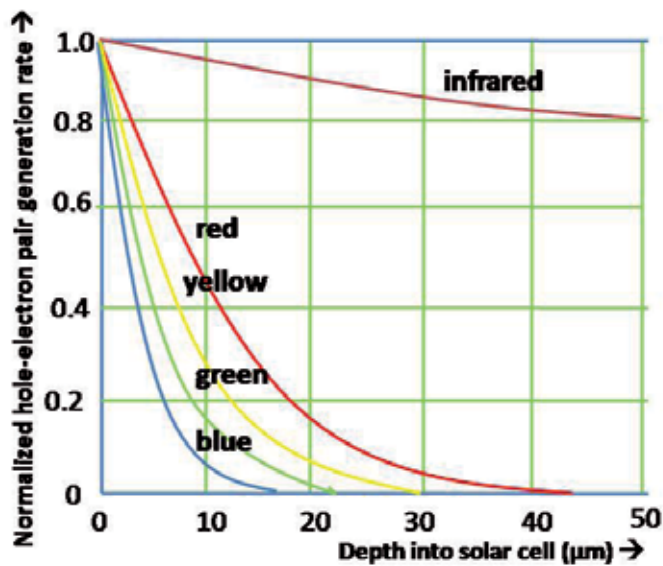


Fig. 6. A normalized hole-electron pair generation rate [2].

when $\exp\left[\left(E-E_f\right)/k_BT\right]\gg 1$, then Equation (10) can be written as

$$f(E)\approx e^{-\left[\left(E-E_f\right)/k_BT\right]} \tag{11}$$

where E represents the energy state in crystalline. Moreover, photon absorption $a(\lambda)$ by material is an equal representation of excitation probability of electron leaving hole towards a state in conduction band after excited by a photon. The probability is the integral accumulation of multiplication between electron occupation probability in valence band

and probability of possible state that can be occupied by the excited electron, furthermore those two are multiplied by a coefficient $\sigma(\lambda)$ as shown in the following equation:

$$\alpha(\lambda) \approx \sigma(\lambda) \cdot \int_{E_c - \frac{hc}{\lambda}}^{E_v} f(E) \cdot (1 - f(E + \frac{hc}{\lambda})) \cdot dE \tag{12}$$

where $\sigma(\lambda)$ is a cross section probability parameter represent of possible occurrence the photon to hole-electron pair generation at wavelength $\lambda$. Parameter $\sigma(\lambda)$ is obtained by the following derivation [2]:

$$\sigma(\lambda) = D\left( \frac{\left(hc / \lambda - E_g + E_p\right)^2}{\exp(E_p / k_B T) - 1} + \frac{\left(hc / \lambda - E_g - E_p\right)^2}{1 - \exp(E_p / k_B T)} \right) \tag{13}$$

where parameters $D$, $Eg$ and $Ep$ depend on material types used and crystalline quality, and usually are obtained by conducting experiments. $Eg$ and $Ep$ each are bandgap energy dan phonon absorption or emission energy respectively, $h$ is the Plank constant and $c$ is the light speed in vacuum. The $\sigma(\lambda)$ parameter is a function of $\lambda$ and naturally depends on the type of the material. Parameter absorption $a(\lambda)$ on Equation (12) when multiplied by illumination intensity $I_{int}(\lambda)$, will represent the generation rate of hole-electron pairs at $\lambda$ or $G(\lambda)$.

$$G(\lambda) = \alpha(\lambda) \cdot I_{int}(\lambda) \approx \sigma(\lambda) \cdot I_{int}(\lambda) \int_{E_c - \frac{hc}{\lambda}}^{E_v} f(E) \cdot (1 - f(E + \frac{hc}{\lambda})) \cdot dE \tag{14-a}$$

Furthermore, the generation rate of hole-electron pair $G$ can be written as the integral of $G(\lambda)$ as following:

$$G = \int_0^{\lambda_{bandgap}} G(\lambda) \, d\lambda \tag{14-b}$$

In a glance, the terms multiplication under the integral and the integral limits of Equations (12 and 14a) show that parameter values $G(\lambda)$ or $a(\lambda)$ getting larger for $\lambda$ becoming shorter (agrees to Figure-6). $\lambda_{bandgap}$ is the $\lambda$ of the bandgap energy as the limit of irradiance photon to electric conversion. At $\lambda > \lambda_{bandgap}$, $\sigma(\lambda)$ is zero and will not be absorbed or there is no electron-hole generation and does not contribute to the conversion. The following Figure-7 illustrates the distribution state of a material with respect to the Fermi function. The transition state probability represents the photon to hole-electron pair generation.

Back to Figure-5, naturally layer $n^+$ is a layer that more easier to generate hole-electron pairs due to photon excitation, in comparison to layer $p^+$. Hence, the $n^+$ layer is called as an electron emitter layer. By considering Figure-5 and 6 that photon absorption and hole-electron generation occurs at the front layer of diode structure, then in order to obtain higher conversion efficiency, the $n^+$ layer as electron emitter layer is located on the top surface of solar cell diode structure such as shown on Figure-5 above.

However, in order to be an effective electron emitter layer, the thickness of the $n^+$ layer must be shorter than the minority carrier diffusion length $L_h$ in $n^+$ layer, where the hole minority
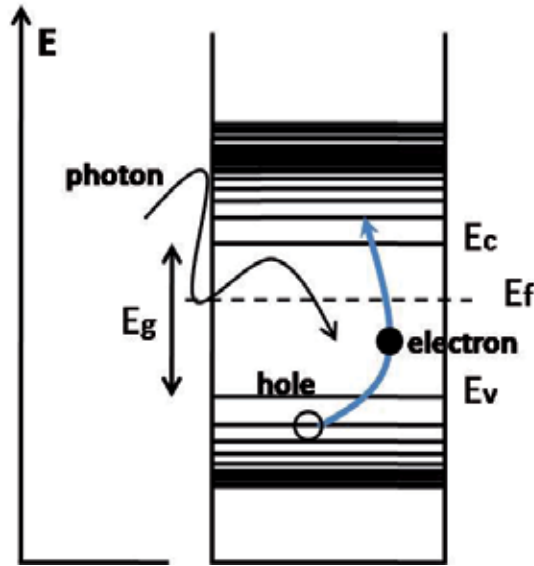
Fig. 7. Transition state probability illustration [4].

carrier diffusion lengths $L_h$ is governed by Equation (3). If the thickness of $n^+$ layer > $L_h$, then most of hole-electron pairs experience local recombination, which means useless for photon to electrical energy conversion. Between $n^+$ and $p^+$ layers, there exists a depletion layer, which has a built in potential $V_{bi}$ to conduct collection probability of the generated hole-electron pairs. The width of depletion layer can be written as follows [1]:

$$W = \left[ \frac{2\varepsilon_r \varepsilon_0}{q} \left( \frac{N_A + N_D}{N_A \cdot N_D} \right) (V_{bi} - V_A) \right]^{1/2} \qquad (15)$$

where W is the depletion layer width, $V_{bi}$ is the diode built in potential and $V_A$ is the applied or solar cell output voltage. The diode built in potential can be approach by the following Equation [1]:

$$V_{bi} = \frac{k_B T}{q} \ln \left( \frac{N_A N_D}{n_i^2} \right) \qquad (16)$$

The collection probability describes the probability that the light absorbed in a certain region of the device will generate hole-electron pairs which will be collected by depletion layer at *p-n* junction. The collected charges contribute to the output current $I_{photon}$. However, the probability depends on the distance to the junction compared to the diffusion length. If the distance is longer than the diffusion length, then instead of contributing to the output current, those hole-electron pairs are locally recombined again, hence the collection probability is very low. The collection probability is normally high (normalized to 1) at the depletion layer. The following Figure-8 shows the occurrence of photon absorption by the device that illustrated as an exponential decay, at the same time, representing generation of hole-electron pairs. The collection probability shows that at the front (top) surface is low

because far from the   built-in voltage at depletion layer. On depletion layer, collection probability very high and give a large contribution on output current $I_{photon}$.
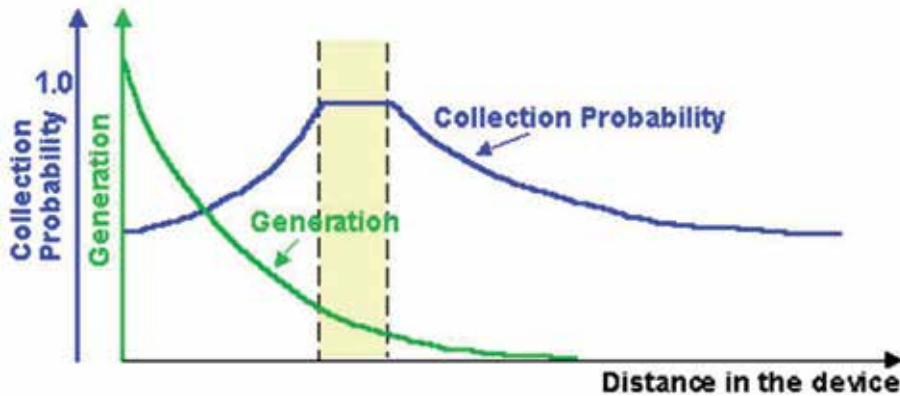


Fig. 8. The collection probability of the generated hole-electron pairs at junction [5].

As explained previously, there are 4 reference parameters in designing solar cell, i.e.: $I_{sc}$, $V_{OC}$, $FF$ and $\eta$. By considering the equations of those 4 parameters, it is likely that the four parameters are correlated each other. For instance, in order to increase $I_{sc}$ or $I_{photon}$ (1st parameter), we have to consider Equation (5), where the structure will depend on 2 parameters i.e. A the area of the cell surface and W the thickness of the depletion layer. While parameters G, $L_e$ and $L_h$ depend on the materials used for the solar cell diode. Increasing A parameter (the area of diode) will not have impact to other parameters, however, increasing W parameter will have impact to other parameters. Of course, by increasing $A$, the total output current $I_{photonic}$ will increase proportionally, the increasing $W$, the length of collection probability of depletion layer will increase as well, where finally it is expected to improve contribution to the output current.

From Equations [15] dan [16], it is shown that structurally $W$ parameter depends on $N_A$ and $N_D$.  In order to increase $W$ proportionally linear, then what we can do is by reducing doping concentration of $N_A$ and $N_D$ or one of both. The consequence of reducing $N_A$ and/or $N_D$ is the linear increment of $I_0$, which in the end causing reducing the total output current such as shown in Equation (4). Don't be panic,  improvement $I_{SC}$ in one side and decreasing in other side due to concentration adjustment of $N_A$ and/or $N_D$ does not mean there is no meaning at all. Because at a certain $N_A$ and/or $N_D$ value $+\Delta I_{SC}$ that caused by $\Delta W$ can be much larger than $-\Delta I_{SC}$ that caused by $I_0$.  Hence, to obtain the optimal design, it is required to apply a comprehensive numerical calculation and analysis to obtain the optimal $I_{SC}$.

For the sake of obtaining an optimal output voltage $V_{OC}$ (2nd parameter), we have to consider Equation (6). The equation shows that $V_{OC}$ is a natural logarithmic function of $I_{SC}/I_0$, it shows that by reducing $N_A$ and/or $N_D$ will cause on increasing $I_{SC}$ in root square manner and linearly proportional to $I_0$ that causes decreasing of  $V_{OC}$. Hence, there is a trade off that to increase $I_{SC}$ by structural engineering will cause to decrease $V_{OC}$. At certain level, the improvement of $I_{SC}$ can be much higher compared to the decrease of $V_{OC}$. Therefore, again, to obtain an optimal design, it is required to apply a comprehensive numerical calculation and analysis to obtain the optimal $I_{SC}$, $V_{OC}$ and output power.

The third parameter is fill factor *FF*, which is a measure on how "square" is the output characteristic of solar cell. It is shown by the curve in the 4th quadrant of *I-V* graph in Figure-4. The shape of the curve is governed by Equation (4). It means *FF* is low for very large $I_0$.

The fourth parameter $\eta$, as shown in Equation (9), linearly depends on the other three parameters. Here, we can conclude that in term of structure design, increasing one of the parameter, for instance $I_{SC}$ will cause reduction on other parameters, for example $V_{OC}$, and so vice versa. Finally, it is concluded that it is required to compromise between thus four output parameters to obtain the optimal condition.

When the optimalization process of four parameters from the structure given on Figure-5 is conducted by reducing the dopant concentration of one part (in general is *p*), then the solar cell will experience and have a relatively high internal resistance, which reducing output the performance parameter $\eta$. Hence, the structure in Figure-5 should be modified by inserting a layer that has a lower dopant concentration as shown in the following Figure-9, and keep the higher dopant concentration layers for ohmic contacts at the top and bottom contacts. By inserting layer *p* in between layer *p+* dan *n+* will cause the contact *p* to the contact + will have a low internal resistance, as same as between *n+* to contact -.
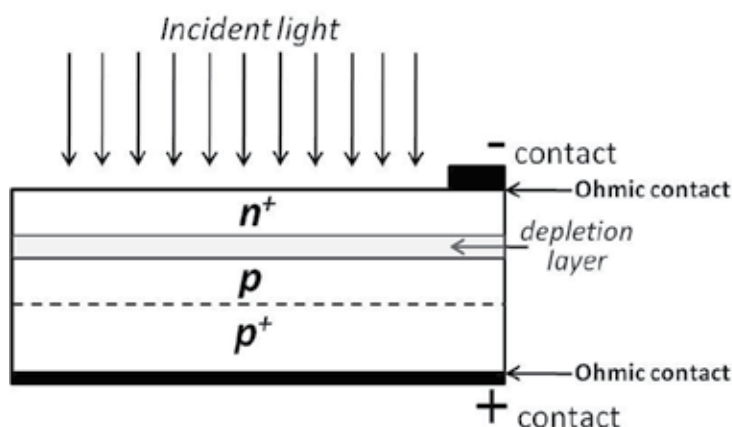


Fig. 9. Insertion of a lower dopant layer p in p-n junction diode to improve collection probability area and keep solar cell internal resistance lower.

### 1st generation of solar cells

1st generation of solar cell is indicated by the usage of material, which is based on silicon crystalline (c-Si). Typically solar cell is made from a single crystal silicon wafer (c-Si), with a simple p+-p-n+ juction diode structure (Figure-9) in large area, with bandgap energy 1.11 eV. In the development process, the usage of c-Si causes the price of solar cell very high, hence emerging the idea to use non-crystalline or poly-crystalline Si for producing solar cells. There was compromising between cost and efficiency. Using poly-crystalline material the price is cut down to the lower one since the fabrication cost is much lower, however the efficiency is going down as well, since the minority carrier lifetimes $\tau_e$ and $\tau_h$ are shorter in poly-crystalline than in single–crystalline Si that makes lower $I_{photon}$ (Equations (3 - 5)). For the ground application with no limitation of area, it is considered to use lower price solar cells with lower conversion efficiency. However, for application with limited areas for

instances on high-rise buildings and even on satellites, space shuttles or space-lab, a higher conversion efficiency is much considered. The first generation of solar cells based on poly-crystalline Si still dominates the market nowadays. The conversion energy efficiency typically reaches 12 to 14 %.

## 3.2 Material engineering to improve conversion parameter *G* (electron-hole pair generation rate)

### 2nd generation of solar cells

Instead of based on traditional Si wafer cystalline and polycrystalline, in the 2nd Generation solar cell, it began to use material alloys such as elemental group IV alloy for instance SiGe (silicon-germanium),  binary and ternary III-V group alloy for instances InGaP, GaAs and AlGaAs. Futhermore, binary to quaternary II-VI group alloy is used as well, such as Cadmium Telluride (CdTe) and Copper Indium Galium Diselenide (CIGS) alloys. The goals of using such material alloys in solar cell diode structure is to improve the irradiance photon to electric conversion rate parameter *G* such as shown in Equation (5) and has been derived in Equations (14-a and b).

By common sense, if $\lambda_{bandgap}$ is as large as possible, then we can expect that the *G* parameter goes up. This is the reason, why one applies SiGe for the solar cell, since the alloy has lower bandgap than Si, where the bandgap energy is governed by the following formula [6] where *x* represents the percent composition of Germanium:

$$E_g(x)= (1.155 – 0.43x + 0.0206x^2 )eV \quad for \quad 0 < x < 0.85 \tag{17}$$

and

$$E_g(x)= (2.010 – 1.27x)eV \quad for \quad 0.85 < x < 1 \tag{18}$$

The usage of SiGe alloy for solar cell results in the improvement of conversion efficiency up to 18% [11].

### Multi-junction solar cells

In the first generation,  Solar cell diode structure used a single type material Si in the form of crystalline, poly-crystalline and amorphous. In the development of 2nd generation solar cell, the researchers use several material alloys in one single device, then it is called as multi-junction solar cell.  As already explained and illustrated in Figure-6 that the shorter the photonic wavelength then it will be absorbed faster inside the material. It means the shorter wavelength part of the sun light spectrum will be absorbed more than the longer part of the spectrum by the same thickness of material. The wavelengths longer than the bandgap wavelength will not be absorbed at all.  The part of the spectrum not absorbed by the diode material is the inefficiency of the solar cell. In order to improve solar cell efficiency performance, then the remaining unabsorbed spectrum must be reabsorbed by the next structure that can converting become electricity. The solar cell structures in the second generation are mostly in the form of tandem structure, which consists of various alloy materials that have different bandgaps with sequence from the top surface, is  the highest bandgap then continued by the lower and finaly the lowest, such as illustrated on Figure-10. There may be a question, if the lower bandgap can absorb more spectrum, why not it is used a single diode structure with very low bandgap material to absorb the overall spectrum energy? without building tandem or cascading structures. The answer is following, it is

correct that more lower the bandgap energy; the material can be categorized as more effective in photon absorption. Hence, for photons with the same wavelength will be absorb faster in lower bandgap typed material in comparison to the larger bandgap material. Thus mechanism is very clear illustrated in math relation by Equations (12 and 14a).
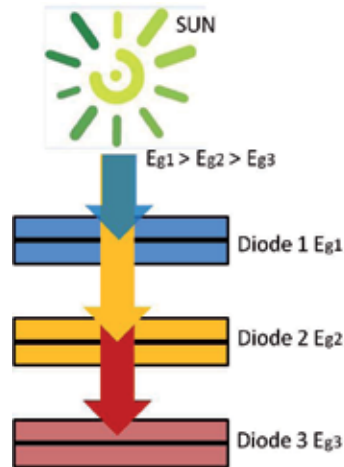


Fig. 10. Multi-junction and cell tandem concept.

The higher energy photon will be very fast absorbed and then generate hole-electron pairs with a high concentration in area close to the top surface of diode, which naturally has abundance surface defects corresponds to deep level trap close the surface. This surface defects cause a fast recombination process. Hence, it can be concluded that the usage of one diode structure with a lower bandgap energy, then a wide photon spectrum can be absorbed, however, the generated electron-hole pairs by the high energy photon will be recombined because located near the surface area with abundance defects and deep level states. Therefore, to make effective absorption and efficient conversion, the solar cell should be in the tandem structure such as illustrated in Figure-10. Further, Figure-11 shows a typical design of multi-junction or tandem solar cell incorporating III-V group of materials.

While the first generation with 12 to 14% efficiency dominates the market nowadays, this second generation of solar cells based on multi-junction structure dominates the market of high efficient solar cell as well, which typically reach 35 to 47 % efficiency. The typical applications of high efficient second generation solar cell with multi-junction technology are for satellite communications and space shuttles. To design multi-junction structure, it is required to have a knowledge about crystalline lattice match. If the crystalline lattice does not match, then there will exist abundance of deep level states in the junction region that cause a short carrier life-time or it causes faster or larger local recombination process. This large local recombination, finally will reduce the output current $I_{photon}$. The information regarding to the bandgap energies dan lattice match of various material are shown on Figures-12 and 13 [4] as follows.

Thus two first generations, besides of dominating solar cell technologies and markets nowadays, also are dominated by the usage of mostly silicon alloy based on semiconductor material. This situation causes the ratio of the solar cell price to the Watt-output power never decrease, because it tightly compete with the usage of Si and other semiconductor
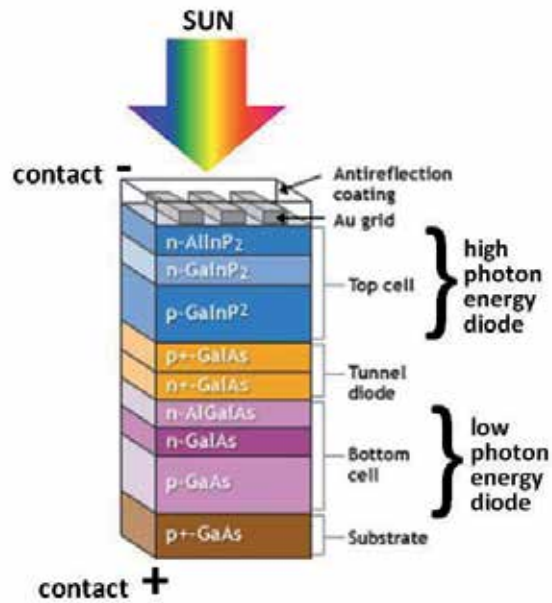
Fig. 11. Typical of high efficient solar cell with dual cell tandem structure[12].
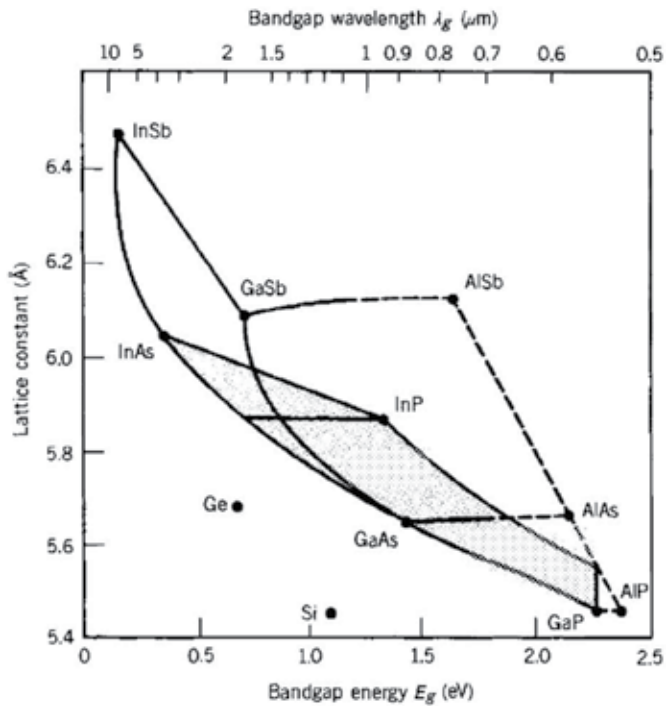


Fig. 12. Lattice constants, bandgap energies and bandgap wavelengths for III-V binary compounds, Si and Ge [4].

material for the global electronics industry demand. The condition encourages the researchers to create a radical technology revolution, by using non-crystalline material that replacing Si and other semiconductor materials, and it is realized in the form of dye-sensitized solar cell (DSSC) as the 3rd generation solar cells.
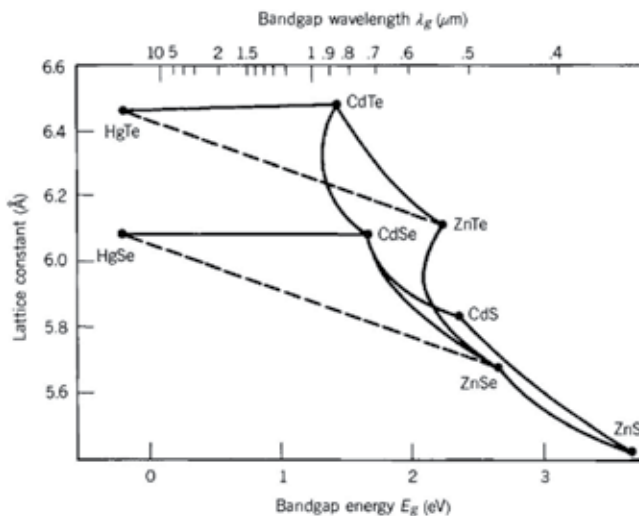


Fig. 13. Lattice constants, bandgap energies and bandgap wavelengths for important II-VI binary compounds [4].

## 3.3 Quantum efficiency engineering (optical design)

### Antireflection (AR) thin-film coating

As already well understood that the sun-light before reaching solar cell, propagates through the vacuum and air. At the moment when the light reaches the solar cell front surface, which is made by silicon material, the light experiences of reflection by the silicon surface due to the index of refraction difference between air and silicon. The reflection causes reduction of overall efficiency of the solar cell. We have to reduce the reflection in order to increase the efficiency. By borrowing the technique that has been well developed in optical science, furthermore to reduce reflection or increase absorption, it uses antireflection thin film coating structure applied on top of the front solar cell surface. Basically this technique uses Bragg reflection phenomenon, that is an interference effect caused by thin film structure. The following Figure-14 illustrates the process of Bragg reflection occurrence by the mirror stack structure. The reflectance occurs when the light incidence on an interface of two material with different index of refraction $n_1 \neq n_2$.

The maximum reflection intensity occurs when the following condition is set and called as Bragg angle [4]

$$\sin\theta = \frac{\lambda}{2d} \tag{19}$$

For normal incidence $\theta = 90^0$, with Bragg equation, distance between mirrors needed for constructive interference reflectance is $d = \lambda/2$. While for the requirement of destructive

interference reflectance or constructive interference transmittance, the distance between mirrors is $d = \lambda/4$.
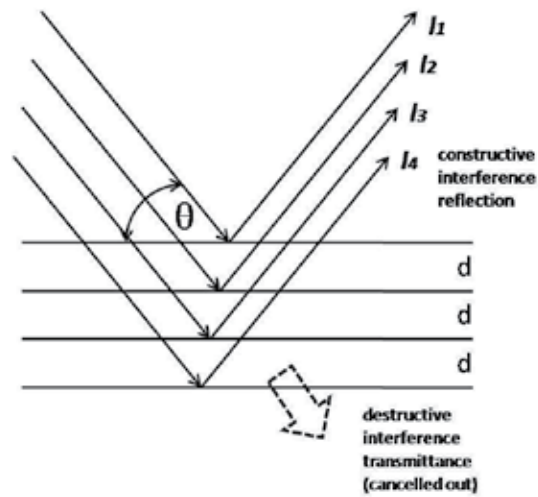


Fig. 14. Bragg reflection effect of mirror stacks structure with distance $d = \lambda/2$.

Furthermore, if there is only a single thin-film structure, as shown on Figure-15, then by using Fresnel equation and assumed that the design is for a normal incidence, then on each interface will occurs reflectance which is written as [2]

$$r_1 = \frac{n_{air} - n_{AR}}{n_{air} + n_{AR}} \quad \text{and} \quad r_2 = \frac{n_{AR} - n_{Si}}{n_{AR} + n_{Si}} \tag{20}$$

where $r_1$ is interface between air and antireflection coating (AR), and $r_2$ is interface between AR and silicon.
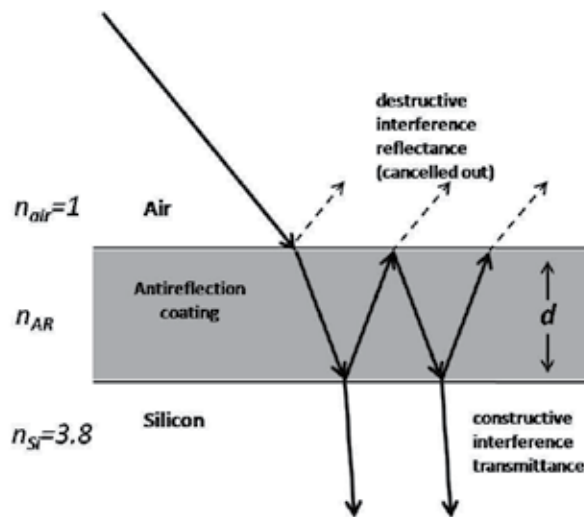


Fig. 15. Bragg reflection effect of mirror stacks structure with distance $d = \lambda/4$.

When the AR coating thickness is designed to be $n_{AR}d = \lambda_0/4$ and in normal incidence, then the total or overall reflectance is minimum and can be written as follows [2]:

$$R_{\min} = \left(\frac{n_{AR}^2 - n_{air}n_{Si}}{n_{AR}^2 + n_{air}n_{Si}}\right)^2 \tag{21}$$

Furthermore, it can be obtained zero reflectance if $n_{AR}^2 - n_{air}n_{Si} = 0$. At this condition, it means that the whole incidence sun light will be absorbed in to Si solar cell diode. As an additional information that refractive index of Si $n_{Si} \approx 3.8$ in the visible spectrum range and $n_{air} = 1$, such that to obtain $R = 0$, then required to use a dielectric AR coating with $n_{AR} \approx \sqrt{n_{air} \cdot n_{Si}} \approx 1.9$. The following Tabel-1 shows a list of materials with their corresponding refractive indices on the wavelength spectrum range in the region of visible and infrared [2].

| Material | Refractive index |
|---|---|
| MgF$_2$ | 1.3 – 1.4 |
| Al$_2$O$_3$ | 1.8 – 1.9 |
| Si$_3$N$_4$ | 1.8 – 2.05 |
| SiO$_2$ | 1.45 – 1.52 |
| SiO | 1.8 – 1.9 |
| TiO$_2$ | 2.3 |
| ZnS | 2.3 – 2.4 |
| Ta$_2$O$_5$ | 2.1 – 2.3 |
| HfO$_2$ | 1.75 – 2.0 |

Tabel 1. List of Refractive Indices of Dielectric Materials

To obtain a minimum reflectance with a single thin film layer AR, we can apply Al$_2$O$_3$, Si$_3$N$_4$, SiO or HfO$_2$ single layer. Other material can be used as AR in multi layer thin-film structure with the consequence of higher fabrication cost.

**Textured Surfaces**

The other method used to reduce reflectance and at the same time increasing photon intensity absorption is by using textured surfaces [2,4]. The simple illustration, how the light can be trapped and then absorbed by solar cell diode is shown on the following Figure-16. Generally, the textured surface can be produced by etching on silicon surface by using etch process where etching silicon in one lattice direction in crystal structure is faster than etching to the other direction. The result is in the form of pyramids as shown in the following Figure-16 [2].

Beside to the one explained above, there are still many methods used to fabricate textured surface, for an example by using large area grating fabrication method on top the solar cell

structure. The large area grating fabrication is started by making photoresist grating with interferometer method, and further continued by etching to the covering layer film of top surface of solar cell structure, as has been done by Priambodo et al [7].

The pyramids shown in Figure-16 are results of intersection crystal lattice planes. Based on Miller indices, the silicon surface is aligned parallel to the (100) plane and the pyramids are formed by the (111) planes [2].
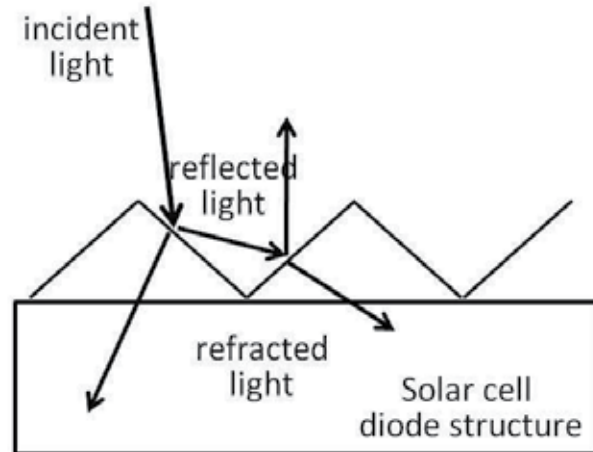


Fig. 16. Textured surface solar cell to improve absorption of solar photons.
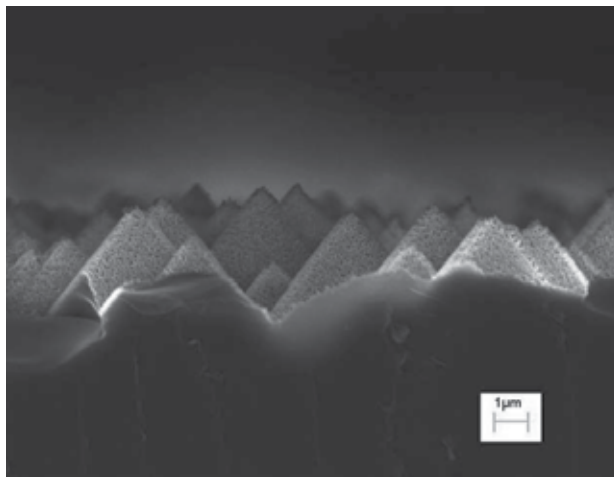


Fig. 17. The Appearance of a textured silicon surface under an SEM [2].

In order to obtain more effective in trapping sun-light to be absorbed, the textured surface design should consider the diffraction effects of textured surface. The diffraction or grating equation is simply written as the following [4]:

$$\sin\theta_q = \sin\theta_i + q\frac{\lambda}{\Lambda} \qquad (22)$$

where $\theta_i$ is the incidence angle to the normal of the grating surface and $\theta_q$ is diffracted order angle, $\Lambda$ is grating period and $\lambda$ is photonic wavelength. When $\theta_i$ is set = 0 or incidence angle normal to the grating and $\Lambda < \lambda$, then the diffracted order photon close 90⁰ or becoming surface wave on the surface of the solar cell structure. Because the refractive index of Si solar cell diode higher than the average textured surface, and if the thickness of textured surface $d_{ts} < \lambda/4n_{Si}$ , then it can be concluded that the whole incident photon energy will be absorbed in to solar cell diode device.

Priambodo et al [7] in their paper shows in detail to create and fabricate textured surface for guided mode resonance (GMR) filter by using interferometric pattern method. We can assume the substrate is solar cell diode structure, which is covered by thin film structure hafnium dioxide (HfO₂) and silicon dioxide (SiO₂). The first step is covering the thin film structure on solar cell by photoresist by using spin-coater, then continued by exposing to a large interferometric UV and developed such that result in large area photoresist grating with period < 400 nm as shown in SEM picture of Figure-18, as follows.
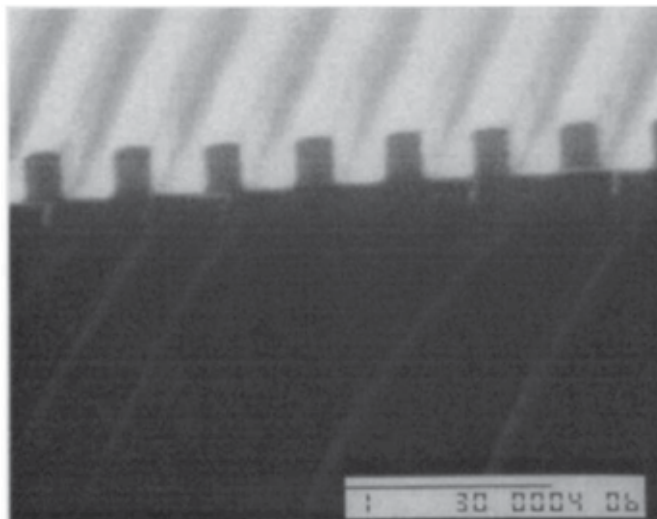


Fig. 18. SEM Picture of grating pattern on large surface with submicron period. This zero order diffracting layer is perfect to be applied for antireflection large area solar cell [7].

Furthermore, on top of the photoresist grating pattern, it is deposited a very thin layer of chromium (Cr) ~ 40-nm by using e-beam evaporator. The next step is removing the photoresist part by using acetone in ultrasonic washer, and left metal Cr grating pattern as a etching mask on top of thin film structure. Moreover, dry etching is conducted to create a large grating pattern on the thin film SiO₂/HfO₂ structure on top of solar cell, by using reactive ion etch (RIE). The whole structure of the solar cell device is shown on Figure-19 below.

However, even though having advantages in improvement of gathering sun-light, but the textured surface has several disadvantages as well, i.e.: (1) more care required in handling; (2) the corrugated surface is more effective to absorb the photon energy in wide spectrum that may some part of it not useful to generate electric energy and causing heat of the solar cell system [2].
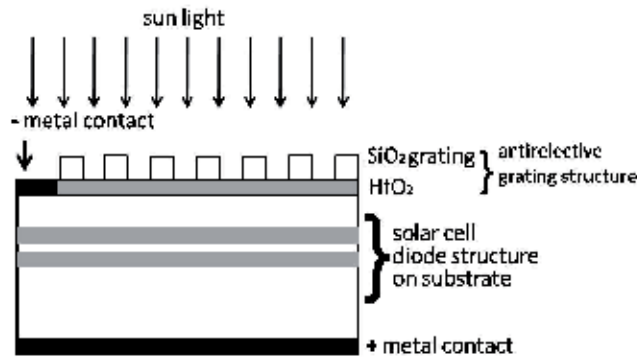
Fig. 19. Solar cell structure incorporating antireflective grating structure.

**Top-contact design**

For solar cell, which is designed to have a large current delivery capacity, the top-contact is a part of solar cell that must be considered. For large current delivery, it is required to have a large top-contact but not blocking the sunlight comes in to the solar cell structure. The design of top-contact must consider that the current transportation is evenly distributed, such that prohibited that a large lateral current flow in top surface. The losses occur in solar cell, mostly due to top-surface lateral current flow and the bad quality of metal contact with semiconductor as well, hence creates a large high internal resistance. For those reasons, the top contact is designed to have a good quality of metal semiconductor contact in the form of wire-mesh with busbars, which are collecting current from the smaller finger-mesh, as shown on Figure-20 [2]. The busbars and the fingers ensure suppressing the lateral current flow on the top surface.
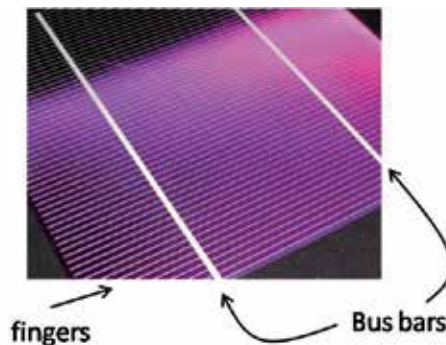


Fig. 20. An Example of top-contact design for solar cells [2].

**Concentrating system engineering**

The solar cell system efficiency without concentrating treatment, in general, is determined by ratio converted electrical energy to the light energy input, which corresponds to total the lumen of sun irradiance per unit area $m^2$. This is a physical efficiency evaluation. In general, the solar cells available in the market have the efficiency value in the range of 12 – 14%. This efficiency value has a direct relationship to the cost efficiency, which is represented in ratio Wattage output to the solar cell area in $m^2$. Device structure and material engineering

discussed in the previous section, are the efforts to improve conversion efficiency in physical meaning. However, the concentrating system engineering we discussed here is an effort to improve the efficiency ratio output wattage to the cost only. In the physics sense, by the concentrating system, the solar cell device efficiency is not experiencing improvement, however in cost efficiency sense, it is improved.

The general method used for concentrating system engineering is the usage of positive (convex) lens to gather the sun irradiance and focus them to the solar cell. By concentrating the input lumen, it is expected there will be an improvement of output electricity. If the lens cost is much lower compared to the solar cell, then it can be concluded that overall it is experiencing improvement in cost efficiency. Another method for concentrating system engineering is the usage of parabolic reflector to focus sun irradiance which is collected by large area of parabolic reflector then focused to the smaller solar cell area. Both examples concentrating system engineering are shown on Figure-21 [2].
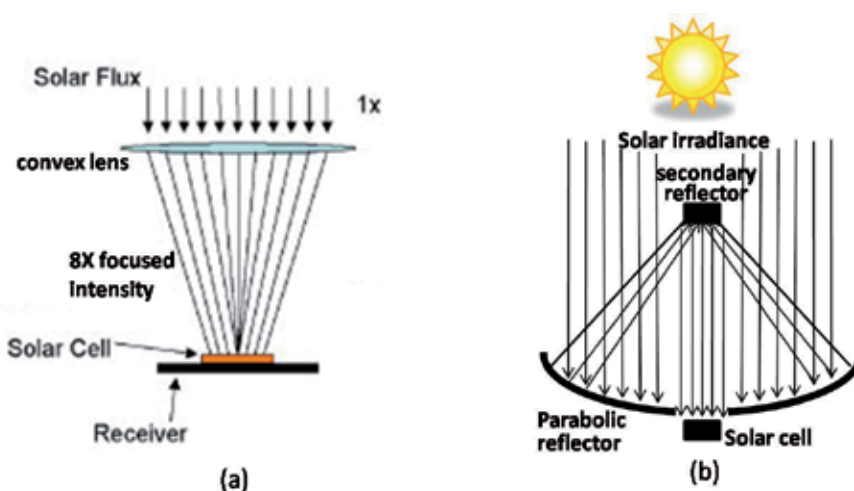


Fig. 21. Two examples of concentrating system engineering concepts with (a) convex lens and (b) parabolic reflector [2].

The technical disadvantages of applying concentrator on solar cell is that the solar cell must be in normal direction to the sun, having larger area and heavier. This means that the system require a control system to point to the sun and finally caused getting more expensive. The cost efficiency should consider thus overall cost.

## 4. Standard solar cell fabrications

Since the first time developed in 1950s, solar cells had been applied for various applications, such as for residential, national energy resources, even for spacecrafts and satellites. To make it systematic, as available in the market today, we classify the solar cell technologies in 3 mainstreams or generations. The first generation is based on Si material, while the second generations are based on material alloys of group IV, III-V and II-VI, as already explained in Section-3. While the third generation is based on organic polymer, in order to reduce the cost, improve Wattage to cost ratio and develop as many as possible solar cell, such as developed by Gratzel et al [10].  In this section, we will discuss the standard fabrication

available for solar cell fabrication for the first and second generations, by using semiconductor materials and the alloys.

**Standard Fab for 1st generation**

Up to now, the market is still dominated by solar cell based on Si material. The reason why market still using Si is because the technology is settled down and Si wafer are abundance available in the market. At the beginning, the solar cells used pure crystalline Si wafers, such that the price was relatively high, because the usage competed with electronics circuit industries. Moreover, there was a trend to use substrate poly crystalline Si with lower price but the consequence of energy conversion efficiency becoming lower. The energy-conversion efficiency of commercial solar cells typically lies in between 12 to 14 % [2].

In this section, we will not discuss how to fabricate silicon substrate, but more emphasizing on how we fabricate solar cell structure on top of the available substrates. There are several mandatory steps that must be conducted prior to fabricate the diode structure.

1.  Cleaning up the substrate in the clean room, to ensure that the wafer free from the dust and all contaminant particles attached on the wafers, conformed with the standard electronic industries, i.e. rinsing detergent (if needed), DI water, alcohol, acetone, TCE dan applying ultrasonic rinsing.
2.  After cleaning step, it is ready to be continued with steps of fabricating diode structure on wafer.

There are several technologies available to be used to fabricate solar cell diode structure on Si wafer. In this discussion, 2 major methods are explained, i.e.: (1) chemical vapor diffusion dan (2) molecular beam epitaxy (MBE).

In Si semiconductor technology, it is common to make p-type Si wafer needs boron dopant to be the dopant acceptor in Si wafer, i.e. the material in group III, which is normally added to the melt in the Czochralski process. Furthermore, in order to make n-type Si wafer needs phosporus dopant to be the dopant donor in Si wafer, i.e. the material in group V. In the solar cell diode structure fabrication process in the 1st generation as shown in Figure-9, it is needed a preparation of p-type Si wafer, in this case a high concentration $p$ or $p^+$. Moreover, we have to deposit 2 thin layers, p and n$^+$ respectively on top of the p+ wafer. In order make the p$^+$pn$^+$ diode structure, we discuss one of the method, which is very robust, i.e. by using chemical vapor diffusion method, such as shown in the following Figure-22 [2].

Instead of depositing layers p and n$^+$ on top of p$^+$ substrate, in this process phophorus dopants are diffused on the top surface of p$^+$ substrate. As already known, phosphorus is a common impurity used. In this common process, a carrier gas (N$_2$) is drifted into the POCl$_3$ liquid creates bubles mixed of POCl$_3$ and N$_2$, then mixed with a small amount of oxygen, the mixed gas passed down into the heated furnace tube with p-type of Si wafers stacked inside. At the temperature about 800$^0$ to 900$^0$ C, the process grows oxide on top of the wafer surface containing phosphorus, then the phosphorus diffuse from the oxide into the p-type wafer. In about 15 to 30 minutes the phosphorus impurities override the boron dopant in the region about the wafer surface, to set a thin-film of heavily doped n-type region as shown in Figure-9. Naturally, phosphorus dopant is assumed to be diffused into p$^+$ type substrate with an exponential function distribution

$$N_d(z) = c_0 e^{-z} \qquad (22)$$

Hypothetically $c_0 = |n^+| + |p^+|$, hence, there will be a natural structure of $p^+pinn^+$ instead of expected $p^+pn^+$. The diffusion depth and c$_0$ are mostly determined by the concentration of

POCl$_3$ and the temperature of furnace. The distribution $N_d(z)$ dapat diatur sehingga the thickness of pin layer between p$^+$ and n$^+$ can be made as thin as possible, such that can be ignored. In the subsequent process, after pulled out the wafers from the furnace, the oxide layer is removed by using HF acid.
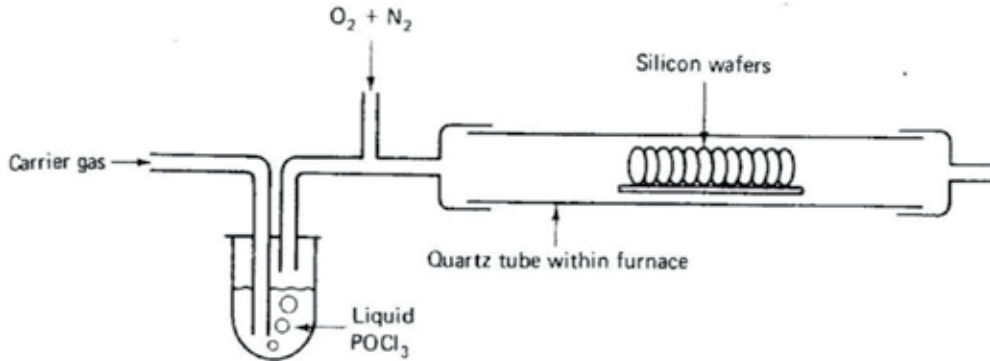


Fig. 22. Chemical (phosphorus) diffusion process [2].

Metal contacts for both top and bottom contacts are applied by using a standard and conventional technology, well known as vacuum metal evaporation. The bottom metal contact of p$^+$ part can be in the form of solid contact; however, the top contact should be in the form of wire-mesh with bus-bars and fingers as explained in previous section. To develop such wire-mesh metal contact for top surface, it is started with depositing photo-resist on the top surface by spin-coating, continued by exposed by UV system, incorporating wire-mesh mask and finally developing the inverse photo-resist wire-mesh pattern. The further step is depositing metal contact layer by using a vacuum metal evaporator, which then continued by cleaning up the photo-resist and unused metal deposition by using acetone in the ultrasonic cleaner. Furthermore, to obtain a high output voltage of solar cell panel, it is required to set a series of several cells.

**Standard Fab for 2$^{nd}$ generation**

The fabrication technology that introduced in the first generation seems to be very simple, however, this technology promises very effective and cost and time efficient for mass or large volume of solar cell production. On the other side, the limited applications such as for spacecrafts and satellites require higher efficiency solar cell, with much higher prices. Every single design should be made as precise and accurate as possible. A high efficient solar cell must be based on single crystalline materials.

For that purposes, it is required an apparatus that can grow crystalline structures. There are several types of technologies the their variances, which are available to grow crystalline structures, i.e. molecular beam epitaxy (MBE) dan chemical vapor deposition (CVD).

Because of limited space of this chapter, CVD is not explained, due to its similarity principles with chemical vapor diffusion process, explained above. Furthermore, MBE is one of several methods to grow crystalline layer structures . It was invented in the late 1960s at Bell Telephone Laboratories by J. R. Arthur and Alfred Y. Cho [8]. For MBE to work, it needs an ultra vacuum chamber condition (super vacuum at 10$^{-7}$ to 10$^{-9}$ Pa), such that it makes possible the material growth epitaxially on crystalline wafer. The disadvantage of this MBE process is the slow growth rate, typically less than 1000-nm/hour.

Due to the limitation space of this Chapter, CVD will not be discussed, since it has similar principal work with chemical vapor difussion process. Furthermore, MBE is one of several methods to grow crystalline layer structures . It was invented in the late 1960s at Bell Telephone Laboratories by J. R. Arthur and Alfred Y. Cho.[1] In order to work, it requires a very high vacuum condition (super vacuum 10^{-7} to 10^{-9} Pa), Such that it is possible to grow material layer in the form of epitaxial crystalline. The disadvantage of MBE process is its very low growth rate, that is typically less than 1000-nm/hour. The following Figure-23 shows the detail of MBE.
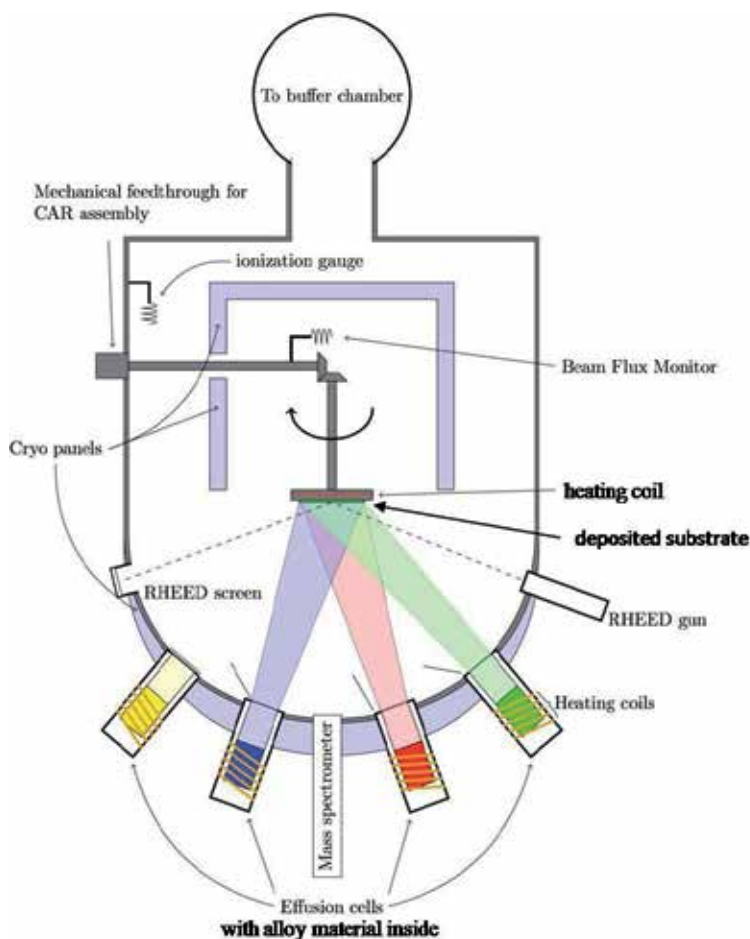


Fig. 23. Molecular beam epitaxy components [8].

In order that the growing thin film layer can be done by epitaxial crystalline, the main requirements to be fulfilled are: (1) Super vacuum, such that it is possible for gaseous alloy material to align their self to form epitaxial crystalline layer. In super vacuum condition, it is possible for heated alloy materials for examples: Al, Ga, As, In, P, Sb and etc can sublimate directly from solid to the gaseous state with relatively lower temperature; (2) Heated alloy materials and the deposited substrate that makes possible the occurrence crystalline condensation form of alloy materials on the substrate; (3) Controlled system temperature,

which makes possible of controlling alloy material and substrate temperatures accurately. Typically, material such as As needs heating up to $250^0$C, Ga is about $600^0$C and other material requires higher temperature. In order to stable the temperature, cooling system like cryogenic system is required; and (4) Shutter system, which is used to halt the deposition process.

For example, alloy material layer such as $Al_xGa_{1-x}As$ growth on GaAs. Controlling the value of x can be conducted by controlling the temperatures of both material alloy sources. The Higher the material temperature means the higher gaseous material concentration in the chamber. More over, the higher material alloy concentration in the chamber, it will cause the higher growth rate of the alloy layer. For that reasons, the data relating to the growth rate of crystalline layer vs temperature, must be tabulated to obtain the accurate and precise device structure.

MBE system is very expensive, because the product output is very low. However, the advantage of using MBE system is accuracy and precision structure, hence resulting in relatively high efficiency and fit to be applied for production of high efficiency solar cells for satellites and spacecrafts.

## 5. Dye Sensitized Solar Cell (DSSC)

### 3rd generation of solar cell

Dye-Sensitized Solar Sel (DSSC) was developed based on the needs of inexpensive solar cells. This type is considered as the third generation of solar cell. DSSC at the first time was developed by Professor Michael Gratzel in 1991. Since then, it has been one of the topical researches conducted very intensive by researchers worldwide. DSSC is considered as first break through in solar cell technology since Si solar cell. A bit difference to the conventional one, DSSC is a photoelectrochemical solar cell, which use electrolyte material as the medium of the charge transport. Beside of electrolyte, DSSC also includes several other parts such nano-crystalline porous $TiO_2$, dye molecules that absorbed in the $TiO_2$ porous layer, and the conductive transparence ITO glass (indium tin oxide) or TCO glass (transparent conductive oxide of $SnO_2$) for both side of DSSC. Basically, there are 4 primary parts to build the DSSC system. The detail of the DSSC components is shown in the following Figure-24 [9-10].

The sun light is coming on the cathode contact side of the DSSC, where TCO is attached with $TiO_2$ porous layer. The porous layer is filled out by the dye light absorbent material. This $TiO_2$ porous layer with the filling dye act as *n*-part of the solar cell diode, where the electrolyte acts as *p*-part of the solar cell diode. On the other side of DSSC, there is a platinum (Pt) or gold (Au) counter-electrode to ensure a good electric contact between electrolytes and the anode. Usually the counter-electrode is covered by catalyst to speed up the redox reaction with the catalyst. The redox pairs that usually used is $I^-/I_3^-$ (iodide/triiodide).

The Dye types can be various. For example we can use Ruthenium complex. However, the price is very high, we can replace it with anthocyanin dye. This material can be obtained from the trees such as blueberry and etc. Different dyes will have different sensitivity to absorb the light, or in term of conventional solar cell, they have different *G* parameter. The peak intensity of the sun light is at yellow wavelength, which is exactly that many dye absorbants have the absorbing sensitivity at the yellow wavelength.
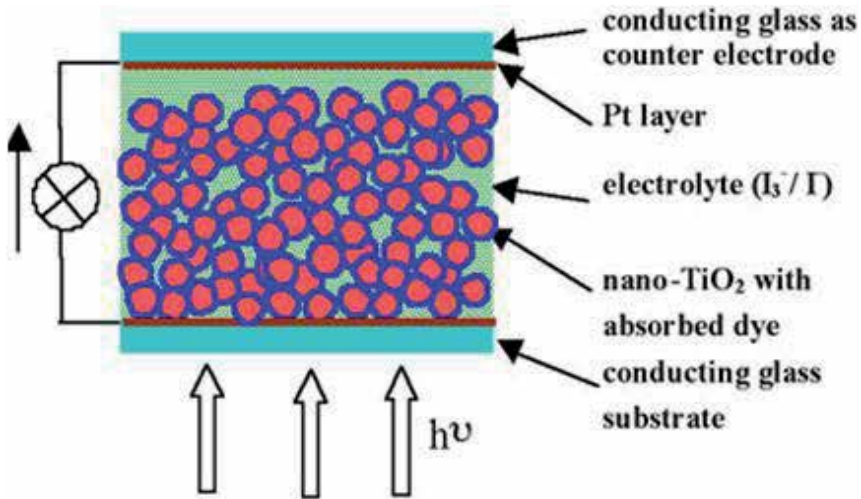
Fig. 24. The schematic diagram of DSSC.

**The principal work of DSSC**

The principle work of DSSC is shown in the following Figure-25. Basically the working principle of DSSC is based on electron excitation of dye material by the photon. The starting process begins with absorption of photon by the dyes, the electron is excited from the groundstate (D) to the excited state (D*). The electron of the excited state then directly injected towards the conduction band (ECB) $TiO_2$, and then goes to the external load, such that the dye molecule becomes more positive (D+). The lower electron energy flow from external circuit goes back to the counter-electrode through the catalyst and the electrolyte then supplies electron back to the dye D+ state to be back to the groundstate (D). The *G* parameter of DSSC depends mainly on the dye material and the thickness of TiO2 layer also the level of porosity of the TiO2 layer.
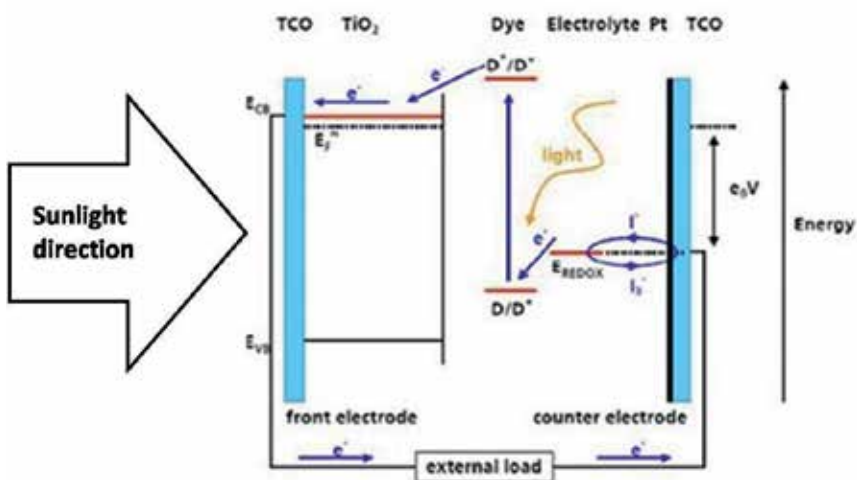


Fig. 25. The principles work of DSSC.

## 6. Summary

The solar cell design has been evolving in many generations. The first generation involved Si material in the form single crystalline, poly-crystalline and amorphous. There is a trade-off in the usage of single crystalline, polycrystalline or amorphous. Using single crystalline can be expected higher efficiency but higher cost than the polycrystalline solar cell. To obtain optimal design, the Chapter also discuss to get the optimal 4 output parameters, $I_{SC}$, $V_{OC}$, FF and η. Moreover, to improve the efficiency, some applying anti-relection coating thin film or corrugated thin film on top of solar cell structure. The second generation emphasize to increase the efficiency by introducing more sophisticated structure such as multi-hetero-junction structure which has a consecuence of increasing the cost. Hence there is a tradeoff in designing solar cell, to increase the conversion efficiency will have a consecuence to lower the cost efficiency or vice verca. Hence, there must be an optimal values for both conversion energy and cost efficiencies.

There is a breaktrough technology that radically changes our dependency to semiconductor in fabricating solar cell, i.e by using organic material. It is called as dye sensitized solar cell (DSSC). This technology, so far still produce lower efficiency. However, this technology is promising to produce solar cell with very low cost and easier to produce.

## 7. References

[1] R.F. Pierret, "Semiconductor Device Fundamentals," Addison-Wesley Publishing Company, ISBN 0-201-54393-1, 1996

[2] M.A. Green, "Solar Cells, Operating Principles, Technology and System Applications," Prentice Hall, ISBN 0-13-82270, 1982

[3] T. Markvart and L. Castaner, "Solar Cells, materials, Manufacture and Operation," Elsevier, ISBN-13: 978-1-85617-457-1, ISBN-10: 1-85617-457-3, 2005

[4] B.E.A. Saleh and M.C. Teich, "Fundamentals of Photonics," Wiley InterScience, ISBN 0-471-83965-5

[5] http://pvcdrom.pveducation.org/CELLOPER/COLPROB.HTM

[6] B.S. Meyerson, "Hi Speed Silicon Germanium Electronics". *Scientific American, March 1994, vol. 270.iii pp. 42-47.*

[7] P.S. Priambodo, T.A. Maldonado and R. Magnusson, " Fabrication and characterization of high quality waveguide-mode resonant optical filters," Applied Physics Letters, Vol. 83 No 16, pp: 3248-3250, 20 Oct 2003

[8] Cho, A. Y.; Arthur, J. R.; Jr (1975). ""Molecular beam epitaxy"". Prog. Solid State Chem. 10: 157–192

[9] J. Poortmans and V. Arkhipov, " Thin film solar cells, fabrications, characterization and applications," John Wiley & Sons, ISBN-13: 078-0-470-09126-5, 2006

[10] M. Grätzel, J. Photochem. Photobiol. C: Photochem. Rev. 4, 145–153 (2003)

[11] Usami, N. ; Takahashi, T. ; Fujiwara, K. ; Ujihara, T. ; Sazaki, G. ; Murakami, Y.; Nakajima, K. "Si/multicrystalline-SiGe heterostructure as a candidate for solar cells with high conversion efficiency", Photovoltaic Specialists Conference, 2002. Conference Record of the Twenty-Ninth IEEE, 19-24 May 2002

[12] Andreev, V.M.; Karlina, L.B.; Kazantsev, A.B.; Khvostikov, V.P.; Rumyantsev, V.D.; Sorokina, S.V.; Shvarts, M.Z.; "Concentrator tandem solar cells based on AlGaAs/GaAs-InP/InGaAs(or GaSb) structures", Photovoltaic Energy Conversion, 1994., Conference Record of the Twenty Fourth. IEEE Photovoltaic Specialists Conference - 1994, 1994 IEEE First World Conference on, 5-9 Dec 1994

# Epitaxial Silicon Solar Cells

Vasiliki Perraki

*Department of Electrical and Computer Engineering, University of Patras,
Greece*

## 1. Introduction

Commercial solar cells are made on crystalline silicon wafers typically 300 μm thick with a cost corresponding to a large fraction of their total cost. The potential to produce good quality layers (of about 50 μm thickness), in order to decrease the cost and improve in the same time the efficiency of cells, has entered to the photovoltaic cell manufacturer priorities. The wafers thickness has been significantly decreased from 400 μm to 200 μm, between 1990 and 2006 while the cell's surface has increased from 100 cm² to 240 cm², and the modules efficiency from 10% to already 13 %, with the highest values above 17% (Photovoltaic Technology Platform; 2007). Advanced technology's solar cells have been fabricated on wafers of 140 μm thicknesses, resulting to efficiencies higher than 20% (Mason.N et al 2006). The cost associated to the substrate of a crystalline silicon solar cell represents about 50-55% on module level and is equally shared between the cost of base material, crystallization and sawing (Peter. K; et al 2008). The cost related to the Si base material can be reduced fabricating thinner cells, while the cost of crystallization and sawing is eliminated by depositing the Si directly on a low cost substrate, like metallurgical grade Si. The epitaxial thin- film solar cells represent an attractive alternative, among the different silicon thin film systems, with a broad thickness range of 1-100μm (Duerinckh. F; et al 2005). Conversion efficiencies of 11.5-12 % have been achieved from epitaxial solar cells grown on Upgraded Metallurgical Grade Silicon (UMG Si) substrates with an active layer of 30 μm, and an efficient BSF (Hoeymissenet. J.V; al 2008). Epitaxial cells with the same active layers deposited on highly doped multi-crystalline Si substrates by Chemical Vapor Deposition and the front and back surfaces prepared by phosphorous diffusion as well as screen printing technique, have confirmed also efficiencies 12.3% (Nieuwenhuysen. K.V; 2006). Solar cells developed by a specific process for low cost substrates of UMG silicon   have led to efficiencies of 12.8% (Sanchez-Friera. P; et al 2006). Better results have been achieved from cells with an emitter epitaxially grown by CVD, onto a base epitaxialy grown (Nieuwenhuysen. K.V; et al 2008). The emitter creates a front surface field which leads to high open-circuit voltages (Voc) resulting to cell efficiencies close to 15% by optimizing the doping profile and thickness of epitaxial layers and by including a light trapping mechanism.

This chapter first describes the manufacturing procedures of epitaxial silicon solar cells, starting from the construction of the base layer until the development of solar cells.

Then a one- dimensional (1D) (Perraki.V; 2010) and a three dimensional (3D) computer program (Kotsovos. K & Perraki.V; 2005), are presented, for the study of the n⁺pp⁺ type

epitaxial solar cells. These cells have been built on impure (low cost) polycrystalline p$^+$ silicon substrates (Upgraded metallurgical grade UMG-Si), by a special step of thin pure Si deposition followed by conventional techniques to build a n$^+$/p junction, contacts and antireflective coating (ARC). The software developed expresses the variations of photovoltaic parameters as a function of epilayer thickness and calculates for different values of structure parameters, the optimised cell's photovoltaic properties.

According to the one dimensional (1D) model, the photocurrent density and efficiency are calculated as a function of epilayer thickness in cases of low and high recombination velocity values, as well as in cases of different doping concentration values (Perraki.V; 2010), and their optimum values are figured.

The parameter chosen for the cell's optimisation is the epitaxial layer thickness, through variation of grain size and grain boundary recombination velocity, according to the three dimensional (3D) model (Kotsovos. K, & Perraki. V, 2005). Furthermore, a comparison among simulated 3D, 1D and corresponding experimental spectral response results under AM 1.5 illuminations, is presented.

## 2. Epitaxial silicon solar cell fabrication

The manufacturing sequence for epitaxial silicon (Si) solar cell can be divided in the following main steps: base/active layer formation, junction formation, antireflective coating (ARC) and metallization (front and back contacts), including the oxidation technology, and auxiliary technologies. A complete flow diagram for the realisation of n$^+$pp$^+$ type epitaxial solar cells is presented in Table 1.

MG-Si → UMG-Si→ HEM process p$^+$ type Si → CVD epitaxy→pp$^+$→ Junction formation $\rightarrow$
  n$^+$pp$^+$ type solar cell ←Back contact formation ←Front grid structuring ←ARC← n$^+$pp$^+$

Table 1. Epitaxial solar cell's process

### 2.1 Base layer

The active layer of n$^+$pp$^+$ type crystalline Si solar cells is a thick layer doped with boron and is thus p-type layer with concentration of $10^{17}$ cm$^{-3}$. The crystalline silicon photovoltaic technology has focused on reducing the specific consumption of the base material and increasing the efficiency of cells and modules and in the same time on using new and integrated concepts. Many research groups have tried to use very thin bases in silicon solar cells, aiming to decrease their cost. One of the possible ways for the achievement of cheap crystalline silicon solar cells on an industrial basis is the "metallurgical route". The different steps of this route are:

*Metallurgical grade* (MG), silicon powder (raw material) is upgraded by water washing, acid etching and melting, resulting to a material with insignificant properties and a measured value of diffusion length, L$_n$, smaller than 5 μm.

*The Upgraded Metallurgical Grade* (UMG), silicon is further purified and recrystallized into ingots by the Heat Exchange Method (HEM) so that to give crack-free ingots associated with large metal impurity segregation and cm size crystals, with better but still insignificant properties. This is due to the fact that the HEM technology allows removing metallic impurities, but the high concentration of boron, phosphorus and the presence of Si carbide precipitates are responsible for again very low measured values of L$_n$, and solar cell

efficiencies. In order to overcome the problem this material is used as a cheap $p^+$ -type substrate, on which a thin p-type epitaxial layer is formatted.

*Epitaxial layer* from pure Si is deposited, by chemical vapor deposition (CVD) on these impure UMG polycrystalline substrates, in an epitaxial reactor (Caymax.M, et al 1986). The wafers are first acid etched and cleaned at 1150 $^0$C, then coated with silicon under $SiH_2Cl_2$ flow in $H_2$ gas at 1120 $^0$C with a growth rate 1μm. min$^{-1}$ (table 2). $B_2H_6$ is used, so that to get p- type layers. When the process has been completed a control is carried out testing the quality, thickness and dopant concentration. On to this layer the $n^+/p$ junction is then built and epitaxial solar cells are realized, using a low cost screen printing technology.

<div align="center">

Remove saw damage by etching

Wafer cleaning

HCl etching in epitaxial reactor

Deposition of the epitaxial layer

</div>

Table 2. Flow diagram of the CVD epitaxial process

The technology of Liquid Phase Epitaxy (LPE) has recently applied on metallurgical grade Si with interesting results as well (Peter.K et al 2002).

## 2.2 Junction formation

Two different approaches exist for the manufacture of the $n^+$-p junction: the ion implantation and the diffusion from the solid phase or from the vapor phase (Overstraeten. R. J. V & Mertens. R, 1986).

a.  The ion implantation is characterized by excellent control of the impurity profile, low temperature processing, higher conversion efficiencies, and is rather used in the manufacture of spatial solar cells, due to the high costs associated with it.

b.  The diffusion process, from both gaseous and liquid phase, is usually applied for silicon solar cell fabrication. $N_2$, Ar and $O_2$ are used as carrier gases, with quantities and mixing proportions as well as temperature, time and dopant concentration on the surface under, a very accurate control.

*Diffusion from the vapor phase* consists of diffusion of phosphorus from the oxide formed onto the silicon surface when $N_2$ carrier gas and $POCl_3$ are used in a heated open-tube furnace process at 800-900 $^0$C. Disadvantages of the method are that, diffusion appears on both sides resulting to a back parasitic junction which has to be removed and non uniformity in cases of very shallow junctions.

*Diffusion from  a solid phase* consists of deposition of a dopant layer at ambient temperature followed by a heat treatment, in an electrically heated tube furnace with a quartz tube, at a temperature ranging from 800 to 900 $^0$C. This process can be performed using chemical vapor deposition (CVD), screen printing technique, spin-on or spray-on, forming thus only a junction on the front surface.

i.  The CVD technique concerns the deposition, at low temperature, of a uniform phosphorus oxide on the wafer's front surface. This technique uses, highly pure, expensive, gases ensuring a uniform profile and defined surface conditions.

ii.  Screen printing is involved to thick film technologies which are characterized by low cost production, automation and reliability. In a first step, a paste rich in phosphorus is screen printed onto the silicon substrate. Then, phosphorus is diffused throughout a heat treatment in an open furnace, under typical peak temperatures between 900 and 950 $^0$C, to form the n-p junction.

iii.  Spin-on and spray-on of doped layers yield to high throughput but non uniform surfaces.

### 2.2.1 Diffusion theory

As the diffusion procedure, is usually applied for silicon solar cell fabrication, it is necessary to refer in brief the theory of diffusion, of various solid elements in the Si solid. This process obeys to Fick's second law, which is expressed in one dimension by the following partial differential equation (Carslaw. H.S; and Jaeger .J.C 1959), (Goetzberger.A, et al 1998).

$$\frac{\partial N(\chi, t)}{\partial t} = D \frac{\partial^2 N(\chi, t)}{\partial \chi^2} \tag{1}$$

Where N ($\chi$, t) stands for the concentration of the diffusing elements at point $\chi$ and time t and D the diffusion coefficient, characteristic of each material. This coefficient strongly depends on temperature according to the following relation (Sze. S. M. 1981).

$$D = D_0 \exp(-\Delta E / kT) \tag{2}$$

$D_0$ and $\Delta E$ (activation energy) are constant for a given element over wide temperature and concentration ranges.

The temperature plays a very important role in the diffusion process due to the temperature exponential dependency of diffusion coefficient. The diffusion coefficients in relation to temperature show that metals like Ti, Ag, Au, have higher diffusion coefficients D by several orders of magnitude compared to dopants As, P, B, and consequently they diffuse faster in Si, while elements such us Cu, Fe diffuse even more quickly. Therefore solar cell technology requires excellent cleanness of laboratory and experimental devices. However diffusion time does not affect so much the depth of penetration as this is proportional to its root square.

Two solutions to the partial differential equation 1 are considered. In the first case the dopant source is inexhaustible, the surface doping concentration $N_s$ is considered constant during the diffusion process and the bulk concentration depends on diffusion time and diffusion temperature. The mathematical solution under boundary conditions concerning the parameters $N_s$, t, $N_x$, and $\chi$ reads:

$$N(\chi, t) = N_S erfc \frac{\chi}{2\sqrt{Dt}} \tag{3}$$

Where, erfc stands for the complementary error function distribution.

In order to calculate the depth $\chi_j$ of the n-p junction, it is necessary to express the ratio of bulk concentration in the base silicon to surface concentration (N $_{\chi t}$ /N$_S$) as a function of $\chi / \sqrt{Dt}$ and choose diffusion constant, temperature, and time.

In the second case, during the diffusion process there is an exhaustible dopant source on the surface with a concentration Q (cm$^{-2}$). The solution of the differential equation 1 N($\chi$,t) (Gaussian distribution) at point $\chi$ and time t is given by Eq 4:

$$N(\chi,t) = \frac{Q}{\sqrt{\pi Dt}} \exp -(\frac{\chi}{2\sqrt{Dt}})^2 \qquad (4)$$

The surface concentration in this case is expressed as a function of the diffusion parameters by Eq 5:

$$N_S = \frac{Q}{\sqrt{\pi Dt}} \qquad (5)$$

The penetration depth $\chi_j$ of the n-p junction is again calculated by the ratio of the concentration in the base silicon to surface concentration (N$_{\chi t}$ /N$_S$) when diffusion constant, temperature and time are also determined.

## 2.2.2 Emitter's diffusion procedure

The silicon base wafers are etched, to remove damage from the wafering process (or to prepare after the CVD process) and cleaned, in order to introduce dopant impurities into the base in a controlled manner and form the n-p junction.

Since the starting wafers for solar cells are p-type, phosphorus is the n- type impurity generally used. The n$^+$-doped emitter of the cell is thus created by the diffusion of phosphorus, in high concentration which is introduced in the form of phosphine (PH) or gaseous oxychloride (POCL3) into the diffusion furnace. The later is introduced using nitrogen N$_2$, as a carrier gas. The disadvantages of this method are the formation of a back parasitic junction as the diffusion occurs on both sides and a non uniformity for very shallow junctions.

At the high temperatures of approximately 800 $^0$C the dopant gases react with the surface of the silicon when oxygen is added, in accordance with the chemical reaction

$$Si + O_2 \rightarrow SiO_2$$
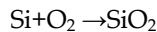
Silicon dioxide (SiO$_2$) is produced on the surface and secondly, phosphine is converted to phosphorus pentoxide (P$_2$O$_5$) according to the following chemical reaction

$$2PH + 3O_2 \rightarrow P_2O_5 + H_2O$$
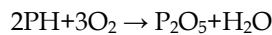
The P$_2$O$_5$ created combines with the SiO$_2$ which is grown on the silicon surface to form liquid phosphorus silicate glass which becomes the diffusion source.

Phosphorus diffusion (at temperatures of 950 $^0$C) as a function of diffusion time shows deviating behaviour from the theory for the case of low penetration depth. This behaviour has been explained by several authors; however it has the disadvantage for solar cells that a dead layer is created, of about 0.3 µm thickness, which reduces efficiency to approximately 10%. According to an advanced process, a dead layer can be impeded using a double diffusion process (Blacker. A. W, et al 1989). The first diffusion step consists of a predisposition coat with a low level diffusion of phosphorus at a temperature of approximately 800 $^0$C. Then the phosphorus silicate glass layer is removed by chemical means and in a second diffusion step, this time at a temperature 1000-1100 $^0$C, the desired

penetration depth of phosphorus is achieved. Surface concentrations of approximately $10^{19}$ cm$^{-3}$ can be obtained.

### 2.2.3 Screen printing for junction formation

A process line based on the use of thick film technology offers advantages of low cost, automation, and reliability. The technology involves the screen printing technique for the junction formation. According to this a phosphorus-doped paste, containing active material, solvents and a thickener is printed through screens, onto a silicon substrate (Overstraeten. R. J 1986). After printing, the substrate is dried at 150 $^0$C allowing thus the solvents to evaporate. The phosphorus diffuses from the printed layer into the silicon during a heat treatment in a belt furnace in nitrogen under typical peak temperatures between 900 and 950 $^0$C. When screen printing is used for junction formation there is no parasitic junction formed at the back as in the case for open tube diffusion. However the layer that remains on the front of the cell after diffusion and the edges of the substrate which are doped due to contamination, have to be removed by etching in a proper chemical solution followed by a cleaning step.

Apart from the junction formation screen printing process can also be applied to the antireflection coating formation and the metallization (front and back contacts).

Epitaxialy growth by CVD may also be used for the n$^+$ doped emitter formation, controlling the doping profile, on an epitaxially grown base. In this way a front surface field (FSF) is created yielding to a high open circuit voltage (Voc) and high efficiency (Nieuwenhuysen. K.V; et al 2008).

### 2.3 Antireflection processes

### 2.3.1 Antireflection Coating (ARC)

Silicon surfaces reflect more than 33% of sunlight depending upon wavelength. For the manufacture of antireflection coatings industrial inks which contain titanium dioxide ($TiO_2$) or tantanium pentoxide ($Ta_2O_5$) as the active coating material, are used.

Two technologies are applied for this purpose:

a. High vacuum evaporation technologies use almost exclusively $TiO_2$, with a refraction index n adjusted between 1.9 and 2.3, a good transparency which favors high efficiencies and high costs.

b. Thick film technologies, which are used in mass production due to their lower cost. At thick film technologies, a paste containing $TiO_2$ compounds is deposited onto the surface of silicon, either by the screen printing technique at temperatures of 600 to 800 $^0$C or by the spinning on technique.

The antireflective coating and the front side grid formation can be combined and made together by screen printing technique. In this case the $TiO_2$ paste is firstly dried at temperatures around 200 $^0$C, then a silver paste is added to it for the grid formation, and both are simultaneously sintered.

A further improvement can reduce total reflection to 3 – 4%. This can be achieved by using two antireflection layers, with a refractive index decreasing from the upper AR layer to the lower.

### 2.3.2 Textured surfaces

The textured surfaces of cells allow most of the light to be absorbed in the cell, after multiple reflections. For the construction of textured silicon surfaces the physical-chemical effect is

used, that the etching rate of silicon in an alkaline solution depends on the crystallographic orientation of silicon's front surface (Price J.B., 1983). The crystal orientation yielding to high efficiency solar cells is <100>.

The anisotropic etching process takes place in weak solutions of KOH or NaOH with a concentration of 10% up to 30% at approximately 70 $^0$C. This configuration results to inverted pyramid structures, under well determined conditions and reduces the reflection of sunlight to approximately 10 % (Goetzberger.A, et al 1998).

An additional ARC allows a further reduction to approximately 3%. In practice the best success has been achieved with inverted pyramids.

## 2.4 Contacts
### 2.4.1 The structuring of the finger grid
The technologies used for the structuring of the finger grid are three:

a.  The vacuum evaporation, which has the disadvantage that the smallest finger width is approximately 100 µm or at best 50 µm,
b.  The photoresist technique which is used if narrower contact fingers are required in order to reduce shadowing.
c.  The screen printing technique, which uses metal pastes, and dominates in a wide range of production techniques as it is particularly cost effective, with the maximum finger width about 100 µm.

This technique is widespread in industrial solar cell manufacturing and has automating processes (Overstraeten. R.J.V; 1986). The screen printing process uses metal pastes containing in addition to 70% Ag approximately 2% sintered glass. After depositing, the layer is sintered at temperatures of about 600 $^0$C, while the sintered glass components melt and dissolve a small layer of silicon. At the same time this melt is enriched by silver. Upon cooling a recrystallized Si layer is created as with normal alloying, which contains a high proportion of Ag and thus creates a good ohmic contact. This process gives quite low contact resistances on the $n^+$ emitter at surface concentrations of approximately $10^{20}$ cm$^{-3}$.

### 2.4.2 Back surface contacts
The realizations of back surface contacts need only aluminum, in the form of paste. This element has the advantage that forms alloys at its eutectic point 577 $^0$C, and has a good solubility with concentrations of about $10^{19}$ cm$^{-3}$ in Si, while a silver palladium paste is often sintered onto this layer in different cases (Overstraeten. R. J. V, & Mertens. R, 1986). Thus a high doping $p^+$ type is achieved in the recrystallised layer providing a Back Surface Field.

Normally sintering takes place at temperatures around 800 $^0$C with the best results. A significant increase in $V_{oc}$ is observed yielding thus higher values of solar cell efficiency.

## 2.5 Oxidation technologies
The oxidation technology is applied for the manufacture of a $SiO_2$ layer in solar cells. It is a relatively simple manufacturing process using high temperature treatment in an electrically heated tube furnace with a quartz tube under oxygen. This layer, nevertheless, plays a crucial role in silicon solar cells, with main characteristics passivation and masking effects of $SiO_2$ regarding impurities, which contributes positively to making silicon the basic material for most semiconductor devices.

*Dry oxidation* is achieved when silicon is heated without the addition of water vapour, and takes place according to the chemical reaction

$$Si + O_2 \rightarrow SiO_2$$
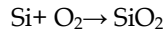
As it is known, oxygen diffuses through the $SiO_2$ layer which is formed, there is no saturation thickness and the layer thickness grows in proportion to time or in proportion to the square root of time at greater layer thickness than 1 μm.

*Wet oxidation*, is achieved when silicon is exposed to water vapor, during the oxidation process and obeys to the following chemical reaction

$$2Si + O_2 + 2H_2O \rightarrow 2SiO_2 + 2H_2$$
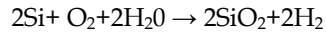
Due to the hydrogen presence in case of wet oxidation the rate of growth is significantly higher than that of dry oxidation (Wolf H. F., 1976). Other influences that also alter the growth rate of $SiO_2$ are the doping concentration of silicon, the orientation of Si surfaces and the addition of chlorine ions during the oxidation process.

The use of $SiO_2$ as a passivating layer in solar cells has shown that dry oxidation under high oxidation temperatures yields very low surface recombination rates, which can be reduced even further by an annealing process at about $450^0$ C, and depends upon the crystallographic orientation of silicon surfaces.

The masking effect of a $SiO_2$ layer in the diffusion process relies upon the fact that the diffusion rate of many diffusants in silicon dioxide is lower by orders of magnitude than in silicon itself. The required $SiO_2$ layer thickness, for different diffusion temperatures and times, shows that boron is masked by significantly thinner $SiO_2$ layers than is phosphorus. Furthermore, $SiO_2$ is used for masking in alkaline etching processes as well as for surface texturing (Goetzberger.A, et al 1998).

## 2.6 Back Surface Field (BSF)

The required $p^+$ doping in the starting wafer, in order to create a Back Surface Field, (BSF), is achieved by diffusion of boron. $BBr_3$ serves as the boron source for this purpose, which can be handled in a very similar manner to $POCl_3$. As it is known, a BSF is necessary for high efficiency solar cells.

In industrial practice, aluminium with a eutectic point 577 $^0$C, is introduced onto the surface for the creation of a BSF. This is processed by vacuum evaporation or by screen printing technique at approximately 800 $^0$C.

## 2.7 Auxiliary technologies

Auxiliary processes such as etching and cleaning are necessary for the manufacture of solar cells.

Etching and cleaning techniques are used in order to make the surfaces of silicon wafers free of contaminants like molecular (residues of the lapping, polishing etc), ionic (from the etching solutions), or atomic (heavy metals). The most widely used procedure for surface cleaning is currently the RCA cleaning (named after the company RCA). This process is based upon the use of hydrogen peroxide ($H_2O_2$) firstly as an addition to a weak solution of ammonium hydroxide ($NH_4OH$) and secondly hydrochloric acid (HCl).

Etching of silicon dioxide layers occurs mainly in a weak solution of hydrofluoric acid, or in combination with ammonium fluoride ($NH_4F$).

Isotropic etching of silicon occurs in a solution of nitric acid and hydrofluoric acid or in combination with acetic acid and phosphoric acid ($H_3PO_4$).

Rinsing with deionised water must take place as the final stage, following all cleaning processes. With this processes, specific resistance values near to the theoretical value are achieved.

## 3. Mathematical model

A one dimensional (1D) analytical model is assessed via a simulation program which takes into account the interaction and the limitations between several parameters. By modeling short circuit current density $J_{sc}$, open circuit voltage $V_{oc}$ and efficiency η, cells of different structure characteristics are studied. The photocurrent density and efficiency are estimated as a function of epilayer thickness d2, for various values of recombination velocity and doping concentration (Perraki V, 2010). Furthermore, the simulated and experimental plots of quantum efficiency are compared, under $1000W/m^2$ irradiation.

A three dimensional (3D) analytical model, which is based on the Green's Function method, is also implemented at the same cells. The model is applied via a simulation program to optimize the efficiency of cells. The parameter chosen for optimization is the epitaxial layer thickness via variation of grain size and grain boundary recombination velocity (Kotsovos K, & Perraki V., 2005). In addition, 3D spectral response data are compared with the 1D results.

### 3.1 One dimensional model

The epitaxial $n^+pp^+$ type Si solar cell is divided in four main regions (front layer $n^+$, Space Charge Region (SCR), epilayer, and substrate), with thickness $d_1-w_n$, $w_n+w_p$, $d_2-w_p$ and $d_3$, respectively, figure 1.
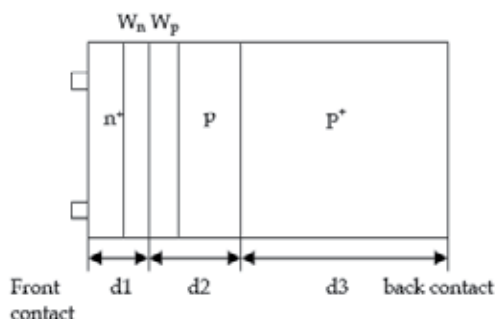


Fig. 1. The cross section for the theoretical model of $n^+pp^+$ type epitaxial solar cell.

There are a number of main assumptions used for modeling which concern, the homogeneity of physical and electrical properties of the grains (doping concentration, minority carrier mobility, life time and diffusion length). The grains are columnar, in Si materials recrystallized by the Heat Exchange Method, becoming increasingly large when considering successively, bottom, middle and top wafers in the ingot. These columnar grains are perpendicular to the front and to the $n^+/p$ junction.

The front surface recombination velocity $S_F$ has a value of $10^4$ cm/s and the back surface $S_B$ $10^{15}$ cm/s. A perfect abrupt interface between the heavily doped substrate with thickness higher

compared to its diffusion length and the lowly doped epilayer, consists a low/high junction $p/p^+$. This junction produces a strong BSF while the $p^+$ layer does not contribute to the total photocurrent (Luque. A, & Hegeduw. S., 2003).

The expression, for the effective recombination velocity, $S_{eff}$, at the epilayer/substrate interface describing the quality of the back surface of the base, is given by the following equation (Godlewski. M; et al 1973):

$$S_{eff} = \frac{N_A D_{n^+}}{N_{A^+} L_{n^+}} \frac{(\frac{S_B L_{n^+}}{D_{n^+}} \cosh\frac{d_3}{L_{n^+}} + \sinh\frac{d_3}{L_{n^+}})}{(\cosh\frac{d_3}{L_{n^+}} + \frac{S_B L_{n^+}}{D_{n^+}} \sinh\frac{d_3}{L_{n^+}})} \tag{6}$$

Where, the terms $N_A$, $N_{A^+}$, $L_n$, $L_{n^+}$, $D_n$, $D_{n^+}$ stand for the material's doping concentration, electron diffusion length and diffusion constant in the epilayer and the substrate respectively and $S_B$ for the recombination velocity at the back surface. Due to the low/ high junction the following simplified relation (Arora. J, et al 1981) gives the expression for $S_{eff}$.

$$S_{eff} = \frac{N_A D_{n^+}}{N_{A^+} L_{n^+}} \tag{7}$$

The terms $N_A$, $N_{A+}$, $D_{n+}$ and $L_{n+}$ are assumed constant all over of these regions' bulk.

The analytical form of the quantum efficiency of the front layer $Q_p$, is described by the following relation (Hovel H J 1975), (Sze. S. M, 1981):

$$Q_P = [1-R]\frac{\alpha_n L_P}{(\alpha_n L_P)^2 - 1} x[\frac{-(\frac{S_F L_P}{D_P} + \alpha_n L_P) + [\frac{S_F L_P}{D_P}\cosh\frac{d_1 - w_n}{L_P} + \sinh\frac{d_1 - w_n}{L_P}]\exp(-\alpha_n d_1 - a_n w_n)}{\frac{S_F L_P}{D_P}\sinh\frac{d_1 - w_n}{L_P} + \cosh\frac{d_1 - w_n}{L_P}}$$

$$+\alpha_n L_p \exp(-\alpha_n d_1 - \alpha_n w_n)] \tag{8}$$

Where $L_p$, $D_p$ and $\alpha_n$ stand for hole diffusion length, diffusion coefficient and absorption coefficient in the front layer and R and $S_F$ stand for reflection coefficient and front surface recombination velocity, respectively.

The base region quantum yield $Q_n$, can be calculated from the following relation

$$Q_n = [1-R]\frac{\alpha_P L_n}{(\alpha_P L_n)^2 - 1}\exp(-(\alpha_n d_1 + \alpha_p W_p))$$

$$[\alpha_P L_n - \frac{\sinh\frac{d_2 - w_p}{L_n} + \frac{S_{eff} L_n}{D_n}\cosh\frac{d_2 - w_p}{L_n} + (\alpha_P L_n - \frac{S_{eff} L_n}{D_n})\exp-\alpha_p(d_2 - w_p)}{\frac{S_{eff} L_n}{D_n}\sinh\frac{d_2 - w_p}{L_n} + \cosh\frac{d_2 - w_p}{L_n}}] \tag{9}$$

$\alpha_p$ stands for the absorption coefficient in the base layer p.

The contribution of the space charge region $Q_{SCR}$ is expressed by the following relation (Sze .S.M 1981)

$$Q_{SCR}=[1-R][exp-(a_nW_n+a_pW_p)-1]exp-a_n(d_1-W_n) \tag{10}$$

The contribution of the three regions of the solar cell is:

$$Q_{tot}=Q_p+Q_n+Q_{SCR} \tag{11}$$

The total photocurrent density $J_{sc}$ arising from the minority carriers generated very near the junction in the n- layer, in the epilayer and in the space charge region can be calculated from the Eq. 12 as a function of the cell's quantum efficiency.

$$J_{SC} = q \int_{0.4}^{1.1} Q_{tot}(\lambda)N(\lambda)d\lambda \tag{12}$$

The flux of photons as a function of wavelength, N ($\lambda$), was defined by a discretized AM1.5 solar spectrum.

The open circuit voltage depends on the Boltzmann constant, k, the solar cell operating temperate, T, the elementary electron charge, q, and the logarithm of the ratio between the photocurrent and dark current density, $J_{sc}$ /$J_0$.

$$V_{OC} = \frac{kT}{q}\ln(\frac{J_{SC}}{J_0}+1) \tag{13}$$

Moreover, efficiency η (%) which is the most important parameter in the evaluation process of photovoltaic cells, is proportional to the open-circuit voltage $V_{oc}$, the photocurrent density $J_{sc}$, fill factor FF, and inversely proportional to the incident power of sunlight.

## 3.2 Three dimensional model (3D)

Several assessments have been admitted in order to simplify the 3D model and obtain the excess minority carrier density from the solution of the three-dimensional diffusion equation in each region.

The p/$p^+$ junction is considered as a low/high junction, incorporating a strong BSF. It is assumed that the $p^+$ region's contribution to the total photocurrent is negligible (Dugas.J, & Qualid. J, 1985).

The heat exchange method provides polycrystalline silicon with columnar grains, as shown in figure 2. The grain boundaries are surfaces of very small width compared to the grain size, characterized by a distribution of interface states. They are perpendicular to the $n^+$/p junction, becoming increasingly large when considering successively, bottom, middle and top wafers in the ingot. Their physical and electrical properties, concerning the doping concentration, the mobility and diffusion length of minority carriers, along the three dimensions are homogeneous, for each region. There are ignored effects of other imperfections of the crystal structure.

The front and back surface recombination velocity $S_F$ and $S_B$ are the same as in (Luque. A, & Hegeduw. S., 2003), and their values are assumed as $10^4$ cm/sec and $10^{15}$ cm/sec respectively. The effective grain boundary recombination velocity is assumed constant all over the surface of the grain and has been estimated to vary from $10^2$ to $10^6$ cm/sec. It
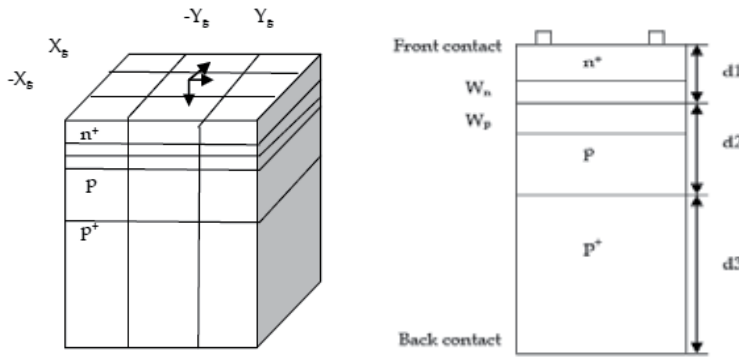
Fig. 2. Ideal crystal orientation and cross section for the theoretical model of n⁺pp⁺ type epitaxial solar cell (with columnar grains).

depends basically on the interface state density at the grain boundary and the doping concentration of the semiconductor material (Card. H.C, & Yang. E.,1977).

The solution of the three-dimensional diffusion equation provides the excess minority carrier density.

The steady state continuity equation for the top side of the junction under illumination is expressed by the following relation (Sze. S. M, 1981):

$$\nabla^2(p_n - p_{n0}) - \frac{p_n - p_{n0}}{L_p^2} = -\frac{\alpha(\lambda)F(\lambda)\exp(-\alpha(\lambda)z)}{D_p} \tag{14}$$

Where, $p_n$-$p_{n0}$ , $L_p$ and $D_p$ stand for the excess minority carrier density in the front layer, the minority carrier diffusion length and the diffusion coefficient respectively. The material absorption coefficient $\alpha(\lambda)$ is given by Runyan (Runyan. W. R, (1976)) and the light generation rate F (number of photons of wavelength $\lambda$ inserting the front side per unit area and unit time) is given by the following relation

$$F(\lambda)=N(0,\lambda)(1-R(\lambda)) \tag{15}$$

With $N(0,\lambda)$ representing the number of photons of wavelength $\lambda$ incident on the surface per unit area and unit time (depth x=0) and $R(\lambda)$ the reflection coefficient of light at the front side. This coefficient is calculated, for an antireflective coating of single layer (TiO₂) with optimal thickness 77 nm, (Heavens. O. S, 1991). There is a metal coverage coefficient of 13.1%, corresponding to the front metal grid and cell series resistance ($R_s$) of about 1.7 Ω.

The boundary conditions which accompany Eq. 14 when the solar cell is short circuited involve the front surface recombination velocity $S_F$ and the grain boundary recombination velocity in the front region $S_{pg}$.

The diffusion equation for the base region is expressed by a similar form like in the front layer:

$$\nabla^2(n_p - n_{p0}) - \frac{n_p - n_{p0}}{L_n^2} = -\frac{\alpha(\lambda)F(\lambda)\exp(-\alpha(\lambda)z)}{D_n} \tag{16}$$

Where, $n_p$-$n_{p0}$ expresses the excess of electron concentration, $L_n$ the corresponding diffusion length and $D_n$ electron diffusion coefficient. The previous equation is subjected also to

specific boundary conditions when the device is operated under short circuit, concerning the grain boundary recombination velocity in the active layer $S_{ng}$ and the effective back surface recombination velocity $S_{eff}$ at the low / high junction. The simplified relation gives the expression for effective electron recombination velocity $S_{eff}$, as a function of the material's doping concentration of the active layer and the substrate ($N_A$, $N_A^+$), assumed constant all over of these regions' bulk (Eq.7). Moreover the grain boundary recombination velocity in the front and the active layer is considered the same and symbolized as $S_{gb}$.

The solution of the continuity equations (14) and (16) is obtained in analytical form using the Green's function method. This procedure is briefly described in (kotsovos. K & Perraki. V; 2005). The analytical expression of the front layer photocurrent density $J_p$ is derived, by differentiating the hole density distribution in the junction edge region $z=d_1-w_n$ presented in the form of infinite series (Halder. N.C, & Williams. T. R., 1983):

$$J_p(x,y,\lambda) = 4q\alpha F \times$$

$$\sum_{m,n}^{\infty} \frac{L_{peff} M_x^2 N_y^2 \sin(mX_g)\sin(nY_g)}{mn(\alpha^2 L_{peff}^2 - 1)} \cos(mx)\cos(ny)$$

$$\times [\frac{N_p + \alpha L_{peff} - \exp(-\alpha(d_1-w_n))\{N_p \cosh(\frac{d_1-w_n}{L_{peff}}) + \sinh(\frac{d_1-w_n}{L_{peff}})\}}{N_p \sinh(\frac{d_1-w_n}{L_{peff}}) + \cosh(\frac{d_1-w_n}{L_{peff}})} - \alpha L_{peff}\exp(-\alpha(d_1-w_n))] \quad (17)$$

where the variables $x$ and $y$ represent arbitrary points inside the grain and $M_x$, $N_y$, $L_{peff}$, $N_p$ are expressed by proper equations as functions of $S_{pg}$, $D_p$, $X_g$, $Y_g$, $L_p$, and $S_F$.

In a similar way the analytical expression of the base region photocurrent density $J_n$ is given, in the form of infinite series, by differentiating the electron density distribution in the junction edge region $z=d_2-w_p$ by the relation

$$J_n = 4q\alpha F e^{-\alpha(d_1+w_p)} \times$$

$$\sum_{k,l}^{\infty} \frac{L_{neff} K_x^2 L_y^2 \sin(kX_g)\sin(lY_g)}{kl(\alpha^2 L_{neff}^2 - 1)} \cos(kx)\cos(ly)$$

$$\times [\alpha L_{neff} - \frac{N_n\{\cosh(\frac{d_2-w_p}{L_{neff}}) - e^{-\alpha(d_2-w_p)}) + \sinh(\frac{d_2-w_p}{L_{neff}})\} + \alpha L_{neff} e^{-\alpha(d_2-w_p)}}{N_n \sinh(\frac{d_2-w_p}{L_{neff}}) + \cosh(\frac{d_2-w_p}{L_{neff}})}] \quad (18)$$

Where $K_x$, $L_y$, $L_{neff}$, $N_n$ are expressed as functions of $S_{eff}$, $S_{ng}$, $D_n$, $X_g$, $Y_g$, $L_n$.

The photogenerated current in the Space Charge Region (equal to the number of photons absorbed), is derived by the 1D model (Sze. S. M, 1981):

$$J_{SCR} = qFe^{-\alpha(d_1-w_n)}\{1 - e^{-\alpha(w_n+w_p)}\} \quad (19)$$

The total photocurrent is given from the sum of all current densities in each region considering as it has been early referred (Dugas. J.& Qualid. J, 1985) that the substrate contribution is negligible:

$$J_{sc} = J_p + J_n + J_{SCR} \qquad (20)$$

A similar analysis might also carried out, for the determination of the dark saturation current ($J_0$) by solving the continuity equations, for both regions, (Halder. N. C, & Williams. T. R., 1983). The derived expression of $J_0$ is then used for the calculation of open circuit voltage from Eq 13.

## 4. Optimization

A computer program has been developed according to the mathematical analysis which implements the 1D model previously described (3.1) for the optimization of cells parameters. The values of ref1ection coefficient R($\lambda$) which depends on the wavelength $\lambda$ and is related to the anti reflecting coating, as well as the photon flux N ($\lambda$) defined by a discretized AM1.5 solar spectrum, are inserted in the program via the modelling procedure. The grid structure of the cell covering about 13.1% of the front surface and the Back Surface Field are inserted in a similar way. Material properties are considered as previously described, however the required data must be inserted by the user manually e.g., data concerning front layer and substrate (thickness, doping concentration), concentration of the front layer $N_D$, front surface recombination velocity $S_F$ and effective recombination velocity $S_{eff}$, e.t.c. This data is then used as the starting point for the optimisation process. The program calculates the external quantum efficiency of the studied cells in a wavelength range from 0.4µm to 1.1µm, under 1000 W/m² illumination (AM1.5 spectrum). The optimisation is carried out by introducing the lower and upper bounds of the epilayer thickness which are 40 and 100 µm respectively (Perraki. V & Giannakopoulos. A.; 2005). The simulation is then performed in batch mode with respect to the input data, controlling the input and output of the simulator at the same time.

After completion of this operation, results are interpreted and assessed by the output interface. The simulated short circuit current density is initially evaluated through numerical integration for the corresponding spectrum, while efficiency of the cells is investigated in the next step.

A 3D model is applied (3.2) to the same type of cells in order to optimize their epitaxial layer thickness, taking into account the structure parameters. The program computes the external quantum efficiency of the studied cells. It also provides, through numerical integration, results for the optimum photocurrent density and efficiency for various values of grain size and grain boundary recombination velocity.

A comparison between the 3D simulated and experimental results of photocurrent, and efficiency under AM1.5 irradiance is performed, as well as between the quantum efficiency curves calculated through 3D model and the corresponding 1D results of the studied cells.

## 5. Influence of structure parameters on cell's properties

The simulations for n⁺pp⁺ type epitaxial silicon solar cells, have been performed under AM 1.5 spectral conditions. The experimental values, of emitter (thickness $d_1$, diffusion length $L_P$

and doping concentration $N_D$), and substrate (thickness $d_3$, diffusion length $L_n^+$ and doping concentration $N_A^+$), assigned to the model parameters are shown in Table 3.

| Cell | $d_1$ (µm) | $L_p$(µm) | $N_D$ (cm$^{-3}$) | $d_3$(µm) | $L_n^+$ (µm) | $N_A^+$(cm$^{-3}$) |
|------|-----------|-----------|-------------------|-----------|--------------|--------------------|
| B2 | 0.4 | 1 | $1.5 \times 10^{20}$ | 300 | 13 | $2.9 \times 10^{19}$ |
| T2 | 0.4 | 1 | $1.5 \times 10^{20}$ | 300 | 18 | $1.9 \times 10^{19}$ |

Table 3. Experimental values of emitter and substrate characteristics.

The experimental values of epilayer properties (thickness $d_2$, base doping concentration $N_A$, diffusion length $L_n$) and the best results of measured photocurrent density $J_{sc}$, open circuit voltage $V_{oc}$ and efficiency $\eta$ for the cells under investigation are shown in table 4.

| Cell | $d_2$ (µm) | $N_A$(cm$^{-3}$) | $L_n$ (µm) | $J_{ph}$(mA/cm$^2$ ) | $V_{oc}$ (V) | $\eta$ (%) |
|------|-----------|------------------|-----------|----------------------|--------------|------------|
| B2 | 64 | $1.5 \times 10^{16}$ | 64 | 25.05 | 542 | 9.3 |
| T2 | 64 | $1.5 \times 10^{16}$ | 71 | 26.17 | 558 | 10.12 |

Table 4. Experimental values of epilayer properties.

### 5.1 One dimensional model

The one dimensional model was utilized to perform simulations that indicate the dependency of cell's photovoltaic properties on recombination velocity and doping level, for the cells (B2, from the bottom of the ingot) as well as for cells (T2, from the top of the ingot). Optimal photocurrent density and efficiency are calculated as a function of epilayer thickness for two different values of recombination velocity, and two different values of doping concentration.

### 5.1.1 Influence of recombination velocity

Figure 3 shows that the photocurrent density is little influenced (Hoeymissen,J. V; et al 2008) in cases of low recombination velocity ($10^2$ cm/sec). On the contrary photocurrent density is heavily affected by the epilayer thickness in case of high recombination velocity ($10^6$ cm/sec) and a value ~30 mA /cm$^2$ is achieved for epilayer thickness values much higher than 65 µm. The evaluation of these results shows that the epilayer thickness of 50 µm represents a second best value, in case of low recombination velocity. The gain, for thicker epilayers than this, is minor with an increment in $J_{sc}$ of approximately ~ 0.05 mA /cm$^2$, when the epilayer thickness increases by steps of 5 µm.

The plots of the efficiency with respect to epilayer thickness for two different values of recombination velocity are illustrated in figure 4.

It is observed that the efficiency of the studied cells, calculated for recombination velocity values of 100 cm/sec saturates ($\eta$~13.8%) for epilayer thickness values higher than ~65µm where the gain is minimal. However for recombination velocity values of $2.5 \times 10^6$ cm/sec the efficiency is lower enough for thin epilayers and saturates for thickness values higher than 85µm. Higher efficiencies are referred to cells with small grains, in comparison to those of large grains, because of the presence of fewer recombination centres. Annotating these results it is found that when the epilayer thickness of these cells decreases to values ≤ 50 µm the maximum theoretical efficiency decreases by a percentage of 0.03 % to 0.07 % for $S_{eff}$ =100 cm/sec. It is particularly recommended that a second best value of epilayer thickness equals to 50 µm, given that the gain for higher epilayer thickness values is of minor importance.
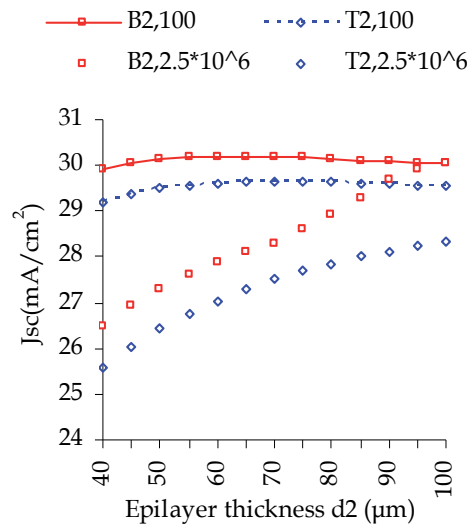
Fig. 3. Variation of short circuit current density, $J_{sc}$, of the studied cells (B2 with small grains, T2 with large grains) versus epilayer thickness d2, calculated for $S_{eff}$=100 cm/sec and 2.5x10^6 cm/sec.
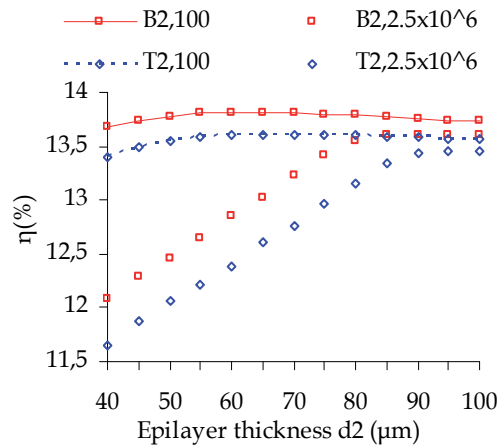


Fig. 4. Efficiency graph versus base thickness d2 of the cells under investigation, calculated for $S_{eff}$ =100 cm/ sec and 2.5x10^6 cm/sec.

### 5.1.2 Influence of doping concentration

The same model was used to perform simulations indicating the relation between photovoltaic properties and doping concentration. When doping concentration increased from $10^{15}$ to $10^{17}$ cm$^{-3}$ simulated data of the short circuit current density, $J_{sc}$, showed a small decrease, due to Auger recombination and minority charge carriers' mobility.

Figure 5, illustrates the variation of $J_{sc}$ with respect to epilayer thickness for two different values of doping. Maximum photocurrent densities are delivered from cells with epilayer thickness equal to 65 and 70 μm (B2 and T2 cells respectively). They vary between 29.6 and
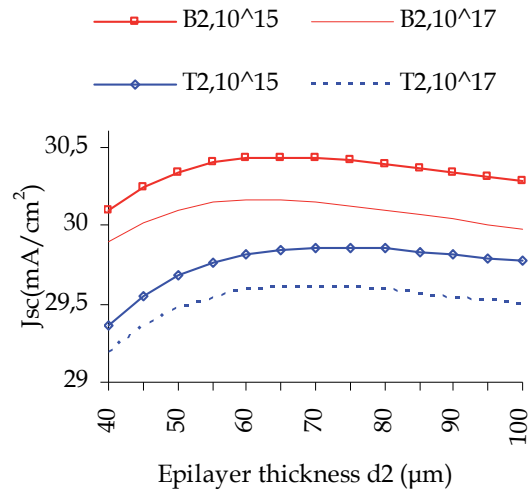
Fig. 5. Variation of the short circuit current density $J_{sc}$ of the cells, as a function of base thickness d2 calculated for doping concentration values of $10^{15}$cm$^{-3}$, and $10^{17}$ cm$^{-3}$.

30.47 mA /cm$^2$, which are higher than experimental values. According to the calculated results when the epilayer thickness of B2 cells decreases to values ≤50 µm, photocurrent density decreases for the different values of doping concentrations by approximately 0.05-0.08 mA/cm$^2$. It can be considered again that 50 µm, represent a second best value, since little is gained when the epitaxial layer becomes thicker.

Simulated data of cell efficiency, η, present a rise of its maximum value, as shown in figure 6, which is well above from maximum values experimentally obtained, and a shift of the optimum epilayer thickness to lower values. Higher efficiency has been calculated for cells with doping concentration of $10^{17}$ cm$^{-3}$ compared to the one calculated for cells with doping
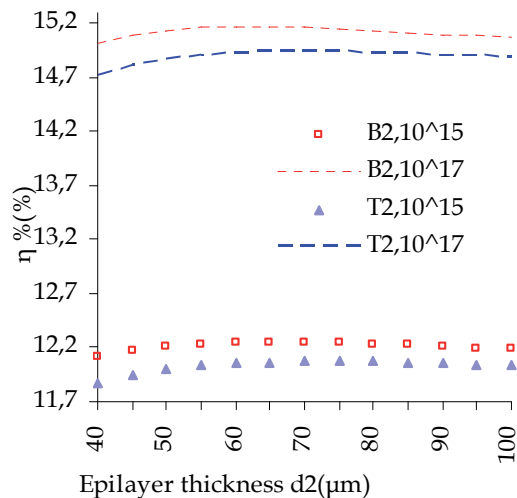


Fig. 6. Variation of the cell's efficiency as a function of epilayer thickness d2 calculated for doping concentrations of $10^{15}$ cm$^{-3}$, and $10^{17}$ cm$^{-3}$.

of $10^{15}$ cm$^{-3}$. It is noticed that solar cell efficiency is insignificantly influenced by epilayer thickness variations. It is pointed that if the epilayer thickness of the small grain cell is reduced to values ≤50 µm, the efficiency decrease is less than 0.03%. Similarly a decrease in epilayer thickness, of T2 cells, to 50 µm results in a decrease of their maximum efficiency by 0.04 %.

The optimized cell parameters $J_{sc}$ and η for an optimum value of doping concentration show that even they are higher compared to the experimental ones, (Perraki. V.; 2010) they do not present significant differences for the two different types of cells. This is due to the fact that cell parameters introduced to the model were not very different and diffusion length values were high in all cases. It must be noted however that the optimum values of photocurrent density, efficiency and epilayer thickness calculated by this model are different than the ones corresponding to maximum $J_{ph}$ and η and equal the values of saturation. When the epilayer thickness increases beyond the optimum value in steps of 5 µm, $J_{sc}$ and η increase by a rate lower than 0.05mA/cm$^2$ and 0.05% respectively. Taking all these into account, we can consider that the optimum value of efficiency is obtained for epilayer thickness values equal to or lower than 50 µm, which is much lower than base thickness and base diffusion length values of any solar cell.

The comparison between the experimental and the optimized quantum efficiency plots of B2 and T2 cells, (calculated by the 1D model) is presented in figure 7. The chosen model parameters, as shown in tables 3 and 4, provide a good fit to the measured QE data for wavelength values above 0.8 µm, whereas optimized curves indicate higher response for the lower part of the spectrum. The response of the experimental devices related to the contribution of the n$^+$ heavily doped front region (for low wavelengths of the solar radiation) is significantly lower than that of the simulated results, due to the non passivated surface.

Moreover, the spectral response of B2 is significantly higher compared to the one of T2 cell near the blue part of the solar spectrum, although cell T2 has higher experimental values of $J_{sc}$, $V_{oc}$, and η. This may be explained by differences of the reflection coefficient between experimental and simulated devices and /or by the presence of fewer recombination centers in smaller inter-grain surfaces.
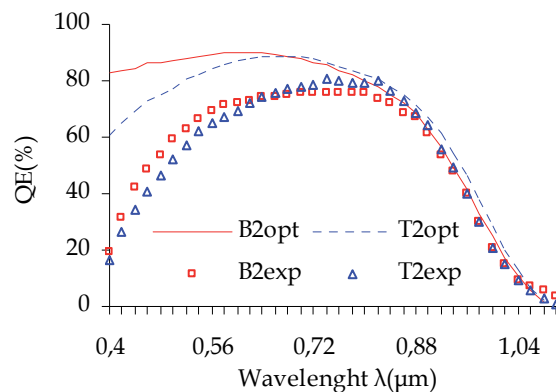


Fig. 7. Optimized external quantum efficiency for cells B2, and T2, evaluated for experimental values included in tables 3 and 4, and comparison with the experimental ones.

## 5.2 Three dimensional model

A 3D model was utilized to perform simulations that show the influence of grain boundary recombination velocity $S_{gb}$ and grain size on cell's properties. The calculated results indicate the influence of grain boundary recombination velocity on the photocurrent and on the efficiency for various values of grain size for the cells B2 (from the bottom of the ingot) as well as for the cells T2 (from the top of the ingot). The plots are obtained for values of epilayer thickness maximizing the photocurrent which are not necessarily equal to the experimental. These optimal values of epilayer thickness used in the graph vary and depend on grain size and $S_{gb}$

The graph of optimal photocurrent as a function of recombination velocity shows, figure 8, that it is seriously affected by recombinations in the grain boundaries of small grains, given that a significant amount of the photogenerated carriers recombine in the grain boundaries when grain's size is lower or comparable to the base diffusion length.
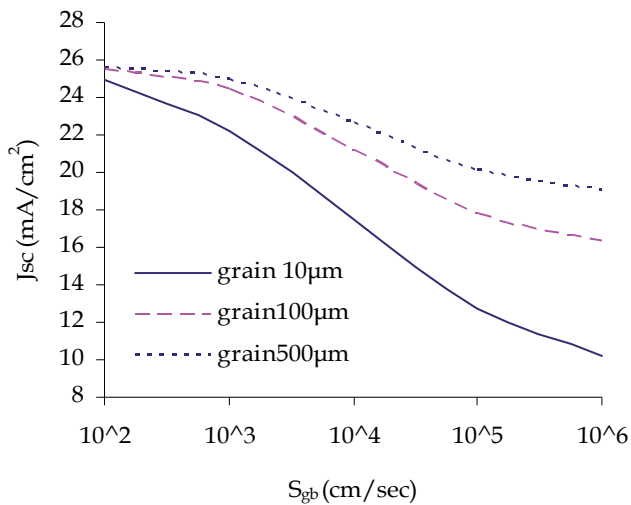


Fig. 8. Optimal short circuit current dependence on grain boundary recombination velocity $S_{gb}$ of the cell B2, with grain size as parameter.

It is shown that the photocurrent density falls rapidly for grains with size 10 µm and high values of grain boundary recombination velocities. However, the effect of grain boundary recombination velocity is not so important for larger grain sizes (100 and 500 µm).

Figure 9 demonstrates the efficiency of the cells B2 in relation with the grain boundary recombination velocity for different grain sizes, which is calculated for optimal base thickness. It can be pointed that for small grain size, the efficiency is largely affected by grain boundary recombination, with a rapid decrease for recombination velocities greater than $10^3$ cm/sec.

For larger grain sizes (500 µm), there is not so strong decrease with the recombination velocity, while insignificant decrease is observed in the efficiency for values lower than $10^3$ cm/sec.

The graphs of optimal photocurrent as a function of grain boundary recombination velocity (figure 10) show that it is less affected from recombination in the grain boundaries for large grain sizes (cells T2), compared to cells with small grain sizes, (cells B2 in figure 8).
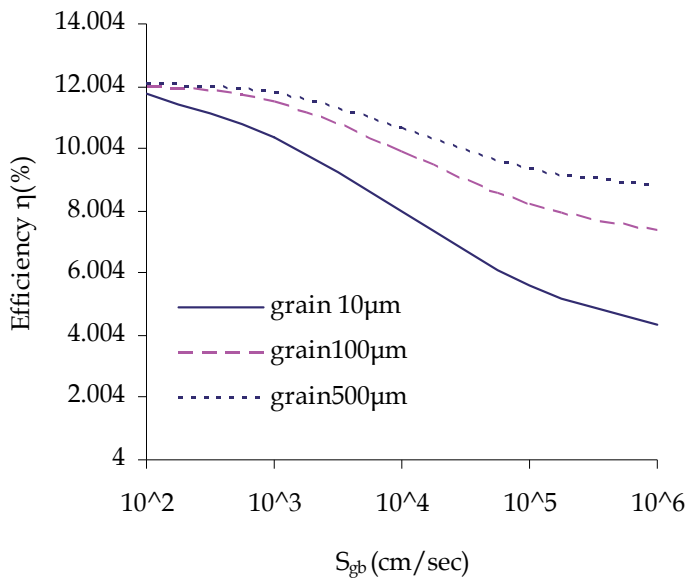
Fig. 9. Variation of efficiency η of the cell B2, as a function of grain boundary recombination velocity $S_{gb}$, calculated for optimal base thickness and variable grain sizes.

Therefore, for grains with size 5000 μm, and high values of grain boundary recombination velocities the photocurrent does not fall rapidly. It is evident that, for cells with even larger grain sizes (10000 μm) the influence of grain boundary recombination velocity is even more insignificant.
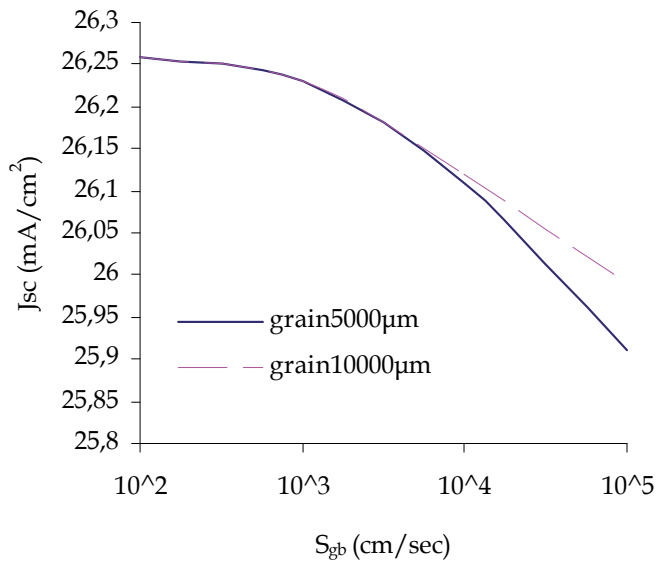


Fig. 10. Optimal short circuit current dependence on grain boundary recombination velocity $S_{gb}$ of the cell T2, with grain size as parameter.
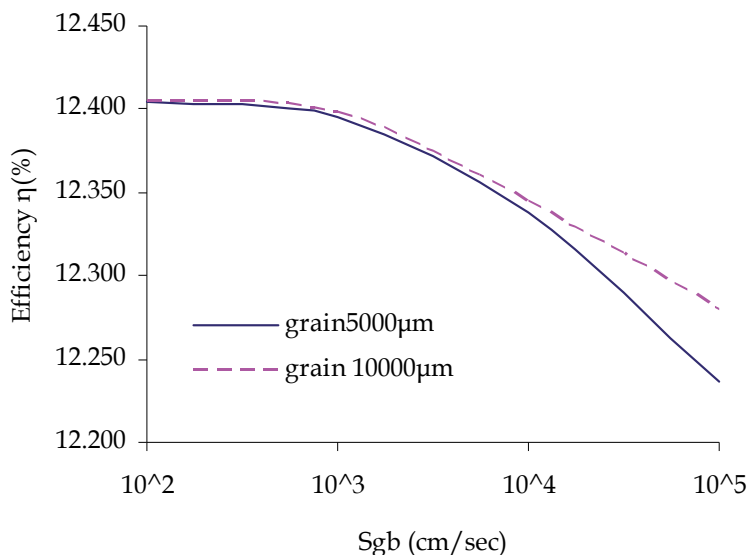
Fig. 11. Variation of the efficiency η as a function of grain boundary recombination velocity $S_{gb}$, calculated for optimal base thickness and variable grain sizes (cell T2).



|     |     |
| :-: | :-: |
| (a) | (b) |
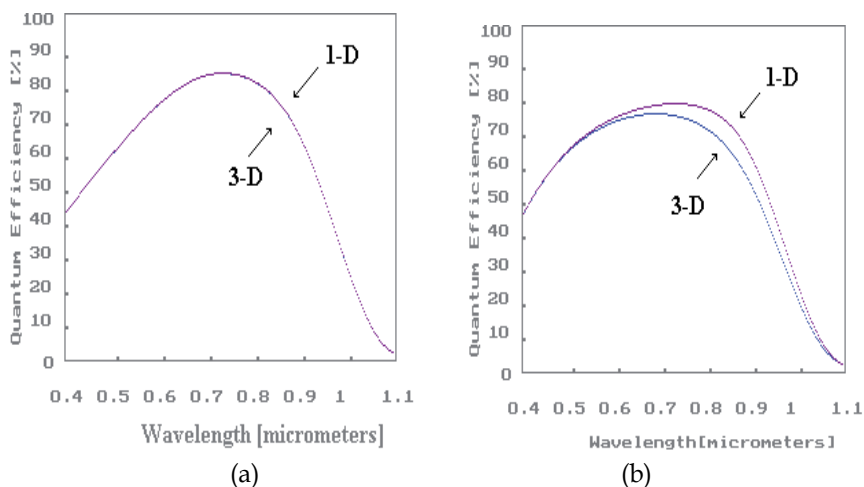
Fig. 12. Optimized external quantum efficiency and comparison with 3D model, for the cells B2 (a) and T2 (b), evaluated for experimental values included in tables 3 and 4.

Figure 11 illustrates the efficiency of the cells T2 as a function of grain boundary recombination velocity for different grain sizes, which is calculated for optimal base thickness. It can be observed that for large grain size, (5000 µm) the efficiency is less affected for grain boundary recombination for $S_{gb}$ values higher than $10^3$ cm/sec, compared to the case of small grain size, Fig. 9. A smoother decrease is observed in case of cells with even

larger grain sizes (10000 μm). It is obvious that solar cell efficiency saturates if $S_{gb}$ is lower than $10^3$ cm/sec and the gain is minimal for smaller values of grain boundary recombination velocity. In this case, efficiency is limited from bulk recombination, which is directly related to the base effective diffusion length $L_n$. However when grain boundary recombination velocity is reduced, the optimal layer thickness increases, until it reaches a value close to the device diffusion length $L_n$ .This parameter seems to affect the value of optimal epilayer thickness. For higher $S_{gb}$ values the maximum efficiency shifts to thickness values lower than the base diffusion length. However, for very elevated values of grain boundary recombination velocities and small grain size, the optimal thickness saturates to a value, which is the same for cells with thin or thick epilayer. The plots of $L_{neff}$ and optimal epilayer thickness as a function of $S_{gb}$, show similar dependence on $S_{gb}$ and grain size, with almost equal values (Kotsovos. K & Perraki.V, 2005).

The optimized 1D external quantum efficiency and the 3D graphs are demonstrated for the cells B2 and T2 in figure 12a and b respectively (kotsovos. K, 1996). Since the influence of grain boundaries has not been taken into account in the 1D model it has shown superior response compared to the 3D equivalent for wavelength values higher than 0.6 μm (cell T2). Lower values of spectral response are observed in case of large grains (cell T2) and λ> 0.6 μm, possible due to the presence of more recombination centers in larger intergrain surfaces. However, very good accordance is observed between 1D and 3D plots for cells B2.

## 6. Conclusions

The optimal photocurrent and conversion efficiency for epitaxial solar cells are influenced by the recombination velocity. The best values of epilayer thickness and the effective base diffusion length are higher for lower values of grain boundary recombination velocities, resulting to higher efficiency values.

The comparison between the simulated 1D and experimental QE curves indicates concurrence for wavelengths greater than 0.8 μm. However, the measured spectral response close to the blue part of the spectrum was considerable lower compared to simulation data. On the other hand   the comparison of the simulated 1D and 3D QE curves shows good agreement only for wavelengths lower than 0.6 μm for cells T2 and very good agreement for cells B2.

## 7. References

Arora. J, Singh. S, and Mathur. P., (1981), *Solid State Electronics*, 24 (1981), p.739-747.

Blacker. A. W, et al (1989) *Proc. 9th EUPVSEC*, Freiburg, Germany, p.328.

Card. H.C, and Yang. E., (1977),  *IEEE Trans. Electron Devices*, 29 (1977) 397.

Carslaw. H.S; and Jaeger .J.C; 1959; *Conduction Heat in Solids*, 2nd ed, Oxford University Press, London 1959.

Caymax. M; Perraki. V; Pastol.J. L; Bourée. J.E; Eycmans. M; Mertens. R; Revel. G; Rodot. M; (1986)"resent results on epitaxial solar cells made from metallurgical grade Si" *Proc.2nd Int.PVSE Conf* (Beijing1986)171.

Duerinckh. F; Nieuwenhuysen. K.V; Kim. H; Kuzma-Filipek. I; Dekkers. H; Beaucarne. G; and Poortmans. J; (2005) "Large –area Epitaxial Silicon Solar Cells Based on Industrial Screen-printing Processes" *Progress in Photovoltaics* 2005,pp673

Dugas.J, and Qualid. J, (1985), "3d modelling of grain size and doping concentration influence on polycrystalline silicon solar cells", *6th ECPVSEC*, (1985) p. 79.

Godlewski. M; Baraona.C.R and Brandhorst.H.W 1973, *Proc 10th IEEE PV Specialist Conf.* (1973) P.40

Goetzberger.A, Knobloch. J, Voss. B; *Crystalline Silicon Solar Cells*, John willey & Sons 1998.

Halder. N.C, and Williams. T. R., (1983);"Grain Boundary Effects in Polycrystalline Silicon Solar Cells", *Solar Cells* 8 (1983) 201.

Heavens. O. S, (1991); *The Optical Properties of Thin solid Films*, Dover, 1991.

Hoeymissen. J.Van; Kuzma-Filipek. I; Nieuwenhuysen. K. Van; Duerinckh. F; Beaucarne. G; J. Poortmans. J; (2008) " Tnin-film epitaxial solar cells on low cost Si substrates: closing the efficiency gap with bulk Si cells using advanced photonic structures and emitters", *Proceedings 23rd EUPVSEC* 2008 pp 2037.

Hovel. H. J. (1975) Solar cells *Semiconductors and Semimetals* vol. II (New York: Academic

Kotsovos. K; 1996, *Final year student Thesis*, University of Patras,Greece,1996

Kotsovos. K and Perraki.V; (2005) "Structure optimisation according to a 3D model applied on epitaxial silicon solar cells :A comparative study" *Solar Energy Materials and Solar Cells* 89 (2005) 113-127.

Luque. A, Hegeduw. S.,(ed) "*Handbook photovoltaic Science and Engineering* '' Wiley, 2003.

Mason. N; Schultz. O; Russel. R; Glunz. S.W; Warta. W; (2006) "20.1% Efficient Large Area Cell on 140 micron thin silicon wafer", *Proc. 21st EUPVSEC*, Dresden 2006, pp 521

Nieuwenhuysen. K. Van; Duerinckh. F; Kuzma. I; Gestel. D.V; Beaucarne. G; Poortmans. J; (2006) " Progress in epitaxial deposition on low-cost substrates for thin- film crystalline silicon solar cells at IMEC" *Journal of Crystal Growth* (2006) pp 438..

Nieuwenhuysen. K.Van; Duerinckx. K; Kuzma. F; Payo. I; Beaucarne. M.R; Poortmans. G; (2008); Epitaxially grown emitters for thin film crystalline silicon solar cells *Thin Solid Film*, 517, (2008) pp 383-384.

Overstraeten. R.J.V, Mertens. R, (1986), *Physics Technology and Use of Photovoltaics*, Adam Hilger Ltd 1986.

Perraki. V and Giannakopoulos.A; (2005); Numerical simulation and optimization of epitaxial solar cells; *Proceedings 20th EPVSEC* Barcelona 2005, pp1279.

Perraki.V; (2010) "Modeling of recombination velocity and doping influence in epitaxial silicon solar cells" *Solar Energy Materials & Solar Cells 94* (2010) 1597-1603.

Peter.K; Kopecer.R; Fath. P; Bucher. E; Zahedi. C; *Sol. Energy Mat. Sol. Cells* 74 (2002) pp 219.

Peter. K; R.Kopecek. R; Soiland. A; Enebakk. E; (2008) "Future potential for SOG-Si Feedstock from the metallurgical process route" *Proc.23rd EUPVSEC* (2008) pp 947

Photovoltaic Technology Platform; (2007) "A Strategic Research Agenda for PV Energy Technology"; *European Communities,* 2007

Price J.B., *Semiconductor Silicon*, Princeton, NJ, 1983, p. 339

Runyan. W. R, (1976) *Southeastern Methodist University Report* 83 -13 (1976).

Sanchez-Friera. P;et al;(2006)"Epitaxial Solar Cells Over Upgraded Metallurgical Silicon Substrates: The Epimetsi Project" *IEEE 4th World Conference on Photovoltaic Energy Conversion*, pp1548-1551.

Sze. S. M; *Physics of Semiconductor Devices*, 2nd Ed, 1981, p 802

Wolf H. F., *Silicon Semiconductor Data*, Pergamon Press, 1976.

# A New Model for Extracting the Physical Parameters from I-V Curves of Organic and Inorganic Solar Cells

N. Nehaoua, Y. Chergui and D. E. Mekki
*Physics Department, LESIMS laboratory,*
*Badji Mokhtar University*
*Algeria*

## 1. Introduction

As worldwide energy demand increases, conventional sources of energy, fossils fuels such as coal, petroleum and natural gas will be exhausted in the near future. Therefore, renewable resources will have to play a significant role in the world's future supply. Solar energy occupies one of the most important places among these various possible alternative energy sources. The direct photovoltaic conversion of sunlight into electricity seems to be extremely promising. Solar cells furnish the most important long-duration power supply for satellites and space vehicles. They have also been successfully employed in terrestrial application. A solar cell (also called photovoltaic cell or photoelectric cell) is a solid state device that converts the energy of sunlight directly into electricity by the photovoltaic effect. Assemblies of cells are used to make solar modules, also known as solar panels. The energy generated from these solar modules, referred to as solar power, is an example of solar energy. photovoltaic system uses various materials and technologies such as crystalline Silicon (c-Si), Cadmium telluride (CdTe), Gallium arsenide (GaAs), chalcopyrite films of Copper-Indium-Selenide (CuInSe2) and Organic materials are attractive because of their light eight, processability, and the ease of designing the materials on the molecular level.

Solar cells are usually assessed by measuring the current voltage characteristics of the device under standard condition of illumination and then extracting a set of parameters from the data. The major parameters are usually the diode saturation current, the series resistance, the ideality factor, the photocurrent and the shunt conduction. The extraction and interpretation has a variety of important application. These parameters can, for instance, be used for quality control during production or to provide insights into the operation of the devices, thereby leading to improvements in devices.

## 2. Equivalent circuit of solar cells

A solar cell is simply diode of large-area forward bias with a photovoltage. The photovoltage is created from the dissociation of electron-hole pairs created by incident photons within the built-in field of the junction or diode. The operating current of a solar cell is given by:

$$I = I_{ph} - I_d - I_p$$

$$= I_{ph} - I_s \left[ \exp\left( \frac{\beta}{n}(V + IR_s) \right) - 1 \right] - \frac{V + IR_s}{R_{sh}} \qquad (1)$$

Where, $I_{ph}$, $I_s$, n, $R_s$ and $G_{sh}$ (=$1/R_{sh}$) being the photocurrent, the diode saturation current, the diode quality factor, the series resistance and the shunt conductance, respectively. $I_p$ is the shunt current and $\beta = q/kT$ is the usual inverse thermal voltage. The shunt resistance is considered $R_{sh}$= ($1/G_{sh}$)>>Rs.

The circuit model of solar cell corresponding to equation (1) is presented in figure (1).
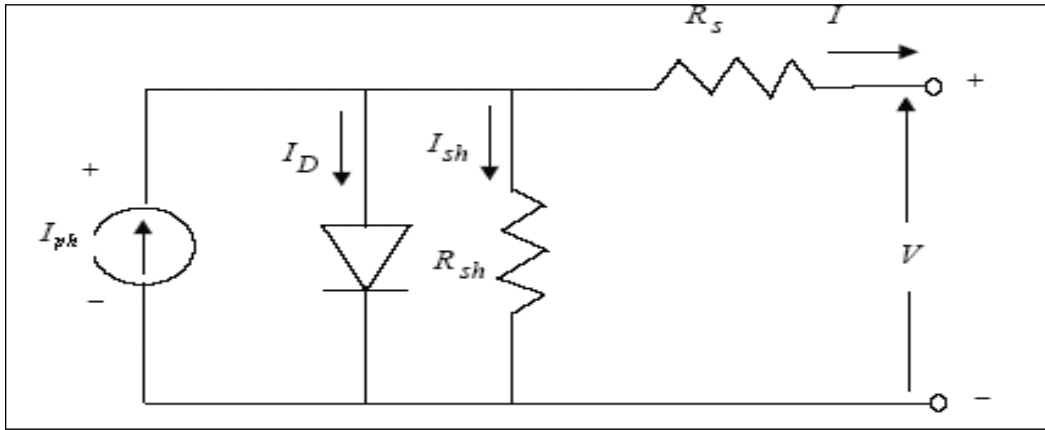


Fig. 1. Equivalent circuit model of the illuminated solar cell.

The single diode model considered here is rather simple, efficient and sufficiently accurate for process optimization and system design tasks. The single diode model can also be used to fit solar modules and arrays where the cells are series and/or parallel connected, provided that the cell to cell variations are not important.

## 3. Solar cell output parameters

The graph of current as a function of voltage I=f (V) for a solar cell passes through three significant points as illustrated in figure 2 below.

- The short circuit current, $I_{sc}$, occurs on a point of the curve where the voltage is zero. At this point, the power output of the solar cell is zero. The current in a device is almost directly proportional to light intensity and size.
- The open circuit voltage, $V_{oc}$, occurs on a point of the curve where the current is zero. At this point the power output of the solar cell is zero. The voltage of the cell does not depend on its size, and remains fairly constant with changing light intensity.
- The fill factor, FF, is the ration of the peak power to the product $I_{sc}$ $V_{oc}$

$$FF = \frac{I_m V_m}{I_{sc} V_{oc}} \qquad (2)$$

The fill factor determines the shape of the solar cell I-V characteristics. Its value is higher than 0.7 for good cells. The series and shunt resistance account for a decrease in the fill factor. The fill factor is useful parameters for quality control test.

- The conversion efficiency, is the ration of the optimal electric power, $P_m$, delivered by the PV module to the solar insolation, $P_0$, received at a given cell temperature, T.

$$\eta = \frac{FF I_{sc} V_{oc}}{P_0} = \frac{P_m}{P_0}$$                    (3)
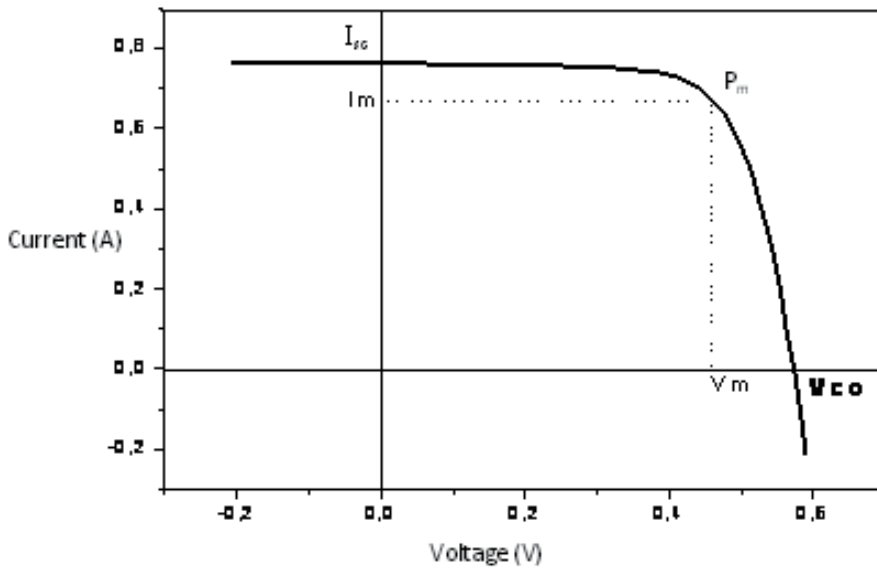


Fig. 2. Solar cell I-V Characteristics.

## 4. Solar cell parameters extraction

### 4.1 Previous works

An accurate knowledge of solar cell parameters from experimental data is of vital importance for the design of solar cells and for the estimates of their performance. The major parameters are usually the diode saturation current, the series resistance, the ideality factor, the photocurrent and the shunt conductance.

The evaluation of these parameters has been the subject of investigation of several authors. Some of the methods use selected parts of the current-voltage (I-V) characteristic (Charles et al, 1981; 1985) and those that exploit the whole characteristic (Easwarakhanthan et al, 1986; phang et al, 1986). (Santakrus et al, 2009)  presents the use of properties of special trans function theory (STFT) for determining the ideality factor of real solar cell. (Priyank et al, 2007) method gives the value of series $R_s$ and shunt resistance $R_{sh}$ using illuminated I-V characteristics in third and fourth quadrants and the $V_{oc}$-$I_{sc}$ characteristics of the cell. In the work of (Bashahu et al, 2007), up to 22 methods for the determination of solar cell ideality factor (n), have been presented, most of them use the single I-V data set. (Ortiz-Conde et al,

2006) have proposed an elegant method to extract the five parameters based on the calculation of the co-content function (CC) from the exact explicit analytical solution of the illuminated current–voltage characteristics, but this method has only been tested on a plastic solar cell. An accurate method using the Lambert W-function has been presented by (Jain and Kapoor, 2004, 2005) to study different parameters of organic solar cells, but it has been validated only on simulated I–V characteristics. A combination of lateral and vertical optimization was used ( Haouari-Merbah et al, 2005; Ferhat-Hamida et al, 2002) to extract the parameters of an illuminated solar cell. (Zagrouba et al, 2010; Sellami et al, 2007) propose to perform a numerical technique based on genetic algorithms (GAs) to identify the five electrical parameters ($I_{ph}$, $I_s$, $R_s$, $R_{sh}$ and n) of multicrystalline silicon photovoltaic (PV) solar cells and modules, but this technique is influenced by the choice of the initial values of population.  A novel parameter extraction method for the one-diode solar cell model is proposed by (Wook et al, 2010) the method deduces the characteristic curve of an ideal solar cell without resistance using the I-V characteristic curve measured.

## 4.2 Proposed method of parameters extraction

The I-V characteristics of the solar cell can be presented by either a two diode model (Kaminsky et al, 1997) or by a single diode model (Sze et al, 1981). Under illumination and normal operating conditions, the single diode model is however the most popular model for solar cells (Datta et al, 1967). In this case, the current voltage (I-V) relation of an illuminated solar cell is given by Equation 1.

Equation 1 is implicit and cannot be solved analytically. The proper approach is to apply least squares techniques by taking into account the measured data over the entire experimental I-V curve and a suitable nonlinear algorithm in order to minimize the sum of the squared errors. In this section we propose a new technique that uses the measured current-voltage curve and its derivative (Chegaar et al, 2004; Nehaoua et al 2010). A non linear least squares optimization algorithm based on the Newton model is hence used to evaluate the solar cell parameters. The problem, we have, is to minimize the objective function S with respect to the set of parameters θ:

$$S(\theta) = \sum_{i=1}^{N} \left[ \frac{G - G_i(V_i, I_i, \theta)}{G_i(V_i, I_i, \theta)} \right]^2 \tag{4}$$

Where $\Theta$ is the set of unknown parameters $\Theta = (I_s, n, R_s, G_{sh})$ and $I_i$, $V_i$ are the measured current, voltage and the computed conductance $G_i = dI_i / dV_i$ respectively at the i-th point among N measured data points. Note that the differential conductance is determined numerically for the whole I-V curve using a method based on the least squares principle and a convolution. The conductance G can be written as:

$$G = -\frac{\psi}{1 + R_s \psi} \tag{5}$$

Where ψ is given by:

$$\Psi = \frac{\beta}{n} \left\{ I_{ph} + I_p - I - G_{sh} \left( V + R_s I \right) \right\} + G_{sh} \tag{6}$$

The term between brackets is equal to $I_s \exp\left(\dfrac{\beta}{n}(V + IR_s)\right)$ and when replaced in equation 6, the conductance G will be independent of the photo-current $I_{ph}$. This equation can be written as:

$$\Psi = \frac{\beta}{n} I_s \exp\left(\frac{\beta}{n}(V + IR_s)\right) + G_{sh} \tag{7}$$

Consequently, by minimizing the sum of the squares of the conductance residuals instead of minimizing the sum of the squares of current residuals as in (Easwarakhanthan et al, 1986). Using this method, the number of parameters to be extracted is reduced from five $\Theta = (I_s, n, R_s, G_{sh}, I_{ph})$ to only four parameters $\Theta = (I_s, n, R_s, G_{sh})$. The fifth parameter, the photocurrent, can be easily deduced using Eq. (1) at V=0, which yield to the following equation (Chegaar et al, 2001, 2004; Nehaoua et al 2010):

$$I_{ph} = I_{sc}\left(1 + R_s G_{sh}\right) + I_p\left(\exp\frac{\beta I_{sc} R_s}{n} - 1\right) \tag{8}$$

Where $I_{sc}$ is the short circuit current.
Newton's method can be used to obtain an approximation to the exact solution. Newton's method is given by:

$$\theta_i = \theta_{i-1} - \left[J(\theta)\right]^{-1} F(\theta) \tag{9}$$

Where $J(\Theta)$ is the Jacobian matrix which elements are defined by:

$$J = \frac{\partial F}{\partial \theta} \tag{10}$$

For minimizing the sum of the squares, it is necessary to solve the equations $F(\Theta)=0$, where $F(\theta)$ is described by the equation:

$$F(\theta) = \frac{\partial S}{\partial \theta} \tag{11}$$

Although Newton's method converges only locally and may diverge under an improper choice of reasonably good starting values for the parameters, it remains attractive with the number of variables being limited (four in this case) and their partial derivatives easily. To illustrate the approach, we have first applied the method to a computer calculated curve reproducing the same solar cell characteristic used by Eswarakhantan et al. To test the effects of different initial values on the method, the known exact solutions were multiplied by the factors [0.5-1.7] respectively and after carrying out the calculations; the extracted solar cell parameters were almost identical to the theoretical ones. Also noticed is the obvious and expected fact that the CPU calculation time decreases quickly when the initial values used are closer to the exact solution. In order to test the quality of the fit to the experimental data, the percentage error is calculated as follows:

$$e_i = \left(I_i - I_{i,cal}\right)\left(100 / I_i\right) \tag{12}$$

Where $I_{i,cal}$ is the current calculated for each $V_i$, by solving the implicit Eq.(1) with the determined set of parameters ($I_{ph}$, $n$, $R_s$, $G_{sh}$, $I_s$). ($I_i$, $V_i$) are respectively the measured current and voltage at the $i$th point among $N$ considered measured data points avoiding the measurements close to the open-circuit condition where the current is not well-defined (Chegaar M et al, 2006). Statistical analysis of the results has also been performed. The root mean square error (RMSE), the mean bias error (MBE) and the mean absolute error (MAE) are the fundamental measures of accuracy. Thus, RMSE, MBE and MAE are given by:

$$RMSE = \left( \sum |e|_i^2 / N \right)^{1/2}$$
$$MBE = \sum e_i / N \qquad\qquad (13)$$
$$MAE = \sum |e|_i / N$$

$N$ is the number of measurements data taken into account.

As test examples, the method has been successfully applied on solar cells under illumination and used to extract the parameters of interest using experimental I–V characteristics of different solar cells and under different temperatures. It has been successfully applied to the measured I–V data of inorganic solar cells. These devices are a 57 mm diameter commercial silicon solar cell at a temperature of 33°C and a solar module in which 36 polycrystalline silicon solar cells are connected in series at 45°C. It has also been successful when applied to an illuminated organic solar cell, where the currents are generally 1000 times smaller and have high series resistances compared to inorganic (silicon) solar cells. The results obtained are compared with previously published data related to the same devices and good agreement is reported. Comparisons are also made with experimental data for the different devices.

## 4.3 Results and discussion

The experimental current–voltage (I–V) data were taken from (Easwarakhantan et al, 1986) for the commercial silicon solar cell and module and from (Ortiz-Conde et al, 2006) for the organic solar cell. The extracted parameters obtained using the method proposed here for the silicon solar cell and modules are given in Table 1. Satisfactory agreement is obtained for most of the extracted parameters. Those of the organic solar cell are shown in Table 2. A comparison with different methods is also given, and good agreement is reported. Statistical indicators of accuracy for the method of this work are shown in Table 3.

The best fits are obtained for the silicon solar cell and module with a root mean square error less than 1% and 2% for the organic solar cell. In figures 3, 4 and 5, the solid squares are the experimental data for the different solar cell and the solid line is the fitted curve derived from Equation (1) with the parameters shown in Table 1 for the silicon solar cell and module and Table 2 for the organic solar cell.

Good agreement is observed, especially for the inorganic solar cells. It is therefore necessary to emphasize that the proposed method is not based on the I-V characteristics alone but also on the derivative of this curve, i.e. the conductance G. Indeed, it has been demonstrated that it is not sufficient to obtain a numerical agreement between measured and fitted I-V data to verify the validity of a theory, but also the conductance data have to be predicted to show the physical applicability of the used theory. The interesting points with the procedure described herein is the fact that it has been successfully applied to experimental I–V

characteristics of different types of solar cells from inorganic to organic solar cells with completely different physical characteristics and under different temperatures. In contrast to other methods that have already been developed for this purpose, the proposed method has no limitation condition on the voltage. Furthermore, the presented method, tested for the selected cases, is more reliable to obtain physically meaningful parameters and is straightforward and easy to use.

| | Method (Easwarakhantan et al, 1986) | Method ( Chegaar M et al ,2006) | Method of this work |
|---|---|---|---|
| Cell (33°C) | | | |
| $G_{sh}$ ($\Omega^{-1}$) | 0.0186 | 0.0094 | 0.0114 |
| $R_s$ ($\Omega$) | 0.0364 | 0.0376 | 0.0392 |
| n | 1.4837 | 1.4841 | 1.4425 |
| $I_s$($\mu A$) | 0.3223 | 0.3374 | 0.2296 |
| $I_{ph}$(A) | 0.7608 | 0.7603 | 0.7606 |
| | | | |
| Module (45°C) | | | |
| $G_{sh}$ ($\Omega^{-1}$) | 0.00182 | 0.00145 | 0.001445 |
| $R_s$ ($\Omega$) | 1.2057 | 1.1619 | 1.2373 |
| n | 48.450 | 50.99 | 47.35 |
| $I_s$($\mu A$) | 3.2876 | 6.3986 | 2.4920 |
| $I_{ph}$(A) | 1.0318 | 1.030 | 1.0333 |

Table 1. Extracted parameters for commercial silicon solar cell and module.

| | Co-content function (Ortiz, 2006) | Method (Chegaar et al,2006) | Method of this work |
|---|---|---|---|
| $G_{sh}$ ($m\Omega^{-1}$) | 5.07 | 5.07 | 4.88 |
| $R_s$ ($\Omega$) | 8.59 | 8.58 | 3.16 |
| n | 2.31 | 2.31 | 2.29 |
| $I_s$($nAcm^{-2}$) | 13.6 | 13.6 | 12.08 |
| $I_{ph}$($mAcm^{-2}$) | 7.94 | 7.94 | 7.66 |

Table 2. Extracted parameters for an organic solar cell.

| | RMSE (%) | MBE (%) | MAE (%) |
|---|---|---|---|
| Solar cell (33°C) | 0.442 | -0.016 | 0.310 |
| Module (45°C) | 0.252 | -0.008 | 0.204 |
| Organic solar cell (27°C) | 1.806 | 0.638 | 1.201 |

Table 3. Statistical indicators of accuracy for the method of this work.
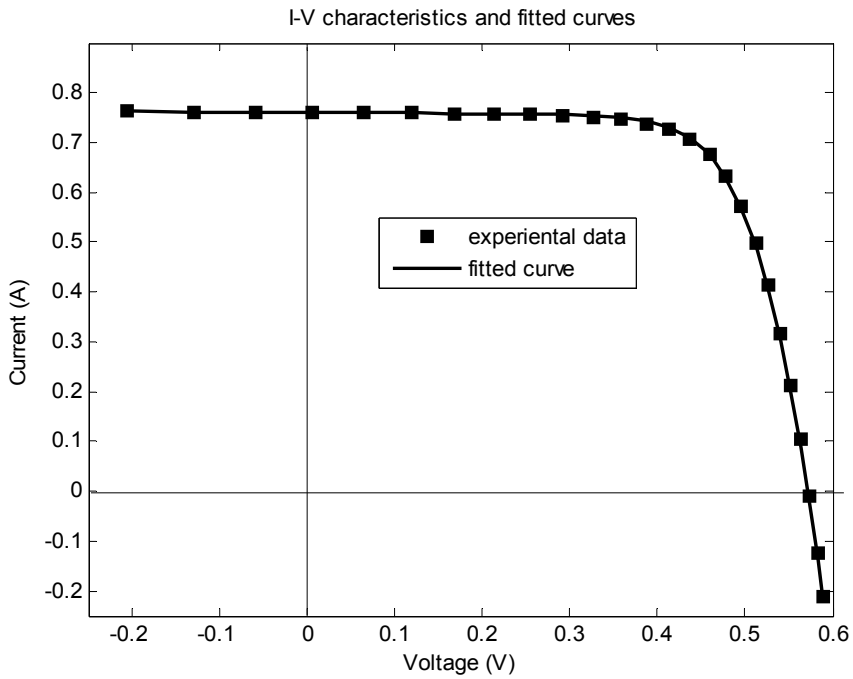
Fig. 3. Experimental data (■) and the fitted curve (-) for the commercial silicon solar cell.
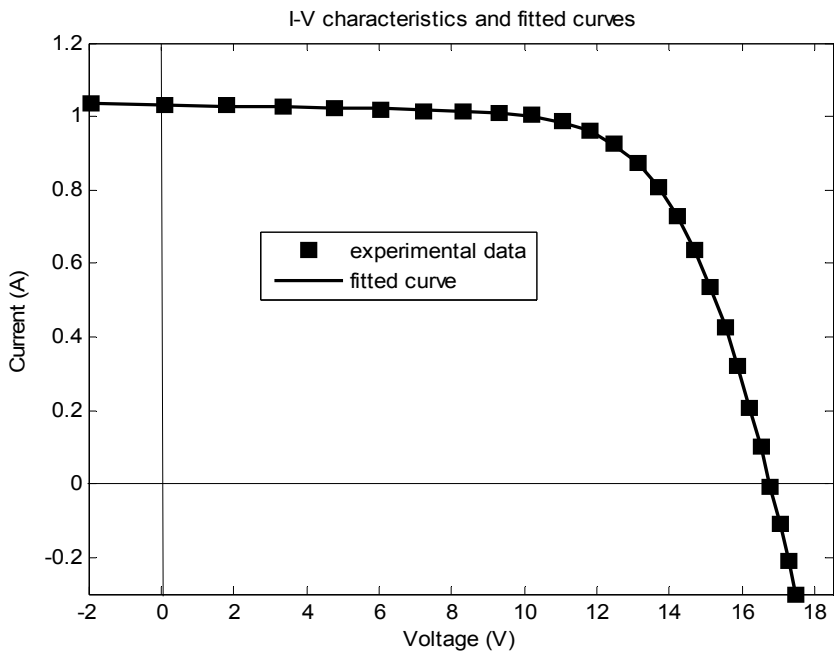


Fig. 4. Experimental data (■) and the fitted curve (-) for the commercial silicon solar module.
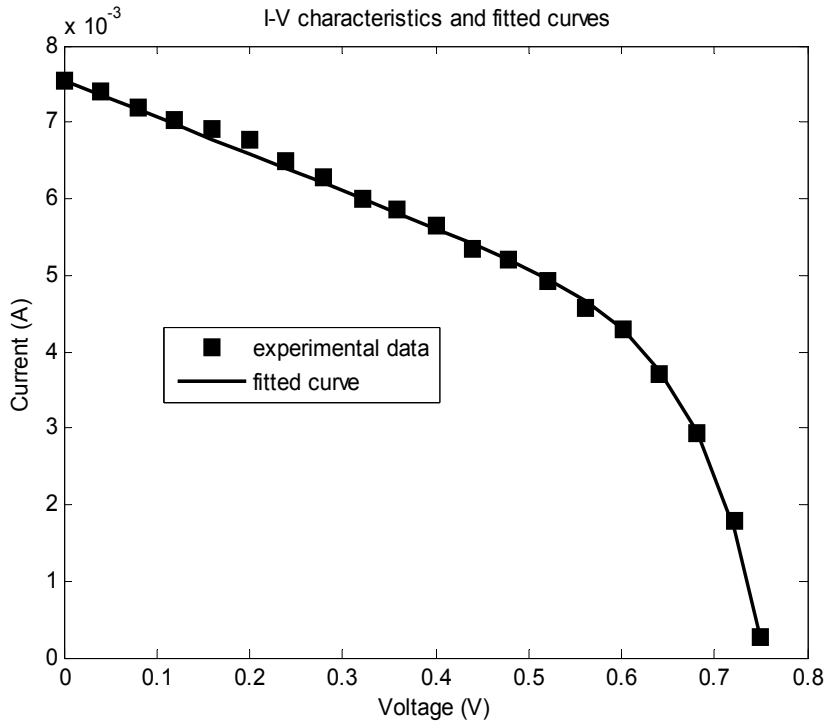
Fig. 5. Experimental data (■) and the fitted curve (-) for the organic solar cell.

## 4.4 Effects of parameters on the shape of the I-V curve

Figures 6-13 show the effect of the series resistance and shunt resistance on the current-voltage (I-V), power-voltage (P-V) characteristics and their effect on the fill factor (FF) and conversion efficiency (η). Change in the shape of the I-V curve due to changes in parameters values. First, as seen in fig.6, the shape of the I-V curve in the voltage source region is depressed horizontally with a gradual increase in the value of series resistance from zero, too, the power conversion decrease with a gradual increase in the value of series resistance. When shunt resistance decreases from infinity, the shape of the I-V curve in the current source region is depressed leftward as shown in fig.10, and the power conversion decrease too. Second, figure 8, 9, 12 and 13 show the effect of the series resistance and shunt resistance on the fill factor (FF) and conversion efficiency (η). Where the fill factor (FF) and conversion efficiency (η) values decrease when the values of series and shunt conductance ($G_{sh}=1/R_{sh}$) increase.
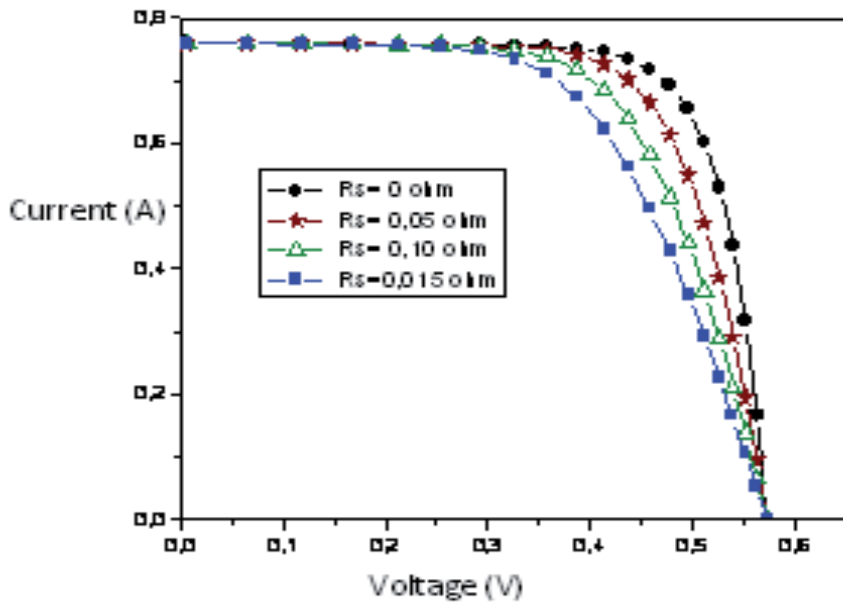
Fig. 6. Effect of series resistance on the I-V characteristics of an illumination solar cell.
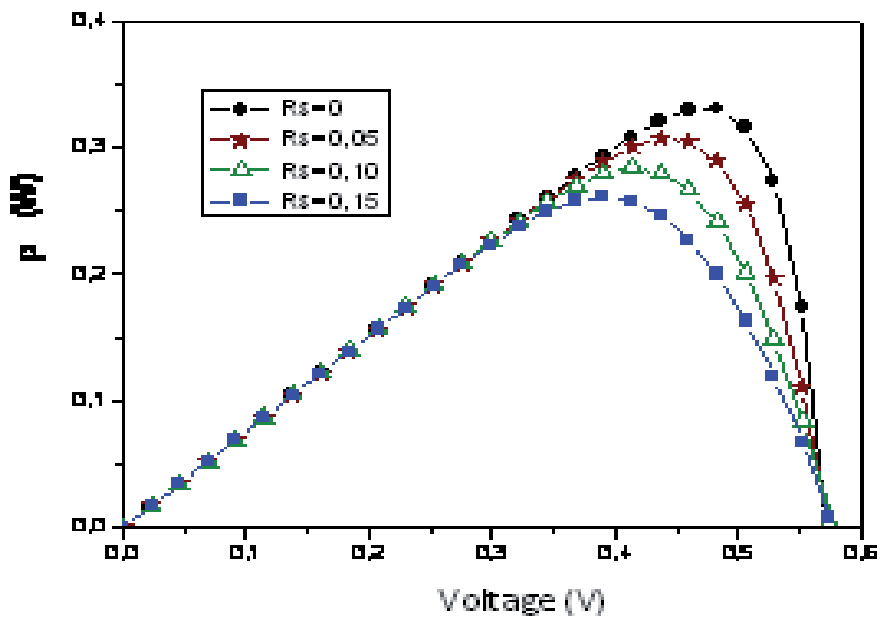


Fig. 7. Effect of series resistance on the P-V characteristics of an illumination solar cell.
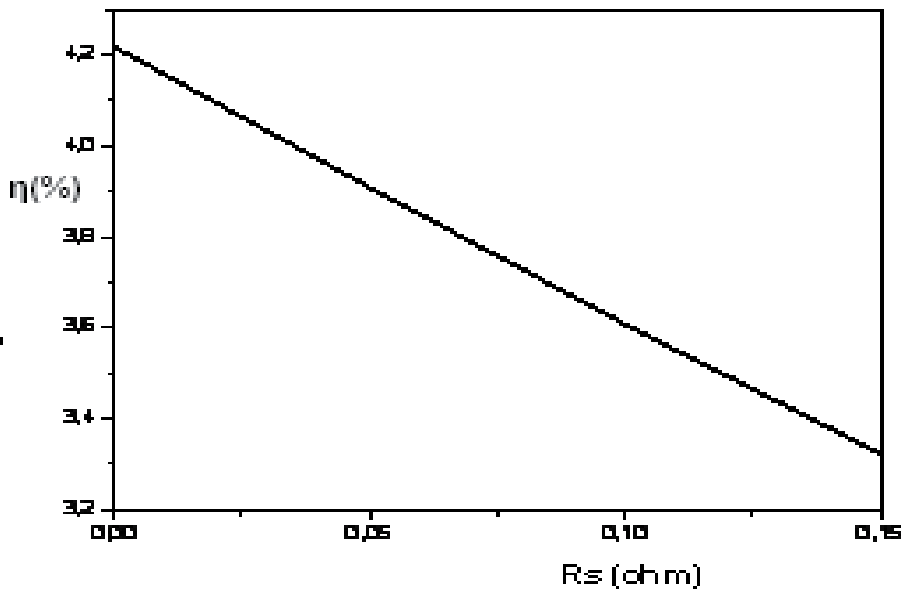
Fig. 8. Effect of series resistance on the η and FF.
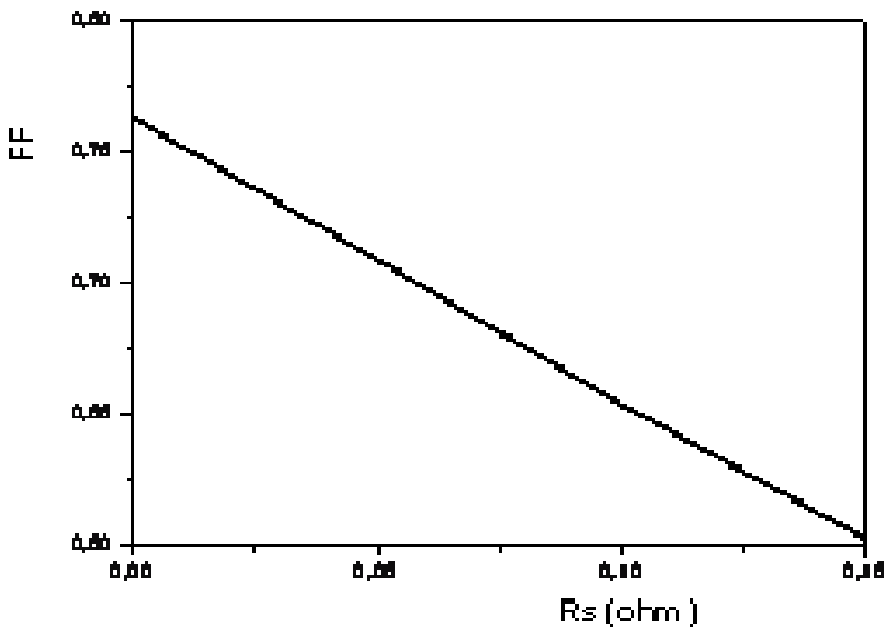


Fig. 9. Effect of series resistance on the η and FF.
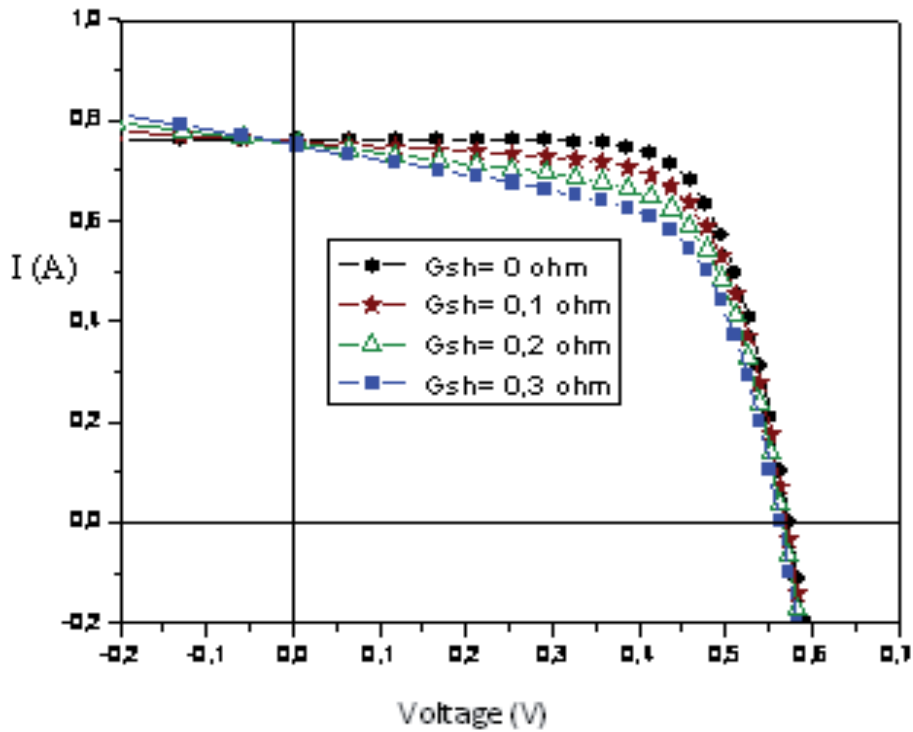
Fig. 10. Effect of shun resistance on the I-V characteristics of an illumination solar.
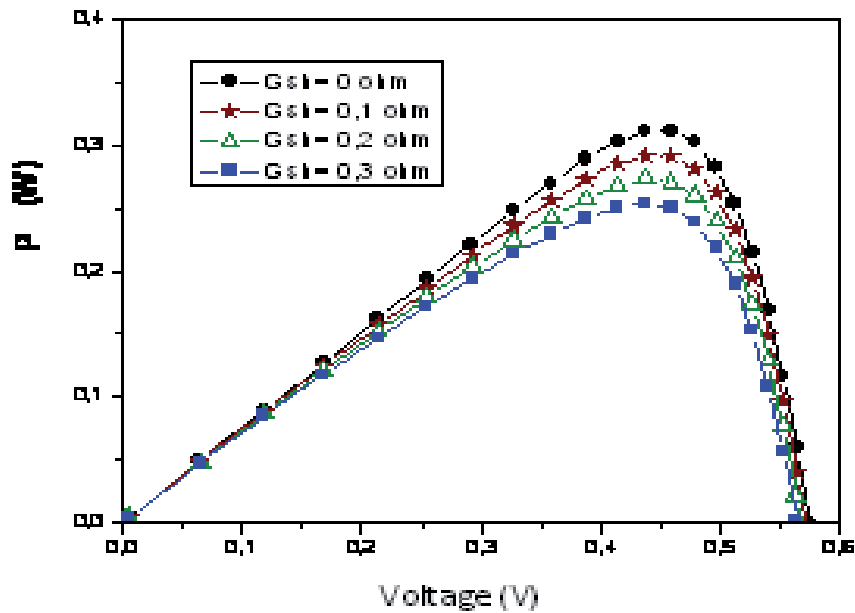


Fig. 11. Effect of shun resistance on the P-V characteristics of an illumination solar.
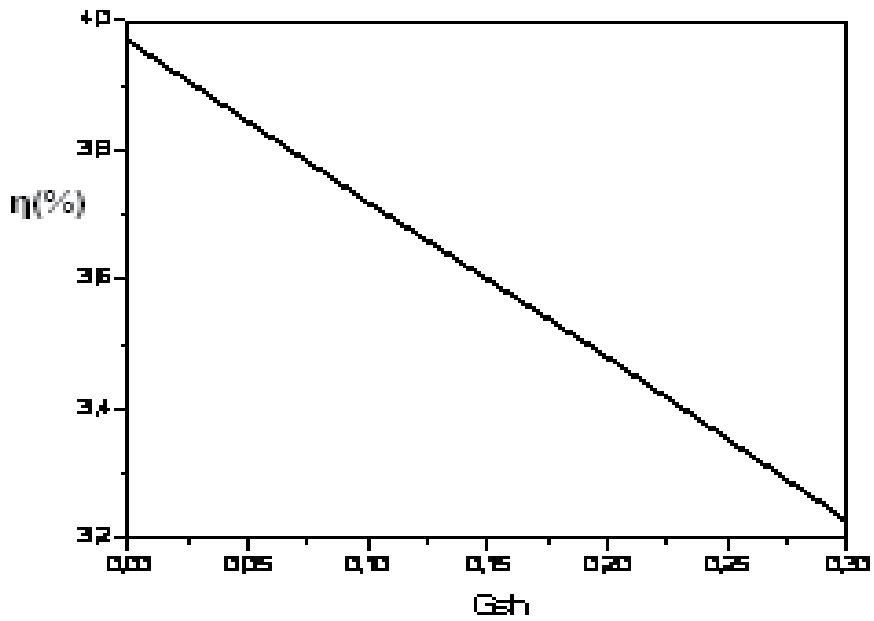
Fig. 12. Effect of shunt resistance on the η and FF.
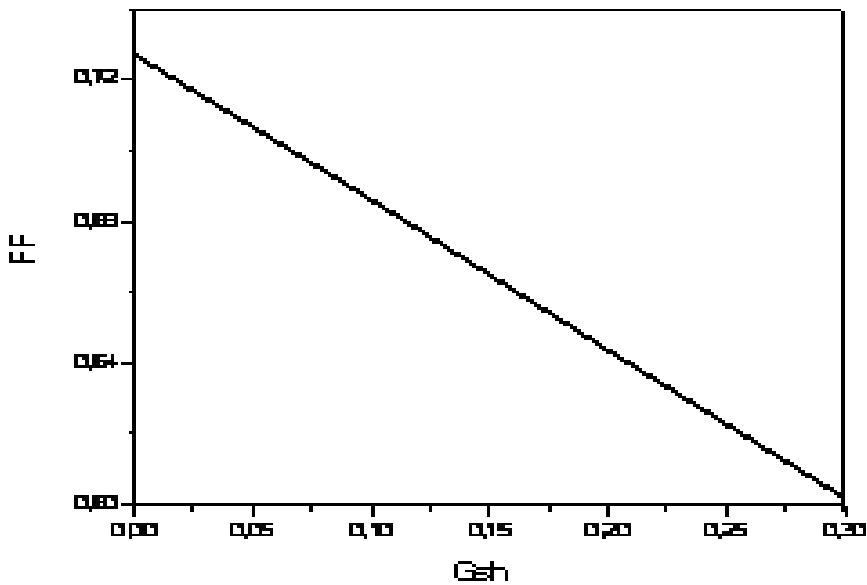


Fig. 13. Effect of shunt resistance on the η and FF.

## 5. Conclusion

This contribution present and analyse a simple and powerful method of extracting solar cell parameters which affect directly the conversion efficiency, the power conversion, the fill

factor and current-voltage shape of the solar cell. These parameters are: the ideality factor, the series resistance, diode saturation current and shunt conductance. This technique is not only based on the current-voltage characteristics but also on the derivative of this curve, the conductance G. by using this method, the number of parameters to be extracted is reduced from five $I_s$, n, $R_s$, $G_{sh}$, $I_{ph}$ to only four parameters $I_s$, n, $R_s$, $G_{sh}$. The method has been successfully applied to a silicon solar cell, a module and an organic solar cell under different temperatures. The results obtained are in good agreement with those published previously. The method is very simple to use. It allows real time characterisation of different types of solar cells and modules in indoor or outdoor conditions.

## 6. References

Bashahu, M. & Nkundabakura,P.(2007) Solar energy. 81 856-863.

Charles, J.P.; Abdelkrim, M.; Muoy, Y.H. & Mialhe,P. (1981). A practical method of analysis of the current-voltage characteristics of solar cells. *Solar cells* 4, 169-178.

Charles, J.P.; Ismail, M.A. & Bordure, G.(1985). A critical study of the effectiveness of the single and double exponential models for I-V characterization of solar cells. *Solide-State electron*. 28 (8), 807-820.

Chegaar, M.; Ouennoughi, Z. & Guechi,F.(2004). Vacuum. 75, 367–72.

Chegaar, M.; Ouennoughi, Z. & Hoffmann, A.(2001). *Solid-state Electronics*. 45, 293- 296.

Chegaar, M.; G. Azzouzi, Mialhe,P.(2006).*Solid-state Electronics*. 50, 1234-1237.

Datta, S.K., mukhopadhyay K., Bandopadhyay, S. & Saha, H.(1967), Solid-State Electron, 192, 35.

Easwarakhanthan, T.; Bottin, J.; Bouhouch,I. & Boutrit, C.(1986) *Int. J. Solar Energy*.4, 1-12.

Ferhat-Hamida, A.; Ouennoughi, Z.; Hoffmann, A.&Weiss,R.(2002), *Solid-State Electronics*. 46, 615–619.

Haouari-Merbah,M.; Belhamel, M.; Tobias & Ruiz, I. J. M.(2005), *Solar Energy Mater Solar Cells*. 87, 225–33.

Jain,A & Kapoor, A.(2005), *Solar energy mater, solar cells*. 86, 197-205.

Jain., A & Kapoor, A.(2004),*Solar energy mater, solar cells*. 81, 269-277.

Kaminsy, A., Marchand J.J. & Laugier, A.(1997). 26th *IEEE Phot*. Specialist conf.1997.

Nehaoua ,N., Chergui ,Y. , Mekki, D. E.(2010) *Vacuum* , 84 : 326–329.

Ortiz-Conde, A. ; F.J. Garcia Sanchez, F. G. & Muci, J.(2006), *Solar Energy Mater, Solar Cells*. 90, 352–61.

Phang, Jacob. Chan, C. H. & Daniel, S. H.(1986). A review of curve fitting error criteria for solar cell I-V characteristics. *Solar cells* 18, 1-12.

Priyanka, M.; Lal, S.; Singh, N. (2007), *Solar energy material and solar cells*. 91,137-142.

Santakrus Singh,N.; Amit Jain & Avinashi Kapoor.(2009), *Solar Energy Materials and Solar Cells*. 93 (2009) 1423–1426.

Sellami, A., Zagrouba, M. & Boua, M.(2007). Application of genetic algorithms for the extraction of electrical parameters of multicrystalline silicon. *Meas. Sci. Technol*. 18, 1472-1476.

Sze & S.M., Physics of semiconductor devices.(1981), 2nd edn, Wiley, new York, 1981.

Wook kim & Woojin choi.(2010), a novel parameter extraction method for the one-diode solar cell model, solar energy 84, 1008-1019.

Zagrouba, M.; Sellami, A.; M. Bouaicha,M. & Ksouri, M.(2010). Identification of PV solar cells and Modules parameters using the genetic algorithms, application to maximum power extraction. *Solar energy* 84, 860-866.

# Trichromatic High Resolution-LBIC: A System for the Micrometric Characterization of Solar Cells

Javier Navas, Rodrigo Alcántara, Concha Fernández-Lorenzo
and Joaquín Martín-Calleja
*University of Cádiz*
*Spain*

## 1. Introduction

Laser Beam Induced Current (LBIC) imaging is a nondestructive characterization technique which can be used for research into semiconductor and photovoltaic devices (Dimassi et al., 2008). Since its first application to p-n junction photodiode structures used in HgCdTe infrared focal plane arrays in the late 1980s, many experimental studies have demonstrated the LBIC technique's capacity to electrically map active regions in semiconductors, as it enables defects and details to be observed which are unobservable with an optical microscope (van Dyk et al., 2007). Thus, the LBIC technique has been used for research in different fields related to photovoltaic energy: the superficial study of silicon structures (Sontag et al. 2002); the study of grain boundaries on silicon based solar cells (Nishioka et al., 2007); the study of polycrystalline solar cells (Nichiporuk et al., 2006); the study of thin film photovoltaic modules (Vorasayan et al., 2009); the study of non-silicon based photovoltaic or semiconductor devices (van Dyk et al., 2007) and the study of dye-sensitized solar cells (Navas et al., 2009).

In this technique, a highly stabilized laser beam is focused on the photoactive surface of a cell and performs a two-dimensional scan of the photoactive surface, measuring the photoresponse generated point to point. A correlation between the number of incident photons and the quantity of photoelectrons generated derived from the photocurrent measurement makes it possible to obtain the photoconverter efficiency, which is the quantum efficiency of the device at each point of the active surface. Thus, the LBIC technique allows images of photovoltaic devices to be obtained dependent upon superficial variation in quantum efficiency. Usually photocurrent values are measured at short circuit as it is a linear function of the radiation power in a wide range and the interaction coefficient is proportional to the quantum photoefficiency (Bisconti et al., 1997). Three main factors can be associated to the level of photocurrent generated by a photovoltaic surface: (a) the limit values of photon energy that are necessary for electron transfer between valence and conduction bands, (b) the intrinsic characteristics of electron-hole recombination, and (c) photon penetration into the active material.

So, the numerical value of the photoefficiency signal generated at each point is computer stored according to its positional coordinates. Using the stored signal, an image is generated

of the photoconversion efficiency of the surface scanned. It is interesting to note that the whole photoactive surface acts as an integrating system. That is, independent of the irradiated area or its position, the entire photogenerated signal is always obtained via the system's two connectors.

The spatial resolution of the images obtained depends on the size of the laser spot. That is, images generated using the LBIC technique have the best possible resolution when the focusing of the beam on the cell is optimum. Thus, it is essential to use a laser as the irradiation system because it provides optimal focusing of the photon beam on the photoactive surface and therefore a higher degree of spatial resolution in the images obtained. This provides enhanced structural detail of the material at a micrometric level which can be related with the quantum yield of the photovoltaic device. However, the monochromatic nature of lasers means that it is impossible to obtain information about the response of the device under solar irradiation conditions. No real irradiation source can simultaneously provide a spectral distribution similar to the emission of the sun with the characteristics of a laser emission in terms of non divergence and Gaussian power distribution.

Nowadays, there are several LBIC systems with different configurations which have been developed by research groups and allowing interesting results to be obtained (Bisconti et al., 1997). In general, these systems are based on a laser source which, by using different optomechanical systems to prepare the radiation beam, is directed at a system which focalizes it on the active surface of the device. There are two options for performing a superficial scan in low spatial resolution systems: using a beam deflection technique or placing the photovoltaic device on a biaxial displacement system which positions the photoactive surface in the right position for each measurement. The system must incorporate the right electrical contacts, as well as the necessary electronic systems, to gather the photocurrent signal and prepare it to be measured so that an image can be created which is related with the quantum efficiency of the device under study. However, high resolution (HR) spatial systems (HR-LBIC) must use a very short focal distance focusing lens, which prevents deflection systems being used to perform the scan and makes it necessary to opt for systems with biaxial displacement along the photoactive surface.

## 2. LBIC system description

The different components which make up the subsystems of the equipment, such as the elements used for focusing the beam on the active surface, controlling the radiant power, controlling the reflected radiant power, etc., are placed along the optical axis (see Figure 1).

In our system we have used the following as excitation radiation emissions: a 632.8 nm He–Ne laser made by Uniphase ©, model 1125, with a nominal power of 10 mW; a 532 nm DPSS laser made by Shangai Dream Lasers Technology ©, model SDL-532–150T, with a nominal power of 150 mW; and a 473 nm DPSS laser by Shangai Dream Lasers Technology©, model SDL-473–040T, with a nominal power of 40 mW. Each of the lasers is mounted on a system allowing optimal adjustment of the optical pathway, with a predetermined angle between them. In turn, a shutter is placed in the optical pathway of each laser which makes it possible to establish the radiation used in each scan. In order to reduce the laser power to the required values, a continuous neutral density filter is placed next the laser exit windows. The layout of the three lasers enables their beams to come together on a mirror supported on a stepper motor, which being set at a predefined angle makes it possible to direct the

radiation from the selected laser through the whole system's main optical pathway. A Micos SMC Pollux stepper motor controller with an integrated two-phase stepper motor, capable of moving 1.8°/0.9° per step has been used for motor control. Command programming and configuration is executed via a RS232 interface, which allows velocity movement definition, point to point moves, and multiple unit control with only one communication port.
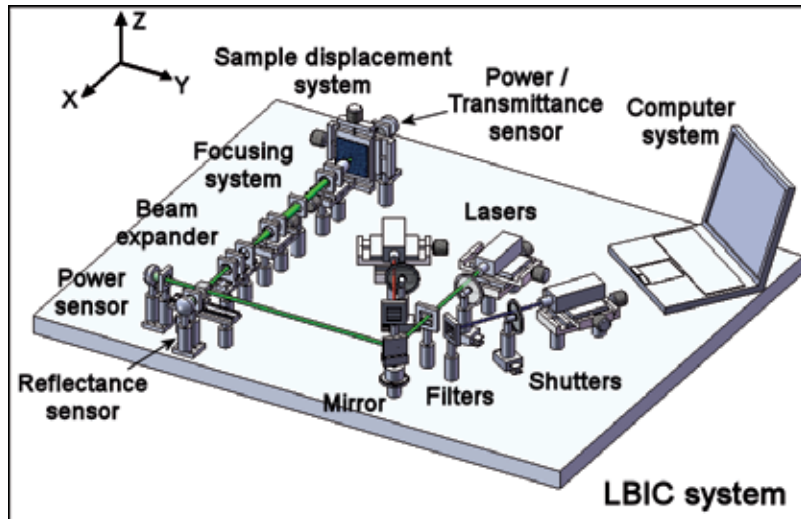


Fig. 1. General outline of the LBIC system.

A highly transparent nonpolarizing beamsplitter, made from BK7 glass with antireflecting coating, has been placed on the optical path. This beamsplitter plays a double role, depending on whether it is working in reflection or in transmission. In reflection, the reflected beam is used for irradiating the sample, whereas the transmitted beam allows one to monitor the stability of the laser power emission by using a silicon photodiode (see Figure 1). By means of the ratio between the induced current and this signal it is possible to obtain a normalized value for the external quantum efficiency.

The optical system between the beamsplitter and the sample works similarly to a confocal system, so that the beam specularly reflected by the sample surface follows an optical path which coincides with the irradiation path, but in the opposite sense. The intensity of this beam that is reflected by beam splitter is measured by a second silicon photodiode which allows one to obtain information on the reflecting properties of the photoactive surface. This information is particularly interesting for the evaluation of the photoconversion internal quantum efficiency. Moreover, when the photovoltaic device under study has a photon transparent support as in dye-sensitized solar cells, the transmittance signal can also be measured (see Figure 1).

This system is most important since an optimum focusing of the laser on the photoactive surface is one of the main limiting factors of the spatial resolution. Any focusing errors will lead to unacceptable results. The focusing system designed consists basically of three subsystems: a focusing lens mounted on a motorized stage with micrometric movement, a beam expander built with two opposing microscope objectives and a calculation algorithm which allows a computer to optimize the focusing process, and which we will analyze in detail later. The spot size at the focus is directly related to the focal distance and inversely

related to the size of the prefocused beam. In this case, the focusing lenses we have used were, either a 16x microscope objective (F:11 mm) or a 10x one (F:15.7 mm), both supplied by Owis GMBH. The beam emitted by the lasers we previously mentioned has a size of 0.81 mm in the $TEM_{00}$ mode, and it has been enlarged up to 7.6 mm by means a beam expander made up of two microscope objectives, coaxially and confocally arranged, with a 63x:4x rate. In order to eliminate as many parasitic emissions as possible, a spatial filter is placed at the confocal point of expander system and the resulting emission of the system is diaphragmed to the indicated nominal diameter (7.6 mm). Focusing with objectives of different magnification values will produce different beam parameters at the focus, affecting the resolution capacity to which photoactive surfaces can be studied.

We have decided to use a system configuration consisting of a fixed beam and mobile sample moving along orthogonal directions (YZ plane) with respect to the irradiation optical axis. The biaxial movement of the photoactive surface is achieved by using a system of motorized stages with numerical control and displacement resolution of 0.5 µm. Special care has been taken to ensure the minimization of the asymmetrically suspended masses so as to avoid the generation of gravitational torsional forces. All optomechanical elements utilized in this system have been provided by Owis GMBH. Moreover, two low ohmic electric contacts are used to extract the electrons generated.

## 3. Focusing algorithm

A $TEM_{00}$ mode laser beam presents a Gaussian irradiance distribution. This distribution is not modified by the focusing or reflecting of the beam by means of spherical optical elements and the irradiance is calculated by means of the expression

$$I(r)=I_0 \cdot \exp\left(-\frac{2r^2}{w^2}\right), \tag{1}$$

where r is the distance from the center of the optical axis and w the so-called Gaussian radius, defined as the distance from the optical axis to the position at which the intensity decreases to $1/e^2$ of the value on the optical axis.

When a monochromatic Gaussian beam is focused, the Gaussian radius in the area near the focus fits the equation

$$w^2(x)=w_0^2\left[1+\left(\frac{\lambda x}{\pi n w_0^2}\right)^2\right], \tag{2}$$

where x is the coordinate along the propagation axis with the origin of coordinates being defined at the focal point, $\lambda$ the wavelength value, n the refraction index of the medium and $w_0$ is the Gaussian radius value at the focus. The latter can be obtained from the expression

$$w_0=\left(\frac{2\lambda}{\pi}\right)\left(\frac{F}{D}\right), \tag{3}$$

where F is the focal distance of the lens and D is the Gaussian diameter of the prefocused beam. For a monochromatic beam, the energy irradiance is proportional to the photon irradiance. As we explained above, in an ideal focusing process, the beam power remains constant, which implies that the number of photons is also kept constant. Assuming that (a) only the photons absorbed can generate electron–hole pairs according to a given quantum yield, (b)

there are no biphotonic processes in normal conditions and (c) the power is low enough as to ignore thermal effects, then we can say that the intensity of the current supplied by the cell must be proportional to the density of incident photons and to the photoconversion efficiency of the cell. This implies that for an ideally homogeneous photoconversion surface, the current intensity generated will be independent of the focusing level, since, except when the size of the beam is larger than the active surface, the total number of photons will be a constant independent of its focusing level. In such a case the measure of current intensity would not be used to judge whether the laser beam is optimally focused.

The situation is quite different if the photoconversion surface has heterogeneities. In that case, the size of the heterogeneity would match the size of the photon beam. The definition of heterogeneity would depend on the type of cell we are working with. In monocrystalline solar cells we may consider the cell's edges or the electron-collecting conducting elements (fingers); in polycrystalline solar cells, in addition to the previously mentioned ones, we may also consider the grain boundaries, the dislocations or any other photoconversion defects and, in dye sensitized solar cells, porous semiconductors density irregularities, dye adsorption concentration, etc. The current $I_{SC}$ generated will depend on the illuminated surface quantum yield average value, which, at the same time is dependant of the spot size and the distribution power. This dependence can be used to optimally focus the laser beam on the active surface.

The basic experimental set-up has been defined before (see Figure 1). According to this diagram, the solar cell or photoelectrical active surface is placed on the YZ plane. Orthogonal to this surface and placed along the X-axis, a laser beam falls on. This laser is focused by a microscope objective lens, which can travel along that axis by means of a computer-controlled motorized stage. In turn, the solar cell is fixed to two motorized stages which allow it to move on the YZ plane, along a coordinate named l so that

$$\Delta l = \sqrt{\Delta y^2 + \Delta z^2} \ . \tag{4}$$

For every position along the l coordinate, a value for the short circuit current is obtained ($I_{SC}$) that is proportional to its quantum efficiency. The graphic representation of $I_{SC}(l)$ versus l gives rise to the so-called $I_{SC}$-curve.

In order to analyze the $I_{SC}$-curve, it is assumed that the photoactive surface is equivalent to an independent set of photoconversion spatial pixels, each one having individual quantum efficiencies in the 0–100% range. These quantum efficiencies can be individually measured only if the size of the laser beam used as probe is equal or lesser than the aforementioned spatial pixels. If the laser beam spot is greater than these basic units, the electric response obtained will be equivalent to the product of the quantum efficiency distribution values of the affected units multiplied by the laser beam geometry photonic intensity.

Figure 2A shows an example of an $I_{SC}$-curve. This one was obtained after performing a scan through a metallic current collector on a Silicon monocrystalline (mc-Si) solar cell. In this case, the laser beam has been focused by means of a 10x microscope objective lens, generating a minimum spot ($w_0$) on the order of 1.2 μm in diameter. Initially, the whole laser spot falls on a high photoconversion efficiency surface, generating a high $I_{SC}$ value, showing small variations caused by little heterogeneities (zone 1), later, when the laser starts to intercept the finger, a gradual $I_{SC}$ decreasing is generated (zone 2). If the collector width is greater than the laser spot diameter, the laser beam must travel through an area in which only a minimum current, associated to the diffuse light, is generated (zone 3). Subsequently the spot will gradually fall again on the photoactive sector (zone 4) until the spot again fully
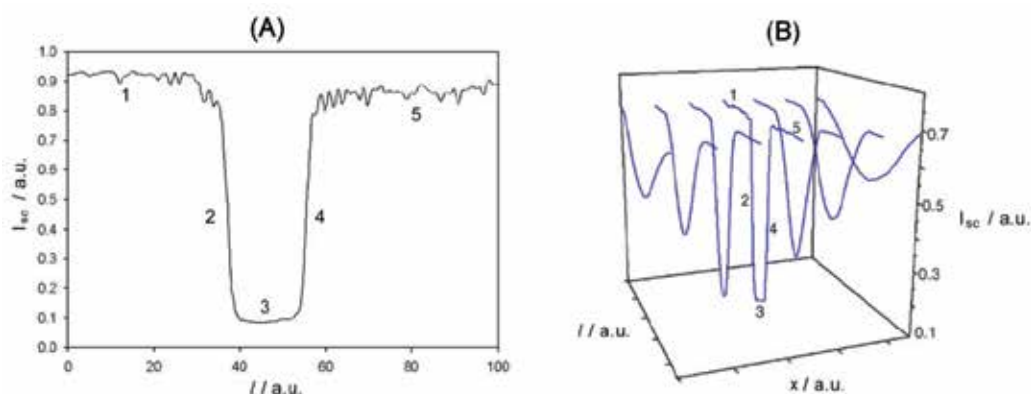
Fig. 2. (A) $I_{SC}$-curve obtained after performing a linear scan along a l superficial coordinate on a Si(MC) solar cell and through a current collector. (B) $I_{SC}$-curve generated at different positions of the focal lens along X-axis.

falls on the high efficiency photoactive surface (zone 5). When the laser is not perfectly focused, the spot size diameter on the surface is larger than $w_0$ and the same scan through the metallic collector generates an $I_{SC}$-curve where signal measured at each position is a mean value of a wide zone. This generates a softer transition between regions with abrupt changes of their quantum efficiencies. In other words, the smaller the spot size, the more abrupt the $I_{SC}$ transition between zones with different superficial photoactivity due to the different photoconversion units are better detected. Figure 2B shows the aforementioned variations of the $I_{SC}$-curve according to the focal lens position. The $I_{SC}$-curve in the center of the figure (numbered as 3) corresponds to that one appearing in Figure 2A, that is, the curve generated when the focal lens is in the optimum focusing position, i.e. the smallest spot size.

### 3.1 Scan methodologies
In order to obtain a data set with information about the optimum focusing position two experimental methodologies can be used. The first one, so called EM1, involves performing successive linear scans along a l coordinate on the photoactive surface, from different $x_f$ focal lens positions. This methodology will lead us to an EM1($I_l$, $x_f$) matrix, whose graphic representation by scan vectors is similar than the one shown in Figure 3B. The second methodology, called EM2, is a particular case of the first one and involves synchronizing the displacement along the l coordinate with the focal lens displacement along the x coordinate. Then, only a vector data set is obtained and it is equivalent to the main diagonal of the aforementioned data EM1($I_l$, $x_f$) matrix, so a substantial reduction in the number of experimental points is achieved. In this case, the evaluation of the EM2($x_f$) data vector is carried out by defining several data subsets of n points of length, ranging from the first point to the total number of points minus n. So, to analyze the previously defined data set, the numerical analysis using derivative function has been used. The purpose is to generate a new data set with a singular point associated to the optimum focusing position. This new data set is named Focal-curve. With this aim, the $I_{SC}$-curve data set properties must be numerically evaluated.

### 3.2 Focal-curve: Derivative analysis

The transition slope between points with different quantum efficiency is defined as the values taken by the $dI_{SC}/dl$ derivative, which is related to the laser beam size. As it has been aforementioned, the smaller the spot size, the more abrupt the $I_{SC}$ transition between points with a different superficial photoactivity and the larger the absolute value of $dI_{SC}/dl$. If the $dl$ is constant, then the derivative can be easily obtained as the $dI_{SC}$.
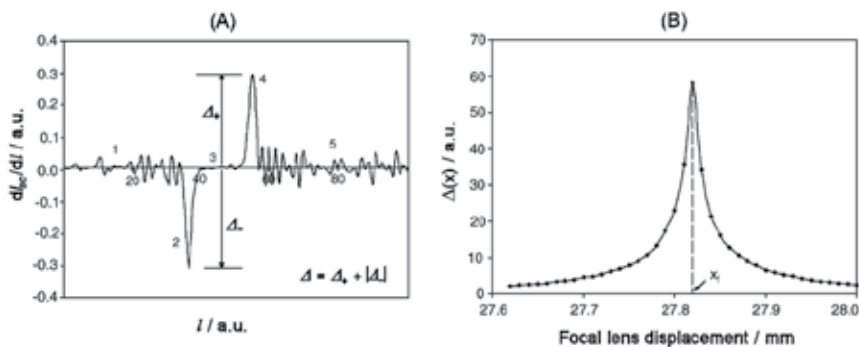


Fig. 3. (A) Numerical derivative of the $I_{SC}$-curve shown in Figure 2A. (B) Representation of the $\Delta$ value versus positions of the focal lens.

Figure 3A shows the derivative of the $I_{SC}$-curve previously shown in Figure 2A in a way that makes possible to recognize the above-mentioned one to five zones. Attention should be drawn to the fact that the absolute maximum values of the derivative are associated to transitions between photoconversion units with greater differential quantum efficiency. From this representation a new magnitude called $\Delta$ can be defined as the absolute difference between the maximum and minimum:

$$\Delta=\Delta_+-\Delta_-=\max\left(\frac{dI_{SC}(l)}{dl}\right)-\min\left(\frac{dI_{SC}(l)}{dl}\right). \tag{5}$$

At this point it is very easy to conclude that, the smaller the spot size (focused laser beam), the higher $\Delta$ value. Then, the representation of $\Delta$ according to the focal lens position, $x$, must result in a Focal-curve showing a peak distribution (Figure 3B). In it, the optimum focusing position, $x_f$, corresponds to that one in which the value of $\Delta$ is the maximum.

### 3.3 Treatment of the Focal-curve

The determination of the $x_f$ position from the Focal-curve can be accomplished by numerical or algebraic methods. In both cases, several artifacts that habitually appear in the Focal-curve obtained as noise, asymmetric contour or multipeaks must be minimized. To diminish the associated noise to each scan point of the Focal-curve, the applying of an accumulation method is the more appropriated way, either to individual points or to full scans. However, the other two artifacts do not show a clear dependence on known procedures. Normally, discerned or undiscerned multilevel photoactive structures can lead to obtain multipeaks and asymmetric contours, but other several circumstances can be cause of them. No particular dependence of these artifacts with the experimental methodology (EM1 or EM2) or with the derivative analysis system has been observed. To apply the numerical method, it

is enough to determine the focal lens position in which the peak distribution shows a maximum, and to associate that value with $x_f$. This is a very quickly methodology but shows significant errors and limitations due to the aforementioned artifacts. The maximum obtainable resolution with this method depends on the incremental value used in the focal lens positioning. A resolution improvement in one order of magnitude implies to measure a number of data two greater orders of magnitude. In the other side, the algebraic method involves adjusting a mathematical peak function to the Focal-curve and then determining $x_f$ as the x value that maximizing the adjusted mathematical peak function. This methodology makes it possible mathematically to determine the maximum of the adjusted curve with as much precision as it is necessary.

In previous tests carried out by means of computerized simulation techniques it was demonstrated that a Pseudo-Voigt type 2 function is one of the peak functions that allows a better adjustment (Poce-Fatou et al., 2002; Fernández-Lorenzo et al., 2006). This function is a linear combination of the Gauss and the Lorentz distribution functions, i.e.

$$V(x)=V_0+V_m\left[sf\frac{2}{\pi}\frac{w_L}{4(x-x_f)^2+w_L^2}+(1-sf)\frac{\sqrt{4ln2}}{\sqrt{\pi}w_G}e^{-(4ln2/w_G^2)(x-x_f)^2}\right], \qquad (6)$$

where $V(x)$ represents the values of $\Delta$, L or $\phi$ according to the position of the focal lens, $w_L$ and $w_G$ are the respectively FWHM (Full Width at Half Maximum) values of the Lorentzian and Gaussian functions, $V_m$ is the peak amplitude or height, sf is a proportionality factor, $V_0$ is the displacement constant of the dependent variable and $x_f$ is the curve maximum position.

With this focusing system and algorithm, a spot size of $7.1 \times 10^{-12}$ m$^2$ is easily obtained.

## 4. LBIC under trichromatic laser radiation: approximation to the solar radiation

Using lasers as the irradiation source is the best solution in LBIC technique as they have a highly monochromatic emission with a quasi parallel beam with minimal divergence and Gaussian power distribution in TEM$_{00}$ mode. These characteristics allow them to be focalized with maximum efficiency. However, using monochromatic radiation beams means that the maps obtained are only representative of the photoefficiency at the wavelength of this type of radiation, and it is not possible to obtain measurements of how the behavior of the system is different at other wavelengths. So, studying the same area with a red-green-blue trichromatic model makes it possible to create characteristic maps associated with each wavelength. Combining them in a suitable way, with irradiation power ratios regulated following a standard emission such as Planck's law or solar emission, makes it possible to approximate to the behavior of the photovoltaic device when it is irradiated with polychromatic radiation, for example, solar emissions. In the literature, it is possible to find a work where LBIC images under solar radiation are obtained (Vorster and van Dyk, 2007). This system uses, as irradiation source, a divergent lamp by which the spot diameter obtained in the focus is about 140 µm and a low spatial resolution can be obtained. So, the methodology that we describe here is a first approach for obtaining high resolution LBIC images that approximate the behavior of a photoactive surface under solar radiation.

The first approach is to assume that the solar emission was blackbodylike with a temperature of 5780 K, as we can assume from literature data (Lipinski et al, 2006). The energy distribution emitted by a black body can be expressed using the Planck's equation

$$Me(\lambda) = \frac{8\pi hc}{\lambda^5} \frac{1}{\exp(hc/\lambda kT)-1}, \tag{7}$$

where h is the Planck constant, c the speed of light, k the Boltzmann constant, T the absolute temperature, and $\lambda$ the wavelength.

With the lasers used in our system, which are described above, in section 2, using Planck's law and setting the initial irradiation power value, the power of the red laser (632.8 nm), as $P_0$, the irradiation power for the other two lasers is calculated to be $1.12P_0$ for both casually. By means of this ratio, the relative powers of the three wavelengths are close to the profile of solar radiation. These three wavelengths are placed in the range of the maximum irradiance in the solar spectrum or black body emission curve, i.e., around the maximum of the energy emission.

## 4.1 Working procedure

The main features for obtaining representative quantum efficiency maps of a photoactive surface are related with the geometry of the system and the different positioning parameters of the optical elements of the system. Furthermore, with the trichromatic system shown in this chapter, it is necessary to take into account the relative irradiation power of the lasers and the unification of the three optical pathways. Thus, the most relevant aspects in the system are considered in the following way:

1. The angle of incidence of the laser must be normal to the photoactive surface in order to minimize the size of the spot. The incidence of the laser beam used perpendicular to the surface can be assured by observing the reflected radiation, the trajectory of which will only coincide with the incident radiation if it is perpendicular to the photoactive surface. Furthermore, this is a necessary condition when trying to obtain reflectance maps correlatable with photoefficiency maps, in accordance with the optical geometry used.

2. The distance between the focal lens and the point of incidence on the surface must remain constant, independent of the laser incidence coordinates over the surface which is derived from the y-z movement of the motorized platform. Thanks to the system being completely automated and controlled by specially designed software, the focusing positions are stored and saved for later use.

3. With the beam selector mirror, the optical trajectory of each of the lasers used must coincide completely with the others, and furthermore, all of them must come into contact on the photoactive surface with the right power to generate radiation resembling that of the black hole, as mentioned earlier.

The bidimensional scans of the surface under study are performed in sequence; first, opening the shutter of the active laser and positioning the mirror; then, setting the focusing lens at the right distance according to the laser to be used; and finally, establishing the irradiation power for each of the lasers. Under these conditions, using the photocurrent values generated in each scan, it is possible to obtain the quantum efficiency values for the device. Thus, using the spectral response, it is possible to obtain a matrix of the external quantum efficiency of the scans performed, following the expression

$$[EQE(\lambda)]_{ij} = [SR(\lambda)]_{ij} \frac{hc}{e\lambda}, \tag{8}$$

where $EQE(\lambda)$ is the external quantum efficiency, $SR(\lambda)$ the spectral response, e the elementary charge, h the Planck constant, c the rate of the light, and $\lambda$ the wavelength.

Taking the definition of the spectral response to be the relationship between the photocurrent generated and the irradiation power, the external quantum efficiency is

$$[EQE(\lambda)]_{ij} = \frac{[I_{SC}(\lambda)]_{ij}}{P_{in}(\lambda)} \frac{hc}{e\lambda}, \tag{9}$$

where $I_{SC}(\lambda)$ is the short-circuit current generated and $P_{in}(\lambda)$ the irradiation power. Likewise, it is also possible to obtain internal quantum efficiency matrixes following

$$[IQE(\lambda)]_{ij} = \frac{[EQE(\lambda)]_{ij}}{1-[R(\lambda)]_{ij}} = \frac{[I_{SC}(\lambda)]_{ij}}{P_{in}(\lambda)} \frac{hc}{e\lambda} \frac{1}{1-[R(\lambda)]_{ij}}, \tag{10}$$

where $IQE(\lambda)$ is the internal quantum efficiency and $R(\lambda)$ is the reflectance.

After calculating the three matrixes of quantum efficiency (internal or external), a colour image can be created reflecting the behaviour of the device under irradiation with the three wavelengths used. To do this, an image analysis program is used which adapts each value of the matrixes obtained to a common scale between 0 and 255 for the three colours red, green and blue; then the three matrixes are combined to obtain a colour image. This image provides information about the behaviour of the material under irradiation with the three wavelengths used.

Furthermore, using the data matrixes obtained, micrometric quantum efficiency values can be obtained which are approximate to those which would be obtained under solar irradiation, as the irradiation power values were set applying Planck's law. Mathematically, according to this approximation, the external quantum efficiency can be expressed as

$$\left[(EQE)_{ij}\right]_{solar} = \frac{hc}{e} \left[ \frac{[(I_{SC})_{ij}]_{632.8nm} + [(I_{SC})_{ij}]_{532nm} + [(I_{SC})_{ij}]_{473nm}}{[P_{in}\lambda]_{632.8nm} + [P_{in}\lambda]_{532nm} + [P_{in}\lambda]_{473nm}} \right], \tag{11}$$

where all the variables have been defined above, and they are expressed for the wavelengths of the laser beam used in each of the scans.

So, the method described in this work investigates the photoresponse of the devices to study at three specific wavelengths. The relative flux distribution of the three wavelengths attempt to match the corresponding wavelengths in the solar spectrum. Obviously, this methodology is an approximation because we attempt to simulate a multispectral radiation as the solar emission with only three specific wavelengths. So, the results obtained will be an approximation to the optoelectrical behavior of the devices under solar illumination.

## 5. Algorithm for improving photoresponse of dye-sensitized solar cells

Dye-sensitized solar cell (DSSC) is an interesting alternative to photovoltaic solar cells based on solid-state semiconductor junctions due to the remarkable low cost of its basic materials and simplicity of fabrication. DSSC technology enables the flexible combination of different substrates (PET, glass), semiconducting oxides, redox shuttles, solvents and dyes (O'Regan and Grätzel, 1991). When a DSSC is illuminated in the range in which the dye absorbs light, the dye molecules are excited to upper electronic states, from which they inject electrons into the conduction band of the semiconductor. The dye molecules become oxidized, whereas the photogenerated electrons diffuse through the semiconductor nanostructure until they are collected by the front electrode. The electrolyte with the redox pair plays the role of a hole conductor, regenerating the oxidized dye molecules and transporting electron acceptors towards the counter electrode. A scheme of a typical DSSC is shown in Figure 4.

Due to the existence of two distinct phases, an electron conducting region and a liquid electrolyte, the electrical response of the device under illumination is not immediate. In contrast, it takes some time (in the order of seconds) before it reaches and keeps its maximum value. This is the socalled characteristic response time. Furthermore, once the irradiation is interrupted, the electrical signal does not disappear instantaneously, but it decays smoothly. This decay time is related to the electron lifetime in the semiconductor (Fredin et al., 2007) and depends on both the trap-limited diffusion transport in the semiconductor (Peter, 2007) and the specific kinetics of the electron transfer reaction in the liquid phase (Gregg, 2004). The decay features in this case can be viewed as a charge/discharge process typical of a capacitor. Rise and decay times should be taken into account when employing techniques to measure quantum yields in DSSCs.
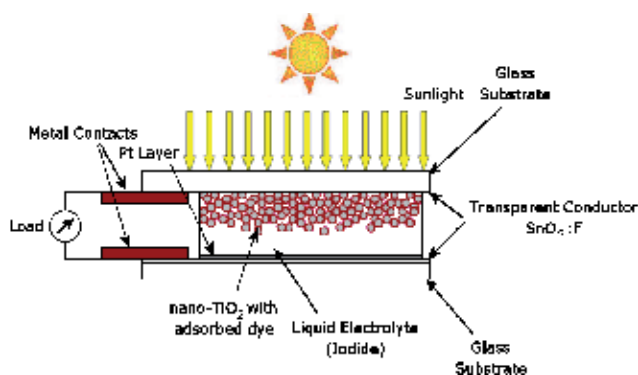


Fig. 4. A scheme of the structure and components of the dye-sensitized solar cells.

The LBIC technique has not been used commonly to characterize DSSCs due to the blurring effect of the slow response of the device to optical excitation and subsequent decay. Hence, to get good spatial resolution the laser beam has to be focused on a very narrow spot. This produces local heating and degradation of the dye/oxide system. This problem can be surmounted by using filters that reduce the light intensity. However, this strategy also reduces the photoconversion signal, which must be amplified to get significant results. Furthermore, as mentioned above, excitation of a single spot requires stopping the scan so that the signal is stabilized properly. This increases the chances of degradation and the time length of the experiment. Hence, a time of 5 s for the rise and decay processes (typical in many DSSCs) implies that to obtain the LBIC signal, we need to (a) irradiate the spot, (b) wait 5 s until the maximum value of the signal (either photocurrent or photovoltage) is achieved, (c) stop the illumination and wait another 5 s until the signal reaches its minimum value and (d) move forward to the next spot and repeat the process. For example, using this procedure we would need 29 days to scan a 500 × 500 $\mu m^2$ cell with 1 µm resolution. In summary, in contrast to silicon solar cells, to obtain clear LBIC images for DSSCs is a difficult task if the standard procedure is used.

Many papers can be found in the literature regarding the response time in DSSCs as a function of the composition and structure of the semiconductor (Cao et al., 1996) and the kinetics of the recombination reaction from open circuit voltage decays (Walker et al., 2006). In this chapter we show an experimental view of the rise and decay signal in DSSCs and the empirical equations that describe their time dependence. Starting from the kinetic constants derived from the experiments, we have devised a mathematical algorithm that makes it possible to correct the photocurrent data so that reliable quantum yields can be extracted.

So, in this chapter, we show a methodology for evaluating and correcting the effects of the charge/discharge processes of DSSCs, enabling clear, high-resolution LBIC images to be obtained without having to increase the scanning time. The methodology is based on a simple, prior evaluation of the time evolution of the photosignal for the charge/discharge processes, before establishing a mathematical algorithm applied point by point over the signal of the cell registered during the LBIC scan, correcting the contribution of previously illuminated points to subsequent ones.
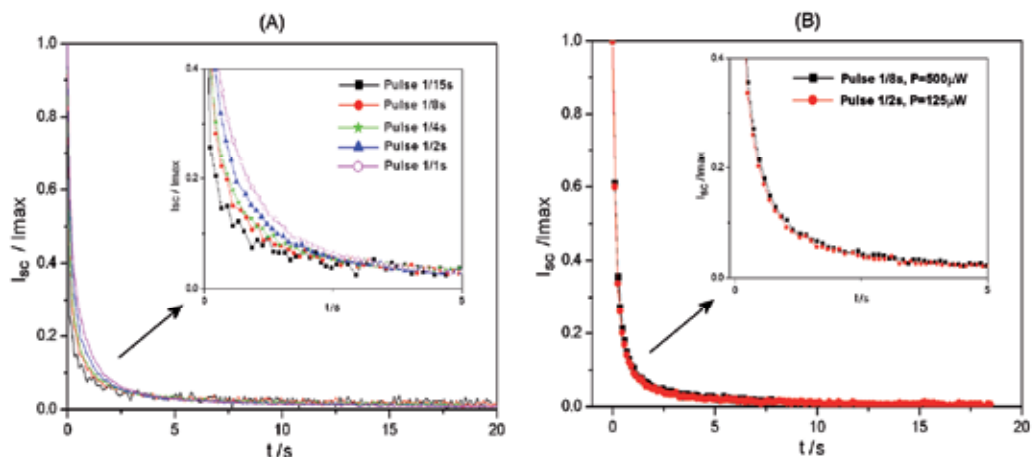


Fig. 5. (A) Time-evolution curve of the discharge process for a cell irradiated with a 532 nm laser, a power of 350 µW, and different exposure times to the radiation. (B) Comparison of two time evolution curve of the discharge process in which the photonic energy is identical but has been generated with different irradiation power and exposure time.

### 5.1 Methodology description

The methodology developed is based on the evaluation of time-evolution curves of the response times for charge/ discharge processes. Based on this, an algorithm corrects the contributions of previous points to the signal of the active one. To perform an LBIC scan within a reasonable time requires dwell times in the order of milliseconds at each point of the scan. This means the system acts as if it were subjected to a set of light pulses, one for each point of the scan. The response of the system depends on the amount of energy received in each pulse. Figure 5A shows time-evolution curves of the photosignal generated by a DSSC at different pulse times using a 532 nm laser and irradiation power of 350 µW. The decay curve is not the same in all cases but rather it depends on the exposure time of the irradiated point. Figure 5B shows two time-evolution curves for the photosignal, one with a 1/8 s pulse and an irradiation power of 500 µW and the other a 1/2 s pulse with an irradiation power of 125 µW so the amount of energy in both cases is constant. This graph shows that the cell behaves the same in both cases, implying that the response during the discharge process of each irradiated point depends on the light energy received. That is, the product of the irradiation power and exposure time. Thus, it is necessary to set the irradiation conditions to be used for performing the scan with the LBIC system in order to obtain the charge/discharge curves of the cell under study under the same conditions.

### 5.1.1 Setting irradiation conditions

Setting the conditions for performing the scan depends on the cell under study, particularly those conditions related to the dwell time of the laser on each point and the amount of energy received. Among these factors are these following considerations: (a) dimensions of the surface to scan, (b) spatial resolution or the distance between points, (c) irradiation power, and (d) dwell time for each point. For the dwell time, the total exposure time must be considered, even when measurements for each point are taken more than once to average the results. From these data the total number of photons affecting each irradiation point can be established with their overall total composing the LBIC image.

### 5.1.2 Determining the time-evolution curves

With the irradiation conditions set, the time-evolution curves for the charge/discharge processes of the cell under study are then developed. To do this, one point of the cell is irradiated with the same amount of photonic energy to be used during the scan. Using a continuous emission laser, irradiation conditions can be established by using a set of neutral density filters and a shutter, such as, for example, the body of a reflex photographic camera. During the selected pulse time, until the system stabilizes, the evolution of the photosignal is recorded. The data obtained for the discharge process are adjusted to a decreasing exponential function following the equation

$$I_{SC} = I_r + I_0 \cdot e^{-A_{SC} t} \, , \tag{12}$$

where $I_{SC}$ is the short circuit photocurrent, $I_r$ is the residual current remaining in the system, $I_0$ is the short circuit steady-state photocurrent, $A_{SC}$ is the rate constant of the discharge process, and t is the time. Using this equation and with specifically designed software, simulations of the photogenerated signal have been developed, which prove the initial hypotheses for the application of this methodology. It is seen that the smaller the rate constant the greater the influence of the discharge process in the LBIC image. Also, it is also concluded that the limit intensity ($I_{lim}$) that the signal of a cell can reach depends on the relationship between the velocity constants of the charge ($A_{SCC}$)/discharge ($A_{SCD}$) process and the short circuit steady-state photocurrent, expressed as

$$I_{lim} = I_0 \frac{A_{SCC}}{A_{SCD}} \, . \tag{13}$$

Furthermore, in most cases, but not always, it is observed experimentally that charge process is faster than the discharge process so the charge process has less influence. In Figure 6A, the charge process lasts about 7 s, while the discharge process takes approximately 16 s. Correcting the charge process effect in the algorithm involves a simple change of scale depending on the response time, calculated with the data of the time-evolution curves and the dwell time. Thus, the correction derived from the charge process, involving multiplying the signal by the correction factor, does not result in a substantial improvement in the quality of the LBIC images. However, it is fundamental for calculating the cell's quantum efficiency. Consequently, the algorithm is based on correcting the contributions of the previously irradiated points, which depend on the discharge process, and correcting the signal level due to the charge process. The time-evolution curves are obtained with the laser beam focalized on one point of the photoactive surface, accepting

that no dependency exists with regards to the position of this point since the discharge process can be associated with the diffusion processes occurring inside the cell.
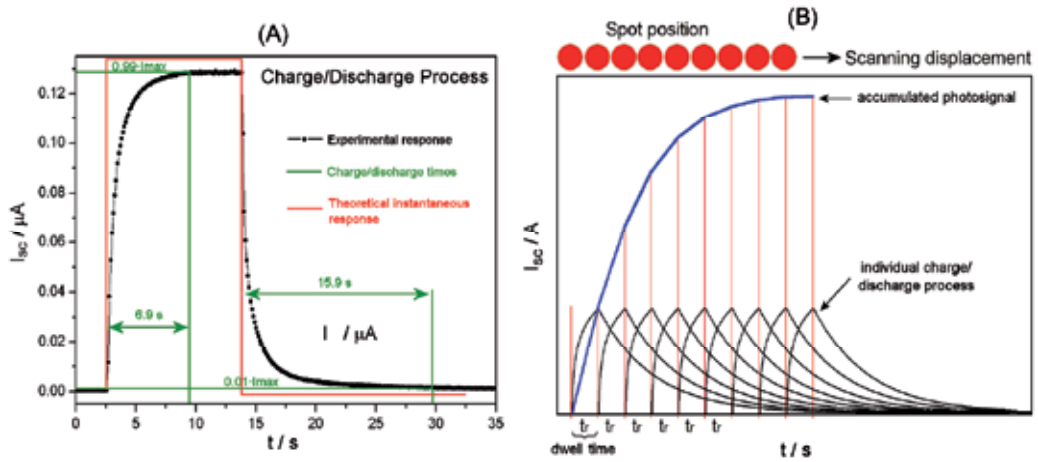


Fig. 6. (A)Representation of experimental data of the charge and discharge process of a cell irradiated with a power of 292 μW, and a comparison with a theoretical instantaneous response. (B) Simulation of the evolution of the irradiated sports showing how the photovoltaic response is influenced by the previously excited points.

### 5.1.3 Correcting the LBIC image

Now, the correction of the discharge process will be describe. From the equation obtained for the cell, the experimental values obtained while taking the LBIC image are corrected, thus eliminating the contribution of the previously irradiated points to the photosignal. The number of points of the scan to be considered as contributing to the signal of one given point is a characteristic of the cell under study and depends on the characteristic parameters of the discharge curve, as is shown in Figure 6B. To evaluate the number of points, the experimental values of the time evolution of the discharge process are adjusted to equation (12), and the time necessary for total discharge is taken as being from when the signal is below 1% of the maximum registered value of the photosignal for that cell in those measuring conditions. With this time, and the dwell time, it is possible to obtain the number of points that have to be considered as contributing to the signal measured and whose contribution has to be corrected to apply the correction to the original image. The extent of this contribution is established using equation (12) and the adjustment parameters obtained, depending on the time passed since a point has been irradiated.

Thus, the real photocurrent signal generated by the irradiated point of the cell is defined as the difference between the photocurrent measured ($I_m$) and the contribution of the previously irradiated points. This is expressed mathematically using the equation

$$I_{SC}=I_m-\sum_{i=1}^{i=n}\left(I_r+I_0 \ e^{-A_{SC}it_r}\right)=I_m-nI_r-I_0\sum_{i=1}^{i=n}e^{-A_{SC}it_r} \ , \tag{14}$$

where $I_{SC}$ is the real short circuit photocurrent generated at the active point, $I_m$ is the signal measured at that active point during the LBIC scan, n is the number of previously irradiated points to consider, $t_r$ is the dwell time; the other variables have been defined above.

## 6. Applications

In order to test the system described here, LBIC scans were performed on various samples. We show results obtained using three different kind of solar cells such as a polycrystalline silicon solar cell, an amorphous thin film silicon solar cell, and a dye-sensitized solar cell.

### 6.1 Polycrystalline silicon solar cell

We include the results obtained with a polycrystalline silicon solar cell manufactured by ISOFOTON, S.A. Different studies were carried out on this device with differing degrees of resolution. Groups of the scans performed with the three lasers are shown below.
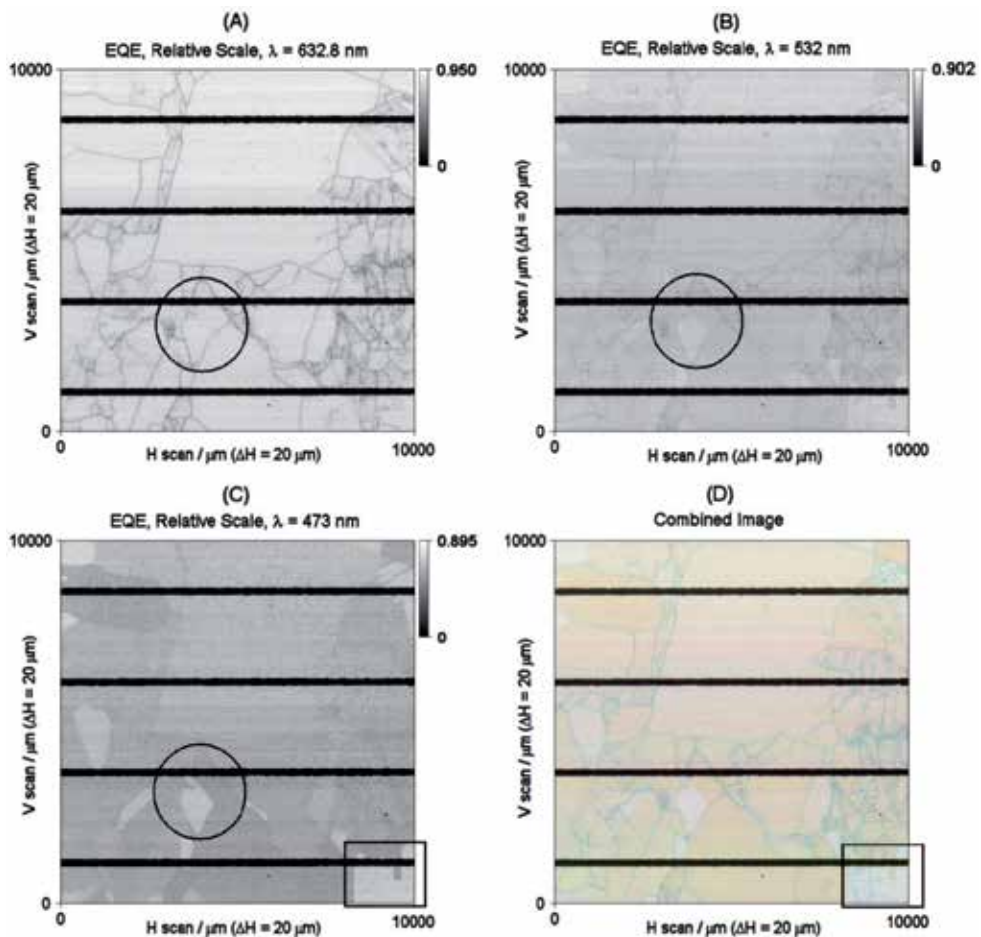


Fig. 7. LBIC images of the three scans performed and the image created by combining these. The data used to construct these images are of EQE on a relative scale for each image.

First, LBIC scans were carried out with the three lasers mentioned above on a 1x1 cm² area of the surface of the cell with a resolution of 20 μm. The irradiation power for the red laser was 5 μW, and 5.6 μW for the green and blue ones. These values comply with the emission of a blackbody at 5780 K, in accordance with Planck's law (equation (7)). Figure 7 shows the

images obtained for the three scans, each one using EQE data on a relative scale. That is, a scale of greys is used which are between the maximum and minimum EQE for each of the images (A-B-C). From Figure 7 it is possible to observe that the conversion of the device depends on the irradiation wavelength used. Macroscopically, a greater quantum efficiency, or photoconversion, is observed when the cell is irradiated with the red laser. This can be seen clearly in Figure 7D, a combined image using those obtained in the scans with each of the lasers, and in which the colour red is seen to dominate most of the image. There are regions where red is not the predominant colour (e.g. the area shown with a square), due to the conversion being greater for one of the other lasers. However, the conversion with blue radiation is similar to that obtained with red. Microscopically, differences can be seen in the scans performed depending on the wavelength used, such as in the area marked with a circle in the images in Figure 7. Furthermore, the maximum and minimum EQE values in each scan are shown in table 2. From these values, an increase in conversion of between 5 and 6 % can be seen in the scan performed with the red laser (632.8 nm) compared with those carried out with the green (532 nm) and blue (473 nm) lasers, just as we had concluded qualitatively before from a simple visual observation.

| λ / nm | EQE | | λ / nm | EQE | |
|--------|---------|---------|-----------------------------|---------|---------|
|        | Maximum | Minimum |                             | Maximum | Minimum |
| 632. 8 | 0.950   | 0       | 473                         | 0.895   | 0       |
| 532    | 0.902   | 0       | Approximation to sunlight   | 0.917   | 0       |

Table 1. Maximum and minimum EQE values for the scans performed and the image obtained as an approximation to solar irradiation.
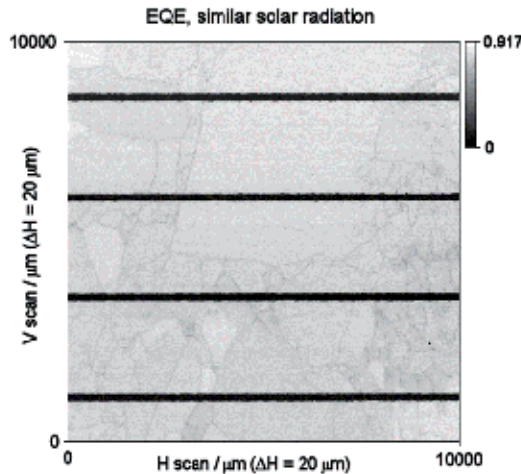


Fig. 8. EQE image approximated to solar radiation using equation (12).

Also, from equation (11) it is possible to obtain EQE values which should be an approximation of the result which would be reached if the device were subjected to solar radiation (see figure 8). The maximum and minimum values obtained are shown in table 1. It is observed that the maximum EQE value for the image constructed with the approximation to solar irradiation is among the maximum values for the three scans

performed. In turn, using the EQE values, an image was constructed using the procedure described which approximates the behaviour of the cell under solar radiation.



Fig. 9. LBIC images of the three intermediate resolution scans performed using EQE values on a relative scale for each image and the combined image using all three.

Secondly, scans are shown which were performed on a small surface area, but with greater resolution. The surface area scanned was 2x1.5 mm² with a resolution of 5 μm. The irradiation conditions were the same as those described above. Figure 9 shows the three scans performed, as well as the combined image. In this figure it is possible to observe small differences in the photoelectric properties of the device depending on the laser used. In the area marked with a circle two clearly distinct regions of differing quantum efficiency can be observed with the green and blue lasers, something which does not happen with the red laser. This difference in efficiency between the two zones becomes more pronounced as the wavelength is reduced. In other words, the depth of penetration decreases, and so we can conclude that this difference in efficiency is due to an artefact on the surface of the cell. It is also possible to observe that the definition of the grain boundaries depends on the wavelength used to do the scan, with the longer wavelength (red laser) leading to better definition, while with the blue laser (shorter wavelength) the grain boundaries can hardly be seen. We will study in greater detail below the differences which can be observed in the grain boundaries depending on the wavelength of the laser.

The maximum and minimum EQE values in each scan are shown in table 2. From these values, greater conversion can be observed in the scan performed with the red laser compared with those performed with the green and blue ones.

| λ / nm | EQE | | λ / nm | EQE | |
| --- | --- | --- | --- | --- | --- |
| | Maximum | Minimum | | Maximum | Minimum |
| 632. 8 | 0.881 | 0.286 | 473 | 0.860 | 0.308 |
| 532 | 0.872 | 0.234 | Approximation to sunlight | 0.873 | 0.284 |

Table 2. Maximum and minimum EQE values for the 2x1.5 mm² scans and those which would be obtained as an approximation to solar irradiation.
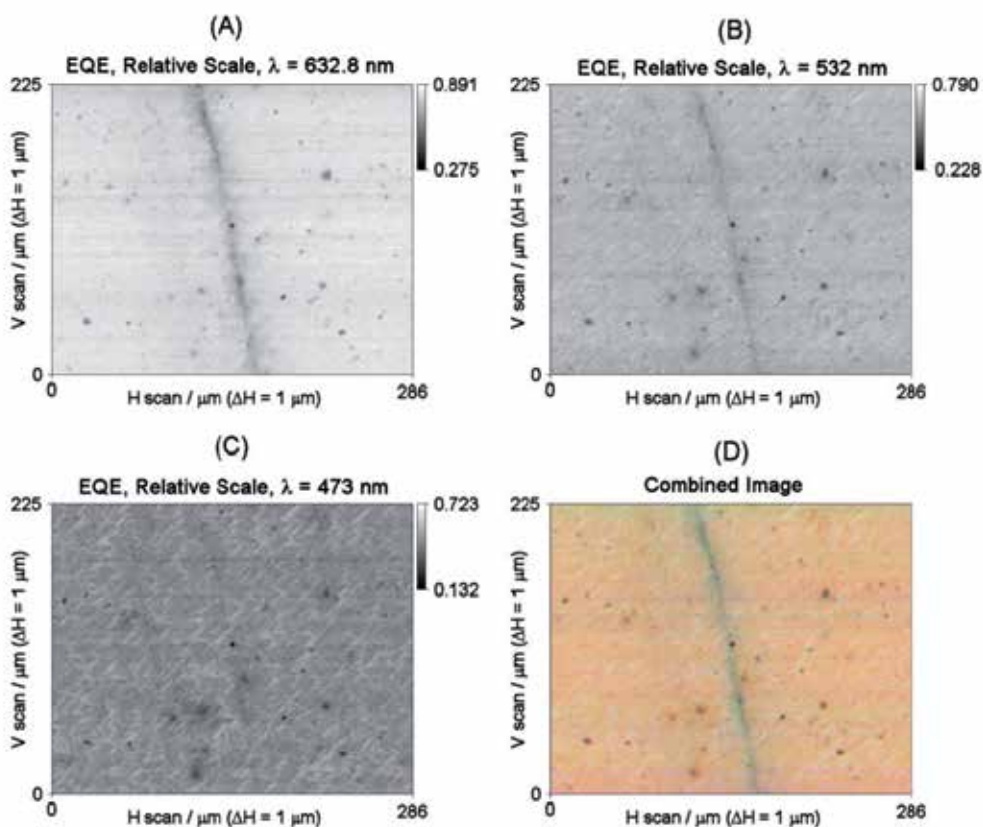


Fig. 10. LBIC images obtained of the three high resolution scans (1 μm) performed using EQE values on a relative scale for each image and the combined images using all three.

Thirdly, high resolution scans were performed. The scans covered a surface area of 286x225 μm², and were performed with a spatial resolution of 1 μm. The irradiation conditions were those described above for the two previous examples. Figure 10 shows the images obtained from the three scans performed. In the images obtained with the red laser, a perfectly defined grain boundary can be observed. On the other hand, this grain boundary is practically impossible to see in the scan performed with the blue laser due to the

difference in the absorption coefficient, which depends on the irradiation wavelength and thus in the difference in the depth of penetration. The green laser provides results halfway between the others. If we wanted to obtain information about carrier diffusion lengths from the grain boundary, the results would differ depending on the irradiation wavelength used. Figure 11 shows the profiles that would be obtained for each scan. These profiles have been obtained as an average of all the horizontal profiles of the scans performed and setting the minimum photocurrent value on the grain boundary common to all the profiles of each scan. Thus, it can be observed that the LBIC signal is influenced in a larger region from the grain boundary as the wavelength increases. These profiles could make it possible to obtain diffusion length values, for example by following the model presented by Yagi et al. using the analysis of the electrical properties of grain boundaries in polycrystalline silicon solar cells (Yagi et al. 2004). But as Figure 11 shows, it would be necessary to bear in mind the irradiation source used.
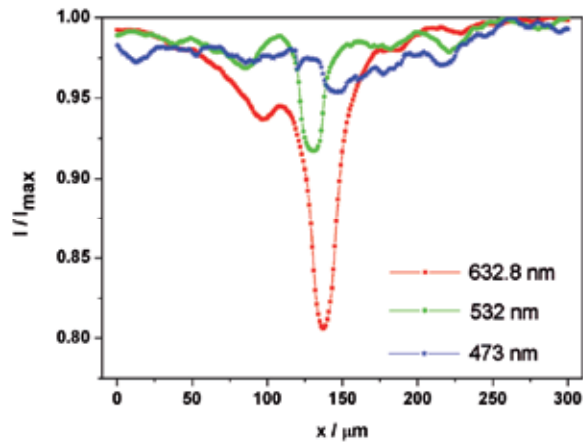


Fig. 11. Average LBIC signal profiles obtained for each of the three high resolution scans performed of a grain boundary.

## 6.2 Amorphous thin film silicon solar cell

We include the results obtained with an amorphous thin film silicon solar cell manufactured by GADIR SOLAR, S.A. LBIC scans were carried out with the three lasers on a 350x350 μm² area of the surface of the cell and were performed with a spatial resolution of 1 μm. The irradiation power for the red laser was 335 μW and 375 μW for the green and blues ones. These values comply with the emission of a blackbody at 5780 K, in accordance with Planck's law. Figure 12 shows the images obtained for the three scans, each one using EQE data on relative scale (maximum and minimum EQE for each of the images A-B-C). The scanned surface is the zone where the solar cell has been marked by laser ablation in order to separate the different cells that make up the solar cell. In the Figure 12 we can see that the laser marking is composed of three lines made point by point with different diameter which leads to the width and depth of each line is different. In the images obtained using the red laser, the three lines are perfectly defined, but it is difficult to see in the scans performed with other two lasers. In turn, macroscopically, greater quantum efficiency is observed
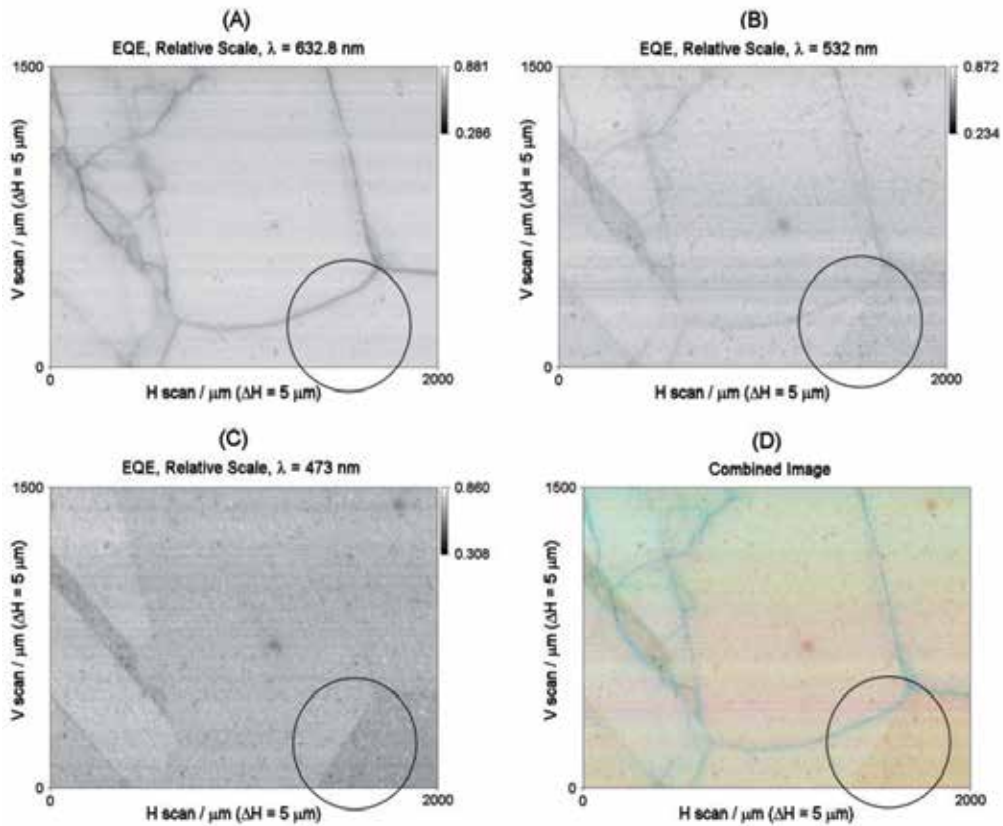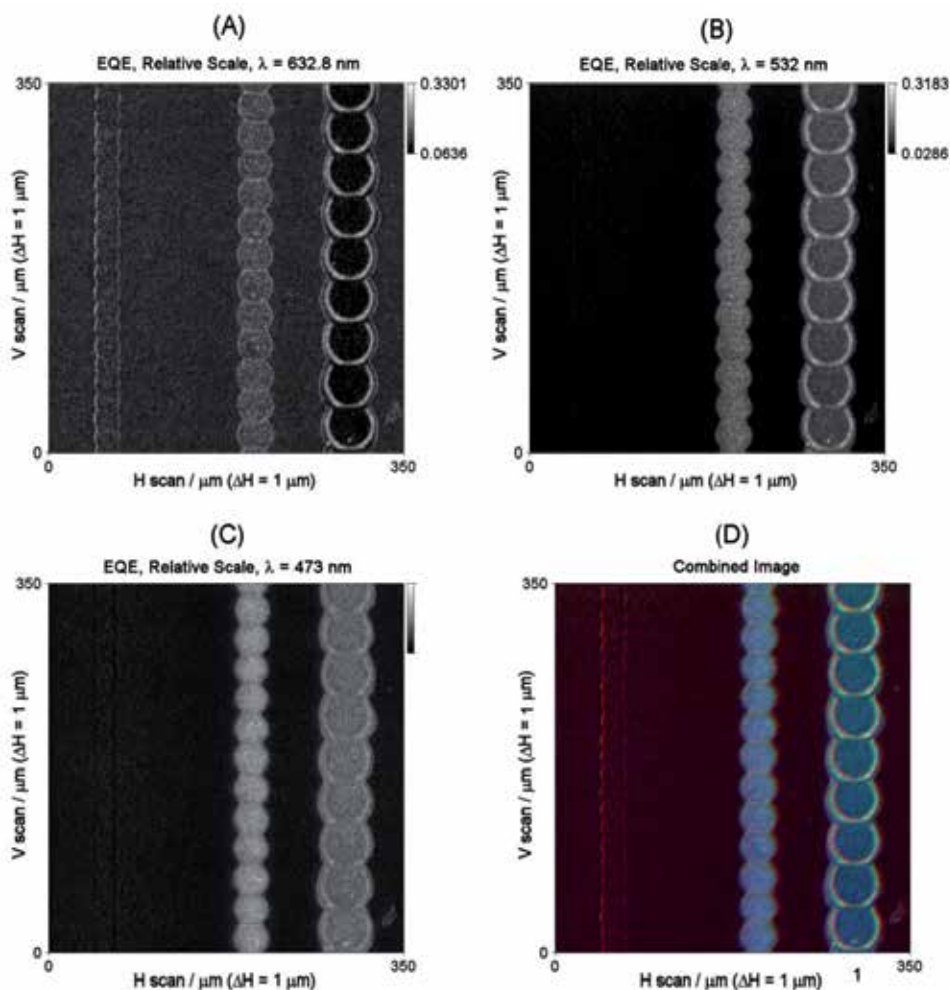
Fig. 12. LBIC images of the three high resolution scans performed using EQE values on a relative scale for each image and the combined image using all three.

when the cell is irradiated with the red laser. This can be seen clearly in Figure 12D, a combined image using those obtained in the scans with each of the lasers, and in which the color red is seen to dominate most of the image. In the zone inside of two of the lines, the red color is not predominant, due to the conversion being greater for one of the other lasers.

| $\lambda$ / nm | EQE | | $\lambda$ / nm | EQE | |
| | Maximum | Minimum | | Maximum | Minimum |
| --- | --- | --- | --- | --- | --- |
| 632. 8 | 0.330 | 0.064 | 473 | 0.303 | 0.011 |
| 532 | 0.318 | 0.029 | Approximation to sunlight | 0.237 | 0.048 |

Table 3. Maximum and minimum EQE values for scans of an amorphous thin film silicon solar cell and those which would be obtained as an approximation to solar irradiation.
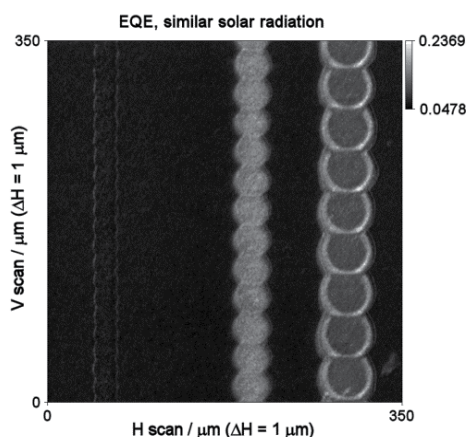
Fig. 13. EQE image approximated to solar radiation using equation (14) for an amorphous thin film silicon solar cell.

The maximum and minimum EQE values in each scan are shown in table 3. From these values, a decrease in conversion of 4 and 8 % can be seen in the scans performed with green laser and blue one, respectively. From equation (11) it is possible to obtain EQE values which should be an approximation of the result which would be reached if the device were subject to solar radiation. The maximum and minimum EQE values in this case are shown in table 4. In turn, an image using EQE values approximated to solar radiation has been constructed using the procedure describes previously. This image is shown in Figure 13.

## 6.3 Dye-sensitized solar cell

The dye-sensitized solar cell used in this chapter was made by authors following the next procedure: Two fluorine-doped tin dioxide coated transparent glass plates (2x2 cm² sheet resistance ~ 15 Ω square⁻¹) supplied by Solaronix were used as the electrode and counter-electrode. Using nanoparticulated $TiO_2$ with a nominal particle size of 25 nm, supplied by Degussa Co., a paste was developed using nitric acid and ethanol at a proportion of 1:3.25. A thin layer of paste was deposited on the electrode plate using the doctor blade method and sintered at 450 °C for 1 h. The thickness of the $TiO_2$ films was 9±0.5 μm. A mixture of 0.5$M$ 4-tert-butylpyridine, 0.1$M$ lithium iodide, and 0.05$M$ iodine in 3-methoxypropionitrile as a solvent, was used as an electrolyte. A catalytic layer of Pt was deposited on the counter-electrode by decomposing a superficially sprayed solution of 0.01$M$ $H_2PtCl_6$ in 2-propanol at 380 °C. Finally, the electrode plate with the sintered layer of $TiO_2$ was immersed in dye solution. The dye used was an ethanolic solution of Ru535 (formerly known as N3, $C_{26}H_{20}O_{10}N_6S_2Ru$).

LBIC scans were carried out with the three lasers mentioned above on a 300x300 μm² area of the surface of the cell and were performed with a spatial resolution of 1 μm. In accordance with Planck's law, the irradiation power for the red laser was 6.62 μW, and 7.41 μW for the green and blues ones. First, the photocurrent values obtained from the three scans were corrected using the algorithm described in section 5. The LBIC images built from photocurrent values measured are shown in Figures 14A, 15A and 16B for lasers red, green and blue, respectively. The images built using the corrected values are shown in Figures

14B, 15B and 16B. In turn, in Figures 14-16 the histograms of the photocurrent values, in both cases, are shown. In these histograms, for the three lasers, it is observed that the measured photocurrent values are higher than the photocurrent values obtained after applying the algorithm. This is obvious because each measured point of the cells has contributions from the previously irradiated (an effect that can be easily observed in Figure 6). The corrected images (Figures 14B, 15B, and 16B) display improvement in clarity. These improvements can be easily observed in the scans made with the red laser, where the artefacts in the surface of the cell can be seen with better definition.

From the values corrected and using the equation (11) the values of EQE can be obtained for each scan. Figure 17 shows the image obtained applying the algorithm described to obtain images which would be obtained as an approximation to solar irradiation. From this image, the maximum and minimum values of EQE are obtained. These values are shown in table 4.

| $\lambda$ / nm | EQE | | $\lambda$ / nm | EQE | |
| | Maximum | Minimum | | Maximum | Minimum |
|---|---|---|---|---|---|
| 632. 8 | 0.309 | 0.096 | 473 | 0.265 | 0.110 |
| 532 | 0.253 | 0.100 | Approximation to sunlight | 0.276 | 0.102 |

Table 4. Maximum and minimum EQE values for scans of a dye-sensitized solar cell and those which would be obtained as an approximation to solar irradiation.
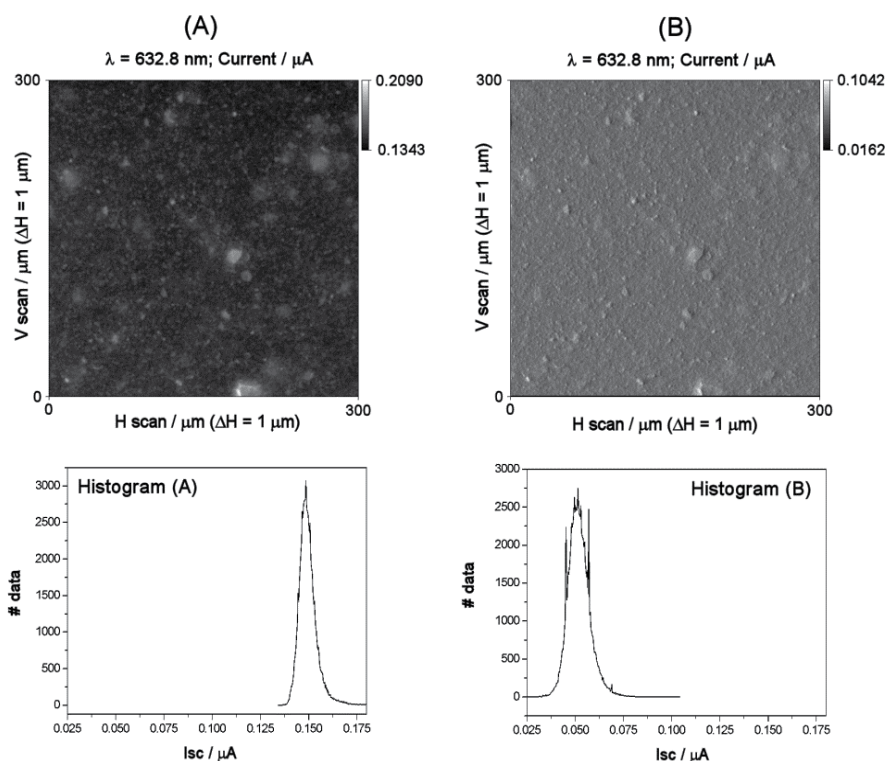


Fig. 14. (A) LBIC image for the DSSC using red laser. (B) The same image modified using our algorithm.
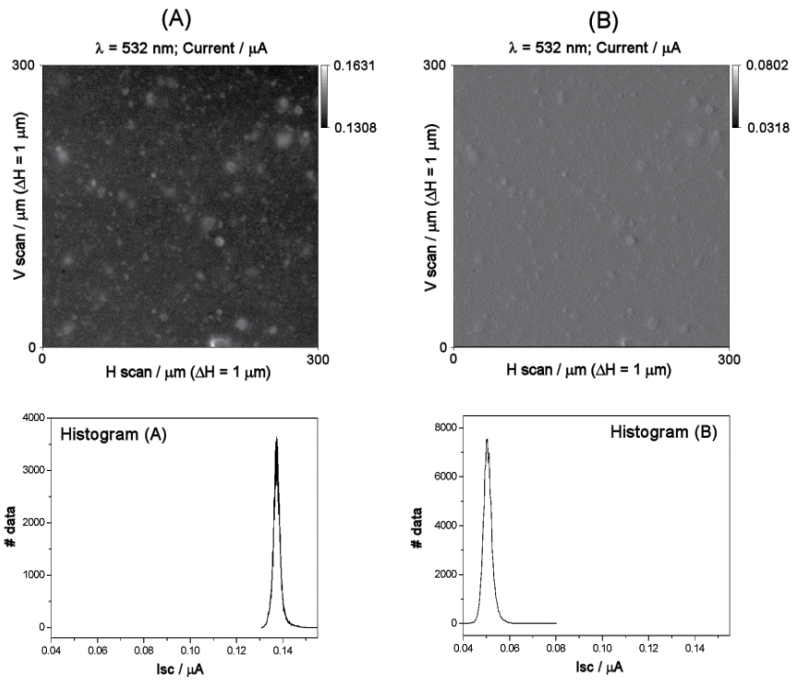
Fig. 15. (A) LBIC image for the DSSC using green laser. (B) The same image modified using our algorithm.
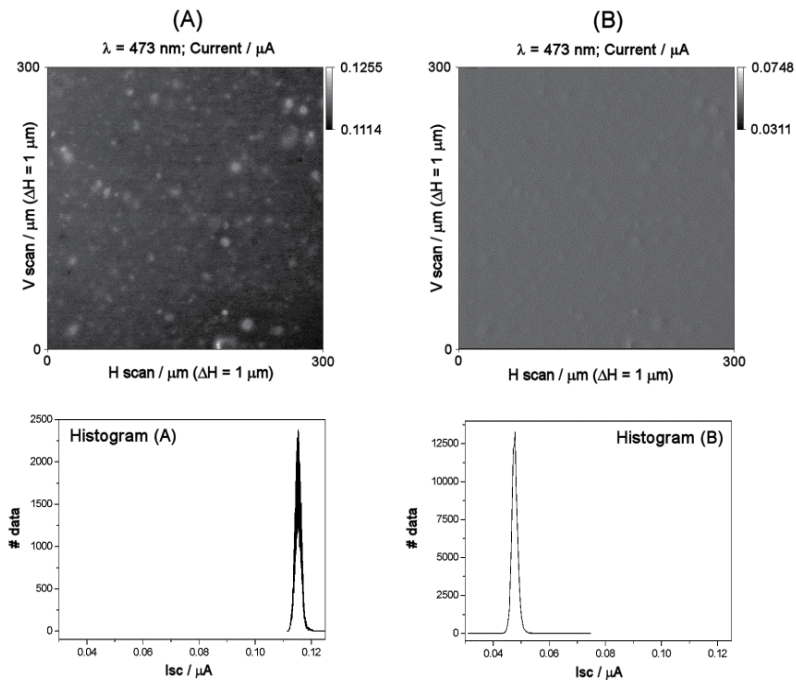


Fig. 16. (A) LBIC image for the DSSC using blue laser. (B) The same image modified using our algorithm.
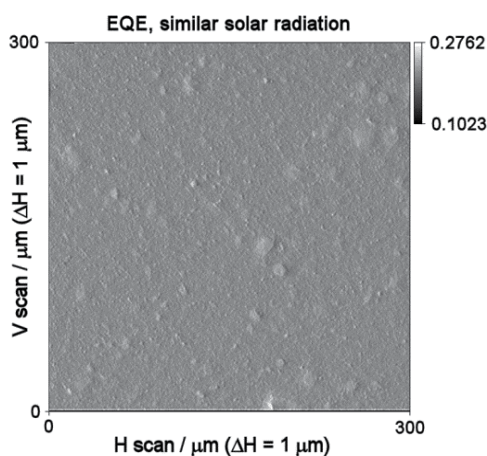
Fig. 17. EQE image approximated to solar radiation for a dye-sensitized solar cell.

## 7. Conclusions

We have described the fundamentals of computer-controlled equipment for scanning the surface of photovoltaic devices, which is capable of obtaining simultaneously LBIC, and specular reflection/transmittance based images. Several algorithm included in the system have been described. These ones are: (a) the algorithm for focusing the laser beam over the photoactive surface in order to obtain high resolution LBIC images; (b) the algorithm for obtaining images which are approximated to the behavior of photovoltaic devices under solar irradiation conditions, and (c) we have showed the algorithm for improving photoresponse of dye-sensitized solar cells. In turn, we have showed results obtained using three different kinds of solar cells such as a polycrystalline silicon solar cell, an amorphous thin film silicon solar cell, and a dye-sensitized solar cell. In this way, we have tested the goodness of our LBIC system for studying different photovoltaic devices.

## 8. References

Bisconti, R.; Kous, R.A.; Lundqvist, M. & Ossenbrink, H.A. (1997). ESTI scan facility. *Solar Energy Materials & Solar Cells*, Vol.48, No.1-4, (November 1997), pp. 61-67, ISSN 0927-0248.

Cao, F.; Oskam, G.; Meyer, G.J., Searson, P.C. (1996). Electron transport in porous nanocrystalline $TiO_2$ photoelectrochemical cells. *Journal of Physical Chemistry B*, Vol. 100, No.42, (October 1996), pp. 17021-17027, ISSN 1520-6106.

Dimassi W.; Bouaïcha, M.; Kharroubi, M.; Lajnef, M.; Ezzaouia, H. & Bessais, B. (2008). Two-dimensional LBIC and internal quantum efficiency investigations of porous silicon-based gettering procedure in multicrystalline silicon. *Solar Energy Materials & Solar Cells*, Vol.92, No.11, (November 2008), pp. 1421-1424, ISSN 0927-0248.

Fernández-Lorenzo, C.; Poce-Fatou, J.A.; Alcántara, R.; Navas, J.; Martín, J. (2006). High resolution laser beam induced current focusing for photoactive surface

characterization. *Applied Surface Science*, Vol.253, No.4 (May 2006), pp. 2179-2188, ISSN 0169-4332.

Fredin, K.; Nissfolk, J.; Boschjloo, G.; Hagfeldt, A. (2007). The influence of cations on charge accumulation in dye-sensitized solar cells. *Journal of Electroanalytical Chemistry*, Vol.609, No.2, (November 2007), pp. 55-60, ISSN 1572-6657.

Gregg, B.A. (2004). Interfacial processes in dye-sensitized solar cell. *Coordination Chemistry Reviews*, Vol.248, No.13-14, (July 2004), pp. 1215-1224, ISSN 0010-8545.

Lipinski, W.; Thommen, D.; Steinfeld, A. (2006). Unsteady radiative heat transfer within a suspension of ZnO particles undergoing thermal dissociation. *Chemical Engineering Science*, Vol.61, No.21, (November 2006), pp. 7039-7035, ISSN 0009-2509.

Navas, F.J.; Alcántara, R.; Fernández-Lorenzo, C. & Martín, J. (2009). A methodology for improving laser beam induced current images of dye sensitized solar cells. *Review of Scientific Instruments*, Vol.80, No.1(June 2009), pp. 063102-1-063102-7, ISSN 0034-6748.

Nichiporuk, O.; Kaminski, A.; Lemiti, M.; Fave, A.; Litvinenko, S. & Skryshevsky, V. (2006). Passivation of the surface of rear contact solar cells by porous silicon. *Thin Solid Films*, Vol.511–512, (July 2006), pp. 248-251, ISSN 0040-6090

Nishioka, k.; Yagi, T.; Uraoka, Y. & Fuyuki, T. (2007). Effect of hydrogen plasma treatment on grain boundaries in polycrystalline silicon solar cell evaluated by laser beam induced current. *Solar Energy Materials & Solar Cells*, Vol.91, No.1, (January 2007), pp. 1-5, ISSN 0927-0248.

O'Regan, B.; Grätzel, M. (1991). A low-cost, high-efficiency solar cell based on dye-sensitized colloidal $TiO_2$ films. *Nature*, Vol.353, No.1 (October 1991), pp. 737-740, ISSN 0028-0836.

Peter, L.M. (2007). Characterization and modeling of dye-sensitized solar cells. *Journal of Physical Chemistry C*, Vol. 111, No.18, (April 2007), pp. 6601-6612, ISSN 1932-7447

Poce-Fatou, J.A.; Martín, J.; Alcántara, R.; Fernández-Lorenzo, C. (2002). A precision method for laser focusing on laser beam induced current experiments. *Review of Scientific Instruments*, Vol.73, No.11, (November 2002), pp. 3895-3900, ISSN 0034-6748.

Sontag, D.; Hahn, G.; Geiger, P.; Fath, P. & Bucher, E. (2002). Two-dimensional resolution of minority carrier diffusion constants in different silicon materials. *Solar Energy Materials & Solar Cells*, Vol.72, No.1-4, (April 2002), pp. 533-539, ISSN 0927-0248.

van Dyk, E.E.; Radue, C. & Gxasheka, A.R. (2007). Characterization of Cu(In,Ga)Se$_2$ photovoltaic modules. *Thin Solid Films*, Vol.515, No.15, (May 2007), pp. 6196-6199, ISSN 0040-6090.

Vorasayan, P.; Betts, T.R.; Tiwari, A.N. & Gottschalg, R. (2009). Multi-laser LBIC system for thin film PV module characterisation. *Solar Energy Materials & Solar Cells*, Vol.93, No.6-7, (June 2009), pp. 917-921, ISSN 0927-0248.

Vorster, F.J.; van Dyk, E.E. (2007). High saturation solar light induced current scanning of solar cells. *Review of Scientific Instruments*, Vol.78, No.1, (January 2007), pp. 013904-1-013904-7, ISSN 0034-6748.

Walker, A.B.; Peter, L.M.; Lobato, K.; Cameron, P.J. (2006). Analysis of photovoltage decay transients in dye-sensitized soar cells. *Journal of Physical Chemistry B*, Vol.110, No.50, (October 2006), pp. 25504-25507, ISSN 1520-6106.

Yagi, T.; Nishioka, K.; Uraoka, Y.; Fuyuki, T. (2004). Analysis of electrical properties of grain boundaries in silicon solar cell using laser beam induced current. *Japanese Journal of Applied Physics*, Vol.43, No.7A, (July 2004), pp. 4068-4072, ISSN 0021-4922.

# Silicon Solar Cells: Structural Properties of Ag-Contacts/Si-Substrate

Ching-Hsi Lin, Shih-Peng Hsu and Wei-Chih Hsu
*Industrial Technology Research Institute ,*
*Taiwan, R.O.C.*

## 1. Introduction

The screen-printed silver (Ag) thick-film is the most widely used front side contact in industrial crystalline silicon solar cells. The front contacts have the roles of efficiently contacting with the silicon (Si) and transporting the photogenerated current without adversely affecting the cell properties and without damaging the p-n junction. Although it is rapid, has low cost and is simplicity, high quality screen-printed silver contact is not easy to make due to the complicated composition in the silver paste. Commercially available silver pastes generally consist of silver powders, lead-glass frit powders and an organic vehicle system. The organic constituents of the silver paste are burned out at temperatures below 500°C. Ag particles, which are ~70-85wt% and can be different in shape and size distribution, show good conductivity and minor corrosive characteristics. The concentration of glass frit is usually less than 5wt %; however, the glass frit in the silver paste plays a critical role for achieving good quality contacts to high-doping emitters. The optimization of the glass frit constitution can help achieve adequate photovoltaic properties.

The melting characteristics of the glass frit and also of the dissolved silver have significant influence on contact resistance and fill factors (FFs). Glass frit advances sintering of the silver particles, wets and merges the antireflection coating. Moreover, glass frit forms a glass layer between Si and Ag-bulk, and can further react with Si-bulk and forms pin-holes on the Si surface upon high temperature firing.

This chapter first describes the Ag-bulk/Si contact structures of the crystalline silicon solar cells. Then, the influences of the Ag-contacts/Si-substrate on performance of the resulted solar cells are investigated. The objective of this chapter was to improve the understanding of front side contact formation by analyzing the Ag-bulk/Si contact structures resulting from different degrees of firing. The observed microscopic contact structure and the resulting solar-cell performance are combined to clarify the mechanism behind the high-temperature contact formation. Samples were fired either at a optimal temperature of ~780°C or at a temperature of over-fired for silver paste to study the effect of firing temperature. The melting characteristics of the glass frit determine the firing condition suitable for low contact resistance and high fill factors. In addition, it was found the post forming gas annealing can help overfired solar cells recover their FF. The results show that after 400°C post forming gas annealing for 25min, the over-fired cells improve their FF. On the other hand, both of the optimally-fired and the under-fired cells did not show similar

effects. The FF remains the same or even worse after post annealing. Upon overfiring, more silver dissolve in the molten glassy phase than that of optimally fired; however, some of the supersaturated silver in the glass was unable to recrystallize because of the rapid cooling process. The post annealing helps the supersaturated silver precipitate in the glass phase or on silicon surface. This helps in recovering high FF and low contact resistance. An increase in the size and number of silver crystallites at the interface and in the glass phase can improve the current transportation.

## 2. Overview of Ag contacts on crystalline Si solar cells

### 2.1 Silver paste

Currently, screen printing a silver paste followed by sintering is used for the deposition of the front contacts on almost all industrial crystalline silicon solar cells. Metallization with a silver paste is reliable and particularly fast. The silver paste have to meet several requirements: opening the dielectric antireflection layer and forming a contact with good mechanical adhesion and low contact resistance. For most crystalline silicon solar cells, $SiN_x$ is used as an antireflection coating. The surface must be easily wetted by the paste. Figure 1 shows a typical front-electrode configuration of a commercial crystalline silicon solar cell. The electrode-pattern consists of several grid fingers that collect current from the neighboring regions and then collected into a bus bar. The bus bar has to be able to be soldered.
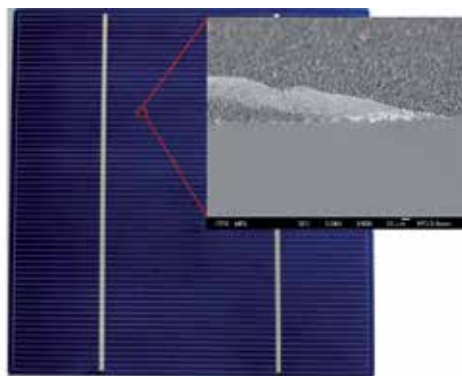


Fig. 1. A typical front-electrode configuration of a commercial crystalline silicon solar cell.

The contact performance is influenced by the paste content, the rheology and the wetting behavior.

Commercially available silver pastes generally consist of silver powders, lead-glass frit powders and an organic vehicle system. The glass frit is used to open the antireflection coating and provide the mechanical adhesion. The glass frit also promotes contact formation. The organic vehicle system primarily includes polymer binder and solvent with small molecular weight. Other additives like rheological material are also included in the paste for better printing. The paste system must have a fine line capability. This requires a well-balanced thixotropy and low flow properties during printing, drying and firing. In addition, the paste should have wide range for firing process window.

## 2.2 Screen printing and firing

Screen printing and the subsequent firing process are the dominant metallization techniques for the industrial production of crystalline silicon solar cells. The front contact of the cell is designed to offer minimum series resistance, while minimizing optical shadowing. The high current density of the cell can be achieved by the low shadowing loss due to the high aspect ratio of the front grid. However, a compromise between the shadowing loss and the resistive loss due to the front grid is needed. The finger-pattern with the bus bar typically covers between 6-10% of the cell surface. To achieve good performance contact, the printing parameters should be selected based on criteria directly related to the silver paste. All parameters such as the screen off-contact distance, squeegee speed and shore hardness of the squeegee rubber must be optimized and matched according to the requirements.

The industrial requirements for technical screen printing regarding excellent print performance, long screen life and higher process yields have increased significantly over recent years. The high mesh count stainless steel mesh is well suited for fine line, high volume printing. The screen should have good tension consistency and suitable flexibility required for the constant deformation associated with off-contact printing. Besides, the combinations of mesh count and thread diameter should be capable of printing the grid thickness electrode requires.

The fast firing techniques are usually applied for electrode formation. During the firing step, the contact is formed within a few seconds at peak temperature around 800°C. A typical firing profile of a commercial crystalline silicon solar cell is shown in Figure 2. The optimal firing profile should feature low series resistance and high fill factor (FF). A high series resistance of a solar cell usually degrades the output power by decreasing the fill factor. The total series resistance is the sum of the rear metal contact resistance, the emitter sheet resistance, the substrate resistance, the front contact resistance, and the grid resistance.
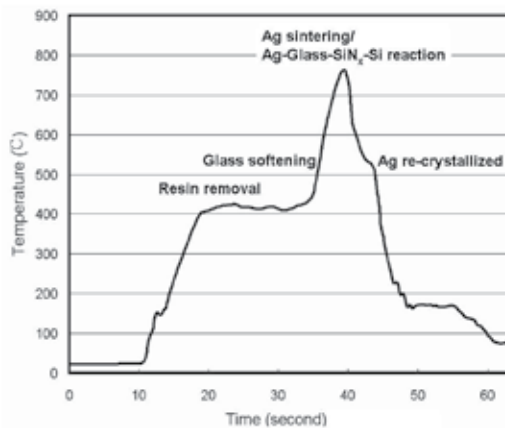


Fig. 2. A typical firing profile of a commercial crystalline silicon solar cell.

## 2.3 Contact mechanisms

A good front-contact of the crystalline silicon solar cell requires Ag-electrode to interact with a very shallow emitter-layer of Si. An overview of the theory of the solar cell contact resistance has been reported (Schroder & Meier, 1984). Despite the success of the screen printing and the subsequent firing process, many aspects of the physics of the front-contact

formation are not fully clear. The major reason is probably because the metal-silicon interface for screen printed fingers is non-uniform in structure and composition. The Ag particles can interact with the Si surface in a few seconds at temperatures that are considerably lower than the eutectic point.

Many mechanisms have been proposed to explain how contact formation is though to occur. The general understanding of the mechanisms agree that the glass frit play a critical role on front-contact formation. Silver and silicon are dissolved in the glass frit upon firing. When cooled, Ag particles recrystallized (Weber 2002, Schubert et al. 2004). It has been suggested that Ag crystallites serve as current pickup points and that conduction from the Ag crystallites to the bulk of the Ag grid takes place via tunneling (Ballif et al., 2003). The effect of glass frit and Ag particles on the electrical characteristics of the cell was also reported (Hoornstra et al. 2005, Hillali et al. 2005, Hillali et al. 2006). It was further suggested that lead oxide gets reduced by the silicon. The generated lead then alloys with the silver and silver contact crystallites are formed from the liquid Ag-Pb phase (Schubert et al. 2004, Schubert et al. 2006). Due to the complicate and non-uniform features of the contact interface, more evidence and further microstructure investigation is still needed. The objective of this chapter was to improve the understanding of front side contact formation by analyzing the Ag-bulk/Si contact structures resulting from different degrees of firing. The influences of the Ag-contacts/Si-substrate on performance of the resulted solar cells are also investigated.

## 3. Structural properties of Ag-contacts/Si-substrate

### 3.1 Sample preparation

This study is based on industrial single-crystalline silicon solar cells with a $SiN_x$ antireflection coating, screen-printed silver thick-film front contacts and a screen-printed aluminum back-surface-field (BSF). The contact pattern was screen printed using commercial silver paste on top of the $SiN_x$ antireflective-coating (ARC) and fired rapidly in a belt furnace. The exact silver paste compositions are not disclosed by the paste manufacturers. The glass frit contents are estimated from the results found in this work. The boron-doped p-type 0.5-2Ωcm, 200-230μm thick (100) CZ single-crystalline Si wafers were used for all the experiments. Si wafers were first chemically cleaned and surface texturized and then followed by $POCl_3$ diffusion to form the n+ emitters. The resulted pyramid-shaped silicon surface is sharp and smooth, as shown in Figure 3. After phosphorus glass removal, a single layer plasma-enhanced chemical vapor deposition (PECVD) $SiN_x$ antireflection coating was deposited on the emitters. Then, both the screen-printed Ag and the Al contacts were cofired in a lamp-heated belt IR furnace.

In this work, cells were fired either at a optimal temperature of ~780°C or at a temperature of over-fired for silver paste to study the effect of firing temperature. Some cells were further post annealed in forming gas ($N_2$:$H_2$=85:15) at 400°C for 25min. The forming gas anneal improve the fill factor (FF) for some over-fired cells.

Transmission electron microscopy (TEM) and Scanning electron microscopy (SEM) was used to study the microstructures and features at contact interface. Microstructural characterization of the contact interface was performed using a JEM-2100F transmission electron microscope (TEM) operated at 200kV. Cross-sectional TEM sample foils were prepared by mechanically thinning followed by focused-ion-beam (FIB) microsampling to electron transparency. Current-voltage (I-V) measurements were taken under a WACOM solar simulator using AM1.5 spectrum. The cells were kept at 25°C while testing.
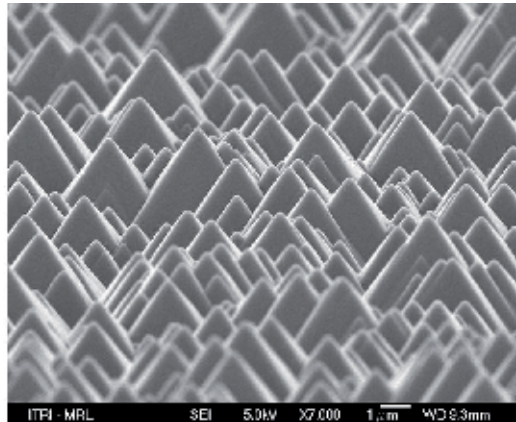
Fig. 3. SEM image of a pyramid-textured silicon surface structure

### 3.2 Interface microstructure

The microstructural properties of the screen-printed Ag-bulk/Si contacts were examined by TEM (Lin et al., 2008). TEM results confirmed that the glassy-phase plays an important role in contact properties. The typical Ag-bulk/Si microstructure, which includes localized large glassy-phase region, is shown in Figure 4(a). The area where Ag-bulk directly contact with Si through SEM observation is actually with a very thin glass layer (<5nm) in between as shown in Figure 4(b). This possibly can be attributed to shape-effect of Ag particles and to the existence of the glassy-phase. Ag particles do not sinter into a very compact structure and a porous Ag-bulk is formed, resulting in a complex contact structure. In this study, it was found that in optimal fired contacts, there are at least three different microstructures, illustrated in Figure 5(a)-(c) (Lin et al., 2008). The combination effects of glassy-phase and the dissolved metal atoms have a crucial influence on Ag-bulk/Si-emitter structures, and consequently, the current transport across the interface is affected.
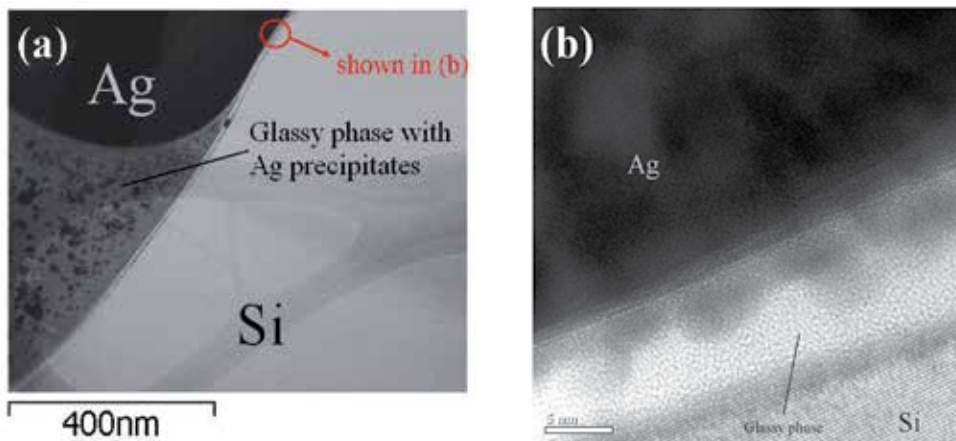


Fig. 4. (a) TEM bright field cross-sectional image of the the Ag-bulk/Si contact structure with localized large glassy-phase region. (b) HRTEM of the Ag-bulk/Si interface. There is a very thin glass layer between Si and Ag-bulk.

Figure 6 shows a high-resolution TEM (HRTEM) contrast of the Ag embryos on Si-bulk. This results in Ag-bulk/thin-glass-layer/Si contact structure which is schematic drawing in Figure 5(a). It is suggested that Ag-bulk/thin-glass-layer/Si contact structure shown in Figure 5(a) is the most decisive path for current transportation (Lin et al., 2008).
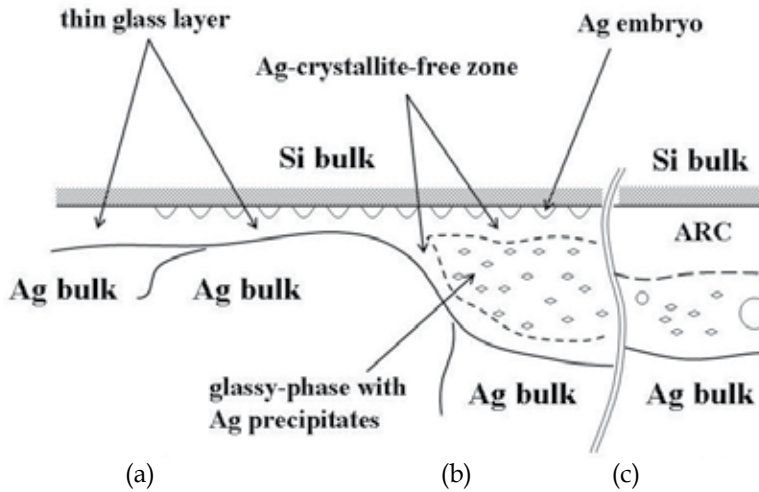


Fig. 5. Schematic drawing of the three major microstructures present in optimal fired Ag-bulk/Si contacts: (a) Ag-bulk/thin-glass-layer/Si; (b) Ag-bulk/thick-glass-layer/Si; and (c) Ag-bulk/glass-layer/ARC/Si contact structure.
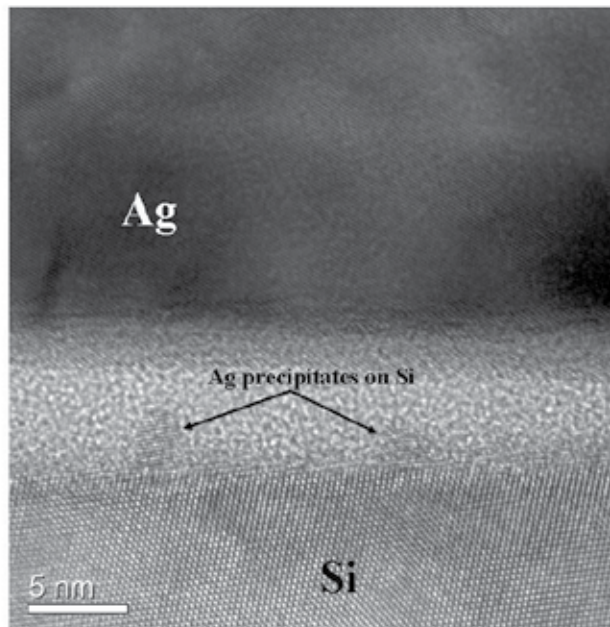


Fig. 6. HRTEM contrast of the Ag embryos on Si-bulk. This results in Ag-bulk/thin-glass-layer/Si contact structure.

The schematic Ag-bulk/thick-glass-layer/Si contact structure shown in Figure 5(b) may arise if there are large glass-frit clusters and/or large voids at the interface plane prior to high temperature treatment. Upon firing, the glass frits soften and flow all around. The flow behavior of the molten glassy-phase, to a degree, is associated with capillary attraction force caused by the tiny spacing between Ag particles, and it also depends on their wetting ability to the antireflection layer. Large and thick glassy-phase region is very likely due to the agglomeration of the molten glass frit at high temperature, and is responsible for a significant variation in glass-layer thickness.

Another interesting feature shown in Fig. 4(a) is the curve-shaped glassy-phase/Si boundary, which suggests the occurrence of mild etching of Si-bulk by the Ag-supersaturated glassy-phase. Penetration of native $SiO_x$ and $SiN_x$ ARC is essential for making good electrical contact with the Si emitter, thus achieving a low contact resistance. However, this must be achieved without etching all the way through the p-n junction and results in shorting the cell. It is found that a smooth curve-shaped Si surface is a distinguishable phenomenon for samples fired optimally (Lin et al., 2008). Underfired samples usually have sharp and straight interface under <110> beam direction, while rough Si surface is usually observed for overfired samples.

Even for optimally fired samples, the residual antireflection coating can be observed at some locations, especially in the valley area of the pyramid-shaped textured structure as shown in Figure 7. Amorphous antireflection layer is thus in between the glassy-phase and Si-bulk. This lead to an Ag-bulk/glass-layer/ARC/Si contact structure as illustrated in Figure 5(c). Here, ARC (~100nm thick prior to firing) includes native $SiO_x$ layer and $SiN_x$ ARC. To some extent, the residual SiNx under the contacts help to reduce surface recombination. Microstructures studies revealed that there is more residual ARC in underfired samples
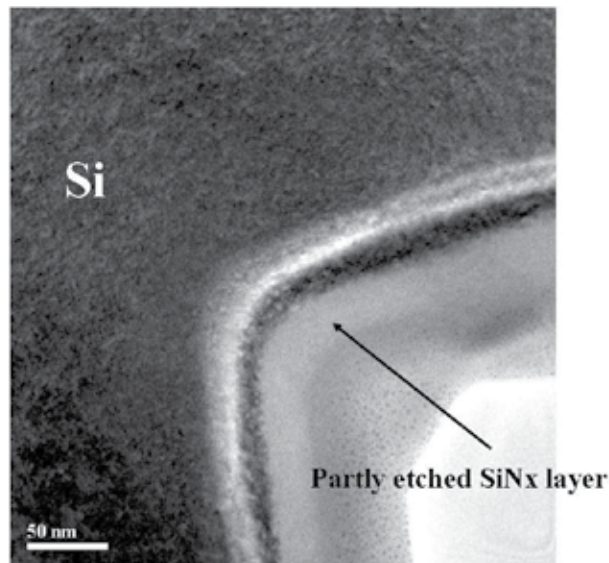


Fig. 7. TEM bright field cross-sectional image. Even for optimally fired samples, the residual antireflection coating can be observed at some locations, especially in the valley area of the pyramid-shaped textured structure. This leads to an Ag-bulk/glass-layer/ARC/Si contact structure.

than in optimally fired samples. In addition, no Ag embryo was found on Si-bulk because the residual ARC helps inhibit Ag diffusion onto Si substrate.

It is still not clear how does glassy-phase, which is a molten phase of the glass frit, etch or interact with the $SiN_x$ ARC? It was reported that the $SiN_x$ ARC can be opened during the firing step by a reaction between the PbO (glass) and $SiN_x$ (Horteis et al., 2010). In the reaction, lead oxide (PbO) was reduced to lead. By tracing Pb content, this work shows that Pb precipitates usually appear in the area where $SiN_x$ ARC can be found. That is, lead embedded in the glassy-phase with an Ag-bulk/glass-layer/ARC/Si contact structure as illustrated in Figure 5(c). The Pb concentration in glassy-phase, which originates from lead silicate glass frit, is much higher than that in ARC. Therefore, Pb can serve as a good tracer to distinguish glassy-phase-area from ARC using energy dispersive spectroscopy (EDS). Figure 8 shows Pb precipitates in the glassy phase. The inset in Figure 8 is an energy dispersive spectroscopy (EDS) mapping. This work suggests that during the firing process, the amorphous $SiN_x$ ARC was incorporated into the already-existing glass phase. It is like two loose glassy-phase merge to each other upon firing. It is shown in this work that the $SiN_x$ ARC in more dense structure, ex. deposited at 850°C through low-pressure CVD (LPCVD), is difficult to merge in the lead silicate glass phase.
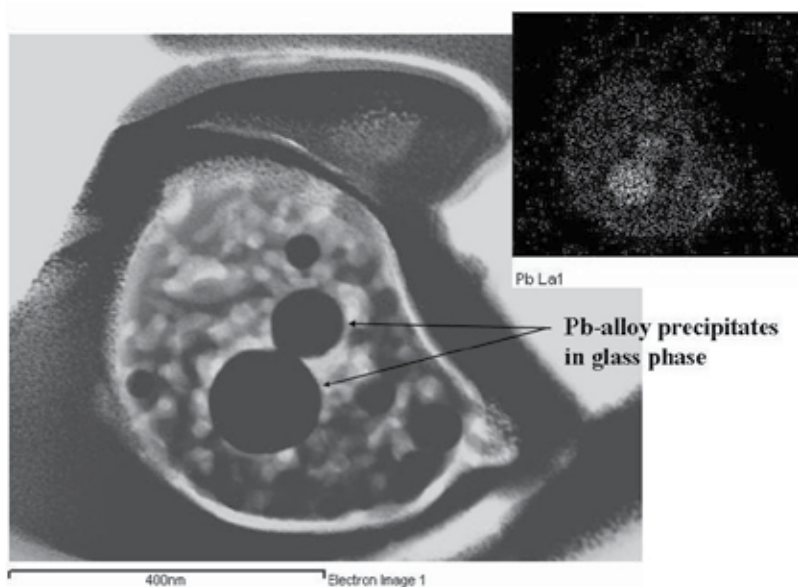


Fig. 8. TEM bright field image shows Pb precipitates in the glassy phase. The inset is the energy dispersive spectroscopy (EDS) mapping.

### 3.3 Crystallite-free zone in glassy phase

Commercially available Ag pastes consist of Ag powders, lead-glass frit powders and an organic vehicle system. It was found that the glass frit plays a very important role during contact formation. Upon firing, the glass frits soften and flow all around. Furthermore, the melted lead silicate glass dissolves the Ag particles. The melted glass also merges the amorphous silicon nitride layer. Upon further heating, the melted glass etches into the silicon bulk underneath and results in non-smooth silicon surface.

TEM micrographs in Figure 9(a) and (c) show the precipitates in the large solidified glassy-phase region which is enclosed with Si and Ag-bulk (Lin et al., 2008). The selected area diffraction (SAD) pattern (Figure 9(d)) reveals that only Ag precipitates exist. As shown in Figure 9(a) and its schematic drawing in Figure 9(b), the dissolved Ag atoms near Si-bulk tend to nucleate on the Si surface and lead to an Ag-crystallite-free zone in close vicinity of the Si surface. Also, an Ag-crystallite-free zone near the bulk-Ag can be found. Few or virtually no Ag microcrystallites were found in the Ag-crystallite-free zone. This indicates that the observed Ag microcrystallites are not un-melted Ag particles which were trapped or suspended in the glassy region; instead, they are precipitates from Ag supersaturation molten glassy-phase.
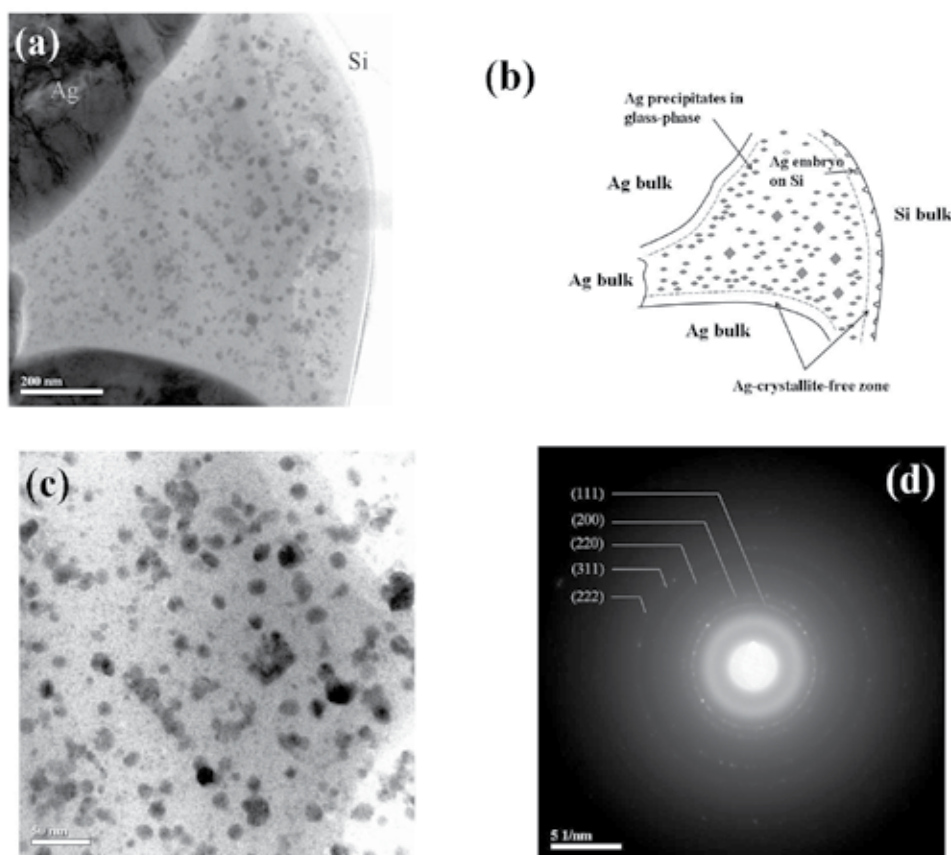


Fig. 9. (a) TEM bright field image. The large glassy-phase enclosed with Si and Ag-bulk. (b) Ag precipitates in the large solidified glassy-phase region. (c) Schematic drawing of image in (b). (d) Selected-area-diffraction pattern of the glassy-phase region shown in (b). Only Ag crystallites exist.

The occurrence of the observed Ag-crystallite-free zone can be accounted for by the diffusion-dependent nucleation mechanism (Porter and Easterling, 1981) as illustrated in Figure 10 (Lin et al., 2008). Upon heating, the dispersed lead silicate glass frits soften into molten phase, in the mean time. They further merged and surrounded the Ag particles due

to capillary attraction force. Some Ag atoms then dissolved in the molten glassy-phase. The observed Ag precipitates confirm the dissolution of Ag because a critical Ag supersaturation must be exceeded for nucleation to occur. Higher temperature increases the Ag dissolution in the glassy-phase. In the mean time, the majority un-dissolved Ag particles, which are in contact with one another, sinter or coalesce to achieve Ag-bulk via interdiffusion of Ag atoms. The molten glassy-phase can further merge (or etch) the amorphous antireflection coating and, therefore, is in direct contact with the Si-bulk. The formation of Ag-crystallite-free zone is attributed to the nucleation and growth of Ag crystallites on Si-bulk. Upon cooling, the dissolved Ag was drained from the surrounding area to Si surface and an Ag-crystallite-free zone results. The width of the Ag-crystallite-free zone is affected by the cooling rate. High cooling rate will produce narrow Ag-crystallite-free zone. This helps in tunneling-assisted carrier transportation. A narrow (width < 20nm) Ag-crystallite-free zone was observed in a large glassy-phase region for optimally fired samples.

It can be found that Ag precipitates in glassy-phase tend to coarsen into larger crystallites with smaller total interfacial area. Also, wide Ag-crystallite-free zones, which surround the large Ag precipitate, were observed. However, the combination effects of low Ag-precipitate density and wide Ag-crystallite-free zone are not favor for current transportation. It, therefore, suggests that long stay in high temperature as well as low cooling rate is of particular concern in the design of firing profile.
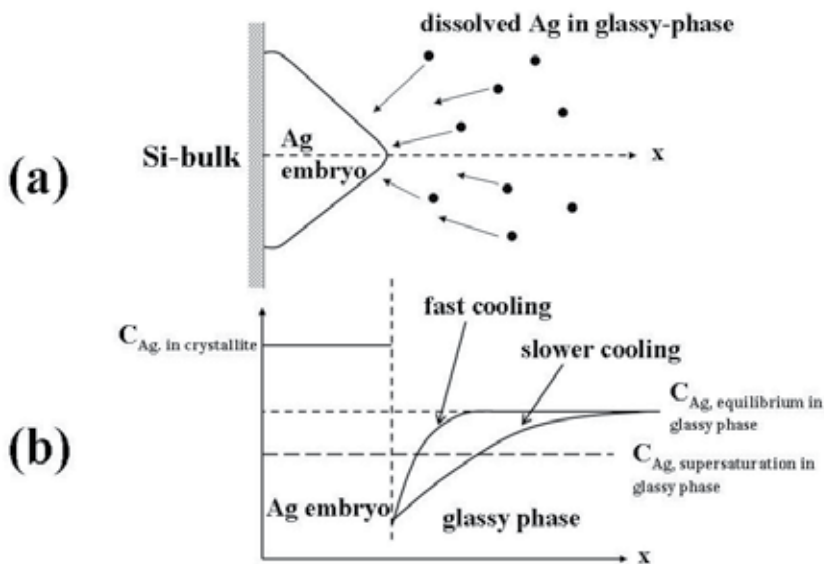


Fig. 10. (a) Schematic cross-section drawing of the Ag-embryo on Si-bulk. (b) Schematic drawing of the dissolved Ag-concentration profile near an Ag embryo.

## 4. Impacts of contact structure on performance of solar cell

### 4.1 A possible mechanism for carrier transportation

The current transport across screen-printed front-side contact of crystalline Si solar cells should be strongly affected by the contact microstructures. This study shows that the area where Ag-bulk directly contact Si, through SEM observation, is actually with a very thin glass layer in

between. In addition, high-density Ag-embryo was found on Si-bulk for samples fired optimally. In Figure 11, Ag embryos with sizes less than 5 nm in diameter nucleate epitaxially on the Si surface. The Ag-embryo density is more than $2\times10^{16}cm^{-2}$, which was counted via TEM. This results in Ag-bulk/thin-glass-layer/Si contact structure. The lack of Ag-bulk/Si direct contact for optimally fired samples leads to a reasonable assumption that Ag-bulk/thin-glass-layer/Si contact structure is the most decisive path for current transporting across the interface. The glass layer between Ag-embryos and Ag-bulk for samples fired optimally is too thin (<5nm) to be an effective barrier to electron transfers, which can occur by tunneling.
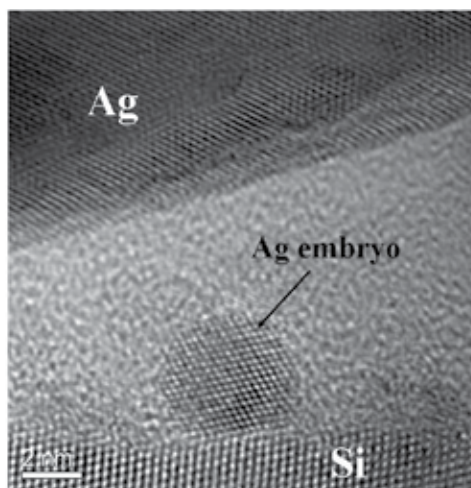


Fig. 11. Cross-sectional HRTEM of the Ag embryos on Si-bulk. This results in Ag-bulk/thin-glass-layer/Si contact structure.

The schematics of a possible conductance mechanisms across the Ag-bulk/thin-glass-layer/Si contact structure is shown in Figure 12. Current transport between Si substrate and front contact is enabled by separated silver crystallites. Since the curved regions of the tiny-pricipitate/glass-phase interface have higher field intensity due to the small radius of curvature; therefore, the breakdown voltage is less (Sze S.M., 1981). Besides the curved-interface effect mentioned above, the metal-supersaturated glassy-phase has better conductivity. The embedded metal precipitates in glassy-phase, as shown in Figure 9, can retain the charge and form the interfacial charge storage centers. In addition, the embedded Ag precipitates can be charged and discharged by quantum-mechanical tunneling of electrons. Moreover, the dissolved Ag can substantially increase the trap density at the interface, thereby allowing shorter times for the transportation. Thus, current can transport through the thick glassy-phase not only by multi-tunneling steps between Ag precipitates, but also by thermally excited electrons hopping from one isolated precipitate to the next. In the case of a current transport by multi-tunneling steps between microscopic Ag precipitates, high Ag-precipitate density in the glassy-phase could help to decrease the specific contact resistance of samples (Gzowski et al. 1982, Ballif et al. 2003).

Many of the ideas that were discussed with regard to Ag-particles/thick-glass-layer/Si microstructure can be carried over to Ag-particles/thin-glass-layer/Si (Figure 5(a)). Only the thick glassy-phase is replaced by an ultrathin glass layer, and this has important consequences for the current conduction across the interface. It was reported (Rollert et al.,

1987) that if the Ag-bulk is in direct contact with the Si and if there was no glass layer in between, the Ag would diffuse at least 5µm deep during the firing cycle and it would shunt the p-n junction. The high-density Ag-embryo on Si found in this study originates from the dissolved Ag in glassy phase, which is in direct contact with Si-bulk. This should play an important role in current transport across the interface. This could be supported by the observation of less Ag-embryo on Si was found for underfired samples, which result in poorer FF of the cell compared to those of optimally fired samples. In the case of underfired samples, the dissolution of Ag is much less; it therefore reduces the supersaturation of Ag. Thus, few Ag precipitates were detected on Si.
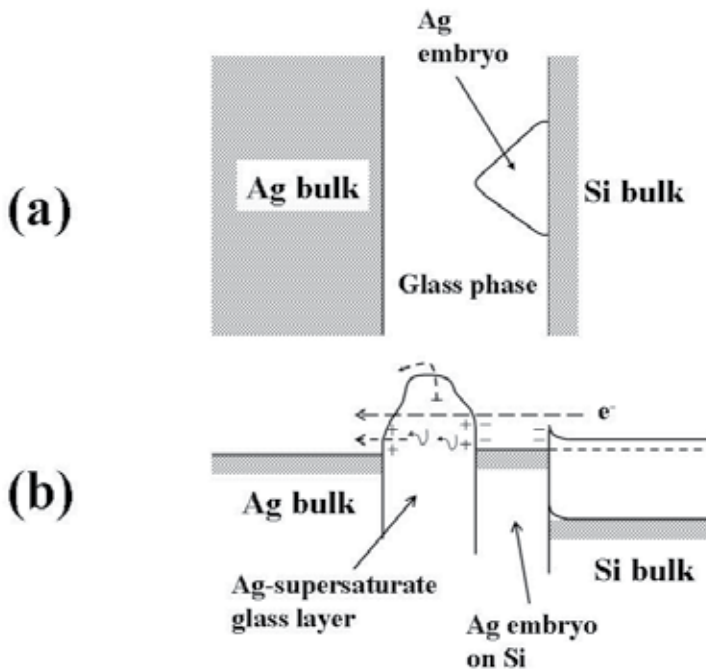


Fig. 12. (a) Schematic cross-section drawing of the Ag-embryo on Si-bulk. (b) Schematic energy-band drawing of a possible conductance mechanisms across Ag-bulk/thin-glass-layer/Si contact structure.

As shown in Figure 12, Ag-embryo on Si could serve as current pickup points and that conduction from the Ag-embryo to Ag-bulk takes place via tunneling through the ultrathin glass layer in between. An increase in the width and the number of Ag precipitates on Si may improve the probability of the encounter of thin glass regions where tunneling can take place. Also, due to tunneling-assisted carrier transport, the fraction of thin glass regions at Ag-bulk/Si interface is critical in reducing the macroscopic contact resistance. Thus, the abilities to generate high-density Ag-embryos on Si-bulk and to keep the glass layer thin are crucial in achieving good electrical contact.

It was reported (Card & Rhoderick 1971, Kumar & Dahlke 1977) that if the insulator layer is sufficiently thick, the tunneling probability through the insulator layer is negligible. Alternatively, if the insulator layer is very thin (< 5nm), little impediment is provided to carrier transport. This study confirms that the spacing between Ag-embryos and Ag-bulk can

be less than 5nm. In addition, the dissolved Ag could improve the electrical conductivity of the glass layer. It, therefore, suggest that carriers through the ultrathin glass layer are the most decisive path for current transportation. A possible mechanism for carriers passing through the thin glass layer is illustrated by considering electron tunnel, as shown in Figure 12.

The interface microstructure analysis of the screen-printed front-side contact shown in this work is based on industrial-type rapid firing-profile, which results in good contact quality. Although Ag-paste composition and characteristics can be different between manufacturers, the results and trends shown in this work have high degree similarity to other screen-printed crystalline Si solar cells using different types of Ag-paste. Further understanding of the effects of the paste constituents and firing conditions on the contact interface can lead to the development of better, more reproducible, and higher performance contacts in the future.

## 4.2 Effects on fill factor

The fill factor, FF, is a measure of the squareness of the I-V characteristic. The fill factor is given: $FF=(V_{max}I_{max})/(V_{oc}I_{sc})$, where $V_{oc}$ is the open-circuit voltage and $I_{sc}$ is the short-circuit current. $V_{max}$ and $I_{max}$ are voltage and current at maximum power point ($P_{max}$) respectively. The graphical interpretation of $P_{max}$ is the area of the largest rectangle below the I-V curve. In practice, FF is less than one because series and parallel resistances will always result in a FF decrease. A good value for industrial silicon solar cells is ~76-78%.

It was found that the glass frit plays an important role during contact formation. During firing procedures, the glass frits firstly get fluid, wet and merge the SiNx dielectric layer. It was then etching into silicon substrate. It was known that defects and impurities tend to move to surface upon high temperature treatments to release their high thermodynamic energies. Therefore, the etching degree of silicon by the glass fluid, to some extent, affects the quality of the contacts. On cooling down, silver precipitates, which serve as a transport medium, recrystallize on silicon surface as well as in the glassy phase. This chapter shows that silver precipitates during cooling and the etching degree of silicon during firing are important for achieving good quality contacts.

On cooling down from high temperature firing, the over-saturated silver tends to precipitate. Figure 13(a) shows a SEM microstructure image of optimally fired sample. Besides precipitating in the glassy phase, high density Ag recrystallizes appear on the silicon substrate. The area where silver directly contacts to Si through SEM observation is actually with a very thin glass layer in between. The dissolved Ag atoms near Si-bulk tend to nucleate on the Si surface. Ag-embryo on Si can serve as current pickup points and that conduction from the Ag-embryo to Ag-bulk takes place via tunneling through the ultrathin glass layer in between. Thus, the abilities to generate high density Ag embryos on Si-bulk and to keep the glass layer thin are crucial in achieving good electrical contact. The observed Ag precipitates confirms the dissolution of Ag because a critical Ag supersaturation must be exceeded for nucleation to occur. In the case of underfiring, the less dissolved Ag reducing the supersaturation, and therefore, fewer Ag precipitates grow on Si during cooling as shown in Figure 13(b).

Penetration of native $SiO_x$ and $SiN_x$ antireflective coating is essential for making good electrical contact to the Si emitter, thus achieving a low contact resistance. However, this must be achieved without etching all the way through the p-n junction and results in shorting the cell. It is found that a smooth curve-shaped Si surface is a distinguishable phenomenon for samples fired optimally. Underfired samples usually have sharp and straight interface, while rough Si surface is usually observed for overfired samples. As shown in Figure 14(a) and (b), overfiring results in rough Si surface. Rough Si surface
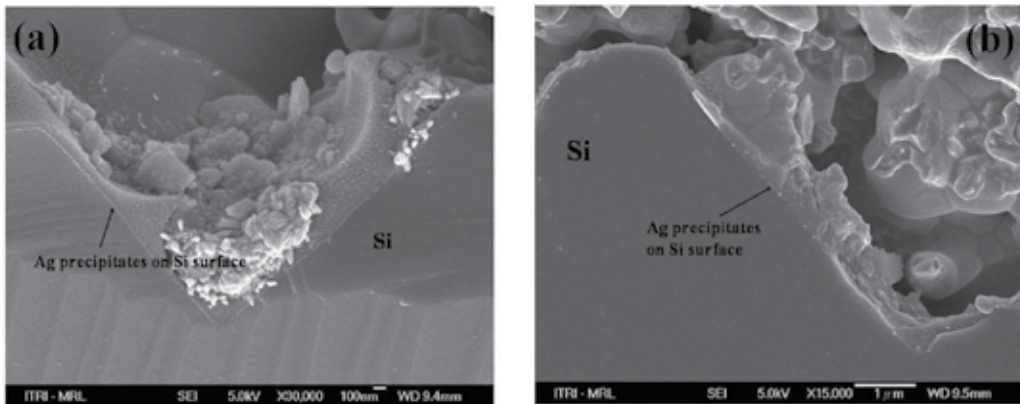
Fig. 13. (a) SEM cross-sectional image of the optimally fired sample. Besides precipitating in the glassy phase, high density Ag recrystallizes on the <111> planes of the pyramid Si. (b) SEM cross-sectional image of the underfired sample. Fewer Ag precipitates grow on Si.
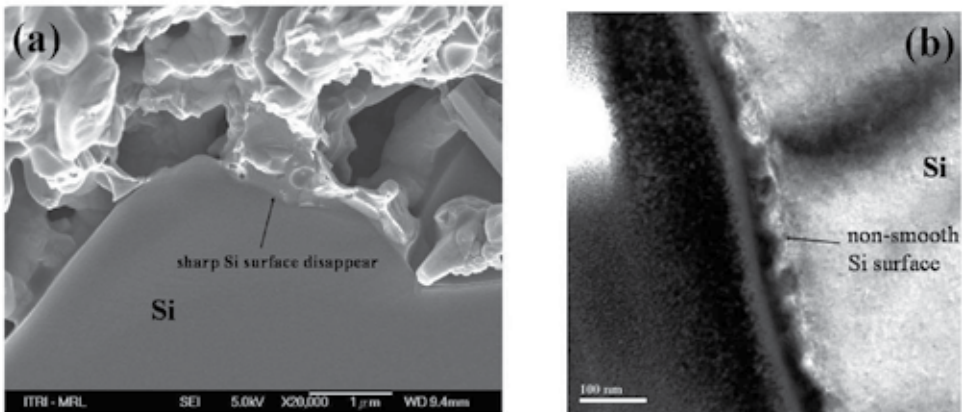


Fig. 14. (a) SEM cross-sectional image of the overfired sample. More bulk Si, especially in the area near the tip of the pyramid, was etched during firing. (b) TEM bright field cross-sectional image of the overfired sample.

increase the possibility of undesired surface recombination. Furthermore, as shown in Figure 14(a), more bulk Si, especially in the area near the tip of the pyramid, was etched during firing. The overetching of Si may result in locally shunt of the cell.

In general, the relation between the current density through the contact and the potential across it is non-linear for metal-semiconductor contacts (Schroder and Meier, 1984). The metal-silicon interface for screen printed fingers is known to be non-uniform in structure and composition. It is found the melting characteristics of the glass frit and its ability to dissolved Ag have significant influence on contact resistance and fill factors (FF). Glass frit advances sintering of the Ag particles, wets and merges the antireflection coating. Moreover, glass frit forms a glass layer between Si and Ag-bulk, and can further react with Si-bulk and forms pin-holes on the Si surface upon high temperature firing. Typical firing temperatures of a commercial solar cell were between 750C and 800C, where the optimum balance between the Ag-crystallite density and the distribution of the glass layer should be found.

For optimum solar cell efficiency, the current-voltage curve must be as rectangular as possible. The new paste design should increase the fill factor of the solar cell without hurting the short-circuit current density. The current-voltage (I-V) characteristic of an ideal silicon solar cell is plotted in Figure 15 denoted as curve-1. In Figure 15, Curve-2 shows the effect of shunt resistance on the current-voltage characteristic of a solar cell (series resistance $R_s$=0). The shunt resistance, $R_{sh}$, has little effect on the short-circuit current, but reduces the open-circuit voltage. Curce-3 shows the effect of series resistance on the current-voltage characteristic of a solar cell ($R_{sh}\rightarrow\infty$). Conversely, the series resistance, $R_s$, has no effect on the open-circuit current, but reduces the short-circuit current. Sources of series resistance include the metal contacts. The extreme current-voltage characteristic, ex. Curve-2 or Curve-3 shown in Figure 15, is not difficult to explain. However, the original sources for I-V curve denoted as Curve-4 in Figure 15 remain unclear. It is not unusually to have I-V feature similar to that of Curve-4. The difference between the curve-1 and curve-4 (the rounded corner of the I-V curve) is probably due to the non-uniform contact resistance of the front contact. Although it is known that the curve can be rounded by series resistance, in practice curve shapes are often found that cannot be explained by the single series resistance.
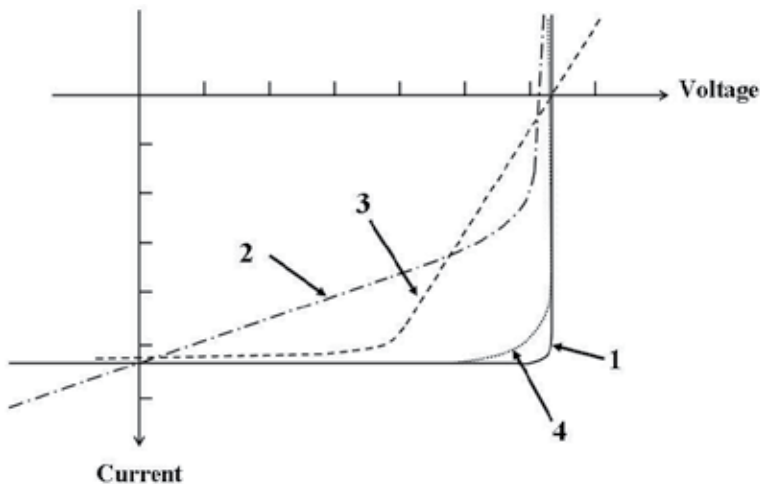


Fig. 15. Current-voltage (I-V) characteristic of a silicon solar cell. The I-V curve for an ideal cell is denoted as curve-1.

The front-contact interface for screen printed fingers is non-uniform in structure and composition. The complicate interface-structure influences the series resistance and the fill factor of the cell. From the view of contact-formation mechanism described in this chapter, the melting characteristics of the glass frit determine whether the paste together with the firing condition is suitable for low contact resistance and high fill factors.

It was found the post forming gas annealing can help overfired solar cells recover their F.F. The results show that after 400°C post forming gas annealing for 25min, the overfired cells improve their FF. On the other hand, both of the optimally-fired and the under-fired cells did not show similar effects. The FF remains the same or even worse after conducting post-annealing.

The mechanism of FF recovers for overfired cells after post forming-gas annealing was further investigated. It was found that the supersaturated silver in the glassy-phase plays a very important role for FF recover. More Ag can dissolve in the molten glassy phase for overfired samples than that of optimally fired counterparts. Either higher temperature or

longer heating time increases the Ag dissolution in the glassy-phase. Some of the supersaturated silver in the glass for overfired cells was unable to recrystallize because of the rapid cooling process. The post-annealing helps the supersaturated silver further precipitate in the glassy-phase or move to already exist Ag crystallites. The number of small precipitates is increased and the conductivity of the insulating glass is improved. Post-annealing the overfired cells thus results in recovering high FF and low contact resistance. An increase in the size and number of silver crystallites at the interface and in the glass phase can improve the current transportation.

Post-annealing of overfired cells helps the supersaturated Ag precipitate. It also coalesce the pre-formed Ag crystallites. More Ag embryos were generated and grew to larger size, which decreased the contact resistance, and enhanced the F.F. As shown in Table 1, the forming-gas anneal reduces the contact resistance, and thus, it improves the FF for the overfired cells. In Table 1, the post-annealing increases the FF by 1.5~9%. However, it should be mentioned that the cells cannot be overfired too much. It must be avoided to etch all the way through the p-n junction, which results in shorting the cell. The overetching of Si underneath may result in locally shunt of the cell. Besides, overfiring results in rough Si surface. Rough Si surface increase the possibility of undesired surface recombination.

| Sample # | $\Delta Jsc/Jsc$ (%) | $\Delta Voc/Voc$ (%) | $\Delta FF/FF$ (%) | $\Delta Eff/Eff$ (%) |
|---|---|---|---|---|
| 1 | -0.68 | -0.25 | 2.66 | 1.71 |
| 2 | -0.30 | -0.27 | 1.75 | 1.16 |
| 3 | -0.36 | -0.05 | 4.68 | 4.25 |
| 4 | -1.92 | -0.61 | 3.19 | 0.58 |
| 5 | -0.01 | -0.68 | 9.13 | 8.38 |

Table 1. The forming gas anneal improves the FF for the overfired cells.

The mechanism for FF enhancement of the overfired cells after post-annealing is related to the supersaturated Ag. Figure 16(a) shows a HRTEM image of the silicon/electrode
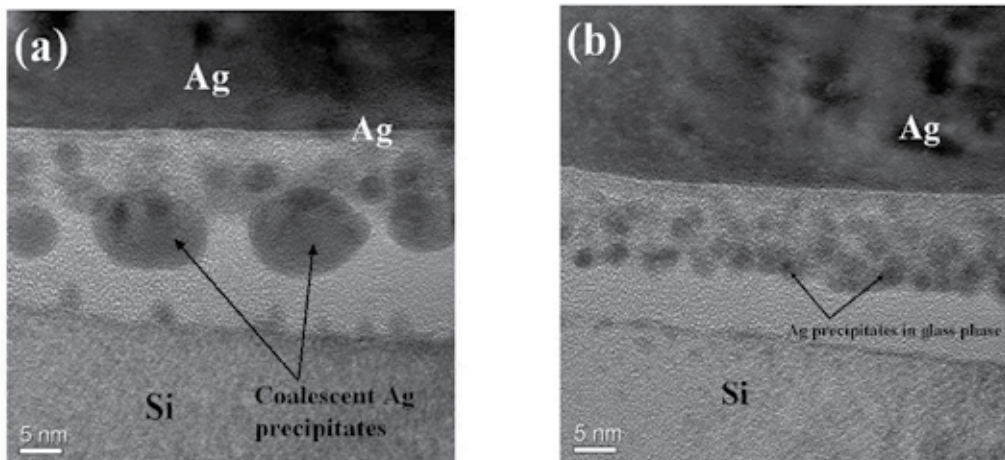


Fig. 16. (a) HR TEM contrast of more and large Ag crystallites in the glassy phase. (b) HR TEM contrast of contact interface. Ag precipitates are closer to Ag-bulk.

interface structure. It can be found that the Ag crystals in the glassy phase grow to larger size either by electron beam annealing or by heat treatments, indicating a better current transportation. The Ag area coverage at the Si-Ag interface is increased. More and larger Ag crystallites in the glassy phase increase the contact area fraction, which improves the probability of tunneling from Ag crystallites to the Ag bulk. The better conductance contributes to lower contact resistance and a higher FF. Also shown in Figure 16(b), more Ag embryos were generated and result in a locally decreased contact resistance. The rounded-corner feature of the I-V curve, as shown as Curve-4 in Figure 15, can be improved. The rounded-corner feature of the I-V curve is caused by combination effects of resistance and recombination. Control the process better and decrease the carriers' jumping-path can improve the fill factor of the cell.

## 5. Conclusion

Despite the success of the screen printing and the subsequent firing process, many aspects of the physics of the front-contact formation are not fully clear. The major reason is probably because the contact-interface for screen printed fingers is non-uniform in structure and composition. The contact microstructures have a high impact on current-transport across the contact-interface.

This chapter first presents the Ag-bulk/Si contact structures of the crystalline silicon solar cells. Then, the influences of the Ag-contacts/Si-substrate on performance of the resulted cells are investigated. The objective of this work was to improve the understanding of front-side contact formation by analyzing the individual contact types and their role in the Ag-bulk/Si contact. Microstructure analyzing confirmed that the glassy-phase plays an important role in contact properties. The location where Ag-bulk directly contact Si-substrate, through SEM observation, is actually a very thin glass layer in between. High density Ag-embryos on Si-bulk were found for samples fired optimally. It is suggested that Ag-bulk/thin-glass-layer/Si contact is the most decisive path for current transportation. Possible conductance mechanisms of electrons across the contact interface are also discussed.

Ag-embryo on Si could serve as current pickup points and that conduction from the Ag-embryo to Ag-bulk takes place via tunneling through the ultrathin glass layer in between. Thus, the abilities to generate high density Ag embryos on Si-bulk and to keep the glass layer thin are crucial in achieving good electrical contact.

This chapter also reports that after 400°C post forming-gas annealing for 25min, the overfired cells improve their FF. The mechanism for FF enhancement of the overfired cells after post-annealing is related to the supersaturated silver in glassy-phase. The post-annealing helps the supersaturated silver further precipitate in the glassy-phase or move to already exist Ag crystallites. More and larger Ag crystallites in the glassy phase increase the contact-area fraction, which improves the probability of tunneling from silver crystallites to the silver bulk.

The interface microstructure analysis of the screen-printed front-side contact shown in this work is based on industrial-type rapid firing-profile. Although Ag-paste composition and characteristics can be different per manufacturer, the results and trends shown in this work have high degree similarity to other screen-printed cell using different type Ag-paste. Further understanding the effects of the paste constituents and firing conditions on the contact-interface can lead to develop a better, more reproducible, and higher performance screen-printed electrode.

## 6. Acknowledgements

## 7. References

Ballif C., D. M. Huljić, G. Willeke, and A. Hessler-Wysser (2003). Silver thick-film contacts on highly doped n-type silicon emitters: structural and electronic properties of the interface, *Applied Physics Letters*, Vol. 82, pp. 1878-1880. ISSN 0003-6951.

Card H.C. and E. H. Rhoderick (1971). Studies of tunnel MOS diodes I. Interface effects in silicon Schottky diodes, *Journal of Physics D: Applied Physics*, Vol. 4, pp. 1589.

Gzowski O., L. Murawski, and K. Trzebiatowski (1982). The surface conductivity of lead glasses, *Journal of Physics D: Applied Physics, Vol*. 15, pp. 1097-1101.

Hilali M.M., K. Nakayahiki, C. Khadilkar, R. C. Reedy, A. Rohatgi, A. Shaikh, S. Kim, and S. Sridharan (2006). Effect of Ag particle size in thick-film Ag paste on the electrical and physical properties of screen printed contacts and silicon solar cells, *Journal of The Electrochemical Society*, Vol. 153, pp. A5-A11. ISSN 0013-4651.

Hilali M.M., M. M. Al-Jassim, B. To, H. Moutinho, A. Rohatgi, and S. Asher (2005). *Journal of The Electrochemical Society,* Vol. 152, pp. G742-G749. ISSN 0013-4651.

Hoornstra J., G. Schubert, K. Broek, F. Granek, C. LePrince (2005). Lead free metallization paste for crystalline silicon solar cells: from model to results, *31st IEEE PVSC conference*, Orlando, Florida.

Horteis M, T. Gutberlet, A. Reller, and S.W. Glunz (2010). High-temperature contact formation on n-type silicon: basic reactions and contact model for seed-layer contacts, *Advanced Functional Mateials*, Vol. 20, pp. 476-484.

Kumar V. and W. E. Dahlke (1977), Solid State Electron., Vol. 20, pp. 143.

Lin C.-H., S.-Y. Tsai, S.-P. Hsu, and M.-H. Hsieh (2008). Investigation of Ag-bulk/glassy-phase/Si heterostructures of printed Ag contacts on crystalline Si solar cells, *Solar Energy Materials & Solar Cells*, Vol. 92, pp. 1011-1015.

Porter D.A. and K.E. Easterling (1981), *Phase Transformations in Metals and Alloys*, Chapman & Hall, New York.

Rollert F., N. A. Stolwijk, and H. Mehrer (1987), Solubility, diffusion and thermodynamic properties of silver in silicon, *Journal of Physics D: Applied Physics*, Vol. 20, pp. 1148-1155.

Schroder D.K. & Meier D.L. (1984). Solar cell contact resistance – a review, *IEEE Transactions on Electron Devices*, Vol. 31, pp. 637-647. ISSN 0018-9383.

Schubert G., F. Huster, P. Fath (2004), Current Transport Mechanism in printed Ag Thick Film Contacts to an n-type Emitter of a Crystalline Silicon Solar Cell, *Proceedings of 19th European Photovoltaic Solar Energy Conference*, Paris, France, pp. 813-817.

Schubert G., F. Huster, and P. Fath (2006). Physical understanding of printed thick-film front contacts of crystalline Si solar cells—Review of existing models and recent developments, *Solar Energy Materials & Solar Cells*, Vol. 90, pp. 3399-3406.

Sze S.M.(1981). *Physics of Semiconductor Devices*, 2nd Edition, John Wiley & Sons, New York, ISBN 10-0471-0566-18.

Weber L. (2002), Equilibrium solid solubility of silicon in silver, *Metallurgical and Materials Transactions A*, Vol. 33, pp. 1145-1150.

# Possibilities of Usage LBIC Method for Characterisation of Solar Cells

Jiri Vanek and Kristyna Jandova
*Brno University of Technology*
*Czech Republic*

## 1. Introduction

Light Beam Induced method works on principle of exposure very small area of a solar cell, usually by laser beam focused directly on the solar cell surface. This point light source moves over measured solar cell in direction of both X and Y axis. Thanks to local current - voltage response the XY current - voltage distribution in investigated solar cell can be measured. Acquainted data are then arranged in form of a current map and the behaviour of whole solar cell single parts is thus visible. Most common quantity measured by Light Beam Induced method is Current (LBIC) which is set near local $I_{SC}$ current.
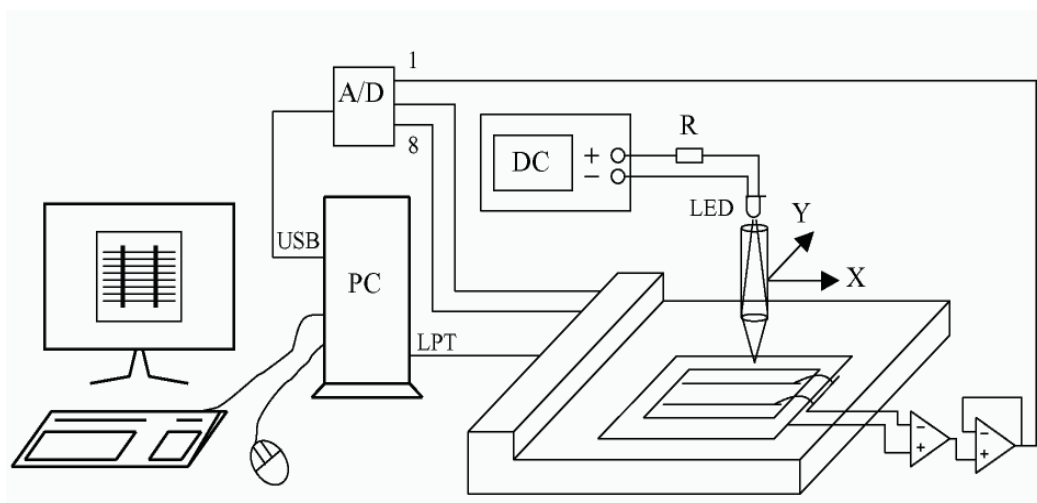


Fig. 1. Diagrammatical demonstration of measuring system (Vanek J, Fort T, 2007)

If the inner resistance of the measured amplifier is set to high value then the response of light is matching to $V_{OC}$ and the method is designed as LBIV. There was some attempt to track the local maximum power point and to record local power value (LBIP) but the most widespread method is LIBC for this predicative feature. In such current map is possible to determine majority of local defects, therefor the LBIC is the useful method to provide a non-destructive characterization of structure of solar cells.
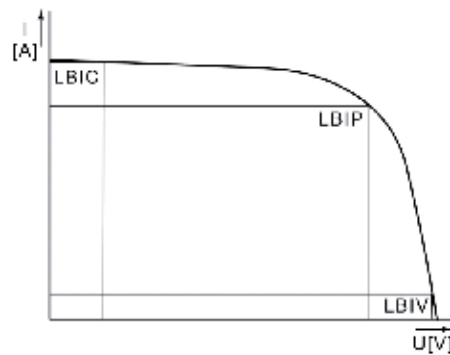
Fig. 2. Operating point of measuring amplifier and resultant method

### 1.1 Different wavelengths of light source used in LBIC

The effect on the absorption coefficient and penetration depth, defined as distance that light travels before the intensity falls to 36% (1/e), is clearly shown in figure 3. Note that the data in figure 3 represent unstrained bulk material with no voltage applied. By introducing strain or electrical bias, it is possible to shift the curves slightly to a higher wavelength due to a reduction in the effective band gap.
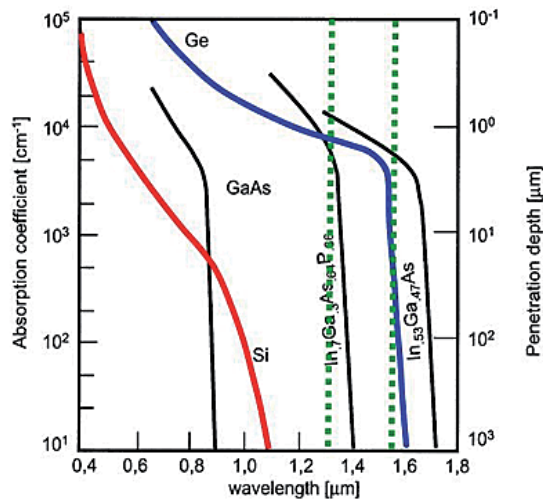


Fig. 3. Absorption coefficient and penetration depth of various bulk materials as a function of wavelength. (Intel,Photodetectors, 2004)

In cases where the photon energy is greater than the band gap energy, an electron has a high probability of being excited into the conduction band, thus becoming mobile. This interaction is also known as the photoelectric effect, and is dependent upon a critical wavelength above which photons have insufficient energy to excite or promote an electron positioned in the valence band and produce an electron-hole pair. When photons exceed the critical wavelength (usually beyond 1100 nanometres for silicon) band gap energy is greater than the intrinsic photon energy, and photons pass completely through the substrate. Table 1 lists the depths (in microns) at which 90 percent of incident photons are absorbed by a typical solar cell.

| Wavelength (Nanometers) | 400 | 450 | 500 | 550 | 600 | 650 | 700 | 750 |
|---|---|---|---|---|---|---|---|---|
| Penetration Depth (Micrometers) | 0.1 | 0.4 | 0.9 | 1.5 | 2.4 | 3.4 | 5.2 | 7.0 |
| Wavelength (Nanometers) | 750 | 800 | 850 | 900 | 950 | 1000 | 1050 | 1100 |
| Penetration Depth (Micrometers | 8.4 | 11 | 19 | 33 | 54 | 156 | 613 | 2857 |

Table 1. Photon Absorption Depth in Silicon (c-Si PC1D 300K)

On the other hand when the wavelength is closer to energy of band gab the spectral efficiency is higher. When photon with high energy impacts silicon atom there is high probability to excitation of valence electron to non-stable energy band and in short time the electron is moving to lower stable energy band. The energy difference is lost and change to heat. Therefor spectral response of higher wavelength photons should be higher than of photons of lower wavelength (even they have higher energy).

## 2. Light beam induced current measurement

Light sources with wavelengths of various colors were used for scanning of samples – Table 2. Various wavelengths of light were used to show the different defects in different depth under the surface of silicon solar cells. See Table 1. Apart from laser, highly illuminating LED diodes installed in a tube similar to that of LASER were used. The tube was a capsule enabling smooth installation of the LED diode instead of laser. It also enabled regulation of illumination.

The LBIC method is realized by the movement of the light source (focused LED diode or laser) fixed on the grid of the pen XY plotter MUTOH IP-210 near the solar cell surface. Thanks to the local response of the solar cell to incident light we get the scan of local current differences (we were using the measurement PC card Tedia PCA-1208). From the obtained data we can get the whole picture of the solar cell current response to light. From this picture we can read the most local type of defect.

For light exposure LASERs and high luminous LED diodes were used. They were inserted into a special container with the same dimensions like the LASERs. The container was used for smooth assembling in the same grid like the LASER and for holding the focusing lens and screening slide.

We have studied set of four samples of solar cells with known defects like swirl defect, scratches, diffusion fail and missing contacts act.

All global parameters of these test cells were known from previous measurements. These parameters are showed in Table 3.

| source | laser | LED | LED | LED |
|---|---|---|---|---|
| color | infrared | red | green | blue |
| wavelength | 830 nm | 660 nm | 560 nm | 430 nm |

Table 2. Used light sources
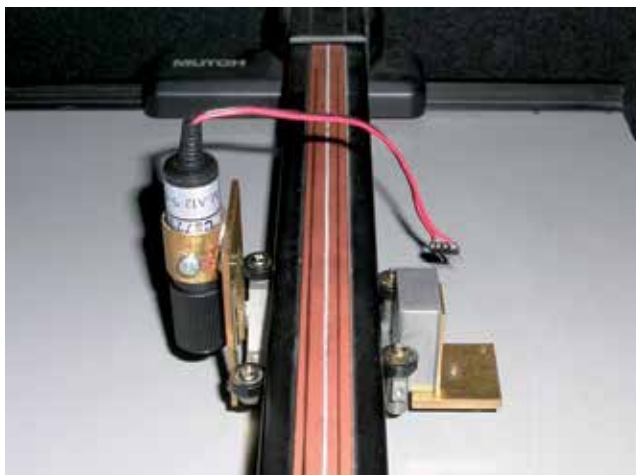
Fig. 4. Laser used in LBIC
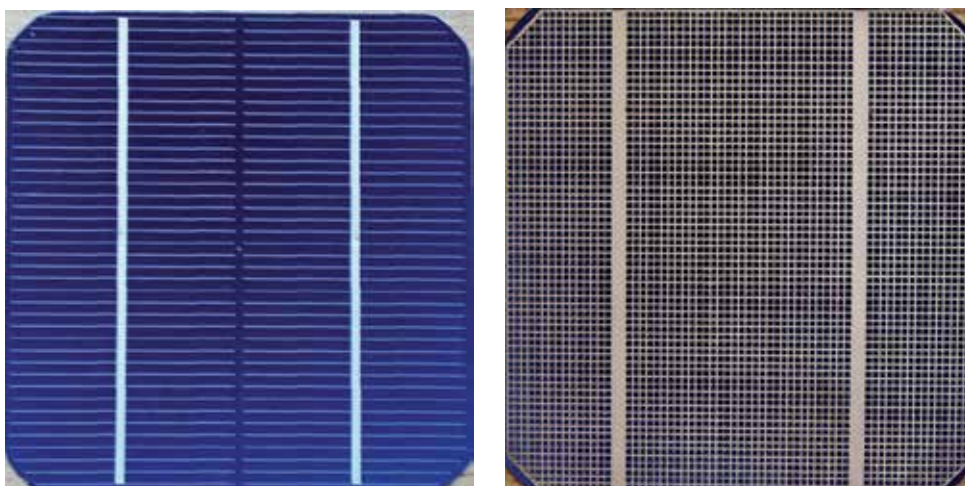


Fig. 5. Front and back side of monocrystaline silicon solar cell.

| Sample | $I_{450}$ [A] | $I_{sc}$ [A] | $U_{oc}$ [V] | $I_m$ [A] | $U_m$ [V] | $P_m$ [W] | FF [%] | EEF [%] |
|---|---|---|---|---|---|---|---|---|
| 1 | 2,729 | 2,842 | 0,576 | 2,628 | 0,476 | 1,252 | 76,5 | 12,04 |
| 2 | 2,344 | 2,511 | 0,559 | 2,293 | 0,461 | 1,057 | 75,4 | 10,17 |
| 3 | 2,426 | 2,602 | 0,560 | 2,344 | 0,466 | 1,092 | 74,9 | 10,50 |
| 4 | 2,500 | 2,670 | 0,567 | 2,473 | 0,459 | 1,136 | 75,1 | 10,92 |

Table 3. Data for global parameters of tested solar cells (Solartec s.r.o, 2005)

There are presented two results for each wavelength (colour of light) of inducing radiation to the chosen samples for a better comparison. There were the sample no. 1 and no 3 chosen. The maximal value of local current is assigned the white color and the minimal current

response is assigned black color. For authenticity of measurement the pictures are kept in their original setting.
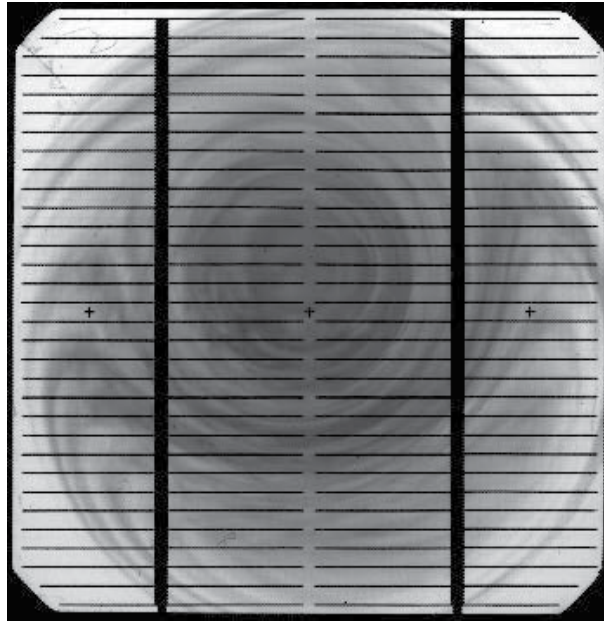


Fig. 6. Analyses of output local current of the sample no. 1 by usage of focused LED diode with middle wavelength 650 nm (red LED, T=297 K)
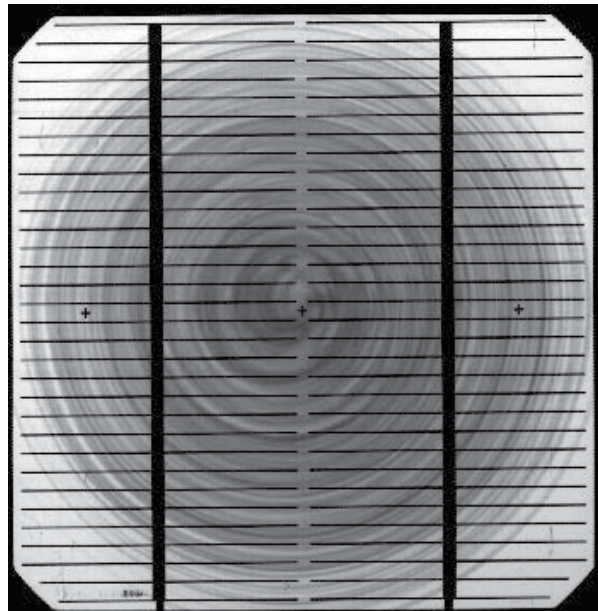


Fig. 7. Analyses of output local current of the sample no. 3 by usage of focused LED diode with middle wavelength 650 nm (red LED, T=297 K)

As mentioned above all samples contain a swirl defect. If you look at the pictures produced by red LED (wavelength 650 nm, figs 6 and 7) this defect is clearly visible.
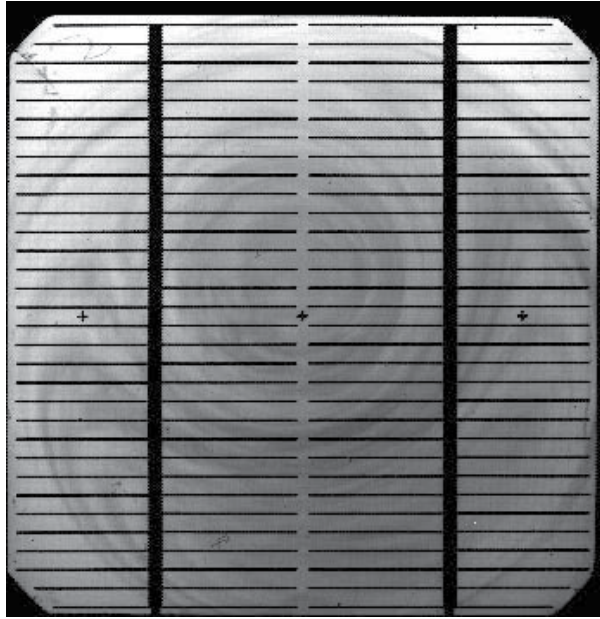


Fig. 8. Analyses of output local current of the sample no. 1 by usage of focused LED diode with middle wavelength 560 nm (green LED, T=297 K)



Fig. 9. Analyses of output local current of the sample no. 1 by usage of focused LED diode with middle wavelength 560 nm (green LED, T=297 K)

For the green LED diode (middle wavelength 560 nm, figures 8 and 9) the defect is still well visible, but not as well-marked as for the red colour (middle wavelength 650 nm).

From the principle of photovoltaic effect it is clear that the light with sufficiently long wavelength passes through the solar cell without generation of photocurrent. With a shorter wavelength the light is absorbed faster from impact light to solar cell and that is why the penetration depth is shorter.

The wavelength of red light is the longest for the used light sources; therefore the penetration depth is the longest. This is proven by well-market visibility of swirl defect which is the defect made in bulk of material.

Along the way the wavelength of blue light is the shortest and it causes the full loss of visibility of this defect. This is caused by the absorption of the light near the solar cell surface where the swirl defect is not taking effect yet.

The wavelength of green color light is between the wavelengths of red and blue color light. Therefore the green color light penetrates to a deeper depth than the blue color light but not so deep as the red color light.

The swirl defect for the blue color (wavelength 430 nm, figures. 10 and 11) is almost invisible.

We may think that the blue color light is not important for LBIC diagnostic because it does not allow the bulk defect detection. If you look at the figure closely, you can observe a decreased affectivity of solar cell in the top right-hand corner of solar cell no 3. (the area of dark gray). These inhomogeneities are due to irregular diffusion during solar cell manufacturing. By the usage of light of red color spectrum this defect is not possible to detect. These defects are surface defects. Even the green colour light can make these inhomogeneities visible, but they can be easily overlooked.
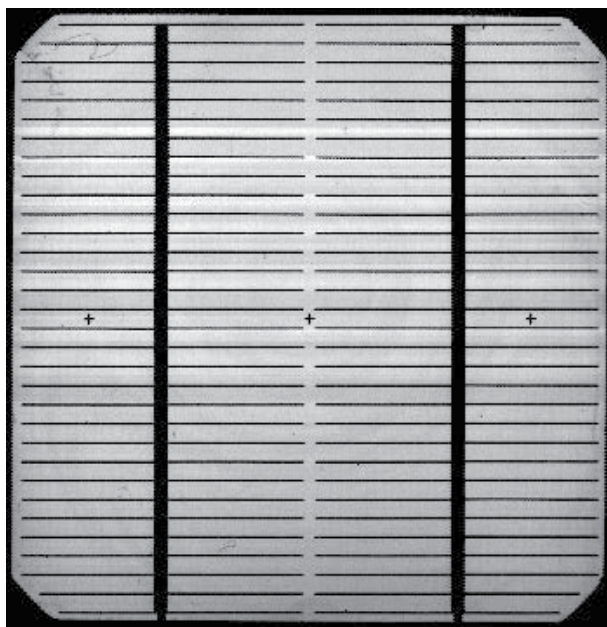


Fig. 10. Analyses of output local current of the sample no. 1 by usage of focused LED diode with middle wavelength 430 nm (blue LED, T=297 K)

Fig. 11. Analyses of output local current of the sample no. 3 by usage of focused LED diode with middle wavelength 430 nm (blue LED, T=297 K)
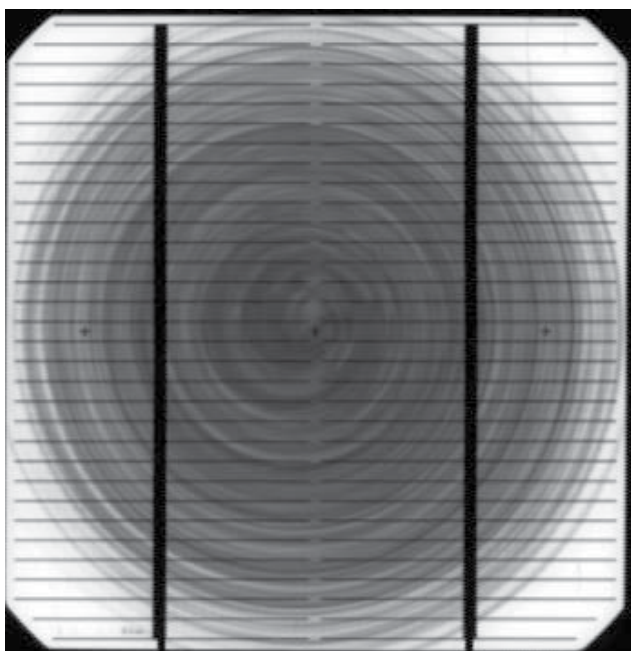


Fig. 12. Analyses of output local current of the sample no. 3 by usage of focused infrared laser (830nm, T=297K)

Among other defects we count scratches and scrapes which are well-marked by all colors even if they are surface defects. This is due to the damage of solar cell structure by higher recombination or higher reflection of damaged surface.

We can compare results for sample no. 3 with the figure produced by the infrared laser M4LA5-30-830 (wavelength 830nm, Fig. 12.). This is the longest wavelength and the penetration depth is the deepest.

The swirl defect displayed by the infrared laser is the most intensive which is the proof of the deepest penetration depth. The obtained picture is slightly defocused in comparison with previous pictures. This is due complicated focusing system of impacting beam because IR light is not visible. The focusing is performed by a special specimen used for focusing the IR laser. The big intensity of defect and a little defocused picture produce a partial loss of information about the surface defect.

### 2.1 Graphic analyses of LBIC data

The result of solar cell scanning is array of values corresponding to local current response to impacting light beam. This array of value is depending on AD convertor but mostly the result is the 12-bit value matrix which is converted to 8 bit (grey tone picture) graphic output. A value 0 corresponds to the darkest black and value 255 corresponds to the lightest white. By the changing of the corresponding colour interval we can visualize the defects which are hidden for graphic analyse and improve the output picture.
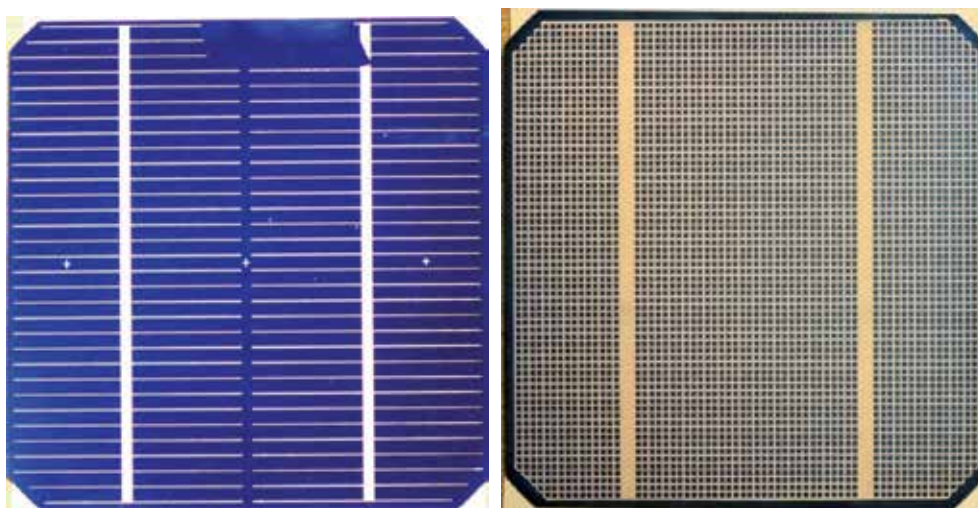


Fig. 13. Front and back side of tested monocrystaline silicon solar cell 710B1.
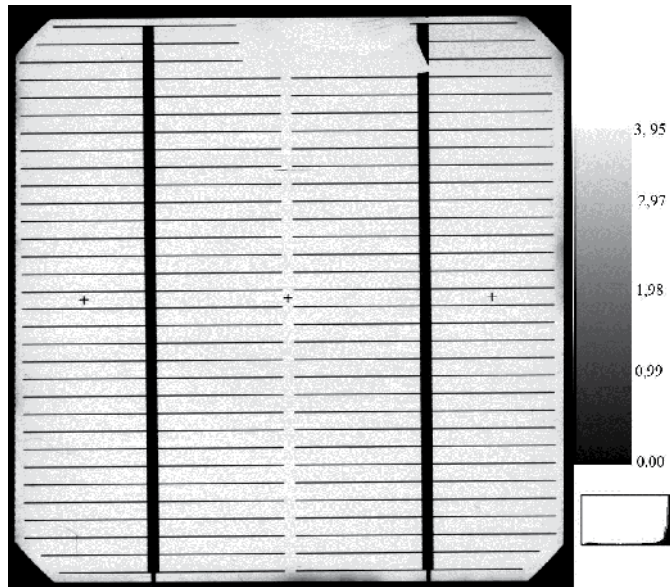
Fig. 14. Output LBIC scan of sample 710B1 in maximal converted interval measured values to grey tone colour (T = 298 K, $\lambda_S$ = 650 nm)
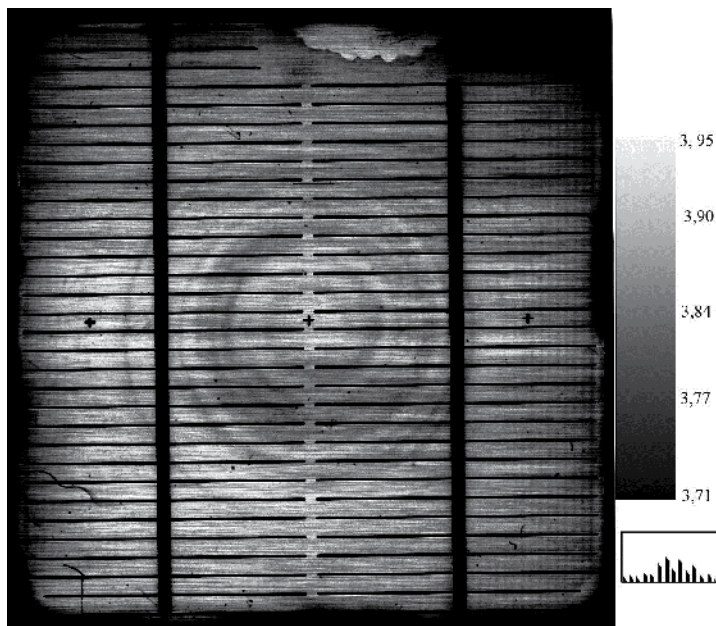


Fig. 15. Output LBIC scan of sample 710B1 in linear selected interval measured values of 3.71 to 3.91 grey tone colour (T = 298 K, $\lambda_S$ = 650 nm)
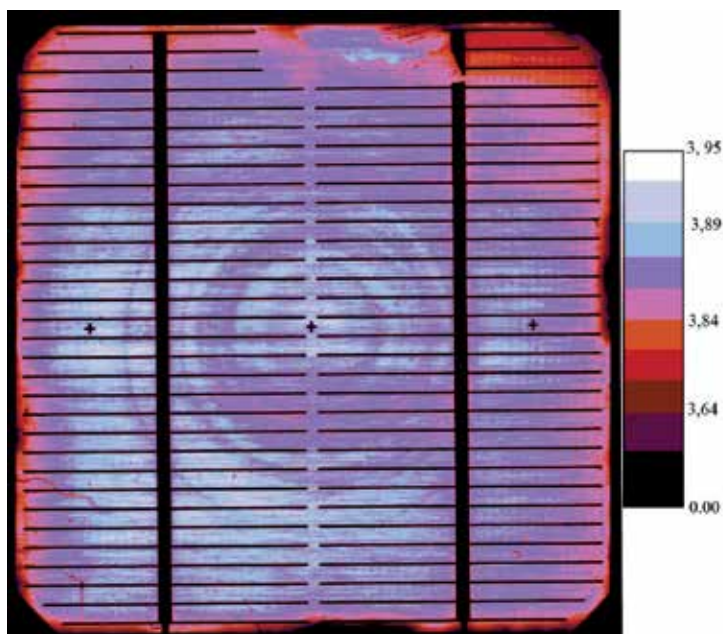
Fig. 16. Output LBIC scan of sample 710B1 in coloured nonlinear selected interval measured values of 0 to 3.95 grey tone colour (T = 298 K, $\lambda_S$ = 650 nm)

## 3. Projection of solar cell back side contact to the LBIC image

 Thanks to different wavelength of used light illumination we can detect different defect and structures depending on penetration depth of light photon. However, the experiments have showed that we can detect structures behind of expected depth like contact bar on the back side of solar cells. This contact we did not detect using long wavelength (IR-980 nm or red-630 nm LED) but they were clearly visible using short wave length (green-525 nm, blue-430 nm or UV-400 nm LED).  Nevertheless using long wavelength enable to clearly detect deep material defects like swirl which are not clearly detectable by UV or blue wavelength but this wavelength enables to detect surface defect.

Projection of back side contact bar to short wavelength LBIC picture can be explain by theory of secondary emission of long wavelength light (~1100 nm) which has penetration depth (~2800μm) much more higher then solar cells depth. Incident high energy light is absorbed in front surface of solar cell and generates electron-hole pair. Part of this carrier charges are separated and generated photocurrent. Because of small penetration depth of impacting photon, most of carrier charges generate near surface area. Thank to high recombination rate on surface a big amount of this carrier charges recombine and emit IR light. The spectral efficiency of impacting photon wavelength is low so the output primary photocurrent is low, too, and do not cover the current induced by secondary emitted photons with energy near silicon band gap and with high spectral efficiency. IR light incidents on back metal contact are absorbed without generation electron-hole pair. Light incident to back surface without metallic contact is reflected back and is absorbed inside substrate volume. This theory was verify by scanning of solar cell illuminated by UV light (Fig. 18) in IR region (Fig. 19).
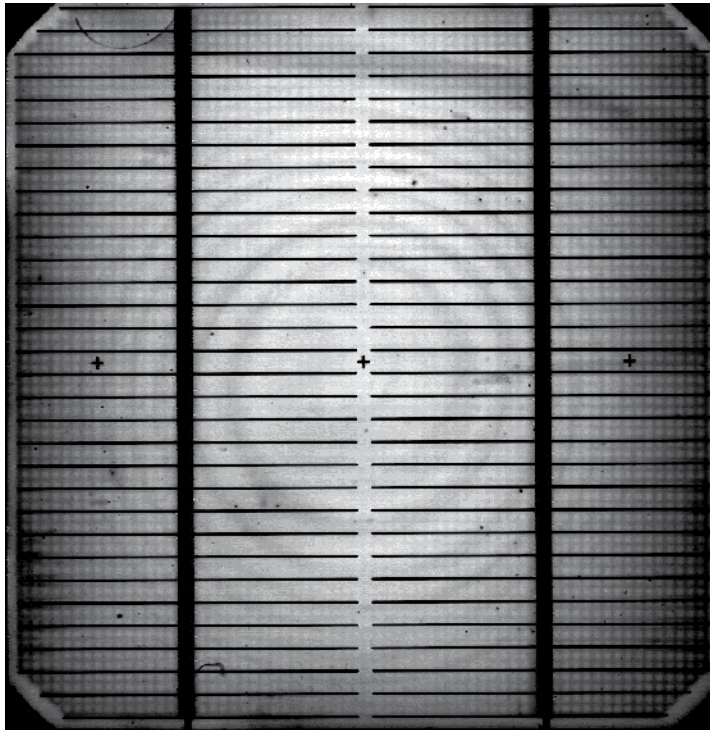
Fig. 17. Projection of back contact bar in LBIC of the sample 57A3 by usage of focused LED diode with middle wavelength 430 nm (blue LED, T=297 K)
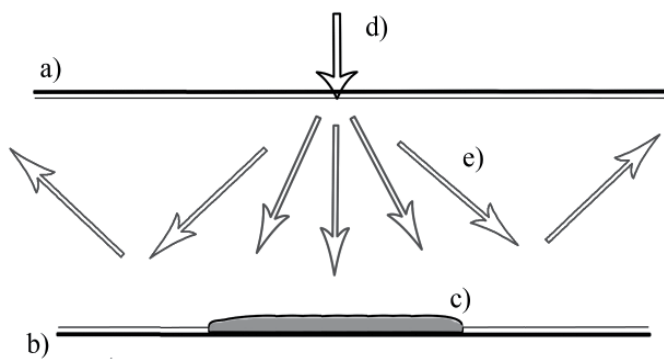


Fig. 18. Theory of projection back side contact during secondary emission of long wavelength light.
a) front side surface, b) back side surface, c) metallic contact on back side, d) short wavelength light e) emitted long wavelength light.
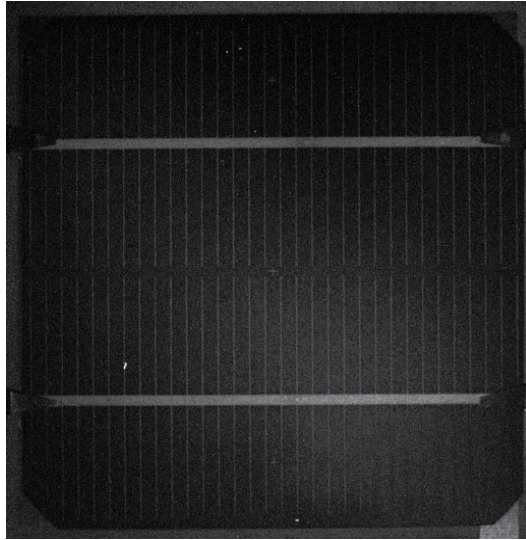
Fig. 19. Photoluminescence of solar cell 24B3 illuminated by UV-400 nm light, scan through blue filter (380- 460nm) – no strong luminescence.
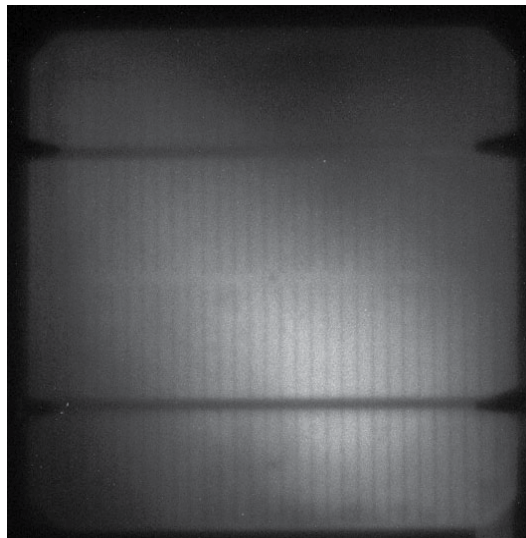


Fig. 20. Photoluminescence of solar cell 24B3 illuminated by UV-400 nm light, scanned through IR filter (742 nm and more) - measurable luminescence.

## 4. Conclusion

The measurement of solar cells using the LBIC method makes possible to most type of defect detection. Various wavelengths of light were used to spot different defects at different depths under the surface of silicon solar cells. This chapter presents the LBIC analysis of set silicon solar cells prepared up-to-date technique. The measurements have demonstrated a strong dependence of LBIC characteristics on the used light source wavelength.

Even better results could be achieved by using LASERs instead of focused LED diodes. The problem of using LED diodes is the weak intensity of light beam connected with low photocurrent and superposition with surrounding noise.

## 5. Acknowledgement

## 6. References

Vasicek, T. Diploma theses, 2004, Brno University of Technology, Brno

Pek, I. Diploma theses , 2005, Brno University of Technology, Brno

Intel, Photodetectors, On-line : http://www.intel.com/technology/itj/2004/ volume08issue02/ art06_siliconphoto/p05_photodetectors.htm, Citeted 2004

Vanek, J., Brzokoupil, V., Vasicek, T., Kazelle, J., Chobola, Z., Barinka, R.  The Comparison between Noise Spectroscopy and LBIC In *The 11th Electronic Devices and Systems Conference. The 11th Electronic Devices and Systems Conference*. Brno: MSD, 2004, s. 454 - 457, ISBN 80-214-2701-9

Vaněk, J., Kazelle, J., Brzokoupil, V., Vašíček, T., Chobola, Z., Bařinka, R. The Comparison of LBIC Method with Noise Spectroscopy. Photovoltaic Devices. Kranjska Gora, Slovenia, *PV-NET*. 2004. p. 60 - 60.

Vaněk, J.; Chobola, Z.; Vašíček, T.; Kazelle, J. The LBIC method appended to noise spectroscopy II. In *Twentieth Eur. Photovoltaic SolarEnergy Conf.* Barcelona, Spain, WIP-Renewable Energies. 2005. p. 1287 - 1290. ISBN 3-936338-19-1.

Vaněk, J., Kazelle, J., Bařinka, R. Lbic method with different wavelength of light source. In *IMAPS CS International Conference* 2005. Brno, MSD s.r.o. 2005. p. 232 - 236. ISBN 80-214-2990-9.

Vaněk, J., Kubíčková, K., Bařinka, R. Properties of solar cells by low an very low illumanation intensity. In *IMAPS CS International Conference* 2005. Brno, MSD s.r.o. 2005. p. 237 - 241. ISBN 80-214-2990-9.

Vaněk, J., Boušek, J., Kazelle, J., Bařinka, R. Different Wavelenghts of light source used in LBIC. In *21st European Photovoltaic Solar Energy Conference*. Dresden, Germeny, WIP-Renewable Energies. 2006. p. 324 - 327. ISBN 3-936338-20-5.

Vaněk, J.; Fořt, T.; Jandová, K. Solar cell back side contact projection to the front side lbic image. In *8th ABA Advanced Batteries and Accumulators*. Brno, TIMEART agency. 2007. p. 253 - 255. ISBN 978-80-214-3424-0.

Vaněk, J.; Fořt, T.; Jandová, K.; Bařinka, R. Projection fo solar cell back side contact to the LBIC image. In *EDS'07*. Brno, TIMEART agency. 2007. p. 253 - 255. ISBN 978-80-214-3470-7.

Vaněk, J.; Dolenský, J.; Jandová, K.; Kazelle, J. Dynamic light beam induced voltage testing method of solar cell. In *EDS ´08 IMAPS Cs International Conference Proceedings*. Brno, Vysoké učení technické v Brně. 2008. p. 153 - 156. ISBN 978-80-214-3717-3.

Vaněk, J.; Jandová, K.; Kazelle, J.; Bařinka, R.; Poruba, A. Secondary photocurrent, current generated from secondary emitted photons. In *23rd European Photovoltaic Solar Energy Conference*, 1-5 September 2008, Valencia, Spain. 2008. p. 323 - 325. ISBN 3-936338-24-8.

# Producing Poly-Silicon from Silane in a Fluidized Bed Reactor

B. Erik Ydstie and Juan Du
*Carnegie Mellon University*
*USA*

## 1. Introduction

The accumulated world solar cell capacity was 2.54 GW in 2006, 89.9% based on mono- or multi-crystalline silicon wafer technology, 7.4% thin film silicon, and 2.6% direct wafering (Neuhaus & Münzer, 2007). The rapidly expanding market and high cost of silicon led to the development of thin-film technologies such as the Cadmium Telluride (CdTe), Copper-Indium-Gallium Selenide (CIGS), Dye Sensitized Solar Cells, amorphous Si on steel and many other. The market share for thin-film technology jumped to nearly 20% of the total 7.7 GW of solar cells production in 2009 (Cavallaro, 2010).

There are more than 25 types of solar cells and modules in current use (Green & Emery, 1993). Technology based on mono-crystalline and multi-crystalline silicon wafers presently dominate and will probably continue to dominate since raw material availability is not a problem given that silicon is abundant and cheap. Solar cells based on rare-earth metals pose a challenge since the cost of the raw materials tend to fluctuate and availability is limited. However the cost of silicon solar cells and the raw material, solar grade poly-silicon is too high and this technology will be displaced unless cost effective alternatives are found to make silicon solar cells.

Figure 1 shows the approximate distributions for the different costs in producing a silicon based solar module (Muller et al., 2006). The figure shows where there is significant incentive to reduce costs. The areas of solar grade silicon (SOG) production and wafer manufacture stand out. These processes are presently not well optimized and many opportunities exist to improve the manufacturing technology through process innovation, retro-fit, optimization and process control.

Poly-silicon, the feedstock for the semiconductor and photovoltaic industries, was in short supply during the beginning of the last decade due to the expansion of the photovoltaic (PV) industry and limited recovery of reject silicon from the semiconductor industry. The relative market share of silicon for the electronic and solar industries is depicted in Figure 2. This figure shows the growing importance of the the solar cell industry in the poly-silicon market. Take last year as an example, a total amount of 170,000 metric tons of poly-silicon was produced and 85% was consumed by solar industry while only 15% was consumed by the semiconductor industry. This represents a complete reversal of the situation less than two decades ago. During the last decade, the total PV industry demand for feedstock grew by more than 20% annually. The forecasted growth rate for the next decade is a conservative 15% per year. The available silicon capacities for both semiconductor and PV industry are limited to 220,000 metric tons for the time being.
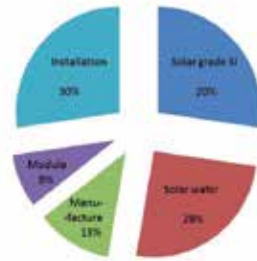
Fig. 1. The cost distribution of a silicon solar module.
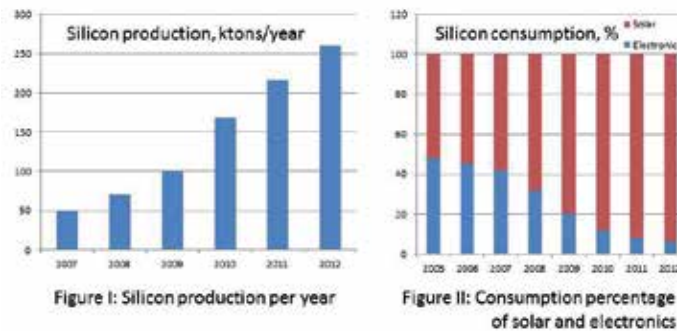


Fig. 2. Poly-Silicon Production and consumption for Electronic and PV Industries (Fishman, 2008).



Fig. 3. The supply chain for solar cell modules.

Six companies supplied most of the poly-silicon consumed worldwide in the year of 2000, namely, REC Silicon, Hemlock Semi-Conductor, Wacker, MEMC, Tokuyama and Mitsubishi (Goetzberger et al., 2002). Those companies still cover most of the world wide production capacity and produced over 75% of the poly-silicon in 2010.

## 2. Solar grade poly-silicon production

Figure 3 illustrates the typical silicon solar cell production. The supply chain starts with the carbothermic reduction of silicates in an electric arc furnace. In this process large amounts of electrical energy breaks the silicon-oxygen bond in the $SiO_2$ via the endothermic reaction with carbon. Molten Si-metal with entrained impurities is withdrawn from the bottom of the furnace while $CO_2$ and fine $SiO_2$ particles escape with the flu-gas (Muller et al., 2006).
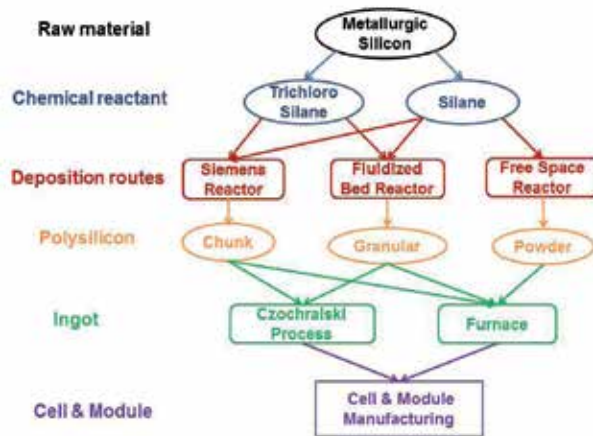
Fig. 4. Silicon based Solar Cell Production Process.
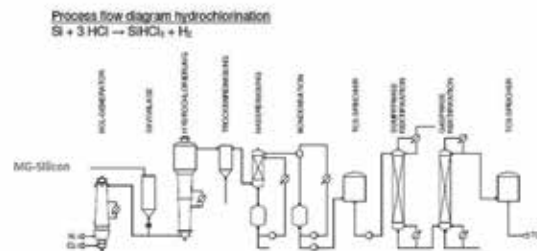


Fig. 5. The production of highly pure TCS from MG-Si.

Metallurgical grade silicon (MG-Si) at about 98.5-99.5% purity is sold to many different markets.   The majority of MG-Si is used for silicones and aluminum alloys (Surek, 2005).   A much smaller portion is for fumed silica, medical and cosmetic products and micro-electronics. A small but rapidly growing proportion is used for solar applications.

Metallurgical silicon is converted to high-purity poly-silicon through two distinct routes. In the metallurgical route the silicon is purified through a combination of steps targeted at different impurities (Muller et al., 2010).  Leaching with calcium based slags may remove some impurities whereas directional solidification takes advantage of the high liquid-solid segregation coefficient of metallic impurities and leaching eliminates metallic silicides in the grain boundaries.   One bottleneck of this process is low purity and yield relative to the chemical route.   Only a small percentage of the current market is based on this approach (Fishman, 2008).

High purity poly-silicon suitable for solar cells and micro-electronics can also be produced by a chemical route which typically proceeds in two steps. In the first step MG-Si reacts with HCl to form a range of chlorosilanes, including tri-chlorosilane (TCS). TCS has a normal boiling point of $31.8^o C$ so that it can be purified by distillation. One process alternative for producing TCS is shown in Figure 5.  Poly-silicon is then produced in the same manufacturing facility by pyrolysis of TCS in reactors that are commonly referred to as Bell or Siemens reactors (del Coso et al., 2007). In the Bell reactor TCS passes over high purity silicon starter rods which are

heated to about $1150^oC$ by electrical resistance heating. The gas decomposes as

$$2HSiCl_3 \rightarrow Si + 2HCl + SiCl_4$$
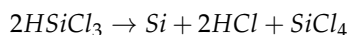
Silicon deposits on the silicon rods as in a chemical vapor deposition process. 9N(99.999999999%) silicon is used for micro-electronics applications. Silicon which is 6N or better is called solar grade silicon (SOG-Si) and it can be used to produce high quality solar cells (Talalaev, 2009).

The free space reactor provides an alternative to the Siemens reactor. It has lower capital and operating cost. However, its disadvantage is that it is difficult to regulate the melting process to generate ingots and wafers. This process has not been used industrially on a large scale yet (Fishman, 2008).

The annual price for solar grade silicon went through a very sharp maximum in 2008 due to high demand and limited poly-silicon production capacity. The increase in price was expected (Woditsch & Koch, 2002) and led to a similar increase in the cost of wafers. The price of solar grade silicon is expected to stabilize in the coming decade as new technologies are introduced and capacity is added to the supply chain: The classical TCS process was designed for micro-electronics manufacture where silicon cost is not as critical as in the solar cell industry. Some companies have retro-fitted their processes to produce solar rather than micro-electronics grade silicon. The pyrolysis process has been made suitable for high volume production of poly-silicon; reactive separation and complex instead of simple distillation has been proposed to reduce energy requirements; and fluid bed reactor technology is set to replace the Bell reactors during the next decade. Finally, progress has been made in making solar grade silicon directly using metallurgical routes. All attempts have not been as successful as was hoped for yet. Nevertheless, it is very likely that solar grade silicon prices can be reduced to $25-30 per kg in the next decade if the tempo of industry expansion is maintained (Neuhaus & Münzer, 2007).

## 3. Fluidized bed reactor

Fluidized bed reactors have excellent heat and mass transfer characteristics and can be utilized for Silane decomposition to overcome the energy waste problem in Siemens process. The energy consumption is reduced because the decomposition operates at a lower temperature and cooling devices are not required. In addition fluidized beds have high throughput rate and operate continuously reducing further capital and operating costs. The final product consist of small granules of high purity silicon that are easy to handle compared to powder produced by free space reactor (Odden et al., 2005).

In the fluidized bed reactor (Kunii & Levenspiel, 1991), the reactive gas is introduced into the reactor together with preheated fluidizing gases, such as hydrogen or helium. Heat for the thermal decomposition is supplied by external heating equipment. Pyrolysis of silicon containing gas produces silicon deposition on seed particles, the subsequent particle growth is due to heterogeneous chemical vapor deposition as well as scavenging of homogeneous silicon nuclei. This results in a high deposition rate by a combination of heterogeneous and homogeneous decomposition reactions. As the silicon seed particles grow, the larger particles move to the lower part of the bed and are removed as a final product. The continuous removal of silicon seed particles after they have grown to the desired size leads to depletion of particles and it is necessary to introduce additional silicon seed particles into the fluidized bed to replace those removed final product (Würfel, 2005).

Two techniques are used to provide a continuous supply of pure silicon seed particles to the fluidized bed reactor. One technique uses a hammer mill or roller crushers to reduce
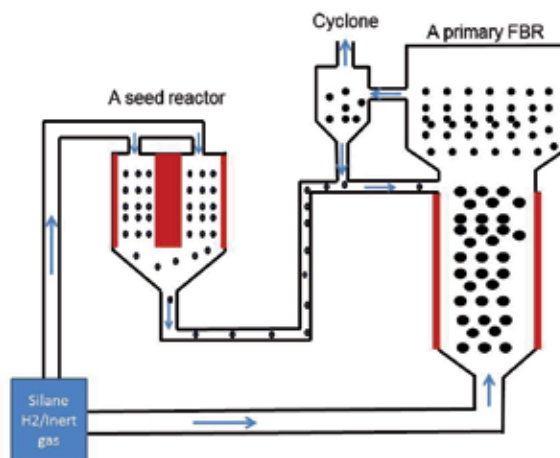
Fig. 6. Fluidized bed reactor with seed generator.

the bulk silicon to a specific particle size distribution suitable for use as seed particles. However, this technique is expensive and causes severe contamination problems. Moreover, the crushing results in a non-spherical seed particle which presents an undesired surface for silicon deposition. The other technique for producing silicon seed particles involves the recycling small particles generated in and removed from the fluidized bed (Odden et al., 2005). In the fluidized bed, the majority of silicon produced during thermal decomposition undergoes heterogeneous deposition on the surface of the seed while a certain amount of silicon is formed homogeneously as gas dust recycled back into the reactor as seed particles (Caussat et al., 1995a). However, those amount of silicon is not sufficient to meet the entire demand for new seed particles. The combination of the recycled homogeneous particles and seed particles produced by crushing (Kojima & Morisawa, 1991) can provide an effective means of re seeding. More importantly, these homogeneously formed particles are amorphous such that they do not provide desirable surface for deposition neither.

A novel seed generator for continuously supplying silicon seed particles solves the above problems (Hsu et al., 1982). This seed generator produces precursor silicon seed via thermal decomposition of silicon containing gas. This device generates uniformly shaped seed particles with desirable fluidization characteristics and silicon deposition. The scheme of silicon production process is illustrated in Figure 6. It comprises a primary fluidized bed reactor and a silicon seed generator. The seed particles are introduced into the primary fluidized bed reactor through seed particle inlet (Steinbach et al., 2002).

## 4. Silane pyrolysis in fluidized beds

Hogness *et al.* (Hogness et al., 1936) was one of the earliest to undertake a series of experiments to study the thermal decomposition of silane. They concluded that the reaction was homogeneous and first order. The hydrogen acted as an inhibitor for the decomposition and no reactions between hydrogen and silicon to form silane was observed. Zambov (Zambov, 1992) investigated the kinetics of homogeneous decomposition of silane and their experimental results showed that homogeneous and heterogeneous pyrolysis coexisted. Furthermore they developed a mathematical model to demonstrate that the ratio of

homogeneous decomposition to heterogeneous deposition grew with increasing temperature and pressure and thus resulted in a substantial degradation of the layer thickness uniformity. A suitable model for silane pyrolysis was developed by Lai *et al.* (Lai et al., 1986) to describe different reaction mechanisms in fluidized bed reactors. They assumed that silane decomposed by heterogeneous and homogeneous decomposition, and occurred via seven pathways as following:

1. Chemical vapor deposition on silicon particles (heterogeneous deposition);

2. Chemical vapor deposition on fines (heterogeneous deposition);

3. Homogeneous decomposition to form Silicon vapor;

4. Coalescence of formation of fines;

5. Diffusion-aided growth of fines;

6. Growth of fines by coagulation;

7. Scavenging of fines by particles;

Heterogeneous decomposition of silane on the existing silicon seed particles (pathway 1) or on the formed nuclei (pathway 2) lead to a chemical vapor deposition of silicon. The reaction rate was described by first order form published by Iya *et al.* (Iya et al., 1982).

Homogeneous decomposition forms a gaseous precursor (pathway 3) that nucleate a new solid phase of silicon, which is called silicon vapor. The concentration of vapor given by Hogness (Hogness et al., 1936) and Caussat (Caussat et al., 1995b) was always negligible as they can be suppressed by diffusion aided growth and coalescence of fines.

By pathway 4 nucleation of critical size nuclei, occurs whenever supersaturation is exceeded. The concentration of silicon vapor can be suppressed by diffusion and condensation on large particles (pathway 5). We assume here that nucleation occurs by the homogeneous nucleation theory. The molecular bombardment rate of small particles (pathway 4) is calculated by the classical expression of kinetic theory while the diffusion rate to large particles (pathway 6) is readily obtained from film theory of mass transfer. The coagulation rate of the fines in pathway 6 was determined by the coagulation coefficient which only depend on the average size of the fines. Scavenging rate was also proportional to a scavenging coefficient depending on the size of particles. Those seven pathways are widely used in practice to describe the reaction mechanism to produce silicon from silane.

Two significant problems exist for industrial practice: fines formation and particle agglomeration (Cadoret et al., 2007). For the problem of fines formation, their experimental study showed that for the inlet concentration of the reactive gas less than 20%, silane conversion was quite complete and fines formation limited. The fines ratio never exceeded 3% regardless of inlet concentration of silane. This encouraging result demonstrated that silicon chemical vapor deposition on powders in a fluidized bed was possible and efficient. The other new observation that chemical reactions of gaseous species on cold surfaces was the cause of fines formation was in complete contradiction with previous works (Hsu et al., 1982) (Lai et al., 1986), for which fines were formed homogeneously in fluidized bed. As to the problem of particle agglomeration, they observed that the presence of silane in the reactor could modify particle cohesiveness. The more plausible explanation for this modification was the reactive species adsorbed on particle surfaces could act as a glue for solids (Caussat et al., 1995a).

$$SiH_4 \rightarrow Si + 2H_2$$
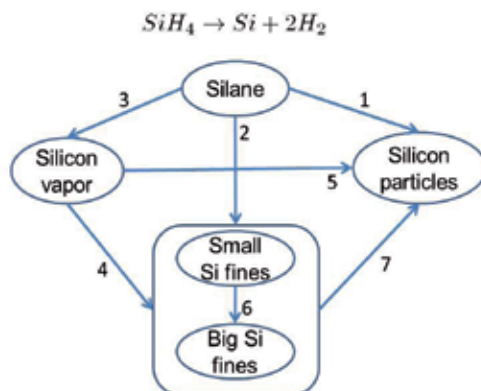


Fig. 7. Reaction pathways for conversion of silane to silicon. (Lai et al., 1986)

## 5. Computational fluid dynamics modeling

Computational fluid dynamics offers a powerful approach to understanding the complex phenomena that occur between the gas phase and the particles in the fluidized bed. The Lagrangian and Eulerian models have been developed to describe the hydrodynamics of gas solid flows for the multiphase systems (Piña et al., 2006). The Lagrangian model solves the Newtonian equations of motion for each individual particle in the gas solid system. However the large number of equations cause computational difficulties to simulate industrial fluidize beds reactors. The Eulerian model treats all different phases as continuous and fully interpenetrating. Generalized Navier-Stokes equations are employed for the interacting phases.

Constitutive equations are necessary to close the governing relations and describe the dynamics of the solid phase. To model solid particles as a separated phase, granular theory is employed to determine its physical parameters. The highly reduced number of equations in the Eulerian model needs much less effort to solve in comparison to the Lagrangian model. Modeling the hydrodynamics of gas-solid multiphase systems with Eulerian models has shown a promising approach for fluidized bed reactors.

Commercial software has been used to solve the models mentioned above. FEMLAB solves the partial differential equations by simulating fluidized bed reactors (Balaji et al., 2010). The simulations account for dynamic transport and hydrodynamic phenomena. Mahecha-Botero *et al.* (Mahecha-Botero et al., 2005) presented a generalized dynamic model to simulate complex fluidized bed catalytic systems. The model describes a broad range of multi-phase catalytic systems subject to mass and energy transfer among different phases, changes in the molar/volumetric flow due to the reactions and different hydrodynamic flow regimes. The generalized model (Mahecha-Botero et al., 2006) dealt with anisotropic mass diffusion and heat conduction and was used for different flow regimes which included bubble phase, emulsion phase and freeboard. The model was applied to simulate an oxychlorination fluidized bed reactor for the production of ethylene dichloride from ethylene. An exchange term was introduced to simulate the fluidized bed reactor as interpenetrating continua, composed of two interacting phases. The numerical results were very similar to those of Abba *et al.* (Abba et al., 2002) and gave good agreement with industrial reactor measured results.

Guenther *et al.* (Guenther et al., 2001) presented an althernative method for simulating fluidized bed reactors using the computational codes MFIX (Multiphase Flow with Interphase eXchanges) developed at the US Department of Energy National Energy Technology Laboratory. Three-dimensional simulations of silane pyrolysis were carried out by using MFIX. The reaction chemistry was described by the homogeneous and heterogeneous reactions described above. The results showed excellent agreement with experimental measurements and demonstrated that these methods can predict qualitatively the dynamical behavior of fluidized bed reactors for silane pyrolysis. Caussat *et al.* (Cadoret et al., 2007) used MFIX for transient simulations for silicon fluidized bed chemical vapor deposition from silane on coarse powders. The three-dimensional simulations provided better results than two-dimension simulations. The model predicts the temporal and spatial evolutions of local void fractions, gas and particle velocities and silicon deposition rate.

White *et al.* (White, 2007) used FLUENT to capture the dynamics of gas flow through a bed of particles with one constant average size. The inputs to FLUENT were reactor geometry, gas flow rates and temperature, heater duty, particle hold-up and average size. The CFD calculations predicted the bed properties such as the overall bed density and the temperature as functions of height. This study formed the basis for a multi-scale model for silane pyrolysis in FBR (Du et al., 2009)

## 6. The dynamics of particulate phase

Fluidized bed reactor dynamics are characterized by the production, growth and decay of particles contained in a continuous phase. Such dynamics can be found everywhere in the chemical engineering field, such as crystallization, granulation and fluidized bed vapor decomposition. Particularly for the solar grade silicon production process in a fluidized bed, the particles grow with heterogeneous chemical vapor deposition and homogeneous decomposition. White *et al.* (White et al., 2006) developed a dynamical model to represent the size distribution for silicon particles growth. The idea for the model development is based on classical population balance proposed by Hulburt and Katz (Hulburt & Katz, 1964). Hulburt *et al.* used the theory of statistical mechanics to develop an infinite dimensional phase space description of the particle behavior. The resulting balance equations express the conservation of probability in the phase space. A set of integro-partial differential equations are generated if the population balance is incorporated with mass balance for the continuous phase. However it requires significant computational efforts to solve those equations. Moment transformation and discretization are two commonly used methods to solve those equations. Randolph and Larson (Randolph & Larson, 1971) proposed the use of moment transformation while Clough (Cooper & Clough, 1985) used orthogonal collocation. Hounslow (Hounslow, 1990) and Henson *et al.* (Henson, 2003) employed various discretization techniques to solve them.

Du *et al.* (Du et al., 2009) reduced the continuous population balance to finite dimensional space by discretizing the size of particles into a finite number of size intervals. In each size interval, both mass balance and number balance are established and the discrete population balance is obtained by comparing those two balance equations. This approach ensures that conservation laws are maintained at all discretization levels and facilitates computation without additional discretization.

Figure 8 illustrates the modeling approach developed by White *et al.* and how it describes how particles change as a function of time. In this method particles are distributed among $N$ discrete size intervals, characterized by an average mass $m_i$ for $i = 1, ..., N$. The relationship between the total mass of particles ($M_i$) in an interval and the number of particles in each
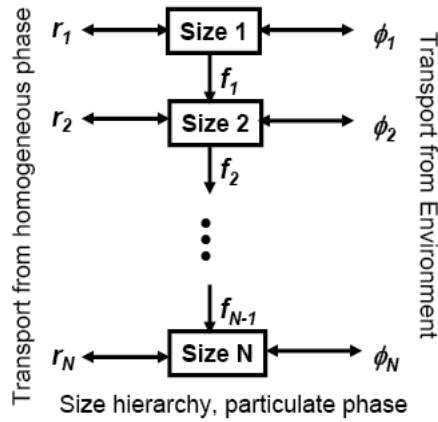
Fig. 8. The network representation of population balance

interval ($n_i$) is thereby given by the expression

$$M_i = m_i n_i. \tag{1}$$

The mass balance for size interval $i$ is written

$$\frac{dM_i}{dt} = q_i + r_i + f_{i-1} - f_i + f_i^a \tag{2}$$

The rate of addition of particles to interval $i$ from the environment is $q_i^{in}$ while particle withdrawal is $q_i^{out}$, so the total external flow of particles is represented by

$$q_i = q_i^{in} - q_i^{out}.$$

The rate of material transfer from the fluid phase to the particle is represented by $r_i$. The term, $f_i^a$ represents the rate of change due to agglomeration, breakage or nucleation. The value can be expressed so that

$$f_i^a = f_i^{a,in} - f_i^{a,out},$$

where $f_i^{a,in}$ represents particle transition to interval $i$ due to agglomeration or nucleation, and $f_i^{a,out}$ represents particle transition out of an interval due to breakage or agglomeration. These terms are often referred to as birth and death in the population balance literature. Finally, the rate of transition of particles from one size interval to the next, caused by particle growth, is represented by $f_{i-1}$ for flow into interval $i$ and $f_i$ for flow out of interval $i$. By connecting several of these balances together we get the network description of the particulate system illustrated in Figure 8. The model was validated by experimental data from pilot plant tests (?) and it was used for pilot plant design and scale-up. It also was used for further development of control strategies and study of dynamical stability of particles' behavior in fluidization processes.

## 7. Multi-scale modeling

Du *et al.* (Du et al., 2009) proposed a multi-scale approach for accurate modeling of the entire process. The hydrodynamics were modeled using CFD, which provides a basis for a simplified reactor flow model. The kinetic terms and the reactor temperature and concentrations are expressed as functions of reactor dimensions, void volume and time in the CFD module. Reactor temperature and concentration from the CFD module provides inputs to the CVD module. The CVD module calculates the overall process yield which provided an input to the population balance module. The average particle diameter is then calculated by population balance module and imported into the CFD module to complete model integration. In continuation of the above mentioned works by White *et al.* (White et al., 2007), Balaji *et al.* (Balaji et al., 2010) presented the complete multi-scale modeling approach including the effect of computational fluid dynamics along with population balance and chemical vapor deposition models. For the first time in the field of silicon production using fluidized beds, they coupled all the effects pertaining to the system (using partial differential equations (CFD), ordinary differential equations (PBM) and algebraic equations (CVD)) and they solved the resulting nonlinear partial differential algebraic equations with a computationally efficient and inexpensive solution methodology.

In order to verify the multi-scale model, we compare the numerical results with experimental data. The relationship between particle flow rates and average particle size at steady state is derived as (White, 2007),

$$1 + \frac{P}{S} = \frac{n_p}{n_s}(\frac{D_{ap}}{D_{as}})^3 \tag{3}$$

where $P$ is the product withdraw flow rate and $S$ is the seed addition rate. $D_{ap}$ is the average particle diameter of product and $D_{as}$ is the average particle diameter of seed. $n_p$ is the number of particles being removed and $n_s$ is the number of particles being added.

If $\ln(1 + P/S) = \ln(n_p/n_s) + 3\ln(D_{ap}/D_{as})$ holds true, then it implies that $n_p/n_s = 1$, which means no nucleation, agglomeration, or breakage is present. On the other hand $n_p/n_s < 1$ indicates that particle agglomeration takes place in the reactor and $n_p/n_s > 1$ means that particle breakage occurs in the pilot plant. The dashed lines in Figure 9 represent the analytical expression. The numerical results in Figure 9 agree with both analytical solution and experimental results which supports that the multi-scale model can be used for further control studies.

## 8. Operation and control

Bed temperature is one key factor for the deposition rate and the quality of the deposition. Inlet silane concentration also affect the deposition rate as well as fines formation and agglomeration. The fluidization mode is determined by a gas velocity ratio between superficial gas velocity $u$ and minimum fluidization velocity $u_{mf}$. All these variables must be coordinated in a multi-variables process control strategy.

A careful selection of the fluidization velocity and silane concentration in the feed limit fines formation and agglomeration. In order to avoid slugging and poor gas-solid contact we adjust fluidization velocity or the ratio bed height to bed diameter during reactor design. Usually hydrogen is used as fluidization gas as it is able to decrease the formation of fines compared to other inert gas such as nitrogen.

Hsu *et al.* (Hsu et al., 1987) proposed that the optimal bed temperature for fluidized bed reactor is $600 - 700^oC$ and gas velocity ratio is between 3 and 5. Within this range, fines elutriation percentage is generally under 10% of the mass of Si in the silane feed. The maximum fine formation is 9.5% at the inlet silane concentration of 57%, no excessive fines
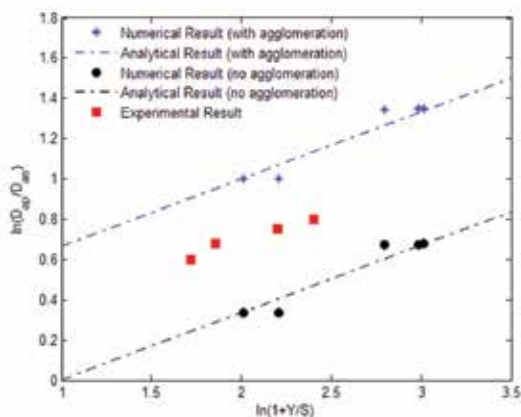
Fig. 9. Model Validation.

are generated with increasing silane concentration from 57% to 100%. Kojima *et al.* (Kojima & Morisawa, 1991) recommended the following operating conditions: bed temperature is $600^{0}C$, gas velocity ratio is 4 and inlet silane concentration is 43%. For both groups, the recommended seed particle size is between 0.15 and 0.3 *melimeter*.

While considerable research effort has been devoted to understanding of the reaction mechanisms and model development for fluidized bed reactors, not much attention has been paid to the study of control technology for the silicon production process. Since this system is complex and typically have limited availability of measurements, complicated control strategies are not suitable to be implemented in the practice. Inventory control (Farschman et al., 1998) is a simple method for control of complex systems and thus has potential for industrial application. It distinguishes itself from other control methods in that it addresses the question of measurement and manipulated variables' selections. We apply inventory control strategy to control particle size distribution by manipulating the total mass of the particles.

The objective of our inventory control system is to control the average particle size in the fluidized bed reactor. We manipulate the seed and product flow rates to achieve the control objective. An inventory control strategy for the total mass hold-up of particles is written as:

$$\frac{dM}{dt} = -K(M - M^*) \tag{4}$$

where $K$ is the proportional control gain. $M$ is the total mass hold up and $M^*$ is the desired hold up. The mass balance of the solid phase is expressed as:

$$\frac{dM}{dt} = S + Y - P \tag{5}$$

where $S$ is the seed addition flow rate, $Y$ is the silicon production rate and $P$ is the product removal rate. The product flow rate can be manipulated to keep the total mass hold-up to a desired value $M^*$ by using the following control action:

$$P = S + Y + K(M - M^*) \tag{6}$$
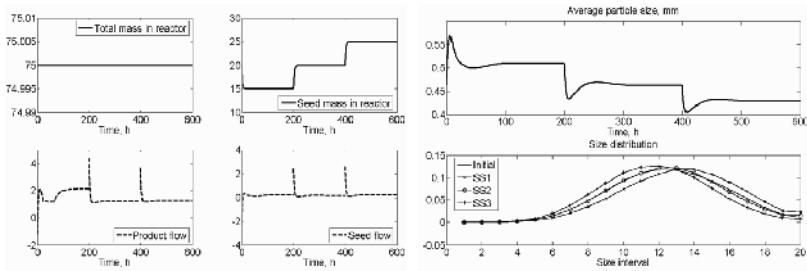
(a) Control total and seed hold up in FBR  (b) Particle size using inventory control

Furthermore we apply inventory control to maintain the seed hold up to a desired value and the control action is in the form of

$$S = -\sum_{i=1}^{N_s} Y_i - K_s \left( \sum_{i=1}^{N_s} M_i - M_{seed}^* \right)$$  (7)

where $N_s$ is the total number of size intervals for the particle seeds and $Y_i$ is the silicon production rate in the seed size intervals, $K_s$ is the proportional gain.

Simulation of controlling the total and seed particle hold-up is shown in Figures 10(a) and 10(b). The hold-up of particles in the system is shown in Figure 10(a). The product and seed flow rates required to achieve the control are also shown. The first steady state (SS1) represents operation when $M_{total}^* = 75$ and $M_{seed}^* = 15$. The subsequent steady states are achieved when $M_{seed}^*$ is increased to 20 and 25. The average particle size and size distribution achieved during each steady state are shown in Figure 10(b). This simulation shows we can control the average product size as well as the product distribution. As the hold up of seed particles increases relative to the total hold up, the average size decreases. The interval representation of the size distribution supports this result. In this simulation, we assumed that the largest seed size interval, $N_s$, was interval 10 out of 20 and that the distribution of seed particles flowing into the system was constant.

## 9. Conclusions

This chapter reviewed the past and current work for modeling and operation of fluidized bed reactor processes for producing solar grade poly-silicon. Currently the shortage of low-cost solar grade silicon is one major factor preventing environmentally friendly solar energy from becoming important in the energy market. Energy consumption is the main cost driver for poly-silicon production process which is highly energy intensive. Fluidized bed reactors serve as an alternative to the Siemens process which dominates the solar grade silicon market. Several companies have attempted to commercialize the fluidized bed reactor process and the process has been scaled up to commercial scale. It has been shown that FBR technology produces poly-silicon at acceptable purity levels and an acceptable price. Extensive research has been carried out to study the chemical kinetics of silane pyrolysis and to model the fluid dynamics in the fluidized beds. The particle growth process due to silicon deposition is captured by discretized population balances which uses ordinary differential and algebraic equations to simulate the distribution function for the particles change as a function of time and operating conditions. A multi-scale modeling approach was applied to couple the population balance with computational fluid dynamics model and reaction model to represented the whole process. The model has been validated with experimental data from

pilot plant tests. An inventory based control is applied to control the total mass hold up of the solid phase and the simulation results demonstrate that such simple control strategy can be used to control the average particle size.

## 10. References

Abba, A., I., R. Grace, J. & T. Bi, H. (2002). Variable-gas-density fluidized bed reactor model for catalytic processes, *Chemical engineering science* 57(22-23): 4797–4807.

Balaji, S., Du, J., White, C. & Ydstie, B. (2010). Multi-scale modeling and control of fluidized beds for the production of solar grade silicon, *Powder Technology* 199(1): 23–31.

Cadoret, L., Reuge, N., Pannala, S., Syamlal, M., Coufort, C. & Caussat, B. (2007). Silicon cvd on powders in fluidized bed: Experimental and multifluid eulerian modelling study, *Surface and Coatings Technology* 201(22-23): 8919–8923.

Caussat, B., Hemati, M. & Couderc, J. (1995a). Silicon deposition from silane or disilane in a fluidized bed–part ii: Theoretical analysis and modeling, *Chemical engineering science* 50(22): 3625–3635.

Caussat, B., Hemati, M. & Couderc, J. (1995b). Silicon deposition from silane or disilane in a fluidized bed–part ii: Theoretical analysis and modeling, *Chemical engineering science* 50(22): 3625–3635.

Cavallaro, F. (2010). A comparative assessment of thin-film photovoltaic production processes using the electre iii method, *Energy Policy* 38(1): 463–474.

Cooper, D. & Clough, D. (1985). Experimental tracking of particle-size distribution in a fluidized bed, *Powder technology* 44(2): 169–177.

del Coso, G., del Canizo, C., Tobias, I. & Luque, A. (2007). Increase on siemens reactor throughput by tailoring temperature profile of polysilicon rods, *Electron Devices, 2007 Spanish Conference on*, IEEE, pp. 25–28.

Du, J., Balaji, S. & Ydstie, B. E. (2009). Multi-scale modeling and inventory control of particle growth processes, *9th International Symposium on Dynamics and Control of Process Systems*.

Farschman, C., Viswanath, K. & Erik Ydstie, B. (1998). Process systems and inventory control, *AIChE Journal* 44(8): 1841–1857.

Fishman, O. (2008). Solar silicon, *Advanced materials & processes* p. 33.

Goetzberger, A., Luther, J. & Willeke, G. (2002). Solar cells: past, present, future, *Solar energy materials and solar cells* 74(1-4): 1–11.

Green, M. & Emery, K. (1993). Solar cell efficiency tables, *Progress in Photovoltaics: Research and Applications* 1(1): 25–29.

Guenther, C., OŠBrien, T. & Syamlal, M. (2001). A numerical model of silane pyrolysis in a gas-solids fluidized bed, *Proceedings of the International Conference on Multiphase Flow*.

Henson, M. (2003). Dynamic modeling of microbial cell populations, *Current opinion in biotechnology* 14(5): 460–467.

Hogness, T., Wilson, T. & Johnson, W. (1936). The thermal decomposition of silane, *Journal of the American Chemical Society* 58(1): 108–112.

Hounslow, M. (1990). A discretized population balance for continuous systems at steady state, *AIChE journal* 36(1): 106–116.

Hsu, G., Levin, H., Hogle, R., Praturi, A. & Lutwack, R. (1982). Fluidized bed silicon deposition from silane. US Patent 4,314,525.

Hsu, G., Rohatgi, N. & Houseman, J. (1987). Silicon particle growth in a fluidized-bed reactor, *AIChE journal* 33(5): 784–791.

Hulburt, H. & Katz, S. (1964). Some problems in particle technology:: A statistical mechanical formulation, *Chemical Engineering Science* 19(8): 555–574.

Iya, S., Flagella, R. & DiPaolo, F. (1982). Heterogeneous decomposition of silane in a fixed bed reactor, *Journal of The Electrochemical Society* 129: 1531.

Kojima, T. & Morisawa, O. (1991). Optimum process conditions for stable and effective operation of a fluidized bed cvd reactor for polycrystalline silicon production.

Kunii, D. & Levenspiel, O. (1991). *Fluidization engineering*, Vol. 101, Butterworth-Heinemann Boston.

Lai, S., Dudukovic, M. & Ramachandran, P. (1986). Chemical vapor deposition and homogeneous nucleation in fluidized bed reactors: silicon from silane, *Chemical Engineering Science* 41(4): 633–641.

Mahecha-Botero, A., Grace, J., Elnashaie, S. & Lim, C. (2005). Femlab simulations using a comprehensive model for gas fluidized-bed reactors, *COMSOL Multiphysics (FEMLAB) Conference Proceedings, Boston, USA*.

Mahecha-Botero, A., Grace, J., Elnashaie, S. & Lim, C. (2006). Comprehensive modeling of gas fluidized-bed reactors allowing for transients, multiple flow regimes and selective removal of species, *International Journal of Chemical Reactor Engineering* 4(4): 11.

Muller, A., Ghosh, M., Sonnenschein, R. & Woditsch, P. (2006). Silicon for photovoltaic application, *Materials Science and Engineering* 134: 257–262.

Muller, M., Birkmann, B., Mosel, F., Westram, I. & Seidl, A. (2010). Silicon efg process development by multiscale modeling, *Journal of Crystal Growth* 312(8): 1397–1401.

Neuhaus, D. & Münzer, A. (2007). Industrial silicon wafer solar cells, *Advances in OptoElectronics*, ID 24521.

Odden, J., Egeberg, P. & Kjekshus, A. (2005). From monosilane to crystalline silicon, part i: Decomposition of monosilane at 690-830ák and initial pressures 0.1-6.6 ámpa in a free-space reactor, *Solar energy materials and solar cells* 86(2): 165–176.

Piña, J., Bucalá, V., Schbib, N., Ege, P. & De Lasa, H. (2006). Modeling a silicon cvd spouted bed pilot plant reactor, *International Journal of Chemical Reactor Engineering* 4(4): 9.

Randolph, A. & Larson, M. (1971). *Theory of particulate processes*, Academic Press.

Steinbach, I., Apel, M., Rettelbach, T. & Franke, D. (2002). Numerical simulations for silicon crystallization processes–examples from ingot and ribbon casting, *Solar energy materials and solar cells* 72(1-4): 59–68.

Surek, T. (2005). Crystal growth and materials research in photovoltaics: progress and challenges, *Journal of Crystal Growth* 275(1-2): 292–304.

Talalaev, R. (2009). Polysim: Modeling of polysilicon deposition by siemens process, *International Semiconductor Technology Conference*.

White, C. (2007). Modeling for design and control of particulate systems.

White, C., Ege, P. & Erik Ydstie, B. (2006). Size distribution modeling for fluidized bed solar-grade silicon production, *Powder technology* 163(1-2): 51–58.

White, C., Zeininger, G., Ege, P. & Ydstie, B. (2007). Multi-scale modeling and constrained sensitivity analysis of particulate cvd systems, *Chemical Vapor Deposition* 13(9): 507–512.

Woditsch, P. & Koch, W. (2002). Solar grade silicon feedstock supply for pv industry, *Solar energy materials and solar cells* 72(1-4): 11–26.

Würfel, P. (2005). *Physics of solar cells: from principles to new concepts*, Vch Verlagsgesellschaft Mbh.

Zambov, L. (1992). Kinetics of homogeneous decomposition of silane, *Journal of crystal growth* 125(1-2): 164–174.

# Silicon-Based Third Generation Photovoltaics

Tetyana Nychyporuk and Mustapha Lemiti

*University of Lyon, Nanotechnology Institute of Lyon (INL),*
*UMR CNRS 5270, INSA de Lyon,*
*France*

## 1. Introduction

In order to ensure the widespread use of photovoltaic (PV) technology for terrestrial applications, the cost per watt must be significantly lower than 1$ / Watt level. Actually, the wafer based Silicon (Si) solar cells referred also as the 1st generation solar cells are the most mature technology on PV market. However such PV devices are material and energy intensive with conversion efficiencies which do not exceed in average 16 %. In 2008 the average cost of industrial 1 Wp Si solar cell with conversion efficiency of 14.5 % (multicrystalline Si cell of 150 x 150 mm², 220 μm of thick, SiN antireflecting coating with back surface field and screen printing contacts) achieved approximately 2.1 € assuming the production volume of 30 – 50 M Wp / per year (Sinke et al., 2008). At that cost level, the PV electricity still remains more expensive comparing with traditional nuclear or thermal power engineering. One of the most promising strategies for lowering PV costs is the use of thin film technology, referred also as 2nd generation solar cells. It involves low cost and low energy intensity deposition techniques of PV material onto inexpensive large area low-cost substrates. Such processes can bring costs down but because of the defects inherent in the lower quality processing methods, have reduced efficiencies compared to the 1st generation solar cells.

Material limitations of the 1st generation solar cells and efficiency limitations of the 2nd generation solar cells are initiated boring of the Si-based 3rd generation photovoltaic. Its main goal is to significantly increase the conversion efficiency of low-cost photovoltaic product. Indeed, the Carnot limit on the conversion of sunlight to electricity is 95% as opposed to the theoretical upper limit of 30% for a standard solar cell (Shockley & Queisser 1961). This suggests the performance of solar cells could be improved 2 – 3 times if different concepts permitting to reduce the power losses were used.

The two most important power loss mechanisms in single-band gap photovoltaic cells are *(1)* the inability to absorb photons with energy less than the band gap and *(2)* thermalisation of photon energy exceeding the gap (Fig. 1). Longer wavelength is not absorbed by the solar cell material. Shorter wavelength generates an electron-hole pair greater than the bandgap of the p-n junction material. The excess of energy is lost as heat because the electron (hole) relaxes to the conduction (valence) band edges. The amounts of the losses are around 23 % and 33 % of the incoming solar energy, respectively (Nelson, 2003). Other losses are junction loss, contact loss and the recombination loss. Theory predicts (Shockley & Queisser 1961) that the highest single – junction solar cell efficiency is roughly 30%, assuming such factors as the intensity of one sun (no sunlight concentration), a one-junction solar cell (a single material with a single bandgap), and one electron-hole pair produced from each incoming photon.

To efficiently convert the whole solar spectrum into the electricity three main families of approaches have been proposed (Green et al., 2005) (Green, 2002): *(i)* increasing the number of bandgaps (*tandem cell* concept); *(ii)* capturing carriers before thermalisation, and *(iii)* multiple carrier pair generation per high energy photon or single carrier pair generation with multiple low energy photons. Up to now, tandem or in other words multijunction cells provide the best-known example of such high-efficiency approaches. Indeed, the loss process *(2)* of Fig. 1 can be largely eliminated if the energy of the absorbed photon is just a little higher that the cell bandgap. The concept of tandem solar cells is based on the use of several solar cells (or subcells) of different bandgaps stacked on top of each other (Fig. 2), with the highest bandgap cell uppermost and lowest on the bottom. The incident light is automatically filtered as it passes through the stack. Each cell absorbs the light that it can most efficiently convert, with the rest passing through to underlying lower bandgap cells (Green et al., 2007). The using of multiple subcells in the tandem cell structure permits to divide the broad solar spectrum on smaller sections, each of which can be converted to electricity more efficiently. Performance increases as the number of subcells increases, with the direct sunlight conversion efficiency of 86.8 % calculated for an infinite stack of independently operated subcells (Marti & Araujo, 1996). The efficiency limit reaches 42.5 % and 47.5 % for 2- and 3-subcell tandem solar cells (Nelson, 2003) as compared to 30% of one junction solar cell.
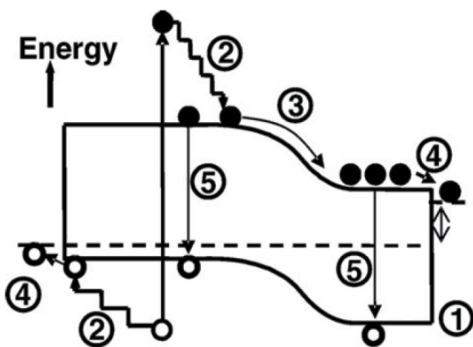


Fig. 1. Loss processes in a standard solar cell: *(1)* non-absorption of below band gap photons; *(2)* lattice thermalisation loss; *(3)* and *(4)* junction and contact voltage losses; *(5)* recombination loss (Green, 2003).
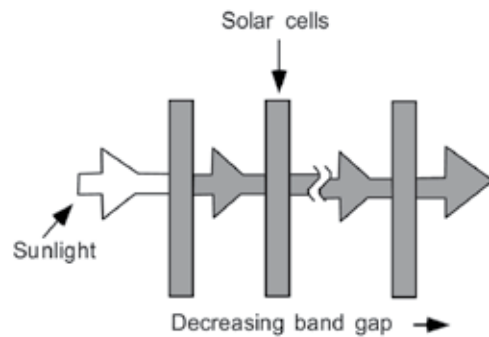
Fig. 2. Tandem cell approach (Green, 2003).

Having to independently operate each subcell is a complication best avoided. Usually, subcells are designed with their current output matched so that they can be connected in series. This constrain reduces performance. Moreover, it makes the design very sensitive to the spectral content of the sunlight. Once the output current of one subcell in a series connection drops more than about 5 % below that of the next worst, the best for overall performance is to short-circuit the low-output subcell, otherwise it will consume, rather than generate power.

It should be also noted the common point of confusion about solar cells efficiency. The measured efficiency of solar cell depends on the spectrum of its light source. The space solar

spectrum or air mass zero (AM0) spectrum is richer in ultraviolet light than the typical terrestrial solar spectrum (air mass 1.5 or AM1.5). Taking into account that the ultraviolet light is converted into electricity less efficiently than the other parts of the spectrum, the resulting efficiencies for AM0 are thus lower (Green et al., 2010). Since cells are typically measured under the spectrum for their intended use and efficiencies are not easily converted, this chapter will indicate efficiencies measured under non-concentrated AM1.5 at 25° unless otherwise specified.
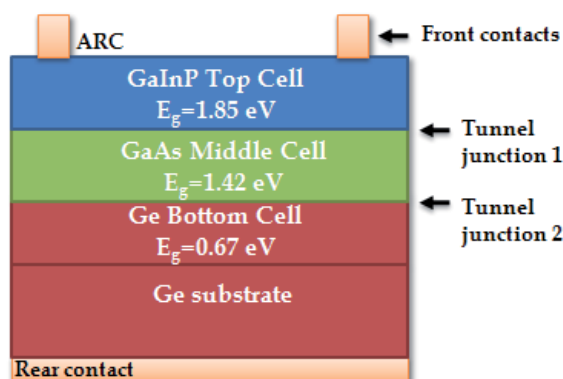


Fig. 3. Schematic view of GaInP/GaAs/Ge solar cell.

Fig. 4. Using of multijunction solar cells for Mars rover missions [1].

Up today the tandem cells have been developing on monolithic integration of non-abundant III –V materials by means of rather expensive technologies of fabrication like molecular beam epitaxy (MBE) or metal-organic chemical vapor deposition (MOCVD). Currently commercially available multijunction cells consist of three subcells (GaInP/GaAs/Ge), which all have the same lattice parameter and are grown in a monolithic stack (Fig. 3). The subcells in this monolithic stack are series connected through the tunnel junctions. The record efficiency of 32% was achieved in 2010 for this type of cells (Green et al., 2010). These high-efficiency solar cells are being increasingly used in solar concentrator systems, where development of both the solar cells and the associated optical and thermal control elements are actively being pursued. The performance of tandem solar cells has been demonstrated, but work is continuing to increase the numbers of junctions and optimize the bandgap junctions. The choice of materials with optimal or near-optimal bandgap is severely limited by the lattice matching constraint of these cells. Another approach to increasing of multijunction solar cell efficiency is the incorporation of materials with a mismatch in the lattice constant. Graded composition buffers between the lattice mismatched subcells are used to reduce the density of the threaded dislocations resulting from the lattice mismatch strain. Lattice mismatch technology opens the parameter space for junction materials, allowing the choice of materials with more optimal bandgaps and a potential for higher cell efficiency.

---

[1] http://marsrovers.nasa.gov/gallery/press/spirit/20060104a.html

In 2010 the cost of multijunction solar cells still remains too high to allow their use outside of specified applications (for example space applications, Mars rover missions (Crisp et al., 2004) (Fig. 4)…). The high cost is mainly due to the complex structure and the high price of materials. In this context the fabrication of multijunction solar cells on the base of abundant low-cost materials that do not cause toxicity in the environment and by using approaches amenable to large scale mass production, like thin film deposition techniques, remains challenging.

## 2. Silicon based tandem cells

Silicon is a benign readily available material, which is widely used for solar cell fabrication. It has a bandgap of 1.12 eV at 300 K, which is close to optimal not only for standard, single p – n junction cell, but also for the bottom cell in a 2-cell or even a 3-cell tandem stack (Conibeer et al., 2008). Therefore a solar cell entirely based of Si and its dielectric compounds (referred also as *all-Si tandem solar cell*) with other abundant elements (i. e. silicon dioxide, nitrides or carbides) fabricated with thin film techniques, is advantageous in terms of potential for large scale manufacturing and in long term availability of its constituents. As was already mentioned previously, thin film low-temperature deposition techniques results in high defect density films. Hence solar cells must be thin enough to limit recombination due to their short diffusion lengths, which in turn means they must have high absorption coefficients.

For AM1.5 solar spectrum the optimal bandgap of the top cell required to maximize conversion efficiency is ~1.7 to 1.8 eV for a 2-cell tandem with a Si bottom cell and 1.5 eV and 2.0 eV for the middle and upper cells for a 3-cell tandem (Meillaud et al., 2006). It should be also noted that for terrestrial applications (AM1.5 solar spectrum), the highest bandgap necessary for the Si-based tandem solar cells is limited to 3.1 eV, the energy at which the absorption from the encapsulation material, such as ethylene-vinyl acetate (EVA), starts to play an important role.

### 2.1 Quantum confinement in Si nanostructures

To increase Si bangap, nanoscale size dependent quantum confinement effect can be used. Indeed, the quantum confinement effect manifests itself by significant modification of electronic band structure of Si nanocrystals when their size is reduced to below the exciton Bohr radius (~4.9 nm) of bulk Si crystals. In particular, quantum confinement effect provokes the increasing of the effective bandgap of Si nanocrystals. Moreover, for indirect bandgap semiconductors, like Si, geometrical confinement of carriers increases the overlap of electron and hole wavefunctions in momentum space and thus enhances the oscillator strength and as a consequence increases its absorption coefficient. From this effect, one can expect Si nanocrystals to behave as direct bandgap semiconductors. However, there is some evidence suggesting that the momentum conservation rule is only partially broken and Si nanocrystal strongly preserves the indirect bandgap nature of bulk Si crystals (Kovalev et al., 1999). Si nanostructures are thus the perfect candidates for higher bandgap materials in all-Si tandem cell approach.

Since the observation in 1990 of strong room-temperature photoluminescence from nanostructured porous Si (Canham, 1990), significant scientific interest has been focused of the simulation of optical and electrical properties of Si nanostructures regarding their size, shape, surface termination, number and degree of interconnections, impurity doping and so

on. Many reviews addressing this problematic since appeared (one of the good recent reviews is Ref (Bulutay & Ossicini, 2010)). In this paragraph we will only underline some important points resulting from quantum confinement effect.

*Ab initio* calculations using density functional theory (DFT) indicate that the increasing of the optical bandgap of Si nanocrystals (or in other words quantum dots (QDs)) is expected to vary from 1.4 to 2.4 eV for a nanocrystal size of 8-2.5 nm (Ögüt et al., 1997). However, further DFT calculations have found that in addition to quantum confinement effect in small QDs, the matrix has a strong influence of the resulting energy levels (König et al., 2009). With increasing polarity of the bonds between the nanocrystal and the matrix, there is an increasing dominance of the interface strain over quantum confinement. For a 2 nm diameter nanocrystal, this strain is such that the highest occupied molecular orbital (HOMO)-lowest unoccupied molecular orbital (LUMO) gap is significantly reduced in a polar $SiO_2$ matrix but not much affected in a less polar $SiN_x$ or nonpolar SiC matrix (König et al., 2009). It is also shown the reduction in gap energy on going from a QD in vacuum to the one embedded in a dielectric. An additional freedom of material design can be also introduced by impurity doping and interconnections between Si QDs, the both ones modify its optical and electrical transport properties (Nychyporuk et al., 2009) (Mimura et al., 1999).

## 3. Silicon quantum dot solar cells

Si QDs offer the potential to tune the effective bandgap, through quantum confinement, and allow fabrication of optimized tandem devices in one growth run in a thin film process.

### 3.1 Fabrication of Si QD nanostructures

Different technological approaches allowing formation of Si quantum dots in a dielectric matrix have already been developed, permitting to obtain Si nanocrystals as small as 1 nm in diameter. Between the most used deposition techniques one can cite reactive evaporation, ion implantation, sputtering and plasma enhanced chemical vapor deposition (PECVD). Considerable work has been done on the growth of Si nanocrystals embedded in silicon oxide dielectric matrices ($SiO_2$) (Zacharias et al., 2002) (Stegemann et al., 2010), silicon nitride ($Si_3N_4$) (Kim et al., 2006) (Cho et al., 2005) (Mercaldo et al., 2010) (So et al., 2010) and silicon carbide (SiC) (Song et al., 2008) (Kurokawa et al., 2006) (Gradmann et al., 2010) (Löper et al., 2010) (Cho et al., 2007). An accurate control of the size and density of Si nanocrystals is mandatory in bandgap engineering for solar cell applications. It should be noted that Si nanocrystals prepared by different methods present slightly different properties which depend on the preparation procedure, because of different defect density, different degree of interconnections between the nanocrystals, different surface termination, and so on.

Conventionally, Si QDs in dielectric matrix like $SiO_2$, $Si_3N_4$ and SiC can be synthetized by self-organized growth from Si rich dielectric layers, which are thermodynamically unstable and therefore undergo phase separation upon appropriate post-annealing step to form nanocrystals. For example for Si rich oxide layer, the precipitation occurs according to the following:

$$SiO_x \rightarrow \frac{x}{2} SiO_2 + \left(1 - \frac{x}{2}\right) Si$$
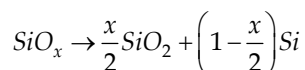
It should be noted that due to the fact that both the polarity and length of the bonds decrease towards those of Si-Si for $SiO_2$ to $Si_3N_4$ and SiC, this implies that the segregation

and precipitation effect for Si in the three matrices would decrease such that in SiC formation of QDs is likely to be most difficult.



(a)



(b)
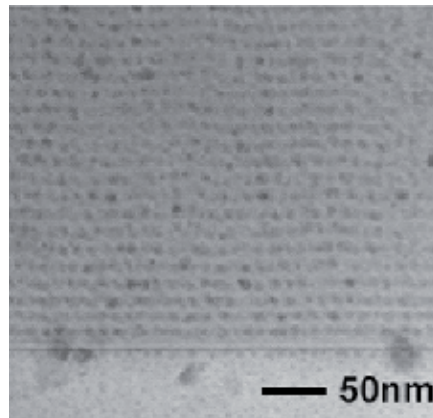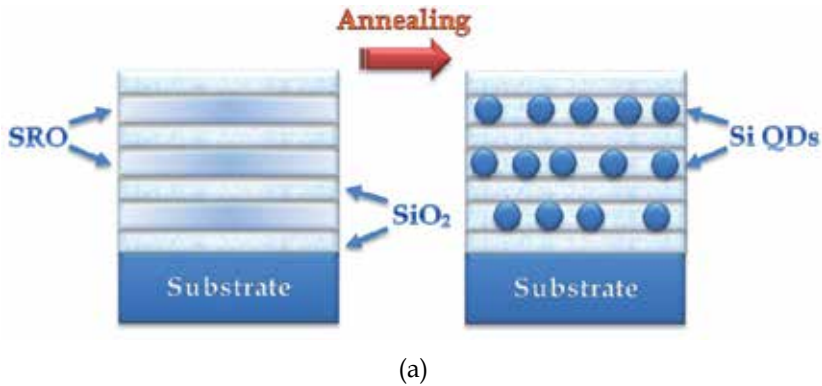
Fig. 5. (a) Multi-layer structure illustrating precipitation of Si QDs in a Si-rich layer; (b) TEM image of a superlattice of Si QDs in $SiO_2$ matrix (Conibeer et al., 2008).

The QD size and density control are normally realized by changing the chemical stoichiometry of the bulk films. By reducing the Si-richness in a bulk Si-based matrix, smaller nanocrystals can be achieved. Nevertheless, this will simultaneously reduce the density of nanocrystals in the film due to the reduced Si-richness. The low density of QDs with desired size leads to a negative effect on the electrical conductivity of the films. Moreover, the assumption that all the excess Si precipitates to nanocrystals turns out to be oversimplification. In fact, it has been observed that only half the excess Si clusters in these precipitates upon annealing at 1000°C for 30 min, in material deposited by PECVD, with a considerable amount of suboxide material forming in the matrix. Therefore, the method allowing a fabrication of high density, but narrow size distributed Si QDs films via superlattice approach, firstly reported by Zacharias (Zacharias et al., 2002) , was adopted by the majority of researchers. It should be mentioned that even without using the multilayer

approach it is still possible to fabricate well – ordered and uniform Si nanocrystals in a film with a high dot density (Surana et al., 2010).

### 3.1.1 Si QDs in silicon oxide matrix

A simple technique to prepare the multilayer structure known also as superlattices of Si QDs in silicon oxide matrix was firstly reported by Zacharias (Zacharias et al., 2002) . It consists in deposition of alternating layers of stoichometric Si oxide ($SiO_2$) and Si rich oxide (SRO) of thicknesses down to 2 nm. This precision is normally achieved by using RF magnetron sputtering or plasma enhanced chemical vapor deposition (PECVD) technique. The deposition consisting typically of 20-50 bi-layers is followed by the annealing step is $N_2$ ambient from 1050 to 1150°C for 1 h. During the annealing step, the surface energy minimization favors the precipitation of Si in the SRO layer into approximately spherical QDs (Conibeer et al., 2008). This process is illustrated on Fig. 5 (a). The diameter of Si QDs is constrained by the SRO layer thickness and quite uniform size dispersion is achieved within about 10% (Zacharias et al., 2002) . The density of the QDs can be varied by the composition of the SRO layer. Fig. 5 (b) shows typical transmission electron microscope (TEM) of the multi-structure SiQDs in $SiO_2$ matrix grown by this method. TEM evidence indicates that these nanocrystals tend to be spherical – as surface energy minimization would dictate - and at this scale would have energy levels confined in all three dimensions and hence can be considered as quantum dots.

Nowadays, the phase separation, solid state crystallization and optical properties of $SiO_2$/SRO/$SiO_2$ superlattices are already well understood. However, it is a major challenge to achieve charge carrier transport through a network of Si QDs embedded in a $SiO_2$ matrix. Therefore, other Si based host matrices such as $Si_3N_4$ or SiC that feature lower energy band offsets with respect to the Si band edges and thus higher carrier mobility are attractive.

### 3.1.2 Si QDs in silicon nitride matrix

For the reasons stated above, it was explored the fabrication of Si QDs in silicon nitride matrix. Thick layers of silicon-rich nitride, when annealed at above 1000°C, precipitate to Si QD (Kim et al., 2005). Multilayered structures also result in Si QD formation with controlled size of the Si QDs (Cho et al., 2005). The annealing temperature can also be used to modify the nitride matrix, with it being amorphous below 1150°C but with crystalline nitride phases, in addition to the Si QDs, appearing at temperatures ranging from 1150 to 1200° (Scardera et al., 2008). Multilayered structures can be deposited by sputtering or by PECVD with growth parameters and annealing conditions very similar to those for oxide giving good control of QD sizes. The main difference is the extra H incorporation with PECVD that requires an initial low-temperature anneal to drive off excess hydrogen and prevent bubble formation during the high-temperature anneal (Cho et al., 2005).

Si QDs can also be grown *in situ* during PECVD deposition, where they form in the gas phase (Lelièvre et al., 2006). There is much less control over size and shape but no high-temperature anneal is required to form the Si QDs (Fig. 6 (a)). Multilayer growth using this *in-situ* technique has also been attempted with irregular shaped but reasonably uniform sized Si QDs (Fig. 6 (b)).

The formation of Si quantum dots in $SiO_2$/$Si_3N_4$ hybrid matrix was also reported (Di et al., 2010). In this approach alternating silicon rich oxide and $Si_3N_4$ layers were produced followed by post-deposition anneals. In addition, it should be noted that $Si_3N_4$ acts as a better diffusion barrier compared to $SiO_2$. It restricts the displacement of Si atoms as well as dopant atoms under high processing temperatures.

(a)                                                    (b)
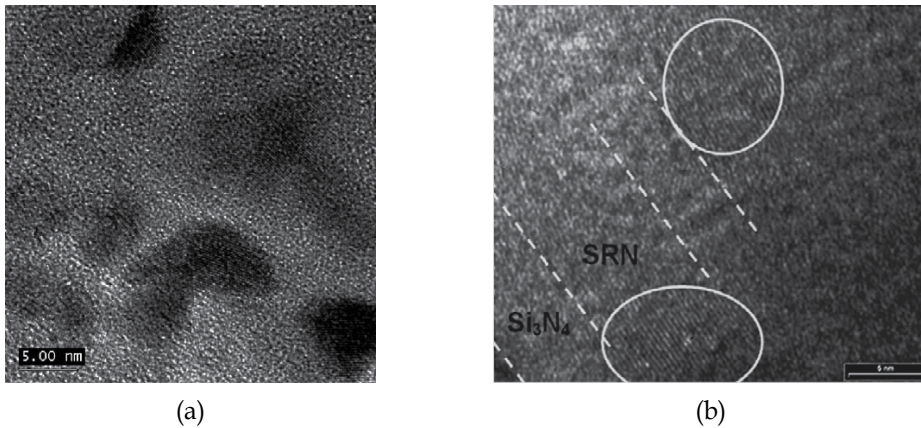
Fig. 6. *In-situ* grown Si QDs in the gas phase and dispersed in $Si_3N_4$ matrix: (a) One layer structure (Lelièvre et al., 2006); (b) multi-layer structure (Conibeer et al., 2008).

### 3.1.3 Si QDs in silicon carbide matrix

Si QDs in a SiC matrix offer an even lower barrier height and hence potentially better electronic transport properties. However, the low barrier height also limits the minimum size of QDs to about 3 nm or else the quantum-confined levels are likely to rise above the level of the barrier, which should be around 2.3 eV for amorphous SiC. Si QDs in SiC matrix have been formed in a single thick layer by Si-rich carbide deposition followed by high-temperature annealing at between 800° and 1100°C in a very similar process to that for oxide (Fig. 7). $Si_{1-x}C_x$/SiC multilayers have also been deposited by sputtering to give better control over the Si QD as with oxide and nitride matrices. However, contrary to these previous matrices, the both Si and SiC QDs have been produced by high temperature annealing of Si –rich SiC layer or in a $SiC_{1-x}C_x$/SiC multistructure. The formation of SiC nanocrystals can hinder the formation of Si QDs.
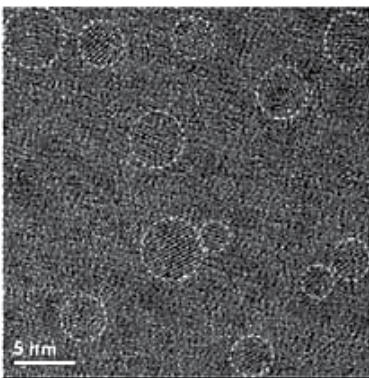


Fig. 7. Cross-sectional HRTEM image of Si-rich SiC layer after the thermal annealing (Conibeer, 2010).
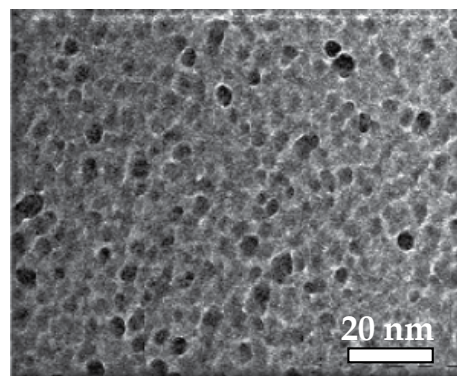


Fig. 8. TEM image interconnected Si QDs forming thin films.

### 3.1.4 Interconnected Si QDs forming thin films

To be successfully applied as a material for all-Si tandem solar cells, the small size of Si QDs is not the single prerequisite. It is also necessary to assure their high density in order to achieve a direct tunneling of the photogenerated charge carriers between the QDs. This still constitutes the bottleneck of the approaches cited above. Recently, the fabrication of thin films composed by highly packed Si QDs with a controlled bandgap values was reported (Nychyporuk et al., 2009). This approach is based on the *in-situ* nucleation of Si QDs in the gas phase during PECVD deposition by using $SiH_4$ as a gas precursor. Indeed, the dust particle formation in Ar-$SiH_4$ plasma is known to be a time-dependent four step process occurring in the gas phase: *(i)* polymerization phase, *(ii)* accumulation phase, *(ii)* coalescence and *(iv)* surface deposition growth. During the polymerization phase, the nucleation of extremely small particles (~1 nm) takes place. They progressively grow in size with time and at the end of the polymerization phase, starting from about 1 nm, a short accumulation phase begins. During this phase the nanoparticles size remains constant and only their density increases in the plasma environment. The coalescence phase starts once the nanoparticles critical density is reached. The small nanoparticles (~1 nm) begin to agglomerate at least two by two to form larger nanoclusters. In consequence, a number of interconnections between the nanoparticles increases. The final phase corresponds to the plasma species deposition on the surface of strongly agglomerated nanoparticles. During this phase a hydrogenated amorphous Si shell layer is formed around the crystalline Si core. The thickness of this amorphous shell increases with time. The square wave modulation of the power amplitude applied to the plasma has been found as a suitable technique permitting to obtain the deposition of Si QDs with required size. It consists of alternating periods of plasma switching time followed by the plasma extinction time. As a result, Si QDs grown in the gas phase during the plasma switching time were deposited on a substrate (Fig. 8). The careful tuning of the plasma switching time permits to precisely control the phase of Si QD growth and as a consequence their size and degree of interconnections between them. Si QD based thin films deposited under dusty plasma conditions appear to be promising candidates for all-Si tandem solar cell applications.

### 3.2 Shallow-impurity doped Si nanostructures

A requirement for a tandem cell element is the presence of some form of junction for carrier separation. Phosphorous (P) and boron (B) are excellent dopants in bulk Si as they have a high solid solubility and alter the conductivity of the bulk Si by several orders of magnitude. Hence they are good initial choices to study the doping in the Si nanocrystals.

Doping of Si nanostructures is a subject of intense research (Tsu et al., 1994) (Holtz & Zhao, 2004) (Erwin et al., 2005) (Norris et al., 2008) (Ossicini et al., 2006). Unfortunately, the main difficult in existing doping techniques arises from the fluctuation of impurity number per nanocrystal in a nanocrystal assembly. For Si nanocrystals as small as few nanometers in diameter, the expression of the doping level in the form of "impurity concentration" is not suitable and it should be expressed as "impurity numbers" because it changes digitally. For example, doping of one impurity atom into a nanocrystal of 3 nm in diameter (~ about 700 atoms) corresponds to an impurity concentration of $7.0 \times 10^{19}$ atoms/cm$^3$. At this doping level, bulk Si is a degenerate semiconductor and exhibits metallic behavior. However, by means of electron spin resonance (ESR) spectroscopy it was shown that Si nanocrystals do not become metallic even under heavily doped conditions. Therefore, in nanocrystals, addition or subtraction of a single impurity atom drastically changes the electronic structure

and the resultant optical and electrical transport properties. So, for solar cell application, the development of a technique permitting to control the "impurity number" with extremely high accuracy is indispensable.

Up to now, an accurate control of "impurity number" in a Si nanocrystal has not been achieved. One of the largest problems of the growth of doped Si nanocrystals is that impurity atoms are pushed out of nanocrystals to surrounding matrices by the so-called self-purification effect. This effect can be understood by considering very high formation energy of doped nanocrystals (Ossicini et al., 2005). Impurity concentration in nanocrystals is thus always different from average concentration in a whole system. In the worst case, the number of impurity in a nanocrystal becomes zero even when average concentration is rather high. The development of viable technique to characterize impurities, especially "active" impurities doped into nanocrystals, is crucial. The resistivity measurements are thus complemented with ESR spectroscopy as well as PL spectroscopy.

As it was discussed previously, numerous methods have been reported for the growth of intrinsic Si QDs. On the other hand, a limited number of studies are published concerning the growth of shallow impurity-doped Si QDs with the diameter below 10 nm. One of the mostly used methods for shallow-impurity doping of Si nanocrystals is plasma decomposition of $SiH_4$ by adding dopant precursors (diborane ($B_2H_6$) and phosphine ($PH_3$)) (Pi et al., 2008) (Stegner et al., 2008). This method permits to obtain a variety of morphologies from densely packed nanocrystalline films to nanoparticle powder by controlling process parameters (Nychyporuk et al., 2009). Another method is incorporation of doping atoms into SRO layers by simultaneous co-sputtering of Si, $SiO_2$ and $P_2O_5$ (or $B_2O_3$) in $SiO_2$/SRO superlattice approach described previously (Mimura et al., 2000). During the annealing, Si nanocrystals are grown in phosphosilicate (PSG) (n-type Si QDs) or borosilicate (BSG) (p-type Si QDs) thin films. It should be also noted that the impurity concentration in nanocrystals is different from that of the matrices because the segregation coefficient strongly depends on the kind of impurities and surrounding medium.
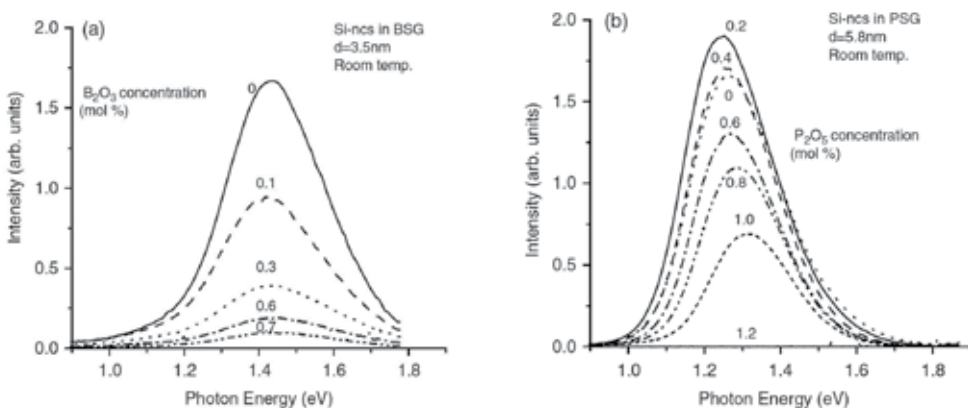


Fig. 9. PL spectra of (a) B-doped (Mimura et al., 1999) and (b) P-doped Si nanocrystals (Fujii et al., 2002) at room temperature for different doping concentrations.

The presence of impurity atoms inside Si nanocrystals can be confirmed by the PL spectroscopy. Indeed, the introduction of extra carriers by impurity doping makes the three-body Auger process possible (Kovalev et al., 2008). In Auger recombination, the energy of

an electron-hole pair is not released in the form of photon. This energy is given to a third carrier, which after the interaction losses its excess energy as thermal vibrations. Since this process is a three-particle interaction, it is normally only significant in strongly non-equilibrium conditions or when the carrier density is very high. For doped nanocrystals the value of Auger rate is four to five orders of magnitude larger than the radiative rate of excitons, and thus one shallow impurity can almost completely kill PL from the nanocrystal. Hence with increasing of average impurity numbers in a nanocrystal assembly, the PL intensity is expected to decrease. This effect was really observed in p-type Si nanocrystals. As one can see on Fig. 9 (a) with increasing of B concentration, the PL intensity monotonously decreases (Fujii et al., 1998) (Müller et al., 1999) (Stegner et al., 2008).

In P-doped Si nanocrystals, the situation is different. When the phosphorous concentration is relatively low, the PL intensity increases slightly compared to that of the undoped Si nanocrystals (Fig. 9 b) (Fujii et al., 2000) (Mimura et al., 2000) (Tchebotareva et al., 2005). The increase of the PL intensity indicates that non-radiative recombination processes are quenched by P doping. One of the possible explanation is that electrons supplied by P are captured by the dangling bonds, which inactivate the nonradiative recombination centers and compensate donors (Stegner et al., 2008) (Lenahan et al., 1998). It should be also noted that the PL intensity also strongly depends on the size of the shallow-doped Si nanocrystals. There are many theoretical studies on preferential localization of impurities in Si nanocrystals. It should to be noted that it is almost impossible to control experimentally the location of impurities in nanocrystals. However, the information on localization was experimentally obtained (Kovalev et al., 1998). It was shown that P dopants are localized at or close to the surface of Si nanocrystal. On the contrary, the B atoms are primary incorporated into the Si nanocrystal core. However, the preferential localization of impurities may depend on nanocrystal growth process and the surface termination. Therefore, properties of dopant may be quite different between Si nanocrystals grown by the decomposition of SiH$_4$, phase separation of SRO and so on. In any cases the doping efficiency by B atoms is much smaller than that of P atoms due to larger formation energy of B-doped Si nanocrystals than P-doped ones (Kovalev et al., 1998) (Ossicini et al., 2005).

To what concerns the optical and electrical properties, contrary to the intrinsic Si nanocrystals, the shallow doped Si nanocrystals present new degree of freedom to control them. For example, the size is one of the main parameters to control optical bandgap of the intrinsic Si nanocrystals. On the other hand, due to the difference in the electronic band structure in the case of doped and codoped Si nanocrystals (obtained by the simultaneous doping by B and P atoms), the optical bandgap is determined by the combination of the size and impurity concentration (Fujii et al., 2010).

It is worth noting that the impurity atoms alter the formation kinetics of Si nanocrystals. Indeed, the average size of P-doped Si nanocrystals is increased compared to the undoped ones under the same experimental conditions (Conibeer et al., 2010), and in some experiments this increasing was almost double. Contrary to the doping with P, the doping with B results in the forming of smaller Si nanocrystals compared to the undoped case (Hao et al., 2009). The crystalline volume fraction was found to decrease with increasing of B concentration (Hao et al., 2009), which suggests that boron suppresses Si crystallization. One of the possible reasons is the local deformations induced by the impurity atoms.

### 3.2.1 Dark resistivity measurements

The resistivity of the Si QD material is an important parameter for photovoltaic applications. The influence of the doping concentration on resistivity of Si QD superlattices was studied

(Hao et al., 2009, 2009a), (Conibeer et al., 2010) (Ficcadenti et al., 2009). The contact resistances in the above measurements were determined by using the TLM (Transmission Line Model) method proposed by Reeves and Harrison (Reeves & Harrison, 1982). This method involves measurement of the resistance between several pairs of contacts, which have identical areas, but are separated by different spaces (Fig. 10). The dark resistivity is then defined as: $\rho_{dark} = V \times d \times w / I \times l$, where $d$ is the thickness of Si QD superlattice, $w$ is the length of Al pad and $l$ is the spacing of Al pads.

To perform the dark resistivity measurements, the Si QD superlattices were grown on the quartz substrate. The ohmic contacts were obtained by thermal evaporation of Al, followed by sintering at a temperature (500-530°C) lower than the Al-Si eutectic temperature to allow the Al to spike down into the film (Voz et al., 2000). The schematic view of the final structure for the lateral resistivity measurements is presented on the Fig. 10.

Fig. 11 (a) and (c) represents the room temperature dark resistivity of Si QD/SiO$_2$ multilayer films for various phosphorous and boron doping levels, respectively. As one can see, the introduction of a slight amount of P and B drastically changes the dark resistivity of the films, from $10^8$ Ωcm for the undoped samples to $10^2 – 10$ Ωcm for doped ones, which is 6 -7 orders of magnitude lower than that of the undoped samples. This decrease in resistivity may be the consequence of an increase in mobile carrier concentration due to a rise in the number of active dopants in the film.

The TLM method was also used to measure the temperature dependence of the resistance of the Si QD films with various (b) phosphorous (Hao et al., 2009) and (d) boron (Hao et al., 2009) concentrations (Fig. 11 (b) and (d), respectively). These measurements permit to estimate the values of the activation energy ($E_a$), that is in a n- (p-) doped semiconductor the energy difference between the conduction (valance) band and Fermi level. The activation energy was calculated by using relation $R \approx exp(E_a/kT)$. As one can see, with the increasing of the doping level, for both types of impurities the activation energy decreases from ~0.5 eV to 0.1 eV. This result is consistent with the view that the observed resistivity decreases are a consequence of an increase in carrier concentration due to more active dopants in the film. The decrease in $E_a$ accompanying the drop in resistivity indicates that the Fermi level energy is moving toward the conduction (valance) band for n- (p-) type doped Si QDs.
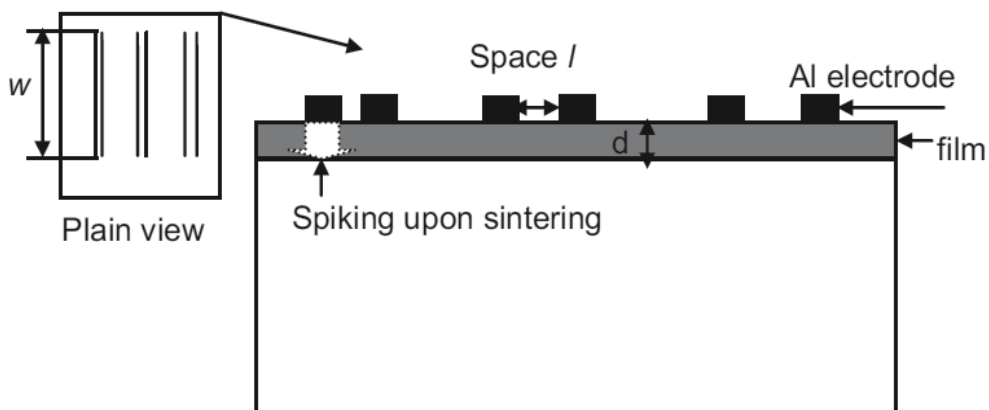


Fig. 10. Schematic layout of the Al contacts on a film for dark resistivity measurements (Hao et al., 2009).

(a)

(b)

(c)

(d)
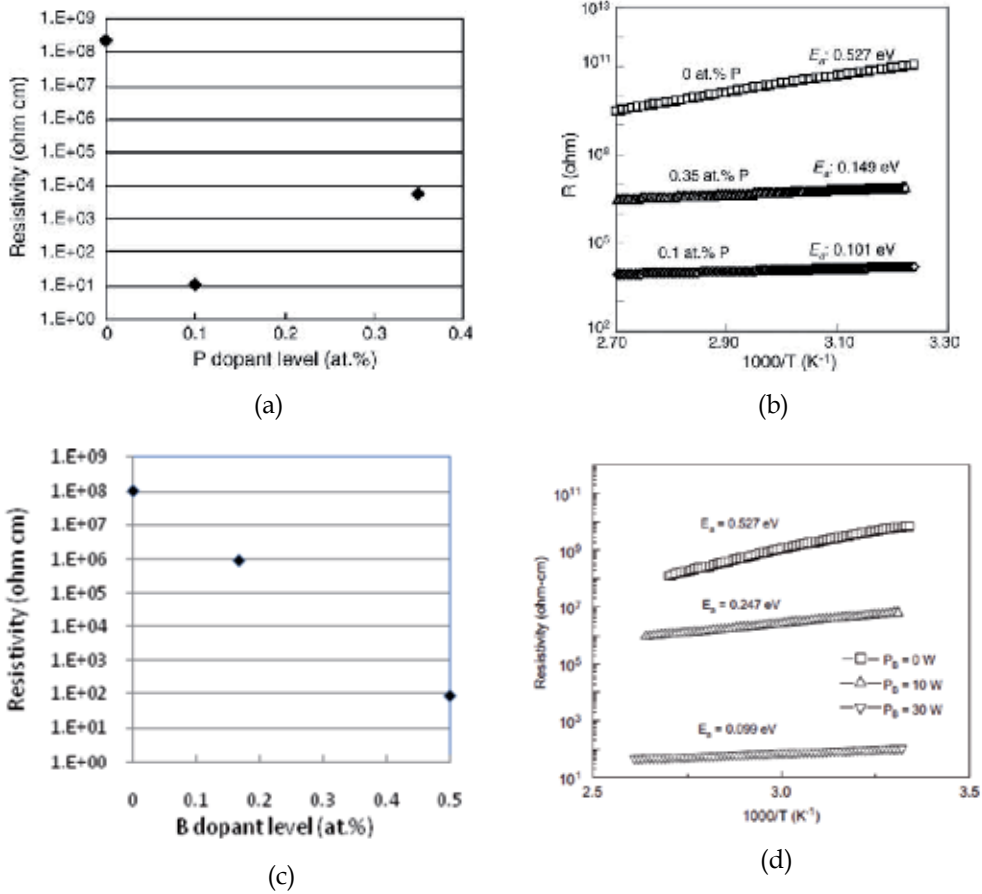
Fig. 11. Dark resistivity of Si QD/SiO$_2$ multilayer films for various (a) phosphorous (Hao et al., 2009) and (c) boron (Conibeer et al., 2010) doping levels.; Temperature dependence of the resistance of the Si QD films with various (b) phosphorous (Hao et al., 2009) and (d) boron (Hao et al., 2009) concentrations .

### 3.3 Optical properties of Si QDs

Regarding to photovoltaic applications, the optical bandgap and the absorption coefficient of Si QDs are the very first physical parameters to be studied and optimized prior to solar cell fabrication. Optical methods provide an easy and sensitive tool for measuring the electronic structure of quantum objects, since they require minimal sample preparation and the measurements are sensitive to the quantum effects. The energy gaps of Si QDs could be determined, for example, from photoluminescence (PL) measurements, whereas the absorption coefficient from the transmission-reflection measurements.

### 3.3.1 Bandgap of Si QDs

Experimental energy gaps of isolated Si QDs in SiO$_2$ and SiN$_x$ matrices reported by several research groups are shown on Fig. 12 (Cho et al., 2004) (Park et al., 2000) (Takeoka

et al., 2000). As one can see the bandgap values of Si nanostructured material could be adjusted in the large range (up to 3.1 eV), covering an important part of the solar spectrum. The results obtained by different teams are in good agreement where the matrix is the same but are quite different for QDs in oxide compared to nitride, particularly for small QDs. They are also qualitatively consistent with the results from *ab-initio* modeling (König et al., 2009) (Ögüt et al., 1997), which had been carried out for the confined energy levels in Si QD consisting of a few hundred atoms. One can observe the expected increasing of confinement energy with decreasing QD size, but also that the amino-terminated QDs (silicon nitride) have energies about 0.5 eV more than the hydroxyl-terminated ones (silicon oxide). The last one observation is consistent with the explanation for the enhanced energies of QDs in nitride given by Yang et al (Yang et al., 2004), that the reason for it is due to better passivation of Si QDs by nitrogen atoms eliminating the strain at the $Si/Si_3N_4$ interface.

Influence of interconnections between the QDs on tuning of their bandgap was also studied (Nychyporuk et al., 2009) (Degoli et al., 2000). Indeed, electronic coupling between the neighboring low-dimensional Si nano-objects constituting a complex quantum system must be considered. This coupling leading to intense energy transfer processes between the electronically communicating quantum objects determines physical properties of the whole quantum system and, therefore, has to be taken into account, of course. It was shown that when the nanocrystals (Allan & Delerue, 2007) (Bulutay, 2007) start to touch each other, the bandgap value of the assembly begins to decrease rapidly (Fig. 13). Thus, the bandgap of the interconnected nanostructures depends not only on the nanocrystal dimension but also on the degree and number of interconnections between them.
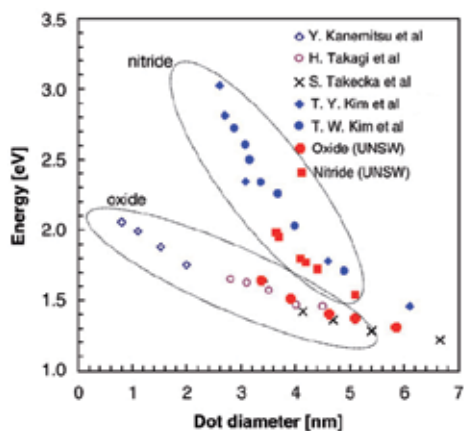


Fig. 12. Experimental energy gaps of three-dimensionally confined Si QDs in $SiO_2$ and $SiN_x$ matrices (300°C) for several research groups (Takeoka et al., 2000) (Kim et al., 2004), (Kim et al., 2005) (Yang et al., 2004) (Fangsuwannarak, 2007).
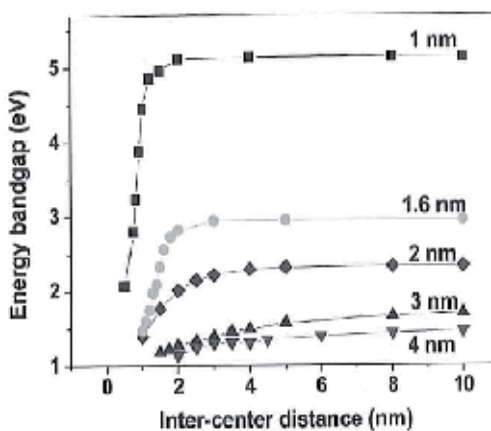
Fig. 13. Evolution of the bandgap of the quantum system constituted of 27 interconnected Si QDs as a function of the distance between the QDs.

### 3.3.2 Optical absorption of Si QDs

The absorption coefficient was experimentally determined for Si QDs in deferent matrices. Fig. 14 shows the global absorption coefficient of $SiN_x$ layers of different stoichiometries with Si QDs embedded inside (Nychyporuk et al., 2008). The absorption coefficient of polycrystalline silicon (poly-Si) is also added for comparison. As it can be seen, the global absorption coefficient of the composite $SiN_x$ decreases with stoichiometric ratio R (i.e. with decreasing of Si QD size and density) and its band-edge shifts to higher energies. Its magnitude is being much lower than that one of the absorption coefficient of poly-Si. No evidence of oscillator strength enhancement was observed and the global absorption coefficient is limited principally by the volume fraction of Si QDs inside the dielectric matrices. These why, the maximum absorption coefficient, approaching this one of the bulk Si, was found in the case of interconnected Si QDs forming thin films (Nychyporuk et al., 2009).
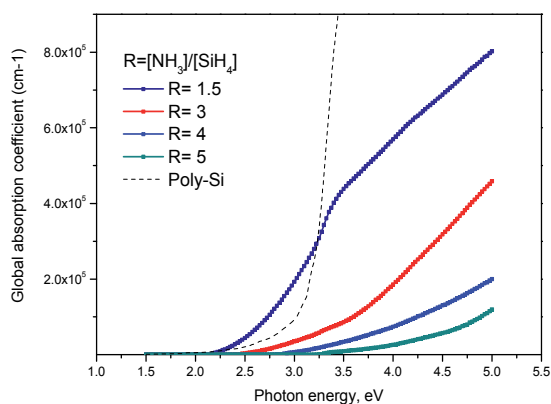


Fig. 14. Global absorption coefficient of $SiN_x$ layers of different stoichiometries with embedded Si QDs. The absorption coefficient of poly-Si is also presented for comparison (Nychyporuk et al., 2008).

### 3.4 Electrical transport mechanisms in Si QD ensembles

While the optical properties of the various ensembles of individual Si nanocrystals have been investigated by many researchers, relatively little attention was paid to the transport properties of 3D ensembles of such QDs. In this paragraph we will only briefly review the main results on the transport mechanisms obtained previously in the literature. A complete review of the electrical transport mechanisms in 3D ensembles of disordered Si nanocrystallites embedded in insulating continuous matrices can be found in Ref. (Balberg et al., 2010). To what concerns the transport processes in nanocrystalline Si superlattices, they were well reviewed in Ref. (Lockwood & Tsybeskov, 2004).

### 3.4.1 Disordered Si QDs in insulating matrix

The transport properties of the ensembles of disordered Si QDs in insulating matrix could be explained in terms of the percolation theory, which has already been successfully implemented to explain the transport processes in granular metals (Abeles et al., 1975).

Indeed, this theory describes the effect of the system's connectivity on its geometrical and physical properties. In the case of granular metals, in a system of $N$ metallic spheres embedded randomly in an insulating matrix, there will be a critical density of spheres $N_c$ above which a "continuous" metallic network will be formed and a metallic bulk-like conduction will dominate. Correspondingly, $N_c$ is the classical percolation threshold (Fonseca & Balberg, 1993) (Balberg et al., 2004). For $N < N_c$, the electron transfer between the individual grains is possible only by tunneling (Abeles et al., 1975) (Balberg et al., 2004).

To what concerns the ensemble of Si QDs, there can be distinguished five different structural-electrical regimes, such that in each of them we may expect a different transport mechanism to dominate. These regimes are *(a)* uniformly dispersed in insulating matrix isolated spherical QDs; *(b)* the transition regime, where some of the QDs starts to "touch" their neighbors; *(c)* the intermediate regime, where clusters of "touching" QDs are formed; *(d)* the percolation transition regime where the above clusters form a global continuous network; and *(e)* the regime where the percolation cluster of "touching" QDs is well formed and geometrically non-"touching" QDs are rarely found. Fig. 15 (a), (b) and (c) present typical examples of ensembles of Si QDs corresponding to regimes *(a)*, *(c)* and *(e)*, respectively. It is worth noting that the connectivity between "touching" QDs in ensembles of semiconductor QDs is different than in granular metals. Usually there are narrow (no more than 0.5 nm wide) boundaries formed between the nanoparticles, which involves at least a different crystallographic orientation of the touching crystallites. This quantum size "grain boundary" limit has not been studied so far. In a literature the charge transfer process between such "touching" QDs was termed as "migration" (Antonova et al., 2008) (Balberg et al., 2007).



(a)                                    (b)                                    (c)
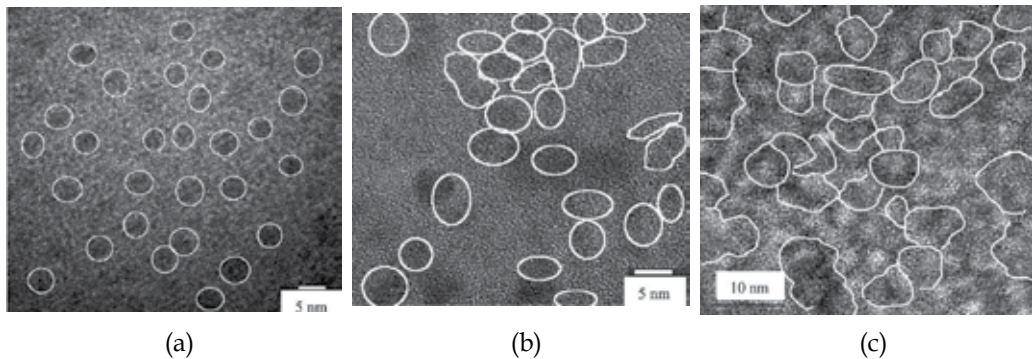
Fig. 15. HRTEM images of the ensembles of Si QDs corresponding to different structural-electrical regimes: (a) uniformly dispersed isolated spherical QDs (regime *a*), (b) clusters of "touching" QDs (regime *c*) and (c) percolation clusters of "touching" QDs (regime e) (Antonova et al., 2008).

The effect of the connectivity on the transport properties (dark and photoconductivity) of the ensembles of Si QD$_S$ is illustrated on Fig. 16. As one can see, the global picture of transport in Si QDs ensembles is reminiscent of that of granular metals, but the details are quite different. For the samples with low Si content (related to the number of Si QDs in the ensemble), which are characterized by the isolated Si QDs (regime *a*), the local conductivity

is determined by the tunneling of charge carriers under Coulomb blockage[2] between adjacent nanocrystallites similar to the case encountered in granular metals in the dielectric regime (Abeles et al., 1975) (Balberg et al., 2004). Indeed, as long as Si QDs or clusters of Si QDs are small enough, they "keep" the carrier that resides in them and become charged when an excess charge carrier reaches them. Hence, the transport through the system can take place only if a corresponding charging (or Coulomb) energy is provided.
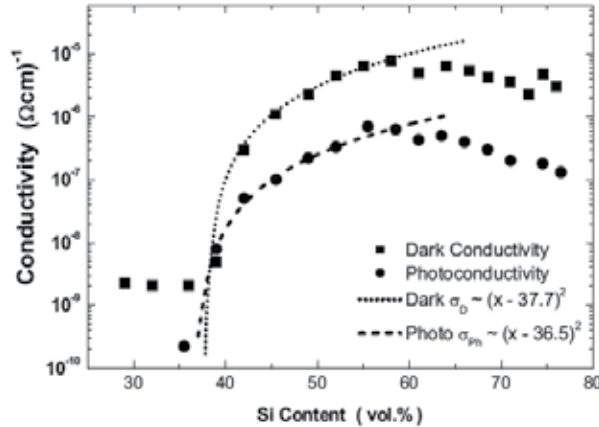


Fig. 16. Dependence of the dark conductivity and the photoconductivity on the Si content (related to the number of Si QDs in ensemble)

With increasing of Si content (Fig. 15 (b)), the interparticle distance decreases and the tunneling-connected quantum dot clusters grow in size. The "delocalization" of the carrier from its confinement in the individual quantum dot to larger regions of the ensemble will take place, i.e., the charge carrier will belong to a cluster of QDs rather than to an individual QD. Correspondingly, this will also yield a decrease in the local charging energy in comparison with that of the isolated QD and the distance to which the charge carrier could wander will increase and as a consequence the conductivity of the ensemble will increase as well. The charge carrier transport in the case of regime *(c)* is thus determined by the intracluster migration and by the intercluster tunneling.

As one can see from the Fig. 16, the maximal possible conductivity is assured in the case of highly percolating system of Si QDs (regime *(e)*). However, the conduction in this regime is quite different from that one of the granular metals since there are still boundaries between touching Si QDs. In fact, the corresponding migration process is similar to that in polycrystalline semiconductors, but now the boundaries are on the quantum scale. It was suggested that in this regime the migration dominates the transport properties and the global conductivity is limited by the interface between the touching QDs (Balberg, 2010).

---

[2] The transfer of an electron from a given neutral particle to an adjacent neutral particle, charges this particle by one (positive) elementary charge *(q)* and that of the adjacent particle by one (negative) elementary charge. If the capacitance of the individual particle in its corresponding environment is $C_0$, the energy needed to be supplied for the above "electron-hole" transfer by tunneling is then: $E=q^2/C_0$. This energy, which opposes to the transfer of charge carriers, is known as the Coulomb blockage energy, which is of the order of a tenth of an eV. In general, one can say, that a tunneling process is thermally activated when it requires a supply of energy.

Form the photovoltaic point of view, the thin films constituted of interconnected Si QDs are the most promising candidates for higher bandgap materials in all-Si tandem cell approach. Indeed, the highly percolating system of Si QDs will ensure the most favorable conditions for the electronic transport between the nanocrystals and, as it was discussed previously, the bandgap value in such structures could be adjusted in the large range covering the major part of the solar spectrum (Nychyporuk et al., 2009).

### 3.4.2 Nanocrystalline Si superlattices

Nanocrystalline Si superlattices have been proposed as candidates for the high bandgap absorber component in all-Si tandem solar cells. They consists of thin dielectric and Si QD based layers alternating in one direction, i.e., heterostructure type –I superlattices. The period of such a superlattice usually is much larger than the lattice constant but is smaller than the electron mean free path. Such a structure possesses, in addition to a periodic potential of the crystalline lattice, a potential due to the alternating semiconductor layers. The existence of such a potential significantly changes the energy bandstructure of the semiconductors from which the superlattice is formed. The coupling among QDs occurs, leading to a splitting of the quantized carrier energy levels of single dots and formation of three-dimensional minibands (Lazarenkova & Balandin, 2001) (Jiang & Green, 2006) as sketched on Fig. 17 (shaded areas).

The charge carrier mobility, which has a crucial impact on a charge-collection efficiency in solar cells, depends on the dominant transport regime at given operating conditions, which may be described by mini-band transport, sequential tunneling or Wannier-Stark hopping (Wacker, 2002). The sequential resonant tunneling (SRT) was suggested to be the most prominent for efficient carrier collection in Si QD solar cells (Raisky et al., 1999).

The schematic view of the sequential resonant tunneling transfer in a multiple-quantum-well structure is depicted on Fig. 18. Electrons tunnel from the ground state of the $j^{th}$ well into an excited state of the $(j+1)^{th}$ well. The tunneling process is then followed by intrasubband energy relaxation from the excited state to the ground state. This two-step scheme can be repeated as many times as needed to build the required thickness for optimal solar absorption. Resonance occurs when the $E_2-E_1 = |q\mathbf{F}d|$ condition is satisfied where $E_1$ and $E_2$ are the ground and first excited subband energies of the quantum well, $q$ the electron charge, $\mathbf{F}$ the internal electric field, and $d$ the spatial structural period. From Fig. 18 it is clear that the bottleneck of electron transfer is the last ($N^{th}$) well, where carriers have to transfer through a significantly thicker right barrier than inside the multiple-quantum-well region. This can lead to charge build up and, consequently, screening of the built-in field.

The photogeneration and transport in superlattice absorbers, on the example of a Si-SiO$_x$ multilayer structure embedded in the intrinsic region of a p-i-n diode was recently numerically investigated (Aeberhard, 2011). The model system under investigation is shown on the Fig. 19. It consists of a set of four coupled quantum wells of 6 monolayer[3] (ML) width with layers separated by oxide barriers of 3-ML thickness, embedded in the intrinsic region of a Si p-i-n diode. The doping density was $10^{18}$ cm$^{-3}$ for both electrons and holes. Insertion of the oxide barriers leads to an increase of the effective bandgap in the central region of the diode from 1.1 to 1.3 eV. The spectral rate of carrier generation in the confined states under illumination with monochromatic light at photon energy 1.65 eV and intensity of 10 kW/m$^2$

---

[3] The monolayer thickness is half the Si lattice constant, i.e., 2.716 Å.

is shown on the Fig. 20. At this photon energy both the lowest and the second minibands are populated. The photocurrent originating in this excitation is shown on Fig. 21. Current flows also in first and second minibands, which means that relaxation due to scattering is not fast enough to confine transport to the band edge. However, transport of photocarriers is strongly affected by the inelastic interactions, and is the closest to the sequential tunneling regime. We can thus conclude that in the case of high internal fields, excess charge is transported via sequential tunneling in the miniband where it is generated.

The sequential resonance tunneling enhances the photocarrier collection and reduces radiative recombination losses (Raisky et al., 1999). However it should be noted that SRT increases both photocurrent (Iph) and dark current (Idc). The total current of a photovoltaic device is the difference of these two currents, and thus, to take advantage of SRT, a solar cell possessing a superlattice structure should be designed to have the resonance in the region where $I_{ph}$» $I_{dc.}$

The main challenge of the tandem structure is to achieve sufficient carrier mobility and hence a reasonable conductivity. This generally requires formation of a true superlattice with overlap of the wave function for adjacent QDs, which in turns requires either close spacing between Si nanocrystals or low barrier height. Transport properties strongly depend on the matrix in which the Si quantum dots are embedded. Indeed, the electron or the hole wavefunctions exponentially decay with distance. Fig. 22 shows the penetration length of the wave function of electron of a single quantum well into different high-bandgap materials having different barrier heights. As one can see, the tunneling probability heavily depends on the barrier height. The penetration length is bigger for the materials with lower barrier height. Thus $Si_3N_4$ and SiC giving lower barriers than $SiO_2$, allow larger dot spacing for a given tunneling current. For example, the QDs in $SiO_2$ matrix would have to be separated by no more than 1-2 nm of matrix, while they could be separated by more than 4 nm of SiC.

The influence of the fluctuations in spacing and size of the QDs on the carrier mobility was also investigated (Jiang & Green, 2006). The calculations have shown that the interdot distance has larger impact on the calculated carrier mobility while the dot size can be used to control the band energy level.

## 3.5 Fabrication of Si QD PV devices

Recently it have been reported on the realization of interdigitated silicon QD solar cells on quartz substrate(Conibeer et al., 2010). Schematic view of the fabricated solar cells is shown on the Fig. 23 (a). The p-n diodes were fabricated by sputtering alternating layers of $SiO_2$ and SRO onto quartz substrate with in situ B and P doping. The top B doped bi-layers were selectively etched to create isolated p-type mesas and to access the buried P doped bi-layers. Aluminium contacts were deposited by evaporation, patterned and sintered to create ohmic contacts on both p- and n-type layers. The area of the fabricated interdigitated solar cells was 0.12 cm$^{-2}$. One of the derivatives of the presented approach was the fabrication of the p-i-n diodes. Indeed, it is expected that the intrinsic layer will have a longer lifetime that the doped material leading to an improved photocurrent.

I-V measurements in the dark and under 1-sun illumination (Fig. 23 (b)) indicate a good rectifying junction and generation of an open-circuit voltage, $V_{OC}$, up to 492 mV (Conibeer, 2010). The high sheet resistance of the deposited layers, in conjunction with the insulating quartz substrates, causes an unavoidable high series resistance in the device.
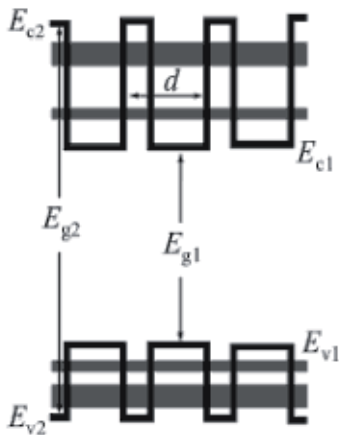
Fig. 17. The energy bandstructure of a semiconductor type-I heterostructure superlattice : $E_{g1}$ and $E_{g2}$ are the bandgaps, $E_{c1}$ and $E_{c2}$ are the bottoms of the conduction bands of narrow bandgap and wide bandgap semiconductors, respectively; d is the period of the heterostructure superlattice (Mitin, 2010).
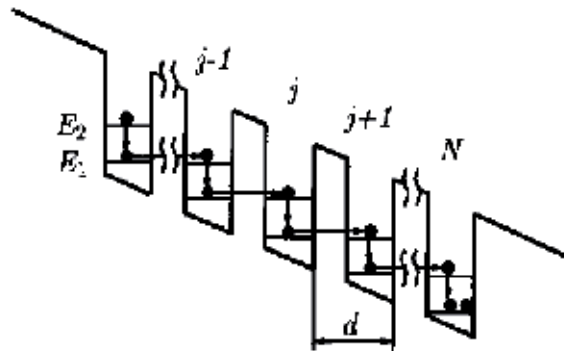


Fig. 18. Sequential resonant tunneling transfer in multiple-quantum-well structure. $E_1$ and $E_2$ are the energies of the ground and first excited states in the quantum well, respectively, and $d$ the superlattice period (Raisky et al., 1999).
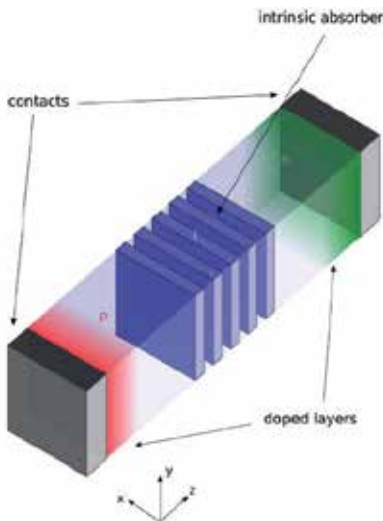


Fig. 19. Spatial structure and doping profile of the p-i-n model system (Aeberhard, 2011).
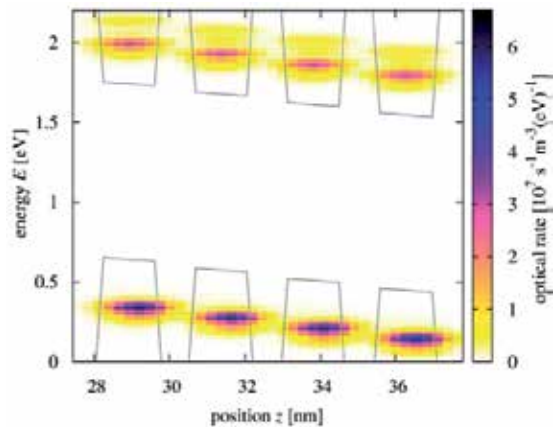


Fig. 20. Spatially and energy resolved charge carrier photogeneration rate in the quantum well region at short-circuit conditions and under monochromatic illumination with energy of 1.65 eV and intensity of 10kW/m² (Aeberhard, 2011).
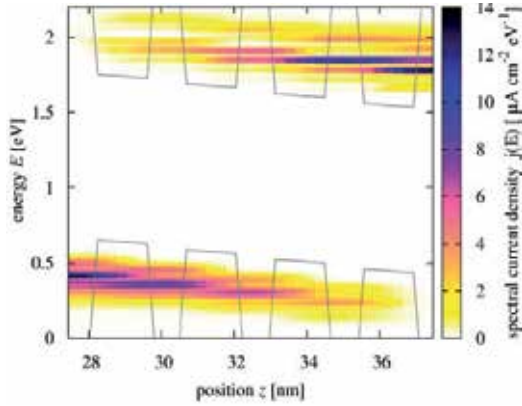
Fig. 21. Spatially and energy-resolved charge carrier short-circuit photocurrent density in the quantum well region under monochromatic illumination with energy of 1.65 eV and intensity of 10kW/m² (Aeberhard, 2011).
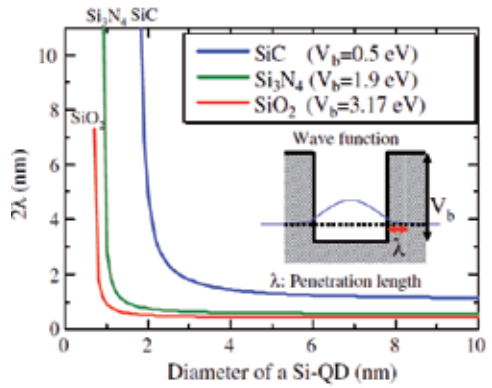
Fig. 22. Penetration length of the wave function of confined electron into barrier layers. $V_b$ represents a barrier height for each barrier material (Aeberhard, 2011).



(a)



(b)
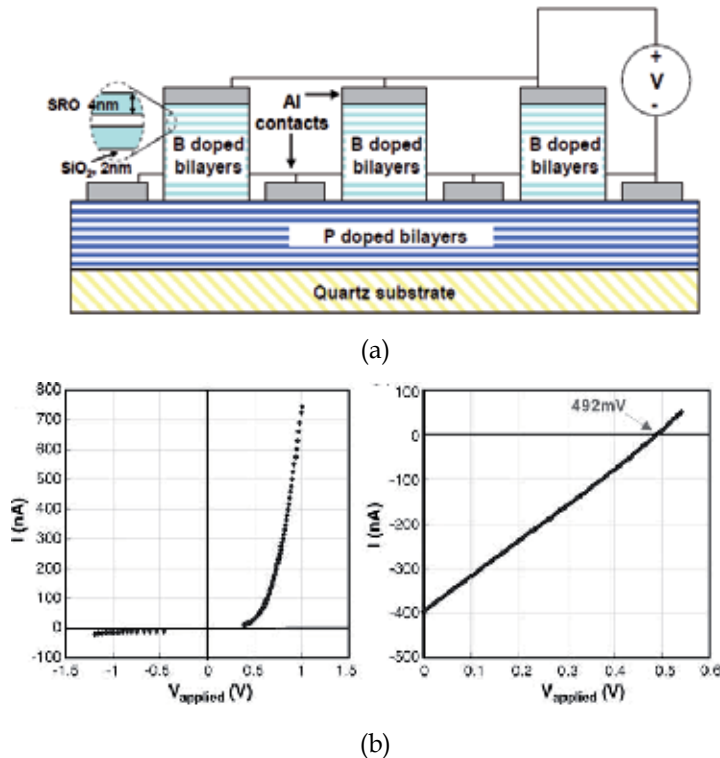
Fig. 23. (a) Schematic representation of the fabricated interdigitated devices (Conibeer et al., 2010); (b) Dark and illuminated I-V measurements of p-i-n diodes with 4 nm SRO/2 nm SiO2 bilayers.

The high resistance severely limits both the short-circuit current and the fill factor of the cells, particularly under illumination. Significant improvement is expected once the parasitic series resistance is eliminated.

Further evidence that this photovoltaic effect occurs in a material with an increased bandgap is given by temperature dependent I-V mesurements, from which an electronic bandgap for the Si QD nanostructure materials can be extracted. A bandgap of 1.8 eV was extracted for a structure containing Si QDs with a nominal diameter of 4 nm. However, this value will be due to a combination of other components in series with the material bandgap, hence the true material bandgap will be less than 1.8 eV.

Homojunction Si QD devices have also been fabricated in a SiC matrix using the superlattice approach (Song et al., 2009). Fig. 24 (a) shows a schematic diagram of a n-type Si QD: SiC/ p-type Si QD:SiC homojunction solar cell fabricated on a quartz substrate. The n-type Si QD emitter was approximately 200 nm thick and the p-type base layer is approximately 300 nm thick. This devices have given $V_{OC}$ of 82 mV that is promising initial value for a Si QDs in SiC solar cells on quartz substrate. Improvement of the device structure and optimization of dopant incorporation is expected to improve this value.



(a)                                                    (b)
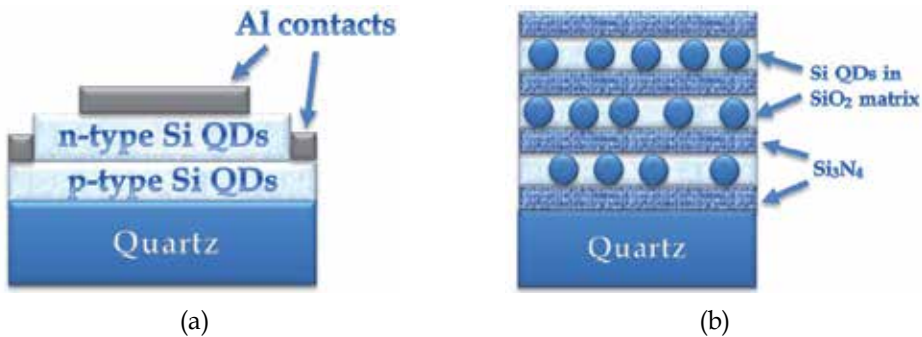
Fig. 24. (a) Schematic diagram of a n-type Si QD: SiC/ p-type Si QD:SiC/ quartz homojunction solar cell (Song et al., 2009); (b) The concept of the transport improvement: alternating layers of $Si_3N_4$ and SRO.

Current in both these $SiO_2$ and SiC matrix devices was very small, due principally to the very high lateral resistance and also because of the small amount of absorption in the approximately 200 nm of material used. Indeed, as it was discussed in the previous paragraph, transport in these devices relies on tunneling and hopping between adjacent QDs. To maximize the tunneling probability, the barrier heights between QDs must be low, but this then compromises the degree of quantum confinement and the height of the confined energy levels and hence the effective bandgap obtained. The solution is to introduce anisotropy between the growth, $z$, direction and the $x$-$y$ plane. This can achieved by maintaining strong confinement through the use of a large barrier height oxide in the plane, but to intersperse these layers with layers of lower barrier height such as $Si_3N_4$ or SiC, thus giving higher tunneling probability in the z direction (Fig. 24 (b)) (Di et al., 2010). The very first results on this approach were rather promising and showed the decreasing in the vertical resistivity of such Si QD nanostructures with $SiN_x$ interlayers (Di et al., 2010). To what concerns the increasing of the $V_{OC}$ the most potential route is the passivation of the defects through the hydrogenation.

The first prototypes of Si QD PV devices were successfully developed. Up today they present $V_{OC}$, $I_{SC}$ and fill factor (FF) values which still lower than those ones of the 1st generation PV cells based on bulk Si – but all these problems are being addressed. The next step implies the further optimization of the fabrication parameters, developing of the efficient doping technique and defect passivation.

## 4. Silicon nanowire solar cells

Nanowire solar cells demonstrated to date have been primarily based on hybrid organic-inorganic materials or have utilized compound semiconductors such as CdSe. Huynh *et al.* utilized CdSe nanorods as the electron-conducting layer of a hole conducting polymer-matrix solar cell (Huynh et al., 2002) and produced an efficiency of 1.7 % for AM 1.5 irradiation. Similar structures have been demonstrated for dye-sensitized solar cells using titania or ZnO nanowires, with efficiencies ranging from 0.5 % to 1.5 % (Law et al., 2005). These results show the benefits of using nanowires for enhanced charge transport in nanostructured solar cells compared to other nanostructured architectures. The Si nanowires (Si NW) solar cells have a potential to provide the equal or better performance to crystalline Si solar cells with processing methods similar to thin film solar cells (Tsakalakos et al., 2007) (Uchiyama et al., 2010) (Andra et al., 2008).

### 4.1 Fabrication of Si nanowires
The techniques to produce nanowires are normally divided into *(i)* bottom up and *(ii)* top down approaches.

### 4.1.1 Bottom up approach
The bottom up approach starts with individual atoms and molecules and builds up the desired nanostructures. One of the mostly used methods in this family of approaches is the Vapor Liquid Solid (VLS) method which uses metal nanotemplates on Si wafer or on Si thin film (Kelzenberg et al., 2008) (Tian et al., 2007) (Tsakalakos et al., 2007, 2007a). In this method a liquid metal cluster acts as the energetically favored site for vapor-phase reactant absorption and when supersaturated, the nucleation site for crystallization. An important feature of this approach for nanowire growth is that phase diagrams can be used to choose a catalyst material that forms a liquid alloy with the nanowire material of interest, i.e. Si in our case. Also, a range of potential growth temperatures can be defined from the phase diagram such that there is coexistence of liquid alloy with solid nanowire phase. The main advantages of the VLS method which should be cited are the rather high growth rate of several 100 nm/min and the fact that perfectly single crystalline nanowires form.

A schematic diagram illustrating the growth of Si nanowires by the VLS mechanism is shown on (Fig. 25 (a)). When the nanocatalysts become supersaturated with Si, a nucleation event occurs producing a solid/liquid Si/Au-Si alloy interface. In order to minimize the interfacial free energy, subsequent solid growth/crystallization occurs at this initial interface, which thus imposes the highly anisotropic growth constrain required for producing nanowires. Its growth continues in the presence of reactant as long as catalyst nanocatalyst remains in the liquid state. Typically the growth is performed by using $SiH_4$ as the Si reactant, and diborane and phosphine as p- and n-type dopants, respectively. The growth can be carried out using Ar, He or $H_2$ as carrier gas, which enables an added degree of freedom for the nanowire growth. For exemple, the use of $H_2$ as a carrier gas can

passivate the growing solid surface and reduce the roughness (Wu et al., 2004) while Ar and He can enhance radial deposition of a specific composition shell.

Most frequently gold is taken as a template for nanowire growth. The Au-Si binary phase diagram (Fig. 25 (b)) predicts that Au nanocatalysts will form liquid alloy droplets with Si at temperatures higher than the eutectic point which is 363°C. The Au nanocatalysts can be prepared either from commercially available gold colloids or by depositing a thin Au film followed by a heating step above the eutectic temperature during which a Au-Si liquid film forms to disintegrate into nano-droplets. Another simple and effective method for producing metal nanoparticles (Au, Ag…) at room temperature is based on their electroless deposition on the surface of Si or hydrogenated Si nitride films (Nychyporuk et al., 2010). It should be mentioned that it is still a controversial issue how gold is incorporated into the wire and thus how it influences the electronic properties of the nanowire. Gold is a deep-level defect in bulk Si and if it is also true for nanowires grown from Au droplets. Hence the alternative metals like In, Sn, Al (Ball et al., 2010) are actually under investigation for using as nanocatalysts during the nanowire growth.

Si NWs grow with a diameter similar to that of the template droplet. The nanowire diameters are on average 1-2 nm larger than the starting nanocatalyst size. As a result a carpet of perfect single crystalline NWs of 10 to 200 nm in diameter and several micrometers in length can be grown on the crystalline substrate (Fig. 26 (a)) (Andra 2008). High-resolution transmission electron microscopy (HRTEM) was used to define in detail the structures of these nanowires (Wu et al., 2004). As synthesized Si NWs are single crystalline nanostructures with uniform diameters. Studies of the ends of the nanowires show that they often terminate with Au nanoparticles (Fig. 26 (b)). In addition, the crystallographic growth directions of Si NWs have also been investigated using HRTEM and systematic measurements reveal that the growth axes are related to their diameters (Wu et al., 2004) (Cui et al., 2001a). For diameters between 3 and 10 nm, 95% of the Si NWs were found to grow along the <110> direction, for diameters between 10 and 20 nm, 61% of the Si NWs grow along the <112> direction, and for diameters between 20 and 30 nm, 64% of the Si NWs grow along the <111> direction. These results demonstrate a clear preference for growth along the <110> direction in the smallest Si NWs and along <111> direction in larger ones (Zhong et al., 2007). Cross-sectional HRTEM analysis has revealed that the nanowires could have triangular, rectangular and hexagonal cross section with well – developed facets (Vo et al., 2006) (Jie et al., 2006) (Zhang et al., 2005).

The VLS method permits to fabricate the nanowires of well-defined length with diameters as small as 3 nm (Wu et al., 2004). The electronic properties can be precisely controlled by introducing dopant reactants during the growth. Addition of different ratios of diborane or phosphine to silane reactant during growth produces p- or n- type Si nanowires with effective doping concentrations directly related to the silane: dopant gas ratios (Cui et al., 2000) (Cui et al., 2001) (Zheng et al., 2004) (Fukata, 2009). It was demonstrated that B and P can be used to change the conductivity of Si NWS over many orders of magnitude (Cui et al., 2000). The carrier mobility in SiNWs can reach that one in bulk Si at a doping concentration of $10^{20}$ cm$^{-3}$ and decreases for smaller diameter wires. Temperature dependent measurements made on heavily doped SiNWs show no evidence for single electron charging at temperatures down to 4.2 K, and thus suggest that SiNWs possess a high degree of structural and doping uniformity. Moreover, TEM studies of boron- and phosphorous doped SiNWs have shown that contrary to Si QDs the introduction of impurity atoms during the nanowire growth does not change their crystallinity. The ability to prepare well-defined doped nanowire during synthesis distinguishes nanowires from QDs.

<center>(a)</center>



<center>(b)</center>
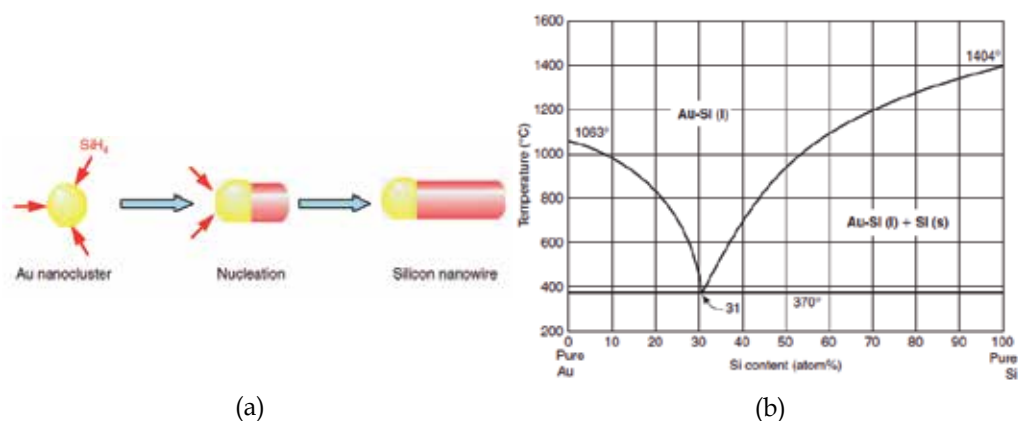
Fig. 25. (a) Schematic diagram illustrating the growth of Si nanowires by the VLS mechanism. (b) Binary phase diagram of Au-Si (Zhong et al., 2007).



<center>(a)</center>



<center>(b)</center>
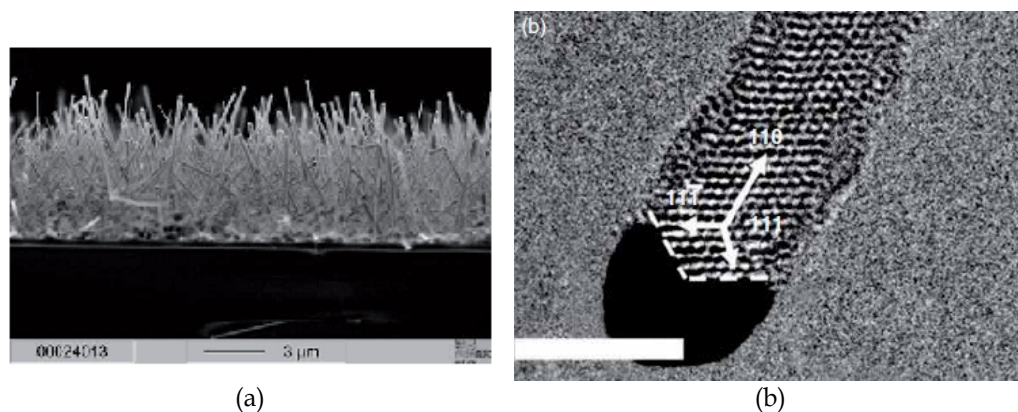
Fig. 26. (a) SEM image of a Si NW carpet grown from Au nanoparticles (150 nm diameter) on a multicrystalline Si wafer (Andra 2008); (b) HRTEM image of the gold catalyst/nanowire interface of a Si NW with a <110> growth axis. Scale bar is 5 nm (Wu et al., 2004).

### 4.1.2 Top down approach

In top down approach relies on dimentional reduction through selective etching and various nanoimprinting techniques. For example, well aligned Si NW arrays can be obtained by electroless metal-assisted chemical etching in $HF/AgNO_3$ solution. Basically, a noble metal is deposited on the surface in the form of nanoparticles which act as catalyst for Si etching in HF solution containing an oxidizing agent. As a consequence, the etching only occurs in the vicinity of the metal nanoparticles and results in the formation of well defined mesopores (20-100 nm in diameter (Fang et al., 2008) (Peng et al., 2005) (Fig. 27 (a)).

One of the main advantages of the top – down methods as compared to the bottom –up is that it is possible to start the processing by using conventional wafers with already performed diffusion regions (ex. $p^+nn^+$ ) and then etch it into SiNWs. Each nanowire will

thus present the p-n junction already formed. However this method presents some drawbacks. One of them is rather poor size control.

To overcome this problem colloidal crystal patterning combined with metal-assisted etching was applied (Wang et al., 2010) (Wang et al., 2010). The main idea is the next one. The sphere lithography is based on the self-organization of micrometer/nanometer spheres into a monolayer with a hexagonal close-packed structure. Typical material used for the spheres are silica and polystyrene, which are commercially available with narrow size distribution. The deposition of a monolayer of the spheres on a substrate is used as a patterning mask for thin metallic film evaporated on the Si wafer. After the sphere dissolution, the Si surface that comes in contact with the metal is selectively etched, leaving behind an array of Si NWs whose diameter is predefined by the size of holes in the metal film, while the length is determined by the etching time. This method enables the formation of large scale arrays with long – range periodicity of vertically standing nanorods/nanowires with well controlled diameter, length and density (Fig. 27 (b)). It should be however noted that this methods does not permit to achieve SiNWs with the diameters lower than 50 nm and thus potentially cannot be applied for all-Si tandem solar cell.
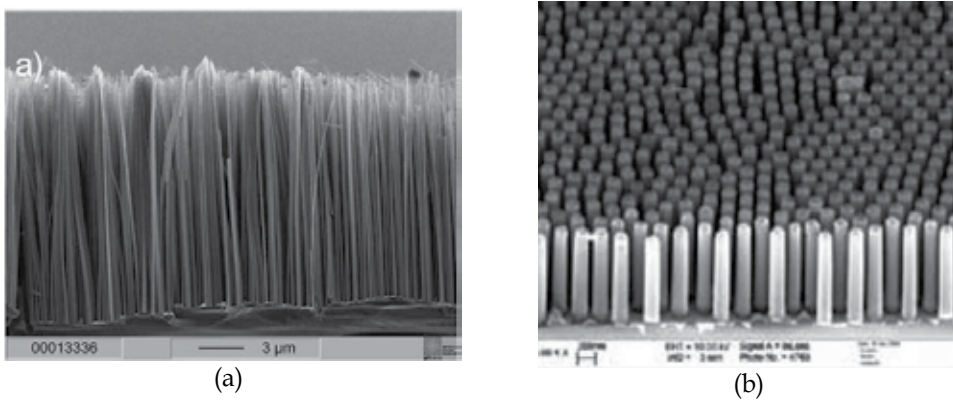


Fig. 27. SEM images of Si NWs obtained by (a) simple metal-assisted etching technique (Andra 2008) and (b) by colloidal crystal patterning combined with metal-assisted etching approach (Wang et al., 2010).

## 4.2 Optical properties of Si nanowires

A variety of the optical techniques have shown that the properties of nanowires are different to those of their bulk counterparts, however the interpretation of these measurements is not always straightforward. The wavelength of light used to probe the sample is usually smaller than the wire length, but larger than the wire diameter. Hence, the probe light used in the optical measurement cannot be focused solely onto the nanowire and the wire and the substrate on which the wire rests (or host material if the wire is embedded in a template) are probed simultaneously. For example, for measurements such as photoluminescence, if the substrate does not luminesce or absorb in the frequency range of the measurements, PL measures the luminescence of the nanowire directly and the substrate can be ignored. In reflection and transmission measurements, even a non-absorbing substrate can modify the measured spectra of nanowires. However, despite these technical difficulties it was

experimentally proved that Si nanowire materials have exhibited properties such as ultra-high surface area ratio, low reflection, absorption of wideband light, and tunable bandgap.

### 4.2.1 Bandgap of quantum SiNWs

In 2003, scanning tunneling spectroscopy measurements on individual oxide-removed Si NWs showed that the optical gap of Si NWs increased with decreasing of Si NW diameter from 1.1 eV for 7 nm to 3.5 eV to 1.3 nm (Ma et al., 2003). Since, a large number of theoretical and experimental works have been done to explore the effect of the chemical passivation, surface reconstruction, cross section geometry and growth orientation on electronic structure of SiNWs (Fernández-Serra et al., 2006) (Yan et al., 2007) (Vo et al., 2006). For example, it was shown than the bandgap of [110] SiNWs is the smallest among those of the [100], [112], and [111] wires of the same diameter (Cui et al., 2000). It should be also noted that the magnitude of the energy increase/decrease in SiNWs induced by quantum confinement is different for each point of the bandstructure. It was predicted that the conduction-band-minimum (CBM) energy increases more near the X point than near the Γ. Therefore for nanowires with sufficiently small dimensions, this difference in the energy shifts at different points in the Brillouin zone is large enough to move the CBM at the X point above the CBM at the Γ point (Vo et al., 2006). Then a transition from an indirect to direct gap material occurs. The indirect to direct transition does not depend on the special cross-sectional shapes and the bandgaps of [110] SiNWs remain direct event for SiNWs with dimensions up to 7 nm. The dependence of the bandgap on SiNW dimension $D$ is shown on the Fig. 28 (a). It is obvious that the smaller the dimension of the nanowire the larger the bandgap due to quantum confinement. As $D$ decreases from 7 to 1 nm, the bandgap increases from 1.5 to 2.7 eV. In addition to the size dependence, the energy gap also shows significantly different change with respect to the cross-sectional shape. The bandgaps of rectangular and hexagonal SiNWs are rather close while distinctly smaller than that of the triangular SiNWs.
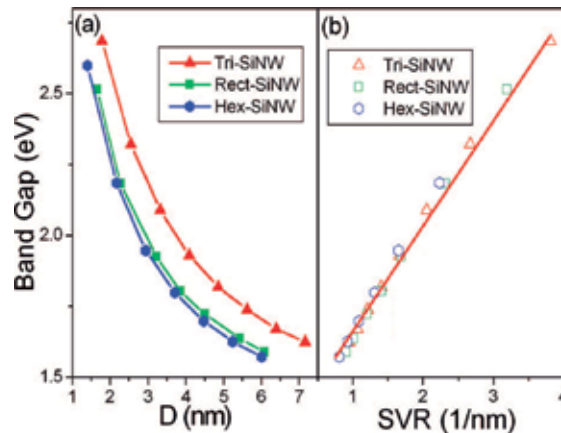


Fig. 28. (a) Bandgap of SiNWs versus the transverse dimension $D$. (b) Bandgap of SiNWs versus SVR (Yao et al., 2008).

The significant cross-sectional shape effects on band gap and size dependence can be understood from the concept of surface –to-volume ratio (SVR). Because of the quantum confinement effect, the band gap increases as the material dimension is reduced, thus

leading to an increase of SVR. In other words, SVR has the impact of enlarging band gap. At the same transverse dimension, triangular SiNW has larger SVR than those of the rectangular SiNW and hexagonal SiNW. As a result, its larger SVR induces the largest band gap among those of the rectangular and hexagonal SiNWs and the strongest size dependence. The bandgap values versus SVR of the SiNWs are shown in Fig. 28 (b). The SVR effect on the bandgap of [110] SiNWs with any cross-sectional shape and area can be described by a universal expression (Yao et al., 2008)

$$E_G \, (eV) = 1.28 + 0.37 \times S \, (nm^{-1}),$$

where $S$ is the value of the SVR in unit of $nm^{-1}$. The bandgap of SiNWs are usually difficult to measure, but their transverse cross-sectional shape and dimension are easy to know, so it is of significance to predict the bandgap values of SiNWs by using the above expression.

### 4.2.2 Optical reflection and absorption in SiNWs

Si NW PV devices show improved optical characteristics compared to planar devices. Fig. 29 (a) shows typical optical reflectance spectra of SiNW film as compared to solid Si film of the same thickness (~10μm) (Tsakalakos et al., 2007a). As one can see, the reflectance of the nanowire film is less than 5% over the majority of the spectrum from the UV to the near IR and begins to increase at ~700°nm to a values of ~41% at the Si band edge (1100 nm), similar to the bulk Si. It is clear that the nanowires impart a significant reduction of the reflectance compared to the solid film. More striking is the fact that the transmission of the nanowire samples is also significantly reduced for wavelength greater than ~700°nm (Fig. 29 (b)). This residual absorption is attributed to strong IR light trapping[4] coupled with the presence of the surface states on the nanowires that absorb below bandgap light. However, the level of optical absorption does not change with passivation, which further indicates that light trapping plays a dominant role in the enhanced absorption of the structures at all wavelength. It should be also noted that the absorption edge of a nanowire film shifts to longer wavelength and approaches the bulk value as the nanowire density is increased. Essentially, the Si nanowire arrays act as sub-wavelength cylindrical scattering elements, with the mactroscopic optical properties being dependent on nanowire pitch, length, and diameter.
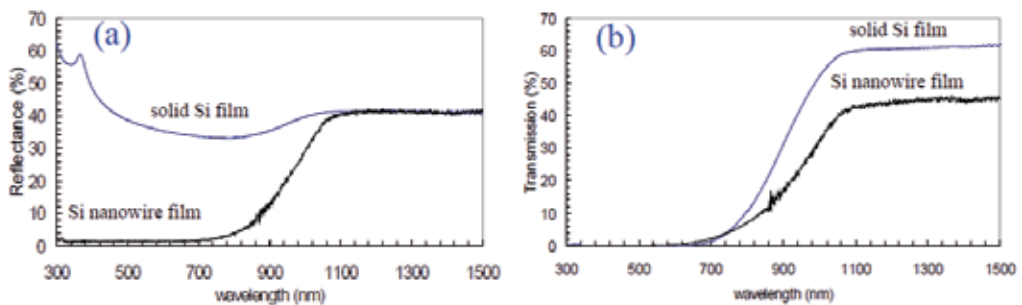


Fig. 29. Total (a) reflectance and (b) transmission data from integrated sphere measurements for 11 μm thick solid Si film and nanowire film on glass substrate (Tsakalakos et al., 2007).

---

[4] Light trapping is typically defined as the ratio of the effective path length for light rays confined within a structure with respect to its thickness.

### 4.3 Electrical transport in SiNWs

Important factors that determine the transport properties of Si nanowires include the wire diameter (important for both classical and quantum size effect), surface conditions, crystal quality, and the crystallographic orientation along the wire axis (Ramayya et al., 2006) (Duan et al., 2002).

Electronic transport phenomena in Si nanowires can be roughly divided into two categories: ballistic transport and diffusive transport. Ballistic transport phenomena occur when the electrons can travel across the nanowire without any scattering. In this case the conduction is mainly determined by the contact between the nanowire and the external circuit. Ballistic transport phenomena are usually observed in very short quantum wires. On the other hand, for nanowires with length much larger than the carrier mean free path, the electrons (or holes) undergo numerous scattering events when they travel along the wire. In this case, the transport is in the diffusive regime, and the conduction is dominated by carrier scattering within the wires, due to lattice vibrations, boundary scattering, lattice and other structural defects and impurity atoms.

The electronic transport behavior of Si nanowires may be categorized based on the relative magnitudes of three length scales: carriers mean free path, the de Broglie wavelength of electrons, and the wire diameter. For wire diameters much larger than the carrier mean free path, the nanowiers exhibit transport properties similar to bulk materials, which are independent of the wire diameter, since the scattering due to the wire boundary is negligible, compared to other scattering mechanisms. For wire diameters comparable or smaller than the carrier mean free path, but still larger than the de Broglie wavelength of the electrons, the transport in the nanowire is in the classical finite regime, where the band structure of the nanowire is still similar to that of the bulk, while the scattering events at the wire boundary alter their transport behavior. For wire diameters comparable to electronic wavelength (de Broglie wavelength of electrons), the electronic density of states is altered dramatically and quantum sub-bands are formed due to quantum confinement effect at the wire boundary. In this regime, the transport properties are further influenced by the change in the band structure. Therefore, transport properties for nanowires in the classical finite size and quantum size regimes are highly diameter-dependent. Experimentally it was shown that the carrier mobility in SiNWs can reach that one in bulk Si at a doping concentration of $10^{20}$ cm$^{-3}$ and decreases for smaller diameter wires (Cui et al., 2000).

Because of the enhanced surface-to-volume ratio of the nanowires, their transport behavior may be modified by changing their surface conditions. For example, it was shown on the n-InP nanowires, that coating of the surface of these nanowires with a layer of redox molecules, the conductance may be changed by orders of magnitude (Duan et al., 2002).

### 4.4 Comparison of axial and radial p-n junction nanowire solar cells

Independently of the nanowire preparation method two designs of NW solar cells are now under consideration with p-n junction either radial or axial (Fig. 30). In the radial case the p-n junction covers the whole outer cylindrical surface of the NWs. This was achieved either by gas doping or by CVD deposition of a shell oppositely doped to the wire (Fang, 2008) (Peng, 2005) (Tian 2007). In the axial variant, the p-n junction cuts the NW in two cylindrical parts and require minimal processing steps (Andra 2008). However, solar cells that absorb photons and collect charges along orthogonal directions meet the optimal relation between the absorption values and minority charge carrier diffusion lengths (Fig. 30 (a)) (Hochbaum 2010). A solar cell consisting of arrays of radial p-n junction nanowires (Fig. 30 (b)) may

provide a solution to this device design and optimization issue. A nanowire with a p-n junction in the radial direction would enable a decoupling of the requirements for light absorption and carrier extraction into orthogonal spatial directions. Each individual p-n junction nanowire in the cell could be long in the direction of incident light, allowing for optimal light absorption, but thin in another dimension, thereby allowing for effective carrier collection.
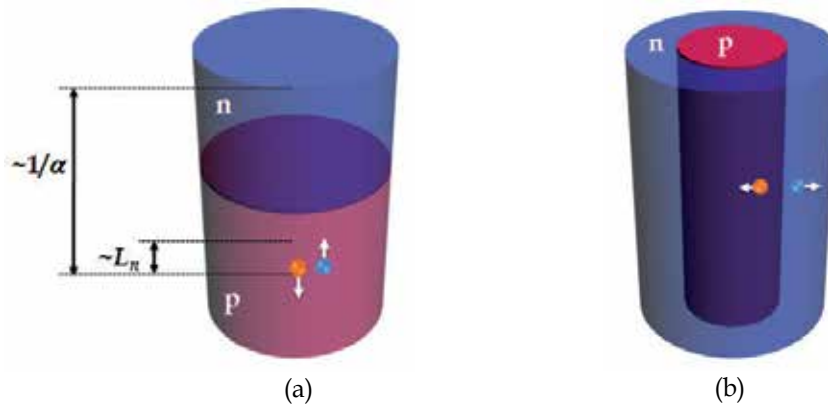


Fig. 30. Schematic views of the (a) axial and (b) radial nanowire solar cell. Light penetration into the cell is characterized by the optical thickness of the material ($\alpha$ is the absorption coefficient), while the mean free path of generated minority carriers is given by their diffusion length. In the case of axial nanowire solar cell, light penetrates deep into the cell, but the electron-diffusion length is too short to allow the collection of all light-generated carriers (Kayes et al., 2005).

The comparison between the axial and radial p-n junction technologies for solar cell applications was performed in details in Ref (Kayes et al., 2005). In the case of radial p-n junction, the short-circuit current ($I_{sc}$) increases with the nanowire length and plateaus when the length of the nanowire become much greater than the optical thickness of the material. Also, $I_{sc}$ was essentially independent on the nanowire radius, provided that the radius ($R$) was less than the minority carrier diffusion length ($L_n$). However, it decreases steeply when $R > L_n$. $I_{sc}$ is essentially independent of trap density in the depletion region. Being rather sensitive to a number of traps in the depletion region, the open circuit voltage $V_{oc}$ decreases with increasing nanowire length, and increases with nanowire radius. On the other hand the trap density in the quasineutral regions had relatively less effect on $V_{oc}$. The optimal nanowire dimensions are obtained when the nanowire has a radius approximately equal to $L_n$ and a length that is determined by the specific tradeoff between the increase in $I_{sc}$ and the decrease in $V_{oc}$ with length. In the case of low trap density in the depletion region, the maximum efficiency is obtained for nanowires having a length approximately equal to the optical thickness. For higher trap densities smaller nanowire lengths are optimal.

Radial p-n junction nanowire cells trend to favor high doping levels to produce high cell efficiencies. High doping will lead to decreased charge-carrier mobility and a decreased depletion region width, but in turn high doping advantageously increases the build-in voltage. Because carriers can travel approximately one diffusion length through a quasineutral region before recombining, making the nanowire radius approximately equal

to the minority –electron diffusion length allows carriers to traverse the cell even if the diffusion length is low, provided that the trap density is relatively low in the depletion region.

An optimally designed radial p-n junction nanowire cell should be doped as high as possible in both n- and p- type regions, have a narrow emitter width, have a radius approximately equal to the diffusion length of the electrons in the p-type core, and have a length approximately equal to the thickness of the material. It is crucial that the trap density near the p-n junction is relatively low. Therefore one would prefer to use doping mechanisms that will getter impurities away from the junction. By exploiting the radial p-n junction nanowire geometry, extremely large efficiency gains up to 11% are possible to be obtained.

## 4.5 Fabrication of Si QD PV devices

By using VLS method (Tian et al., 2007) (Kelzenberg et al., 2008) (Rout et al., 2008) (Fang et al., 2008) (Perraud et al., 2009) as well as by the etching method (Garnett et al., 2008) (Peng et al., 2005). SiNW based photovoltaic devices were experimentally demonstrated. Nearly all the works were concerned with Si wafers as a substrate. However, it should be noted that for competitive solar cells, low cost substrates, such as glass or metal foils are to be preferred. Schematic view of the VLS fabricated structure of the SiNW array solar cells is illustrated on Fig. 31 (a). The n-type SiNWs were prepared by the VLS method on (100) p-type Si substrate (14-22 $\Omega$cm). Device fabrication started from the evaporation of 2-nm thick gold film followed by annealing at 550°C for 10 min under $H_2$ flow to form Au nanocatalyzers. SiNWs were subsequently grown at 500° with $SiH_4$ diluted in $H_2$ as the gas precursor. N-type doping was achieved by adding $PH_3$ to $SiH_4$, with $PH_3/SiH_4$ ratio of $2x10^{-3}$ corresponding to a nominal phosphorous density of $10^{20}cm^{-3}$. After the VLS growth the gold catalysts were etched off in $KI/I_2$ solution, and the doping impurities were activated by rapid thermal annealing at 750° for 5 min. The SiNW array was then embedded into spin-on-glass (SOG) matrix. Indeed, SOG matrix ensures a good mechanical stability of the SiNW array and enables further processing steps, such as front surface planarization and electrical contact deposition. The planarization step is normally performed by the chemical-mechanical polishing. To form the front contacts indium-tin-oxide (ITO) was firstly deposited on planarized SOG surface followed by the deposition of Ni/Al contact grid. As back electrical contact, the sputtered and annealed Al was used. The area of the fabricated SiNW solar cell was 2.3 cm$^{-2}$.

The sheet resistance of n-type SiNWs embedded into SOG matrix was estimated to be $10^{-4}$ $\Omega$/sq. I-V measurements in the dark and under 1-sun illumination (Fig. 31 (b)) indicate a good rectifying junction. The measured $I_{SC}$, $V_{OC}$ and FF were 17 mA/cm², 250mV and 44%, respectively, leading to an energy-conversion efficiency of 1.9%. The $V_{OC}$ of Si NW solar cell was shown to be increased up to 580 mV (Peng et al., 2005). The parasitic series resistance found for SiNW solar cells (~5 $\Omega$ cm$^{-2}$) was slightly larger than in the standard 1st generation solar cells (~2 $\Omega$ cm$^{-2}$), however the p-n junction reverse current was of the order of 1 $\mu$A/cm² with is about 100 times bigger than in typical Si solar cells (~1 pA/cm²). Such a high pn junction reverse current indicates a high density of localized electronic states within the bandgap, which act as generation-recombination centers. These states may come from contamination of Si by gold which is used as catalyst for VLS growth. Other types of metallic catalysers, like Sn, were also used (Uchiyama et al., 2010).

However, for a moment by using this catalyzer it is difficult to achieve the diameter of SiNWs less that 200 nm. The electronic states in the bandgap may also come from a lack of passivation of surface defects. The passivation step is rather crucial for SiNW solar cells, since SiNW have very high SVR ratio and their opto-electronic properties strongly depends on the surface passivation.



|  (a)  |  (b)  |
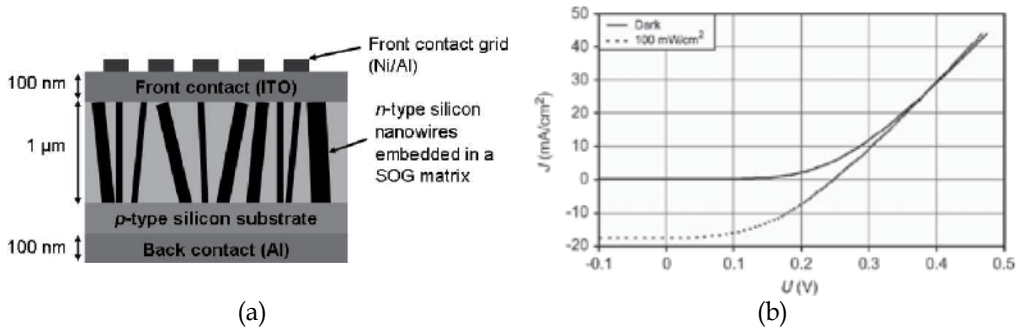
Fig. 31. (a) Structure of the SiNW array solar cell. A p-n junction is formed between the n-type SiNWs and the p-type Si substrate; (b) Dark and illuminated I-V measurements of n-type SiNWs on p-type Si substrate (Perraud et al., 2009).

The theoretical value of the efficiency for Si nanowire solar cells is predicted to be as high as 16%, which makes them perfect candidates for higher bandgap bricks in all-Si tandem cell approach. The first prototypes of SiNW solar cells have excellent antireflection capabilities and shown the presence of the photovoltaic effect. However, up today there was no evidence that this photovoltaic effect occurred in a material with an increased bandgap.

## 5. Conclusions

Silicon based third generation photovoltaics is a quickly developing field, which integrates the knowledge from material science and photovoltaics. Today the first prototypes of both Si QD solar cells and Si NWs solar cells have already been developed. For a moment they present $V_{OC}$, $I_{SC}$ and FF values which still lower than those ones of the 1st generation PV cells based on bulk Si – but all these problems are being addressed. It is too prematurely to draw the conclusions while the further optimization steps of the fabrication parameters were not performed. We should not forget that, for example, although the airplane was not invented until the early 20th century, Leonardo da Vinci sketched a flying machine four centuries earlier.

## 6. References

Abeles, B.; Pinch, H. L. & Gittleman, J. I. (1975), Percolation conductivity in W-Al₂O₃ granular metal films, *Phys. Rev. Lett.*, Vol. 35, pp. 247-250.
Aeberhard, U. (2011), Theory and simulation of photogeneration and transport in Si-SiOx superlattice absorbers, *Nanoscale Research Letters*, Vol. 6, p. 242.

Allan, G. & Delerue, C. (2007), Energy transfer between semiconductor nanocrystals: Validity of Förster's theory, *Phys. Rev. B*, Vol. 75, pp. 195311.

Andra, G.; Pietsch, M.; Sivakov, V.; Stelzner, Th.; Gawlik, A.; Christiansen, S.& Falk, F. (2008). Thin film solar cells based on single crystalline silicon nanowires, *Proceedings of 23th European Photovoltaic Solar Cell Energy Conference.*, Spain, pp. 163-167

Antonova, A.; Gulaev, M.; Savir, E.; Jedrzejewski, J, & Balberg, I. (2008), Charge storage, photoluminescence, and cluster statistics in ensembles of Si QDs, *Phys. Rev. B.*, Vol. 77, pp. 123318.

Balberg, I,; Azulay, D.; Toker, D. & Millo, O. (2004), Percolation and tunneling in composite materials, *Int. J. Mod. Phys. B*, Vol. 18, pp. 2091-2121.

Balberg, I.; Savir, E.; Jedrzejewski, J, Nassiopoulou, A. & Gardelis, S. (2007), Fundamental transport processes in ensembles of silicon quantum dots, *Phys. Rev. B.*, Vol. 75, pp. 235329.

Balberg, I. (2010) Chapter 4, in *Silicon Nanocrystals: Fundamentals, Synthesis and Application* (ed. L. Pavesi and R; Turan), Wiley, Weinheim.

Ball, J. & Reehal, H. (2010), The effect of substrate bias on the growth of silicon nanowires from Tin catalyst layers,, *Proceedings of 25th European Photovoltaic Solar Cell Energy Conference*, Spain, September 6-10, pp. 769-772.

Bulutay,C. (2007), Electronic structure and optical properties of silicon nanocrystals along their aggregation stages , *Physica E*, Vol. 38, pp. 112.

Bulutay, C. & Ossicini, S. (2010) Chapter 2, in *Silicon Nanocrystals: Fundamentals, Synthesis and Application* (ed. L. Pavesi and R; Turan), Wiley, Weinheim.

Canham, L. T. (1990), Silicon quantum wire array fabrication by electrochemical and chemical dissolution of wafers, *Appl. Phys. Lett.*, Vol. 57, pp. 1046.

Cho, E-Ch,; Green, M.; Xia, J.; Corkish, R.; Reece, P.; & Gal, M (2004), Clear quantum-confined luminescence from silicon/$SiO_2$ single quantum wells, *Appl. Phys. Lett.*, Vol. 84, p. 2286.

Cho, Y. H.; Green, M. A.; Cho, E-Ch.; Huang, Yu.; Trupke, Th. & Conibeer, G. (2005), Silicon quantum dots in SiNx matrix for third generation photovoltaics, *Proceedings of 20th European Photovoltaic Solar Cell Energy Conference*, Spain, June 6-10, pp. 47-50

Cho, E.C.; Green, M.A.; Conibeer, G.; Song, D.Y.; Cho, Y.H.; Scardera, G.; Huang, S.J.; Park, S.; Hao, X.J.; Huang, Y. & Dao, L.V. (2007) Silicon quantum dots in a dielectric matrix for all-silicon tandem solar cells. *Adv. OptoElectr.*, 2007, Article ID 69578.

Conibeer, G.; Green, M.; Cho, Cho, Eu-Ch.; König, D.; Cho, Y-H.; Fangsuwannarak, T.; Scardera, G.; Pink, E.; Huang, Yi.; Puzzer, T.; Huang, Sh.; Song, D.; Flynn, Ch.; Park, S.; Hao, X.& Mansfield, D. (2008), Silicon quantum dot nanostructures for tandem photovoltaic cells, *Thin Solid Films*, Vol. 516, pp. 6748-6756.

Conibeer, G. (2010) Chapter 20, in *Silicon Nanocrystals: Fundamentals, Synthesis and Application* (ed. L. Pavesi and R; Turan), Wiley, Weinheim.

Conibeer, G.; Green, M.; König, D.; Perez-Wurfl, I.; Huang, S.; Hao, X.; Di, D.; Shi, L.; Shrestha, S.; Puthen-Veetil, B.; So, Y.; Zhang, B. & Wan, Z. (2010a), Silicon quantum dot based solar cells: addressing the issues of doping, voltage and current

transport, *Proceedings of 25th European Photovoltaic Solar Cell Energy Conference*, Spain, September 6-10, pp. 182-190.

Crisp, D.; Pathare, A. & Ewell, R.C. (2004), The performance of gallium arsenide/germanium solar cells at the Martian surface, *Acta Astronautica,* Vol. 54, pp. 83-101.

Cui, Y.; Duan, X.; Hu, J. & Lieber, C.M., (2000), Doping and electrical transport in Si nanowires, *J. Phys. Chem. B* Vol. 104, pp. 5213-5216.

Cui Y., & Lieber, C.M. (2001), Functional Nanoscale Electronic Devices Assembled Using Silicon Nanowire Building Blocks, *Science* Vol. 291, pp. 851-853.

Cui, Y.; Lauhon, L.J.; Gudiksen, M.S.; Wang J. & Lieber, C.M. (2001a), Diameter-controlled synthesis of single-crystal silicon nanowires, *Appl. Phys. Lett.* Vol. 78, pp. 2214

Degoli, E.; Luppi, M. & Ossicini, S. (2000), From Undulating Si Quantum Wires to Si Quantum Dots: A Model for Porous Silicon, *Phys. Stat. Solidi (a)*, Vol. 182, pp. 301

Di. D.; Perez-Wurfl, I.; Conibeer, G. & Green, M. (2010) Formation and photoluminescence of Si quantum dots in $SiO_2/Si_3N_4$ hybrid matrix for all-Si tandem solar cells, *Sol. Energy Mater. Sol. Cells*. Vol. 94, pp. 2238-2243.

Duan, X.; Huang, Y. & Lieber, C. (2002) Nonvolatile memory and programmable logic from molecule-gated nanowires, Nano Lett., Vol. 2, pp. 487-490.

Erwin, S.C.; Zu, L.J.; Haftel, M.I.; Efros, A.L.; Kennedy, T.A.; & Norris, D.J. (2005) Doping semiconductor nanocrystals. *Nature*, Vol. 436, pp.91–94.

Fang, H.; Li, X.; Song, S.; Xu, Y. & Zhu, J. (2008), Fabrication of slantingly-aligned silicon nanowire arrays for solar cell applications, *Nanotechnology,* Vol. 19, pp.255703

Fangsuwannarak, T. (2007) Electronic and optical characterisations of silicon quantum dots and its applications in solar cells, PhD Thesis, University of New South Wales, Australia.

Fernández-Serra, M.; Adessi, Ch. & Blasé, X. (2006) Conductance, Surface Traps, and Passivation in Doped Silicon Nanowires, *Nano Lett.* Vol. 6, pp. 2674-2678.

Ficcadenti, M.; Pinto, N.; Morresi, L.; Murri, R.; Serenelli, L.; Tucci, M.; Falconieri, M.; Krasilnikova Sytchkova, A.; Grilli, M.L.; Mittiga, A.; Izzi, M.; Pirozzi, L. & Jadkar, S.R. (2009) Si quantum dots for solar cell fabrication, *Materials Science and Engineering B*, Vol. 159-160, pp. 66-69.

Fujii, M.; Hayashi, S.; & Yamamoto, K. (1998) Photoluminescence from B-doped Si nanocrystals. *J. Appl. Phys.,* Vol. 83, pp. 7953–7957

Fujii, M.; Mimura, A.; Hayashi, S.; Yamamoto, K.; Urakawa, C.; & Ohta, H. (2000) Improvement in photoluminescence efficiency of $SiO_2$ films containing Si nanocrystals by P doping: an electron spin resonance study. *J. Appl. Phys.*, Vol. 87, pp. 1855–1857.

Fujii, M.; Mimura, A.; Hayashi, S.; Yamamoto, Y.; & Murakami, K. (2002) Hyperfine structure of the electron spin resonance of phosphorus-doped Si nanocrystals. *Phys. Rev. Lett.,* Vol. 89, pp. 206805.

Fujii, M. (2010) Chapter 3, in *Silicon Nanocrystals: Fundamentals, Synthesis and Application* (ed. L. Pavesi and R; Turan), Wiley, Weinheim.

Fukata, N. (2009), Impurity doping in silicon nanowires, *Adv. Mater*. Vol. 21, pp. 2829-2832.

Garnett, E. & Yang, P. (2008) Silicon Nanowire Radial p−n Junction Solar Cells, *J. Am. Chem. Soc.* Vol. 130, pp.9224-9225.

Gradmann, R.; Löper, Ph.; Künle M.; Rothfelder, M.; Janz, S.; Hermle, M.& Glunz, S. (2010), Silicon nanocrystals in SiC: the influence of doping on crystallization and electrical properties, *Proceedings of 25th European Photovoltaic Solar Cell Energy Conference*, Spain, September 6-10, pp. 199-202.

Green, M. (2002), Third generation photovoltaics: solar cells for 2020 and beyond, *Physica E*, Vol. 14, pp. 65-70.

Green, M. (2003). *Third generation photovoltaics (advanced solar energy conversation),* Springer, pp.160.

Green, M. A.; Cho, E.-C.; Huang, Y.; Pink, E.; Trupke, T.; Lin, A.; Fangsuwannarak T.; Puzzer, T.; Conibeer, G. & Corkish, R. (2005), All-Si tandem cells based on "artificial" semiconductor synthesized using silicon quantum dots in dielectric matrix , *Proceedings of 20th European Photovoltaic Solar Cell Energy Conference*, Spain, June 6-10, pp. 3-7

Green, M. A.; Conibeer, G.; Cho, E.-C.; König, D.; Huang, S.; Song, D.; Scardera, G.; Cho, Y.; Hao, X.; Fangsuwannarak T.; Park, S. W.; Perez-Wurfl, P.; Huang, Y.; Chang, S.; Pink, E.; Bellet, D.; Bellet-Almaric, E. & Puzzer, T. (2007), Progress with Si-based tandem cells using quantum dots in dielectric matrix, *Proceedings of 22th European Photovoltaic Solar Cell Energy Conference*, Italy, September 3-7, pp. 1-4

Green, M.; Emery, K.; Hishikawa, Y. & Warta, W. (2010), Solar cell efficiency tables (version 36), *Progress in photovoltaics: research and applications*, Vol. 18, pp. 346-352.

Hao, X.J.; Cho, E.-C.; Scardera, G.; Shen, Y.S.; Bellet-Amalric, E.; Bellet, D.; Conibeer, G.; & Green, M.A. (2009) Phosphorus doped silicon quantum dots for all-silicon quantum dot tandem solar cells. *Sol. Energy Mater. Sol. Cells*, Vol. 93, pp. 1524.

Hao, X.J.; Cho, E-C.; Flynn, C.; Shen, Y.S.; Park, S.C.; Conibeer, G. & Green, M. (2009a), Synthesis and characterization of boron-doped Si quantum dots for all-Si quantum dot tandem solar cells, *Sol. Energy Mater. Sol. Cells*, Vol. 93, pp. 273-279.

Holtz, P.O. & Zhao, Q.X. (2004) Impurities Confined in Quantum Structures, Springer-Verlag, Berlin.

Huynh, W.; Dittmer, J. & Alivisatos, A. (2002) Hybrid nanorod-polymer solar cells, *Science*, Vol. 295, pp. 2425-2427.

Jiang Ch. & Green. M. (2006), Silicon quantum dot superlattices: modeling of energy bands, densities of states and mobilities for silicon tandem solar cell applications, *J. Appl. Phys.*, Vol. 99, p. 114902.

Jie, J. S.; Zhang, W. J.; Jiang, Y.; Meng, X. M.; Li, Y. Q. & Lee S. T. (2006), Photoconductive Characteristics of Single-Crystal CdS Nanoribbons, *Nano Lett.* Vol. 6, pp. 1887-1892.

Kayes, B.; Atwater, H. & Lewis, N. (2005), Comparison of the device physics principles of planar and radial p-n junction nanorod solar cells, *J. Appl. Phys.*, Vol. 97, pp. 114302.

Kelzenberg, M.; Turner-Evans, D.; Kayes, B.; Filler, M.; Putnam, M.; Lewis, N. & Atwater, H. A. (2008), Photovoltaic Measurements in Single-Nanowire Silicon Solar Cells, *Nano Lett.* Vol. 8, pp. 710-714.

Kim, T.; Park, N.; Kim, K.; Yong Sung, G.; Ok, Y.; Seong, T. & Choi, Ch. (2004), Quantum confinement effect of silicon nanocrystals in situ grown in silicon nitride films, *Appl. Phys. Lett.*, Vol. 85, pp. 5355.

Kim, B.H., Cho, C., Kim, T., Park, N., Sung, G., and Park, S. (2005) Photoluminescence of silicon quantum dots in silicon nitride grown by NH3 and SiH4. *Appl. Phys. Lett.*, 86, 091908., idem

Kim, T.-W.; Cho, Ch-H,; Kim, B-H, & Park, S-Ju. (2006), Quantum confinement effect in crystalline silicon quantum dots in silicon nitride growth using $SiH_4$ and $NH_3$, *Appl. Phys. Lett.*, Vol. 88, p. 123102.

König, D.; Rudd, J.; Green, A. & Conibeer, G. (2009) Impact of interface on the effective bandgap of Si quantum dots, *Sol. Energy Mater. Sol. Cells*, Vol. 93, pp. 753-758.

Kovalev, D.; Heckler, H.; Ben-Chorin, M.; Polisski, G.; Schwartzkopff, M. & Koch, F. (1998) Breakdown of the k-conservation rule in Si nanocrystals. *Phys. Rev. Lett.*, Vol. 81, pp. 2803–2806.

Kovalev, D.; Heckler, H.; Polisski, G.; & Koch, F. (1999) Optical properties of Si nanocrystals. *Phys. Status Solidi B*,Vol. 215, pp. 871–932.

Kovalev, D. & Fujii, M. (2008) Chapter 15, in *Silicon Nanophotonics: Basic Principles, Present Status and Perspectives* (ed. L. Khriachtchev), World Scientific, Singapore.

Kurokawa, Y.; Miyajima, S.; Yamada, A.& Konagai, M. (2006) Preparation of nanocrystalline silicon in amorphous silicon carbide matrix, *Jpn. J. Appl. Phys.* Vol. 45, pp. L1064-L1066.

Law, M.; Greene, L.; Johnson, J.; Saykally, R. & Yang P. (2005), Nanowire dye-sensitiezed solar cells, *Nat. Mater,* Vol. 4, pp. 455-459.

Lazarenkova, O. & Balandin, A. (2001), Miniband formation in a quantum dot crystal, *J. Appl. Phys.*, Vol. 89, p. 5509.

Lelièvre, J.-F.; De la Torre, J.; Kaminski, A.; Bremond, G.; Lemiti, M.; El Bouayadi, R.; Araujo, D.; Epicier, T.; Monna, R.; Pirot, M.; Ribeyron, P.-J. & Jaussaud, C. (2006), Correlation of optical and photoluminescence properties in amorphous SiNx:H thin films deposited by PECVD or UVCVD, *Thin Solid Films*, Vol. 511-512, pp. 103-107

Lenahan, P.M. & Conley, J.F. (1998) What can electron paramagnetic resonance tell us about the Si/SiO2 system? *J. Vac. Sci. Technol. B*, Vol. 16, pp. 2134–2153.

Lockwood, D. J.& Tsybeskov, L. (2004) Nanocrystalline Silicon Superlattices, in *Encyclopedia of Nanoscience and Nanotechnology* (ed. By H. S. Nalwa), Vol. 6, pp. 477-494.

Löper, P.; Hiller, D.; Künle, M.; Grandmann, R.; Rothfelder, M.; Janz, S.; Hermle, M.; Zacharias, M. & Glunz, S. W. (2010), Carrier confinement and transport in high band gap materials with embedded Si QDs, *Proceedings of 25th European Photovoltaic Solar Cell Energy Conference*, Spain, September 6-10, pp. 269-273

Ma, D.; Lee, C. S.; Au, F.; Tong, S. & Lee, S. T. (2003), Small-Diameter Silicon Nanowire Surfaces, *Science*, Vol. 299, pp. 1874-1877.

Marti, A. & Araujo, A. (1996) Limiting efficiencies for photovoltaic energy conversion in multigap systems, *Sol. Energy Mater. Sol. Cells*. Vol. 43, pp. 203-222.

Meillaud, F.; Shah, A.; Droz, C.; Vallat-Sauvain, E. & Miazza, C. (2006) Efficiency limits for single-junction and tandem solar cells, *Sol. Energy Mater. Sol. Cells*. Vol. 90, pp. 2952-2959.

Mercaldo, L.; Veneri, P.; Esposito, E. & Fameli, G. (2010), Micro-raman investigation of silicon nitride embedding Si nanostructures, *Proceedings of 25th European Photovoltaic Solar Cell Energy Conference*, Spain, September 6-10, pp. 223-228.

Mimura, A.; Fujii, M.; Hayashi, S.; & Yamamoto, K. (1999) Quenching of photoluminescence from Si nanocrystals caused by boron doping. *Solid State Commun.*, Vol. 109, pp.561–565.

Mimura, A.; Fujii, M.; Hayashi, S.; Kovalev, D. & Koch, F. (2000) Photoluminescence and free-electron absorption in heavily phosphorous – doped si nanocrystals, *Phys. Rev. B.*, Vol. 62, p. 12625-12627.

Mitin, V. (2010), Quantum mechanics for nanostructures, Cambridge University Press, p. 431.

Müller, J.; Finger, F.; Carius, R.; & Wagner, H. (1999) Electron spin resonance investigation of electronic states in hydrogenated microcrystalline silicon. *Phys. Rev. B*, Vol. 60, p.11666.

Nelson, J. (2003). *The physics of solar cells,* Imperial College, *UK*, pp.384.

Norris, D.J.;  Efros, A.L., & Erwin, S.C. (2008) Doped nanocrystals. *Science*, Vol. 319, pp. 1776–1779.

Nychyporuk, T.; Marty, O.; Rezgui, B.; Sibai, A.; Lemiti, M. & Bremond, G. (2008), Towards the 3rd generation photovoltaics: absorption properties of silicon nanocrystals embedded in silicon nitride matrix, *Proceedings of 23th European Photovoltaic Solar Cell Energy Conference*, Spain, September 1-5, pp. 491-494.

Nychyporuk, T.; Zakharko, Yu.; Lysenko, V. & Lemiti, M. (2009), Interconnected Si nanocrystals forming thin films with controlled bandgap values, *Appl. Phys. Lett.*, Vol. 95, pp. 083124.

Nychyporuk, T.; Zhou, Z.; Fave, A.; Lemiti, M. & Bastide, S. (2010) Electroless deposition of Ag nanoparticles on the surface of $SiN_x$:H dielectric layers, *Sol. Energy Mater. Sol. Cells*, Vol. 94, pp. 2314-2317.

Ögüt, S. & Chelikowsky, J. R. (1997), Quantum confinement and optical gaps in Si nanocrystals, *Phys. Rev. Lett.*, Vol. 79, pp. 1770-1773.

Ossicini, S.; Degoli, E.; Iori, F.; Luppi, E.; Magri, R.; Cantele, G.; Trani, F. & Ninno, D. (2005), Simultaneously B- and P- doped silicon nanoclusters: formation energies and electronic properties, *Appl. Phys. Lett.*, Vol. 87, p. 173120.

Ossicini, S.; Iori, F.; Degoli, E.; Luppi, E.; Magri, R.; Poli, R.; Cantele, G.; Trani, F. & Ninno, D. (2006) Understanding doping in silicon nanostructures. *IEEE J. Sel. Top. Quant.*, Vol. 12, pp. 1585–1591.

Park, N.; Choi, Ch.; Seong, T. & Park, S. (2000), Quantum confinement in amorphous Si quantum dots embedded in silicon nitride, *Phys. Rev. Lett.*, Vol. 86, p. 1355.

Peng, K.; Xu,; Y. Wu,; Y.; Yan, Y.; Lee, S. & Zhu, J. (2005), Aligned Single-Crystalline Si Nanowire Arrays for Photovoltaic Applications, *Small*, Vol. 1, pp. 1062-1067.

Perraud, S.; Poncet, S.; Noël, S.; Levis, M.; Faucherand, P.; Rouvière, E.; Thony, P.; Jaussaud, C. & Delsol, R. (2009), Full process for integrating silicon nanowire arrays into solar cells, *Sol. Energy Mater. Sol. Cells*, Vol. 93, pp. 1568-1571.

Pi, X.; Gresback, R.; Liptak, R. W. & Krtshagen, U. (2008), Doping efficiency, dopant location, and oxidation of Si nanocrystals, *Appl. Phys. Lett.*, Vol. 92, p. 123102.

Raisky, O.Y.; Wang, W.B; Alfano, R.R.; Reynolds, C.L.; Stampone, D.V. & Focht, M.W. (1999) Resonant enhancement of the photocurrent in multiple-quantum-well photovoltaic devices, *Appl. Phys. Lett.*, Vol. 74, pp. 129.

Ramayya, E.; Vasileska, D.; Goodnick, S. & Knezevic, I. (2006), Electron transport in Si nanowires, *Journal of Physics: Conference Series*, Vol. 38, pp. 126-129.

Reeves, G. K. & Harrison, H. B. (1982) Contact resistance of polysilicon silicon interconnections, Electronic Letters, Vol. 18, pp. 1083-1085.

Rout, Ch. & Rao, C. N. R. (2008), Electroluminescence and rectifying properties of heterojunction LEDs based on ZnO nanorods, *Nanotechnology,* Vol. 19, pp.285203

Scardera, G.; Puzzer, T.; Perez-Wurfl, I. & Conibeer, G. (2008) The effects of annealing temperature on the photoluminescence from silicon nitride multilayer structures. *J. Crystal Growth*, Vol. 310, pp. 3680–3684.

Shockley, W. & Queisser, H. J. (1961), Detailed balance limit of efficiency of p-n junction solar cells, *J. Appl. Phys.*, Vol. 32, p. 510.

Sinke, W.C.; del Canizo, C. & del Coso G. (2008). 1 € per Watt-peak advanced crystalline silicon modules: the Crystal Clear integrated project, *Proceedings of 25th European Photovoltaic Solar Cell Energy Conference*, Spain, pp.3700-3705.

So, Y. H.; Perez-Wurfl, I.; Shi, L;; Huang, S;; Conibeer, G. & Green, M. (2010), Silicon nitride as alternative matrix for all-Si tandem solar cell, *Proceedings of 25th European Photovoltaic Solar Cell Energy Conference*, Spain, September 6-10, pp. 690-692.

Song, D.; Cho, Eu-C.; Conibeer, G.; Huang, Yi.; Flynn, Ch. & Green, M. A. (2008), Structural characharization of annealed $Si_{1-x}C_x$/SiC multilayers targeting formation of Si nanocrystals in a SiC matrix, *J. Appl. Phys*, Vol. 103, p. 083544

Song, D.; Cho, E.-C.; Conibeer, G. & Green M. (2009) Solar cells based on Si-NCs embedded in a SiC matrix, Technical Digest of the 18th International Photovoltaic Science and Engineering Conference, India, 19-23 January.

Stegemann, B.; Lussky, T.; Schöpke, A.; Cermak, J.; Rezek, B.; Kocka, J. & Schmidt, M. (2010), Formation kinetics and electrical transport of silicon quantum dot layers, *Proceedings of 25th European Photovoltaic Solar Cell Energy Conference*, Spain, September 6-10, pp. 260-264.

Stegner, A.R.; Pereira, R.N.; Klein, K.; Lechner, R.; Dietmueller, R.; Brandt, M.S.; Stutzmann, M. & Wiggers, H. (2008) Electronic transport in phosphorus-doped silicon nanocrystal networks. *Phys. Rev. Lett.*, Vol. 1, p. 026803.

Surana, K.; Lebrun, J. M.; Lepage, H.; Doisneau, B.; Vellet, D.; Le Carval, G.; Thony, P. & Mur, P. (2010), Enhanced conduction in Si QD superlattice in $SiO_2$ matrix, *Proceedings of 25th European Photovoltaic Solar Cell Energy Conference*, Spain, September 6-10, pp. 654-656.

Tae-Wook Kim, Chang-Hee Cho, Baek-Hyun Kim, and Seong-Ju Park, Quantum confinement effect in crystalline silicon quantum dots in silicon nitride grown using SiH4 and NH3, *Appl. Phys. Lett.*, Vol. 88, pp. 123102. Idem

Takeoka, S.; Fujii, M.; & Hayashi, S. (2000) Size-dependent photoluminescence from surface-oxidized Si nanocrystals in a weak confinement regime. *Phys. Rev. B*, Vol. 62, pp. 16820–16825.

Tchebotareva, A.L.; Dooda, M.J.A.d.; Biteenb, J.S.; Atwaterb, H.A. & Polman, A. (2005) Quenching of Si nanocrystal photoluminescence by doping with gold or phosphorous. *J. Lumin.*, Vol. 114, pp. 137–144.

Tian, B.; Zheng, X.; Kempa, T.; Fang, Y.; Yu, N.; Yu, G.; Huang, J. & Lieber, C. M. (2007), Coaxial silicon nanowires as solar cells and nanoelectronic power sources, *Nature*, Vol. 449, pp. 885-890.

Tsakalakos, L.; Balsh, J.; Fronheiser, J.; Korevaar, B.; Sulima, O.; Rand, J. (2007), Silicon nanowire solar cells, *Appl. Phys. Lett.* Vol. 91, pp. 233117

Tsakalakos, L.; Balsh, J.; Fronheiser, J.; Shih, M.; LeBoeuf, S.; Pietrzykowski, M.; Codella, P.; Korevaar, B.; Sulima, O.; Rand, J.; Davuluru, A. & Rapol, U. (2007a), Strong broadband optical absorption in silicon nanowire films, *Journal of Nanophotonics*, Vol. 1, p. 013552

Tsu, R. & Babic, D. (1994) Doping of a quantum dot. *Appl. Phys. Lett.*, Vol. 64, pp. 1806–1808.

Uchiyama, H.; Nemoto, Y.; Dhamrin, M. & Kamisako, K. (2010),fabrication and evaluation of silicon nanowire solar cells, *Proceedings of 25th European Photovoltaic Solar Cell Energy Conference*, Spain, September 6-10, pp. 700-702.

Vo, T.; Williamson, A. & Galli, G. (2006), First principles simulations of the structural and electronic properties of silicon nanowires, *Phys. Rev. B.*, Vol. 74, pp. 045116.

Voz, C.; Peiró, D.; Bertomeu, J.; Soler, D.; Fonrodona, M. & Andreu, J. (2000), Optimisation of doped microcrystalline silicon films deposited at very low temperatures by hot-wire CVD, *Materials Science and Engineering B*, Vol. 69-70, pp. 278-283.

Wacker, A. (2002), Semiconductor superlattices: a model system for nonlinear transport, *Physics Reports*, Vol. 357, pp. 1-111.

Wang, X.; Pey, K. L.; Yip, C. H.; Fitzgerald, E. A. &Antoniadis, D. A. (2010), Vertically arrayed Si nanowire/nanorod-based core-shell p-n junction solar cells, *J. Appl. Phys.*, Vol. 108, pp. 124303.

Wang, X.; Pittet, P.; Gentil, P.; Noë, P. & Lévy-Clément, C. (2010a), Silicon nanowire arrays using colloidal crystal lithography and metal-assisted etching, *Proceedings of 25th European Photovoltaic Solar Cell Energy Conference*, Spain, September 6-10, pp. 191-194.

Wu, Y.; Cui, Y.; Huynh, L.; Barrelet, C.; Bell, D. & Lieber, C. (2004), Controlled growth and structures of molecular-scale silicon nanowires,.Vol. 4, pp. 433-436.

Yan, J.; Yang, L. & Chou, M. (2007), Size and orientation dependence in the electronic properties of silicon nanowires, *Phys. Rev. B.*, Vol. 76, pp. 115319.

Yang, M.; Cho, K.; Jhe, J.; Seo, S.; Shin, J.; Kim, K. & Moon, D. (2004) Effect of nitride passivation on the visible photoluminescence from Si-nanocrystals, *Appl. Phys. Lett.*, Vol. 85, pp. 3408.

Yao, D.; Zhang, G. & Li, B. (2008), A Universal Expression of Band Gap for Silicon Nanowires of Different Cross-Section Geometries, *Nano Lett.* Vol. 8, pp. 4557-4561.

Zacharias, M.; Heitmann, J.; Scholz, R.; Kahler, U.; Schmidt, M & Bläsing, J. (2002), Size controlled highly luminescent nanocrystals: A SiO/SiO2 superlattice approach, *Appl. Phys. Lett.*, Vol. 80, p. 661.

Zhang, R. Q.; Lifshitz, Y.; Ma, D. D. D.; Zhao, Y. L.; Frauenheim, Th.; Lee, S. T. & Tong S. Y., (2005) Structures and energetics of hydrogen-terminated silicon nanowire surfaces, *J Chem Phys*, Vol. 123, pp. 144703.

Zheng, G.; Lu, W.; Jin, S. & Lieber, C.M. (2004), Synthesis and Fabrication of High-Performance n-Type Silicon Nanowire Transistors, *Adv. Mater*. Vol. 16, pp. 1890-1893.

Zhong, Z.; Yang C. & Lieber, C. (2007) Chapter 5, in *Nanosilicon* (ed. By V. Kumar), Elsevier.

# Optical Insights into Enhancement of Solar Cell Performance Based on Porous Silicon Surfaces

Asmiet Ramizy[1,3], Y. Al-Douri[2], Khalid Omar[1] and Z. Hassan[1]
*[1]Nano-Optoelectronics Research and Technology Laboratory,*
*School of Physics, Universiti Sains Malaysia, Penang,*
*[2]Institute of Nano Electronic Engineering, University Malaysia Perlis*
*[3]University of Anbar-collage of sciences-physics department,*
*[1,2]Malaysia*
*[3]Iraq*

## 1. Introduction

The amount of light reflection from the surface is the main obstacle in efficient solar cell performance because reflection is related to the refractive index of the material. For instance, the silicon (Si) refractive index is 3.5, (which can rise by up to 35%), which prevents an electron-hole pair from being generated and could reduce the efficiency of photovoltaic converters. Antireflection coatings ARC are able to reduce surface reflection, increase conversion efficiency, extend the life of converters, and improve the electrophysical and characterization of photovoltaic converters [1].

Porous Si (PS) is attractive in solar cell applications because of its efficient ARC and other properties such as band gap broadening, wide absorption spectrum, and optical transmission range (700–1000 nm). Furthermore, PS can also be used for surface passivation and texturization [2–6]. The potential advantages of PS as an ARC for solar cells include surface passivation and removal of the dead-layer diffused region. Moreover, PS is able to convert higher energy solar radiation into spectrum light, which is absorbed more efficiently into bulk Si [7].

The vibrations, electronic, and optical properties of PS have been studied using various experimental techniques. Of these, the electrochemical etching process is a promising technique for fabricating PS [8–11]. According to the quantum confinement model, a heterojunction can be formed between the Si substrate and porous layers because the latter has a wider band gap (1.8–2.2 eV) compared with crystalline Si (c-Si) [12].

Recently, Ben Rabha and Bessais [13] used chemical vapor etching to perform the front PS layer and buried metallic contacts of multicrystalline silicon solar cells to reduce reflectivity to 8% in the 450–950 nm wavelength range, yielding a simple and low-cost technology with 12% conversion efficiency. Yae et al. [14] deposited fine platinum (Pt) particles on multicrystalline n-Si wafers by electroless displacement reaction in a hexachloroplatinic acid solution containing HF. The reflectance of the wafers was reduced from 30% to 6% by the formation of porous layer. Brendel [15] performed electrochemical etching of PS layer into the substrate based on homoepitaxial growth of monocrystalline Si films, yielding a module efficiency of 10%.

The present work aims to investigate the effect of PS on performance of Si solar cells. Optical properties such as refractive index and optical dielectric constant are investigated.

Enhancing solar cell efficiency can be realized by manipulating back reflected mirrors, and the results are promising for solar cell manufacturing because of the simplicity, lower-cost technology, and suitability for mass production of the method.

## 2. Experimental procedure

### 2.1 PS Structure formation

An n-type Si wafer with a dimension of 1 cm x 1 cm x 283 µm, (111) orientation, resistivity of 0.75 Ω.cm, and doping concentration of $1.8 \times 1017 \times$ cm$^{-3}$ was etched through an electrochemical process to produce the porous structure. The wafer was placed in an electrolyte solution [hydrofluoric acid (HF): Ethanol, 1:4] with a current density of 60 mA/cm$^2$ at an etching time of 30 min. To produce solar cells on both sides of the PS, the PS wafer was fabricated by electrochemical etching at the current density of 60 mA/cm$^2$ for 15 min on each side.

Before the etching process, the Si substrate was cleaned using the Radio Corporation of America (RCA) method to remove the oxide layer, and then immersed in HF acid to remove the native oxide. The electrochemical cell is made of Teflon and has a circular aperture with a radius of 0.4 cm, with the silicon wafer sealed below. The cell consists of a two-electrode system with the Si wafer as the anode and platinum as the cathode, as shown in Fig. 1. The process was carried out at room temperature. After etching, all samples were rinsed with ethanol and air-dried. Surface morphology and structural properties of the samples under treatment were characterized using scanning electron microscopy (SEM). The PS optical reflectance was obtained using an optical reflectometer (Filmetrics F20) with an integrating sphere. Fourier transform infrared spectroscopy (FTIR) of the PS samples was performed, and photoluminescence (PL) spectroscopy was performed at room temperature using He-Cd laser (λ=325 nm).
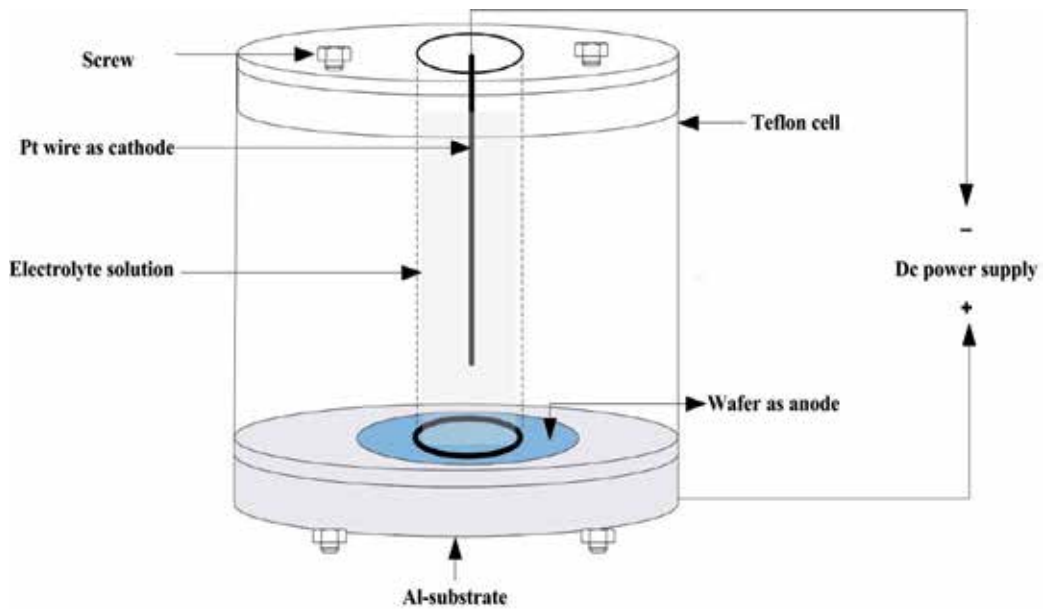


Fig. 1. Schematic of the electrochemical etching setup
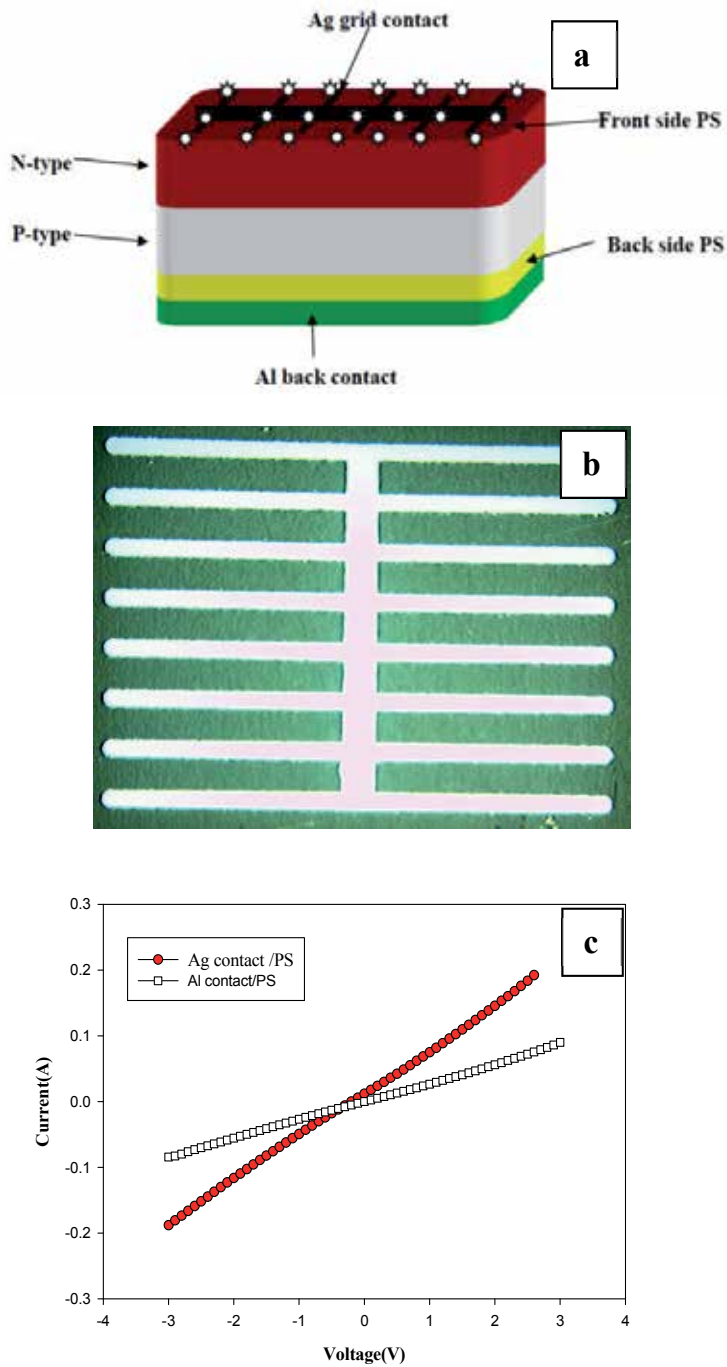
Fig. 2. Solar cells setup (a) p-n junction layers, (b) metal mask, and (c) contact I-V
characterization

## 2.2 Solar cell fabrication

After the (RCA) cleaning and oxidation, the silicon wafer underwent spin-coating. A liquid containing photoresistant material was placed at the center of the wafer. The spinning process was conducted at room temperature at the speed of 300 rpm for 20 s. After spin-coating, the wafer was placed back into the furnace for 20 min at 200 °C to remove moisture. The mask was designed by the photoplotter technique placed directly above the sample and exposed to UV-light for 25 s to form a patterned coating on the surface. Doping diffusion was carried out using a tube furnace at the temperature of 1100 °C for 60 min using $N_2$ flow gas. The top surface area of the wafer was doped with boron to be P-type. Prior to the contact evaporating process, the oxidation layer was removed using an etching solution of $NH_4F:H_2O$, and then mixed with HF with a mole ratio of 1:7. Aluminum evaporation was used for the back metal contact, whereas silver was used for front metallization. Figure 1 shows the setup of the solar cells. Contact annealing was performed at 400 °C for 20 min to pledge ohmic contact (see Fig. 1), as well as to improve the contact properties. A back reflected mirror with reflectivity >89% was used to enhance solar cell efficiency. The structure of the PS solar cells consists of a metal mask contact of grid pattern with a finger width of 300 µm and finger spacing of 600 µm.

The fabricated device was analyzed using current-voltage (I-V) measurement, with the lens placed under solar simulator illumination. A solar cell using unetched c-Si was fabricated under the same conditions for comparison.
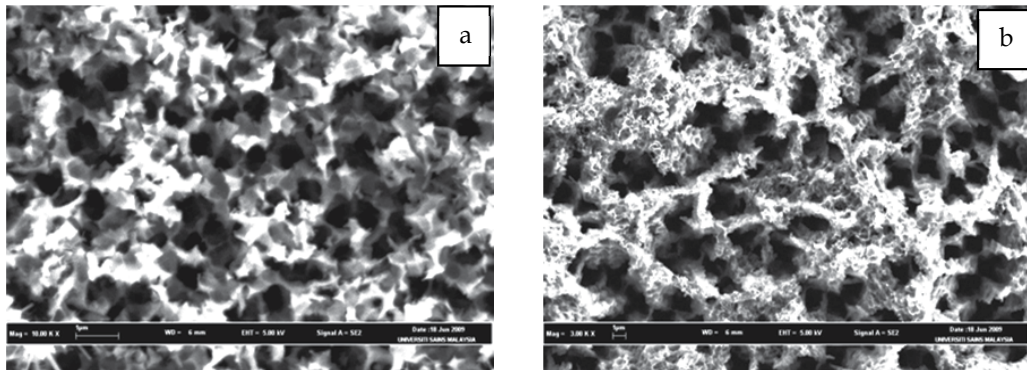


Fig. 3. SEM images of PS formed on (a) N (100), (b) P (100)
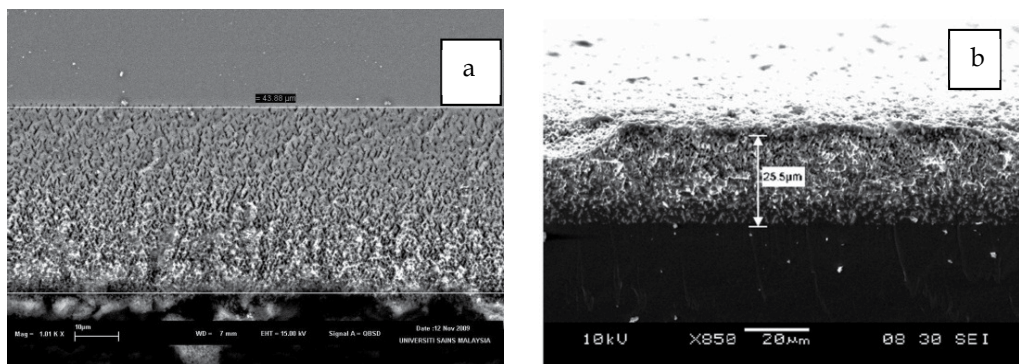


Fig. 4. Cross-sectional SEM images of PS on (a) both sides of the c-Si wafer and (b) on the 47 polished front

## 3. Effect of doping-type of porous on silicon solar cell performance

The SEM images in Figs. 3 (a) and (b) reveal the grains of the surface texturing with similar grain geometry, which is caused by the isotropic character of the HF/ethanol etching and the optimal conditions for current density and etching time. Moreover, similar morphology is apparent in the SEM images of all etched surfaces. The depth of porosity increased with the N-type silicon wafers compared with P-type, as shown in Figs. 4 (a) and (b), which may be due the abundance of electron-hole pair charge carriers that lead to extra chemical interaction between the electrolyte solution and the surface of the silicon wafer, resulting in the formation of PS.

The surface reflections of PS N (100) show a reduction of incoming light reflection and an increase in capturing the light of the wide wavelength range compared with PS P (100) reflection, as illustrated in Fig. 5. This caused the N (100) surface formed to be preferentially dissolved because of the preferred pore tips. However, the P (100) surface is most effective for preferred pore walls during the etching processing.

Figure 6 reveals the Raman spectra of bulk silicon, which show a sharp line in the spectra with FWHM of 3.5 cm$^{-1}$ shifted by 522 cm$^{-1}$ relative to the laser line incident. However, the PS spectra became broader relative to the 517 cm-1 sharp with FWHM of 8.2 cm$^{-1}$ in PS P (100) and shifted to 510 cm$^{-1}$ with (FWHM) of 17.3 cm$^{-1}$ in PS N (100), which is attributed to the quantum confinement effect on electronic wave function of silicon nanocrystals [16]

Figure 7 shows the PL spectrum of PS P (100) at 698.9 nm (1.77 eV) with FWHM of about 140 nm. In PS N (100), PL at 670.35 nm (1.82 eV) with FWHM of 123 nm is evident. The PL output intensity in the N-type becomes stronger because of an increase in the number of emitted photons on the porous surface. The peak shift increase with N-type PS compared with P-type wafers, which can be attributed to the abundance of charge carriers, enhances the spontaneous etching rate of silicon. The particles are confined into a lower dimension, leading to higher efficiency. Without these charge carriers, the etching process substantially slows down.
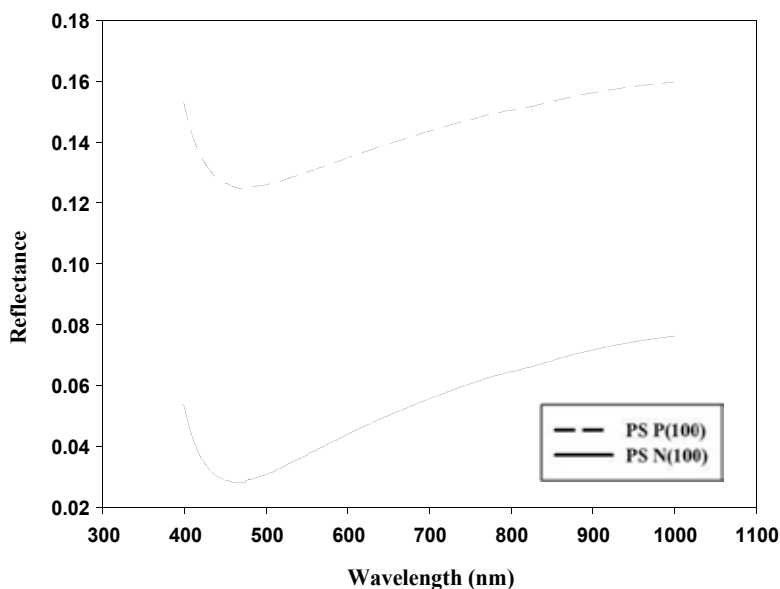


Fig. 5. Reflectance spectra for PS N (100) and P (100)
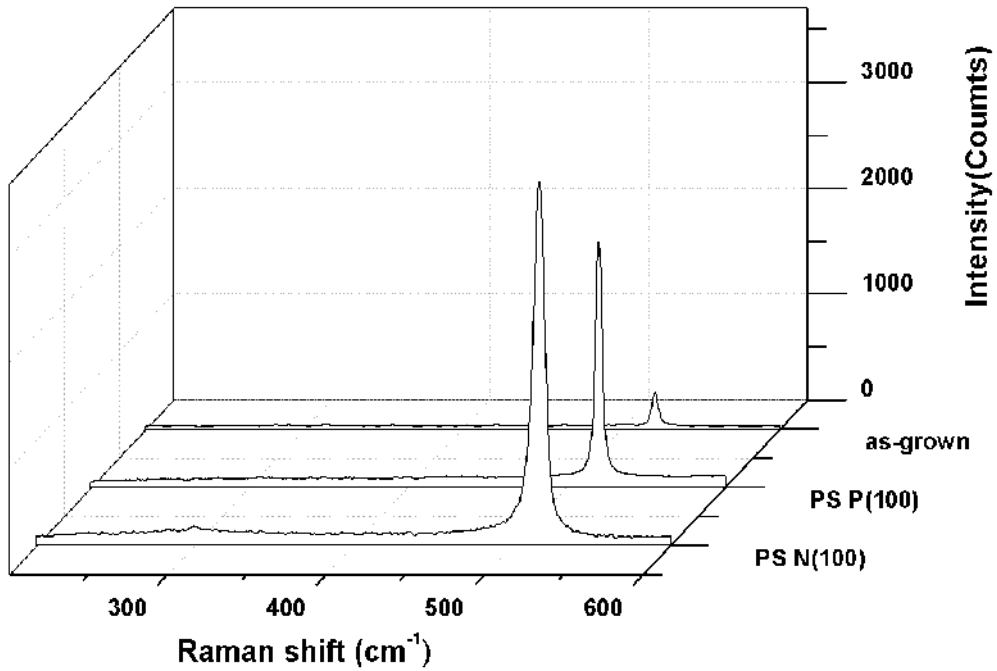
Fig. 6. Raman spectra of PS prepared by electrochemical etching
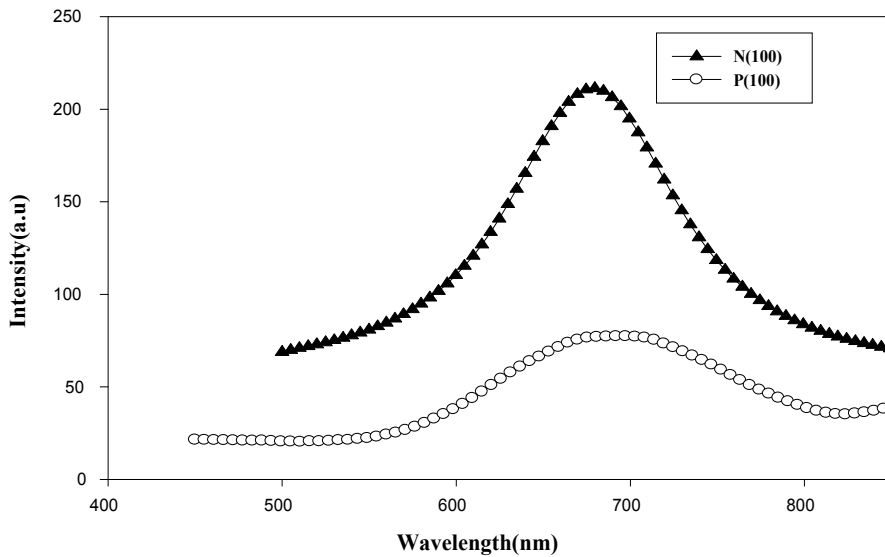


Fig. 7. PL spectra of PS prepared by electrochemical etching

The experimental data in Fig. 8 and Table 1 show that the solar cell with PS N (100) increases the short-circuit current to 12.2, open current voltage to 0.36, and conversation efficiency to 10.85 in comparison to the solar cell fabricated with PS P (100).
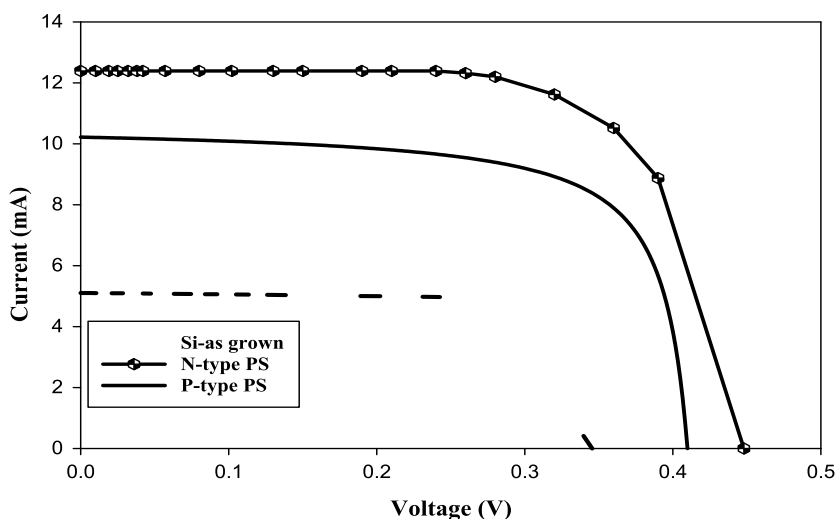
Fig. 8. Current-voltage characteristics of PS N (100) and P (100) solar cells

| Samples | Vm(V) | Im(mA) | Voc(V) | Isc (mA) | FF | Efficiency($\eta$) |
|---------|-------|--------|--------|----------|-----|---------------------|
| Si as- grown | 0.26 | 5.09 | 0.34 | 5.1 | 0.77 | 3.34 % |
| P-type PS | 0.33 | 10.03 | 0.41 | 10.2 | 0.81 | 8.4 % |
| N-type PS | 0.36 | 12.1 | 0.42 | 12.2 | 0.85 | 10.85 % |

Table 1. Fill factor (FF) and efficiency $(\eta)$ of PS N (100) and P (100)

## 4. New optical features to enhance solar cell performance based on porous silicon surfaces

The efficiency of photovoltaic energy conversion must be enhanced to reduce the cost of solar cell modules for energy generation. In this process, photons from solar radiation fall on a solar cell that generate electron and hole pairs, which are then collected at the contact points. However, a drawback of solar photovoltaic energy conversion is that most of the semiconducting materials used are sensitive only to a part of the solar radiation spectrum. Figure 9a shows cross-sectional SEM images of chemically treated samples. These images show that the thickness is uniform throughout the obtained porous layer, indicating that the etching process forms a uniform porous density layer on the surface. The SEM images in Figs. 9 (b) and (c) illustrate the treated surface with similar grain geometry because of the isotropic character of HF/ethanol etching and the optimal conditions of the current density and etching time. The images show that the entire surface of the sample is etched, and that most of the pores are spherical. In addition to the short-branched pores, the porous surface formed on the front polished side has discrete pores. In contrast, the PS surface formed on the unpolished backside is shaped in small pores, which could be attributed to an increase in surface roughness for the unpolished backside that is proportional to the etching parameter.
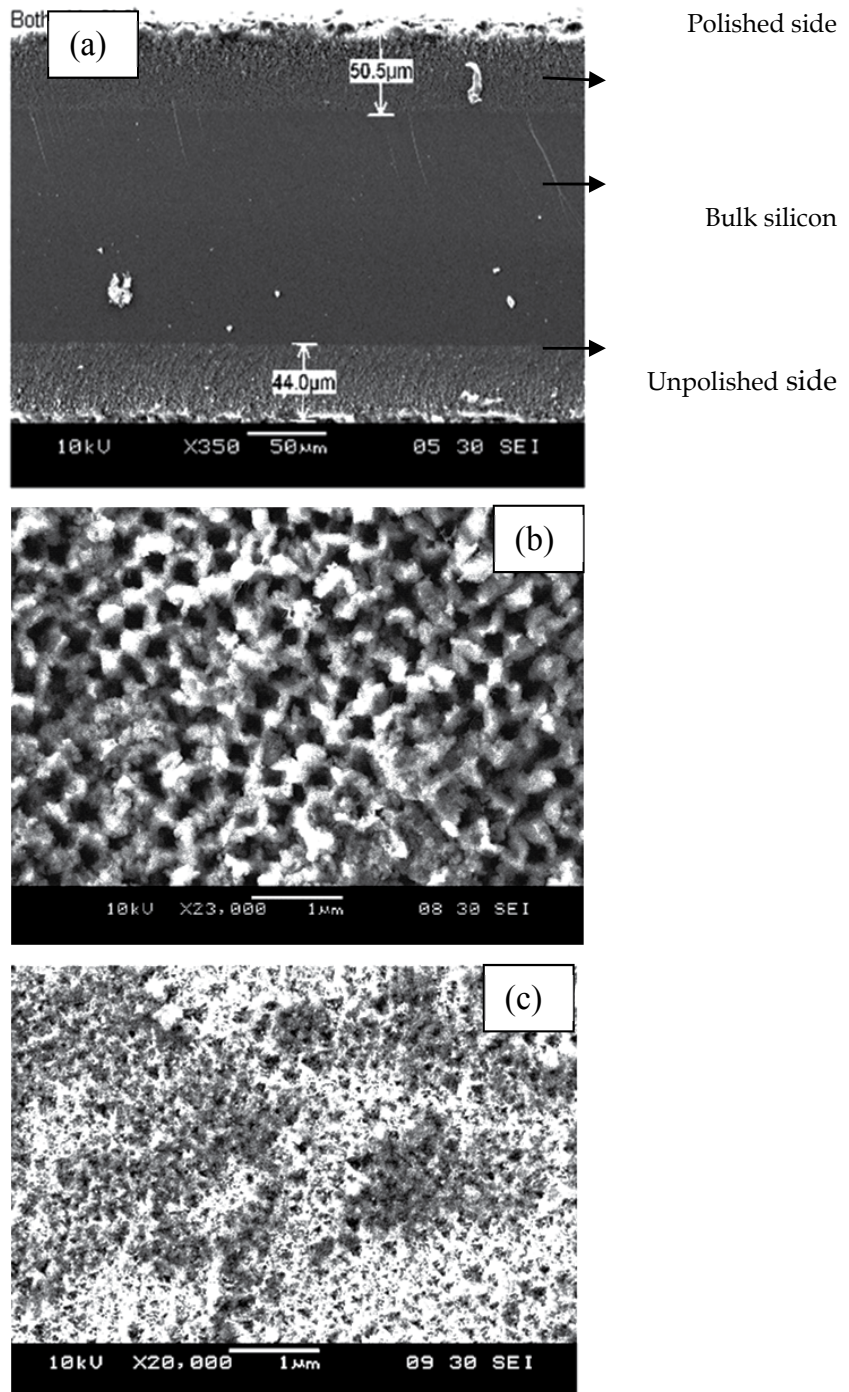
Fig. 9. Cross-sectional SEM images of PS on (a) both sides of the c-Si wafer, (b) on the polished front side c-Si wafer, and (c) on the unpolished backside c-Si wafer

Figure 10 shows the three-dimensional topographic images of the PS etched surfaces with the pyramidal shape distributed over the entire surface. The pyramidal shape indicates that the increase in surface roughness is because of the effect of the etching parameters on surface characterization. The high degree of roughness of the PS surface implies the possibility of using the porous layer as an ARC because the surface texture reduces light reflection. The scattering in PS is possibly because of the roughness in relation to the thickness of the porous layer [17], whereas the attenuation of the reflectivity is because of scattering and transmission at the porous and bulk interfaces [17, 18]. This parameter is important in enhancing the photoconversion process for solar cells, which confirms that PS can be utilized as an ARC. Meanwhile, the reflection measurement was taken using optical reflectometry.
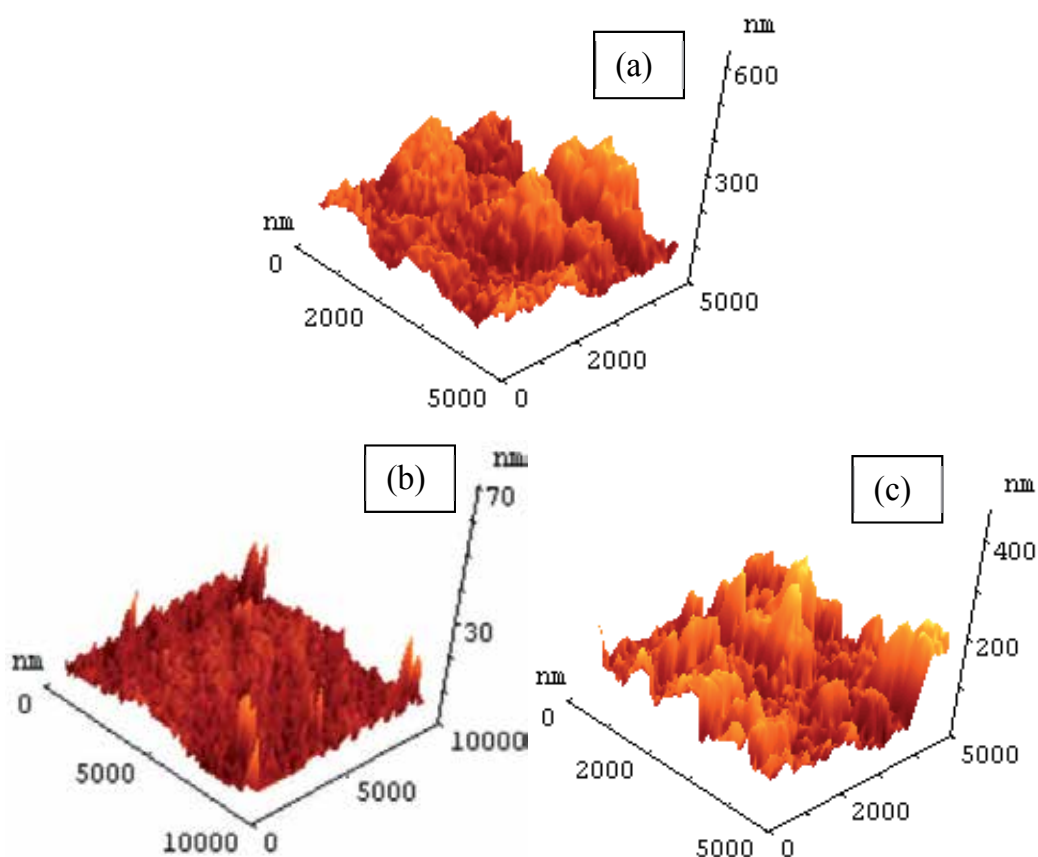


Fig. 10. AFM images of PS (a) as-grown, (b) polished front side, and (c) unpolished back side

The results in Fig. 11 demonstrate that the PS that formed on both sides has lower reflectivity value compared with results of other studies [13–15]. These results were confirmed by the absorption spectrum, as shown in Fig. 12.
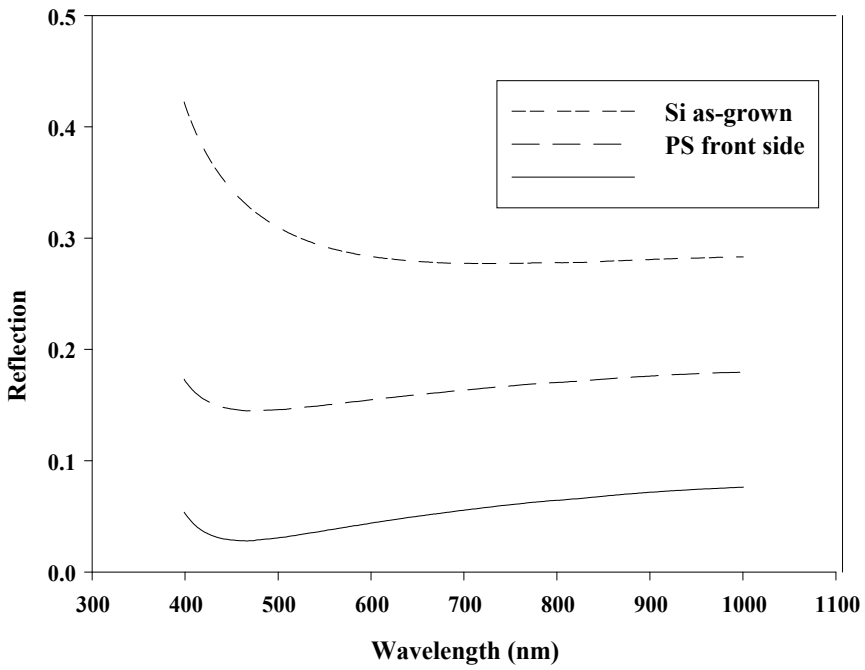
Fig. 11. The reflectance spectra of Si (as grown) and PS of both sides
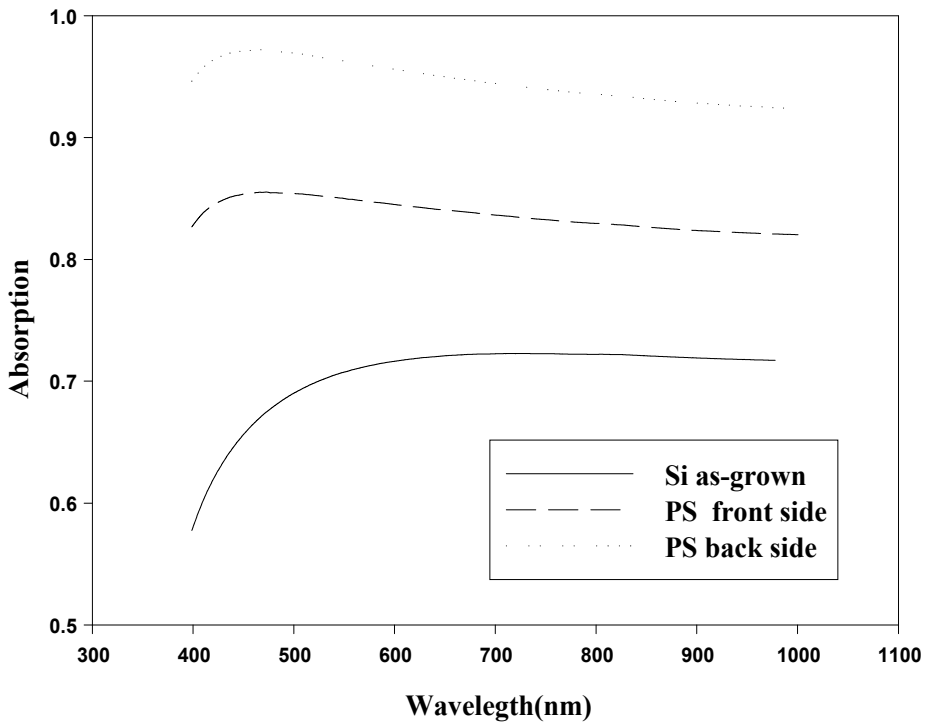


Fig. 12. The reflectance spectra of Si (as grown) and PS of both sides.

Figures 13 and 14 show the FTIR spectra of the silicon as grown and PS as a function of reflectivity and absorptivity, respectively. The results show an agreement with the results demonstrated in Figs. 4 and 5, indicating that our PS sample has high absorption and low reflection spectra compared with the as-grown sample. This may be attributed to the increase of porosity that leads to an increase in PS density over the surface of the sample.
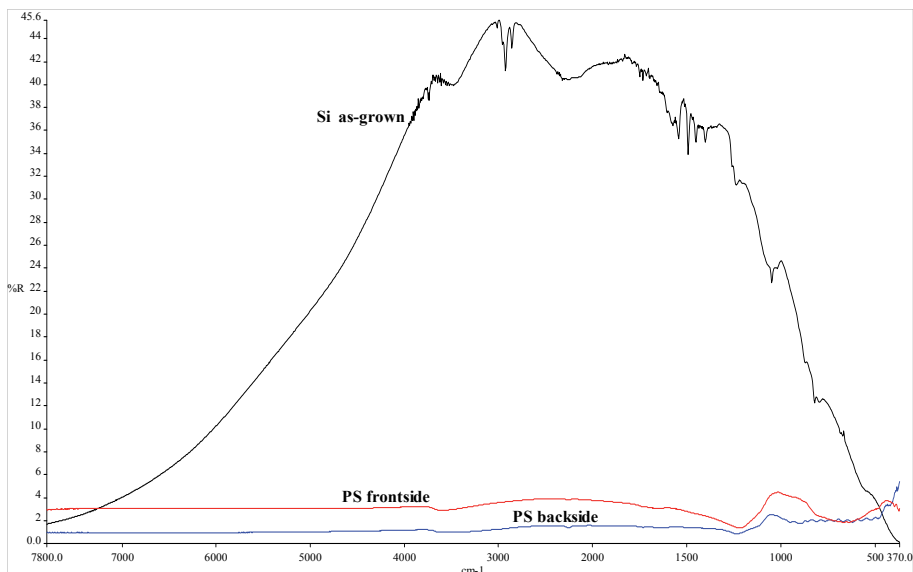


Fig. 13. FTIR reflection spectra of Si (as grown) and PS of both sides
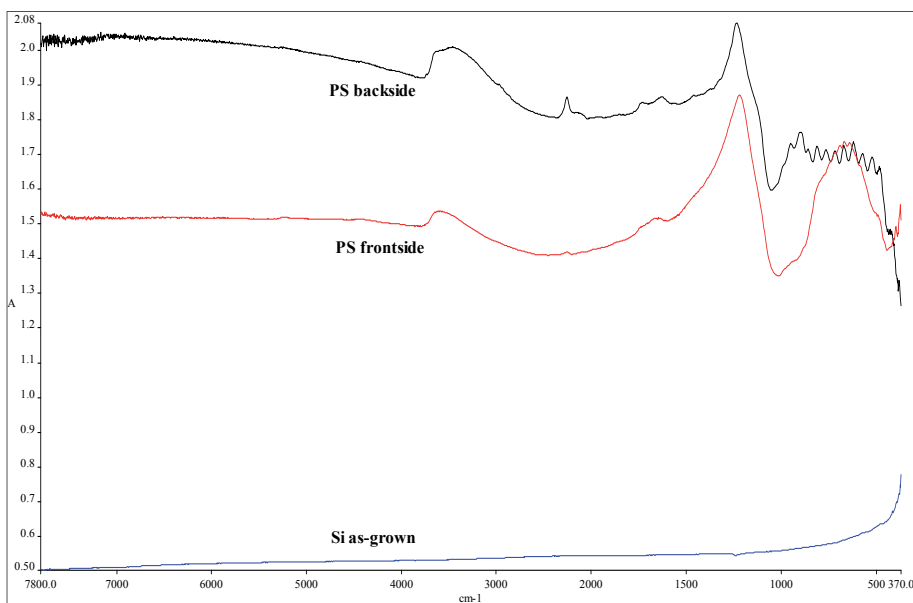


Fig. 14. FTIR absorption spectra of Si (as grown) and PS of both sides

Figure 15 illustrates the PL spectrum of the PS formed on the unpolished side, revealing a peak at 681.3 nm (1.82 eV) with FWHM of 330 mV. For the PS formed on the front polished side, the peak located at 666.9 nm (1.86 eV) with a FWHM of approximately 180 mV is obtained. The PS formed on the front polished side has a blue shift luminescence, indicating that the particles are confined into the lower dimension. The energy gaps of the PS increased to 1.82 and 1.86, respectively, and the broadening of the energy gap occurs with a decrease in the crystallite size.
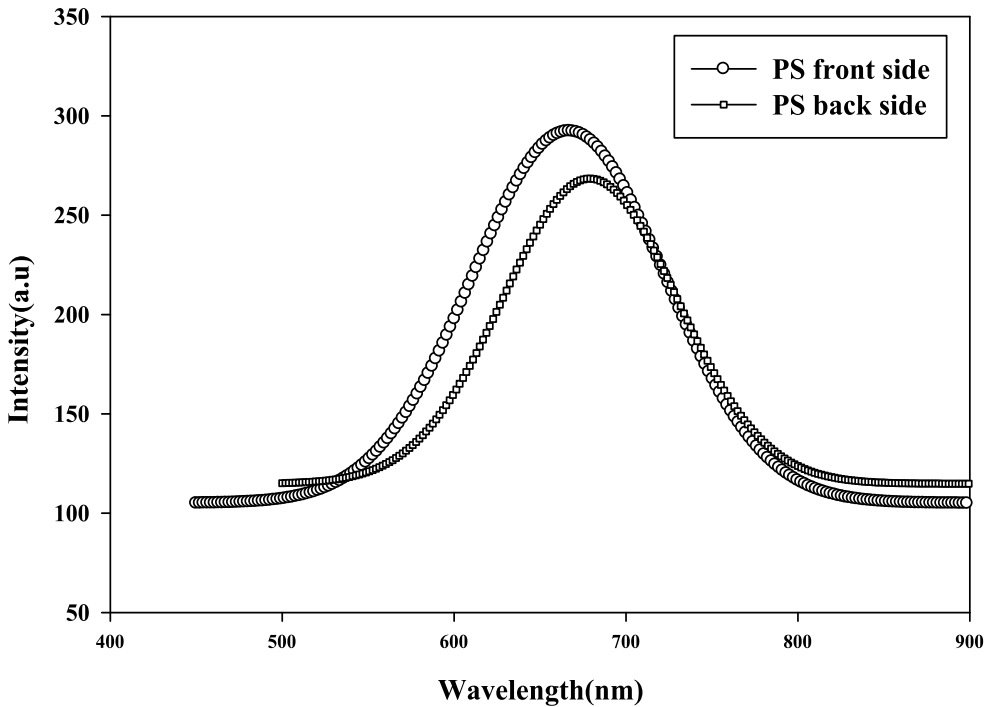


Fig. 15. PL spectra of PS on both sides of the c-Si wafer

The efficiency of the solar cells fabricated with PS formed on both sides of the wafer increased compared with one side of the PS and bulk Si solar cells, respectively, as shown in Fig. 16. This can be attributed to an increase in the open circuit voltage without losing the short circuit current of the solar cells, as shown in Table 2. The porous surface texturing properties are able to enhance and increase the conversion efficiency of Si solar cells, and the resulting efficiency from this procedure is more promising compared with the other solar cells fabricated under similar conditions [19].

## 5. Optical properties

The results in Figs. 4 and 6 are used to calculate the refractive index and optical dielectric constant of Si and PS using the following equation [20]:

$$n = \frac{1 + R^{1/2}}{1 - R^{1/2}} \tag{1}$$
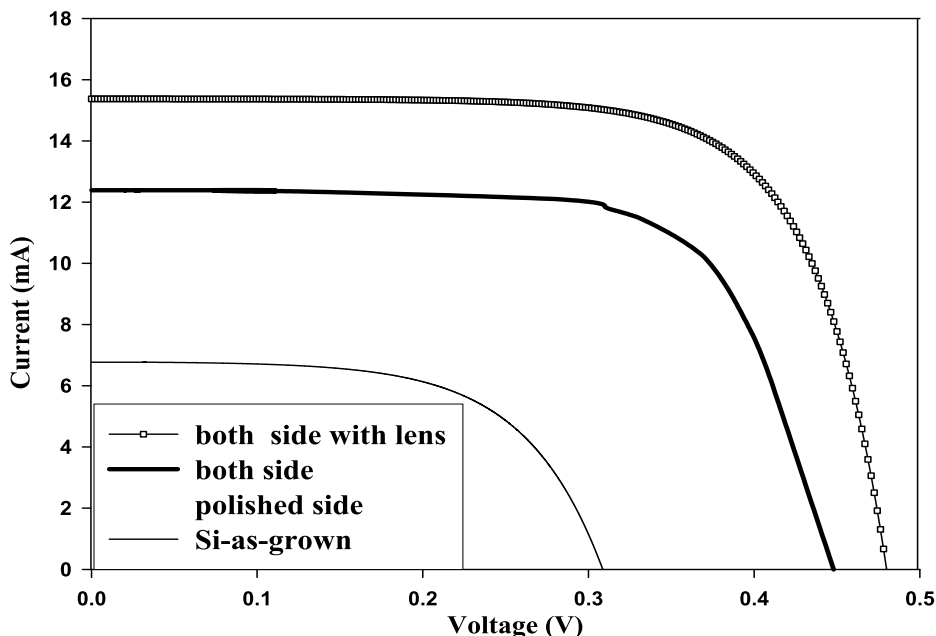
Fig. 16. Current-voltage (IV) characteristics of Si (as grown) and Si of different sides

| Samples | $R_s$ (Ω) | $R_{sh}$ (kΩ) | $V_m$ (V) | $I_m$ (mA) | $V_{oc}$ (V) | $I_{sc}$ (mA) | $FF$ (%) | Efficiency ($\eta$) (%) |
|---|---|---|---|---|---|---|---|---|
| Si as-grown | 70.4 | 2.98 | 0.26 | 6.71 | 0.31 | 6.72 | 83 | 4.34 |
| PS formed on the unpolished side | 7.14 | 149.8 | 0.41 | 7.24 | 0.43 | 8.83 | 78 | 7.38 |
| PS formed on both sides | 7.9 | 4.86 | 0.44 | 11.65 | 0.45 | 12.37 | 84 | 12.75 |
| PS on both sides with lens | 2.81 | 18.77 | 0.41 | 15.12 | 0.49 | 15.5 | 88 | 15.4 |

Table 2. Investigated series resistance Rs, shunt resistance Rsh, maximum voltage Vm, maximum current Im, open-circuit voltage Voc, short-circuit current Isc, FF, and efficiency (η) of Si and PS

where R is reflectivity. The refractive index $n$ is an important physical parameter related to microscopic atomic interactions. Theoretically, the two different approaches in viewing this subject are the refractive index related to density and the local polarizability of these entities [21].

In contrast, the crystalline structure represented by a delocalized picture, $n$, is closely related to the energy band structure of the material, complicated quantum mechanical analysis requirements, and the obtained results. Many attempts have been made to relate

the refractive index and the energy gap Eg through simple relationships [22–27]. However, these relationships of $n$ are independent of temperature and incident photon energy. Here, the various relationships between $n$ and $E_g$ are reviewed. Ravindra et al. [27] suggested different relationships between the band gap and the high frequency refractive index and presented a linear form of $n$ as a function of $E_g$ :

$$n = \alpha + \beta E_g ,$$

(2)

where α = 4.048 and β = −0.62 eV−1.

To be inspired by the simple physics of light refraction and dispersion, Herve and Vandamme [28] proposed the empirical relation as

$$n = \sqrt{1 + \left( \frac{A}{E_g + B} \right)^2} ,$$

(3)

where A = 13.6 eV and B = 3.4 eV. Ghosh et al. [29] took a different approach to the problem by considering the band structure and quantum-dielectric formulations of Penn [30] and Van Vechten [31]. Introducing A as the contribution from the valence electrons and B as a constant additive to the lowest band gap Eg, the expression for the high-frequency refractive index is written as

$$n^2 - 1 = \frac{A}{\left( E_g + B \right)^2} ,$$

(4)

where A = 25Eg + 212, B = 0.21Eg + 4.25, and (Eg+B) refers to an appropriate average energy gap of the material. Thus, these three models of variation $n$ with energy gap have been calculated. The calculated refractive indices of the end-point compounds are shown in Table 3, with the optical dielectric constant $\varepsilon_\infty$ calculated using $\varepsilon_\infty = n^2$ [32], which is dependent on the refractive index. In Table 1, the calculated values of $\varepsilon_\infty$ using the three models are also investigated. Increasing the porosity percentage from 60% (front side) to 80% (back side) uses weight measurements [33] that lead to a decreasing refractive index. As with Ghosh et al. [29], this is more appropriate for studying porous silicon solar cell optical properties, which showed lower reflectivity and more absorption as compared to other models.

| Samples | $n$ | $\varepsilon_\infty$ |
|---|---|---|
| Si | 3.35[a]  2.91[b]  2.89[c]  3.46[d] 3.46[e] | 11.22[a]  8.46[b]  8.35[c] 11.97[e] |
| PS formed on the unpolished side | 3.17[a]   2.79[b]   2.77[c] 1.8[e] | 10.04[a]   7.78[b]   7.67[c] 3.24[e] |
| PS formed on the front polished side | 2.94[a]   2.68[b]   2.66[c] 2.38[e] | 8.64[a]   7.18[b]   7.07[c] 5.66[e] |

[a]Ref. [27], [b]Ref. [28], [c]Ref. [29], [d]Ref. [20] exp. eusing Equation (1)

Table 3. Calculated refractive indices for Si and PS using Ravindra et al. [27], Herve and Vandamme [28], and Ghosh et al. [29] models compared with others that corresponds to the optical dielectric constant

## 6. Ionicity character

The systematic theoretical studies of the electronic structures, optical properties, and charge distributions have already been reported in the literature [34,35]. However, detailed calculations on covalent and ionic bonds have not reached the same degree of a priori completeness as what can be attained in the case of metallic properties. The difficulty in defining the ionicity lies in transforming a qualitative or verbal concept into a quantitative, mathematical formula. Several empirical approaches have been developed [36] in yielding analytic results that can be used for exploring the trends in materials properties. In many applications, these empirical approaches do not give highly accurate results for each specific material; however, they still can be very useful. The stimulating assumption of Phillips [36] concerning the relationship of the macroscopic (dielectric constant, structure) and the microscopic (band gap, covalent, and atomic charge densities) characteristics of a covalent crystal is based essentially on the isotropic model of a covalent semiconductor, whereas Christensen et al. [37] performed self-consistent calculations and used model potentials derived from a realistic GaAs potential where additional external potentials were added to the anion and cation sites. However, in general, the ionicities found by Christensen et al. tend to be somewhat larger than those found by Phillips. In addition, Garcia and Cohen [38] achieved the mapping of the ionicity scale by an unambiguous procedure based on the measure of the asymmetry of the first principle valence charge distribution [39]. As for the Christensen scale, their results were somewhat larger than those of the Phillips scale. Zaoui et al. [40] established an empirical formula for the calculation of ionicity based on the measure of the asymmetry of the total valence charge density, and their results are in agreement with those of the Phillips scale. In the present work, the ionicity, fi, was calculated using different formulas [41], and the theory yielded formulas with three attractive features. Only the energy gap EgΓX was required as the input, the computation of fi itself was trivial, and the accuracy of the results reached that of ab initio calculations. This option is attractive because it considers the hypothetical structure and simulation of experimental conditions that are difficult to achieve in the laboratory (e.g., very high pressure). The goal of the current study is to understand how qualitative concepts, such as ionicity, can be related to energy gap EgΓX with respect to the nearest-neighbor distance, d, cohesive energy, $E_{coh}$, and refractive index, $n_0$. Our calculations are based on the energy gap EgΓX reported previously [34,42–45], and the energy gap that follows chemical trends is described by a homopolar energy gap. Numerous attempts have been made to face the differences between energy levels. Empirical pseudopotential methods based on optical spectra encountered the same problems using an elaborate (but not necessarily more accurate) study based on one-electron atomic or crystal potential. As mentioned earlier, d, $E_{coh}$, and $n_0$ have been reported elsewhere for Si and PS. One reason for presenting these data in the present work is that the validity of our calculations, in principle, is not restricted in space. Thus, they will no doubt prove valuable for future work in this field. An important observation for studying ionicity, $f_i$, is the distinguished difference between the values of the energy gaps of the semiconductors, EgΓX, as seen in Table 2; hence, the energy gaps EgΓX are predominantly dependent on fi . The differences between the energy gaps Egrx have led us to consider these models, and the bases of our models are the energy gaps, EgΓX, as seen in Table 4. The fitting of these data gives the following empirical formulas [41]:

$$f_i = \lambda \left( \frac{(d / E_{g\Gamma X})}{4} \right) \tag{5}$$

$$f_i = \lambda \left( \frac{(E_{coh} / E_{g\Gamma X})}{2} \right) \tag{6}$$

$$f_i = \lambda \left( \frac{(n_0 / E_{g\Gamma X})}{4} \right) \tag{7}$$

where $E_{g\Gamma X}$ is the energy gap in (eV), d the nearest-neighbor distance in (Å), $E_{coh}$ the cohesive energy in (eV), $n_0$ the refractive index, and $\lambda$ is a parameter separating the strongly ionic materials from the weakly ionic ones. Thus, $\lambda$ = 0, 1, and 6 are for the Groups IV, III–V, and II–VI semiconductors, respectively. The calculated ionicity values compared with those of Phillips [36], Christensen et al. [37], Garcia and Cohen [38], and Zaoui et al. [40] are given in Table 2. We may conclude that the present ionicities, which were calculated differently than in the definition of Phillips, are in good agreement with the empirical ionicity values, and exhibit the same chemical trends as those found in the values derived from the Phillips theory or those of Christensen et al. [37], Garcia and Cohen [38], and Zaoui et al. [40] (Table 2).

| Samples | $d$ [a] (Å) | $E_{coh}$ [b] (eV) | $n_0$ | $f_i$ cal. | $f_i$[g] | $f_i$[h] | $f_i$[i] | $f_i$[j] | $E_{g\Gamma X}$ (eV) |
|---|---|---|---|---|---|---|---|---|---|
| Si | 2.35 | 2.32 | 3.673[c] | 0[e] 0[f] | 0 | 0 | 0 | 0 | 1.1 |
| PS formed on the unpolished side | | | 2.77[d] | 0 | 0 | 0 | 0 | 0 | 1.82 |
| PS formed on the front polished side | | | 2.66[d] | 0 | 0 | 0 | 0 | 0 | 1.86 |

[a]Ref. [46], [b]Ref. [47], [c]Ref. [48], [d]Ref. [29], [e]Ref. [41]: Formulas (5–7), [f]Ref. [49], [g]Ref. [36], [h]Ref. [37], [i]Ref. [38], [j]Ref. [40]

Table 4. Calculated ionicity character for Si and PS along with those of Phillips [36], Christensen et al. [37], Garcia and Cohen [38], Zaoui et al. [40], and Al-Douri et al. [41]

The difficulty involved with such calculations resides with the lack of a theoretical framework that can describe the physical properties of crystals. Generally speaking, any definition of ionicity is likely to be imperfect. Although we may argue that, for many of these compounds, the empirically calculated differences are of the same order as the differences between the reported measured values, these trends are still expected to be real [47]. The unchanged ionicity characters of bulk Si and PS are noticed. In conclusion, the empirical models obtained for the ionicity give results in good agreement with the results of other scales, which in turn demonstrate the validity of our models to predict some other physical properties of such compounds.

## 7. Material stiffness

The bulk modulus is known as a reflectance of the crucial material stiffness in different industries. Many authors [50–55] have made various efforts to explore the thermodynamic properties of solids, particularly in examining the thermodynamic properties such as the inter-atomic separation and the bulk modulus of solids with different approximations and best-fit relations [52–55]. Computing the important number of structural and electronic properties of solids with great accuracy has now become possible, even though the ab initio calculations are complex and require significant effort. Therefore, additional empirical approaches have been developed [36, 47] to compute properties of materials. In many cases, the empirical methods offer the advantage of applicability to a broad class of materials and to illustrate trends. In many applications, these empirical approaches do not provide highly accurate results for each specific material; however, they are still very useful. Cohen [46] established an empirical formula for calculating bulk modulus $B0$ based on the nearest-neighbor distance, and the result is in agreement with the experimental values. Lam et al. [56] derived an analytical expression for the bulk modulus from the total energy that gives similar numerical results even though this expression is different in structure from the empirical formula. Furthermore, they obtained an analytical expression for the pressure derivative $B0$ of the bulk modulus. Meanwhile, our group [57] used a concept based on the energy gap along Γ-X and transition pressure to establish an empirical formula for the calculation of the bulk modulus, the results of which are in good agreement with the experimental data and other calculations. In the present work, we have established an empirical formula for the calculation of bulk modulus $B0$ of a specific class of materials, and the theory yielded a formula with three attractive features. Apparently, only the energy gap along Γ -X and transition pressure are required as an input, and the computation of $B0$ in itself is trivial. The consideration of the hypothetical structure and simulation of the experimental conditions are required to make practical use of this formula.

The aim of the present study is to determine how a qualitative concept, such as the bulk modulus, can be related to the energy gap. We [57] obtained a simple formula for the bulk moduli of diamond and zinc-blende solids using scaling arguments for the relevant bonding and volume. The dominant effect in these materials has been argued to be the degree of covalence, as characterized by the  homopolar gap, $Eh$ of Phillips, [36] and the gap along Γ-X [57]. Our calculation is based upon the energy gap along Γ-X which has been reported previously [42–45], and the energy gaps that follow chemical trends are described by homopolar and heteropolar energy gaps. Empirical pseudopotential methods based on

optical spectra encounter the same problems using an elaborate (but not necessarily more accurate) study based on one electron atomic or crystal potential. One of the earliest approaches [58] involved in correlating the transition pressure with the optical band gap [e.g., the band gap for α-Sn is zero and the pressure for a transition to β-Sn is vanishingly small, whereas for Si with a band gap of 1 eV, the pressure for the same transition is approximately 12.5 GPa (125 kbar)]. A more recent effort is from Van Vechten [59], who used the dielectric theory of Phillips [36] to scale the zinc-blende to β-Sn transition with the ionic and covalent components of the chemical bond. The theory is a considerable improvement with respect to earlier efforts, but is limited to the zinc-blende to β-Sn transition. As mentioned, EgΓX and Pt have been reported elsewhere for several semiconducting compounds. One reason for presenting these data in the current work is that the validity of our calculations is not restricted in computed space. Thus, the data is bound prove valuable for future work in this field.

An important reason for studying B0 is the observation of clear differences between the energy gap along Γ-X in going from the group IV, III–V, and II–VI semiconductors in Table 4, where one can see the effect of the increasing covalence. As covalence increases, the pseudopotential becomes more attractive and pulls the charge more toward the core region, thereby reducing the number of electrons available for bonding. The modulus generally increases with the increasing covalence, but not as quickly as predicted by the uniform density term. Hence, the energy gaps are predominantly dependent on B0. A likely origin for the above result is the increase of ionicity and the loss of covalence. The effect of ionicity reduces the amount of bonding charge and the bulk modulus. This picture is essentially consistent with the present results; hence, the ionic contribution to B0 is of the order 40%–50% smaller. The differences between the energy gaps have led us to consider this model.

The basis of our model is the energy gap as seen in Table 4. The fitting of these data gives the following empirical formula [57]:

$$B_0 = (30 + \lambda 10)\left[\left(P_t^{1/2} / E_{g\Gamma X}\right) / 3\right] \tag{8}$$

where EgΓX is the energy gap along Γ-X (in eV), Pt is the transition pressure (in GPa ''kbar''), and λ is an empirical parameter that accounts for the effect of ionicity; λ = 0; 1, 5 for group IV, III–V, and II–VI semiconductors, respectively. In Table 5, the calculated bulk modulus values are compared with the experimental values and the results of Cohen [46], Lam et al. [56], and Al-Douri et al. [57].

We may conclude that the present bulk moduli calculated in a different way than in the definition of Cohen are in good agreement with the experimental values. Furthermore, the moduli exhibit the same chemical trends as those found for the values derived from the experimental values, as seen in Table 5. The results of our calculations are in reasonable agreement with the results of Cohen [46] and the experiments of Lam et al. [56], and are more accurate than in our previous work [57]. As mentioned previously, an approach [57] that elucidates the correlation of the transition pressure with the optical band gap exists. This procedure gives a rough correlation and fails badly for some materials such as AlSb that have a larger band gap than Si but have a lower transition pressure [64]. From the above empirical formula, a correlation is evident between the transition pressure and B0

[e.g., the $B_0$ for Si is 100.7 GPa and the pressure for the transition to β-Sn is 12.5 GPa (125 kbar), whereas for GaSb, B0 is 55.5 GPa and the transition pressure to β-Sn is 7.65 GPa (76.5 kbar)]. This correlation fails for a compound such as ZnS that has a smaller value of B0 than Si but has a larger transition pressure. In conclusion, the empirical model obtained for the bulk modulus gives results that are in good overall agreement with previous results.

| Samples | $B_0$ cal. (GPa) | $B_0$ exp.[b] (GPa) | $B_0$ [46] (GPa) | $B_0$ [56] (GPa) | $B_0$ [57] (GPa) | $B_0$ (GPa) | $P_t$ [e] (GPa) |
|---|---|---|---|---|---|---|---|
| Si | 101[a'] 91.5[a''] 100[a'''] | 98 | 98 | 100 | 92 | 92[c] 93.6[d] | 12.5 |
| PS formed on the unpolished side | 61.4[a'] 150.7[a''] 165[a'''] | | | | | | |
| PS formed on the front polished side | 60.1[a'] 148.5[a''] 169[a'''] | | | | | | |

a'Ref. [57], a''Ref. [60], a'''Ref. [61], bRef. [46], cRef. [62], dRef. [63], eRef. [64]

Table 5. Calculated bulk modulus for Si and PS together with experimental values, and the results of Cohen [46], Lam et al. [56], Al-Douri et al. [57] values, and others [43,44]

## 8. Conclusions

PS formed on the unpolished backside of the c-Si wafer showed an increase in surface roughness compared with one formed on the polished front side. The high degree of roughness along with the presence of the nanocrystal layer implies that the surface used as an ARC, which can reduce the reflection of light and increase light trapping on a wide wavelength range. This parameter is important in enhancing the photo conversion process for solar cell devices. PS formed on both sides has low reflectivity value. Fabricated solar cells show that the conversion efficiency is 15.4% compared with the unetched sample and other results [13, 15]. The results of the refractive index and optical dielectric constant of Si and PS are investigated. The results of Ghosh et al. proved the appropriate for studying porous silicon solar cell optical properties. The mentioned models of ionicity in our study indicated a good accordance with other scales .other side, the empirical model obtained for the bulk modulus gives results that are in good overall agreement with previous results.

## 9. Acknowledgement

## 10. References

[1] V.M. Aroutiounia, K.S.h. Martirosyana, S. Hovhannisyana, G. Soukiassianb, J. Contemp. Phys. 43 (2008) 72.

[2] Wisam J Aziz, Asmat Ramizy, K. Ibrahim, Khalid Omar, Z. Hassan, Journal of Optoelectronic and Advanced Materials (JOAM), Vol. 11, No. 11, p. 1632 - 1636, Nov. (2009)

[3] Asmiet Ramizy, Wisam J Aziz, Z. Hassan, Khalid Omar and K. Ibrahim, Microelectronics International, Vol. 27, No. 2, pp. 117-120, 2010.

[4] Wisam J. Aziz, Asmiet Ramizy, K. Ibrahim, Z. Hassan, Khalid Omar, In Press, Corrected Proof, Available online 17 January 2011,OPTIK, Int. J. Light Electron Opt.

[5] Asmiet Ramizy, Wisam J. Aziz, Z. Hassan, Khalid. Omar and K. Ibrahim, In Press, Corrected Proof, Available online 9 March 2011, OPTIK,

[6] Asmiet Ramizy, Z. Hassan, Khalid Omar, Y. Al-Douri, M. A. Mahdi. Applied Surface Science, Applied Surface Science, Vol. 257, Iss. 14, (2011) pp. 6112–6117.

[7] Asmiet Ramizy, Wisam J. Aziz, Z. Hassan, Khalid Omar, and K. Ibrahim, Accepted, Materials Science-Poland.

[8] D.-H. Oha, T.W. Kim, W.J. Chob, K.K. D, J. Ceram. Process. Res. 9 (2008) 57.

[9] G. Barillaro, A. Nannini, F. Pieri, J. Electrochem. Soc. C 180 (2002) 149.

[10] J. Guobin, S. Winfried, A. Tzanimir, K. Martin, J. Mater. Sci. Mater. Electron. 19 (2008) S9.

[11] F. Yan, X. Bao, T. Gao, Solid State Commun. 91 (1994) 341.

[12] M. Yamaguchi, Super-high efficiency III–V tandem and multijunction cells, in: M.D. Archer, R. Hill (Eds.), Clean Electricity from Photovoltaics, Super-High Effi- ciency III–V Tandem and Multijunction Cells, Imperial College Press, London, 2001, p. 347.

[13] M. Ben Rabha, B. Bessaïs, Solar Energy 84 (2010) 486.

[14] S. Yae, T. Kobayashi, T. Kawagishi, N. Fukumuro, H. Matsuda, Solar Energy 80 (2006) 701.

[15] R. Brendel, Solar Energy 77 (2004) 969.

[16] Adam. A, Susan. S, and Raphael. T, J Vac Sci Technol., B 14 6 (1996) 3431

[17] G. Lerondel, R. Romestain, in: L. Canham (Ed.), Reflection and Light Scat tering in Porous Silicon, Properties of porous silicon, INSPEC, UK, 1997, p. 241.

[18] Asmiet Ramizy, Z. Hassan, K. Omar, J. Mater. Sci. Elec, (First available online).

[19] J. A. Wisam, Ramizy.Asmiet, I. K, O. Khalid, and H. Z, Journal of Optoelectronic and Advance Materials 11 (2009) pp.1632

[20] M. A. Mahdi, S. J. Kasem, J. J. Hassen, A. A. Swadi, S. K. J.Al-Ani, Int. J.Nanoelectronics and Materials 2 (2009) 163

[21] N. M. Balzaretti, J. A. H. da Jornada, Solid State Commun. 99 (1996) 943

[22] T. S. Moss, Proc. Phys. Soc. B 63 (1950) 167

[23] V. P. Gupta, N. M. Ravindra, Phys. Stat. Sol. B 100 (1980) 715

[24] Y. Al-Douri, Mater. Chem. Phys. 82 (2003) 49

[25] Y. Al-Douri, Y. P. Feng, A. C. H. Huan, Solid State Commun. 148 (2008) 521

[26] P. Herve, L. K. J. Vandamme, Infrared Phys. Technol. 35 (1993) 609

[27] N. M. Ravindra, S. Auluck, V. K. Srivastava, Phys. Stat. Sol. (b) 93 (1979) K155

[28] P. J. L. Herve, L. K. J. Vandamme, J. Appl. Phys. 77 (1995) 5476

[29] D. K. Ghosh, L. K. Samanta, G. C. Bhar, Infrared Phys. 24 (1984) 34

[30] D. R. Penn, Phys. Rev. 128 (1962) 2093

[31] J. A. Van Vechten, Phys. Rev. 182 (1969) 891

[32] G. A. Samara, Phys. Rev. B 27 (1983) 3494

[33] Halimaoui A. 1997, 'Porous silicon formation by anodization', in: L. Canham (Ed.), Properties of porous silicon, INSPEC, UK (1997) 18

[34] J.R. Chelikowsky, M.L. Cohen, Phys. Rev. B14 (1976) 556

[35] C.S. Wang, B.M. Klein, Phys. Rev. B24 (1981) 3393

[36] J.C. Phillips, Bonds and Bands in Semiconductors, Academic Press, San Diego, 1973

[37] N.E. Christensen, S. Stapathy, Z. Pawlowska, Phys. Rev. B36 (1987) 1032

[38] A. Garcia, M.L. Cohen, Phys. Rev. B47 (1993) 4215

[39] A. Garcia, M.L. Cohen, Phys. Rev. B47 (1993) 4221

[40] A. Zaoui, M. Ferhat, B. Khelifa, J.P. Dufour, H. Aourag, Phys. Stat. Sol. (b) 185 (1994) 163

[41] Y. Al-Douri, H. Abid, H. Aourag, Mater. Chem. Phys. 65 (2000) 117

[42] I.M. Tsidilkovski, Band Structure of Semiconductors, Pergamon, Oxford, 1982

[43] K. Strossner, S. Ves, Chul Koo Kim, M. Cardona, Phys. Rev. B33 (1986) 4044

[44] C. Albert, A. Joullié, A.M. Joullié, C. Ance, Phys. Rev. B27 (1984) 4946

[45] R.G. Humphreys, V. Rossler, M. Cardona, Phys. Rev. B18 (1978) 5590

[46] M.L. Cohen, Phys. Rev. B32 (1985) 7988

[47] W.A. Harison, Electronic Structure and the Properties of Solids, General Publishing Company, Toronto, 1989

[48] Landolt-Bornstein, Numerical Data and Functional Realtionships in Science and Technology — Crystal and Solid State Physics, vol. 22, Springer, Berlin, 1987

[49] Y. Al-Douri, J. Eng. Res. Edu. 4 (2007) 81

[50] A.M. Sherry, M. Kumar, J. Phys. Chem. Solids 52 (1991) 1145

[51] J.L. Tallon, J. Phys. Chem. Solids 41 (1980) 837

[52] M. Kumar, S.P. Upadhyaya, Phys. Stat. Sol. B 181 (1994) 55

[53] M. Kumar, Physica B 205 (1995) 175

[54] R.K. Pandey, J. Phys. Chem. Solids 59 (1998) 1157.

[55] Qing He, Zu-Tong Yan, Phys. Stat. Sol. B 223 (2001) 767.

[56] P.K. Lam, M.L. Cohen, G. Martinez, Phys. Rev. B 35 (1987) 9190.

[57] Y. Al-Douri, H. Abid, H. Aourag, Physica B 322 (2002) 179.

[58] J.C. Jamieson, Science 139 (1963) 845.

[59] J.A. Van Vechten, Phys. Rev. B 7 (1973) 1479.

[60] Y. Al-Douri, H. Abid, H. Aourag, Mater. Chem. Phys. 87 (2004) 14.

[61] Y. Al-Douri, Res. Lett. Mater. Sci. 57 (2007) 143.

[62] Y. Al-Douri, H. Abid, H. Aourag, Physica B 305 (2001) 186

[63] Y. Al-Douri, H. Abid, H. Aourag, Mater. Lett. 59 (2005) 2032
[64] J.R. Chelikowsky, Phys. Rev. B 35 (1987) 1174.

# Evaluation the Accuracy of One-Diode and Two-Diode Models for a Solar Panel Based Open-Air Climate Measurements

Mohsen Taherbaneh, Gholamreza Farahani and Karim Rahmani
*Electrical and Information Technology Department,*
*Iranian Research Organization for Science and Technology, Tehran,*
*Iran*

## 1. Introduction

Increasingly, using lower energy cost system to overcome the need of human beings is of interest in today's energy conservation environment. To address the solution, several approaches have been undertaken in past. Where, renewable energy sources such as photovoltaic systems are one of the suitable options that will study in this paper. Furthermore, significant work has been carried out in the area of photovoltaic system as one of the main types of renewable energy sources whose utilization becomes more common due to its nature. On the other hand, modeling and simulation of a photovoltaic system could be used to predict system electrical behaviour in various environmental and load conditions. In this modeling, solar panels are one of the essential parts of a photovoltaic system which convert solar energy to electrical energy and have nonlinear I-V characteristic curves. Accurate prediction of the system electrical behaviour needs to have comprehensive and precise models for all parts of the system especially their solar panels. Consequently, it provides a valuable tool in order to investigate the electrical behaviour of the solar cell/panel. In the literature, models that used to express electrical behaviour of a solar cell/panel are mostly one-diode or two-diode models with a specific and close accuracy with respect to each other. One-diode model has five variable parameters and two-diode model has seven variable parameters in different environmental conditions respectively.

During the last decades, different approaches have been developed in order to identify electrical characteristics of both models. (Castaner & Silvestre, 2002) have introduced and evaluated two separate models (one-diode and two-diode models) for a solar cell but dependency of the models parameters on environmental conditions has not been fully considered. Hence, the proposed models are not completely accurate. (Sera et al., 2007) have introduced a photovoltaic panel model based on datasheet values; however with some restrict assumptions. Series and shunt resistances of the proposed model have been stated constant and their dependencies on environmental conditions have been ignored. Furthermore, dark-saturation current has been considered as a variable which depend on the temperature but its variations with irradiance has been also neglected. Model equations have been merely stated for a solar panel which composed by several series cells.

(De Soto et al., 2006) have also described a detailed model for a solar panel based on data provided by manufacturers. Several equations for the model have been expressed and one of them is derivative of open-circuit voltage respect to the temperature but with some assumptions. Shunt and series resistances have been considered constant through the paper, also their dependency over environmental conditions has been ignored. Meanwhile, only dependency of dark-saturation current to temperature has been considered. (Celik & Acikgoz, 2007) have also presented an analytical one-diode model for a solar panel. In this model, an approximation has been considered to describe the series and shunt resistances; they have been stated by the slopes at the open-circuit voltage and short-circuit current, respectively. Dependencies of the model parameters over environmental conditions have been briefly expressed. Therefore, the model is not suitable for high accuracy applications.

(Chenni et al., 2007) have used a model based on four parameters to evaluate three popular types of photovoltaic panels; thin film, multi and mono crystalline silicon. In the proposed model, value of shunt resistance has been considered infinite. The dark-saturation current has been dependent only on the temperature. (Gow & Manning, 1999) have demonstrated a circuit-based simulation model for a photovoltaic cell. The interaction between a proposed power converter and a photovoltaic array has been also studied. In order to extract the initial values of the model parameters at standard conditions, it has been assumed that the slope of current-voltage curve in open-circuit voltage available from the manufacturers. Clearly, this parameter is not supported by a solar panel datasheet and it is obtained only through experiment.

There are also several researches regarding evaluation of solar panel's models parameters from different conditions point of view by (Merbah et al., 2005; Xiao et al., 2004; Walker, 2001). In all of them, solar panel's models have been proposed with some restrictions.

The main goal of this study is investigation the accuracy of two mentioned models in the open-air climate measurements. At first step of the research, a new approach to model a solar panel is fully introduced that it has high accuracy. The approach could be used to define the both models (on-diode and two diode models) with a little bit modifications. Meanwhile, the corresponding models parameters will also evaluate and compare. To assess the accuracy of the models, several extracted I-V characteristic curves are utilized using comprehensive designed measurement system. In order to coverage of a wide range of environmental conditions, almost one hundred solar panel I-V curves have been extracted from the measurement system during several days of the year in different seasons. Hence, the rest of chapter is organized as follows.

In section 2 of the report, derivation of an approach to evaluate the models accuracy will be described. Nonlinear mathematical expressions for both models are fully derived. The Newton's method is selected to solve the nonlinear models equations. A measurement system in order to extract I-V curves of solar panel is described in section 3. In section 4, the extracted unknown parameters of the models for according to former approach are presented. Results and their interpretation are presented in section 5. Detailed discussion on the results of the research and conclusions will provide in the final section.

## 2. Study method

The characteristics of a solar cell "current versus voltage" under environmental conditions (irradiance and temperature) is usually translated either to an equivalent circuits of one-

Evaluation the Accuracy of One-Diode and Two-Diode
Models for a Solar Panel Based Open-Air Climate Measurements
203

diode model (Fig. 1a) or to an equivalent circuit of two-diode model (Fig. 1b) containing photocurrent source, a diode or two diodes, a shunt resistor and a series resistor in the load branch.
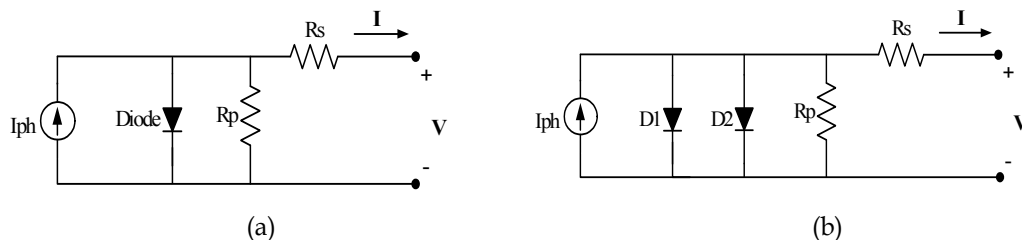


Fig. 1. The equivalent circuits of one-diode and two-diode models of a solar cell.

One-diode model and two-diode model can be represented by Eqs. (1) and (2) accordingly:

$$i = I_{ph} - I_0(e^{\frac{v+iR_s}{V_T}} - 1) - \frac{v + iR_s}{R_p} \quad , \quad V_T = \frac{nkT}{q} \tag{1}$$

$$i = I_{ph} - I_{01}(e^{\frac{v+iR_s}{V_{T1}}} - 1) - I_{02}(e^{\frac{v+iR_s}{V_{T2}}} - 1) - \frac{v + iR_s}{R_p} \quad , \quad V_{Tj} = \frac{n_j kT}{q} \quad j = 1,2 \tag{2}$$

Where, one-diode model has five unknown parameters; $I_{ph}, I_0, n, R_s$ and $R_p$ and the two-diode model has seven unknown parameters; $I_{ph}, I_{01}, n_1, I_{02}, n_2, R_s$ and $R_p$. On the other hand, a solar panel is composed of parallel combination of several cell strings and a string contains several cells in series. Therefore, the both models can be also stated for a solar panel. In this research, the idea is to compare the accuracy of the two mentioned models for a solar panel. As it is known, the unknown parameters of the models are functions of the incident solar irradiation and panel temperature; hence dependency between them should be taken into account.

In this section, evaluation of the unknown one-diode model parameters based on five equations are presented. The specific five points (are shown in Fig. 2) on the I-V curve are used to define the equations, where $I_{sc}$ is the short circuit current, $I_x$ is the current at $V_x = 0.5V_{oc}$, $I_{xx}$ is current at $V_{xx} = 0.5(V_{oc} + V_{mp})$, $V_{oc}$ is the open circuit voltage and $V_{mp}$ is the voltage at the maximum power point. In this study, the mentioned points are generated for 113 operating conditions between 15-65°C and 100-1000W/m² to solve the five coupled implicit nonlinear equations for a solar panel that consists of 36 series connected poly-crystalline silicon solar cells at different operating conditions. By solving the nonlinear equations in a specific environmental condition, we will find five unknown parameters of the model in one operating condition. Equation (3) shows the system nonlinear equations for one-diode model.

$$F_j = -i_j + I_{ph} - I_0(e^{\frac{v+iR_s}{a}}) - \frac{v + iR_s}{R_p} \quad , \quad a = \frac{nkT}{q} \quad j = 1,2,...,5 \tag{3}$$
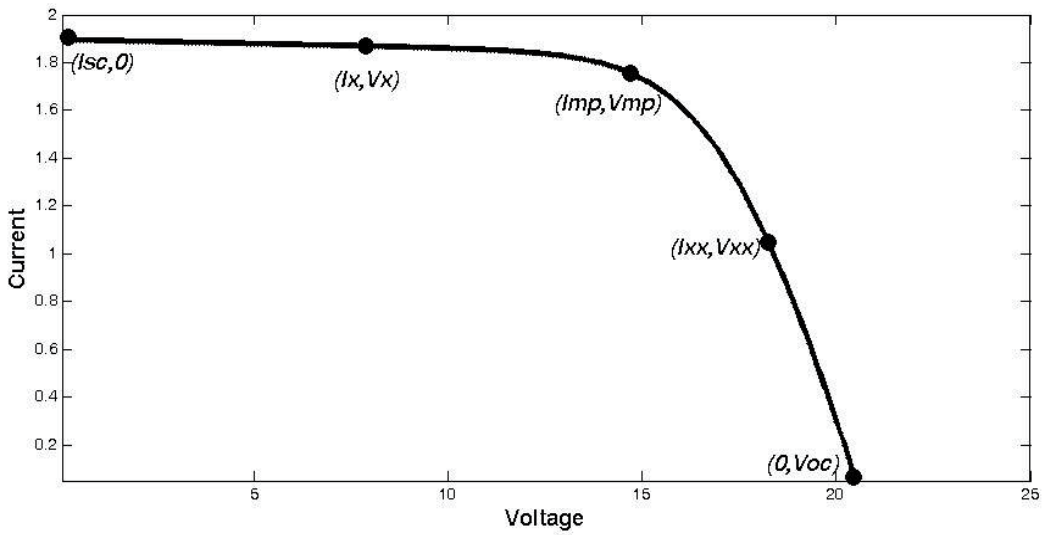
Fig. 2. Five points on the I-V curve of a solar panel are used to solve the nonlinear equations.

Former approach is used to solve seven coupled implicit nonlinear equations of the two-diode model for a solar panel. The specific seven points (are shown in Fig. 3) on the I-V curve are used to define the equations, where $I_b$ is the current at $V_b = \dfrac{V_{mp}}{3}$, $I_c$ is the current at $V_c = \dfrac{2V_{mp}}{3}$, $I_e$ is the current at $V_e = \dfrac{2V_{mp} + V_{oc}}{3}$ and $I_f$ is the current at $V_f = \dfrac{V_{mp} + 2V_{oc}}{3}$.
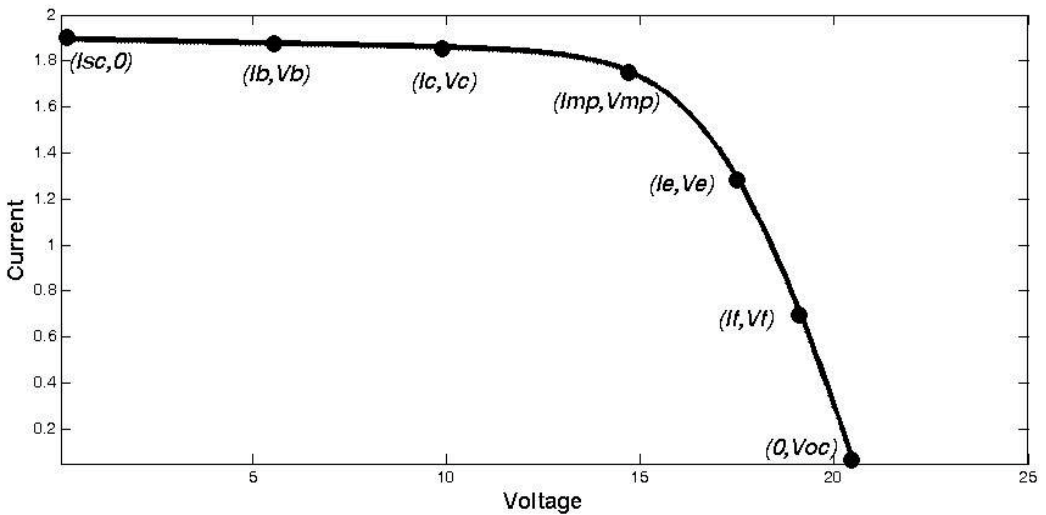


Fig. 3. Seven points on the I-V curve of a solar panel to solve the nonlinear equations.

The points are also generated for the 113 operating conditions to solve the seven coupled implicit nonlinear equations for the solar panel. Solving the nonlinear equations in a specific environmental condition leads to define seven unknown model parameters in one operating condition. Equation (4) shows the system nonlinear equations for the two-diode model.

$$G_j = -i_j + I_{ph} - I_{01}(e^{\frac{v+iR_s}{a_1}} - 1) - I_{02}(e^{\frac{v+iR_s}{a_2}} - 1) - \frac{v+iR_s}{R_P},$$

$$a_k = \frac{n_k kT}{q}, \qquad k = 1,2 \ , \ j = 1,2,...,7$$

(4)

Figs. 4 and 5 show the implemented algorithms in order to solve the nonlinear equations for the both models.

## 3. Measurement system

A block diagram of a measurement system is shown in Fig. 6. The main function of this system is extracting the solar panel's I-V curves. In this system, an AVR microcontroller (ATMEGA64) is used as the central processing unit. This unit measures, processes and controls input data. Then the processed data transmit to a PC through a serial link. In the proposed system, the PC has two main tasks; monitoring (acquiring the results) and programming the microcontroller. Extracting the solar panel's I-V curves shall be carried out in different environmental conditions. Different levels of received solar irradiance are achieved by changing in solar panel's orientation which is performed by controlling two DC motors in horizontal and vertical directions. Although the ambient temperature changing is not controllable, the measurements are carried out in different days and different conditions in order to cover this problem. A portable pyranometer and thermometer are used for measuring the environmental conditions; irradiance and temperature. Hence, 113 acceptable I-V curves *(out of two hundred)* were extracted. Motor driver block diagram is also shown in Fig. 7. Driving the motors is achieved through two full bridge PWM choppers with current protection. Table 1 reports electrical specifications of the under investigation solar panel at standard conditions based on datasheets.

| Solar Panel | | Poly-Crystalline Silicon Solar Panel |
|---|---|---|
| *Standard conditions* | **Irradiance (W/m²)** | 1000 |
| | **Temperature (°C)** | 25 |
| $I_{sc}$ (A) | | 2.98 |
| $V_{oc}$ (V) | | 20.5 |
| $I_{mpp}$ (A) | | 2.73 |
| $V_{mpp}$ (V) | | 16.5 |
| $P_{mpp}$ (W) | | 45 |
| $n_s$ | | 36 |
| $n_p$ | | 1 |
| $k_i$ (%/°C ) | | 0.07 |
| $k_v$ (mv/°C) | | -0.038 |

Table 1. Datasheet information of the under investigation solar panel

Extraction the Solar Panel I-V
Curves using Measurement System

Measuring Irradiance and Temperature of all Curves
Power = Current×Voltage

Extracting (for all Curves)
Open Circuit Voltage ($V_{oc}$), Short Circuit Current ($I_{sc}$)
Maximum Power ($P_{max}$)
Voltage at Maximum Power Point ($V_{mp}$)
Current at Maximum Power Point ($I_{mp}$)

Defining 5 Points on Each Curve
$V_x = 0.5V_{oc}$
$V_{xx} = 0.5(V_{oc}+V_{mp})$
$I_x$ current at $V_x$
$I_{xx}$ current at $V_{xx}$

Solving 5 Nonlinear Equations for Each Curve

$$F_j = -i_j + I_{ph} - I_0(e^{\frac{v+iR_s}{a}}) - \frac{v+iR_s}{R_p} = 0 \qquad , \qquad a = \frac{nkT}{q} \quad j = 1,2,...,5$$

Extracting 5 Parameters of the Model for any Environmental Condition
$I_{ph}$, $I_0$, n, $R_s$, $R_p$

Fig. 4. Flowchart of extraction the one-diode model parameters
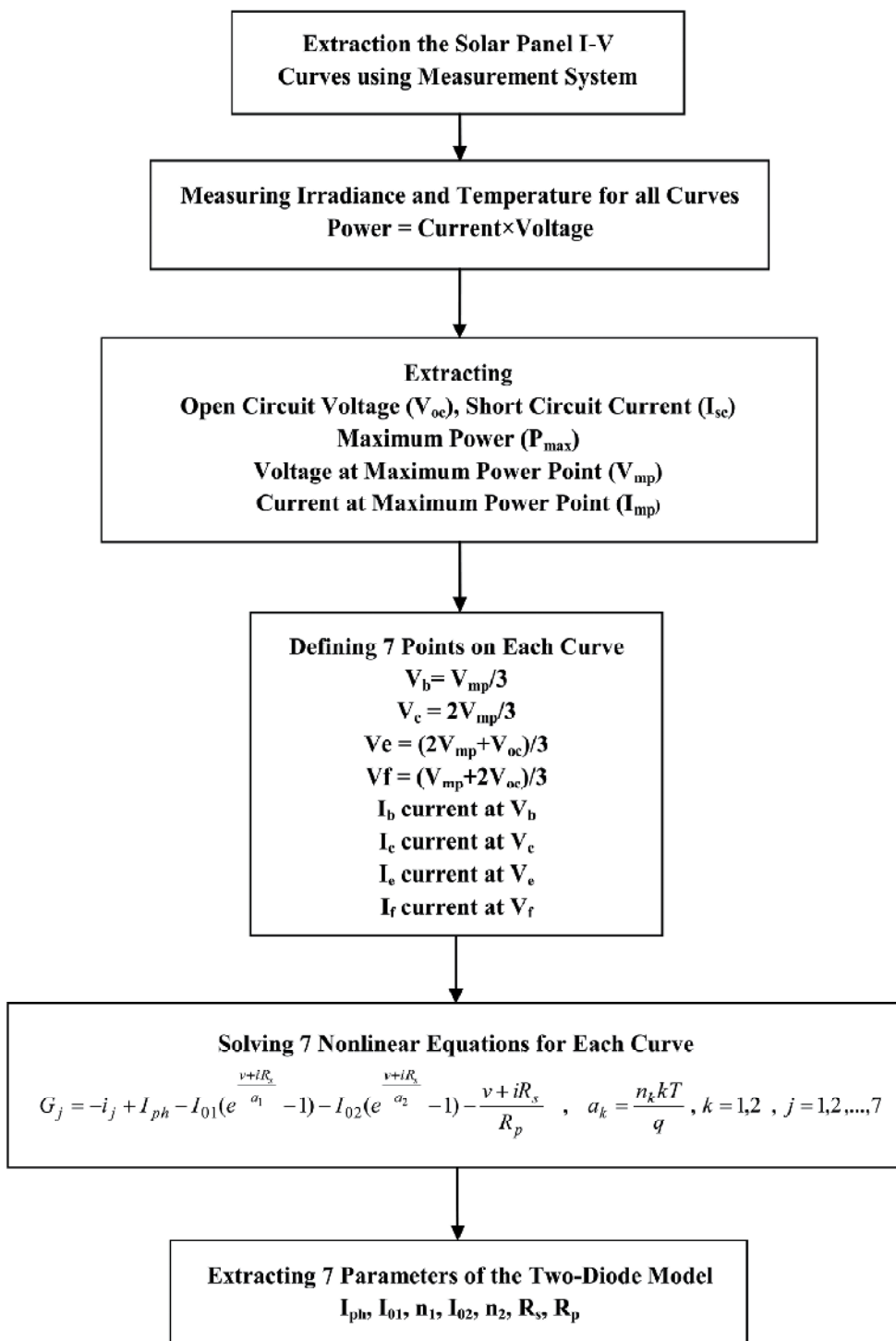
Fig. 5. Flowchart of extraction the two-diode model parameters
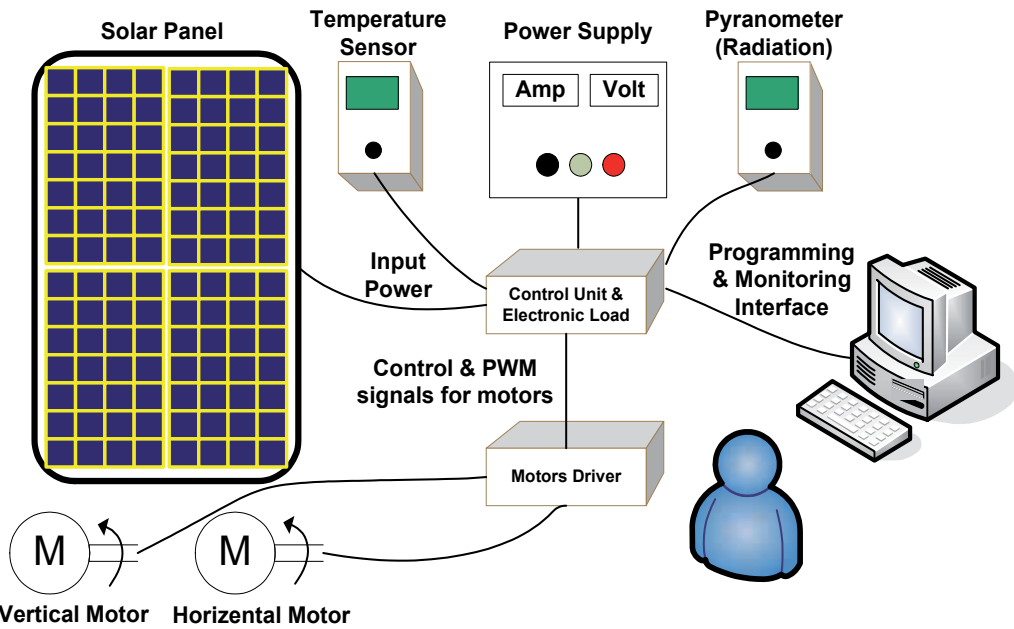
Fig. 6. Block diagram of the proposed measurement system
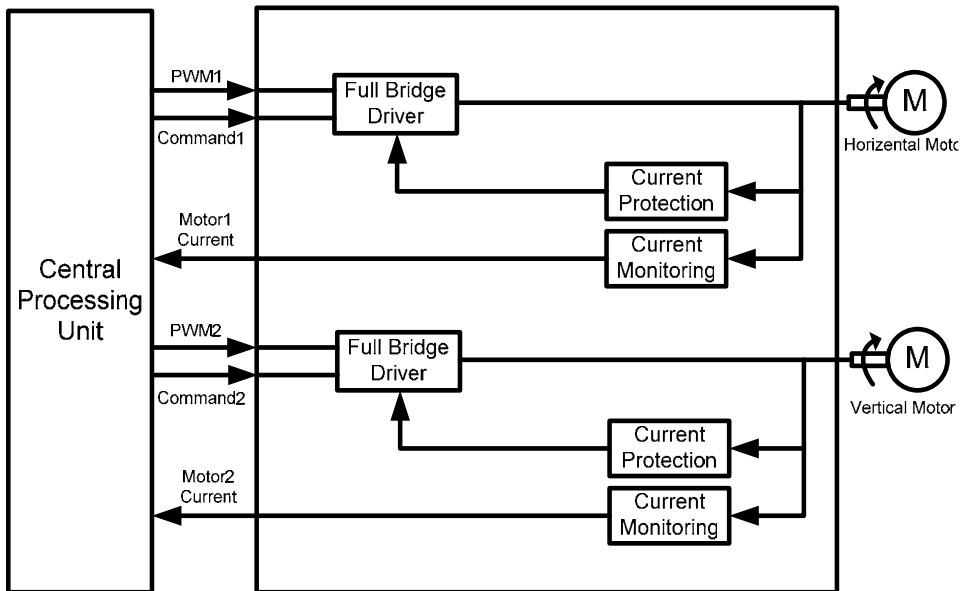


Fig. 7. Motor driver block diagram

### 3.1 The I-V curve extractor

There is an important rule for solar panel's I-V curves in photovoltaic system designing. Although the manufacturers give specifications of their products (cell or panel) generally in the standard condition, behavior of solar cells and panels are more required in non-standard

Evaluation the Accuracy of One-Diode and Two-Diode
Models for a Solar Panel Based Open-Air Climate Measurements
209

environmental conditions. In order to extract a solar panels' I-V curve, it is sufficient to change the panel current between zero (open-circuit) to its maximum value (short-circuit) continuously or step by step when environmental condition was stable (the incident solar irradiance and panel temperature). Then the characteristic curve could be obtained by measuring the corresponding voltages and currents. Therefore, a variable load is required across the panel output ports.

Since the solar panel's I-V curve is nonlinear, the load variation profile has a significant impact on the precision of the extracted curve. If the load resistance (or conductance) varies linearly, the density of the measured points will be high near $I_{sc}$ or $V_{oc}$ and it is not desired. Hence, the nonlinear electronic load is more suitable. There are generally two methods for implementation a variable load, which will be discussed below.

### 3.1.1 Discrete method

As mentioned above, extracting the solar panel I-V curve could be carried out by its output load variation. An easy way is switching of some paralleled resistors to have different loads. If the resistors have been chosen according to Eq. (5), it is possible to have $2^n$ different load values by switching of n resistors.

$$R_n = \frac{1}{2} R_{n-1} \tag{5}$$

The schematic for the proposed switching load is shown in Fig. 8. This method may cause some switching noise in the measurement system. Therefore, a controllable continuous electronic load is suitable.
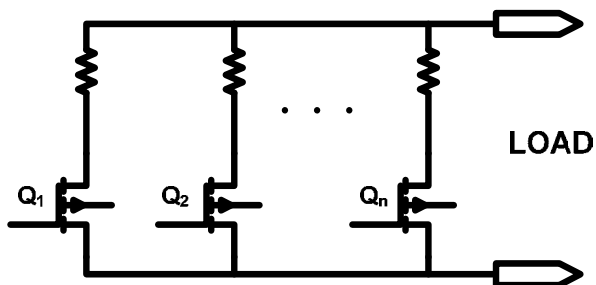


Fig. 8. The proposed switching load circuit

### 3.1.2 Continuous method

The schematic diagram for the proposed continuous electronic load is shown in Fig. 9. The drain-source resistor of a MOSFET in linear area of its electrical characteristic curves is used as a load. As we know, the value of this resistor could be controlled by gate-source voltage. Mathematical relationship between the value of this resistor and applied voltage is described in Eq. (6).

$$R_{ds} = \frac{t_{ox}L}{\mu\varepsilon W} \left( \frac{1}{V_{gs} - V_T} \right) \tag{6}$$
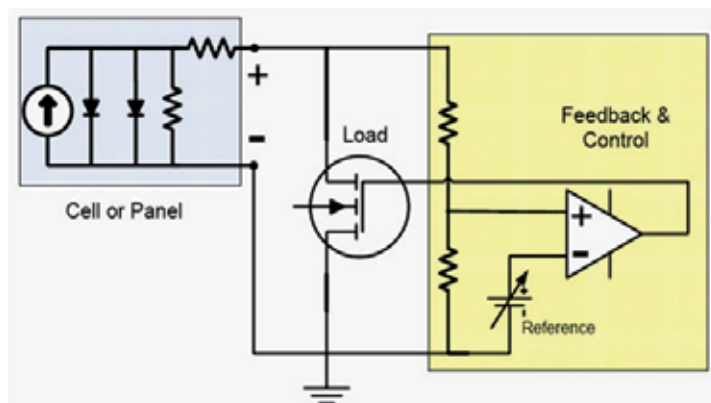
Fig. 9. The proposed continuous electronic load

In this equation, L is channel length, W is channel width, $\varepsilon$ is electric permittivity, $\mu$ is electron mobility and $t_{ox}$ is oxide thickness in the MOSFET. Implementation of this method is much quicker and easier than the previous one, and doesn't induce any switching noise in the measurement system. Simulation results and the measured data for the proposed electronic load (continuous method) are performed by Orcad/Pspice 9.2. The simulation result and experimental data are shown in Fig. 10. We observed that the simulation result and experimental data have similar electrical behavior. Their difference between curves was raised because of error in measurement and inequality real components with components in the simulation program. Anyway, the proposed electronic load (continuous method) was suitable for our purpose.
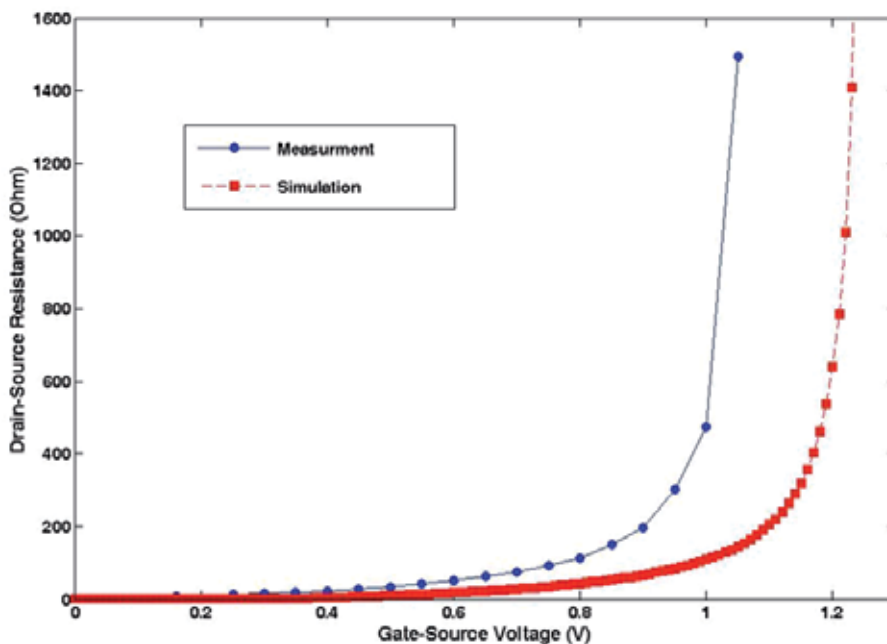


Fig. 10. Experimental data and simulation results of continuous electronic load profile

The schematic diagram of the implemented continuous electronic load is shown in Fig. 11.
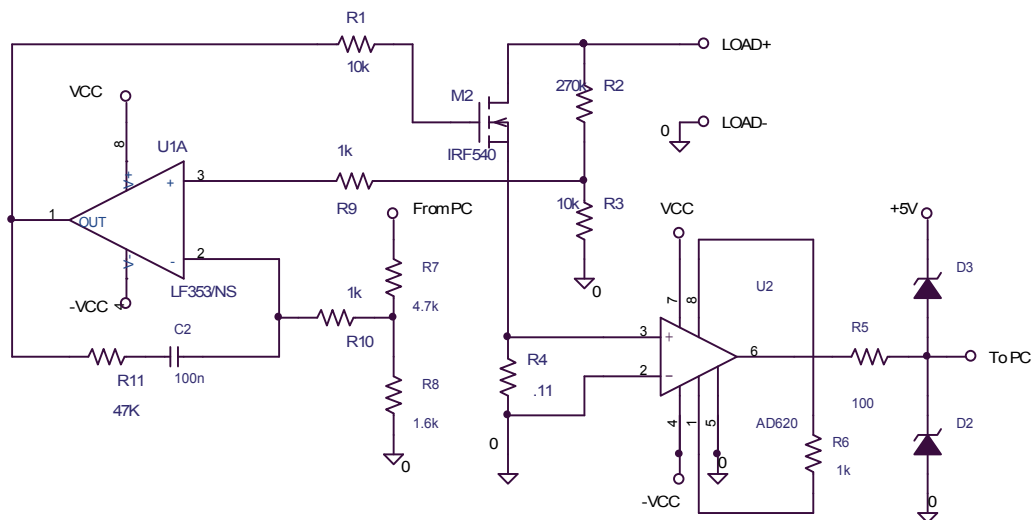


Fig. 11. The schematic diagram of continuous electronic load

Fig. 12 shows a typical extracted I-V and P-V curves by this method in the following conditions; irradiance = 500 w/m² and temperature = 34.5 °C. It is observed that the proposed electronic load could be suitable to extract the solar panel's I-V curves.
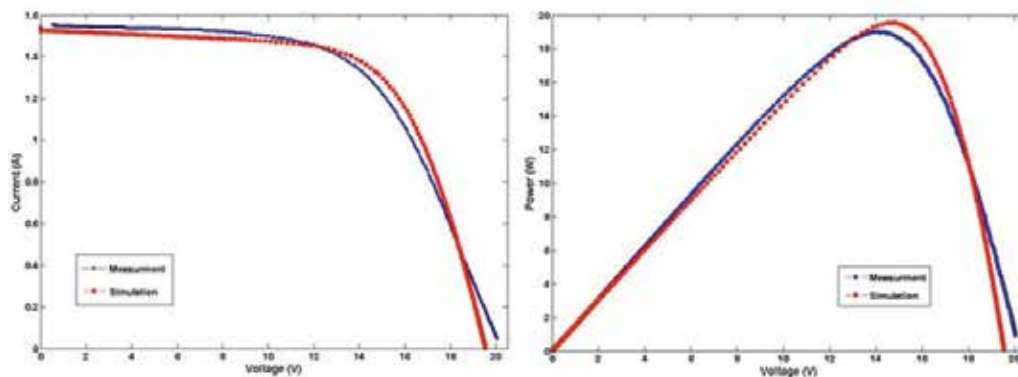


Fig. 12. A typical extracted solar panel's I-V curve

## 4. The extracted models unknown parameters

The Newton method is chosen to solve the nonlinear equations. A modification is also reported in the Newton's solving approach to attain the best convergence. MATLAB software environment is used to implement the nonlinear equations and their solving method. At first, the main electrical characteristics $(I_{sc}, V_{oc}, V_{mp} \& I_{mp})$ are extracted for all I-V curves of the solar panel (extracted by the measurement system) which Table 2 shows them. The main electrical characteristics of the solar panel are used in nonlinear equations models.

| The I-V Curves | Environmental Conditions | | $V_{oc}$ (V) | $I_{sc}$ (A) | $V_{mp}$ (V) | $I_{mp}$ (A) |
| --- | --- | --- | --- | --- | --- | --- |
| | Irradiance (W/m²) | Temperature (°C) | | | | |
| 1 | 644.30 | 22.95 | 20.58 | 1.90 | 15.55 | 1.67 |
| 2 | 657.70 | 24.00 | 20.53 | 1.94 | 15.52 | 1.70 |
| 3 | 662.18 | 24.50 | 20.50 | 1.95 | 15.55 | 1.70 |
| 4 | 665.16 | 25.20 | 20.50 | 1.97 | 15.60 | 1.71 |
| 5 | 668.85 | 25.20 | 20.50 | 1.98 | 15.40 | 1.74 |
| 6 | 456.36 | 15.20 | 21.10 | 1.35 | 16.43 | 1.21 |
| 7 | 467.55 | 14.50 | 21.15 | 1.39 | 16.50 | 1.22 |
| 8 | 478.00 | 14.15 | 21.15 | 1.43 | 16.50 | 1.24 |
| 9 | 558.50 | 17.80 | 21.00 | 1.63 | 16.14 | 1.47 |
| 10 | 529.50 | 17.90 | 20.90 | 1.57 | 16.17 | 1.38 |
| 11 | 575.00 | 17.40 | 20.90 | 1.70 | 16.10 | 1.49 |
| 12 | 601.00 | 18.10 | 20.90 | 1.77 | 16.00 | 1.55 |
| 13 | 605.50 | 18.45 | 20.90 | 1.78 | 16.10 | 1.56 |
| 14 | 474.25 | 13.65 | 21.00 | 1.38 | 16.40 | 1.22 |
| 15 | 495.15 | 14.20 | 21.00 | 1.45 | 16.30 | 1.27 |
| 16 | 528.00 | 18.30 | 20.60 | 1.53 | 16.00 | 1.34 |
| 17 | 528.00 | 18.45 | 20.60 | 1.54 | 15.95 | 1.36 |
| 18 | 537.00 | 18.30 | 20.58 | 1.56 | 15.86 | 1.37 |
| 19 | 557.80 | 21.00 | 20.28 | 1.61 | 15.35 | 1.44 |
| 20 | 548.80 | 22.00 | 20.25 | 1.59 | 15.47 | 1.40 |
| 21 | 524.25 | 21.5 | 20.22 | 1.51 | 15.50 | 1.36 |
| 22 | 517.50 | 20.65 | 20.19 | 1.47 | 15.47 | 1.31 |
| 23 | 533.15 | 19.85 | 20.45 | 1.53 | 15.92 | 1.39 |
| 24 | 946.25 | 40.85 | 18.95 | 2.65 | 13.00 | 2.29 |
| 25 | 945.50 | 42.90 | 18.93 | 2.64 | 12.91 | 2.30 |
| 26 | 778.50 | 33.40 | 20.30 | 2.26 | 14.60 | 1.97 |
| 27 | 762.30 | 33.15 | 20.22 | 2.22 | 14.70 | 1.94 |
| 28 | 789.00 | 34.15 | 20.22 | 2.28 | 14.48 | 2.03 |
| 29 | 782.25 | 33.80 | 20.27 | 2.27 | 14.60 | 2.01 |
| 30 | 391.20 | 41.80 | 18.34 | 1.43 | 13.67 | 1.26 |
| 31 | 914.95 | 21.95 | 20.50 | 2.56 | 14.76 | 2.21 |
| 32 | 917.95 | 23.85 | 20.30 | 2.58 | 14.42 | 2.25 |
| 33 | 923.20 | 27.00 | 20.00 | 2.60 | 14.15 | 2.25 |
| 34 | 1004.50 | 34.60 | 19.10 | 2.82 | 13.00 | 2.42 |
| 35 | 1004.50 | 35.15 | 19.07 | 2.83 | 12.91 | 2.43 |
| 36 | 994.75 | 34.25 | 19.04 | 2.80 | 13.08 | 2.39 |
| 37 | 900.80 | 34.90 | 18.98 | 2.62 | 13.05 | 2.26 |
| 38 | 899.30 | 35.55 | 18.98 | 2.63 | 13.33 | 2.22 |
| 39 | 808.30 | 36.40 | 18.84 | 2.45 | 13.16 | 2.11 |
| 40 | 811.30 | 36.80 | 18.84 | 2.47 | 13.08 | 2.13 |
| 41 | 630.90 | 36.10 | 18.73 | 2.13 | 13.36 | 1.85 |

| The I-V Curves | Environmental Conditions | | $V_{oc}$ (V) | $I_{sc}$ (A) | $V_{mp}$ (V) | $I_{mp}$ (A) |
| | Irradiance (W/m²) | Temperature (°C) | | | | |
|---|---|---|---|---|---|---|
| 42 | 633.85 | 36.20 | 18.79 | 2.13 | 13.39 | 1.85 |
| 43 | 637.55 | 35.85 | 18.84 | 2.14 | 13.44 | 1.86 |
| 44 | 406.40 | 34.10 | 18.70 | 1.59 | 13.81 | 1.40 |
| 45 | 412.35 | 33.00 | 18.87 | 1.61 | 14.10 | 1.40 |
| 46 | 1006.70 | 33.05 | 19.46 | 2.82 | 13.30 | 2.43 |
| 47 | 1014.20 | 33.20 | 19.38 | 2.85 | 13.22 | 2.45 |
| 48 | 1014.90 | 33.95 | 19.32 | 2.86 | 13.19 | 2.45 |
| 49 | 599.50 | 44.10 | 17.86 | 2.00 | 12.54 | 1.73 |
| 50 | 756.85 | 50.55 | 17.92 | 2.23 | 12.63 | 1.86 |
| 51 | 776.20 | 50.35 | 17.97 | 2.29 | 12.37 | 1.94 |
| 52 | 759.90 | 50.10 | 18.06 | 2.32 | 12.54 | 1.93 |
| 53 | 769.55 | 49.55 | 18.11 | 2.33 | 12.71 | 1.96 |
| 54 | 590.60 | 48.20 | 18.00 | 1.93 | 12.94 | 1.64 |
| 55 | 392.25 | 45.35 | 17.94 | 1.45 | 13.28 | 1.27 |
| 56 | 701.00 | 36.40 | 19.13 | 2.17 | 13.75 | 1.88 |
| 57 | 822.55 | 36.55 | 19.21 | 2.41 | 13.53 | 2.09 |
| 58 | 815.00 | 36.25 | 19.21 | 2.39 | 13.44 | 2.07 |
| 59 | 937.35 | 35.90 | 19.35 | 2.61 | 13.36 | 2.27 |
| 60 | 948.10 | 35.40 | 19.43 | 2.61 | 13.73 | 2.24 |
| 61 | 458.65 | 37.40 | 19.60 | 1.72 | 14.60 | 1.52 |
| 62 | 455.65 | 37.60 | 19.58 | 1.72 | 14.43 | 1.53 |
| 63 | 602.50 | 38.40 | 19.63 | 1.99 | 14.34 | 1.75 |
| 64 | 706.90 | 38.45 | 19.66 | 2.17 | 14.20 | 1.90 |
| 65 | 705.40 | 36.60 | 19.69 | 2.16 | 14.32 | 1.89 |
| 66 | 703.90 | 38.70 | 19.66 | 2.16 | 14.37 | 1.87 |
| 67 | 780.75 | 37.00 | 19.86 | 2.27 | 14.43 | 1.96 |
| 68 | 777.75 | 36.40 | 19.91 | 2.25 | 14.32 | 1.98 |
| 69 | 777.00 | 35.80 | 19.97 | 2.24 | 14.57 | 1.95 |
| 70 | 886.60 | 44.45 | 19.38 | 2.52 | 13.84 | 2.14 |
| 71 | 879.15 | 44.25 | 19.41 | 2.43 | 13.75 | 2.12 |
| 72 | 830.70 | 40.05 | 19.58 | 2.41 | 14.03 | 2.10 |
| 73 | 818.80 | 40.30 | 19.60 | 2.40 | 14.06 | 2.07 |
| 74 | 749.45 | 38.95 | 19.66 | 2.26 | 14.12 | 1.99 |
| 75 | 746.45 | 38.70 | 19.69 | 2.26 | 14.23 | 1.98 |
| 76 | 604.75 | 45.95 | 17.75 | 2.00 | 12.49 | 1.73 |
| 77 | 987.30 | 48.80 | 17.89 | 2.71 | 11.93 | 2.3 |
| 78 | 981.05 | 50.00 | 17.83 | 2.68 | 12.09 | 2.23 |
| 79 | 519.00 | 33.70 | 19.29 | 1.79 | 14.09 | 1.59 |
| 80 | 516.00 | 34.90 | 19.24 | 1.79 | 14.29 | 1.56 |
| 81 | 615.95 | 36.35 | 19.10 | 2.00 | 13.95 | 1.74 |
| 82 | 615.20 | 36.50 | 19.07 | 2.00 | 13.81 | 1.74 |

| The I-V Curves | Environmental Conditions | | $V_{oc}$ (V) | $I_{sc}$ (A) | $V_{mp}$ (V) | $I_{mp}$ (A) |
| | Irradiance (W/m²) | Temperature (°C) | | | | |
|---|---|---|---|---|---|---|
| 83 | 648.75 | 37.90 | 19.38 | 2.08 | 14.23 | 1.79 |
| 84 | 778.50 | 35.70 | 19.80 | 2.37 | 14.46 | 2.02 |
| 85 | 836.70 | 25.00 | 20.78 | 2.4 | 15.16 | 2.12 |
| 86 | 850.10 | 25.40 | 20.78 | 2.45 | 15.24 | 2.13 |
| 87 | 839.65 | 23.15 | 20.90 | 2.43 | 15.22 | 2.14 |
| 88 | 838.16 | 23.05 | 20.90 | 2.42 | 15.22 | 2.14 |
| 89 | 844.15 | 23.35 | 20.90 | 2.43 | 15.22 | 2.14 |
| 90 | 781.50 | 20.80 | 21.07 | 2.24 | 15.55 | 2.00 |
| 91 | 775.50 | 20.45 | 21.07 | 2.23 | 15.75 | 1.96 |
| 92 | 612.25 | 15.55 | 21.43 | 1.78 | 16.54 | 1.57 |
| 93 | 609.25 | 15.00 | 21.46 | 1.77 | 16.48 | 1.57 |
| 94 | 601.75 | 14.75 | 21.46 | 1.75 | 16.68 | 1.55 |
| 95 | 240.85 | 31.40 | 18.59 | 1.08 | 14.46 | 0.93 |
| 96 | 241.60 | 31.65 | 18.48 | 1.08 | 14.26 | 0.94 |
| 97 | 876.20 | 35.40 | 19.13 | 2.42 | 13.53 | 2.08 |
| 98 | 873.25 | 36.45 | 19.13 | 2.40 | 13.56 | 2.06 |
| 99 | 453.40 | 34.10 | 18.90 | 1.64 | 14.03 | 1.44 |
| 100 | 617.40 | 38.50 | 19.60 | 2.00 | 14.54 | 1.74 |
| 101 | 620.40 | 37.40 | 19.60 | 2.00 | 14.43 | 1.75 |
| 102 | 453.40 | 37.00 | 19.35 | 1.64 | 14.63 | 1.48 |
| 103 | 678.60 | 14.75 | 21.54 | 1.91 | 16.26 | 1.70 |
| 104 | 718.10 | 13.15 | 21.71 | 2.05 | 16.43 | 1.83 |
| 105 | 615.20 | 33.10 | 19.77 | 2.09 | 14.48 | 1.79 |
| 106 | 589.10 | 33.55 | 19.72 | 1.95 | 14.63 | 1.70 |
| 107 | 649.50 | 37.85 | 19.35 | 2.09 | 13.92 | 1.83 |
| 108 | 648.05 | 37.90 | 18.79 | 2.08 | 13.42 | 1.82 |
| 109 | 653.95 | 38.15 | 18.76 | 2.08 | 13.33 | 1.83 |
| 110 | 665.20 | 39.20 | 18.73 | 2.13 | 13.19 | 1.87 |
| 111 | 947.05 | 42.55 | 18.90 | 2.65 | 13.02 | 2.28 |
| 112 | 454.90 | 37.75 | 18.73 | 1.64 | 13.84 | 1.44 |
| 113 | 458.65 | 36.10 | 18.68 | 1.64 | 13.92 | 1.42 |

Table 2. The main electrical characteristic of the panel

Then, the five and the seven nonlinear equations of the models are implemented and the nonlinear least square approach is used to solve them. Tables 3 and 4 show the extracted unknown parameters of the models for environmental conditions.

| | Irradiance (W/m²) | Temperature (°C) | $I_{ph}$ (A) | $I_0$ (A) | a | Rs(Ω) | Rp(Ω) |
|---|---|---|---|---|---|---|---|
| 1 | 644.30 | 22.95 | 1.9054 | $1.3645 \times 10^{-7}$ | 1.2544 | 1.2078 | 279.6413 |
| 2 | 657.70 | 24.00 | 1.9406 | $2.0381 \times 10^{-7}$ | 1.2807 | 1.1805 | 287.2463 |
| 3 | 662.18 | 24.50 | 1.9579 | $1.0977 \times 10^{-7}$ | 1.2311 | 1.2276 | 252.0760 |

| | Irradiance (W/m²) | Temperature (°C) | $I_{ph}$ (A) | $I_0$ (A) | a | Rs(Ω) | Rp(Ω) |
|---|---|---|---|---|---|---|---|
| 4 | 665.16 | 25.20 | 1.9738 | $9.0465 \times 10^{-8}$ | 1.2164 | 1.2520 | 255.1335 |
| 5 | 668.85 | 25.20 | 1.9776 | $1.4502 \times 10^{-7}$ | 1.2513 | 1.2238 | 253.4728 |
| 6 | 456.36 | 15.20 | 1.3443 | $2.0084 \times 10^{-7}$ | 1.3468 | 1.0289 | 475.3187 |
| 7 | 467.55 | 14.50 | 1.3822 | $5.7962 \times 10^{-8}$ | 1.2489 | 1.1676 | 303.7811 |
| 8 | 478.00 | 14.15 | 1.4235 | $5.2113 \times 10^{-8}$ | 1.2401 | 1.1492 | 228.1600 |
| 9 | 558.50 | 17.80 | 1.6448 | $1.6758 \times 10^{-7}$ | 1.3089 | 1.1391 | 488.4681 |
| 10 | 529.50 | 17.90 | 1.5640 | $1.3622 \times 10^{-7}$ | 1.2908 | 1.1252 | 305.8098 |
| 11 | 575.00 | 17.40 | 1.6993 | $1.4140 \times 10^{-7}$ | 1.2872 | 1.1635 | 280.1520 |
| 12 | 601.00 | 18.10 | 1.7753 | $1.0810 \times 10^{-7}$ | 1.2614 | 1.1667 | 252.2827 |
| 13 | 605.50 | 18.45 | 1.7854 | $1.8325 \times 10^{-7}$ | 1.3034 | 1.1494 | 313.9411 |
| 14 | 474.25 | 13.65 | 1.3814 | $2.0780 \times 10^{-7}$ | 1.3435 | 0.9994 | 307.3284 |
| 15 | 495.15 | 14.20 | 1.4413 | $2.1472 \times 10^{-7}$ | 1.3430 | 1.0062 | 275.3528 |
| 16 | 528.00 | 18.30 | 1.5321 | $2.1087 \times 10^{-7}$ | 1.3087 | 1.0844 | 307.3237 |
| 17 | 528.00 | 18.45 | 1.54442 | $1.8252 \times 10^{-7}$ | 1.2961 | 1.1175 | 303.6138 |
| 18 | 537.00 | 18.30 | 1.5615 | $9.6833 \times 10^{-8}$ | 1.2447 | 1.1485 | 245.5091 |
| 19 | 557.80 | 21.00 | 1.6145 | $3.2875 \times 10^{-7}$ | 1.3193 | 1.1212 | 354.5386 |
| 20 | 548.80 | 22.00 | 1.5919 | $2.1440 \times 10^{-7}$ | 1.2835 | 1.1649 | 305.2178 |
| 21 | 524.25 | 21.50 | 1.5309 | $5.5771 \times 10^{-7}$ | 1.3667 | 1.0884 | 474.5784 |
| 22 | 517.50 | 20.65 | 1.4714 | $3.9398 \times 10^{-7}$ | 1.3375 | 1.0842 | 405.6716 |
| 23 | 533.15 | 19.85 | 1.5753 | $2.1603 \times 10^{-7}$ | 1.2953 | 1.1464 | 805.5353 |
| 24 | 946.25 | 40.85 | 2.6666 | $8.9271 \times 10^{-7}$ | 1.2757 | 1.3558 | 146.2230 |
| 25 | 945.50 | 42.90 | 2.6574 | $1.2424 \times 10^{-6}$ | 1.3030 | 1.3219 | 150.3004 |
| 26 | 778.50 | 33.40 | 2.1973 | $3.1128 \times 10^{-7}$ | 1.2892 | 1.2567 | 515.2084 |
| 27 | 762.30 | 33.15 | 2.2171 | $5.3812 \times 10^{-7}$ | 1.3316 | 1.1894 | 210.1448 |
| 28 | 789.00 | 34.15 | 2.2886 | $3.9798 \times 10^{-7}$ | 1.3028 | 1.2315 | 214.3753 |
| 29 | 782.25 | 33.80 | 2.2765 | $5.0119 \times 10^{-7}$ | 1.3266 | 1.1978 | 212.4934 |
| 30 | 391.20 | 41.80 | 1.4409 | $2.2284 \times 10^{-6}$ | 1.3744 | 1.2030 | 357.0918 |
| 31 | 914.95 | 21.95 | 2.5657 | $2.9407 \times 10^{-7}$ | 1.2866 | 1.2771 | 178.6504 |
| 32 | 917.95 | 23.85 | 2.5853 | $4.0314 \times 10^{-7}$ | 1.2993 | 1.2704 | 179.9606 |
| 33 | 923.20 | 27.00 | 2.6220 | $5.5929 \times 10^{-7}$ | 1.3065 | 1.2800 | 142.9452 |
| 34 | 1004.50 | 34.60 | 2.8279 | $1.2215 \times 10^{-6}$ | 1.3071 | 1.3467 | 155.7048 |
| 35 | 1004.50 | 35.15 | 2.8362 | $1.5357 \times 10^{-6}$ | 1.3258 | 1.3260 | 151.6557 |
| 36 | 994.75 | 34.25 | 2.8140 | $1.2354 \times 10^{-6}$ | 1.3051 | 1.3258 | 141.9868 |
| 37 | 900.80 | 34.90 | 2.6385 | $2.1545 \times 10^{-6}$ | 1.3585 | 1.3032 | 170.0669 |
| 38 | 899.30 | 35.55 | 2.6449 | $1.5551 \times 10^{-6}$ | 1.3278 | 1.3082 | 152.1797 |
| 39 | 808.30 | 36.40 | 2.4663 | $1.5142 \times 10^{-6}$ | 1.3214 | 1.3244 | 186.9949 |
| 40 | 811.30 | 36.80 | 2.4866 | $8.9032 \times 10^{-7}$ | 1.2740 | 1.3574 | 152.6324 |
| 41 | 630.90 | 36.10 | 2.1335 | $7.5213 \times 10^{-7}$ | 1.2650 | 1.3213 | 179.3817 |
| 42 | 633.85 | 36.20 | 2.1493 | $1.4614 \times 10^{-6}$ | 1.3279 | 1.2659 | 172.9979 |
| 43 | 637.55 | 35.85 | 2.1526 | $1.3956 \times 10^{-6}$ | 1.3272 | 1.2720 | 181.0577 |
| 44 | 406.40 | 34.10 | 1.5971 | $1.7433 \times 10^{-6}$ | 1.3672 | 1.1656 | 253.3236 |
| 45 | 412.35 | 33.00 | 1.6220 | $1.0427 \times 10^{-6}$ | 1.3288 | 1.1815 | 221.4351 |

| | Irradiance (W/m²) | Temperature (°C) | $I_{ph}$ (A) | $I_0$ (A) | a | Rs(Ω) | Rp(Ω) |
|---|---|---|---|---|---|---|---|
| 46 | 1006.70 | 33.05 | 2.8445 | $7.7494 \times 10^{-7}$ | 1.2922 | 1.3580 | 132.0408 |
| 47 | 1014.20 | 33.20 | 2.8548 | $9.1903 \times 10^{-7}$ | 1.3001 | 1.3490 | 162.1626 |
| 48 | 1014.90 | 33.95 | 2.8757 | $7.7393 \times 10^{-7}$ | 1.2816 | 1.3650 | 135.7198 |
| 49 | 599.50 | 44.10 | 2.0093 | $3.2553 \times 10^{-6}$ | 1.3443 | 1.3202 | 193.5047 |
| 50 | 756.85 | 50.55 | 2.2630 | $2.0566 \times 10^{-6}$ | 1.2958 | 1.3584 | 98.4074 |
| 51 | 776.20 | 50.35 | 2.3183 | $9.4350 \times 10^{-6}$ | 1.4552 | 1.3151 | 131.0878 |
| 52 | 759.90 | 50.10 | 2.3446 | $1.3496 \times 10^{-6}$ | 1.2650 | 1.4109 | 86.7692 |
| 53 | 769.55 | 49.55 | 2.3492 | $3.1359 \times 10^{-6}$ | 1.3436 | 1.3764 | 173.6641 |
| 54 | 590.60 | 48.20 | 1.9461 | $1.7518 \times 10^{-6}$ | 1.2990 | 1.3753 | 152.9589 |
| 55 | 392.25 | 45.35 | 1.4551 | $7.3811 \times 10^{-6}$ | 1.4749 | 1.1449 | 513.8872 |
| 56 | 701.00 | 36.40 | 2.1809 | $6.3023 \times 10^{-7}$ | 1.2744 | 1.3197 | 181.3692 |
| 57 | 822.55 | 36.55 | 2.4333 | $1.4581 \times 10^{-6}$ | 1.3457 | 1.2695 | 154.6094 |
| 58 | 815.00 | 36.25 | 2.3989 | $8.6293 \times 10^{-7}$ | 1.2995 | 1.3051 | 148.3509 |
| 59 | 937.35 | 35.90 | 2.6353 | $7.8507 \times 10^{-7}$ | 1.2924 | 1.3333 | 140.9158 |
| 60 | 948.10 | 35.40 | 2.6281 | $6.5875 \times 10^{-7}$ | 1.2819 | 1.3362 | 198.5875 |
| 61 | 458.65 | 37.40 | 1.7341 | $2.3307 \times 10^{-7}$ | 1.2435 | 1.2222 | 202.9395 |
| 62 | 455.65 | 37.60 | 1.7262 | $2.9317 \times 10^{-7}$ | 1.2605 | 1.2122 | 202.2739 |
| 63 | 602.50 | 38.40 | 2.0061 | $2.2729 \times 10^{-7}$ | 1.2318 | 1.2910 | 179.7304 |
| 64 | 706.90 | 38.45 | 2.1841 | $6.2885 \times 10^{-7}$ | 1.3100 | 1.2227 | 176.9047 |
| 65 | 705.40 | 36.60 | 2.1762 | $3.4172 \times 10^{-7}$ | 1.2607 | 1.2898 | 185.8031 |
| 66 | 703.90 | 38.70 | 2.1727 | $4.4171 \times 10^{-7}$ | 1.2803 | 1.2778 | 178.6681 |
| 67 | 780.75 | 37.00 | 2.2865 | $2.7213 \times 10^{-7}$ | 1.2499 | 1.2911 | 155.5827 |
| 68 | 777.75 | 36.40 | 2.2661 | $6.4822 \times 10^{-7}$ | 1.3257 | 1.2351 | 196.1866 |
| 69 | 777.00 | 35.80 | 2.2597 | $3.5896 \times 10^{-7}$ | 1.2797 | 1.2661 | 180.5390 |
| 70 | 886.60 | 44.45 | 2.4968 | $5.9216 \times 10^{-7}$ | 1.2747 | 1.2546 | 153.3574 |
| 71 | 879.15 | 44.25 | 2.4217 | $1.7378 \times 10^{-6}$ | 1.3740 | 1.2205 | 360.6990 |
| 72 | 830.70 | 40.05 | 2.4218 | $6.8898 \times 10^{-7}$ | 1.3016 | 1.2563 | 247.4058 |
| 73 | 818.80 | 40.30 | 2.4188 | $7.9099 \times 10^{-7}$ | 1.3181 | 1.2113 | 137.7473 |
| 74 | 749.45 | 38.95 | 2.2718 | $6.9207 \times 10^{-7}$ | 1.3136 | 1.2329 | 232.5429 |
| 75 | 746.45 | 38.70 | 2.2801 | $5.1192 \times 10^{-7}$ | 1.2905 | 1.2244 | 168.6507 |
| 76 | 604.75 | 45.95 | 2.0164 | $1.5572 \times 10^{-6}$ | 1.2660 | 1.3880 | 165.8156 |
| 77 | 987.30 | 48.80 | 2.7459 | $3.1186 \times 10^{-6}$ | 1.3124 | 1.4018 | 115.7579 |
| 78 | 981.05 | 50.00 | 2.7064 | $4.3017 \times 10^{-6}$ | 1.3400 | 1.4091 | 151.9670 |
| 79 | 519.00 | 33.70 | 1.7947 | $5.8455 \times 10^{-7}$ | 1.2951 | 1.2475 | 281.8090 |
| 80 | 516.00 | 34.90 | 1.8017 | $4.0818 \times 10^{-7}$ | 1.2618 | 1.2594 | 205.2749 |
| 81 | 615.95 | 36.35 | 2.0075 | $6.1718 \times 10^{-7}$ | 1.2774 | 1.2940 | 218.7826 |
| 82 | 615.20 | 36.50 | 2.0152 | $4.5464 \times 10^{-7}$ | 1.2507 | 1.3113 | 168.6899 |
| 83 | 648.75 | 37.90 | 2.0960 | $4.6946 \times 10^{-7}$ | 1.2710 | 1.2501 | 148.6441 |
| 84 | 778.50 | 35.70 | 2.3769 | $3.8760 \times 10^{-7}$ | 1.2713 | 1.2666 | 160.5721 |
| 85 | 836.70 | 25.00 | 2.4144 | $2.1683 \times 10^{-7}$ | 1.2840 | 1.2112 | 228.6814 |
| 86 | 850.10 | 25.40 | 2.4656 | $1.6939 \times 10^{-7}$ | 1.2639 | 1.2282 | 180.5302 |
| 87 | 839.65 | 23.15 | 2.4409 | $2.2484 \times 10^{-7}$ | 1.2938 | 1.1793 | 183.7797 |

Evaluation the Accuracy of One-Diode and Two-Diode
Models for a Solar Panel Based Open-Air Climate Measurements
217

| | Irradiance (W/m²) | Temperature (°C) | $I_{ph}$ (A) | $I_0$ (A) | a | Rs(Ω) | Rp(Ω) |
|---|---|---|---|---|---|---|---|
| 88 | 838.16 | 23.05 | 2.4333 | $1.6491×10^{-7}$ | 1.2697 | 1.1971 | 181.9877 |
| 89 | 844.15 | 23.35 | 2.4391 | $1.0187×10^{-7}$ | 1.2337 | 1.2319 | 168.4823 |
| 90 | 781.50 | 20.80 | 2.2502 | $2.4789×10^{-7}$ | 1.3180 | 1.1315 | 249.5637 |
| 91 | 775.50 | 20.45 | 2.2299 | $1.8167×10^{-7}$ | 1.2934 | 1.1539 | 269.1192 |
| 92 | 612.25 | 15.55 | 1.7732 | $1.1189×10^{-7}$ | 1.2958 | 1.0877 | 317.2956 |
| 93 | 609.25 | 15.00 | 1.7761 | $2.6497×10^{-8}$ | 1.1944 | 1.1797 | 232.1886 |
| 94 | 601.75 | 14.75 | 1.7631 | $5.0466×10^{-8}$ | 1.2390 | 1.1252 | 252.8796 |
| 95 | 240.85 | 31.40 | 1.0841 | $2.8277×10^{-6}$ | 1.4522 | 0.8406 | 328.3110 |
| 96 | 241.60 | 31.65 | 1.0842 | $2.9811×10^{-6}$ | 1.4494 | 0.8720 | 323.0246 |
| 97 | 876.20 | 35.40 | 2.4382 | $5.6696×10^{-7}$ | 1.2564 | 1.3492 | 157.0273 |
| 98 | 873.25 | 36.45 | 2.4151 | $1.3653×10^{-6}$ | 1.3337 | 1.3058 | 180.0039 |
| 99 | 453.40 | 34.10 | 1.6490 | $1.1006×10^{-6}$ | 1.3337 | 1.1999 | 245.1651 |
| 100 | 617.40 | 38.50 | 2.0113 | $3.5727×10^{-7}$ | 1.2650 | 1.2431 | 213.8478 |
| 101 | 620.40 | 37.40 | 2.0119 | $4.5098×10^{-7}$ | 1.2847 | 1.2074 | 196.3093 |
| 102 | 453.40 | 37.00 | 1.6437 | $1.0425×10^{-6}$ | 1.3602 | 1.1132 | 275.7352 |
| 103 | 678.60 | 14.75 | 1.8721 | $1.7176×10^{-7}$ | 1.3306 | 1.1480 | 837.2890 |
| 104 | 718.10 | 13.15 | 2.0527 | $7.0015×10^{-8}$ | 1.2647 | 1.2034 | 427.2372 |
| 105 | 615.20 | 33.10 | 2.0934 | $1.15866×10^{-7}$ | 1.2124 | 1.2524 | 113.7532 |
| 106 | 589.10 | 33.55 | 1.9420 | $3.2678×10^{-7}$ | 1.2673 | 1.2389 | 257.1990 |
| 107 | 649.50 | 37.85 | 2.1063 | $6.5590×10^{-7}$ | 1.2966 | 1.2533 | 163.5833 |
| 108 | 648.05 | 37.90 | 2.0915 | $1.5511×10^{-6}$ | 1.3355 | 1.2439 | 198.8860 |
| 109 | 653.95 | 38.15 | 2.0951 | $1.2615×10^{-6}$ | 1.3138 | 1.2757 | 209.6240 |
| 110 | 665.20 | 39.20 | 2.1463 | $1.0031×10^{-6}$ | 1.2899 | 1.3034 | 166.9648 |
| 111 | 947.05 | 42.55 | 2.6799 | $1.6611×10^{-6}$ | 1.3274 | 1.3070 | 133.4828 |
| 112 | 454.90 | 37.75 | 1.6428 | $2.2538×10^{-6}$ | 1.3913 | 1.1596 | 331.7340 |
| 113 | 458.65 | 36.10 | 1.6525 | $2.1133×10^{-6}$ | 1.3810 | 1.1576 | 251.5761 |

Table 3. One-diode model parameters in different environmental conditions

| | Irradiance (W/m²) | Temperature (°C) | $I_{ph}$ (A) | $I_{01}$ (A) | $a_1$ | $I_{02}$ (A) | $a_2$ | Rs (Ω) | Rp(Ω) |
|---|---|---|---|---|---|---|---|---|---|
| 1 | 644.30 | 22.95 | 1.9043 | $3.0432×10^{-8}$ | 1.1883 | $1.3697×10^{-7}$ | 1.3197 | 1.2341 | 294.5317 |
| 2 | 657.70 | 24.00 | 1.9446 | $2.0588×10^{-8}$ | 1.1240 | $2.0918×10^{-7}$ | 1.5696 | 1.3141 | 254.2053 |
| 3 | 662.18 | 24.50 | 1.9536 | $1.3177×10^{-7}$ | 1.3606 | $4.0695×10^{-7}$ | 1.3606 | 1.1380 | 318.7178 |
| 4 | 665.16 | 25.20 | 1.9729 | $2.9981×10^{-8}$ | 1.1706 | $1.7914×10^{-7}$ | 1.3537 | 1.2339 | 248.5131 |
| 5 | 668.85 | 25.20 | 1.9745 | $2.8887×10^{-8}$ | 1.2215 | $2.0565×10^{-7}$ | 1.3069 | 1.2181 | 281.0450 |
| 6 | 456.36 | 15.20 | 1.3453 | $2.4504×10^{-8}$ | 1.2271 | $2.6436×10^{-7}$ | 1.4485 | 1.0603 | 474.6605 |
| 7 | 467.55 | 14.50 | 1.3809 | $2.7889×10^{-8}$ | 1.2443 | $1.4274×10^{-7}$ | 1.3800 | 1.1122 | 340.2013 |
| 8 | 478.00 | 14.15 | 1.4212 | $2.7554×10^{-8}$ | 1.2449 | $1.6846×10^{-7}$ | 1.3907 | 1.0636 | 250.2702 |
| 9 | 558.50 | 17.80 | 1.6464 | $2.9720×10^{-8}$ | 1.2208 | $1.6773×10^{-7}$ | 1.3810 | 1.1662 | 443.9569 |
| 10 | 529.50 | 17.90 | 1.5654 | $3.4963×10^{-9}$ | 1.0648 | $7.7917×10^{-7}$ | 1.6272 | 1.2959 | 306.1568 |
| 11 | 575.00 | 17.40 | 1.7003 | $2.2433×10^{-8}$ | 1.1666 | $2.1302×10^{-7}$ | 1.5016 | 1.2351 | 268.6247 |
| 12 | 601.00 | 18.10 | 1.7728 | $2.8641×10^{-8}$ | 1.2150 | $1.8419×10^{-7}$ | 1.3616 | 1.1607 | 275.4929 |

|  | Irradiance (W/m²) | Temperature (°C) | $I_{ph}$ (A) | $I_{01}$ (A) | $a_1$ | $I_{02}$ (A) | $a_2$ | Rs (Ω) | Rp(Ω) |
|---|---|---|---|---|---|---|---|---|---|
| 13 | 605.50 | 18.45 | 1.7850 | $2.5508 \times 10^{-8}$ | 1.1760 | $1.8028 \times 10^{-7}$ | 1.4433 | 1.2442 | 316.8041 |
| 14 | 474.25 | 13.65 | 1.3797 | $3.0408 \times 10^{-8}$ | 1.3842 | $2.9990 \times 10^{-7}$ | 1.3846 | 0.9578 | 312.5028 |
| 15 | 495.15 | 14.20 | 1.4398 | $2.7505 \times 10^{-8}$ | 1.2616 | $1.9085 \times 10^{-7}$ | 1.3710 | 1.0181 | 268.2193 |
| 16 | 528.00 | 18.30 | 1.5321 | $2.3850 \times 10^{-8}$ | 1.1597 | $1.9136 \times 10^{-7}$ | 1.4811 | 1.2332 | 302.4667 |
| 17 | 528.00 | 18.45 | 1.5458 | $5.7239 \times 10^{-9}$ | 1.0782 | $6.9380 \times 10^{-7}$ | 1.5793 | 1.2685 | 298.4500 |
| 18 | 537.00 | 18.30 | 1.5612 | $2.8985 \times 10^{-8}$ | 1.1918 | $1.8355 \times 10^{-7}$ | 1.3790 | 1.1295 | 254.8772 |
| 19 | 557.80 | 21.00 | 1.6153 | $2.9673 \times 10^{-8}$ | 1.2465 | $2.6445 \times 10^{-7}$ | 1.3220 | 1.1547 | 356.6941 |
| 20 | 548.80 | 22.00 | 1.5912 | $2.9889 \times 10^{-8}$ | 1.1972 | $1.6498 \times 10^{-7}$ | 1.3094 | 1.1999 | 289.9760 |
| 21 | 524.25 | 21.50 | 1.5337 | $2.4210 \times 10^{-8}$ | 1.1624 | $3.3020 \times 10^{-7}$ | 1.4010 | 1.1874 | 396.9221 |
| 22 | 517.50 | 20.65 | 1.4707 | $2.9247 \times 10^{-8}$ | 1.1909 | $2.4577 \times 10^{-7}$ | 1.3534 | 1.1742 | 395.9226 |
| 23 | 533.15 | 19.85 | 1.5767 | $2.9454 \times 10^{-8}$ | 1.1883 | $1.9557 \times 10^{-7}$ | 1.3592 | 1.1708 | 611.9569 |
| 24 | 946.25 | 40.85 | 2.6531 | $2.5017 \times 10^{-6}$ | 1.4644 | $3.6255 \times 10^{-6}$ | 1.4643 | 1.2576 | 222.6724 |
| 25 | 945.50 | 42.90 | 2.6524 | $2.4917 \times 10^{-7}$ | 1.3377 | $1.5983 \times 10^{-6}$ | 1.3396 | 1.3038 | 165.3972 |
| 26 | 778.50 | 33.40 | 2.1998 | $1.1948 \times 10^{-8}$ | 1.0729 | $1.4190 \times 10^{-6}$ | 1.7427 | 1.3897 | 355.8168 |
| 27 | 762.30 | 33.15 | 2.2196 | $2.7598 \times 10^{-8}$ | 1.1455 | $2.8448 \times 10^{-7}$ | 1.3577 | 1.2938 | 200.6356 |
| 28 | 789.00 | 34.15 | 2.2859 | $2.8133 \times 10^{-8}$ | 1.2301 | $4.0767 \times 10^{-7}$ | 1.3213 | 1.2504 | 226.2728 |
| 29 | 782.25 | 33.80 | 2.2787 | $1.9512 \times 10^{-8}$ | 1.1067 | $4.2830 \times 10^{-7}$ | 1.4745 | 1.3242 | 187.2231 |
| 30 | 391.20 | 41.80 | 1.4425 | $2.5260 \times 10^{-7}$ | 1.3334 | $1.5355 \times 10^{-6}$ | 1.3554 | 1.2526 | 350.9833 |
| 31 | 914.95 | 21.95 | 2.5641 | $2.9959 \times 10^{-8}$ | 1.2141 | $2.4595 \times 10^{-7}$ | 1.2967 | 1.3091 | 195.5702 |
| 32 | 917.95 | 23.85 | 2.5827 | $5.4386 \times 10^{-8}$ | 1.3181 | $5.0320 \times 10^{-7}$ | 1.3275 | 1.2698 | 199.2378 |
| 33 | 923.20 | 27.00 | 2.6221 | $9.0452 \times 10^{-9}$ | 1.0543 | $1.2920 \times 10^{-6}$ | 1.4846 | 1.3512 | 137.6304 |
| 34 | 1004.50 | 34.60 | 2.8311 | $6.8694 \times 10^{-8}$ | 1.1262 | $9.0237 \times 10^{-7}$ | 1.3614 | 1.4110 | 152.6305 |
| 35 | 1004.50 | 35.15 | 2.8410 | $6.4888 \times 10^{-8}$ | 1.1394 | $8.3690 \times 10^{-7}$ | 1.3241 | 1.3880 | 142.3507 |
| 36 | 994.75 | 34.25 | 2.8144 | $1.1388 \times 10^{-7}$ | 1.2995 | $1.0543 \times 10^{-6}$ | 1.2999 | 1.3414 | 148.7050 |
| 37 | 900.80 | 34.90 | 2.6371 | $2.5877 \times 10^{-7}$ | 1.3474 | $1.7108 \times 10^{-6}$ | 1.3502 | 1.3179 | 171.1347 |
| 38 | 899.30 | 35.55 | 2.6451 | $7.9309 \times 10^{-8}$ | 1.2414 | $6.1660 \times 10^{-7}$ | 1.2594 | 1.3682 | 150.0456 |
| 39 | 808.30 | 36.40 | 2.4660 | $1.4170 \times 10^{-7}$ | 1.3019 | $1.1481 \times 10^{-6}$ | 1.3073 | 1.3361 | 184.8603 |
| 40 | 811.30 | 36.80 | 2.4842 | $1.8339 \times 10^{-7}$ | 1.3129 | $1.1981 \times 10^{-6}$ | 1.3128 | 1.3281 | 159.9860 |
| 41 | 630.90 | 36.10 | 2.1256 | $2.5422 \times 10^{-6}$ | 1.4743 | $3.6746 \times 10^{-6}$ | 1.4743 | 1.1656 | 248.2853 |
| 42 | 633.85 | 36.20 | 2.1413 | $2.2951 \times 10^{-6}$ | 1.4692 | $3.4374 \times 10^{-6}$ | 1.4690 | 1.1719 | 217.3854 |
| 43 | 637.55 | 35.85 | 2.1516 | $9.4216 \times 10^{-8}$ | 1.3134 | $1.1090 \times 10^{-6}$ | 1.3134 | 1.3044 | 184.2421 |
| 44 | 406.40 | 34.10 | 1.5958 | $2.9422 \times 10^{-7}$ | 1.3599 | $1.3358 \times 10^{-6}$ | 1.3611 | 1.1440 | 237.6602 |
| 45 | 412.35 | 33.00 | 1.6175 | $1.2768 \times 10^{-6}$ | 1.4603 | $2.4944 \times 10^{-6}$ | 1.4605 | 1.0597 | 258.8879 |
| 46 | 1006.70 | 33.05 | 2.8442 | $5.6206 \times 10^{-8}$ | 1.1902 | $6.3607 \times 10^{-7}$ | 1.3014 | 1.3825 | 134.8388 |
| 47 | 1014.20 | 33.20 | 2.8506 | $2.0098 \times 10^{-7}$ | 1.3564 | $1.5479 \times 10^{-6}$ | 1.3583 | 1.3247 | 197.6830 |
| 48 | 1014.90 | 33.95 | 2.8735 | $1.1218 \times 10^{-7}$ | 1.3243 | $1.1483 \times 10^{-6}$ | 1.3243 | 1.3351 | 140.4835 |
| 49 | 599.50 | 44.10 | 2.0076 | $9.6057 \times 10^{-7}$ | 1.3467 | $2.3573 \times 10^{-6}$ | 1.3467 | 1.3091 | 178.8528 |
| 50 | 756.85 | 50.55 | 2.2601 | $1.9992 \times 10^{-6}$ | 1.3906 | $3.3102 \times 10^{-6}$ | 1.3904 | 1.3121 | 108.5623 |
| 51 | 776.20 | 50.35 | 2.3243 | $6.7891 \times 10^{-7}$ | 1.3131 | $2.3084 \times 10^{-6}$ | 1.3385 | 1.4005 | 110.3408 |
| 52 | 759.90 | 50.10 | 2.3479 | $1.6993 \times 10^{-7}$ | 1.1701 | $5.8437 \times 10^{-7}$ | 1.2368 | 1.4630 | 84.6207 |
| 53 | 769.55 | 49.55 | 2.3457 | $2.2463 \times 10^{-6}$ | 1.4075 | $3.5604 \times 10^{-6}$ | 1.4074 | 1.3535 | 201.9657 |
| 54 | 590.60 | 48.20 | 1.9409 | $5.6130 \times 10^{-7}$ | 1.3287 | $1.8279 \times 10^{-6}$ | 1.3287 | 1.3952 | 158.5665 |

| | Irradiance (W/m²) | Temperature (°C) | $I_{ph}$ (A) | $I_{01}$ (A) | $a_1$ | $I_{02}$ (A) | $a_2$ | Rs (Ω) | Rp(Ω) |
|---|---|---|---|---|---|---|---|---|---|
| 55 | 392.25 | 45.35 | 1.4567 | $6.3763\times10^{-7}$ | 1.3514 | $2.1097\times10^{-6}$ | 1.3685 | 1.2832 | 449.1823 |
| 56 | 701.00 | 36.40 | 2.1796 | $5.9120\times10^{-8}$ | 1.2659 | $6.4841\times10^{-7}$ | 1.2862 | 1.3258 | 185.9257 |
| 57 | 822.55 | 36.55 | 2.4292 | $8.8912\times10^{-8}$ | 1.3149 | $9.5018\times10^{-7}$ | 1.3149 | 1.2908 | 148.4283 |
| 58 | 815.00 | 36.25 | 2.3942 | $7.8008\times10^{-8}$ | 1.3071 | $8.6383\times10^{-7}$ | 1.3071 | 1.3137 | 158.4158 |
| 59 | 937.35 | 35.90 | 2.6380 | $5.6508\times10^{-8}$ | 1.1643 | $5.8327\times10^{-7}$ | 1.3081 | 1.3438 | 125.1391 |
| 60 | 948.10 | 35.40 | 2.6253 | $7.7330\times10^{-8}$ | 1.3167 | $9.1644\times10^{-7}$ | 1.3172 | 1.3343 | 238.5130 |
| 61 | 458.65 | 37.40 | 1.7340 | $2.0356\times10^{-8}$ | 1.0972 | $4.2763\times10^{-7}$ | 1.4106 | 1.2842 | 196.2692 |
| 62 | 455.65 | 37.60 | 1.7239 | $3.0959\times10^{-8}$ | 1.1392 | $4.4560\times10^{-7}$ | 1.3674 | 1.2573 | 216.5685 |
| 63 | 602.50 | 38.40 | 2.0035 | $3.1412\times10^{-8}$ | 1.1813 | $4.8461\times10^{-7}$ | 1.3212 | 1.2244 | 180.2013 |
| 64 | 706.90 | 38.45 | 2.1800 | $5.4562\times10^{-8}$ | 1.3504 | $9.3287\times10^{-7}$ | 1.3503 | 1.2132 | 194.9991 |
| 65 | 705.40 | 36.60 | 2.1695 | $2.9715\times10^{-8}$ | 1.3401 | $8.3436\times10^{-7}$ | 1.3401 | 1.2273 | 210.6548 |
| 66 | 703.90 | 38.70 | 2.1708 | $2.9240\times10^{-8}$ | 1.3187 | $6.6092\times10^{-7}$ | 1.3187 | 1.2416 | 177.3929 |
| 67 | 780.75 | 37.00 | 2.2875 | $1.2985\times10^{-8}$ | 1.0604 | $1.8326\times10^{-6}$ | 1.6166 | 1.3705 | 151.6619 |
| 68 | 777.75 | 36.40 | 2.2669 | $7.9289\times10^{-8}$ | 1.0395 | $2.0258\times10^{-6}$ | 1.6016 | 1.3944 | 189.5926 |
| 69 | 777.00 | 35.80 | 2.2613 | $1.0495\times10^{-8}$ | 1.0530 | $2.1107\times10^{-6}$ | 1.6648 | 1.3922 | 174.3726 |
| 70 | 886.60 | 44.45 | 2.4906 | $5.3519\times10^{-8}$ | 1.1734 | $5.0326\times10^{-7}$ | 1.2961 | 1.2738 | 151.7814 |
| 71 | 879.15 | 44.25 | 2.4246 | $4.7363\times10^{-8}$ | 1.2251 | $8.2091\times10^{-7}$ | 1.3194 | 1.2895 | 317.8984 |
| 72 | 830.70 | 40.05 | 2.4173 | $2.0975\times10^{-7}$ | 1.3619 | $1.1345\times10^{-6}$ | 1.3619 | 1.2276 | 289.4507 |
| 73 | 818.80 | 40.30 | 2.4138 | $4.3268\times10^{-8}$ | 1.3130 | $7.0331\times10^{-7}$ | 1.3130 | 1.2228 | 141.9730 |
| 74 | 749.45 | 38.95 | 2.2701 | $8.8746\times10^{-8}$ | 1.3359 | $9.5496\times10^{-7}$ | 1.3522 | 1.1952 | 238.7603 |
| 75 | 746.45 | 38.70 | 2.2769 | $3.4376\times10^{-8}$ | 1.3022 | $6.5867\times10^{-7}$ | 1.3174 | 1.2048 | 173.1026 |
| 76 | 604.75 | 45.95 | 2.0155 | $2.1057\times10^{-7}$ | 1.2517 | $1.4359\times10^{-6}$ | 1.2742 | 1.3825 | 166.8131 |
| 77 | 987.30 | 48.80 | 2.7327 | $3.8961\times10^{-6}$ | 1.4222 | $5.1035\times10^{-6}$ | 1.4221 | 1.3555 | 150.1287 |
| 78 | 981.05 | 50.00 | 2.7015 | $2.1267\times10^{-6}$ | 1.3779 | $4.0844\times10^{-6}$ | 1.3779 | 1.4000 | 164.3968 |
| 79 | 519.00 | 33.70 | 1.7890 | $3.6873\times10^{-7}$ | 1.4160 | $1.7341\times10^{-6}$ | 1.4160 | 1.1666 | 388.5935 |
| 80 | 516.00 | 34.90 | 1.7966 | $2.8663\times10^{-7}$ | 1.3823 | $1.2693\times10^{-6}$ | 1.3824 | 1.1770 | 259.5067 |
| 81 | 615.95 | 36.35 | 2.0065 | $5.4318\times10^{-8}$ | 1.2134 | $5.3810\times10^{-7}$ | 1.2844 | 1.2897 | 206.7961 |
| 82 | 615.20 | 36.50 | 2.0134 | $5.5856\times10^{-8}$ | 1.1890 | $4.8161\times10^{-7}$ | 1.2822 | 1.3032 | 171.1018 |
| 83 | 648.75 | 37.90 | 2.0925 | $4.2362\times10^{-8}$ | 1.1432 | $5.3933\times10^{-7}$ | 1.3437 | 1.2704 | 149.7204 |
| 84 | 778.50 | 35.70 | 2.3755 | $3.8038\times10^{-8}$ | 1.1490 | $4.7462\times10^{-7}$ | 1.3515 | 1.2931 | 161.9807 |
| 85 | 836.70 | 25.00 | 2.4100 | $3.0253\times10^{-8}$ | 1.3337 | $3.7734\times10^{-7}$ | 1.3361 | 1.1797 | 260.1578 |
| 86 | 850.10 | 25.40 | 2.4609 | $3.0968\times10^{-8}$ | 1.3033 | $2.4821\times10^{-7}$ | 1.3033 | 1.2173 | 195.0512 |
| 87 | 839.65 | 23.15 | 2.4396 | $2.5111\times10^{-}$ | 1.1490 | $1.9083\times10^{-7}$ | 1.4551 | 1.2452 | 169.0755 |
| 88 | 838.16 | 23.05 | 2.4322 | $2.4870\times10^{-8}$ | 1.1509 | $2.0781\times10^{-7}$ | 1.4440 | 1.2393 | 172.6510 |
| 89 | 844.15 | 23.35 | 2.4427 | $1.2633\times10^{-8}$ | 1.0985 | $1.0025\times10^{-9}$ | 1.7022 | 1.3270 | 152.1720 |
| 90 | 781.50 | 20.80 | 2.2524 | $9.4105\times10^{-9}$ | 1.1001 | $1.4127\times10^{-6}$ | 1.7709 | 1.2685 | 219.9114 |
| 91 | 775.50 | 20.45 | 2.2298 | $1.6292\times10^{-8}$ | 1.1488 | $4.3632\times10^{-7}$ | 1.4821 | 1.1884 | 260.3549 |
| 92 | 612.25 | 15.55 | 1.7738 | $2.4899\times10^{-8}$ | 1.1970 | $1.3638\times10^{-7}$ | 1.5022 | 1.1488 | 289.5701 |
| 93 | 609.25 | 15.00 | 1.7733 | $2.9613\times10^{-8}$ | 1.2056 | $6.0005\times10^{-8}$ | 1.5044 | 1.1616 | 247.4696 |
| 94 | 601.75 | 14.75 | 1.7590 | $2.7260\times10^{-8}$ | 1.2505 | $1.9787\times10^{-7}$ | 1.3990 | 1.0152 | 277.5651 |
| 95 | 240.85 | 31.40 | 1.0832 | $7.6864\times10^{-7}$ | 1.4388 | $1.7435\times10^{-6}$ | 1.4391 | 0.9077 | 320.8844 |
| 96 | 241.60 | 31.65 | 1.0832 | $1.0096\times10^{-6}$ | 1.4575 | $2.1944\times10^{-6}$ | 1.4580 | 0.8800 | 315.9751 |

| | Irradiance (W/m²) | Temperature (°C) | $I_{ph}$ (A) | $I_{01}$ (A) | $a_1$ | $I_{02}$ (A) | $a_2$ | Rs (Ω) | Rp(Ω) |
|---|---|---|---|---|---|---|---|---|---|
| 97 | 876.20 | 35.40 | 2.4400 | $5.9112 \times 10^{-8}$ | 1.1237 | $6.9247 \times 10^{-7}$ | 1.3634 | 1.3776 | 148.9166 |
| 98 | 873.25 | 36.45 | 2.4181 | $5.7254 \times 10^{-8}$ | 1.1237 | $6.8324 \times 10^{-7}$ | 1.3591 | 1.3861 | 154.3058 |
| 99 | 453.40 | 34.10 | 1.6455 | $4.0638 \times 10^{-7}$ | 1.3908 | $1.5872 \times 10^{-6}$ | 1.3921 | 1.1546 | 268.8136 |
| 100 | 617.40 | 38.50 | 2.0073 | $3.3293 \times 10^{-8}$ | 1.2287 | $4.8840 \times 10^{-7}$ | 1.3040 | 1.2366 | 241.8706 |
| 101 | 620.40 | 37.40 | 2.0146 | $2.7671 \times 10^{-8}$ | 1.0959 | $4.7090 \times 10^{-7}$ | 1.4730 | 1.3276 | 181.4589 |
| 102 | 453.40 | 37.00 | 1.6427 | $4.6296 \times 10^{-8}$ | 1.3259 | $6.7511 \times 10^{-7}$ | 1.3262 | 1.1444 | 253.0705 |
| 103 | 678.60 | 14.75 | 1.8738 | $2.7386 \times 10^{-8}$ | 1.2386 | $1.8163 \times 10^{-7}$ | 1.4012 | 1.1645 | 756.5171 |
| 104 | 718.10 | 13.15 | 2.0557 | $1.1487 \times 10^{-8}$ | 1.1480 | $9.7984 \times 10^{-7}$ | 1.8497 | 1.2781 | 404.3674 |
| 105 | 615.20 | 33.10 | 2.0924 | $2.7213 \times 10^{-8}$ | 1.1383 | $6.1137 \times 10^{-7}$ | 1.3848 | 1.1947 | 116.7962 |
| 106 | 589.10 | 33.55 | 1.9408 | $2.9259 \times 10^{-8}$ | 1.1168 | $3.8318 \times 10^{-7}$ | 1.4000 | 1.3141 | 242.0028 |
| 107 | 649.50 | 37.85 | 2.1087 | $3.3872 \times 10^{-8}$ | 1.1031 | $7.3445 \times 10^{-7}$ | 1.4255 | 1.3455 | 152.8020 |
| 108 | 648.05 | 37.90 | 2.0881 | $9.7714 \times 10^{-7}$ | 1.4012 | $2.0786 \times 10^{-6}$ | 1.4040 | 1.1869 | 209.7529 |
| 109 | 653.95 | 38.15 | 2.0926 | $2.2252 \times 10^{-7}$ | 1.3486 | $1.6059 \times 10^{-6}$ | 1.3486 | 1.2456 | 228.6922 |
| 110 | 665.20 | 39.20 | 2.1417 | $2.5978 \times 10^{-7}$ | 1.3349 | $1.3822 \times 10^{-6}$ | 1.3349 | 1.2873 | 185.4866 |
| 111 | 947.05 | 42.55 | 2.6777 | $4.5174 \times 10^{-7}$ | 1.3483 | $1.7329 \times 10^{-6}$ | 1.3546 | 1.2946 | 139.3115 |
| 112 | 454.90 | 37.75 | 1.6429 | $8.0987 \times 10^{-8}$ | 1.3366 | $1.3234 \times 10^{-6}$ | 1.3447 | 1.2234 | 311.6319 |
| 113 | 458.65 | 36.10 | 1.6527 | $1.3443 \times 10^{-7}$ | 1.3189 | $1.2103 \times 10^{-6}$ | 1.3386 | 1.2193 | 244.6175 |

Table 4. Two-diode model parameters in different environmental conditions

## 5. Results and their commentary

As discussed earlier, Tables 3 and 4 show the models parameters for the poly-crystalline silicon solar panel. It is easily seen any parameters in both models is not equal together. There are many interesting observations that could be made upon examination of the models. Figs. 13 and 14 show the I-V and P-V characteristic curves of #33 and their corresponding one-diode and two-diode models.

Comparison among the extracted I-V curves show that the both models have high accuracy. It can be seen that the one-diode model with variable diode ideally factor (n) can also models the solar panel accurately. The mentioned approach was repeated for all the curves and similar results were obtained.

Table 5 shows the main characteristics ($P_{max}$, $V_{oc}$, $I_{sc}$ and Fill Factor) of the solar panel for several measured curves and the corresponding one-diode and two-diode models corresponding parameters. The Fill Factor is described by Equation (7) [1].

$$FF = \frac{V_{mp}I_{mp}}{V_{oc}I_{sc}} \qquad (7)$$

In continue dependency of the models parameters over environmental conditions is expressed. Figures 15, 16 and 17 show appropriate sheets fitted on the distribution data (i.e. some of one-diode model parameters) drawn by MATLAB (thin plate smoothing splint fitting). Dependency of the model parameters could be seen from the figures. It could be easily seen that the relation between $I_{ph}$ and irradiance is approximately increasing linear and its dependency with temperature is also the same behavior. Other commentaries could be expressed for other model parameters. Thin plate smoothing splint fitting could be also carried out for two-diode model.
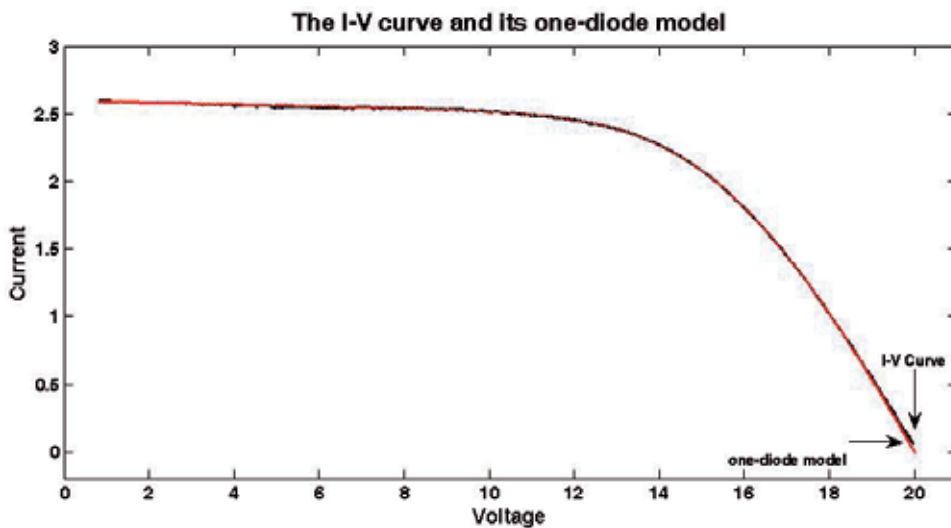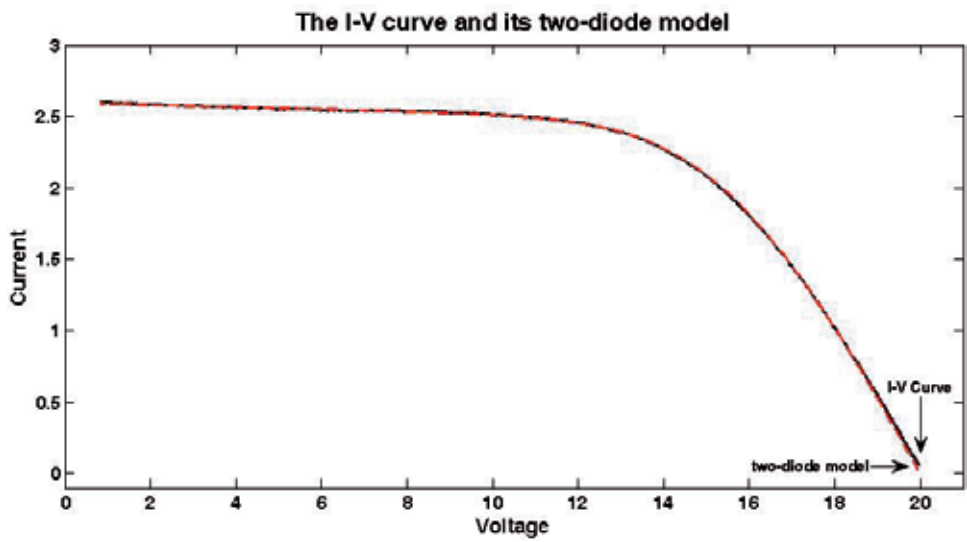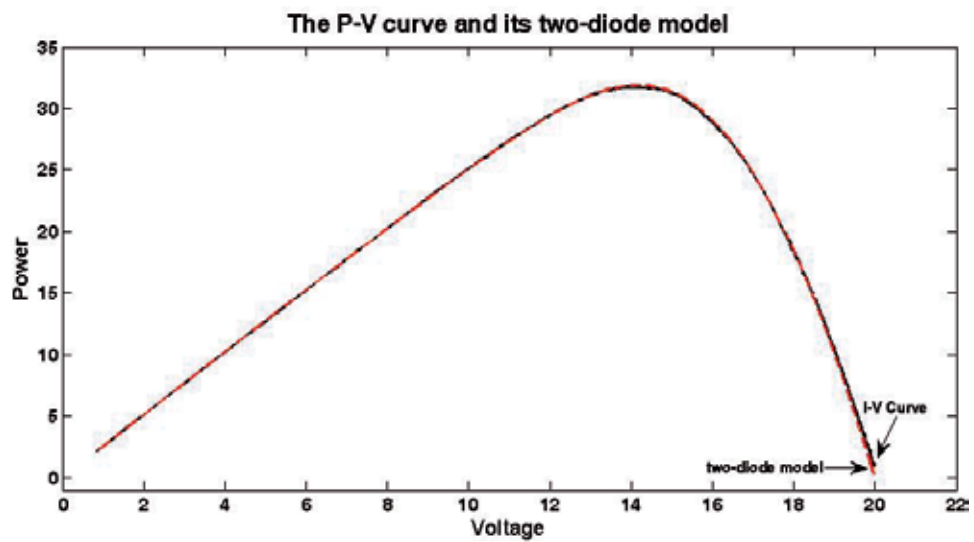
(a)
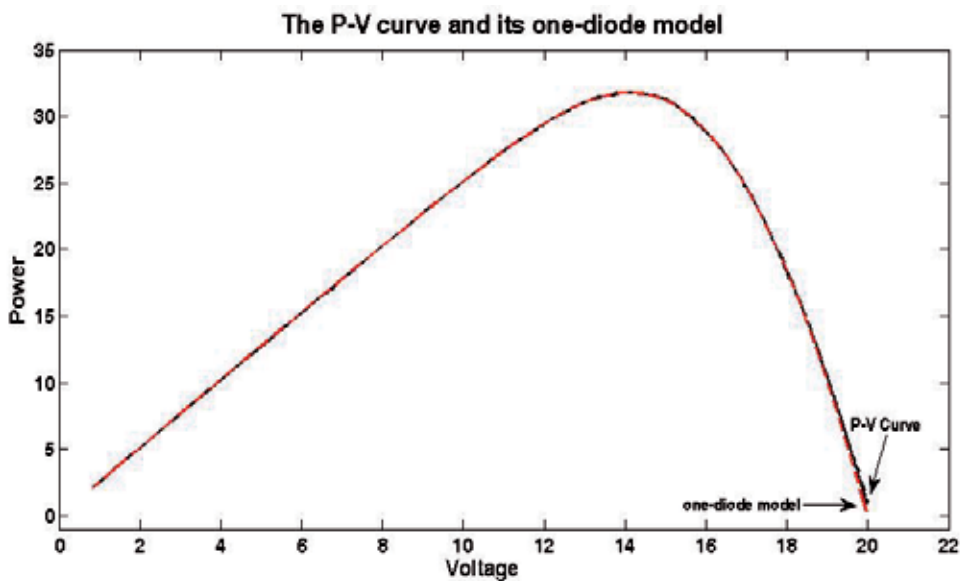


(b)

Fig. 13. The I-V curves #33 and its one-diode model

(a)



(b)

Fig. 14. The I-V curves #33 and its two-diode model

| Curve No. | $P_{max}$(W) | | | $I_{sc}$(A) | | | $V_{oc}$(V) | | | Fill Factor (FF) | | |
|---|---|---|---|---|---|---|---|---|---|---|---|---|
| | Measurements | 1-diode model | 2-diode model | Measurements | 1-diode model | 2-diode model | Measurements | 1-diode model | 2-diode model | Measurements | 1-diode model | 2-diode model |
| 33 | 31.8064 | 31.8 | 31.9203 | 2.5993 | 2.5929 | 2.5908 | 19.9972 | 19.9972 | 19.9972 | 0.6119 | 0.6134 | 0.6161 |
| 63 | 25.1194 | 25.1201 | 25.0915 | 1.9918 | 1.9884 | 1.9866 | 19.6316 | 19.6316 | 19.6316 | 0.6424 | 0.6427 | 0.6434 |
| 79 | 22.4528 | 22.4681 | 22.3444 | 1.7867 | 1.7848 | 1.7822 | 19.2940 | 19.2940 | 19.2940 | 0.6513 | 0.6509 | 0.6498 |
| 90 | 31.0414 | 31.0373 | 31.1237 | 2.2443 | 2.2371 | 2.2362 | 21.066 | 21.066 | 21.066 | 0.6566 | 0.6582 | 0.6607 |

Table 5. The main characteristics of the solar panel
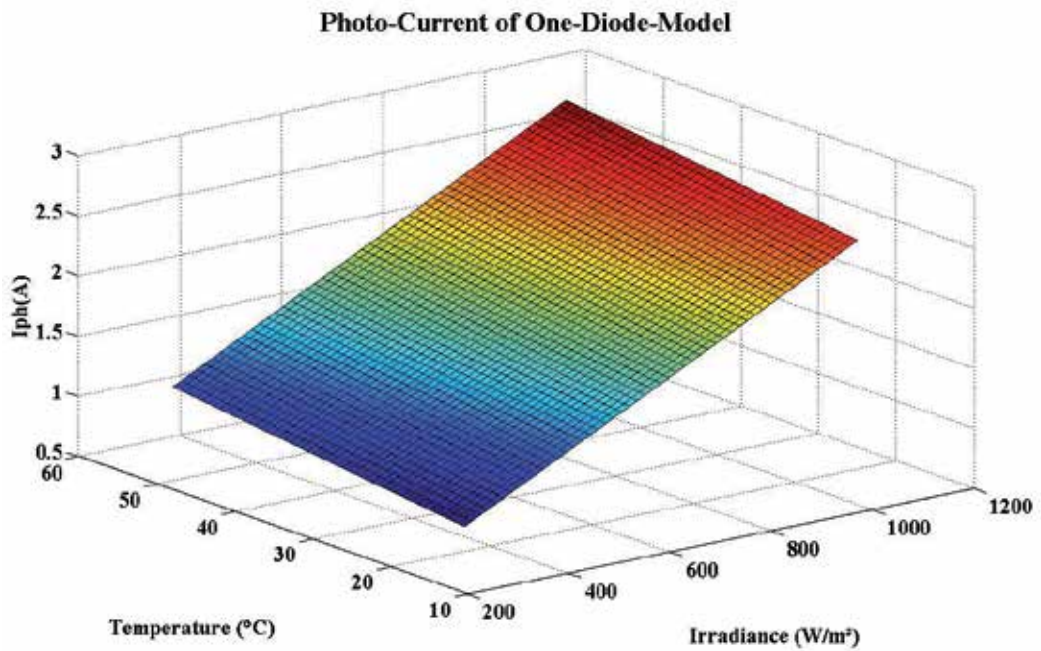
Fig. 15. Fitted sheet on photo-current of one-diode model by MATLAB.
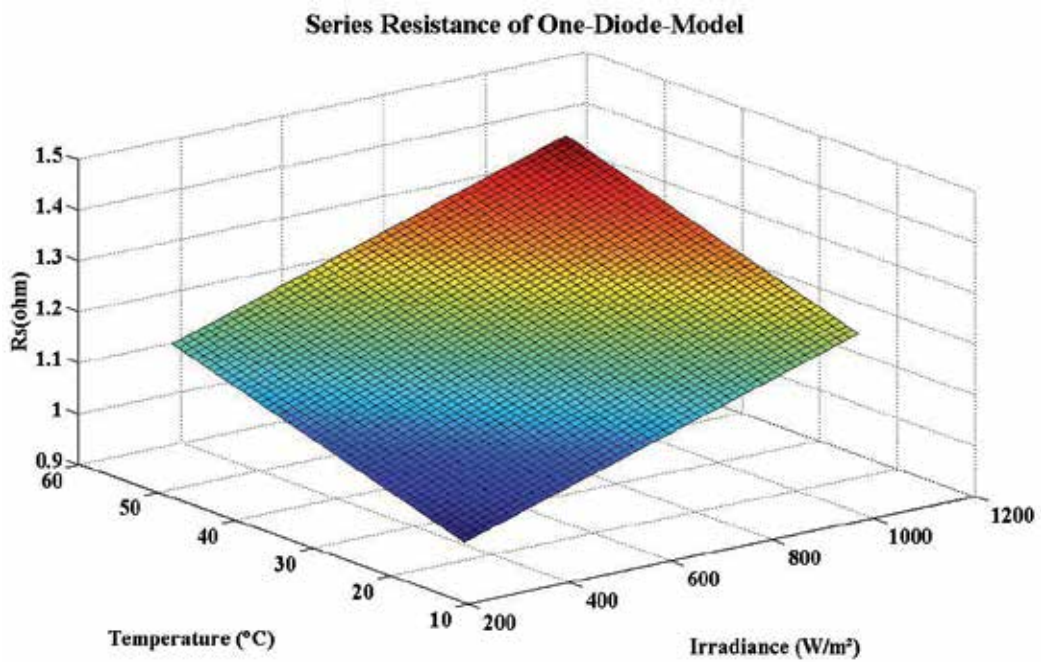


Fig. 16. Fitted sheet on series resistance of one-diode model by MATLAB.
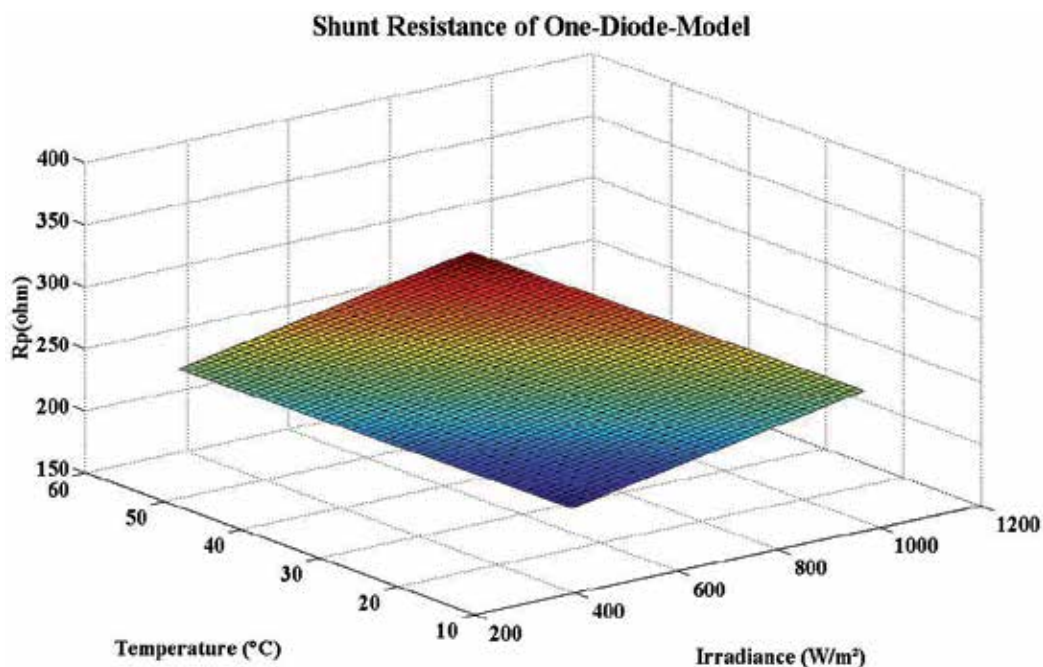
Fig. 17. Fitted sheet on shunt resistance of one-diode model by MATLAB.

## 6. Conclusion

In this research, a new approach to define one-diode and two-diode models of a solar panel were developed through using outdoor solar panel I-V curves measurement. For one-diode model five nonlinear equations and for two-diode model seven nonlinear equations were introduced. Solving the nonlinear equations lead us to define unknown parameters of the both models respectively. The Newton's method was chosen to solve the models nonlinear equations A modification was also reported in the Newton's solving approach to attain the best convergence. Then, a comprehensive measurement system was developed and implemented to extract solar panel I-V curves in open air climate condition. To evaluate accuracy of the models, output characteristics of the solar panel provided from simulation results were compared with the data provided from experimental results. The comparison showed that the results from simulation are compatible with data form measurement for both models and the both proposed models have the same accuracy in the measurement range of environmental conditions approximately. Finally, it was shown that all parameters of the both models have dependency on environmental conditions which they were extracted by thin plates smoothing splint fitting. Extracting mathematical expression for dependency of the each parameter of the models over environmental conditions will carry out in our future research.

## 7. Appendix

Equations (8-12) state the one-diode model nonlinear equations for a solar panel. Five unknown parameters; $I_{ph}, I_0, n, R_s$ and $R_p$ should be specified.

$$I_{sc} = I_{ph} - I_0 e^{\frac{I_{sc}R_s}{V_T}} - \frac{I_{sc}R_s}{R_p} \tag{8}$$

$$I_{oc} = 0 = I_{ph} - I_0 e^{\frac{V_{oc}}{V_T}} - \frac{V_{oc}}{R_p} \tag{9}$$

$$I_{mpp} = I_{ph} - I_0 e^{\frac{V_{mpp} + I_{mpp}R_s}{V_T}} - \frac{V_{mpp} + I_{mpp}R_s}{R_p} \tag{10}$$

$$I_x = I_{ph} - I_0 e^{\frac{V_x + I_x R_s}{V_T}} - \frac{V_x + I_x R_s}{R_p} \tag{11}$$

$$I_{xx} = I_{ph} - I_0 e^{\frac{V_{xx} + I_{xx}R_s}{V_T}} - \frac{V_{xx} + I_{xx}R_s}{R_p} \tag{12}$$

Therefore, the five aforementioned nonlinear equations must be solved to define the model. Newton's method is chosen to solve the equations which its foundation is based on using Jacobean matrix. MATLAB software environment is used to express the Jacobean matrix.

$$R = \begin{cases} f_1(I_{ph}, I_0, V_T, R_s, R_p) = 0 \\ f_2(I_{ph}, I_0, V_T, R_s, R_p) = 0 \\ f_3(I_{ph}, I_0, V_T, R_s, R_p) = 0 \\ f_4(I_{ph}, I_0, V_T, R_s, R_p) = 0 \\ f_5(I_{ph}, I_0, V_T, R_s, R_p) = 0 \end{cases} , \qquad J = \begin{bmatrix} \frac{\partial f_1}{\partial x_1} & \frac{\partial f_1}{\partial x_2} & \frac{\partial f_1}{\partial x_3} & \frac{\partial f_1}{\partial x_4} & \frac{\partial f_1}{\partial x_5} \\ \frac{\partial f_2}{\partial x_1} & \frac{\partial f_2}{\partial x_2} & \frac{\partial f_2}{\partial x_3} & \frac{\partial f_2}{\partial x_4} & \frac{\partial f_2}{\partial x_5} \\ \frac{\partial f_3}{\partial x_1} & \frac{\partial f_3}{\partial x_2} & \frac{\partial f_3}{\partial x_3} & \frac{\partial f_3}{\partial x_4} & \frac{\partial f_3}{\partial x_5} \\ \frac{\partial f_4}{\partial x_1} & \frac{\partial f_4}{\partial x_2} & \frac{\partial f_4}{\partial x_3} & \frac{\partial f_4}{\partial x_4} & \frac{\partial f_4}{\partial x_5} \\ \frac{\partial f_5}{\partial x_1} & \frac{\partial f_5}{\partial x_2} & \frac{\partial f_5}{\partial x_3} & \frac{\partial f_5}{\partial x_4} & \frac{\partial f_5}{\partial x_5} \end{bmatrix}$$

To solve the equations, a starting point $x_0 = [I_{ph}, I_0, V_T, R_s, R_p]$ must be determined and both matrixes R & J are also examined at that point. Then $\delta x$ is described based on the Eq. (13) and consequently Eq. (14) states the new estimation for the root of the equations.

$$J^k \delta x^k = -R^k \tag{13}$$

$$x_{new} = x_{old} + \delta x \tag{14}$$

Finally, the above iteration is repeated by the new start point $(x_{new})$ while the error was less than an acceptable level. The above iterative numerical approach is implemented for the two-diode models with seven nonlinear equations system. It was seen that to have an appropriate convergence, a modification coefficient $(0 < \alpha < 1)$ is added to Eq. (14) and it leads to Eq. (15).

$$x_{new} = x_{old} + \alpha \times \delta x \tag{15}$$

The modified approach has good response to solve the models equations by tuning the proposed coefficient.

## 8. Acknowledgment

## 9. References

Castaner, L.; Silvestre, S. (2002). *Modeling Photovoltaic Systems using Pspice,* John Wiley & Sons, ISBN: 0-470-84527-9, England

Sera, D.; Teodorescu, R. & Rodriguez, P. (2007). PV panel model based on datasheet values, *IEEE International Symposium on Industrial Electronics*, ISBN: 978-1-4244-0754-5, Spain, June 2007

De Soto, W.; Klein, S.A. & Beckman, W.A. (2006). Improvement and validation of a model for photovoltaic array performance, *Elsevier, Solar Energy,* Vol. 80, No. 1, (June 2005), pp. 78–88, doi:10.1016/j.solener.2005.06.010

Celik, A.N.; Acikgoz, N. (2007). Modeling and experimental verification of the operating current of mono-crystalline photovoltaic modules using four- and five-parameter models, *Elsevier, Applied Energy,* Vol. 84, No. 1, (June 2006), pp. 1–15, doi:10.1016/j.apenergy.2006.04.007

Chenni, R.; Makhlouf, M.; Kerbache, T. & Bouzid, A. (2007). A detailed modeling method for photovoltaic cells, *Elsevier, Energy,* Vol. 32, No. 9, (Decembere 2006), pp. 1724–1730, dio:10.1016/j.energy.2006.12.006

Gow, J.A. & Manning, C.D. (1999). Development of a Photovoltaic Array Model for Use in Power-Electronic Simulation Studies, *IEE proceeding, Electrical Power Applications,* Vol. 146, No. 2, (September 1998), pp. 193-200, doi:10.1049/ip-epa:19990116

Merbah, M.H.; Belhamel, M.; Tobias, I. & Ruiz, J.M. (2005). Extraction and analysis of solar cell parameters from the illuminated current-voltage curve, *Elsevier, Solar Energy Material and Solar Cells,* Vol. 87, No. 1-4, (July 2004), pp. 225-233, doi:10.1016/j.solmat.2004.07.019

Xiao, W.; Dunford, W. & Capel, A. (2004). A novel modeling method for photovoltaic cells, *35th IEEE Power Electronic Specialists Conference*, ISBN: 0-7803-8399-0, Germany, June 2004

Walker, G. R. (2001). Evaluating MPPT converter topologies using a MATLAB PV model, *Journal of Electrical and Electronics Engineering,* Vol. 21, No. 1, (2001), pp. 49–55, ISSN: 0725-2986

# Non-Idealities in the I-V Characteristic of the PV Generators: Manufacturing Mismatch and Shading Effect

Filippo Spertino, Paolo Di Leo and Fabio Corona
*Politecnico di Torino, Dipartimento di Ingegneria Elettrica*
*Italy*

## 1. Introduction

A single solar cell can generate an electric power too low for the majority of the applications (2,5 - 4 W at 0,5 V). This is the reason why a group of cells is connected together in series and encapsulated in a panel, known as PhotoVoltaic (PV) module. Moreover, since the output power of a PV module is not so high (few hundreds of watts), then a photovoltaic generator is constituted generally by an array of strings in parallel, each one made by a series of PV modules, in order to obtain the requested electric power.

Unfortunately, the current-voltage (I-V) characteristic of each cell, and so also of each PV module, differs nearly from that of the other ones. The causes can be found in the manufacturing tolerance, i.e. the pattern of crystalline domains in poly-silicon cells, or the different aging of each element of the PV generator, or in the presence of not uniformly distributed shade over the PV array. These phenomena can cause important losses in the energy production of the generator, but they could also lead to destructive effects, such as "hot spots", or even the breakdown of single solar cells. The aim of this chapter is to examine the mismatch in all its forms and effects, exposing some experimental works through simulation and real case studies, in order to investigate the solutions which were thought to minimize the effects of the mismatch.

## 2. Series/parallel mismatch in the I-V characteristic

Firstly, it will be worthy to explain the I-V mismatch in general for the solar cells, making a classification in series and parallel mismatch. In the first case the effect of the different short-circuit current (and maximum power point current) of each solar cell is that the total I-V characteristic of a string of series-connected cells can be constructed summing the voltage of each cell at the same current value, fixed by the worst element of the string. This means that the string I-V curve is strongly limited by the short-circuit current of the bad cell, and consequently the total output power is much less than the sum of each cell maximum power. This phenomenon is more relevant in the case of shading than in presence of production tolerance. It will be shown that the bad cell does not perform as an open circuit, but like a low resistance (a few ohms or a few tens of ohms), becoming a load for the other solar cells. In particular, it is subject to an inverse voltage and it dissipates power, then if the power dissipation is too high, it will be possible the formation of some "hot spots", with

degradation and early aging of the solar cell. Furthermore, if the inverse voltage applied to a shaded cell exceeds its breakdown value, it could be destroyed. The worst situation is with the string in short-circuit, when all the voltage of the irradiated cells is applied to the shaded ones. It is clear that the most dangerous case occurs if the shaded cell is only one, while the experience shows that usually with two shaded cells the heating is still acceptable.

The solution adopted worldwide for this problem is the by-pass diode in anti-parallel connection with a group of solar cell for each module. In this way, the output power decreases only of the contribution of the group of bad cells and the inverse voltage is limited by the diode.

In the case of parallel of strings, it is the voltage mismatch which becomes important. The total I-V characteristic can be constructed summing the current of each string at the same voltage value. The total open-circuit voltage will be very close to that of the bad string. The worst case for the bad or shaded string is that one of the open circuit, because it will become the only load for the other strings. Consequently, it will conduct inverse current with unavoidable over-heating, which can put the string in out of service. In the parallel mismatching a diode in series with the string can avoid the presence of inverse currents.

After this basic introduction to the mismatch, the equivalent circuit of a solar cell with its parameters will be illustrated.

## 2.1 Solar cell model for I-V curve simulation

The equivalent circuit of a solar cell with its parameters is a tool to simulate, for whatever irradiance and temperature conditions, the *I-V* characteristics of each PV module within a batch that will constitute an array of parallel-connected strings of series-connected modules. With this aim, the literature gives two typical equivalent circuits, in which a current source I is in parallel with a non linear diode. $I_{ph}$ is directly proportional to the irradiance G and the area of the solar cell A, simulating the photovoltaic effect, according to the formula

$$I_{ph} = K_S \cdot G \cdot A \qquad (1)$$

Since PV cells and modules are spectrally selective, their conversion efficiency depends on the daily and monthly variations of the solar spectral distribution (Abete et al., 2003) . A way to assess the spectral influence on PV performance is by means of the effective responsivity $K_S$ (A/W):

$$K_S = \frac{\int g(\lambda) \cdot S(\lambda) d\lambda}{\int g(\lambda) d\lambda} \qquad (2)$$

where S($\lambda$) is the absolute spectral response of a silicon cell (A/W) and g($\lambda$) the irradiance spectrum (W/m²$\mu$m).

A suitable software, which calculates the global radiation spectrum on a selected tilted plane, has been used. Apart from month, day and time, the input parameters are meteorological and geographical data: global and diffuse irradiance on horizontal plane (W/m²), ambient temperature (°C), relative humidity (%), atmospheric pressure (Pa); latitude and longitude. Among the output parameters, it is important the global irradiance spectrum (on the tilted plane) versus wavelength. By the spectral response of a typical mono-crystalline silicon cell, it is possible to calculate $K_S$. As an example, Figure 1 shows the quantities S($\lambda$), $g_1(\lambda)$ and $g_2(\lambda)$ at 12.00 of a clear day in winter and summer, respectively. It

is noteworthy that between 0.9 and 1μm, where S(λ) is high, the winter spectrum exceeds the summer spectrum. Figure 2 shows the quantities S(λ)·g₁(λ) and S(λ)·g₂(λ), named spectral current density $\delta_{I1}$ e $\delta_{I2}$, which have units of A/(m²μm). Not only in this example, but in many cases $K_S$ is higher in winter than in summer and the deviations are roughly 5%.
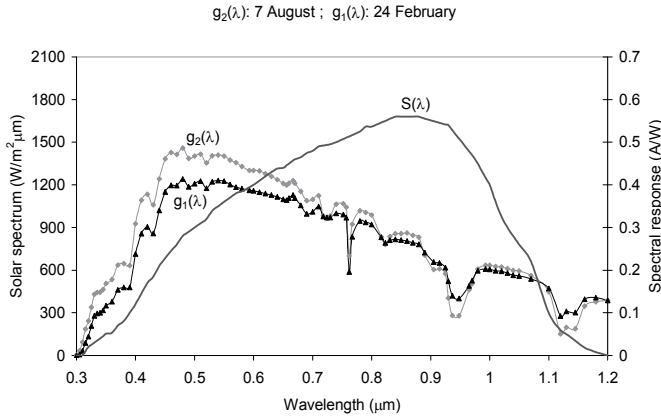

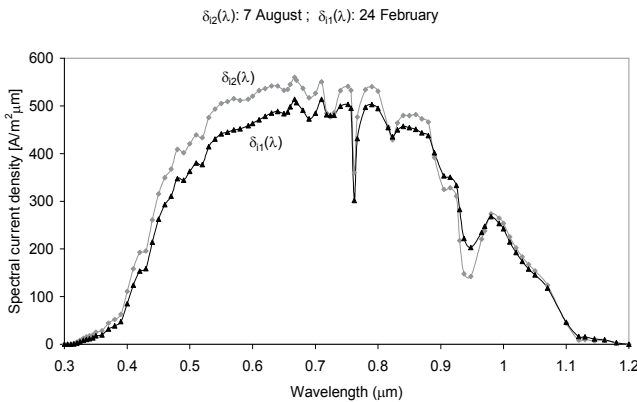
Fig. 1. Comparison of solar spectra in winter and summer.



Fig. 2. Comparison of spectral current density in winter and summer.

The rated power of the PV devices is defined at Standard Test Conditions (STC), corresponding to the solar spectrum at noon in the spring/autumn equinox, with clear sky. This global irradiance ($G_{STC}$ = 1000 W/m²) is also referred as Air Mass (AM) equal to 1.5. Then, considering the non linear diode, on the one hand, the first equivalent circuit is based on a single exponential model for the P-N junction, in which the reverse saturation current $I_o$ and quality factor of junction *m* are the diode parameters to be determined:

$$I_j = I_o \cdot \left( e^{\frac{qV_j}{mkT_c}} - 1 \right) \tag{3}$$

where $V_j$ is the junction voltage, $k$ the Boltzmann constant, $q$ the electron charge and $T_c$ the cell temperature.

On the other hand, the second model involves a couple of exponential terms, in which the quality factors assume fixed values (1 and 2 usually), whereas $I_{o1}$ and $I_{o2}$ must be inserted.

$$I_j = I_{o1} \cdot \left( e^{\frac{qV_j}{m_1 kT_c}} - 1 \right) + I_{o2} \cdot \left( e^{\frac{qV_j}{m_2 kT_c}} - 1 \right) \tag{4}$$

The model with a single exponential is used in this chapter (Fig. 3). In this one, the series resistance $R_s$ accounts for the voltage drop in bulk semiconductor, electrodes and contacts, and the shunt resistance $R_{sh}$ represents the lost current in surface paths.

Thus, five parameters are sufficient to determine the behaviour of the solar cell, namely, the current source $I_{ph}$, the saturation current $I_o$, the junction quality factor $m$, the series resistance $R_s$, the shunt resistance $R_{sh}$. If we examine the silicon technologies, mono-crystalline (m-Si), poly-crystalline (p-Si) and amorphous (a-Si), the shape of the *I-V* curve is mainly determined by the values of $R_s$ and $R_{sh}$.
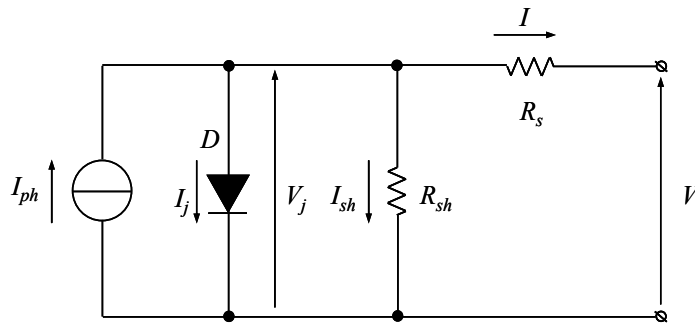


Fig. 3. Equivalent circuit of solar cell with one exponential.

Finally, the dependence on the solar irradiance $G(t)$ and on the cell temperature $T_c(t)$ is explained for the ideal PV current $I_{ph}$ and the reverse saturation current $I_0$ in the following expression:

$$I_{ph} = I_{SC|STC} \frac{G}{G_{STC}} \left[ 1 + \alpha_T \left( T_c - 298 \right) \right] \tag{5}$$

$$I_0 = I_{0|STC} \left( \frac{T_c}{298} \right)^3 \frac{e^{-\frac{E_g}{kT_c}}}{e^{-\frac{E_g}{k \cdot 298}}} \tag{6}$$

where $I_{SC|STC}$ is the short-circuit current evaluated at STC ($T_{STC} = 25°C = 298$ K), $\alpha_T$ is the temperature coefficient of $I_{ph}$, $E_g$ is the energy gap and $k$ is the Boltzmann constant. The cell temperature is evaluated by considering a linear dependence on the ambient temperature $T_a$

and the irradiance G, according to the NOCT definition valid for modules installed in mounting structures which allow the natural air circulation (maximum wind speed equal to 1 m/s):

$$T_c = T_a + \frac{G}{G_{NOCT}} (NOCT - 20°C) \tag{7}$$

in which $G_{NOCT}$ = 800 W/m². By using the aforementioned model, the PV-array $I(V)$ characteristic, corresponding to the actual irradiance and cell temperature, is calculated on a specific program implemented in MATLAB.

Through this model of a solar cell it is possible to simulate the mismatch due to shading effect on different configurations of a PV generator made of an array of solar panels. Usually the shading effect is studied changing the number of shaded solar cells of a single module for each configuration considered. The current-voltage (I-V) curve is then determined, together with the maximum power available with the shading $P_m'$ (normalized with the power $P_m$ without shades and defined as µ), the power dissipated and the inverse voltage on the shaded solar cells.

For example, the following simulation is relative to a series mismatch due to shading. Let us consider a 35 $W_p$ rated power PV module of 36 solar cells in poly-crystalline silicon, with a short circuit current of 2.4 A in STC. Figure 4 shows the I-V curves of:

a. 36 cells totally irradiated;
b. 35 cells totally irradiated;
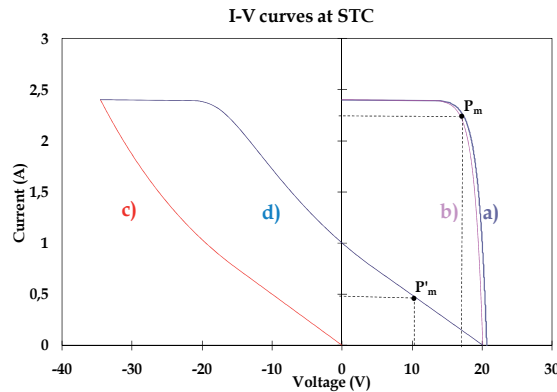c. 1 completely shaded cell;
d. 36 cells with 1 shaded cell.



Fig. 4. I-V curves of different number of series-connected solar cells.

In the d) curve the normalized power µ is reduced significantly (nearly 10%) as it is shown in Table 1. In the shaded cell the worst condition, in terms of dissipated power $P_c$ and inverse voltage $U_c$, occurs when the PV module is in short circuit. Its working point can be obtained from the interception between curve c) and curve b), in figure 1, if the curve b) is reversed respect the current axis. This point gives the dissipated power and inverse voltage on the shaded cell ($U_c$=18V e $P_c$=24W). Raising the number of shaded solar cells ($N_c$) the values of µ, $P_c$ and $U_c$ shown in table 1 are obtained. It is clear that if $N_c$ grows $P_c$ and $U_c$ decrease, namely the working conditions of the PV module are less dangerous for the solar cells.

| $N_c$ | $\mu$ | $P_c$ [W] | $U_c$ [V] |
|---|---|---|---|
| 1 | 0.11 | 24 | 18 |
| 2 | 0.06 | 4.3 | 9.2 |
| 3 | 0.04 | 1.8 | 6.1 |
| 4 | 0.03 | 1 | 4.4 |
| 18 | 0 | 0 | 0 |
| 36 | 0 | 0 | 0 |

Table 1. Normalized power of the PV module $\mu$, dissipated power $P_c$ and inverse voltage $U_c$ on shaded solar cell, under STC, depending on the number of shaded solar cells.

## 3. Manufacturing I-V mismatch

Considering at first the mismatch among PV modules due to production tolerance, a first study is presented in the paper (Abete et al., 1998) in which an experimental set up has been developed to detect the mismatching of the current-voltage characteristics between a reference PV module and another one under test, in the same environmental conditions. Two dual bridge circuits have been set up, one with series and the other one with parallel connected modules, which have produced the direct measurement of the difference characteristic and the mismatching parameters. Therefore it has been achieved a better accuracy as regard to the indirect determination of the difference from the two I-V characteristics. The measuring circuits reported could be profitably employed for optimum module connection in the array, manufacturer quality control, customer acceptance testing and field test on PV array.

### 3.1 Production tolerance detection

The optimum performance of a photovoltaic module or array is achieved if the current-voltage I(U) characteristics of the solar cells in the module or the I(U) characteristics of the modules in the array are identical (matched). Otherwise, that is when an I-U mismatch occurs due to manufacturing tolerance, the electrical output power of the PV array decreases and the increasing internal power losses may cause "hot spots" up to the failure of the module with lower performance. The mismatch of the I(U) curves of PV modules is measured by the difference between two I(U) characteristics, one of a reference module and the other of a testing module, in the same ambient conditions. For the direct measurement of this difference curve (to achieve uncertainty lower than with indirect measurement), two dual measuring circuits are presented, one with series and the other with parallel connected modules.

To obtain this difference between the reference and the testing I(U) curves, it is required to measure the voltage difference of series connected modules, for equal current value, and the current difference of parallel connected modules for equal voltage value. The two measuring circuits can be regarded as a bridge comparing, point by point, the dynamic I(U) characteristics of two PV modules, the reference and the other under test. In the first circuit ("series type") the PV modules are series connected: in case of mismatch, the voltage output measurement of the unbalanced bridge, for each current value, is directly proportional to the difference of the module's voltages $\Delta U$. This $\Delta U$ vs. current I represents the difference characteristic $U_2(I) - U_1(I)$. In the dual circuit ("parallel type") the

PV modules are parallel connected: in case of mismatch, the voltage output measurement of the unbalanced bridge, for each voltage value, is directly proportional to the difference of the module's currents $\Delta I$. This $\Delta I$ vs. voltage U represents the voltage difference characteristics $I_2(U) - I_1(U)$.

Fig. 5 and Fig. 6 show the series and parallel bridge measuring circuits. Each bridge has two active branches constituted by two modules, $PV_1$ (reference) and $PV_2$ (testing), which are subject to the same irradiance G and cell temperature T. The other two branches of each bridge are two equal resistors, $R_s$ with high resistance in Fig. 5 and $R_p$ with low resistance in Fig. 6, such as to have a negligible loading effect on the I(U) characteristics of $PV_1$ and $PV_2$ modules. C is a capacitor such as to give a suitable du/dt, i.e., not so quick to interfere with the parasitic junction capacitance of the solar cells and not so slow to permit the variation of the ambient conditions. Usually, values around a few millifarad are adequate. The PR devices are Hall-effect probes for accurate and non-intrusive measurement of current. At closing of switch s, the transient charge of the capacitor C provides, in a single sweep, the I(U) dynamic curves of the two modules.
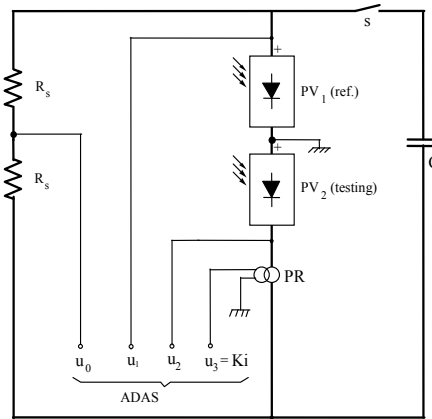


Fig. 5. "Series type" bridge measuring circuit.
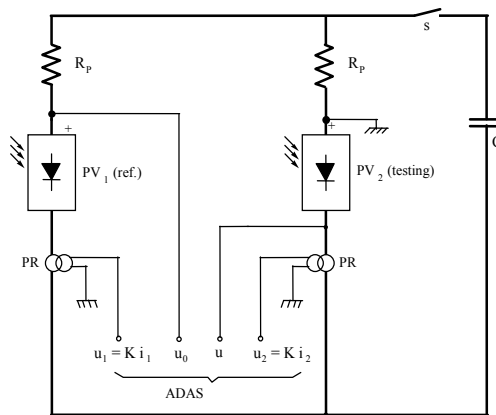


Fig. 6. "Parallel type" bridge measuring circuit.

The circuit analysis proves that:

- in the series circuit, for each current value, the voltage output $U_0$ of the unbalanced bridge measures the difference $\Delta U$ of the two module's voltages by $\Delta U = U_0(2+R_s/R_0)$;
- in the parallel circuit, for each voltage values, the voltage output $U_0$ of the unbalanced bridge measures the difference $\Delta I$ of the two modules currents by $\Delta I = U_0(1/R_P+2/R_0)$ with $R_0$ input resistance of the instrument which measures the voltage output $U_0$.

Therefore, the measurement of the voltage difference $\Delta U$ vs. the current I gives the difference curve of the series connected modules; the measurement of the current difference $\Delta I$ vs. the voltage U gives the difference curve of the parallel connected modules. For mismatch assessment, besides the difference of open circuit voltages $\Delta U_{oc}$ and of short circuit currents $\Delta I_{sc}$, it is profitable, in the maximum power point $P_M = (I_M, U_M)$ of the reference module, to know the following parameters:

- the voltage difference $\Delta U_M$ and the power reduction $\Delta P_{MI} = I_M \Delta U_M$ for series connected modules;
- the current difference $\Delta I_M$ and the power reduction $\Delta P_{MU} = U_M \Delta I_M$ for parallel connected modules.

These quantities $\Delta U_M$, $\Delta P_{MI}$, $\Delta I_M$ and $\Delta P_{MU}$ can be assumed as "mismatch parameters".

The measuring signals of the circuits in Fig. 5 and Fig. 6 (K current probe constant), with a suitable sampling rate (10-100 kSa/s), are digitized by an Automatic Data Acquisition System (ADAS). This ADAS processes the signals for providing current-voltage curves of the PV modules, the difference characteristics and the mismatch parameters. These experimental results, concerning series and parallel connected polycrystalline silicon modules, are shown respectively in Fig. 7 and Fig. 8. In Fig. 7 the testing module $I(U_2)$ curve extends as far as the second quadrant, while the reference module $I(U_1)$ curve does not run through all the first quadrant. This proves that the short circuit currents of the two modules are different and consequently the testing module can operate as a load of the reference module. In Fig. 8, likewise, the testing module $I_2(U)$ curve extends as far as the fourth quadrant, while the reference module $I_1(U)$ curve does not run through all the first quadrant. This proves that the open circuit voltages of the two modules are different and thus the testing one can operate as a load. Once the power reduction are $\Delta P_{MI}$ and $\Delta P_{MU}$ are measured, it is possible to choose the connection of the modules in the array to achieve the optimum performance. Finally, the presented circuits can be profitably employed in manufacturer quality control and customer acceptance testing.
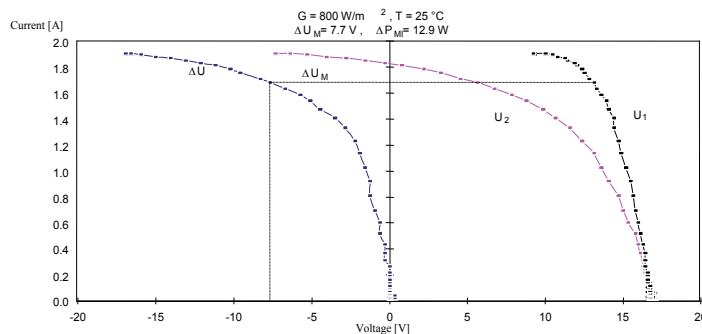


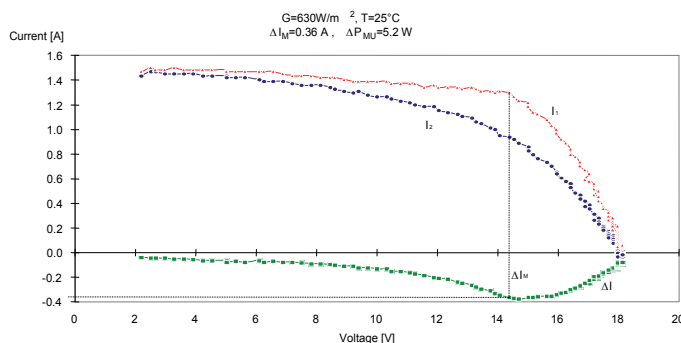Fig. 7. Experimental results with series connected polycrystalline silicon modules.

Fig. 8. Experimental results with parallel connected polycrystalline silicon modules.

### 3.2 Manufacturing I-V mismatch and reverse currents in large Photovoltaic arrays

As an example of the consequences of the production tolerance in large PV plants, a brief summary of a study on this topic is reported here. This work has dealt with the current-voltage mismatch consequent to the production tolerance as a typical factor of losses in large photovoltaic plants (Spertino & Sumaili, 2009). The results have been simulated extracting the parameters of the equivalent circuit of the solar cell for several PV modules from flash reports provided by the manufacturers. The corresponding I-V characteristic of every module has been used to evaluate the behavior of different strings and the interaction among the strings connected for composing PV arrays. Two real crystalline silicon PV systems of 2 MW and 20 kW have been studied. The simulation results have revealed that the impact of the I-V mismatch is negligible with the usual tolerance, and the insertion of the blocking diodes against reverse currents can be avoided with crystalline silicon technology. On the other hand, the experimental results have shown a remarkable power deviation (3%-4%) with respect to the rated power, mainly due to the lack of measurement uncertainty in the manufacturer flash reports.

### 4. Optimal configuration of module connections for minimizing the shading effect in multi-rows PV arrays

In another study, the periodic shading among the rows in the morning and in the evening in grid-connected PV systems, installed e.g. on the rooftop of buildings, has been investigated (Spertino et al. 2009). This phenomenon is quite common in large PV plants, in fact often the designer does not take into account this shading when he decides the module connections in the strings, the number of modules per string and the arrangement, according to the longest side of the modules, in horizontal or vertical direction. The study has discussed, by suitable comparisons, various cases of shading pattern in PV arrays from multiple viewpoints: power profiles in clear days with 15-min time step, daily energy as a monthly average value for clear and cloudy days. The simulation results have proved that, with simple structure of the array and important amount of shading, it is better to limit the shading effect within one string rather than to distribute the shading on all the strings: the gains are higher than 10% in the worst month and 1% on yearly basis. Contrary, with more complex structure of the array and low amount of shading, it is practically equivalent to concentrate or to distribute

the shading on all the strings. Finally, in the simulation conditions the impact of the shading losses on yearly basis is limited to 1-3%.

## 4.1 Analysis of some shading patterns

In order to establish some guidelines for minimising the shading effect in multi-rows PV arrays, a comparison among different configurations of module connections is carried out within simplifying assumptions, i.e., *all the shaded modules are located only in a single string* vs. *the shaded modules are equally distributed in all the strings*. In particular, the shading implies the collection of the diffuse irradiance without the direct or beam irradiance; thus, the parameters which determine the behaviour of the PV arrays in these conditions are:

- $N_S$: number of series connected modules per string ($N_S > 1$ otherwise the meaning is vanishing);
- $N_P$: number of parallel connected strings per array ($N_P > 1$ otherwise the meaning is vanishing);
- $N_{Ssh}$(one_str): number of shaded modules in the case of shading concentrated in a single string;
- $N_{Ssh}$(all_str): number of shaded modules per each string in the case of shading distributed in all the strings.

All the comparisons are performed by satisfying the equation:

$$\frac{N_{Ssh}\left(one\_str\right)}{N_S} = N_P \cdot \frac{N_{Ssh}\left(all\_str\right)}{N_S} \tag{8}$$

Obviously, the previous parameter $N_{Ssh}$(all_str) ≥ 1 only if $N_P \leq N_S$.

In our study, the chosen arrays are two, the first one with usual number of modules per string ($N_S$ = 16) and low number of parallel strings ($N_P$ = 4) concerns a decentralized inverter (Figures 9 and 10), whereas the second one deals with a centralized inverter ($N_S$ = 16, $N_P$ = 8 in Figures 11 and 12). In order to gain deeper understanding, the pattern of shading (i.e. modules subject to diffuse radiation without beam radiation) can be:

1. either one or a half shaded string in the array, i.e., $N_{Ssh}$(one_str) = 16 or $N_{Ssh}$(one_str) =8;
2. whereas only one or more modules with shading for every string of the array, i.e., $N_{Ssh}$(all_str) = 1 or $N_{Ssh}$(all_str) = 4.

On one hand, in the first array with 25%- shading amount the situations are: *4 shaded modules in every string* (conf. 1 in Figure 9) vs. *all the 16 modules shaded in the same string* (conf. 2 in Fig. 10). The eq. (8) becomes

$$\frac{N_{Ssh}\left(one\_str\right)}{N_S} = N_P \cdot \frac{N_{Ssh}\left(all\_str\right)}{N_S} = 1 \tag{9}$$

with $N_{Ssh}$(one_str) = 16 and $N_{Ssh}$(all_str) = 4 corresponding to the maximum number of shaded modules per string in this example. In Figure 9 in every string, even if there are both shaded modules (four) and totally irradiated modules (twelve), it is assumed the same temperature for uniformity reasons and this one is equal to the temperature of the totally irradiated modules. Consequently, the I-V curve can be calculated.

On the other hand, in the second array with 6.25%- shading amount the situations are *8 shaded modules in the same string* (half a string in Conf. 4 of Fig. 12) vs. *one shaded module for every string* (Conf. 3 of Fig. 11), i.e., the eq. (8) becomes

$$\frac{N_{Ssh}(one\_str)}{N_S} = N_P \cdot \frac{N_{Ssh}(all\_str)}{N_S} = \frac{1}{2} \tag{10}$$

with $N_{Ssh}(one\_str) = 8$ and $N_{Ssh}(all\_str) = 1$ corresponding to the minimum number of shaded modules.
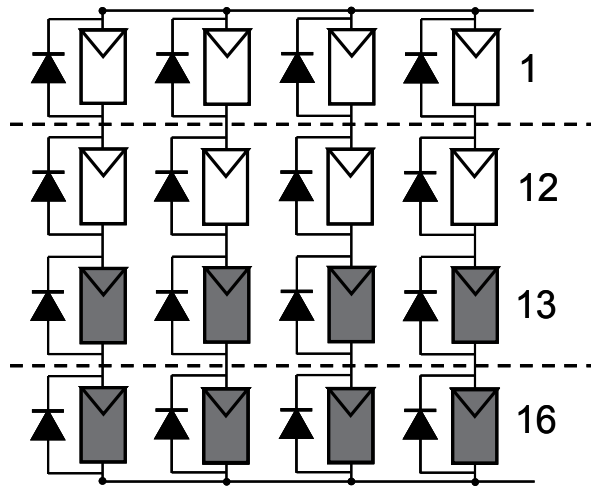


Fig. 9. Array ($N_S$ = 16, $N_P$ = 4) with shading patterns - Configuration 1
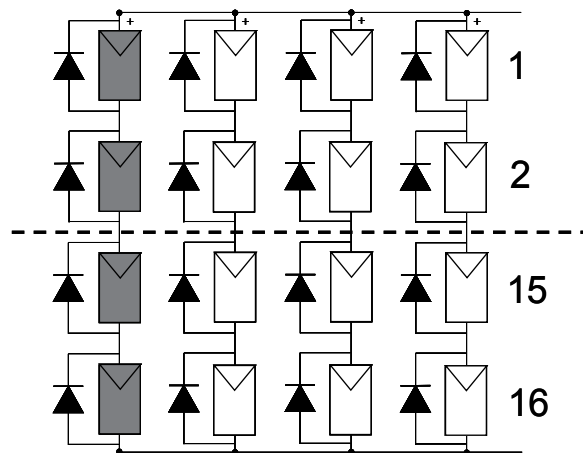


Fig. 10. Array ($N_S$ = 16, $N_P$ = 4) with shading patterns - Configuration 2
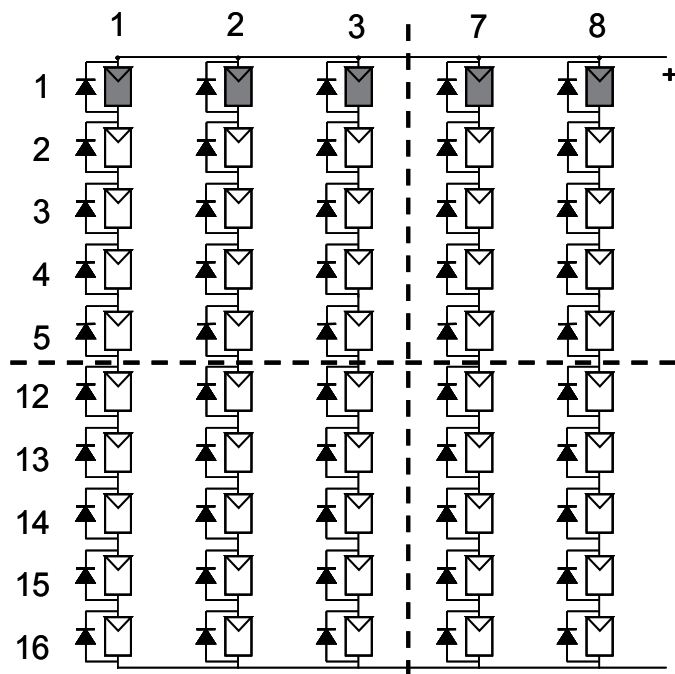
Fig. 11. Array ($N_S$ = 16, $N_P$ = 8) with shading patterns - Configuration 3
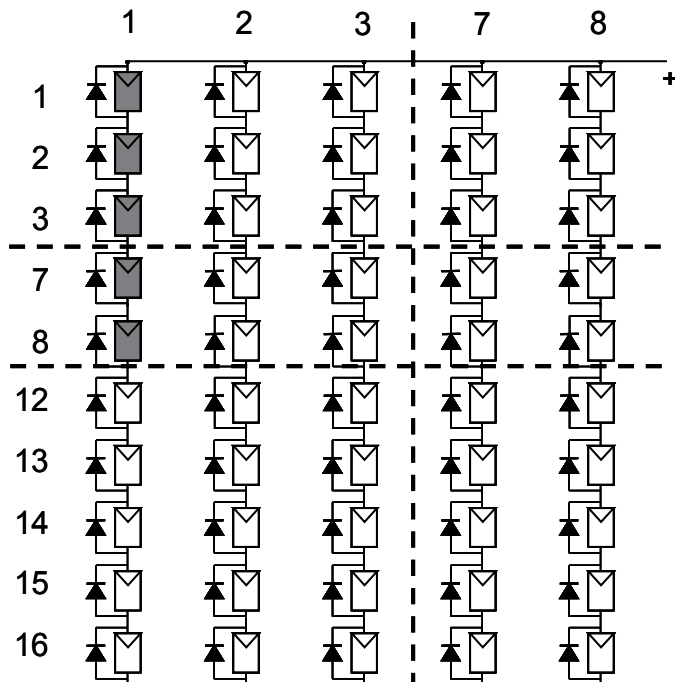


Fig. 12. Array ($N_S$ = 16, $N_P$ = 8) with shading patterns - Configuration 4

## 4.2 Simulation results of the considered shading patterns

The study cannot be limited to the irradiance values in the clear days, but requires the simulation of real-sky conditions by using an average day which takes into account both clear and cloudy days (e.g. Page and Liu-Jordan models). In this case, the PVGIS tool, available on the web-site of JRC of the European Commission, is used. Simulation results are presented in the following with reference to a South-Italy location (latitude $\varphi \approx 41.5°$, tilt angle $\beta = 15°$ for maximum installation density and azimuth $\psi = 30°$ W). The installation option is the PV-rooftop array in order to earn higher amount of money within the Italian feed-in tariff (partial building integration). The obstruction which produces the shading effect is the *balustrade* of the building roof: consequently, only the PV-modules of the closest row are subject to the shading because the successive rows are sufficiently separate each other ($d > d_{min}$ in Figure 13 where $d_{min}$ is calculated on the Winter solstice at noon with Sun-height angle $\alpha$).
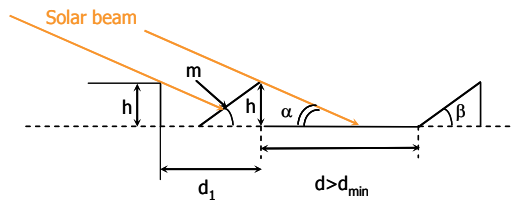


Fig. 13. The row arrangement and the balustrade obstruction with height h

The figures 14 and 15 show the two patterns of shading for the first PV array ($N_S=16$, $N_P=4$) with 4 rows: in the configuration 1 (Fig. 14) there are 4 modules per string in each row and in configuration 2 (Fig. 15) there are all the 16 modules of each string in a single row.
The figures 16 and 17 show the two patterns of shading for the second PV array ($N_S = 16$, $N_P = 8$) with 16 rows: in the configuration 3 (Fig. 16) there is only one module per string in each row and in configuration 4 (Fig. 17) there are 8 modules of each string in a single row.
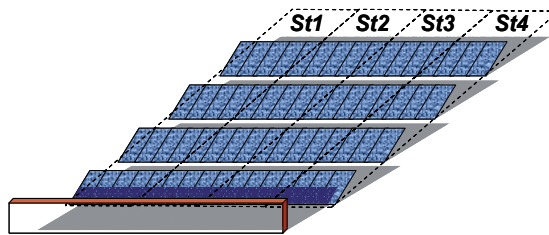


Fig. 14. The row arrangement and the balustrade in the first array - Configuration 1
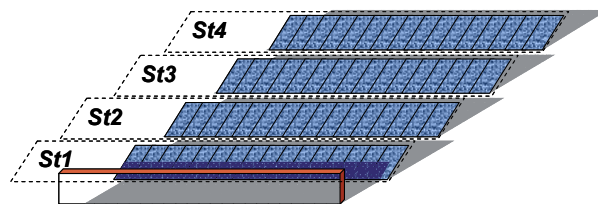


Fig. 15. The row arrangement and the balustrade in the first array - Configuration 2
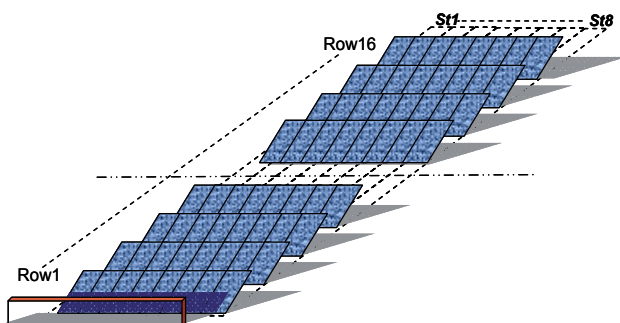
Fig. 16. The row arrangement and the balustrade in the second array - Configuration 3
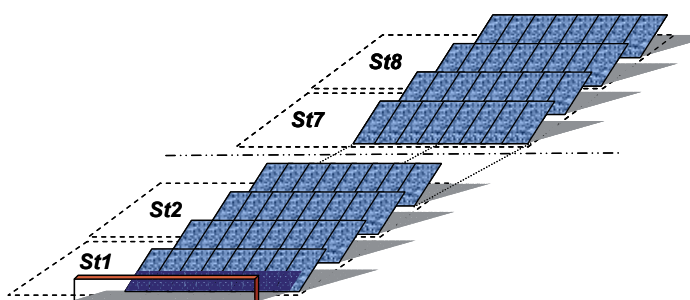


Fig. 17. The row arrangement and the balustrade in the second array - Configuration 4

The selected technology for the PV-module is the conventional poly-crystalline-silicon one with rated power of 215 $W_p$. The main specifications are presented in Table 2 (rated power $P_{max}$, voltage $V_{MPP}$ and current $I_{MPP}$ at rated power, open circuit voltage $V_{OC}$, short circuit current $I_{SC}$, temperature coefficients of $V_{OC}$, $I_{SC}$, and normal operating cell temperature NOCT).
Notice that all the PV-modules are equipped with 3 bypass diodes, each protecting a group of 20 cells.

| $P_{max}$ = 215 $W_p$ | $V_{MPP}$ = 28.5 V | $I_{MPP}$ = 7.55 A |
|---|---|---|
| | $V_{OC}$ = 36.3 V | $I_{SC}$ = 8.2 A |
| | $\beta_{Voc}$ = -0.35%/°C | $\alpha_{Isc}$ = +0.05%/°C |
| | NOCT = 48 °C | |

Table 2. Specifications of the PV modules

As an example of the simulation outputs for each time step (15 min), Figure 18 illustrates the I-V curve , while Figure 19 shows the P-V characteristics of the array 1 with rated power $P_r$ = 13.76 kW in the configurations 1, 2, and without shading in particular conditions of global irradiance $G_g$ (direct + diffuse), diffuse irradiance alone $G_d$, and ambient temperature. It is worth noting that the configuration 2 with shading concentrated on a single string is better that the other configuration with shading equally distributed on all the strings. Moreover, the action of the bypass diodes is clear in the abrupt variation of the derivative in the curve of configuration 1 (blue colour).
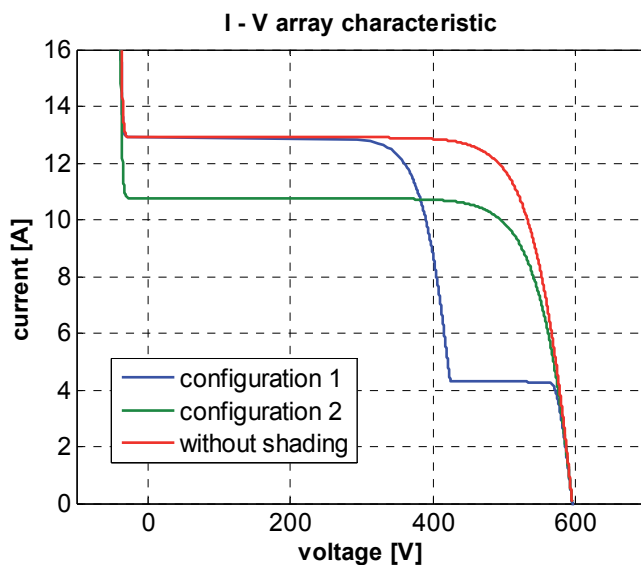
**I - V array characteristic**



Fig. 18. The I-V curve at $G_g$ = 395 W/m², $G_d$ = 131 W/m² and $T_a$ = 4.1 °C

P - V array characteristic
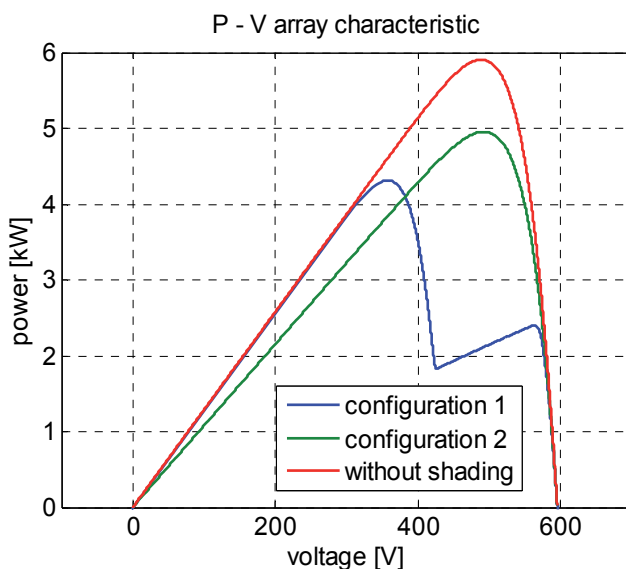


Fig. 19. The P-V curve at $G_g$ = 395 W/m², $G_d$ = 131 W/m² and $T_a$ = 4.1 °C

Furthermore, the simulation outputs provide also the daily power diagrams for both real (Fig. 20) and clear sky (Fig. 21) conditions for the configurations 1 and 2. It is possible to point out that the shading causes power losses in the afternoon, due to the azimuth of the PV array, and the produced energy is higher for configuration 2 with shading concentrated in a single string, as in the previous case.
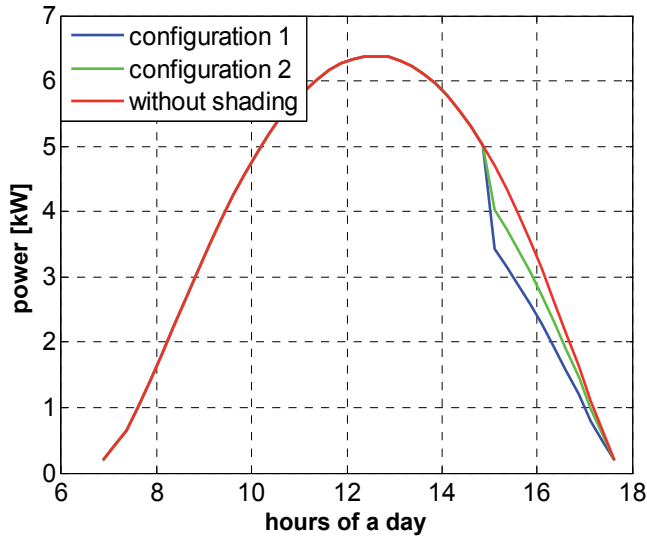
Fig. 20. The daily power diagrams in October for configurations 1 and 2 (Real Sky)
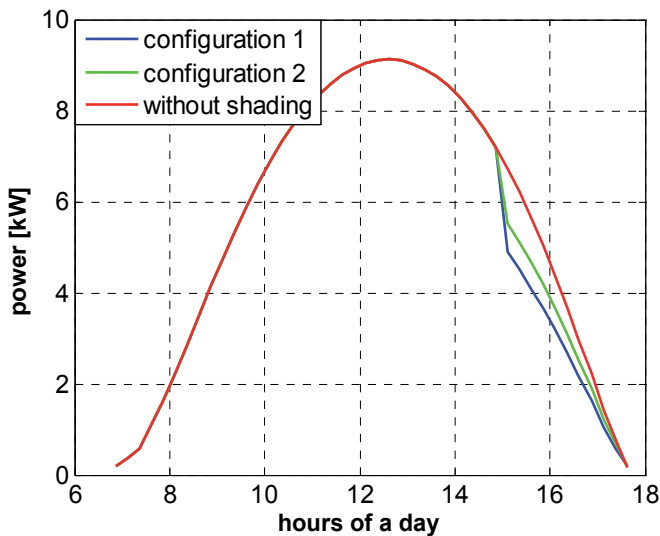


Fig. 21. The daily power diagrams in October for configurations 1 and 2 (Clear-sky)

Concluding the study on the two configurations of the first array, it can be stressed that the simulations on the average day of the months subject to shading effect give greater losses in configuration 1 than in configuration 2, both for real-sky days and clear-sky days. Obviously, the losses are maximum in December with values of 17.8% (Conf. 1) vs. 9.4% (Conf. 2) but, if we consider the losses on yearly basis (including the months without shading), the mean value of losses is 2.5% (Conf. 1) vs. 1.3% (Conf. 2). Hence, in this case it is more profitable to adopt the module connection which allows to concentrate the shading in a single string.

| Day | No shad. Energy [kWh] | Configuration 1 Energy [kWh] | Configuration 1 Losses (%) | Configuration 2 Energy [kWh] | Configuration 2 Losses (%) |
|-----|-----|-----|-----|-----|-----|
| Oct | 43.83 | 41.83 | 4.30 | 42.80 | 2.08 |
| Nov | 30.47 | 27.10 | 11.06 | 28.71 | 5.78 |
| Dec | 25.01 | 20.57 | 17.76 | 22.65 | 9.41 |
| Jan | 30.81 | 26.73 | 13.23 | 28.55 | 7.33 |
| Feb | 37.46 | 34.77 | 7.19 | 36.13 | 3.55 |

Table 3. Energies and losses in the shading patterns (Real sky)

| Day | No shad. Energy [kWh] | Configuration 1 Energy [kWh] | Configuration 1 Losses (%) | Configuration 2 Energy [kWh] | Configuration 2 Losses (%) |
|-----|-----|-----|-----|-----|-----|
| Oct | 61.30 | 58.65 | 4.33 | 59.68 | 2.65 |
| Nov | 47.15 | 41.81 | 11.33 | 43.56 | 7.61 |
| Dec | 40.08 | 32.75 | 18.29 | 35.04 | 12.54 |
| Jan | 44.74 | 38.66 | 7.19 | 40.64 | 3.55 |
| Feb | 56.87 | 52.70 | 7.32 | 54.17 | 4.75 |

Table 4. Energies and losses in the shading patterns (Clear sky)

Now, addressing the focus on the two configurations of the second array, it can be stressed that the simulations on the average day of the months subject to shading effect give slightly greater losses in configuration 3 than in configuration 4 for real-sky days whereas the opposite occurs for clear-sky days with higher values of losses. More in detail, in clear-sky conditions the losses are maximum in December with values of 4.69% (Conf. 3) vs. 6.24% (Conf. 4) but, if we consider the losses on yearly basis (including the months without shading), the mean value of losses is 0.65% (Conf. 3) vs. 0.64% (Conf. 4). Hence, with more complex structure of array and less amount of shading, it is almost equivalent either to concentrate the shading in a single string or to distribute equally in all the strings.

| Day | No shad. Energy [kWh] | Configuration 3 Energy [kWh] | Configuration 3 Losses (%) | Configuration 4 Energy [kWh] | Configuration 4 Losses [kWh] |
|-----|-----|-----|-----|-----|-----|
| Oct | 87.42 | 86.46 | 1.10 | 86.57 | 0.98 |
| Nov | 60.94 | 59.23 | 2.81 | 59.26 | 2.76 |
| Dec | 50.02 | 47.75 | 4.53 | 47.76 | 4.50 |
| Jan | 61.61 | 59.54 | 3.37 | 59.44 | 3.53 |
| Feb | 74.92 | 73.55 | 1.83 | 73.66 | 1.68 |

Table 5. Energies and losses in the shading patterns (Real-sky).

| Day | No shad. Energy [kWh] | Configuration 3 Energy [kWh] | Configuration 3 Losses (%) | Configuration 4 Energy [kWh] | Configuration 4 Losses [kWh] |
|-----|-----|-----|-----|-----|-----|
| Oct | 122.27 | 121.27 | 1.09 | 120.99 | 1.32 |
| Nov | 94.30 | 91.58 | 2.88 | 90.73 | 3.79 |
| Dec | 80.16 | 76.40 | 4.69 | 75.15 | 6.24 |
| Jan | 89.48 | 86.35 | 3.51 | 85.40 | 4.56 |
| Feb | 113.74 | 111.62 | 1.86 | 111.01 | 2.40 |

Table 6. Energies and losses in the shading patterns (Clear-sky).

### 4.3 Concluding remarks

Since the PV-system designer does not take into account possible periodic shading when he decides the connections of the modules in the strings, the paper has discussed, by proper comparisons, various cases of shading pattern in PV arrays from multiple viewpoints: power profiles in clear days with 15-min time step, daily energy as a monthly average value for clear and cloudy days.

The simulation results prove that, with *simple structure* of the array and *important amount of shading*, it is better to limit the shading effect within one string rather than to distribute the shading on all the strings. Contrary, with more complex structure of the array and low amount of shading, it is practically equivalent to concentrate or to distribute the shading on all the strings.

Finally, in the simulation conditions the impact of the shading losses on yearly basis is limited to 1-3%.

## 5. Decrease of inverter performance for shading effect

The last paragraph of this chapter deals with other consequences of the mismatch, because it has a significant impact also on the inverter performance and the power quality fed into the grid (Abete et al., 2005).

The real case of two systems installed in Italy within the Italian program "PV roofs" is presented. They have been built on the south oriented façades of the headquarters of two different municipal Companies. Due to the façade azimuth, besides the distances among the floors, a partial shading occurs during morning periods from April to September. The shading effect determined an important decrease of the available power. However the attention has been focused on the inverter performance, both at the DC and AC side in these conditions, during which experimental data have been collected. The DC ripples in voltage and current signals can be higher than 30%, with a fundamental frequency within 40-80 Hz; the Maximum Power Point Tracker (MPPT) efficiency resulted around 60%, because the tracking method relied on the wrong assumption that the voltage at maximum power point (MPP) was a constant fraction of the open circuit voltage, while with shading the fraction decreased down to roughly 50%; the Total Harmonic Distortion (THD) of AC current resulted higher than 20% with a great spread and presence of even harmonics, whereas the THD of voltage is slightly influenced by the shading; the power factor was within 0.75-0.95, due to the previous current distortion and the capacitive component, which becomes important in these conditions.

### 5.1 Two real case PV systems built on façades

Within an Italian grid connected PV Programme, two systems (20 $kW_P$ and 16 $kW_P$, respectively) have been installed in Torino on the south oriented façades of the headquarters of AMIAT (municipal company for the waste-materials management) and of "Provincia di Torino" public administration.

The first system consists of six PV plants, 3.3 $kW_P$ each: the array of a single plant counts 30 modules and supplies a single-phase inverter. The low-voltage three-phase grid is fed by two parallel connected inverters per phase (230 V line to neutral wire). The second system consists of six PV plants, 2.6 $kW_P$ each: the array of a single plant counts 24 modules and

supplies a single-phase inverter of the same model as in the first system. Also the scheme of grid connection is the same as in the previous system.

These PV systems are among the first examples of PV building integration in Italy, even if they are a *retro-fit* work: in fact, their modules behave as saw-tooth curtains (or "sun shields") providing a protection against direct sunlight, principally in summer season. Due to the façade azimuth (≈25° west), besides the comparative distances among the rows of arrays, a partial shading effect occurs during morning periods from April to September. All the PV fields are involved by this partial shading during these periods except for the array 4, which is entirely located above the last floor in the first system (Fig. 22) and for the arrays 5 and 6, which are located on the roof, in the second system (Fig. 23).



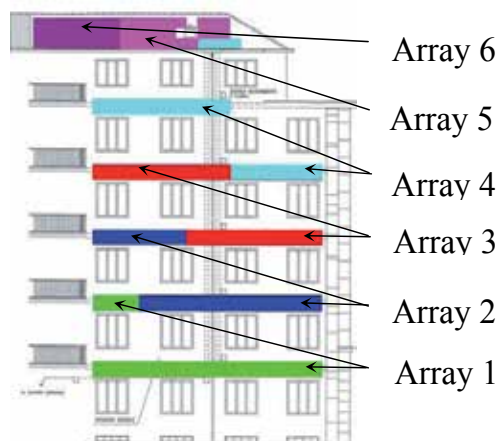Fig. 22. PV arrays on the façade of the 1st system.



Fig. 23. PV arrays on the façade of the 2nd system.

The amount of shaded array, the beginning and duration of these conditions, obviously, are depending on the calendar day. As well known, the shading effect, concentrated on

some cells of a PV array, determines a mismatch of cell current-voltage I(V) characteristics, with an important decrease (only limited by the bypass diodes) of the available power; furthermore, the shaded cells can work as a load and the hot spots can rise. However the attention has been focused on the inverter performance, both at the DC side and at the AC side in shading conditions, during which experimental data have been collected.

## 5.2 Parameters of inverter performance and their measurement system

The inverter performance can be defined by the following parameters, besides the DC-AC efficiency:

- the ripple peak factors of DC voltage $V_{pp} = \dfrac{V_{\max} - V_{\min}}{V_{mean}}$ and current $I_{pp} = \dfrac{I_{\max} - I_{\min}}{I_{mean}}$ ;

- the MPP Tracker efficiency $\eta_{MPPT} = P_{DC}/P_{MAX}$ (how close to maximum power $P_{MAX}$ the MPPT is operating), where $P_{DC}$ is the input power of the inverter and $P_{MAX}$ is the maximum power calculated on the current-voltage I(V) characteristic;

- the total harmonic distortion of grid AC voltage $THD_V = \sqrt{V_2^2 + V_3^2 + ... + V_n^2}\Big/V_1$ and AC current $THD_I = \sqrt{I_2^2 + I_3^2 + ... + I_n^2}\Big/I_1$ , where $V_1$ ($I_1$), $V_2$ ($I_2$),…, $V_n$ ($I_n$) are the harmonic r.m.s. values;

- the power factor $PF = P_{AC}\big/\left(V_{trms} \cdot I_{trms}\right)$, with $P_{AC}$ active power, $V_{trms}$ and $I_{trms}$ true r.m.s. voltage and current.

The measurements have been carried out by a Data Acquisition board (DAQ), integrated into a notebook PC. The real-time sampling has been performed at the sampling rate of 25.6 kSa/s, with a resolution of 12 bits. This rate corresponds to 512 samples per period at grid frequency of 50 Hz, in such a way as to allow the calculation of the harmonics up to 50th. Three voltage probes and three current ones are used as a signal conditioning stage to extend the range of the measured quantities above the voltage range of ±10 V. These probes are equipped with operational amplifiers with low output resistance (≈ 50 Ω), for obtaining low time constants with the capacitance of the Sample & Hold circuit in the DAQ board, which accepts up to eight input channels by its multiplexer.

A proper software, developed in LabVIEW environment, implements Virtual Instruments behaving as storage oscilloscope and multimeter for measurement of r.m.s. voltage (up to 600 V), current (up to 20 A), active power and power factor. The oscilloscope, in order to obtain the I(V) curves of the PV arrays, is equipped with a trigger system, useful for the capture of the transient charge of a capacitor. The multimeter also performs harmonic analysis for the calculation of THD by the Discrete Fourier Transform (DFT) and operates as data logger with user-selected time interval between two consecutive measurements.

## 5.3 Distortion of waveforms in case of shading effect

In case of shading effect, which causes the distortion of the I(V) shape, the ripples at the DC side of inverter increase and cannot be sinusoidal: the waveforms, thus, have harmonic content, as pointed out in (11) for the power, with a fundamental-harmonic frequency different from 100 Hz (double of grid frequency):

$$P_{DC} = V_{mean} \cdot I_{mean} + \sum_{k=1}^{n} V_k \cdot I_k \cdot \cos\varphi_k \qquad (11)$$

$V_k$, $I_k$ represent the r.m.s. values of harmonic voltage and current at the same frequency, whereas $\varphi_k$ is the phase shift between voltage and current: here every $\cos\varphi_k$ is negative and so the harmonics decrease the DC power.

A remarkable distortion arises also at the AC side of inverter with reference to the current: even harmonics, which cause that the positive half-wave is different from the negative half-wave, can be noticeable. The even harmonics do not contribute AC active power, since the grid voltage, generally, has only odd harmonics: the DC-AC efficiency, consequently, decreases.

Summarizing the previous items, the inverter parameters worsen with shading effect:

- the DC ripples can be higher than 10% and the waveforms have harmonic content, with a fundamental-harmonic frequency down to 30 Hz, because the I(V) characteristics are distorted and multiple MPPs arise ;

- the MPPT efficiency can be lower than 95%, because the tracking method, employed in the inverters under study, relies on the statement that the voltage $V_{MPP}$ at MPP is a constant fraction of the open circuit voltage, but with shading the fraction is lower;

- the THD of AC current can be higher than 10% with great spread and presence of even harmonics (especially the 2nd one), whereas the THD of voltage is slightly influenced by the shading;

- the power factor can be lower than 0.9, due to both the previous distortion of AC current and a capacitive component, which becomes important when the active component is low, as in this case.

## 5.4 Experimental tests to detect the inverter behaviour

The experimental tests, presented in this section, include:

1. measurements of DC and AC waveforms by the oscilloscope on the inverters of the most shaded arrays of the first system (array 1 and 2) during the morning period and immediately after the shading;

2. measurements of AC waveforms by the oscilloscope on the inverters of the second system after the morning shading, in order to compare the behaviour, without shading, of inverters of the same model;

3. daily monitoring of the parameters of inverter performance at the AC side, by the data logger in three phase configuration, on the first system.

Concerning the item 1., the MPPT efficiency is obtained by two tests, carried out as close as possible because of the ambient conditions (irradiance and temperature) must be equal.

The first test determines the I(V) characteristics by a suitable method (transient charge of a capacitor. Hence, it is possible to calculate the maximum power $P_{MAX}$. As an example, Figure 24 shows ten I(V) curves of the array 2 during the morning evolution of the shading (from 9.50 to 11.35 in August). It is possible to note different conditions of irradiance: at 9.50 the shading is complete above all the PV modules (only diffuse radiation gives its contribution) and the I(V) shape is regular; from 10.25 to 10.35 the irradiance is not uniform, some modules begin to be subject to the beam radiation and the I(V) shape has abrupt changes of derivative (bypass diodes action): the power, hence, decreases.
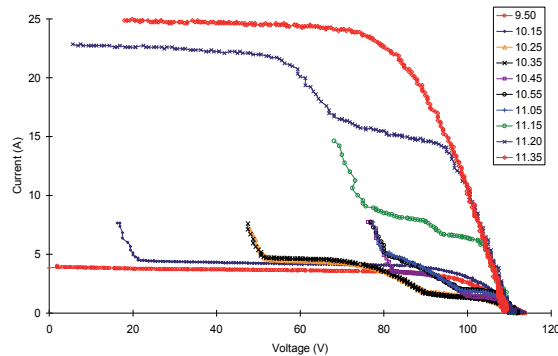
Fig. 24. I(V) curves of the array 2 during the shading.

Only after 11.05, when the most of modules are subject to beam radiation, the power begins again to increase; the shading, around 11.35, is vanishing. In Fig. 3 the I(V) curves are not complete because we have preferred to obtain the maximum accuracy of current measurement in the portion of I(V) that is used by the MPPT of the inverter (in this case 66-120 V is the voltage range of the MPPT).

The second test, for the same ambient conditions, provides the input signals of the inverter: voltage $v_{DC}(t)$, current $i_{DC}(t)$ and power $p_{DC}(t)$ affected by the ripples. It is worth noting that the amplitude and frequency of DC ripple can influence the normal work of the input DC filter and the DC-DC converter. Fig. 25 shows some profiles of DC current ripples, corresponding to the previous I(V) measurements: the waveforms have many changes of derivative with even harmonics, whereas the DC voltage ones have always a slow ascent and a steep descent (not represented here). This behaviour of $i_{DC}(t)$ can be responsible for higher losses in the iron inductor of DC-DC converter.
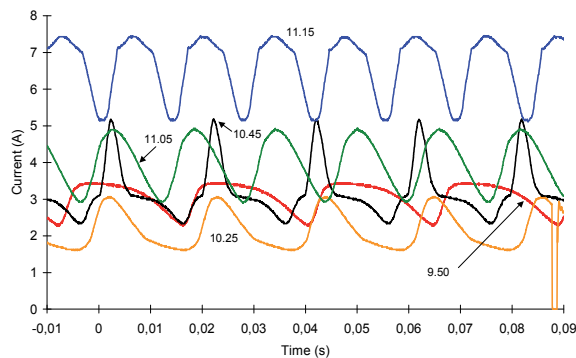


Fig. 25. DC current ripples during shading (inverter 2).

By combining the results of the two tests (Fig. 24 and Fig. 25), if the functions I(V) and $i_{DC}(v_{DC})$ are plotted in the same diagram, it is possible to assess the operation of the MPPT in shading condition. As an example, Fig. 26 shows what happens at 10.25 in the inverter 2: the curves are not complete for the previous reason and the voltage $V_{MPP} < 47$ V (less than 43% of the PV open circuit voltage). The MPPT is not able to work in the absolute maximum

power point (out of current scale here), due to the algorithm that imposes a voltage $v_{DC}$ equal to 78% of PV open circuit voltage. Moreover in this case $P_{DC}$ is 62% of the local MPP corresponding to 73 V.

Table 7 summarizes the experimental results in terms of: the ripple frequency $f_{ripple}$; the ripple indices of DC voltage $V_{PP}$ and current $I_{PP}$; the MPPT efficiency $\eta_{MPPT}$.
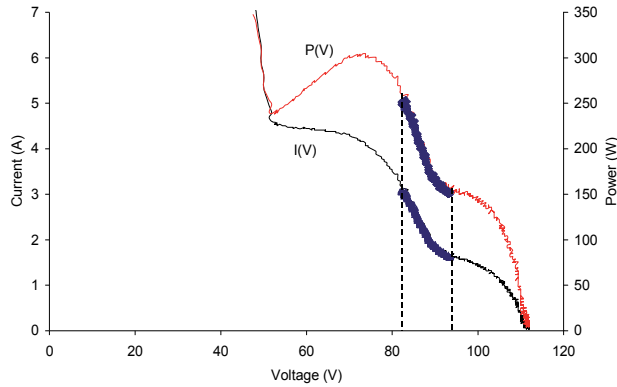


Fig. 26. Bad operation of MPPT in the inverter 2.

| Hours | $f_{ripple}$ (Hz) | $V_{PP}$ % | $I_{PP}$ % | $\eta_{MPPT}$ % |
|---|---|---|---|---|
| 9.50 | 41 | 27 | 38 | 89 |
| 10.15 | 47 | 27 | 33 | 92 |
| 10.25 | 48 | 13 | 69 | <54 |
| 10.35 | 53 | 8.5 | 59 | <49 |
| 10.45 | 50 | 20 | 89 | <47 |
| 10.55 | 62 | 16 | 52 | <56 |
| 11.05 | 64 | 16 | 51 | <57 |
| 11.15 | 73 | 20 | 35 | <58 |
| 11.20 | 80 | 9.2 | 4.5 | 81 |
| 11.35 | 101 | 2.9 | 4.5 | 94 |

Table 7. The DC performance parameters (inverter 2)

Concerning the AC measurements of the items 1. and 2., the results show, during the shading, high distortion of current waveforms, which however does not worsen significantly the voltage waveforms (THD$_V$ within the range of 2-3%). The positive half-waves are not all the same (on the time scale of few grid periods) and are very different from the negative half-waves (due to the even harmonics also present at the DC side). A capacitive component, enough remarkable, produces a phase shift with respect to the grid voltage. Figure 27 shows the voltage and current signals at 10.45 for inverter 2: the first positive half-wave has one sharp peak, whereas the last positive half-wave has two peaks, as it occurs for the negative half-waves.

The computation of the total harmonic distortion of AC current proves that the values are always higher than 15% (up to 22%). With respect to the individual harmonics, the following

remarks can be done: the second harmonic arises up to 8% in the first part (9.50-10.35), then vanishes; the seventh harmonic is the highest (10-14%) for all the duration of the shading; the third harmonic maintains itself nearly constant at 6% until 11.20, when it rises up to 10%, that is the main component after the conclusion of shading; finally the fifth, ninth and eleventh harmonics maintain their selves around the 5% level during the shading. Figure 28 summarizes these results in a histogram.
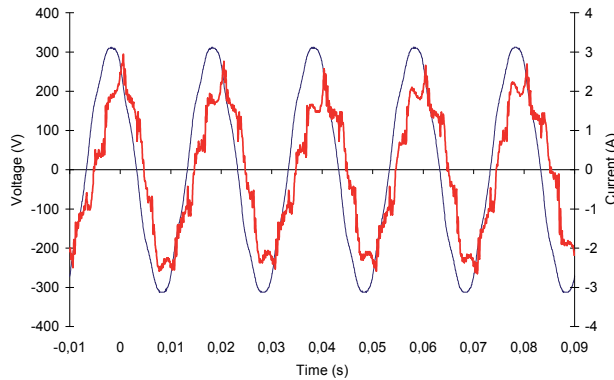


Fig. 27. AC waveforms of inverter 2 at 10.45.

After the conclusion of the shading, all the six inverters of the first system have values of THD of AC current around 10 %, with the main component given by the third harmonic. In order to check whether this is the behaviour also for the inverters of the second system, the measurements of the AC waveforms, without the shading, have been carried out by the oscilloscope.
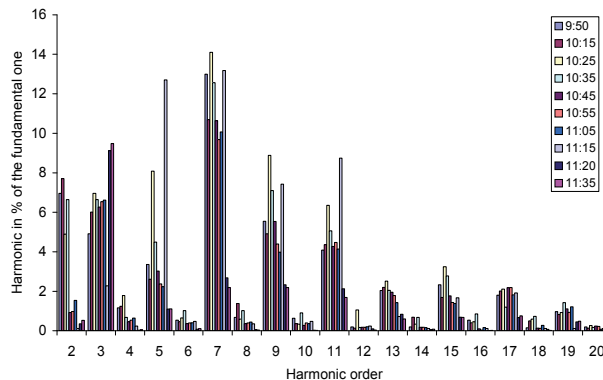


Fig. 28. Histogram of the harmonic currents (inverter 2).

As an example for the inverter 5, the waveforms of AC current and voltage are shown in Figure 29, in which it is worth noting that: no phase shift exists between voltage and current; a sharp peak, which causes a THD around 9%, is detected in the current. Also the other inverters have confirmed the same behaviour for the current waveform and the harmonic distortion.
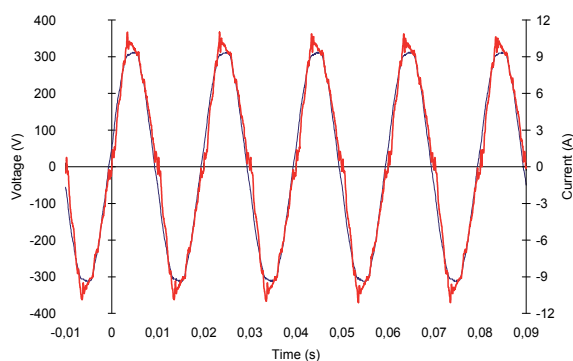
Fig. 29. AC waveforms of inverter 5 (2nd system).

Concerning the item 3., by using the data logger, periodic measurements of r.m.s. voltage, current and power, besides harmonic analysis with THD, have been performed for each phase of the three-phase grid. In the first system, phase 1 supplies the currents of inverter 1 and 2 (the most shaded), phase 2 feeds the currents of inverter 3 and 4 (supplied by the only array without shading) and phase 3 feeds the currents of inverter 5 and 6. In Figure 30, relevant to a data acquisition in May, it is clear the shading effect until 13.00. During the shading, the main results are: the power factors $PF_1$ and $PF_3$ are continuously variable within the range 0.75-0.95, due to not only the high harmonic distortion $THD_I$ (15-20%), but also the phase shift between voltage and current.
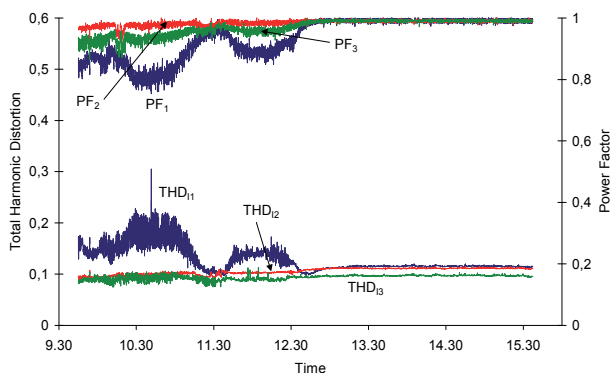


Fig. 30. Daily monitoring of PF and THD (1st system).

## 5.5 Concluding remarks

Concerning two grid connected PV systems, it has been described the negative influence, owing to shading effect of PV arrays, on the inverter performance both at the DC and the AC sides. The experimental results point out that:

- the DC ripples are higher than 30% and the waveforms have harmonic content, with a fundamental frequency within 40-80 Hz;
- the MPPT efficiency is around 60%, because the tracking method relies on the assumption that the voltage at MPP is a constant fraction of the open circuit voltage, but with shading the fraction decreases down to roughly 50%;

- the THD of AC current is higher than 20% with a great spread and presence of even harmonics, whereas the THD of voltage is slightly influenced by the shading;
- the power factor is within 0.75-0.95, due to the previous current distortion and the capacitive component, which becomes important in shading condition.

## 6. References

Abete, A.; Ferraris, L. & Spertino, F. (1998). Measuring Circuits to detect Mismatching of the Photovoltaic cells or modules Current-Voltage Characteristics, *IMEKO TC-4 Symposium on Development in Digital Measuring Instrumentation and 3rd Workshop on ADC Modeling and Testing*, pp. 313-315, Naples, Italy, September 17-18, 1998.

Abete, A.; Napoli, R. & Spertino, F. (2003). A simulation procedure to predict the monthly energy supplied by grid connected PV systems, *3rd World Conference on Photovoltaic Energy Conversion*, pp. 1-4 (CD ROM), ISBN 4-9901816-3-8, Osaka, Japan, May 11-18, 2003.

Abete, A.; Napoli, R. & Spertino, F. (2005). Grid connected PV systems on façade "Sun Shields": Decrease of inverter performance for shading effect, *20th European Photovoltaic Solar Energy Conference*, pp. 2135-2138, ISBN 3-936338-19-1, Barcelona, Spain, June 6-10, 2005.

Spertino, F.; Di Leo, P. & Sumaili Akilimali, J. (2009). Optimal Configuration of module connections for minimizing the shading effect in multi-rows PV arrays, *24th European Photovoltaic Solar Energy Conference*, pp. 4136-4140, ISBN 3-936338-25-6, Hamburg, Germany, September 21-25, 2009.

Spertino, F. & Sumaili Akilimali, J. (2009). Are manufacturing I-V mismatch and reverse currents key factors in large Photovoltaic arrays?, *IEEE Transactions on Industrial Electronics*, Vol. 56, No.11, (November 2009), pp. 4520-4531, ISSN 0278-0046.

# Light Trapping Design in Silicon-Based Solar Cells

Fengxiang Chen and Lisheng Wang
*Physics science and technology, Wuhan University of Technology*
*China*

## 1. Introduction

When the sunlight illuminates the front surface of solar cell, part of the incident energy reflects from the surface, and part of incident energy transmits to the inside of solar cell and converts into electrical energy. Typically, the reflectivity of bare silicon surface is quite higher; more than 30% of incident sunlight can be reflected. In order to reduce the reflection loss on the surface of solar cell, usually the following methods were adopted. One is to corrode and texture the front surface [Gangopadhyay et al., 2007; Ju et al., 2008; Basu et al., 2010; Li et al., 2011], so that incident light can reflect back and forth between the inclined surfaces, which will increase the interaction between incident light and semiconductor surface. The second is coated with a single-layer or multi-layer antireflection film coating [Chao et al., 2010]. Generally, these coatings are very thin, the optical thickness is nearly quarter or half of incident wavelength. Single-layer antireflection coating only has good anti-reflection effect for a single wavelength, so multi-layer antireflection coating is commonly used in high efficiency solar cells, for it has good anti-reflection effect within the wide spectrum of solar radiation. Third, surface plasmons offer a novel way of light trapping by using metal nanoparticles to enhance absorption or light extraction in thin film solar cell structures [Derkacs et al., 2006; Catchpole et al., 2008; Moulin et al.,2008; Nkayama et al.,2008; Losurdo et al.,2009;]. By manipulating their size, the particles can be used as an efficient scattering layer. One of the benefits of this light trapping approach is that the surface area of silicon and surface passivation layer remain the same for a planar cell, so surface recombination losses are not expect to increase.

The above light tapping methods can be used individually or in combination. In the following section we will introduce them in detail.

## 2. Principle and preparation of textured surface

Textured solar cells can not only increase the absorption of the incident sunlight, it also has many other advantages [Fesquet et al., 2009]. For solar cells, the higher efficiency and the lower cost are always main topic in scientific research. Because the crystalline silicon is non-direct band gap semiconductor material, the absorption of sunlight is relatively weak, the thickness of the solar cell need to exceed a few millimeters to absorb 99% of the solar spectrum, which increased the weight of materials and the production cost, and increased the recombination probability in the bulk, resulting in reduced anti-radiation performance.

The textured surface can be realized by many methods. These methods are different for mono-crystalline silicon and multi-crystalline silicon material. Next, we will introduce the textured methods for silicon solar cells in detail.

### 2.1 Textured surface for single crystalline silicon

Textured surface is fulfilled on mono-crystalline silicon surface by a selective corrosion. At high temperature, the chemical reaction between silicon and alkali occurs as follows:

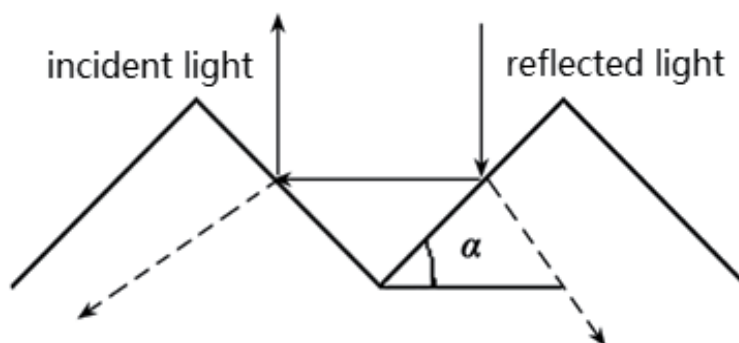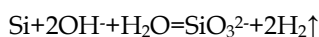$$Si+2OH^-+H_2O=SiO_3^{2-}+2H_2\uparrow$$



Fig. 1. Light trapping by "pyramid" covered at the textured surface.

So hot alkaline solution is usually used to corrode the silicon. For different crystalline faces and crystalline directions, the atoms are arranged differently, so the strength between the atoms is different. According to principles of electrochemical corrosion, their corrosion rate will be different. For {100} planes, the spacing of the adjacent two planes is maximum and the density of covalent bonds is the minimum, so the adjacent layer along the {100} atomic planes are most prone to breakage. On the other hand, atoms within the {111} planes have the minimum distance, and the surface density of covalent bonds is the maximum, which results in that the corrosion rate is the minimum along the <111> direction. Therefore, the corrosion faces revealed by preferential etching solution are (111) planes. After single crystalline silicon material with <100> orientation was corroded preferentially, the pyramids on the surface of mono-crystalline silicon come from the intersection of (111) planes. The "pyramid" structure was shown in Fig. 1.

The low concentrations alkaline solution, such as 1.25% of sodium hydroxide (NaOH) solution is usually used as a selective etching solution, because the corrosion rates of (100) plane and the (111) plane are not the same, the pyramid structure can be obtained on mono-crystalline Si surface, which increased light absorption greatly. In the preparation processes, temperature, ethanol content, NaOH content, and corrosion time are the factors which affect the morphology of the pyramids. Fig.2 shows the SEM pictures of textured surfaces with changes of the corrosion time. It can be seen from Fig.2 that the formation of the pyramids with the corrosion time. For example, after 5min, the pyramid began to appear; after 15min, the silicon surface was covered by small pyramids, and a few have begun to grow up; after 30min, the silicon surface covered with pyramids.
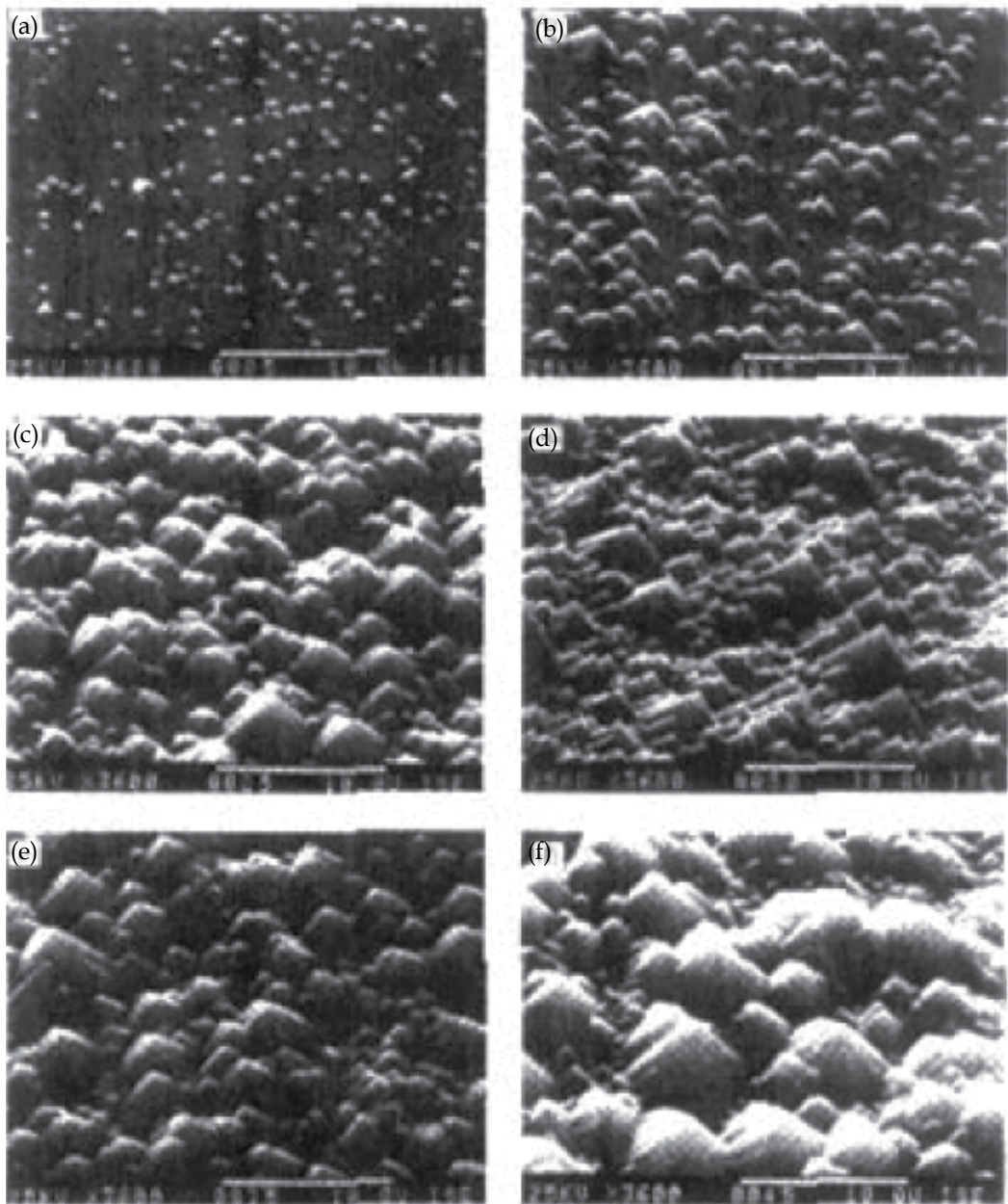
Fig. 2. The SEM pictures of textured surface with the corrosion time, the corrosion time are: (a)5min,(b)15min,(c)25min, (d)30min,(e)35min, (f)40min, respectively.[Wang, 2005]
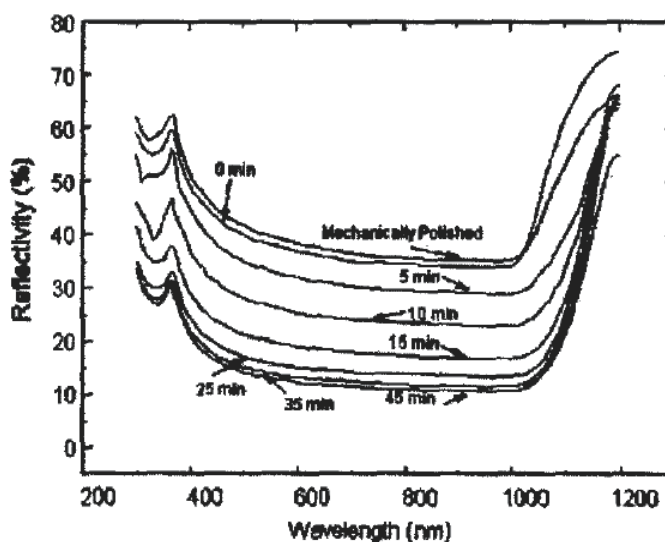
Fig. 3. The reflectivity of silicon wafers after different etching time.[Wang, 2005]

Fig.3 shows the reflectivity of mono-crystalline silicon wafer after different corrosion time (5-45min). We can find that in the visible range (450-1000nm), the reflectivity decreases with increasing corrosion time, the minimum reflectivity is 11%. For the corrosion time is in the 25-45min range, the corresponding reflectivity is nearly 11-14%. If etching time is further increased, no significant change happens in reflectivity.

### 2.2 Textured surface for polycrystalline silicon

For single crystalline silicon with <100> orientation, the ideal pyramid structure can be etched by NaOH solution. However, for polysilicon, only a very small part of the surface is covered with (100) orientation, so the use of anisotropic etching for textured surface is not feasible. Because the orientations of the grains in polysilicon are arbitrary and alkaline solution such as NaOH or KOH, are anisotropic etching, these can easily result in uneven texture, this alkaline etching method is not suitable for texturing polysilicon. In view of optics, the acid solution (the mixture of HF, $HNO_3$, and $H_2O$) and the RIE (reactive ion etching) method are the isotropic surface texture methods for textured surface of polysilicon.

The acid etching solution for polysilicon is mixture of HF, $HNO_3$ and deionized water mixed by certain percentages, where $HNO_3$ is used as strong oxidant, so that silicon became $SiO_2$ after oxidation. The whole silicon surface is covered by dense $SiO_2$ film after oxidation and this $SiO_2$ film will protect the silicon from further reaction. HF solution is used as complexing agent and this solution can dissolve $SiO_2$ film, the resulting $H_2[SiF_6]$ complexes is soluble in water. $H_2[SiF_6]$ is a strong acid, which is stronger than sulfuric acid and easily dissociate in solution. So this reaction is a positive feedback corrosion reaction, with the generation of $H_2[SiF_6]$, and the dissociation from the $H^+$ concentration increased, then the corrosion rate also increased. If corrosion speed is too fast, the reaction process is difficult to control, leading to poor corrosion. To mitigate the corrosion reaction, by mass action law, reducing the HF concentration can slow the reaction speed. The reaction mechanism is as follows [Yang, 2010]:

$$3Si+4HNO_3=3SiO_2+2H_2O+4NO \uparrow$$

$$SiO_2+6HF=H_2[SiF_6]+2H_2O$$

$$H_2[SiF_6] \Leftrightarrow 2H^+ +[SiF_6]^{2-}$$
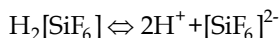
This etching method is isotropic corrosion, which has nothing to do with the orientations of the grains, so it will form a uniform textured surface on the polysilicon surface.

Fig.4 shows the SEM pictures for polysilicon wafers after alkaline etching, acid etching, and first acid corrosion with the second alkaline etching. From Fig.4(a), we can see that after alkaline corrosion the surface is uneven and has more steps. Fig.4(c) shows the morphology of the first acid corrosion with the second alkaline etching, we can find that the pyramid shape and the surface are uneven. So these two surface conditions are not suitable to the sequent screen printing procedure. And SEM picture for acid corrosion is shown in Fig.4 (b). We can get the required thickness by changing the ratio of acid solution and controlling the response speed.



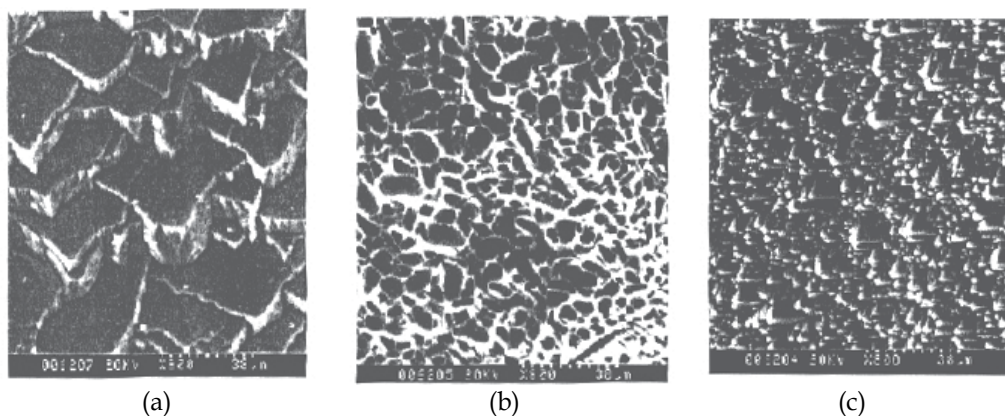|       (a)       |       (b)       |       (c)       |

Fig. 4. The SEM pictures for (a)polysilicon with alkaline etching;(b)polysilicon with acid etching; (c)polysilicon with first acid etching and second alkaline etching.[Meng, 2001]

Acid etching method for polysilicon has many advantages: firstly, it can remove surface damage layer and texture surface in a very short period of time, this will save the production time; Secondly, the surface after etching is relatively flat and thin, which is easy to make thin battery; Thirdly, NaOH solution is not used, which avoid the contamination from Na ions; and the wafer after the acid corrosion is flat, which is easy to form a relatively flat pn junction, thereby it help to improve the stability of the solar cells; Finally, the flat surface is suitable for the screen printing process and the electrode contact is not prone to break.

The reflectance curves of different polysilicon surfaces are shown in Fig.5. We can found the reflectivity with acid etching is no more than 20% in the range 400-1000nm; after the deposition of silicon nitride anti-reflection coating (ARC), the average reflectivity is less than 10%; and the reflectivity reaches 1% at 600nm wavelength. Thus, the reflection loss with acid etching is very small. In contrast, for the alkaline texture, the reflectivity is relatively higher, while the reflectivity with acid and alkaline double texture is intervenient.
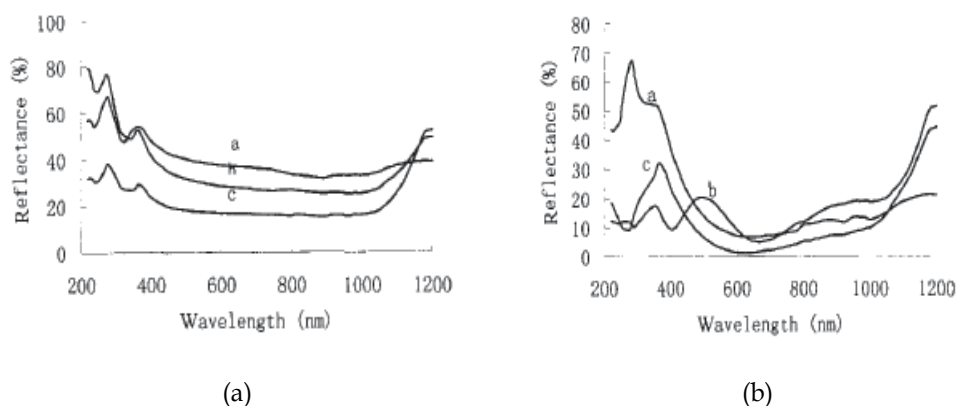
(a)                                                                      (b)

Fig. 5. Reflectance curves of polysilicon textured with the chemical etching. (a) Without ARC; (b)With SiN ARC. (a-NaOH texturing; b-NaOH after acidic texturing; c-Acidic texturing). [Meng, 2001]

In the RIE preparation process, the gas species, gas flow, pressure and RF power both will influent the etching result. Combined with the gas plasma etching with chlorine gas ($Cl_2$) and the antireflection coating method, the lower reflectivity can be realized in a wide range of wavelengths. According to [Inomato, 1997], the flow rate of chlorine gas can be easily controlled to adjust the surface aspect ratio, which is helpful to form the similar pyramid structure on the polysilicon surface. The maximum short circuit current and the maximum open circuit voltage can be obtained under the condition the chlorine flow is 4.5sccm. The experimental results show that for the mono-crystalline silicon, the reflectivity is about 1-2% in the 400-1000nm wavelength range. In RIE method, because the chlorine or fluorine was used as etching gas, the influence on the environment should be considered.

The textured structure also has some drawbacks. Firstly, in the production process of pyramids, the acid or alkaline solution is often used, which need to be careful; Secondly, the pyramids on the surface increase the surface area, which reduces the average light intensity. And the multiple reflections on the textured surface will result in the uneven distribution of incident illumination. Both these will affect the open circuit voltage of the solar cell; Thirdly, the textured structure not only decreases the reflectivity, but also increases the absorption of the infrared light. The absorption of infrared light will heat the solar cell and decrease the conversion efficiency of solar cell; seriously it will disable the solar cell.

## 3. Principle and design of the antireflection coating

### 3.1 The basic theory of antireflection coating

Most solar cells were coated with an antireflection coating layer to reduce light reflection on the front surface [Kuo et al., 2008]. This is why crystalline silicon solar cells appears to be blue or black while silicon material appears to be grey. A set of optimized and well designed anti-reflection coating on the front surface is an effective way to improve the optical absorption of the solar cell. For certain range in sunlight spectrum, reflectivity on the front surface varies from more than 30% down to less than 5% [Geng et al., 2010], which greatly increase the absorption of incident sunlight energy of the solar cell.

The following figure shows the basic principles of the anti-reflection film. When the reflection of light on second interface returns to the first interface, and if the phase difference between the two lights is 180 degrees, the former will offset the latter to some extent.
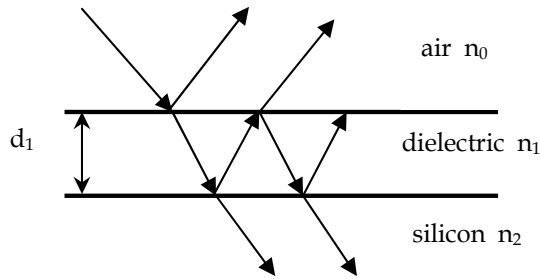


Fig. 6. The principles of the antireflection coating.

When the incident light is normally illuminated, and the silicon material covered with a transparent layer with thickness $d_1$, the expression of the reflected energy is [Wang, 2001]:

$$R = \frac{r_1^2 + r_2^2 + 2r_1r_2\cos 2\theta}{1 + r_1^2r_2^2 + 2r_1r_2\cos 2\theta} \tag{1}$$

Where $r_1$ and $r_2$ are: $r_1 = \frac{n_0 - n_1}{n_0 + n_1}, r_2 = \frac{n_1 - n_2}{n_1 + n_2}$

Where $n_i$ represents the diffraction index. The $\theta$ is given by:

$$\theta = \frac{2\pi n_1 d_1}{\lambda_0}$$

When $n_1 d_1 = \lambda_0/4$ is fulfilled, the reflectivity has the minimum.

$$R_{min} = (\frac{n_1^2 - n_0 n_2}{n_1^2 + n_0 n_2})^2$$

If the transparent layer has the greatest antireflective effect, the zero reflectivity R = 0 should be required. This means $n_1 = \sqrt{n_0 n_2}$. Thus for the desired wavelength $\lambda_0$, the refractive index of the antireflective film can be calculated by the above expression. But when the incident wavelength deviates from $\lambda_0$, the reflectivity will increase. Therefore, in order to increase the output of solar cell, the distribution of solar spectrum and the relative spectral response of crystalline silicon should be taken into account, and a reasonable wavelength $\lambda_n$ will be chosen. The peak energy among the terrestrial solar spectrum occur in 0.5um, while the peak of relative spectrum response of silicon cells is in the range 0.8-0.9um wavelength, so the wavelength range of the best anti-reflection is in 0.5-0.7um.

In the actual processes of crystalline silicon solar cells, commonly used anti-reflective materials are $TiO_2$, $SiO_2$, $SiN_x$, $MgF_2$, ZnS, $Al_2O_3$, etc. Their refractive indexes were listed in Table 1. Their thicknesses are generally about 60-100nm. Chemical vapor deposition (CVD), plasma chemical vapor deposition (PECVD), spray pyrolysis, sputtering and evaporation techniques can be used to deposit the different anti-reflection film.

| Materials | Refraction index n |
|-----------|--------------------|
| $MgF_2$ | 1.38 |
| $SiO_2$ | 1.46 |
| $Al_2O_3$ | 1.76 |
| $Si_3N_4$ | 2.05 |
| $Ta_2O_5$ | 2.2 |
| ZnS | 2.36 |
| SiOx | 1.8-1.9 |
| $TiO_2$ | 2.62 |

Note: The wavelength 590nm (the corresponding energy is 2.1eV) was used in calibration.

Table 1. The refractive index of common anti-reflective materials [Markvart & Castner, 2009]

Among all antireflection coatings, $TiO_x(x \leq 2)$ is one of commonly used antireflection coatings in preparation of crystalline silicon solar cells. This film is usually used as an ideal antireflection coating (ARC) for its high refractive index, and its transparent band center coincides with visible spectrum of sunlight well. And silicon nitride ($SiN_x$) is another commonly used ARC. Because $SiN_x$ film has good insulating ability, density, stability and masking ability for the impurity ions, it has been widely used in semiconductor production as an efficient surface passivation layer. And in the preparation process of $SiN_x$ coating, it can be easily achieved that the reflection-passivation dual effect, which will improve the conversion efficiency of silicon solar cells significantly. Therefore, since the 90s of the 20th century, the use of $SiN_x$ thin film as antireflection coating has become research and application focus.

## 3.2 Optimization of the antireflection coating

When conducting coatings optimization design, generally the following assumptions were assumed [Wang, 2001]: 1) The film is an isotropic optical media, and its dielectric properties can be characterized by the refractive index n, where n is a real number. For metals and semiconductors, their dielectric properties can be represented by the complex refractive index N = n-jk (or optical admittance), where N is a plural, and its real part n still represents refractive index, imaginary part k is the extinction coefficient, j is imaginary unit. 2) Two adjacent media was separated with an interface, and the refractive index occurs on both sides change discontinuously. 3) Except the interface, the variation of the refractive index along the film thickness direction is continuous; 4) Films can be separated by two parallel planes, and it is assumed to be infinite in horizontal direction. The thickness of the film has the same magnitude with the light wavelength; 5) The incident light is a plane wave.

In the design of multi-layer coating, the main parameters of the coating structure are: the thickness of each layer $d_1$, $d_2$, ...,$d_k$; incident media, refractive indexes of each layer and the substrate $n_0$, $n_1$ ... $n_k$; light incidence angle $\theta$ and wavelength $\lambda$. The optical properties of the coating, such as the reflectivity R, depend on these structural parameters. In general, the spectral distribution of incident light is known, so the desired reflectivity R can be achieved by adjusting the values of $n_i$, $d_i$ (i = 1,2, ... k) and so on.

Fig.7 shows the typical reflectivity curves for single and double layer antireflection coating under normal incidence. We can find the curve shapes in Fig.7(a) and Fig.7(b) are different. The reflectivity curve for single-layer ARC is V-shape, which means the minimum reflectivity only can be achieved in one specific wavelength. If the incident wavelength is far

from this wavelength, the reflectivity increases very much. While the reflectivity curve for double ARC is W-shape. This means that the reflectivity reaches the minimum in two specific wavelengths, which is helpful to suppress the reflectivity in the range 300-1200nm. It is clear from Fig.7 that the antireflection effect of double layer ARC is better than that of single layer ARC.
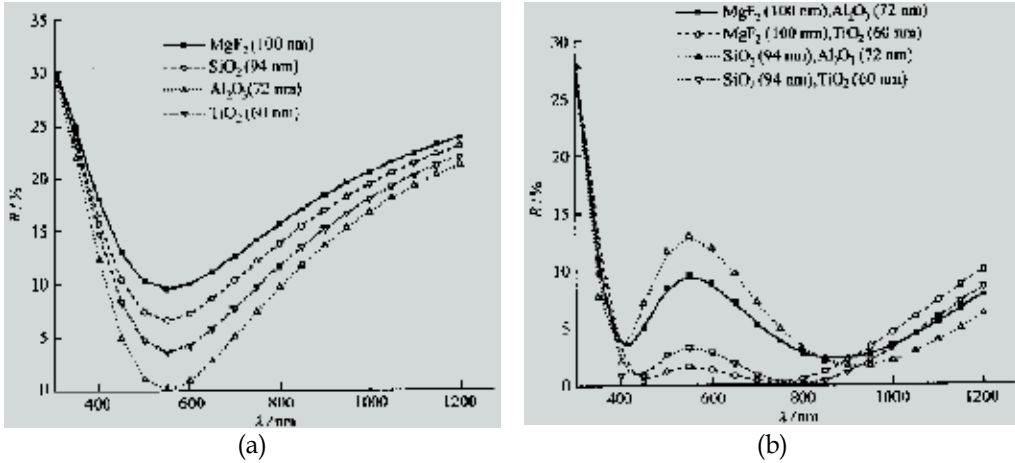


Fig. 7. The typical reflectivity curves for single and double layer antireflection coating. [Wang et al., 2004]

Besides the normal incidence, the oblique incidence should also be considered. This is because in the practical application, except for concentrated solar cells, most solar cells are fixed in a certain direction in accordance with local longitude and latitude. In the whole cycle of the sun rising and landing, the antireflection coating is not always perpendicular to the incident light. The incident angle is always changing and this case is known as oblique incidence. When the ARC designed under normal incidence is applied to the oblique incidence, due to the polarization effect, the reflective properties will change dramatically. Therefore, the antireflection coatings used in the wide-angle should be redesigned to meet the needs of all-weather use.

In the case of oblique incidence, for a single-layer system, the reflectivity can be obtained by Fresnel formula; for a multi-layer system, each layer can be represented by an equivalent interface. If the equivalent admittance of the interface is obtained, the reflectivity of the whole system can be acquired. The basic calculation is as follows [Lin & Lu, 1990]:

For m layers coating system, the refractive index and thickness of each membrane material are known as $n_k, d_k (k = 1, 2, .... m)$, respectively. The refractive index of incident medium and the substrate material are $n_0, n_{m+1}$, respectively. The light incident angle is $\theta_0$. $\eta_k$ is the optical admittance. The interference matrix for the k-layer is:

$$M_k = \begin{bmatrix} \cos\delta_k & i(\sin\delta_k)/\eta_k \\ i\eta_k \sin\delta_k & \cos\delta_k \end{bmatrix} \tag{1}$$

where $\delta_k = 2\pi n_k d_k \cos\theta_k / \lambda \quad (k = 0, 1...m)$ is the phase thickness of the k-layer.

Then the interference matrix for the whole m layers system is:

$$M = \prod_{k=1}^{m} M_k \tag{2}$$

In the case of oblique incidence, the admittance values of s polarization and p polarization are different. For the number k layer, they are:

$$\eta_k = \begin{cases} n_k/\cos\theta_k & p \text{ component} \\ n_k\cos\theta_k & s \text{ component} \end{cases} \tag{3}$$

Where $\theta_k$ can be given by the Snell law,

$$n_0\sin\theta_0 = n_k\sin\theta_k, k = 1,2....m, m+1 \tag{4}$$

The expression $Y = C/B$ is the admittance for combinations of multi-layer coatings and the substrate, and B, C were determined by:

$$\begin{bmatrix} B \\ C \end{bmatrix} = M\begin{bmatrix} 1 \\ \eta_{m+1} \end{bmatrix} \tag{5}$$

Where $\eta_{m+1}$ is the admittance of the substrate layer.

The energy reflectivity $R$ of the thin film system is:

$$R = \left|\frac{1 - Y/\eta_0}{1 + Y/\eta_0}\right|^2 \tag{6}$$

For the $R_s$ component, the $Y, \eta_0$ values in above expression should be replaced by $Y_s, \eta_{0s}$. For the $R_p$ component, the corresponding $Y, \eta_0$ should be substituted by $Y_p, \eta_{0p}$. The total energy reflectivity $R$ is:

$$R = \frac{R_s + R_p}{2} \tag{7}$$

The reflectivity R of the whole system depends on the structural parameters of each layer. Since the spectral response of silicon ranges from 300 to 1200nm, so only incident light in the 300-1200nm wavelength range is considered. Taking into account the inconsistent between the solar spectrum and the spectral response curve of silicon, the evaluation function is chosen as:

$$F = \frac{\int_{0.3}^{1.2} S(\lambda)SR(\lambda)R(\lambda)d\lambda}{\int_{0.3}^{1.2} S(\lambda)SR(\lambda)d\lambda} \tag{8}$$

where $S(\lambda), SR(\lambda)$ and $R(\lambda)$ represent the spectral distribution of the sun, the spectral response of silicon and the reflectivity of the antireflection coating in the specific wavelength, respectively. So the weighted average reflectivity F can be calculated within the entire solar spectrum.

### 3.3 The optimization results

Fig.8 (a), (b), (c), (d) show the results of $SiN_x/SiO_2$ ARC when 15°, 30°, 45°, 60° were selected as the optimal angles, where the angles marked in the figure are the incident angles. It can be seen from Fig.8 (a) that the reflectivity is too high when the incident angle is large, especially for the longer wavelength range. And comparing the results of the case 60° and 15°, we can find that the 60° optimization can significantly reduce the long-wavelength reflectivity within the 10%, but the reflectivity rises in short-wave area inevitably, which inhibits the absorption of high-energy photons in the solar spectrum. While optimization with 30° shows a good antireflection property. Under this case when the incident angles range from 0° to 45°, the reflectivity curve is relatively stable; even for the 60° incident angle, the reflectivities in short wavelength and long wavelength still maintain below 15%. The optimization results of 45° is similar with those of 60°, the reflectivity for long wavelength under large incident angle is lower, but for small angle case, the reflectivity for short wavelength is too high.
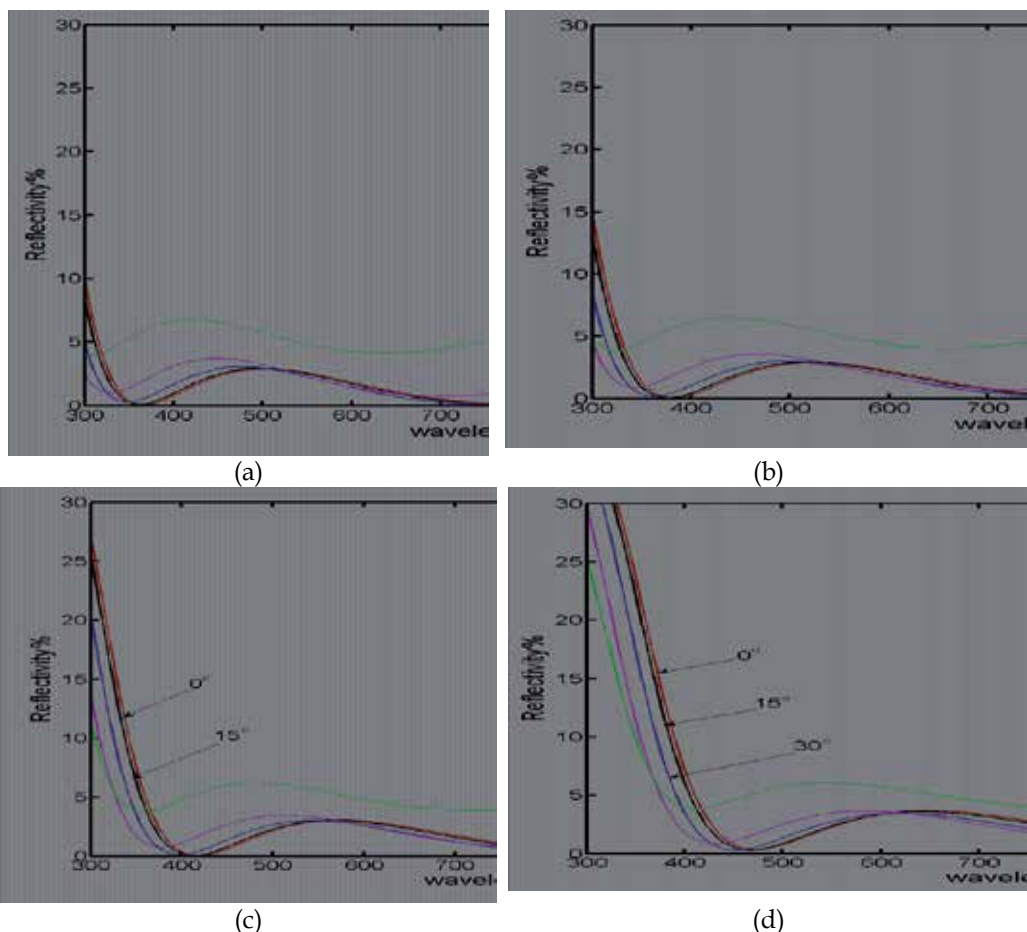


Fig. 8. Under different optimal angles, the reflectivities of optimal $SiN_x/SiO_2$ ARC vary with the incident angles and wavelength. The different optimal angles equal to
(a) 15°; (b) 30°; (c) 45°; (d) 60°, respectively.[Chen & Wang, 2008]

To further comparing the impact of the optimal angles on the antireflection, combining the intensity distribution of the solar spectrum and spectral response of silicon solar cells, Fig. 9 shows the variation of the weighted average reflectance F with the incident angle. It can be seen from Fig. 9 that if 0° or 15° was selected as an optimal angle, F is just low in small incident angle, with the incident angle increases, F increases rapidly; and if 45° or 60° was used as an optimal angle, although F is low for the large angle, but F is higher in small angle range, especially for 60° case. The value of F is more than 1 percentage point higher than that of 0° in small-angle region. These suggest that if the large angle is selected as the optimal angle, a good anti-reflection effect can't be achieved for the small incident angle. And if 30° is selected, it is clear from the figure that this angle has the minimum average F in this range, so 30°is the best optimization angle.
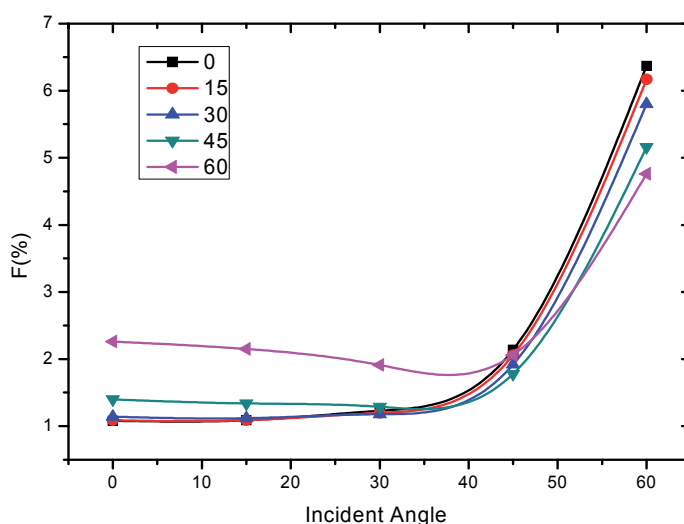


Fig. 9. Weighted average reflectance of double-layer anti-reflection coatings versus different incident angles.[ Chen & Wang, 2008]

In conclusion, in practical applications, the oblique incidence is a more common situation. In the oblique incidence case, 30° is the best degree for designing and optimizing ARC.

## 4. Surface Plasmons [Atwater & Polman, 2010; Pillai et al., 2007]

For thin-film silicon solar cells, the Si absorber has a thickness on the order of only a few micrometers and is deposited on foreign substrates such as glass, ceramics, plastic, or metal for mechanical support. However, the efficiency of such silicon thin-film cells at the moment are low compared to wafer-based silicon cells because of the relatively poor light absorption, as well as high bulk and surface recombination. Fig.10 shows the standard AM1.5 solar spectrum together with a graph that illustrates what fraction of the solar spectrum is absorbed on a single pass through 2-um-thick crystalline Si film. Clearly, a large fraction of the solar spectrum, in particular in the intense 600-1100nm spectral range, is poorly

absorbed. This is the reason that conventional wafer-based crystalline Si solar cells have a much larger thickness of typically 180-300um.
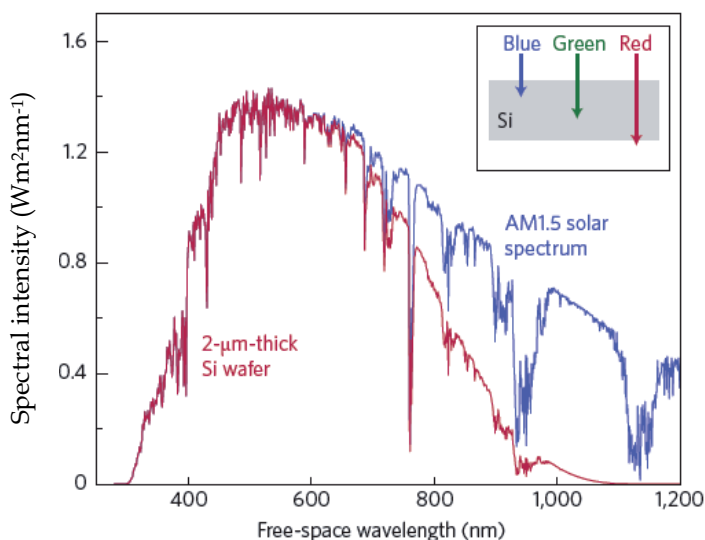


Fig. 10. AM1.5 solar spectrum, together with a graph that indicates the solar energy absorbed in a 2um-thick crystalline Si film (assuming single-pass absorption and no reflection). [Atwater & Polman, 2010]

Because thin-film solar cells are only a few microns thick, standard methods of increasing the light absorption, which use surface textures that are typically around 10 microns in size, cannot be used. Plasma etching techniques, which can be used to etch submicron-sized feature, can damage the silicon, thereby reducing the cell efficiency. Another alternative to direct texturing of Si is the texturing of the substrate. However, this also results in increased recombination losses through increased surface area. Though in practice it has been experimentally proven to be very difficult to reduce recombination losses beyond a certain limit, theoretically energy conversion efficiency of above 24% even for 1um cells can be achieved. This highlights the need to incorporate better light-trapping mechanisms that do not increase recombination losses in thin-film solar cells to extract the full potential of the cells. A new method of achieving light trapping in thin-film solar cells is the use of plasma resonances in metal.

The electromagnetic properties of metal particles have been known for a long time since the work of Wood and Ritchie, but there has been renewed interest in recent years following the development of new nanofabrication techniques which makes it easy to fabricate these nanostructures. Plasmons can exist in bulk, can be in the form of propagating waves on thin metal surface or can be localized to the surface. So the plasmons are termed bulk plasmons, surface plasmon polariton (SPP) and localized surface plasmons (LSP) respectively. Bulk plasmons are studied using electron or x-ray spectroscopy. The excitation of bulk plasmons using visible light is difficult.

Surface Plasmon polaritions (SPPs) are combined excitations of the conduction electrons and a photon, and form a propagating mode bound to the interface between a thin metal and a

dielectric travelling perpendicular to the film plane. This phenomenon only occur at the interface between metals and dielectrics where the Re($\varepsilon$) (where $\varepsilon$ is the dielectric function) have opposite signs, and decay exponentially with distance from the interface, as shown in Fig.11.
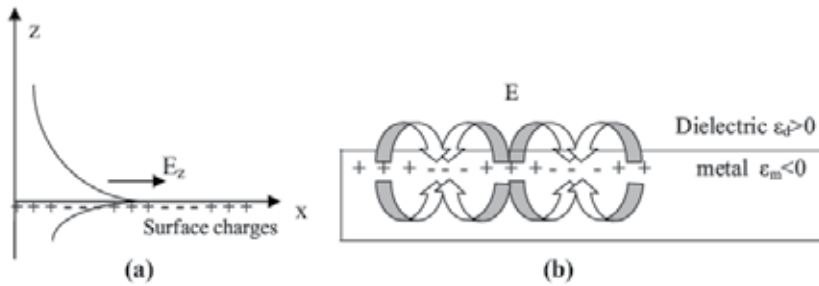


Fig. 11. (a) Schematic of a surface plasmon at the interface of a metal and dielectric showing the exponential dependence of the field E in the z direction along with charges and (b) electromagnetic field of surface plasmons propagating on the surface in the x direction. [Pillai, 2007]

According the theory, the propagating waves can travel up to 10-100um in the visible for silver owing to its low absorption losses and can increase up to 1mm in the near-infrared. Generally the surface plasmon resonant frequency is in the ultra-violet for metals and the infra-red for heavily doped semiconductors.

LSP are collective oscillations of the conduction electrons in metal particles. Movement of the conduction electrons upon excitation with incident light leads to a buildup of polarization charges on the particle surface. This acts as a restoring force, allowing a resonance to occur at a particular frequency, which is termed the dipole surface plasmon resonance frequency. A consequence of surface plasmon excitation in the enhancement of the electromagnetic field around the vicinity of the particles is shown in Fig.12.
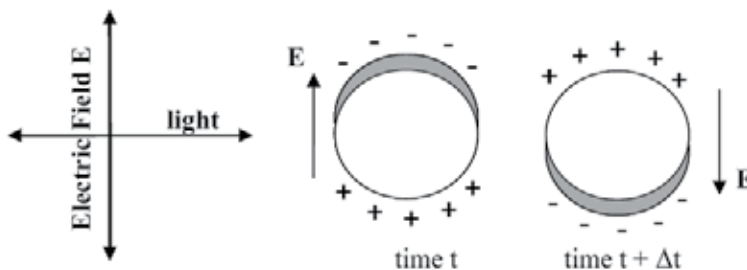


Fig. 12. Incident light excites the dipole localized surface Plasmon resonance on a spherical metal nanoparticle. [Pillai, 2007]

By proper engineering of this metallodielectric structures, light can be concentrated and "folded" into a thin semiconductor layer, thereby increasing the absorption. Both local surface plasmons excited in metal nanoparticles and surface plasmons polaritions propagating at the metals/semiconductor interface are of interest.

Plasmonic structures can offer at least three ways of reducing the physical thickness of the photovoltaic absorber layer while keeping their optical thickness constant, as shown in Fig.13. First, metallic nanoparticles can be used as subwavelength scattering elements to couple and trap freely propagating plane waves from the Sun into an absorbing semiconductor thin film, by folding the light into a thin absorber layer. Second, metallic nanoparticles can be used as subwavelength antenna in which the plasmonic near-field is coupled to the semiconductor, increasing its effective absorption cross-section. Third, a corrugated metallic film on the back surface of a thin photovoltaic absorber layer can couple sunlight into SPP modes supported at the metal/semiconductor interface as well as guided modes in the semiconductor slab, whereupon the light is converted to photocarrier in the semiconductor.
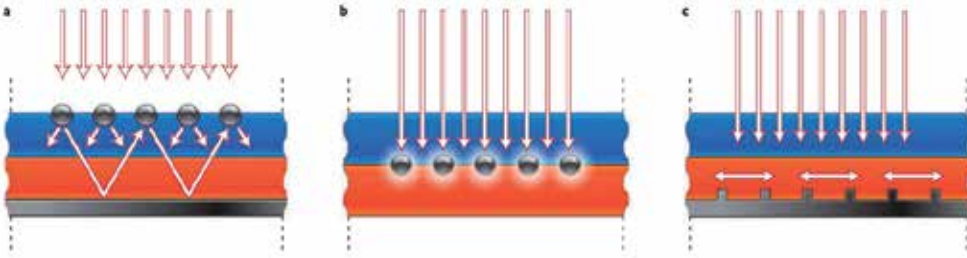


Fig. 13. Plasmonic light-trapping geometric for thin-film solar cells.[Atwater & Polman, 2010]

## 4.1 Light scattering using particle plasmons

Incident light that is in the region of the resonance wavelength of the particles is strongly scattered or absorbed, depending on the size of the particles. The extinction of the particle is defined as the sum of the scattering and absorption. For small particles in the quasistatic limit, the scattering and absorption cross section are given by [Bohren, 1983; Bohren & Huffman, 1998]

$$C_{sat} = \frac{1}{6\pi}\left(\frac{2\pi}{\lambda}\right)^4 |\alpha|^2$$

and
$$C_{abs} = \frac{2\pi}{\lambda}\text{Im}[\alpha]$$

Here, $\alpha$ is the polarizability of the particle, given by

$$\alpha = 3V\frac{(\varepsilon-1)}{(\varepsilon+2)}$$

for a small spherical particle in vacuum, where V is the volume of the particle and $\varepsilon$ is the permittivity of the metal. The scattering efficiency $Q_{sca}$ is given by $Q_{sca} = C_{sca}/\pi r^2$ , where

$\pi r^2$ is the geometric cross section of the particle. Near the surface plasmon resonance, light may interact with the particle over a cross-sectional area larger than the geometric cross section of the particle because the polarizability of the particle becomes very high in this frequency range [Bohren, 1983]. Metals exhibit this property due to excitations of surface plasmons at the frequency where $\varepsilon \cong -2$ .

Both shape and size of metal nanoparticles are key factors determining the incoupling efficiency [Pillai & Green, 2010]. This is illustrated in Fig.14a, which shows that smaller particles, with their effective dipole moment located closer to the semiconductor layer, couple a large fraction of the incident light into the underlying semiconductor because of enhanced near-field coupling. Indeed, in the limit of a point dipole very near to a silicon substrate, 96% of the incident light is scattered into the substrate, demonstrating the power of the particle scattering technique. Fig.14b shows the path-length enhancement in the solar cells derived from Fig.14a using a simple first-order scattering model. For 100-nm-diameter Ag hemispheres on Si, a 30-fold enhancement is found. These light-trapping effects are most pronounced at the peak of the plasmon resonance spectrum, which can be tuned by engineering the dielectric constant of the surrounding medium. For example, small Ag or Au particles in air have plasmon resonances at 350nm and 480nm respectively; they can be redshifted in a controlled way over the entire 500-1500nm spectral range by (partially) embedding them in $SiO_2$, $Si_3N_4$ or Si, which are all standard materials in solar cell manufacturing. The scattering cross-sections for metal nanoparticle can be as high as ten times the geometrical area, and a nearly 10% coverage of the solar cell would sufficient to capture most of the incident sunlight into plasmon excitations.
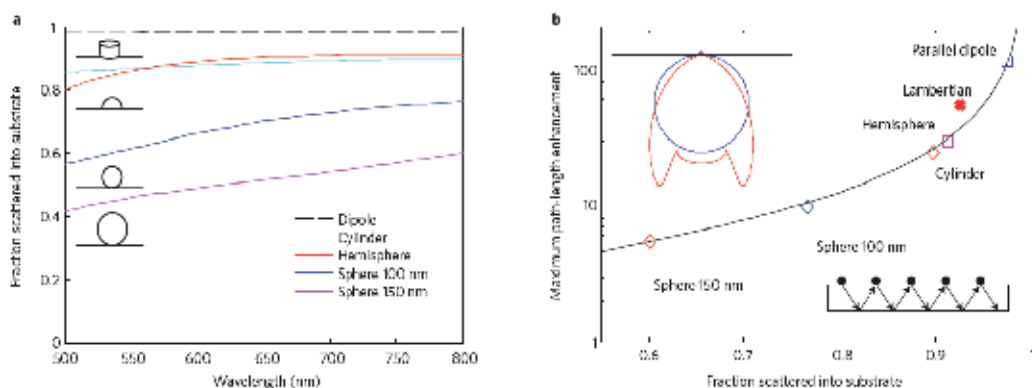


Fig. 14. Light scattering and trapping is very sensitive to particle shape. a. Fraction of light scattered into the substrate, divided by total scattered power, for different sizes and shapes of Ag particles on Si. Also plotted is the scattered fraction for a parallel electric dipole that is 10nm from a Si substrate. b. Maximum path-length enhancement for the same geometries as in left figure at a wavelength of 800nm. Absorption within the particles is neglected for these calculations and an ideal rear reflector is assumed. The line is a guide for eyes. Insets (top left) angular distribution of scattered power for a parallel electric dipole that is 10nm above a Si layer and Lambertian scatter; (bottom-right) geometry considered for calculating the path length enhancement. [Catchpole & Polman, 2008]

## 4.2 Light concentration using particle plasmons.

An alternative use of resonant plasmon excitation in thin-film solar cells is to take advantage of the strong local field enhancement around the metal nanoparticle to increase absorption in a surrounding semiconductor material. The nanoparticles then act as an effective 'antenna' for the incident sunlight that stores the incident energy in a localized surface plasmon mode (Fig.13b). This works particularly well for small (5-20nm diameter) particles for which the albedo is low. These antennas are particularly useful in materials where the carrier diffusion lengths are small, and photocarriers must be generated close to the collection junction area.

Several examples of this concept have recently appeared that demonstrate enhanced photocurrents owing to the plasmonic near-field coupling. Enhanced efficiencies have been demonstrated for ultrathin-film organic solar cells doped with very small (5nm diameter) Ag nanoparticles. An increase in efficiency by a factor of 1.7 has been shown for organic bulk heterojunction solar cells. Dye-sensitized solar cells can also be enhanced by embedding small metal nanoparticles. Also, the increased light absorption and increased photocurrent also reported for inorganic solar cells, such as CdSe/Si heterojunction, Si and so on. The optimization of the coupling between plasmons, excitons and phonons in metal-semiconductor nanostructures is a rich field of research that so far has not received much attention with photovoltaics in mind.

## 4.3 Light trapping using SPPs

In a third plasmonic light-trapping geometry, light is converted into SPPs, which are electromagnetic waves that travel along the interface between a metal back contact and the semiconductor absorber layer, as shown in Fig.13c. Near the Plasmon resonance frequency, the evanescent electromagnetic SPP fields are confined near the interface at dimensions much smaller than the wavelength. SPPs excited at the metal/semiconductor interface can efficiently trap and guide light in the semiconductor layer. In this geometry the incident solar flux is effectively turned by 90°, and light is absorbed along the lateral direction of the solar cell, which has dimensions that are orders of magnitude larger than the optical absorption length. As metal contacts are a standard element in the solar-cell design, this plasmonic coupling concept can be integrated in a natural way.

At frequencies near plasmon resonance frequency (typically in the 350-700nm spectral range, depending on metal and dielectric) SPPs suffer from relatively high losses. Further into the infrared, however, propagation lengths are substantial. For example, for a semi-infinite $Ag/SiO_2$ geometry, SPP propagation lengths range from 10 to 100um in the 800-1500nm spectral range. By using a thin-film metal geometry the plasmon dispersion can be further engineered. Increased propagation length comes at the expense of reduced optical confinement and optimum metal-film design thus depends on the desired solar-cell geometry. Detailed accounts of plasmon dispersion and loss in metal-dielectric geometries are found in references [Berini, 2000; Berini, 2001; Dionne et al., 2005; Dionne et al., 2006].

The ability to construct optically thick but physically very thin photovoltaic absorbers could revolutionize high-efficiency photovoltaic device designs. This becomes possible by using light trapping through the resonant scattering and concentration of light in arrays of metal nanoparticles, or by coupling light into surface plasmon polaritons and photonic modes that propagate in the plane of the semiconductor layer. In this way extremely thin photovoltaic absorber layers (tens to hundreds of nanometers thick) may absorb the full solar spectrum.

## 5. References

Atwater, H. A. & Polman, A. (2010). Plasmonics for improved photovoltaic devices. *Nature Materials*, vol. 9, pp.205–213, ISSN 1476-1122

Basu, P.K.; Pujahari, R.M; Harpreet K. et al. (2010). Impact of surface roughness on the electric parameters of industrial high efficiency NaOH-NaOCl textured multicrystalline silicon solar cell, *Solar Energy*, vol.84, No.9, pp.1658-1665, ISSN 0038-092X

Berini P, (2000). Plasmon-polariton waves guided by thin lossy metal films of finite width: bound modes of symmetric structures. *Phys. Rev.B*, Vol.61, pp.10484-10503, ISSN 1098-0121

Berini P, (2001). Plasmon-polariton waves guided by thin lossy metal films of finite width: bound modes of asymmetric structures. *Phys. Rev.B*, Vol.63, pp.125417, ISSN 1098-0121

Bohren C.F., (1983). How can a particle absorb more than the light incident on it? *Am. J.Phys.* vol.51, No.4, pp.323-327, ISSN 0002- 9483

Bohren C.F. & Huffman D.R., (1998). *Absorption and scattering of light by small particles*, Wiley Interscience, ISBN 0471293407, New York

Catchpole K. R. & Polman A., (2008). Plasmonic solar cells. *Optics Express*, vol.16, No.26, pp.21793-21800, ISSN 1094-4087

Catchpole K.R. & Polman A., (2008). Design principles for particle plasmon enhanced solar cells. *Appl. Phys. Lett.* Vol.93, pp.191113-1-191113-3, ISSN 0003-6951

Chen F.X. & Wang L.S., (2008). Optimized Design of Antireflection Coating for Silicon Solar Cells with Board Angle Usage, *Acta Energiae Solaris Sinica*, vol.29, pp.1262-1266, ISSN 0254-0096

Derkacs D., Lim S. H., Matheu P., et al. (2006). Improved performance of amorphous silicon solar cells via scattering from surface plasmon polaritons in nearby metallic nanoparticles. *Appl. Phys. Lett.*, vol.89, pp. 093103-1-093103-3, ISSN 0003-6951

Dionne J.A, Sweatlock I, Atwater H.A & Polman, A. (2005). Planar plasmon metal waveguides: frequency-dependent dispersion, propagation, localization, and loss beyond the free electron model. *Phys. Rev.B*, vol.72, pp.075405, ISSN 1098-0121

Dionne J.A, Sweatlock I, Atwater H.A & Polman A. (2006). Plasmon slot waveguides: towards chip-scale propagation with subwavelength-scale localization. *Phys. Rev.B*, vol.73, pp.035407, ISSN 1098-0121

Fesquet L, Olibet S, Damon-Lacoste J et al. (2009). Modification of textured silicon wafer surface morphology for fabrication of heterojunction solar cell with open circuit voltage over 700mV. *34th IEEE Photovoltaic Specialists Conference (PVSC)*, ISBN 978-1-4244-2950-9, Philadelphia, June, 2009

Gangopadhyay U, Dhungel S.K, Basu P.K, et al. (2007). Comparative study of different approaches of multicrystalline silicon texturing for solar cell fabrication. *Solar Energy Materials and Solar Cells*, vol.91, No.4, pp.285-289, ISSN 0927-0248

Geng Xue-Wen, Li Mei-Cheng & Zhao Lian-Cheng, (2010). Research development of light trapping structures for thin-film silicon solar cells, *Journal of Function Materials*, vol.41, No.5, pp.751-754, ISSN 1001-9731

Inomata Y., Fukui K. & Shirasawa K., (1997). Surface texturing of large area multi-crystalline silicon solar cells using reactive ion etching method. *Solar Energy Materials and Solar Cells*, vol. 48, pp.237-242, ISSN 0927-0248

Ju M, Gunasekaran M, Kim K, et al. (2008). A new vapor texturing method for multicrystalline silicon solar cell applications, *Materials Science and Engineering B: Solid-State Materials for Advanced Technology*, vol.153, pp.66-69, ISSN 9215-5107

Kuo Mei-Ling, Poxson David J, Kim Yong Sung et al. (2008). Realization of a near-perfect antireflection coating for silicon solar energy utilization, *Optics Letters*, vol.33, No.21,pp.2527-2529, ISSN 0146-9592

Li Qun Wu, Yan Chao & Jian Shao, (2011). Texturing of multi-crystalline silicon wafers through ionized bubble for solar cell fabrication, *Advanced Materials Research*, vol.216, pp. 592-595, ISSN 1022-6680

Lin Y.C. & Lu W.Q., (1990). *Principles of Optical Thin Films*, National Defense Industry Press, ISBN 978-7-118-00543-1, China:Beijing

Maria Losurdo, Maria M. Giangregorio, Giuseppe V. Bianco, et al. (2009). Enhanced absorption in Au nanoparticles/a-Si:H/c-Si heterojunction solar cells exploiting Au surface plasmon resonance. *Solar Energy Materials & Solar Cells,* vol.93, pp.1749-1754, ISSN 0927-0248

Markvart Tom & Castner Luis, (2009). *Solar cells: Materials, Manufacture and Operation,* China Machine Press, ISBN 978-7-111-26798-0, China:Beijing

Meng F.Y., (2001). Grain boundary theory and photovoltaic characteristics of solar cell on polycrystalline silicon material, *Ph.D thesis,* Shanghai Jiaotong University, Shanghai, China

Moulin E., Sukmanowski J., Luo P., et al, (2008). Improved light absorption in thin-film silicon solar cells by integration of silver nanoparticles. *J. Non-Cryst. Solids,* vol.354, pp.2488–2491, ISSN: 0022-3093

Nakayama K., Tanabe K. & Atwater H.A., (2008). Plasmonic nanoparticle enhanced light absorption in GaAs solar cells. *Appl. Phys. Lett.*, vol.93, pp.121904-1–121904-3, ISSN 0003-6951

Pillai S., (2007). Surface plasmons for enhanced thin-film silicon solar cells and light emitting diodes, *Ph.D thesis,* University of NewSouth Wales, Sydney, Australia

Pillai S., Catchpole K. R., Trupke T., et al. (2007). Surface plasmon enhanced silicon solar cells. *J.Appl. Phys.* Vol.101, pp.093105-1-093105-8, ISSN 0021-8979

Pillai S. & Green M.A., (2010). Plasmonics for photovoltaic applications. *Solar Energy Materials and Solar Cells,* Vol.94, No. 9, pp.1481-1486, ISSN 0927-0248

Wang H.Y., (2005), The research on light-trapping materials and structures for silicon-based solar cells. *Ph.D thesis*, Zhengzhou University, Zhengzhou, China

Wang Y.D., (2001). Study on optical properties of solar cells, *Ph.D thesis,* Shanghai Jiaotong University, Shanghai, China

Wang W.H., Li H.B. & Wu D.X., (2004). Design and analysis of anti-reflection coating for solar cells, *Journal of Shanghai University (Nature Science)*, vol.10, No.1, pp.39-42, ISSN 1007-2861

Xiong C., Yao R.H. & Gen K.W., (2010). Two low reflectance of triple-layer broadband antireflection coating for silicon solar cells. *Proceeding on 10th IEEE International Conference on Solid-State and Integrated Circuit Technology*, ISBN 978-1-4244-5798-4, Shanghai, China, Nov.2010

Yang Deren. (2010). *Materials for solar cells*, Chemical Industry Press, ISBN 978-7-5025-9580-7, China:Beijing

# Characterization of Thin Films for Solar Cells and Photodetectors and Possibilities for Improvement of Solar Cells Characteristics

Aleksandra Vasic[1], Milos Vujisic[2],
Koviljka Stankovic[2] and Predrag Osmokrovic[2]
*[1]Faculty of Mechanical Engineering, University of Belgrade*
*[2]Faculty of Electrical Engineering, University of Belgrade*
*Serbia*

## 1. Introduction

Faced with an alarming increase of energy consumption on one side, and very limiting amounts of available conventional energy sources on the other, scientists have turned to the most promising, renewable energy sources. Possibilities for the application of solar systems based on photovoltaic conversion of solar energy are very wide, primarily because of their relatively low cost and very important fact that solar energy is most acceptable source of electrical energy from the environmental point of view. Recently, increased investments in the development of PV technology are observed worldwide. Photovoltaic (PV) conversion of solar energy is one of the most up-to-date semiconductor technologies that enables application of PV systems for various purposes. The wider substitution of conventional energies by solar energy lies in the rate of developing solar cell technology. Silicon is still the mostly used element for solar cell production, so efforts are directed to the improvement of physical properties of silicon structures. Silicon solar cells belong to a wide group of semiconductor detector devises, though somewhat specific in its design (larger than most of the detectors). Basic part of solar cell is p-n junction, which active part is less that 0.2μm thick, so it could be treated as thin film. This photosensitive layer have the most important influence on solar cell functioning, primarily on creation of electron-hole pairs under solar irradiation, transport properties in cells, formation of internal field, and finally, output characteristics of the device such as short circuit current, open circuit voltage and efficiency. Furthermore, in order to function as a voltage generator with the best possible performances, beside p-n junction other thin films such as contact, antireflective, protective (oxide) thin films must be applied both on the front and on the back surface of solar cells. Also, in order to improve characteristics of the device, MIS structure (thin oxide layers) and back surface field layers are routinely used.

Since thin films are very important in many fields of modern science (solar cell technology, for example), a large number of methods were developed for their characterization. Characterization of thin films includes investigations of physical processes in them, developing of the methods for measuring major physical and electrical properties and their

experimental determination. From the aspect of quality assessment of semiconductor device performance, characterization of the whole device gives best results especially in working conditions.

## 2. Characterization of thin films for solar cells and photodetectors

Contemporary trends in microelectronics and electronics in general are oriented to thin films, both from technological and scientific standpoints. Thin film devices as a whole or just a parts of the of devices such as surface, protective, antireflective, contact, or other thin films, have significant advantages over bulk materials. Beside obvious advantage in material and minimization of the device dimensions, methods for obtaining thin films are simpler and less demanded when the quality of the material is concerned than for thicker films. Moreover, characteristics of thin films could be significantly different from the bulk material and could lead to better performances of the device.

Great importance of thin films in modern science, as well as diversity of their characteristics made necessary the development of numerous methods for their research. Investigations of both physical and electrical properties of thin films are necessary primarily in order to determine the best combination for given working conditions (for example, high temperature, exposure to radiation, etc.). On the other hand, ion implantation, laser beams, epitaxial growth in highly controlled environment, etc., are commonly used for structural changes and obtaining better output characteristics of the devices. All of that was made possible by development, availability and improvement of sensitivity of methods for composition and structural characterization of materials. Although also very important in the process of thin film formation, these methods are essential for the quality assessment of the whole device in working conditions. In solar cells, for example, measurement of the output characteristics such as ideality factor, serial and parallel resistance, fill factor and efficiency, could directly or indirectly indicate the possibilities for the improvement of the production technology (from the basic material, formation of thin films, contact films, etc.). The choice of the appropriate method in each case depends on the type of the investigations and expected results. The most commonly used method for characterization of electrical properties of semiconducting devices (such as solar cells) is current-voltage ($I$-$V$) measurement. Versatility of the data obtained in this way gives very important information about the device (solar cell), both from the fundamental standpoint (ideality factor, series and parallel resistance) and from the standpoint of the output characteristics (short-circuit current, open-circuit voltage, fill factor, efficiency).

Also, since contact films have significant influence on the output characteristics of all semiconducting devices, they must possess certain properties such as: low resistivity, good connection to the basic material, temperature stability, and low noise. One of the most important characteristic of detectors such as solar cells is their energy resolution that primarily depends on noise. That is why measuring and lowering noise is important for obtaining good quality detectors. It is known that low frequency noise (1/f and burst noise) is manifested as random fluctuation of the output current or voltage, leading to lowering of the efficiency of the device. Because of the large surface to volume ration, surface effects are expected to be a major cause of 1/f noise, so good quality contacts are of great importance. That is why measurements of 1/f noise and improvement of silicides characteristics by lowering 1/f noise in them leads to the production of reliable contacts.

## 2.1 Noise in thin film semiconducting devices

Negative influence of noise on the photodetector characteristics could be observed in widening of the spectral line of the signal as well as in rising of the detection threshold. That is the reason why investigation of physical basis of different types of noises is necessary for their minimizing. Noise level primarily depends on fabrication procedures and is connected to the fundamental physical processes in semiconducting devices, so it could be said that noise appears in every detector regardless to their type or quality. Noise is commonly classified into three categories: thermal noise, frequency dependent noise and shot noise. Also, noise could be classified according to the physical processes as generation-recombination noise, diffusion noise and modulation noise. Low frequency noise, 1/f and burst noise are especially important in semiconducting devices. Various experiments suggests (Jayaweera et al., 2005, 2007) that the origin of this noise is fluctuation of the number free charge carriers connected to existence of the traps located in the vicinity or directly in the junction area, or fluctuation of the mobility of charge carriers. In both cases these fluctuations arise from the interactions of carriers with defects, surface states and impurities, that are either introduced during manufacturing of the device, or as a consequence of the hostile working conditions (radiation, high temperature, humidity). In the case of surface films such as contacts, their electical characteristics modulate potential and electric field in the surface area, controlling in that way transport mechanisms between the surface and bulk area. This is particularly important for photodetectors and metal semiconductor barriers including contacts.

Beside 1/f noise, burst noise could also induce discreate fluctuations of current between two or more levels. This type of noise is considered the most limiting factor in the performance of photodetectors. The origin of this noise, as well as its appearance in different voltage regions depends on the type of polarization and on the type of actual device, but it is usually ascribed to the presence of the defects in crystal lattice such as dislocations. Since burst noise is manifested in the presence of the so called excess current, investigations of its origin and factors that influence its amplitude could lead to better understanding of the burst noise. It was supposed that current flowing through the defects is modulated by the change in the charge state of the generation-recombination (GR) centers located near defects in the space charge region. When such GR center captures electron, local increase of the barrier height occurs. Electron flux passing through the barrier in the vicinity of GR center decrease, as a consequence of the barrier height increase, modulating (decreasing) excess current. Vice versa, emmision of the charge carrier from the trap center leads to the local decrease of the barrier height, thus increasing the excess current. Depending on the type of the device, this phenomenon could occur on the surface of the device also.

Amplitude of the excess current (i.e. burst noise) $\Delta I_F$, depends on the applied voltage $V_F$ in the exponential manner:

$$\Delta I_F = \Delta I_{sat} \exp \frac{qV_F}{n_{BN}kT} \qquad (1)$$

where $\Delta I_{sat}$ and $n_{BN}$, are saturation current and ideality factor, respectively. Since in this model current $\Delta I_F$ is considered to be generation-recombination current, $n_{BN} > 1$, and depends on the lifetime and concentration of the charge carriers, recombination probability, thermal velocity of the electrons, etc.

### 2.1.1 Minimization of 1/f noise in silicides by ion implantation

Both burst noise and 1/f noise are considered to be especially important in contact layers, so a large number of investigations are based on measurements of these type of noises in contacts, for example, silicides. Silicides belong to a very promising group of materials with low resistivity and good temperature stability that are used for fabrication of reliable and reproducible contacts. Investigations of this type of contacts include both their experimental development and the development of methods for their characterization such as noise level measurements and RBS analysis. The noise level measurements enable the control of the noise, which is important characteristic of metal-semiconductor electrical contacts (especially 1/f noise). Surface effects such as surface recombination fluctuations in carrier mobility, concentration of surface states, etc., have great influence on frequency dependent noise in silicides. Many authors in their investigation of silicides discuss the problem related to the application of ion beam mixing of As+ ions for the formation of silicides (Stojanovic et al., 1996a). Although introduction of As+ ions and their diffusion could change impurity concentration resulting in an increased noise level (especially for 1/f noise) in the structure, carefull optimization of the implantation dose and subsequent thermal treatment such as annealing could result in the formation of stable contacts with a low noise level. Every step of the silicides fabrication including preparation of Si substartes, deposition of metal layer (Pd, Ti, TiN, for example), As+ ion implantation, and annealing must be taking into consideration in order to achieve the best possible result. It has been found (Stojanovic et al., 1996a, 1996b) that both the implantation dose and ion energy, and annealing have a pronounced influence on the noise level in silicides. When Pd silicides are concerned, structural RBS analysis have shown that $Pd_2Si$ phase, which was already formed during pre-implantation annealing is not affected by ion implantation. The spectra exibit slight changes in the slopes of the signal, corresponding to the $Pd_2Si$-Si interface. These changes can be attributed to additional intermixing of silicon and palladium atoms due to the presence of radiation-induced defects. It was also found (Stojanovic et al., 1996a) that the sequence of the fabrication steps influence the noise level in the formed silicides. The noise level was lowest in the samples implanted after annealing, so optimized ion implantation concerning implantation energy and dose, and average projected range of As+ ions near Pd-Si interface, does not reorder the silicides formed by annealing (also shown by RBS analysis), and induce more homogenous silicide/silicon interface. This suggests that thermal treatment induce relaxation of crystal lattice and improvement of the crystal structure of the silicides. On the other hand, noise measurements have confirmed that a more homogenous structure of Pd-silicides results in a lower frequency noise level.

The influence of the implantation dose on the noise level could clearly be seen for the Ti-TiN silicides example (Vasic et al., 2011). Structural RBS analysis has shown that ion implantation did not induce redistribution of components for lower implantation doses (Fig. 1). The spectra indicate that the entire titanium layer has interdiffused with the silicon substrate.

The presence of the $TiSi_2$ and $TiSi_2$ phase in the implanted samples was observed. In all cases top TiN layer remains unaffected, but for higher doses of implantation ($1x10^{16}$ ions/cm$^2$) a disordered structure was registered. This corresponds to the amorphization of silicon substrate, which is moving deeper with the ion dose, showing that the physical properties of TiN/Ti/Si are influenced by the implantation.
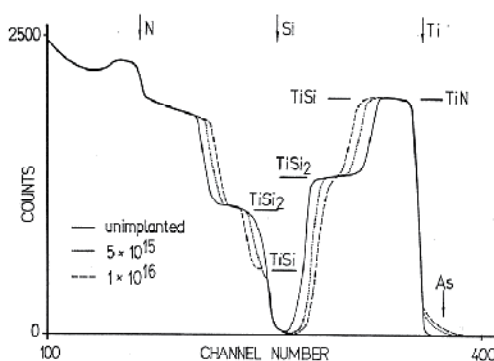
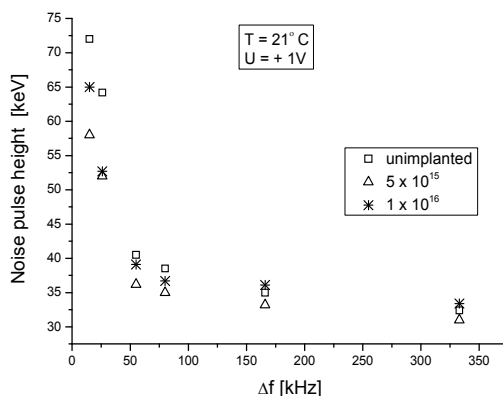Fig. 1. RBS spectra of TiN/Ti/Si samples (Vasic et al., 2011).



Fig. 2. Frequency noise level for TiN/Ti/Si samples at 21°C (Vasic et al., 2011).

This influence was confirmed by noise level measurements (all of the samples exhibit similar behaviour). Noise spectra were measured for different time constants $\tau$ (frequency range $\tau \sim 1/f$) of the low noise amplifier. Analysis of the results of these measurements shows that implantation could have influence on the noise level (Fig.2), but the main effect depends on the implantation dose. As discussed above, implantation dose of $1 \times 10^{16}$ ions/cm$^2$ induces some disorder in the structure that could lead to higher noise level. Ion dose of $5 \times 10^{15}$ ions/cm$^2$ shows the best results for the entire measuring range, suggesting that this dose of implantation induce a more homogeneous silicidation and the formation of Ti-Si phase with a lower concentration of crystal defects (after annealing). The lower concentration of point defects and dislocations and a more homogeneous silicide/silicon interface result in a lower frequency noise level of the analyzed structures.

## 2.2 *I-V* measurements and the ideality factor

Another commonly used and relatively simple method for obtaining output characteristics of photodetectors and solar cells related to the transport processes is current-voltage (*I-V*) measurement. Any deviation of the transport mechanism from the ideal model of thermionic emission directly reflexes on the shape of current-voltage characteristics. Main

parameter that could be extracted from *I-V* data is the ideality factor (*n*), direct indicator of the output parameter dependence on the electrical transport properties of the junction. Output characteristic of all semiconductor devices are primarily defined by fundamental parameters (resistance, lifetime and mobility of charge carriers, diffusion length etc.), and processes in them. Analytical connections between fundamental and output characteristics of solar cells are matter of theoretical analysis, but experimentally obtained results are more complex than theoretical suppositions. Both in production process of solar cells, and during their performance, the distribution of dopants, impurities and especially defects is usually not uniform and predictable, and could directly influence the processes in the cells. Factors that influence internal parameters of solar cells such as series and parallel resistance lead to changes in efficiency and maximum generated power in solar cell. Capability of solar cell to convert solar energy into electrical, depends on various fundamental and technological parameters (Stojanovic et al., 1998). Empirically obtained influence of fundamental parameters is usually mathematically defined by formal introduction of the ideality factor, *n*, in the exponent of current – voltage characteristics of solar cells. Ideality factor combines all variations of current flow from the ideal case, induced by various internal and external influences of physical parameters during the manufacturing process or as a consequence of aging. The non-ideal behavior of the device is reflected in the values of *n* greater than 1, and that is the result of the presence of different transport mechanisms that can contribute to the diode current. Determination of the dominant current mechanism is very difficult because the relative magnitude of these components depends on various parameters, such as density of the interface states, concentration of the impurities and defects, height of the potential barrier, device voltage, and device temperature (Vasic et al., 2004). Obtaining of the ideality factor from *I-V* measurements is simple, non-invasive and effective way to evaluate possible degradation of output characteristics of solar cells and photodetectors in general in working conditions.

### 2.2.1 Extraction of parameters from *I-V* measurements

Characteristic parameters of the semiconducting devices are often very difficult to determine and their values could depend on the used measurement methods. Current-voltage measurements are widely used to characterize the barrier height, carrier transport mechanisms and interface states both in Schotky barriers and p-n junctions. This relatively simple method provides reliable and reproducible results, but the extraction of the diode parameters could be influenced by their voltage dependence and the presence of series resistance (Vasic et al., 2000, 2005).

In an ideal case of thermionic emmision as a dominant trasport mechanism of charge carriers, current flow across the junction diode under forward bias and in the case when $V - IR_s \gg 3kT/q$, is usually represented by the equation:

$$I = I_s \left[ \exp \frac{q(V - IR_s)}{nkT} \right] \tag{2}$$

where *I* is diode current, $I_s$ the saturation current, *V* the applied bias voltage, $R_s$ the series resistance, *n* the ideality factor, *T* the temperature, *q* the electron charge and *k* the Boltzman constant. The saturation current $I_s$ depends on the carrier transport mechanism across the junction, and the formally introduced ideality factor *n* reflects the influence of various parameters (presence of the interface states, generation-recombination current, tunneling,

spatial inhomogenities, etc.), and frequently is a function of the applied voltage (Vasic et al., 2005). Parameters $n$ and $I_s$ are direct indicators of the output characteristics of the semiconducting devices on the electric transport processes in the junction. Deviations of the ideal (Shockley) case of the carrier transport are mostly the result of the combined influence of following factors: surface effects, generation and recombination of the cerriers in the depletion region, tunneling between states in the energy gap, series resistance, etc. For homo-junctions with homogenous distribution of recombination centers, two limiting values for the ideality factor are usually taken into consideration: $n = 1$ for the injection and diffusion in the depletion layer, and $n = 2$ in the case of the domination of the generation-recombination current in the depletion layer (due to the recombination of the electron-hole pairs in the recombination centers - traps). Very rarely values of the ideality factor are exactly 1 or 2, and they usually depend on the applied voltage also. Variations from the predicted values are the consequence of many factors. On the microscopic level impurities and defects induced during manufacture could form regions of low carrier lifetime, and that could have influence on the *I-V* characteristics, and hence the ideality factor also. Beside that, surface states could act as a recombination centers as well, and in that case ideality factor depends on the energy states of that recombination centers. If the space distribution of the recombination centers within the depletion region is nonuniform, the ideality factor could have values greater than 2.

All of these factors make the extraction of the diode parameters very complicated since, usually, the first step in extraction of the diode parameters is the linear approximation of the ln*I-V* plot. Determination of the ideality factor value could be used as a measure of the validity of such a method. Namely, if the value of $n$ is approximately 1, such approximation could be considered accurate enough, but if $n > 1.4$, transport mechanisms that produce the deviation from the ideal model and non-linearity of the ln*I-V* plot should also be considered. Even when the type of the transport mechanism could be more or less precisely determined, series and parallel resistance of the device should also be taken into consideration. Introduction of these parameters in the *I-V* characteristic (eq.2) gives following dependence:

$$I = I_{s1}\left[\exp\frac{q(V - IR_s)}{kT} - 1\right] + I_{sn}\left[\exp\frac{q(V - IR_s)}{nkT} - 1\right] + \frac{V - IR_s}{R_{sh}} \qquad (3)$$

In this case, ln*I-V* plot is clearly not linear, because depending on the applied voltage, there could exsist one or more linear regions. The decrease of the ln*I-V* slope, i.e. increase of the ideality factor for lower voltage is a result of the presence of parallel resistance, $R_{sh}$ (due to "leakage" current across the junction). The same effect on the values of the ideality factor has series resistance, $R_s$ for higher voltages.

Since in the real semiconductiong device (solar cell, photodetector) many unpredictable factors (concentration of defects and impurities, exsistance of the energy states in the forbidden zone, etc.) influence their parameters ($n$, $I_s$, $R_s$), determination of the ideality factor as a macroscopic quantity, could give accurate information about the quality of each device. The basis of most of methods for obtaining the diode parameters from *I-V* curves (Vasic et al., 2005) is the correction of the experimentaly obtained data due to the presence of the series resistance $R_s$, but some of them also treat the diode parameters (especially $n$ and $I_s$) as voltage dependent. Analysis of the linear part of ln*I* vs *V* plot and fitting of the experimental results is used in the so called numerical methods, whereas in other methods auxiliary functions based on some physical parameters are introduced.

**Standard linearization method**

This method is based on the analysis of the linear part of $\ln I = f(V)$ plot using equation (2) when diode parameters are voltage independent - $I_s$ is calculated from the extrapolated intercept with the y (current) axis, and $n$ is deduced from the slope. However, when measured plot deviates from straight line shape (in the presence of $R_s$), calculated parameters are significantly different from the values obtained using other methods. This is very distinct when $R_s$ is high and the shape of the $I$-$V$ curve is not the same in different voltage regions (especially for high forward bias).

**Numerical method**

Enhanced version of the standard method also includes presence of the series reistance, but the diode parameters could be determined without linearization of the $I$-$V$ curve (Vasic et al., 2005). Method is based on a least square method of fitting the experimentally obtained results in order to yield optimal values of $I_s$, $n$, and $R_s$.

When an applied voltage $V_A$ is provided across the device terminals, actual barrier (junction) voltage $V$ is given by:

$$V = V_A - I_E R_s \tag{4}$$

($I_E$ is experimentally measured diode current). Then, from the equation (2) and using equation (4), applied voltage is given by:

$$V_A = I_E R_s + a \ln I_E + b \tag{5}$$

where:

$$a = nkT/q \ \text{ and } b = -a \ln I_s \tag{6}$$

Thus if $R_s$, $a$, and $b$ could be determined, then $n$ and $I_s$ could also be obtained. One of the ways for optimization of $R_s$, $a$, and $b$ is method of least squares, and for this purpose function S is defined as:

$$S = \sum_{i=1}^{m} \left\{ I_{Ei} R_s + a \ln I_{Ei} + b - V_{Ei} \right\}^2 \tag{7}$$

where $m$ is the number of diode pairs of experimentally determined $I_E$ and $V_E$. The optimal combination of parameters would result in a minimum value of S, and from the set of matrix equations values of $R_s$, $a$, and $b$ could be calculated. Then, using equation (6) $n$ and $I_s$ are easily obtained.

It has been shown (Vasic et al., 2005) that the agreement between experimental data and numerical simulation is very good, especially when parasitic series resistance effects are present, and when the measured $\ln I = f(V)$ plot shows no linear regime. However, since this method is not based on any physical model of current transport, there are no sufficient indications of the validity of these results.

**Methods based on the physical models**

Physical parameters such as differential conductance and resistance, for example, are the basis of some methods that use auxiliary functions or parameters for the determination of real diode parameters. Novel methods take into account that for the real diodes $n \neq 1$, and

also the fact that at high bias voltages series resistance could significantly influence the shape of the *I-V* plot, making the linear fit for the whole voltage region impossible. Nevertheless, these methods usually treat such problems separately. Namely, most of the methods do not take into account that the diode parameters ($n$, $I_s$) are voltage-dependent. On the other hand, methods that analyze voltage-dependent parameters produce correct results only under assumption that the influence of the series resistance is negligible. However, generally speaking, for real diodes neither series resistance nor voltage dependence are negligible, so most of the proposed methods have limited application and give unreliable results.

There are several approaches for determination of the voltage-dependent ideality factor:

1.  differentiation of the simplified expression of equation (2):

$$\frac{1}{n(V)} = \frac{kT}{q}\frac{\partial}{\partial V}(\ln I) \tag{8}$$

but numerical differentiation is, in effect, a total (complete) and not partial differentiation, so the obtained result is some function f($n$), and not the true ideality factor $n(V)$,

2.  calculation of the function $n(V)$ at each point of the experimental *I-V* data (method "point by point") using equation:

$$n(V) = \frac{qV}{kT}\ln\left(\frac{I}{I_s} + 1\right) \tag{9}$$

with the assumption that the saturation current is previously determined in accordance with the influence of the series resistance,

3.  method of adding an external resistance, based on two consecutive measurements:
    a.  conventional *I-V* measurements, and
    b.  *I-V* measurement with external resistance $R_{ex}$ in series with the diode.
        From the equation (2) and after adding $R_{ex}$, following set of equations were obtained:

$$\ln I = \ln I_s + \frac{q}{n(V)kT}(V - IR_s) \tag{10}$$

$$\ln(I + \Delta I) = \ln I_s + \frac{q}{n(V)kT}\left[V - (I + \Delta I)(R_s + R_{ex})\right] \tag{11}$$

where $\Delta I$ is the change in *I* produced by adding $R_{ex}$. From those equations follows:

$$\frac{\Delta(\ln I)}{R_{ex}} = -\frac{q}{n(V)kT}\left[(R_s + R_{ex})\frac{\Delta I}{R_{ex}} + I\right] \tag{12}$$

Equations (10) and (12) form the system of two equations with three unknown diode parameters ($R_s$, $I_s$ and $n$), so some relationship must be established between any two of the unknown parameters. There are two methods of eliminating one unknown parameter; first method ("A") is based on establishing the relationship between the ideality factor and

saturation current by eliminating series resistance from the equation (10), and obtaining from the equation (11):

$$f_2(I, \Delta I) = \ln I_s + \frac{q}{n(V)kT} f_1(V, I, \Delta I, R_{ex}) \tag{13}$$

$$f_2(I, \Delta I) = \ln I - \frac{\Delta I}{I} \ln\left(1 + \frac{\Delta I}{I}\right) \qquad and \qquad f_1(V, I, \Delta I, R_{ex}) = V + R_{ex}I\left(1 + \frac{I}{\Delta I}\right)$$

Using the $f_2 = f(f_1)$ dependence, saturation current $I_s$ and ideality factor $n$ could be obtained from the slope and the vertical axis intercept of the plot, independently of the series resistance ($R_s$ could be calculated from the equation (2), afterwards).

However, in the case of voltage-dependent $n$, dependence $f_2 = f(f_1)$ is not a straight line, so second method ("B") that allows determination of all parameters in the case of non-linearity, must be used. The ideality factor $n$ is, at the beginning, eliminated from the equations (11) and (12), thus establishing the relationship between $I_s$ and $R_s$:

$$R_s = -\frac{1}{\Delta I}\left[\frac{f_1}{f_2 - \ln I_s}\ln\left(1 + \frac{\Delta I}{I}\right) + R_{ex}\left(I + \Delta I\right)\right] \tag{14}$$

assuming that both $I_s$ and $R_s$ are voltage independent over the range of interest. Saturation current could be determined by fitting in such a way that series resistance would have approximately constant value. The obtained values of $I_s$ and $R_s$ could then be used to extract the voltage-dependent $n(V)$ from the equation (2).

It was shown that both of these methods that use the auxiliary function $f_1$ and $f_2$ give reliable and reproducible results. First one ("A") is limited on the cases of voltage independent parameters, but gives good results in the presence of noise, while method "B" provides the possibility of analyzing the general case of voltage-dependent ideality factor in the presence of series resistance and experimental noise.

**Verification of the presented methods**

The validity of the above-described methods was examined by analyzing *I-V* characteristics (primarily obtaining the values of the ideality factor) of real photodiodes (Vasic et al., 2005). Samples used in the experiment were commercially available p-i-n and p-n silicon photodiodes (trademarks BPW 34, BPW 43, SFH 205, and BP 104). Forward bias dark *I-V* characteristics of the diodes were measured using standard configuration for the *I-V* measurements. In all samples presence of the series resistance was detected (calculated range of $R_s$ was from 20÷30 Ω for BPW 34 and SFH 205 p-i-n type, to 100÷200 Ω for BPW 43 p-n type of photodiodes). Values of the ideality factor calculated using standard method were in the range of 1.2÷1.6, depending on the type of the samples. Similar range of values was obtained by numerical method, while application of the auxiliary functions (method "A") results in lower values of $n$ (1.05÷1.5). Considering physical meaning of the ideality factor (measure of non-ideality of the junction), the only way to verify the validity of a given method is evaluation of the agreement between experimentally measured data and numerically calculated *I-V* curves (with calculated diode parameters), i.e., determination of the correlation factor $r$. For standard and numerical method correlation factor was higher than 0.99, but the best values of $r$ were for the method "A". Figure 3 shows agreement for

standard method and method "A" for one sample, 3 BPW 43 (dots represent experimental data, and lines – calculated characteristics). Correlation factor for all three used methods was good (r > 0.99), so the choice of the exact method depends on the complexity of the procedure and experiment requirements.
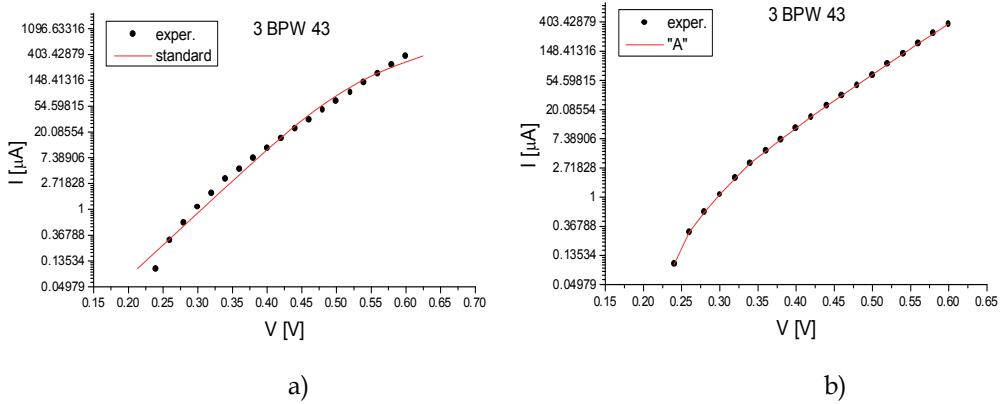


a)                                                                                      b)

Fig. 3. Agreement: experimental and calculated data for a) standard, b) method "A" (Vasic et al., 2005).

In order to test the assumption that the ideality factor is voltage-independent and that the determination of only one, "summary" ideality factor is sufficient, diagrams of $f_2 = f(f_1)$ dependence were plotted (two characteristic examples are shown in Fig. 4). Correlation factor for those functions for the sample 3 BPW 43 was the highest ($r = 0.99751$), and that, together with the obvious good linearity of the $f_2 = f(f_1)$ diagram, shows that for this sample ideality factor has approximately constant value for whole voltage range. However, although the agreement between experimental and calculated data for both shown samples were good, from Fig. 4b) could be seen that $f_2 = f(f_1)$ dependence for sample 9 BPW 34 was not linear, so junction parameters are voltage dependent. This makes the determination of the local ideality factor $n_{loc}$ (i.e., determination of the $n(V)$ dependence) necessary.



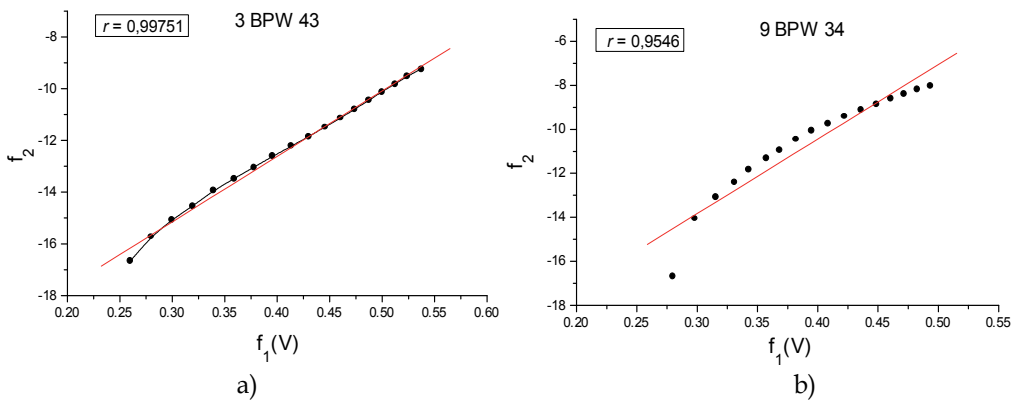a)                                                                                      b)

Fig. 4. Diagram of the $f_2 = f(f_1)$ dependence for samples a) 3 BPW 43 and b) 9 BPW 34 (Vasic et al., 2005).

Differentiation of the equation (2) leads to as previously explained, some function f($n$), due to the presence of $Rs$:

$$f(n) = \frac{kT}{q}\frac{d}{dV}(\ln I) = \frac{1}{n} - \frac{V}{n^2}\frac{dn}{dV} \qquad (15)$$

Except in cases when $dn/dV \ll n(V)/V$ at the same bias, second term in the right hand side of the equation (15) cannot be neglected. Therefore, the exact values of the ideality factor could be obtained by integration of the equation (15), which is difficult, due to the unknown initial conditions.
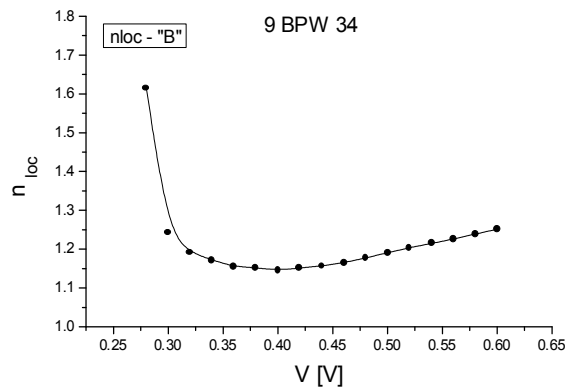


Fig. 5. Method "B" (Vasic et al, 2005).
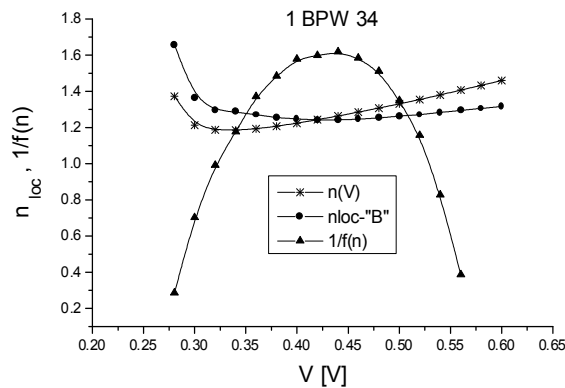


Fig. 6. Comparison for $n_{loc}$ (Vasic et al., 2005).

Above-mentioned deviations of the $f_2 = f(f_1)$ plot from the linearity are ascribed to the bias dependence of the ideality factor. Reliable and accurate method for obtaining the local ideality factor directly, is method "B". For the sample 9 BPW 34 ($f_2 = f(f_1)$ significantly deviates from the linearity, Fig. 4 b)), bias dependent $n_{loc}$ was calculated using proposed method, and the result is shown in Fig. 5. From this figure it could be seen that the ideality factor is constant only in the very narrow voltage region (from 0.32 to 0.42 V). The correlation factor for method "B" was very good (near 1). However, beside very high

precision of the obtained results, the complexity of the method presents in some cases, the major limiting factor for its application. Adding an external resistance, together with the problem of selection of an optimal value for $R_{ex}$, makes these methods (both "A" and "B") inappropriate in the field conditions for example, or when a quick evaluation of the *I-V* data is necessary. In this case, method based on the calculation of the $n(V)$ at each point of the experimental *I-V* data – method "point by point", should be used (equation (9)). In Fig. 6, bias dependent ideality factor calculated using method "B" (filled circles) and "point by point" (asterisk) for one sample (1 BPW 34) is presented. It could be seen that both methods give similar values of *n*, as well as the same $n(V)$ behavior (high values of $n_{loc}$ at low bias, decrease for medium, and slight increase for higher bias). For the comparison, in the same figure $1/f(n)$ dependence was also plotted (triangles). The only condition that should be fulfilled for using equation (9) is to determine the value of the saturation current previously, and this could be done by any of the proposed methods.

The extraction of diode parameters is difficult due to the presence of the series resistance, and values of $I_s$, *n*, and $R_s$ usually depend on the methods used for their calculation. The choise of the exact method depends both on the complexity of the method and on the experimental demands (conditions). Methods of using auxiliary functions (methods "A" and "B") demand adding (optimal) external resistance and additional measurements. Also, calculation of the diode parameters is more complex than for other methods due to the extended numerical procedure. In laboratory conditions, these methods undoubtedly give the best results, but in the field conditions both of these methods are very complex and the extraction of the parameters is slow. This is more emphasized if the devices are exposed to the severe working conditions when quick assessment of their performance is needed. Even in the laboratory conditions, when the relative change of the diode parameters is measured for the estimation of the "worst-case scenario", both standard and numerical method gave good results for voltage-independent parameters, and "point by point" method for voltage-dependent parameters. Based on the experimental verification, it could be concluded that, although the results obtained by the methods of adding an external resistance have the best agreement with the experimental data, standard and numerical methods are more suitable for quick extraction of diode parameters.

## 3. Radiation effects and possibilities of improvement of solar cells characteristics

Beside the diversity of the device technologies used for designing of the optical and other detectors, there are a variety of radiation environments in which they are used (natural space and atmospheric, as well as military and civil nuclear environments, etc.). Reliability of electrical devices in a radiation environment is very important, and extensive studies concerning the development of semiconductor devices that can operate normally in such conditions have been seriously undertaken. Possible degradation of the electrical performance of solar cells and  photodetectors induced by irradiation means that very strict conditions for their application must be predetermined for the worst case scenario. Performance failure in such conditions could have negative impact both on the financial and environmental aspects of the device application. Therefore, from the technological point of view, it is important to study the variations induced by irradiation of semiconductor

junction characteristic parameters (ideality factor, saturation current, etc.), that affect the performance of the photodiodes and solar cells.

Investigations of radiation effects in solids are primarily based on the study of the characteristics based on structure. Since radiation unduced deffects are connetcted to the defects in the crystal lattice, physical evidence of such a damage must br found through those characteristics that are most sensitive to the unperfections of the lattice. Due to the microscopic nature of such a defects, measurements of variations in those charcateristics are almost the only method of evaluation of radiation influence (Loncar et al., 2005, 2006, 2007). In semiconductor devices, radiation induced defects are connected to the localized energy states that could change concentration and mobility of the charge carriers. Namely, the main charactersitics of semiconducting devices is precisely the change (in a large range) of the charge carriers concentration, weather because of the defects and impurities, or under the influence of the raised temperature. When the equilibrium concentration of electrons and holes is disturbed by the radiation, for example, their mutual anihillation is possible only in the localized energy states in the crystal. These are, so called, recombination centers, and radiation induced defects represent very good example of such a centers.

Interaction of radiation with the semiconducting devices basically produses three effects: permenent ionization damage in insulator layers, ionization effects in semiconductors, and dislocation damage. During interction of γ radiarion with the device, and depending on the radiation energy, primarilly three effects could occur: photoelectric effect, Compton effect, and electron-hole creation. In all of these processe, absorbed photon energy couses ionization and excitation of the created electrons, with the electron-hole creation. These effects lead to the generation of parasitic charge (noise) collected in the depletion region. Also, ionization effects could produce recombination centers in the energy gap. In silicon, all of these effects could be permenent or quasi-permenent.

On the other hand, dislocation damage usually arise after the interaction of the particled such as protons, neutrons and electrons. Processes that could happen during those collisions depend on the type of particles and their energy. Collision of the particles with the atoms of crystal lattice could produce vacances, interstities, and other types of defects. These defects could be traped in the impurity centers, for example, and could form active defects leading to the changes in the characteristics of the photodetectros, primarilly the decrease of the minority carrier lifetime. Radiation damage due to neutrons (heavy particles) is, as mentioned above, primarily connected to the displacement of silicon atoms from their lattice sites in the crystalline silicon solar cells, leading to destruction and distortion of local lattice structure and formation of defects. If, under the influence of neutrons, stable defects are made, they could, together with impurity atoms, donors and for example implanted atoms, form complex defects acting as recombination sites or traps, significantly decreasing minority carrier lifetime.

## 3.1 Radiation damage in solar cells and photodiodes

The main effect of radiation on photodiodes and solar cells is an increase in the dark current generated within or at the surface of the depletion region. Generation of electron–hole pairs due to ionization effects and displacement damage induced by neutrons, result in the generation and increase of the noise and the minimum signal that can be detected. Since presence of the noise could be connected to the excess current, measurement of the *I-V*

characteristics before and after irradiation reveals the extent of degradation of electrical properties of photodiodes.

Although polycrystalline and monocrystalline solar cells are more reliable than amorphous, inherent presence of defects and impurities in the basic material could, during time, produce some negative effects. This is specially emphasized if those states are located within the energy gap and are activated during work. In such a case they become traps for optically produced electron-hole pairs, and thus decrease the number of collected charge carriers. Macroscopically, this effect could be observed as a decrease of the output current and voltage, and ultimately could lead to the decrease of the efficiency of solar cell. Lower values of short-circuit current indicate the existence of the recombination centers that decrease the mobility and diffusion length of the charge carriers, making the recombination in the depletion region dominant transport in such solar cells (Vasic et al., 2000, 2003). The lifetime of the solar cell is restricted by the degree of radiation damage that the cell receives. This is an important factor that affects the performance of the solar cell in practical applications. The permanent damage in the solar cells materials is caused by collisions of the incident radiation particles with the atoms in the crystalline lattice, which are displaced from their positions. These defects degrade the transport properties of the material and particularly the minority carrier lifetime (Alurralde et al., 2004, Horiushi et al., 2000, Zhenyu et al., 2004). This lifetime decrease produces degradation of the parameters of the cell ultimately leading to an increase of the noise level. The interaction between vacancies, self-interstitials, impurities, and dopants in Si leads to the formation of undesirable point defects such as recombination and compensator centers which affects performance of the solar cells, especially in space. Introduction of radiation-induced recombination centers reduce the minority carrier lifetime in the base layer of the p-n junction increasing series resistance. After very high doses of radiation series resistance of the base layer could be so high that most of the power generated by the device is dissipated by its own internal resistance (Khan et al., 2003).
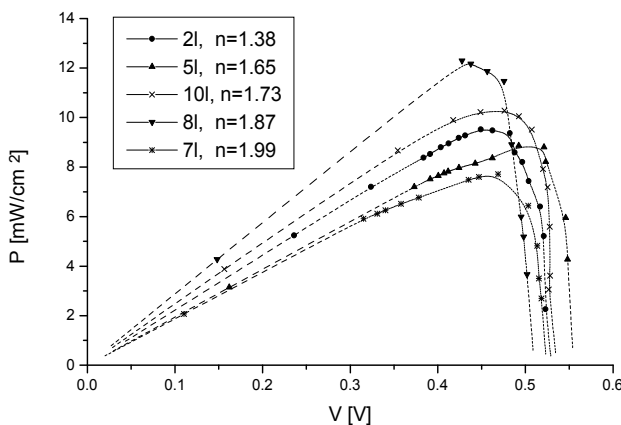


Fig. 7. Simulation of the dependence of *P-V* characteristics on *n* (Vasic et al., 2011).

Capability of solar cell to convert solar energy into electrical, depends on various fundamental and technological parameters. Variations from the ideal case of current transport could be represented by the ideality factor that could be easily obtained from *I-V* characteristics of solar cells. The non-ideal behaviour of the device is reflected in the values of *n* greater than 1, and that is the result of the presence of different transport mechanisms that can contribute to the diode current.

Determination of the dominant current mechanism is very difficult because the relative magnitude of these components depends on various parameters, such as density of the interface states, concentration of the impurities and defects, height of the potential barrier, device voltage, and device temperature. The dependence of the maximum power on the ideality factor could be seen in Fig. 7.

Considering the fact that maximum power point depends on the resistance (and ideality factor as well), series and parallel resistance should be maintained at such a values to obtain maximum efficiency. Also, voltage decrease in the maximum power point ($P_m$) has great influence on the efficiency. One of the main reasons for this decrease is the increase of the ideality factor, so it could be said that the influence of the ideality factor on the solar cell efficiency is through the voltage. Set of the experimentally obtained $\eta$ = f(*n*) dependencies for different solar cells is shown in Fig. 8 (Vasic et al., 2000).
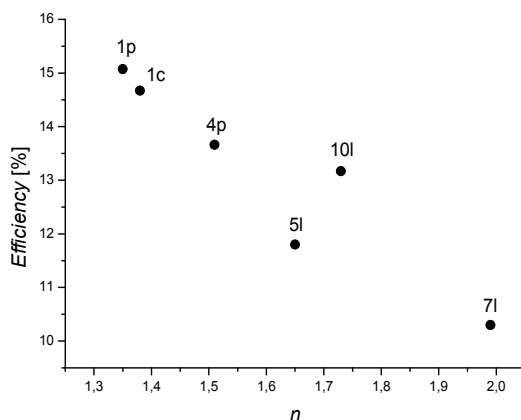


Fig. 8. Efficiency dependence on the ideality factor (Vasic et al., 2000).

Regardless to the type of radiation used, damage to even a small portion of the individual solar cell results in an increase in saturation (leakage) current for whole cell. The cell diode saturation current (or more commonly used its density) $J_0$, increases with the decreased minority carrier lifetime. On the other hand, the minority carrier lifetime decreases due to the ionization effects and displacement damage in the depletion region, caused by the incident radiation. In consequence, this reduces the cell open circuit voltage $V_{oc}$. Since forward-biased cell diode current increases for all diode voltages, the current available to the load decreases, so that the maximum power delivered to the load, $P_{max}$, will also decrease, leading to the substantial drop of the cell efficiency $\eta$. Such non-ideal behavior of the device is usually reflected in the values of the ideality factor *n* greater than 1, as the result of the presence of different transport mechanisms in different voltage regions that can

contribute to the diode current. Since the ideality factor is the direct indicator of the output parameter dependence on the electrical transport properties, measurements of the $n(V)$ dependence along with the $I$-$V$ measurements at different irradiation doses, could narrow down possibilities of the dominant current component. Also, values of the ideality factor could indicate not only the transport mechanism, but indirectly, the presence and possible activation of the defects and impurities, acting as recombination and/or tunneling centers.

The influence of the ideality factor on the solar cell efficiency is predominantly through the voltage, i.e. the decrease of the efficiency with the increase of the ideality factor is the result of the voltage decrease in the maximum power point. Physical basis of such dependence lies in the connection between the ideality factor and saturation current density shown in Fig. 9 (for different types of solar cells).
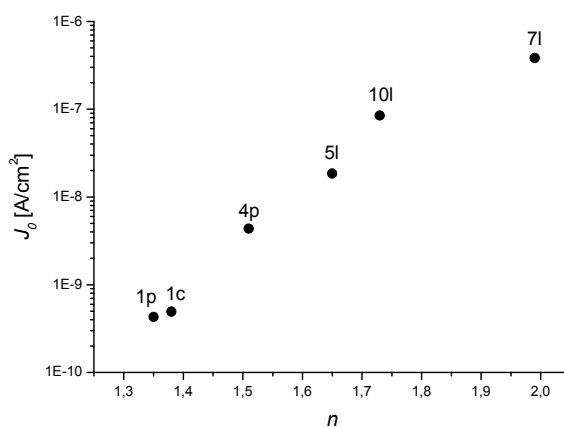


Fig. 9. Saturation current dencity dependence on ideality factor (Vasic et al., 2000).

Direct connection between $J_0$ and $n$ (nearly exponential increase of saturation current density with the increase of $n$) produces the decrease of the efficiency with the increase of either of these parameters. In the radiation environment, such an increase is usually the result of induced defects and/or activation of the existent impurities that could act as a recombination centers for the charge carriers, altering the dominant current transport.

Determination of the dominant current mechanism is very difficult because the relative magnitude of these components depend on various parameters such as, density of the interface states, concentration of the impurity defects, and also devises operating voltage. Existence of the $n(V)$ dependence is the result of such a junction imperfections, leading to domination of different transport mechanisms in different voltage regions. Therefore, measuring and monitoring the $n(V)$ dependence which is possible even in working conditions, could reveal not only the degree of degradation, but also, possible instabilities of the device in certain voltage regions. This is especially important if those instabilities occur in the voltage region where maximum power is transferred to the load. Although still in working condition, performances of such solar cells (efficiency, for most) are considerably degraded, so that monitoring of the device characteristics should be performed

continuously, especially if solar cells are exposed to severe working conditions, such as radiation environment.

Although effects of gamma irradiation on the solar cells are known to be primarily through ionization effects, increase of series resistance could also be observed, Fig. 10 (Vasic et al., 2007, 2010).
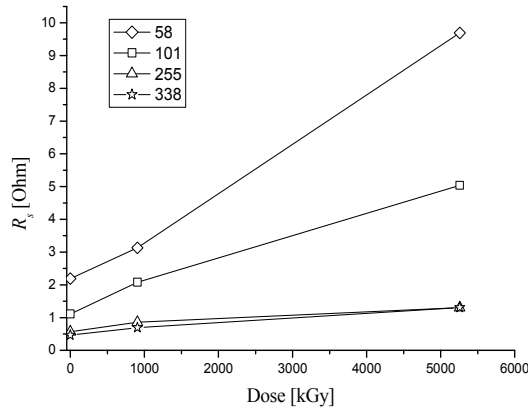


Fig. 10. Dependence of $R_s$ on doses for polycrystalline solar cells (Vasic et al., 2007).

Almost   linear dependence of series resistance on the absorbed irradiation dose indicates that some changes in the collection of the charge carriers have occurred. This behaviour of $R_s$ is reflected mostly on the short-circuit current density $J_{sc}$, since radiation induced activation of defects and impurities mainly affects the transport mechanisms in the device. Dependence of the $J_{sc}$ on the absorbed dose for different illumination levels was shown in Fig. 11.
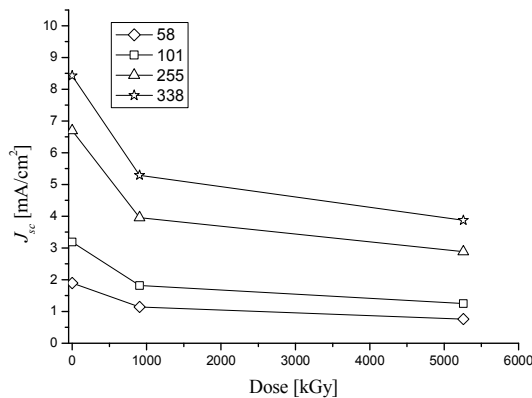


Fig. 11. Dependence of the $J_{sc}$ on doses for polycrystalline solar cells (Vasic et al., 2007).

Due to the inevitable presence of surface energy states (as a result of lattice defects, dislocations, impurities, etc.), after silicon is irradiated with gamma photons, both the surface recombination velocity and the density of surface states increase. If those states

correspond to deep energy level in the silicon energy gap, they act as efficient surface recombination centers for charge carriers. Generation of electron-hole pairs due to ionization effects usually result in the generation and an increase of the noise and minimum signal that can be detected. All of these effects lead to the decrease of output current. Steeper decrease of the $J_{sc}$ for higher illumination levels indicates that recombination centers could be both optically activated and activated by irradiation. Therefore, solar cells exposed to the higher values of solar irradiation during their performance could exhibit greater decrease in the initial $J_{sc}$.

Additionally, if solar cells are polycrystalline, so presence of grain boundaries, characteristic for the polycrystalline material, has great influence on the collection of the photogenerated carriers. Presence of the recombination centers, small diffusion length and minority carrier lifetime, as a result of either irradiation or aging, finally leads to the decrease of the efficiency of solar cells. As could be seen in Fig. 12, this decrease is very pronounced, regardless of the illumination level. Although initial efficiencies were slightly different for different illumination levels, after irradiation they became almost equal, indicating that radiation gas greater influence on production and transport of charge carriers than illumination. That, from the standpoint of solar cells, could be very limiting factor for their performance. Combined influence of the increased 1/f and burst noise due to radiation induced damage has significant negative influence on major solar cells characteristics.
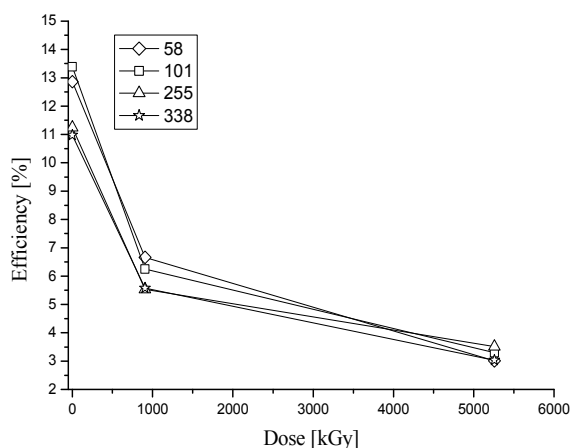


Fig. 12. Dependence of the efficiency on doses (Vasic et al., 2007).

All of this inevitably leads to the decrease of the resolution of the photodetector devices, lowering solar cells efficiency and for this reason, monitoring of the device characteristics should be performed continuously, especially when solar cells are exposed to the severe working conditions.

## 3.2 Possibilities of the improvement of solar cells and photodetectors

The lifetime decrease of the charge carriers due to the radiation damage induced by neutrons, produces degradation of electrical parameters of the cell, such as series resistance ($R_s$), output current and finally efficiency ($\eta$). High level of series resistance usually indicate

the presence of impurity atoms and defects localized in the depletion region acting as traps for recombination or tunneling effects, increasing dark current of the cell (Alexander, 2003, Holwes-Siedle & Adams, 2002). Moreover, shallow recombination centers in the vicinity of conducting zone enhance tunneling effect, further degrading output characteristics of the cell by increasing noise level (especially burst noise that is connected to the presence of excess current).

Such negative impact of neutron radiation was observed higher illumination level, as could be seen in Fig. 13 (Vasic et al., 2008). But interesting phenomena – the decrease of series resistance, was observed for lower values of illumination. (Different behavior for different illumination level is due to the presence of finite series and parallel resistance in the cell.) This decrease is very significant from the solar cell design standpoint because it indicates possible beneficent influence of low doses of irradiation, even with neutrons. It could be explained by the fact that during fabrication process of any semiconducting device, structural defects and impurities that were unavoidably made, produce tension in the crystal lattice. Low doses of radiation could act similarly to annealing, relaxing lattice structure and decreasing series resistance. Subsequently, this leads to lowering of noise level and an increase of the output current as shown in Fig.14 ($J_m$ – current in the maximum power point).
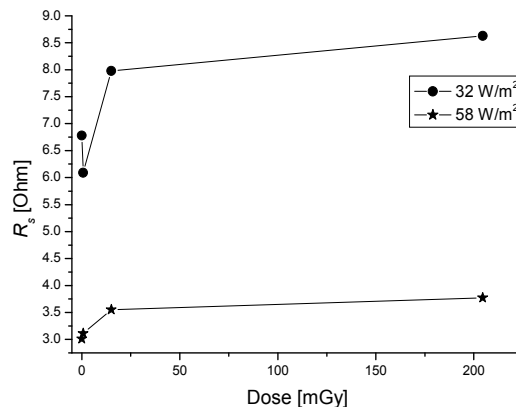


Fig. 13. Dependence of $R_s$ on doses for two illumination levels (Vasic et al., 2008).

Other parameters of solar cells (voltage in the maximum power point $V_m$ , fill factor *ff* and efficiency) have shown the similar tendencies, which is not surprising since, as it is well known, high series resistance of the solar cell is one of the main limiting factors of the efficiency. So, it could be expected that all the main output parameters of the solar cell should exhibit the same behavior as series resistance in the relation to the irradiation dose.

Finally, improvement of output characteristics after the first irradiation step for low illumination level is registered for the efficiency also, Fig. 15. Although higher doses of neutron radiation undoubtedly have negative impact on the performance of solar cells, observed phenomena give possibilities for using radiation as a method for the improvement of solar cell characteristics.
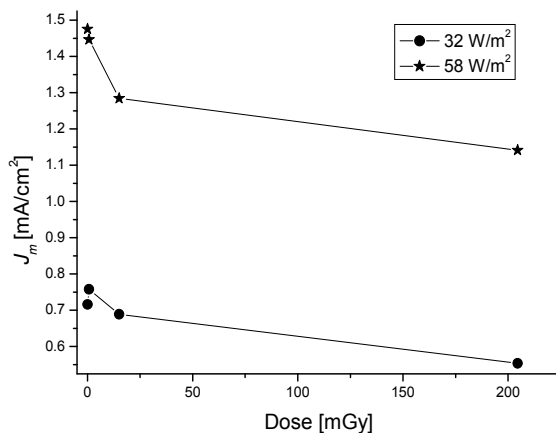
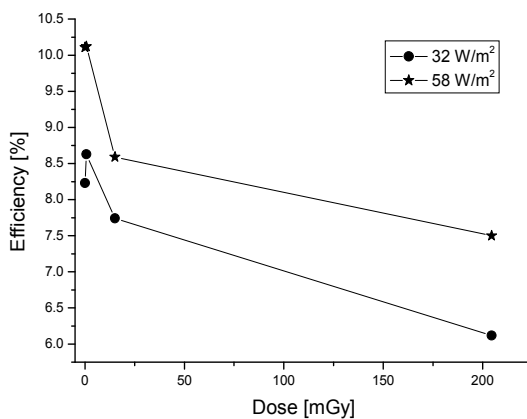Fig. 14. Dependence of the $J_m$ on doses (Vasic et al., 2008).



Fig. 15. Dependence of the efficiency on doses (Vasic et al., 2008).

Though commonly referred to as a source of noise in semiconducting devices, radiation induced effects (interaction of neutrons with Si solar cells, in particular) could have in some cases positive effect on main electrical characteristics ($R_s$, $J_m$, $\eta$). Initial improvement of the characteristics observed for small doses of neutron radiation and low illumination level, indicates that there is a possibility of using irradiation for enhancement of the solar cells quality.

## 4. Conclusion

Single element optical detectors such as solar cells and photodiodes are the final component needed for a communications or optical information processing systems. Due to wide area of application, they are often exposed to the variety of radiation effects (natural space environment, atmospheric environment, military and civil nuclear environment). Therefore, the extensive studies concerning the development of semiconductor devices that can operate normally in a radiation environment have been undertaken. Although proven to be reliable in terrestrial applications, solar systems are (like other semiconductor devices) sensitive to variety of radiation environments in which they are used. Performance failure could have negative impact both on the financial and environmental aspects of the device application. From a technological point of view, it is important to study the variations induced by irradiation of semiconductor junction characteristic parameters (reverse saturation current, ideality factor etc.), that affect the performance of the solar cells and photodiodes.

## 5. Acknowledgment

## 6. References

Alexander, D.R. (2003). Transient Ionizing Radiation Effects in Devices and Circuits, *IEEE Transaction on Nuclear Sciences,* Vol.50, No. 3, pp. 565-582, (2003), ISSN 0018-9499

Alurralde, M., Tamasi, M. J. L., Bruno, C. J., Martinez Bogado, M. G., Pla, J., Fernandez Vasquez, J., Duran, J., Shuff, J., Burlon, A. A., Stoliar, P., & Kreiner, A. J. (2004). Experimental and theoretical radiation damage studies on crystalline silicon solar cells, *Solar Energy Materials & Solar Cells,* Vol. 82, pp.531-542, (2004), ISSN 0927-0248

Holwes-Siedle, A.G., & Adams, L. (2002). *Handbook of Radiation* (Second Edition), Oxford University Press, ISBN13 9780198507338, Oxford

Horiushi, N., Nozaki, T., & Chiba, A. (2000). Improvement in electrical performance of radiation-damaged silicon solar cells by annealing, *Nuclear Instruments and Methods A,* Vol. 443, pp. 186-193, (2000), ISSN 0168-9002

Hu, Z., He, S., & Yang, D. (2004). Effects of <200 keV proton radiation on electric properties of silicon solar cells at 77 K, *NIM B Beam Interaction with Materials & Atoms*, Vol. 217, pp. 321-326, (2004), ISSN 0168-583X

Jayaweera, P.V.V. , Pitigala, P.K.D.D.P., Perera, A.G.U., & Tennakone, K. (2005). 1/f noise and dye-sensitized solar cells, *Semiconductor Science Technology,* Vol. 20, pp.L40-L42, (2005), ISSN 0268-1242

Jayaweera, P.V.V. , Pitigala, P.K.D.D.P., Senevirante, M.K.I., Perera, A.G.U, & Tennakone, K. (2007). 1/f noise in dye-sensitized solar cells and NIR photon detectors, *Infrared Physics & Technology,* Vol. 50, pp. 270-273, (2007), ISSN 1350-4495

Khan, A., Yamaguchi, M., Ohshita, Y., Dharmaraso, N., Araki, K., Khanh, V.T., Itoh, H., Ohshima, T. , Imaizumi, M., & Matsuda, S. (2003). Strategies for improving

radiation tolerance of Si space solar cells, *Solar Energy Materials & Solar Cells,* Vol.75, pp. 271-276, (2003), ISSN 0927-0248

Kovačević-Markov, K., Vasić, A., Stanković, K., Vujisić, M. & Osmokrović, P. (2011). Novel trends in improvement of solar cell characteristics, *Radiation Effects and Defects in Solids,* Vol. 166, No. 1, pp. 8-14, (2011), ISSN 1042-0150

Lončar, B., Stanković, S., Vasić, A., & Osmokrović, P. (2005). The influence of gamma and X-radiation on pre-breakdown currents and resistance of commercial gas filled surge arresters, *Nuclear Technology & Radiation Protection*, Vol. XX, No. 1, pp. 59-63, (2005), ISSN 1451-3994

Lončar, B., Osmokrović, P., Vasić, A., & Stanković, S. (2006). Influence of gamma and X radiation on gas-filled surge arrester characteristics, *IEEE Transactions on Plasma Science*, Vol. 34, No. 4, pp. 1561-1565, (2006), ISSN 0093-3813

Lončar, B., Osmokrović, P., Vujisić, M., & Vasić, A. (2007). Temperature and radiation hardness of polycarbonate capacitors, *Journal of Optoelectronics and Advanced Materials*, Vol. 9, No. 9, pp. 2863-2867, (2007), ISSN 1070-9789

Stojanović, M., Vasić, A., & Jeynes, C. (1996a). Ion implanted silicides studies by frequency noise level measurements, *Nuclear Instruments and Methods B*, Vol. 112, pp. 192-195, (1996),ISSN 0168-583X

Stojanović, M., Jeynes, C., Bibić, N., Milosavljević, M., Vasić, A., & Milošević, Z. (1996b). Frequency noise level of As ion implanted TiN-Ti-Si structures, *Nuclear Instruments and Methods B*, Vol. 115, pp. 554-556, (1996), ISSN 0168-583X

Stojanović, M., Stanković, S., Vukić, D., Osmokrović, P., Vasić, P., & Vasić, A. (1998). PV solar systems and development of semiconductor materials, *Materials Science Forum*, Vols. 282-283, pp. 157-164, (1998), ISSN 0255-5476

Vasić, A., Stojanović, M., Osmokrović, P., & Stojanović, N. (2000). The influence of ideality factor on fill factor and efficiency of solar cells, *Materials Science Forum*, Vol. 352, pp. 241-246, (2000), ISSN 0255-5476

Vasić, A., Stanković, S., & Lončar, B. (2003). Influence of the radiation effects on electrical characteristics of photodetectors, *Materials Science Forum*, Vol. 413, pp. 171-174, (2004), ISSN 0255-5476

Vasić, A., Osmokrović, P., Stanković, S. & Lončar, B. (2004). Study of increased temperature influence on the degradation of photodetectors through ideality factor, *Materials Science Forum*, Vol. 453-454, pp. 37-42, (2004), ISSN 0255-5476

Vasić, A., Osmokrović, P., Lončar, B., & Stanković, S. (2005). Extraction of parameters from I-V data for nonideal photodetectors: a comparative study, *Materials Science Forum*, Vol. 494, pp. 83-88, (2005), ISSN 0255-5476

Vasić, A., Vujisić, M., Lončar, B., & Osmokrović, P. (2007). Aging of solar cells under working conditions, *Journal of Optoelectronics and Advanced Materials*, Vol. 9 , No. 6, pp. 1843-1846, (2007), ISSN 1070-9789

Vasić, A., Osmokrović, P., Vujisić, M., Dolićanin, C., & Stanković, K. (2008). Possibilities of improvement of silicon solar cell characteristics by lowering noise, *Journal of Optoelectronics and advanced Materials*, Vol. 10, No 10, pp. 2800-2804, (2008), ISSN 1070-9789

Vasic,A., Loncar, B., Vujisic, M., Stankovic, K., & Osmokrovic, P. (2010). Aging of the Photovoltaic Solar Cells, Proceedings of 27th IEEE International Conference on Microelectronics, pp. 487-490, ISBN 1-4244-0116-x, Nis, Serbia, May 2010

# Solar Cells on the Base of Semiconductor-Insulator-Semiconductor Structures

Alexei Simaschevici, Dormidont Serban and Leonid Bruc
*Institute of Applied Physics, Academy of Sciences,*
*Moldova*

## 1. Introduction

The conventional energy production is not based on sustainable methods, hence exhausting the existing natural resources of oil, gas, coal, nuclear fuel. The conventional energy systems also cause the majority of environmental problems. Only renewable energy systems can meet, in a sustainable way, the growing energy demands without detriment to the environment.

The photovoltaic conversion of solar energy, which is a direct conversion of radiation energy into electricity, is one of the main ways to solve the above-mentioned problem. The first PV cells were fabricated in 1954 at Bell Telephone Laboratories (Chapin et al., 1954); the first applications for space exploration were made in the USA and the former USSR in 1956. The first commercial applications for terrestrial use of PV cells were ten years later. The oil crisis of 1972 stimulated the research programs on PV all over the word and in 1975 the terrestrial market exceeds the spatial one 10 times. Besides classical solar cells (SC) based on p-n junctions new types of SC were elaborated and investigated: photoelectrochemical cells, SC based on Schottky diodes or MIS structures and semiconductor-insulator-semiconductor (SIS) structures, SC for concentrated radiation, bifacial SC. Currently, researchers are focusing their attention on lowering the cost of electrical energy produced by PV modules. In this regard, SC on the base of SIS structures are very promising, and recently the SIS structures have been recommended as low cost photovoltaic solar energy converters. For their fabrication, it is not necessary to obtain a p-n junction because the separation of the charge carriers generated by solar radiation is realized by an electric field at the insulator-semiconductor interface. Such SIS structures are obtained by the deposition of thin films of transparent conductor oxides (TCO) on the oxidized silicon surface. A overview on this subject was presented in (Malik et al., 2009).

Basic investigations of the ITO/Si SIS structures have been carried out and published in the USA (DuBow et al., 1976; Mizrah et al., 1976; Shewchun et al., 1978; Shewchun et al, 1979) Theoretical and experimental aspects of the processes that take place in these structures are examined in those papers. Later on the investigations of SC based on SIS structures using, as an absorber component, Si, InP and other semiconductor materials have been continued in Japan (Nagatomo et al., 1982; Kobayashi, et al., 1991), India (Vasu & Subrahmanyam, 1992; Vasu et al., 1993), France (Manifacier & Szepessy, 1977; Caldererer et al., 1979), Ukraine

(Malik et al., 1979; Malik et al., 1980), Russia (Untila et al., 1998), the USA (Shewchun et al., 1980; Gessert et al., 1990; Gessert et al., 1991), Brasil (Marques & Chambouleyron, 1986) and the Republic of Moldova (Adeeb et al., 1987; Botnariuc et al., 1990; Gagara et al., 1996; Simashkevich et al., 1999). The results of SIS structures fabrication by different methods, especially by pyrolitic pulverization and radiofrequency sputtering, are discussed in those papers. The investigation of electrical and photoelectrical properties of the Si based SIS structures shows that their efficiency is of the order of 10% for laboratory-produced samples with an active area that does not exceed a few square centimeters. The spray deposition method of ITO layer onto the silicon crystal surface results in an efficient junction only in the case of n-type Si crystals, whereas in the case of p-type silicon crystals radiofrequency sputtering must be used to obtain good results.

Bifacial solar cells (BSC) are promising devices because they are able to convert solar energy coming from both sides of the cell, thus increasing its efficiency. Different constructions of BSC have been proposed and investigated. In the framework of the classification suggested in (Cuevas, 2005) the BSC structures could be divided into groups according to the number of junctions: a) two p-n junctions, b) one p-n junction and one high-low junction, and c) just one p-n junction. In all those types of BSC are based on a heteropolar p-n junction. In this case, it is necessary to obtain two junctions: a heteropolar p-n junction at the frontal side of the silicon wafer and a homopolar $n/n^+$ or $p/p^+$ junction at its rear side. Usually these junctions are fabricated by impurity diffusion in the silicon wafer. The diffusion takes place at temperatures higher than $800^0C$ and requires special conditions and strict control. In the case of the back surface field (BSF) fabrication, these difficulties increase since it is necessary to carry out the simultaneous diffusion of impurities that have an opposite influence on the silicon properties. Therefore the problem arises concerning the protection of silicon surface from undesirable impurities.

The main purpose of this overview is to demonstrate the possibility to manufacture, on the base of nSi, monofacial as well as a novel type of bifacial solar cells with efficiencies over 10%, containing only homopolar junctions with an enlarged active area, using spray pyrolysis technique, the simplest method of obtaining SIS structures with a shallow junction. The utilization of such structures removes a considerable part of the above-mentioned problems in BSC fabrication. The results of the investigations of ITO/pInP SC obtained by spray pyrolysis are also discussed.

## 2. The history of semiconductor-insulator-semiconductor solar cells

First, it must be noted that SC obtained on the base of MIS and SIS structures are practically the same type of SC, even though they are sometimes considered as being different devices. The similarity of these structures was demonstrated experimentally and theoretically for two of the most common systems, $Al/SiO_x/pSi$ and $ITO/SiO_x/pSi$ (Schewchun et al, 1980). The tunnel current through the insulator layer at the interface is the transport mechanism between the metal or oxide semiconductor and the radiation-absorbing semiconductor, silicon in this case.

One of the main advantages of SIS based SC is the elimination of high temperature diffusion process from the technological chain, the maximum temperature at the SIS structure fabrication not being higher than 450ºC. The films can be deposited by a variety of techniques among which the spray deposition method is particularly attractive since it is simple, relatively fast, and vacuumless (Chopra et al., 1983). Besides, the superficial layer of

the silicon wafer where the electrical field is localized is not affected by the impurity diffusion. The TCO films with the band gap of the order of 3.3-3.7eV are transparent in the whole region of solar spectrum, especially in the blue and ultraviolet regions, which increase the photoresponce comparative to the traditional SC. The TCO layer assists with the collection of separated charge carriers and at the same time is an antireflection coating. In SC fabrication the most utilized TCO materials are tin oxide, indium oxide and their mixture known as indium tin oxide (ITO). Thin ITO layers have been deposited onto different semiconductors to obtain SIS structures: Si (Malik et al., 1979), InP (Botnariuc et al., 1990), CdTe (Adeeb et al., 1987), GaAs (Simashkevich et al., 1992). Therefore, solar cells fabricated on the base of SIS structures have been recommended as low cost photovoltaic solar energy converters. The reduction in cost of such solar cells is due to the simple technology used for the junction fabrication. The separation of light generated carriers is achieved by a space charge region that in the basic semiconductor is near the insulator layer.

The number of publications concerning the fabrication and investigation of SIS structures is very big, therefore we will limited our consideration of the given structures only to those on the base of the most widespread solar materials – silicon and indium phosphide. To be exact, main attention will be focused on SC on the base of ITO/nSi and ITO/pInP.

## 2.1 SIS structures on the base of silicon crystals

As shown above, one of the ways to solve the problem of the cost reduction of the electrical energy provided by SC is to use SIS structures. First publications regarding the obtaining and investigation of ITO/nSi structures appeared in 1976. (Mizrah & Adler, 1976). Power conversion efficiencies of 1% were reported for an ITO/nSi cell, obtained by the magnetron dispersion of ITO layers on the surface of nSi crystals with an active area of 0.13 cm$^2$. The data obtained from the investigated I-V dark characteristics and known band gaps and the work functions of ITO and Si allows to make the band diagram of these structures (Fig. 1). The efficiency of 10% was observed for ITO/nSi cells, obtained by the spray deposition of ITO layers onto nSi crystals with the area of 0.1 cm$^2$ (Manifacier & Szepessy 1977; Calderer et al., 1979). ITO/nSi SC with the power conversion efficiencies of 10% were fabricated by deposition onto n-type Si crystals by the electron- beam evaporation of a mixture of 90:10 molar % In$_2$O$_3$: SnO$_2$ powder (Feng et al., 1979).

The results of those works have been analyzed in detail (Shewchun et al., 1978; Shewchun et al., 1979) from both experimental and theoretical points of view. Given the general theory of heterojunctions is incomprehensible, how they can work as effective SC formed by materials with different crystalline types and lattice constants, when an intermediate layer with many defects appears at the interface. It is intriguing to note here that various authors have received quite contradictory results. Examining these data, authors in (Shewchun et al., 1979) concluded that the performance of those SC depended on the intermediate thin insulator layer. Its main function is the compensation of the defects due to the mismatches of the crystalline lattices. Its thickness is not greater than 30Å, which ensures the tunnel transport of the carriers through the barrier. The theoretical analysis of ITO/nSi solar cell has shown that they are similar to MIS structures: their parameters depend on the thickness of the insulating layer at the interface, the substrate doping level, concentration of surface states, oxide electric charge and temperature. The optimization of these parameters can provide 20% efficiency.

In (Shewchun et al., 1979) this issue was examined in terms of energy losses during conversion of sunlight into electricity. Different mechanisms of energy loss that limit

ITO/nSi solar cell efficiency are probably valid for other SIS structures too. Dark current-voltage characteristics were used as experimental material and it was shown that after a certain threshold of direct voltage these characteristics do not differ from similar characteristics of p-n junctions in silicon, and the current is controlled by diffusion processes in silicon volume. Different mechanisms of energy loss that limit ITO/nSi solar cell efficiency are presented in Table 1 (Shewchun et al., 1979).
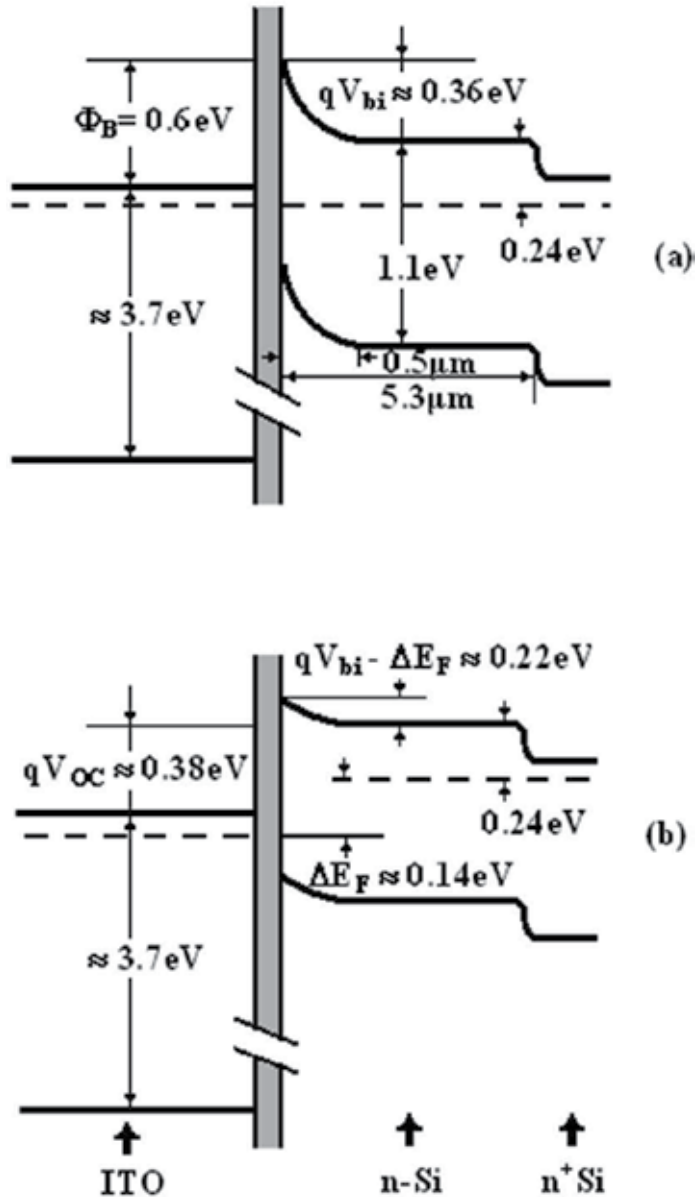


Fig. 1. Energy band diagram of the ITO/nSi/n +Si structure (a) - in the dark, (b) - at solar illumination under open circuit conditions. The shaded area - the insulating SiOx layer.

| Mechanism | Loss rate |
|---|---|
| 1. Absorption and reflection in the ITO layer | up to 8% |
| 2. Recombination in space charge region | 0.1 1% |
| 3. $V_{CD}$ height reduction | 0 – 12% |
| too high work function | 0-3% |
| inhomogeneous $SiO_x$ layer | 0-3% |
| low doped ITO layer | 0-3% |
| too large saturation current | 0-3% |
| 4. Low fill factor | 0-10% |
| series resistance of the intermediate layer | |
| series resistance of the contacts | |
| shunt | |

Table 1. The energy loss mechanisms, which do not provide the maximum possible efficiency of 20%

An increase of the conversion efficiency of SC based on ITO/nSi structures can be achieved by the optimization of the thickness of the frontal ITO layer and of the insulator $SiO_2$ layer; the optimization of the concentration of electrons in absorbing Si wafers; the texturing of the Si wafers surface.

The thickness of the frontal ITO layer is a very important factor because it affects the quantity of the absorbed solar radiation depending on both absorption and reflection. It is necessary to select such ITO layer thickness that determines a large minimum of the reflection in the region of maximum sensitivity of the $n^+ITO/SiO_2/nSi$ SC. At the same time, the thickness of the frontal ITO layer determines their electrical resistance and, therefore, the value of the photocurrent, but for all that, the growing of the ITO layer thickness has an contrary effect on the solar cells efficiency, diminishing the absorption and increasing the photocurrent. At the same time, the thickness of the frontal ITO layer determines the efficiency of this layer as an anti reflection coating.

The properties of the SIS structures, largely, also depend on the thickness of the $SiO_2$ insulator layer at ITO/Si interface. This $SiO_2$ layer increases the height of the junction potential barrier and diminishes the saturation current. Besides, the insulator $SiO_2$ layer must be tunnel transparent for charge carrier transport. The optimal $SiO_2$ insulator layer thickness must be not more than some tens of Å.

All silicon wafers must be oriented in the (100) plane because only such crystallographic orientation could be used to get a potential barrier by ITO spray deposition. Single crystalline Si wafers with different carrier concentration from $10^{15}cm^{-3}$ up to $10^{18}cm^{-3}$ have been used to fabricate ITO/nSi SIS structures by spray deposition.

The influence of the structural state of the Si single crystalline wafers on the conversion efficiency will be discussed in the next section of this overview.

The paper (Feng et al., 1979) studied the current transport mechanism of ITO/Si structures, the TCO layer beings obtained by evaporation under the action of an electron beam. Pre-treatment of Si crystals with $Cl_2$ has led to the increased yield from 2.3% to 5.5%. In this case the current transport mechanism was dominated by recombination in the space charge

layer, while there is the thermo emission over the potential barrier in the absence of $Cl_2$. Systematical studies of the properties of the ITO/nSi structures, obtained by spray pyrolysis, were carried out in 1980 (Ashok et al., 1980). The optical and electrical characteristics of the IT0 layer as well as the thickness of the insulator layer have been optimized to yield the following photovoltaic parameters on 0.5Ohm cm nSi: $V_{oc}$= 0.52V, $J_{sc}$=31.5mA/cm², FF=0.70, conversion efficiency is 11.5%. The dark I-V and C-V characteristics have also been evaluated to identify the mechanisms of barrier formation and current flow. C-V data indicate an abrupt heterojuncton, while dark I-V characteristics are suggestive of a tunneling process to determine current flow in these devices in conformity with the Riben and Feucht model (Riben & Feucht, 1966). A comparison of spray deposited ITO/nSi and $SnO_2$/nSi was presented by Japanese researchers (Nagatomo et al. 1982). The diode and photovoltaic properties of these structures are very similar, but the conversion efficiency of ITO/nSi is higher, up to 11-13%, whereas for $SnO_2$/nSi these values do not exceed 7.2% (Nagatomo et al., 1979). As is reported in the paper (Malik et al., 2008; Malik et al., 2009), the authors fabricated ITO/nSi solar cells using n-type single crystalline silicon wafers with a 10Ohm cm resistivity and an 80nm thick ITO film with a sheet resistance of 30Ohm/□ that was deposited by spray pyrolysis on the silicon substrate treated in the $H_2O_2$ solution. This ITO thickness was chosen in order to obtain an effective antireflection action of the film. The cells obtained in such a way can be considered as structures presenting an inverted p-n junction (Fig. 2).
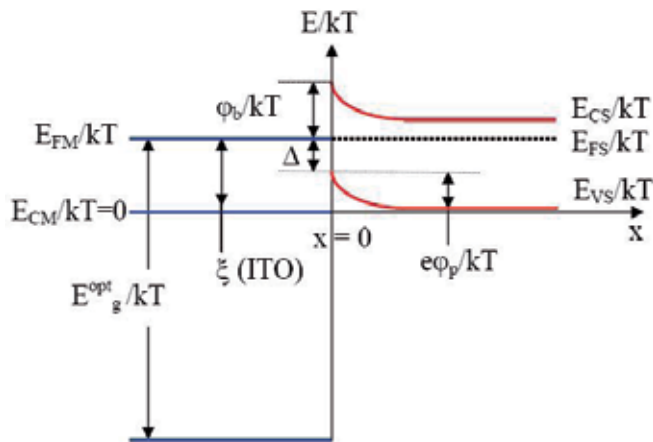


Fig. 2. Energy diagram (in *kT* units) of the heavy doped ITO/n-Si heterojunction

Under the AM0 and AM1.5 solar illumination conditions, the efficiency is 10.8% and 12.2%, respectively. The theoretical modeling based on p-n solar cells shows an excellent agreement between the theoretical and the experimental results. It is also shown that using 1Ω cm silicon substrates is a promising alternative for obtaining solar cells with 14% efficiency under AM1.5 illumination conditions.

Various models for energetic band diagrams and the carrier transport mechanism in SIS ITO/nSi cells have been proposed so far. Among them are the thermo ionic emission as the dominant charge transport mechanism in the SC obtained by spray deposition of $SnO_2$ onto nSi crystals (Kato et al., 1975), and the recombination current in the depletion layer for the CVD deposited ITO/nSi junction (Varma et al., 1984). Majority of authors suggested that

trap –assisted multi step tunneling through the depletion layer is the determinant current flow mechanism (Ashok et al., 1980; Saim & Campbell, 1987; Kobayashi et al., 1990; Simashkevich et al., 2009).

The mechanism of the current transport through the potential barrier is determined by the energetic band diagram and the height of the barrier. When the later is very high, a physical p-n junction is formed in Si crystals near the surface (Fig. 2). Otherwise, the ITO/nSi SC operate as MIS structures or Schottky diodes (Fig. 1). Some data about the efficiencies of ITO/nSi SC are presented in Table 2.

| References | ITO deposition method | Area (cm$^2$) | Eff. (%) | Note |
|---|---|---|---|---|
| Mizrah et al., 1976 | R.F. Sputtering | 0.13 | 1 | |
| Manifacier et al., 1977 | Spray | 1.5 | 10 | |
| Feng et al., 1979 | Electron beam | 1 - 4 | 10 | |
| Calderer et al., 1979 | Spray | 1.5 | 10 | |
| Ashok et al., 1980 | Spray | 0.3 | 11.5 | BSF |
| Nagatomo et al., 1982 | Spray | | 11-13 | |
| Gagara et al., 1996 | Spray | | 10.1 | |
| Vasu et al., 2005 | Electron beam | 1.0 | 5.5 | |
| Malik et al., 2008 | Spray | 1 - 4 | 11.2 | |

Table 2. Efficiencies of ITO/nSI solar cells fabricated by various deposition techniques of ITO films on smooth (non textured) Si crystal surfaces

The analysis of the works referred to shows that the conversion efficiency of ITO/nSi solar cells obtained by various methods is about 10% and in some cases reaches 12%. Their active area is not more than a few square centimeters, which is not enough for practical application.

## 2.2 ITO/nSi solar cells with textured surface of Si crystalls

As can be seen from Table 1, the optical losses of ITO/nSI solar cells are up to 8%, other estimates show that they can exceed 10% (Garcia et al., 1982). Those losses depend on the surface state of silicon wafers and can be minimized by creating a textured surface of the light absorbing semiconductor material, thus reducing the reflection and increasing the absorption. The texturization leads to the enlargement of the junction area of a photovoltaic cell and to the increase of the conversion efficiency. The enlargement of the junction area in the case of silicon crystals is usually achieved by means of selective chemical etching in KOH (Bobeico et al., 2001; Dikusar et al., 2008; Simashkevich et al., 2011). As a result, pyramids or truncated cones with the base dimensions of 5μmx5μm or with a diameter of 10μm on the Si surface are formed.

The efficiency of 12.6% under AM1 simulated irradiation was obtained for $SnO_2$: P/$SiO_2$/nSi SC with the active area of 2cm$^2$(Wishwakarma et al., 1993) Those cells were fabricated by deposition of $SnO_2$ layers doped with P by CVD method on the textured surface of the Si crystals with resistivity of 0.1 Ohm.cm. $SiO_2$ insulating layer was obtained by chemical

methods. The textured surface of the Si crystals reduces the frontal reflectivity, and consequently increases the short circuit current by around 10%.

ITO/nSI obtained by spray deposition of ITO layers on nSi wafers oriented in (100) plane, were obtained in Japan (Kobayashi et al, 1990). The final size of the active area of the cell was 0.9cm x 0.9cm. Mat-textured Si surfaces were produced by the immersion of the Si wafers in NaOH solution at $85^0$C. For so treated specimens the solar energy conversion efficiency of 13% was attained under AM1 illumination.

The paper (Simashkevich et al., 2011) studied the properties of ITO/nSi SC with improved parameters. The performed optimization consists in the following: the optimization of the thickness of the frontal ITO layer and of the thickness of the insulator $SiO_2$ layer; the optimization of the concentration of the electrons in absorbing Si wafers; the texturing of the Si wafers surface.

The performed investigations make it possible to come to the following conclusions. The optimum thickness of the frontal ITO layer was determined experimentally from the photoelectric investigations and is equal to 0.5µm. The $SiO_2$ layer can be obtained by different methods. In the case of fabrication n+ITO/SiO₂/nSi solar cells by spray pyrolysis, the optimal $SiO_2$ layer thickness was obtained by a combined thermo chemical method selecting the temperature regime and the speed of the gas flow during ITO layer deposition. The optimal $SiO_2$ insulator layer thickness, measured by means of ellipsometric method, is about 30-40Å.

To determine the optimal electron concentration ITO/nSi SIS structures were investigated obtained by ITO spray deposition on the surface of phosphor and antimony doped single crystalline Si wafers with different carrier concentrations: $10^{15}cm^{-3}$, $5 \cdot 10^{15}cm^{-3}$, $6 \cdot 10^{16}cm^{-3}$, and $2 \cdot 10^{18}cm^{-3}$, produced in Russia (STB Telecom) and Germany (Siltronix, Semirep). The investigation of the electrical properties of n+ITO/SiO₂/nSi SC shows that the optimum values of the barrier height, equal to 0.53eV and the space charge region thickness equal to W=0.36µm, have been obtained in the case of Si crystals with the electron concentration $5 \cdot 10^{15}cm^{-3}$. Carrier diffusion length (L) is one of the main parameters for bifacial solar cells. For this silicon crystal L is about 200µm. The BSF region at the rear side of the cell was obtained by phosphor diffusion.

To enlarge the active area and reduce optical losses due to radiation reflection, the active area of Si wafer, oriented in a plane (100), was exposed to the anisotropic etching.

The etching was spent by two expedients for reception of the irregular and regular landform. In both cases, the boiling 50% aqueous solution of KOH was used as the etching agent. The processing time was 60 - 80s. In the first case, the etching process was yielded without initially making a landform on the silicon wafer surface for the subsequent orientation of the etching process.

Fig. 3a shows that the landform of the silicon surface is irregular and unequal in depth. The depth of poles of etching is within the limits of 2-3µm.

In the second case, the method of making the ranked landform in the form of an inverse pyramid was applied. The chemical micro structurisation of the silicon wafer surface was carried out in the following order: the deposition of a $SiO_2$ thin film with 0.1µm thickness by electron beam method; the deposition on the $SiO_2$ thin film of a photo resists layer and its exposure to an ultraviolet radiation through a special mask; removal of the irradiated photo resist and etching $SiO_2$ with HF through the formed windows; removal of the remaining photo resist thin film. The anisotropic etching of the silicon surface through the windows in $SiO_2$ thin film was carried out. The result of this type of etching is shown in Fig. 3b.
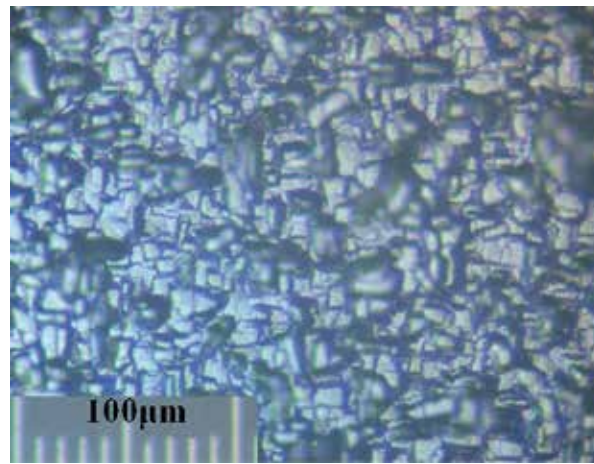
(a)
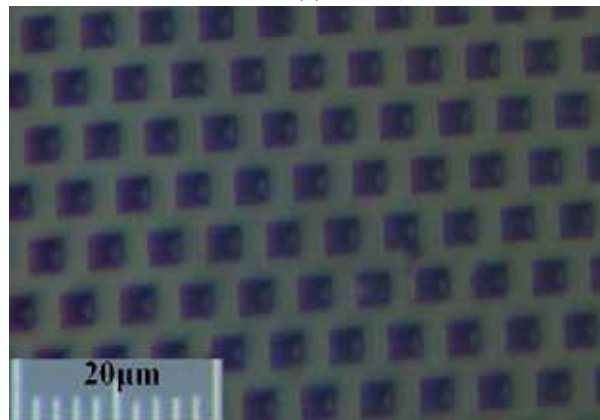


(b)

Fig. 3. Images of the silicon wafers surface landform a) irregular etching; b) regular etching

It is evident that the micro structured surface represents a plane with a hexagonal ornament formed by inverse quadrangular pyramids with 4µm base and 2-3µm depth.

After the deposition of ITO layers on the both types of the textured surfaces of the silicon wafers (Fig. 3) and Cu evaporated grid on the frontal side and continuous Cu layer on the rear side, two types of the optimized structures have been fabricated (Fig. 4).
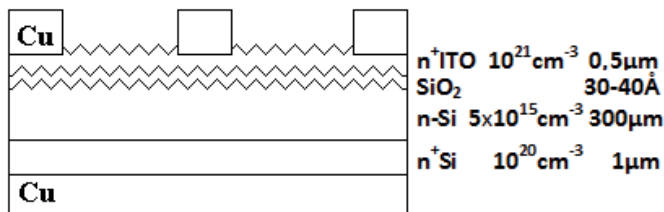


Fig. 4. The schematic image of ITO/SiO$_2$/nSi/n$^+$Si solar cell with optimized parameters and textured Si surface

The measurements of these characteristics and of solar energy conversion efficiency have been carried out under standard conditions (AM1.5, 1000W/m2, 250C) with the solar simulator ST 1000. The load I-V characteristics of the $n^+ITO/SiO_2/n/n^+Si$ SC are presented in Fig. 5 and Fig. 6.
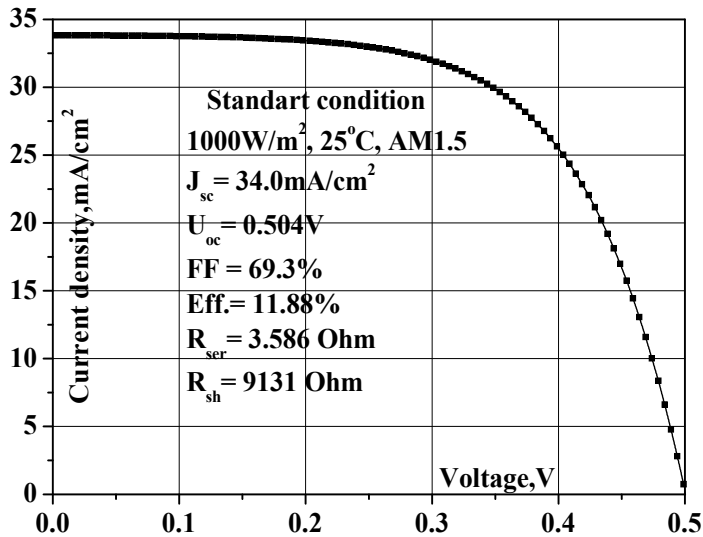


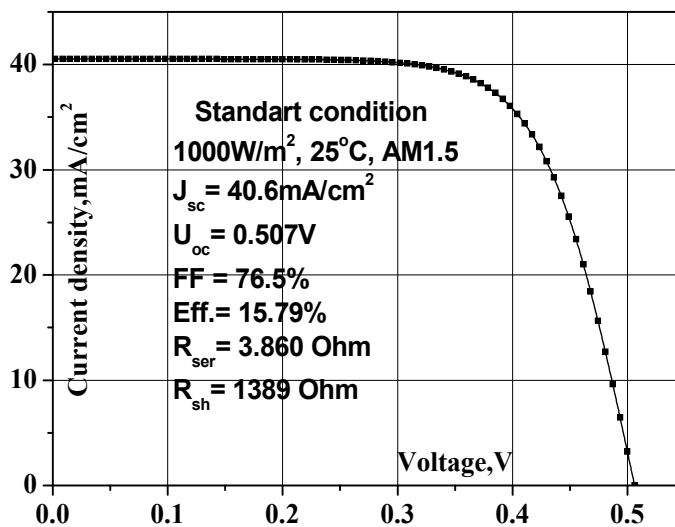Fig. 5. Load I-V characteristic of ITO/SiO$_2$/nSi solar cells with irregular landform Si surface



Fig. 6. Load I-V characteristic of ITO/SiO$_2$/nSi solar cells with regular landform Si surface

For samples obtained on textured Si wafers with irregular landform (Fig. 5), the efficiency and other photoelectric parameters increased in comparison with the SC described earlier (Gagara et al, 1996, Simashkevich et al, 1999). Besides, the results improved when Si wafers

with regular landform (Fig.3b) were used for ITO/$SiO_2$/nSi solar cell fabrication. The respective load I-V characteristic is presented in Fig. 6.

The summary data regarding the methods of ITO layer deposition onto the textured silicon wafers and the obtained efficiencies are presented in Table 3.

| References | ITO deposition method | Area (cm²) | Eff. (%) | Note |
|---|---|---|---|---|
| Kobayashi et al., 1991 | Spray | 2.25 | 13 | Textured Si surface |
| Vishvakarma et al., 1993 | CVD | 2.0 | 12.6 | Textured Si surface |
| Simashkevich et al., 2011 | Spray | 4.0 | 11.88 | Irregular texture Si surface |
| Simashkevich et al., 2011 | Spray | 4.0 | 15.79 | Regular texture Si surface |

Table 3. Efficiencies of ITO/$SiO_2$/nSi solar cells fabricated by various deposition techniques of ITO layers onto the textured silicon wafers

## 2.3 SIS structures on the base of InP and other crystals

Indium phosphide is known to be one of the most preferable materials for the fabrication of solar cells due to its optimum band gap; therefore, it is possible to obtain solar energy conversion into electric power with high efficiency. On the base of InP, SC have been fabricated with the efficiency of more than 20 % (Gessert, et al, 1990). In addition, InP based SC are stable under harsh radiation conditions. It was shown (Botnaryuk, Gorchiak et al., 1990, Yamamoto et al, 1984, Horvath et al, 1998) that the efficiency of these SC after proton and electron irradiation decreases less than in the case of Si or GaAs based SC. However, due to the high price of InP wafers, in terrestrial applications, indium phosphide based SC could not be competitive with SC fabricated on other existing semiconductor solar materials such as silicon.

## 2.3.1 Fabrication of ITO/InP photovoltaic devices

Let us consider the fabrication process of ITO/InP photovoltaic devices. Two main methods of the ITO layer deposition onto InP crystals are used. The first method consists in the utilization of an ion beam sputtering system (Aharoni et al., 1986). The fabrication process of InP photovoltaic devices using this method and the obtained results are described in detail elsewhere (Gessert et al., 1990; Aharoni et al., 1999).

A schematic diagram of the ITO/InP solar cell fabricated by the above-mentioned method is presented in Fig. 7. The operation of solar cells shown in Fig. 7 can be attributed to two possible mechanisms. One is that the conductive ITO and the substrate form an nITO/pInP Schottky type barrier junction. The second is the formation of a homojunction due to the formation of a "dead" layer (thickness – d) at the top of the InP substrate. This "dead" layer is caused by the crystal damage, which results from the impingement of the particles sputtered from the target on the InP top surface. The "dead" layer volume is characterized by extremely short free carrier's life times, i.e. high carrier recombination rates, with respect to the underlying InP crystal.
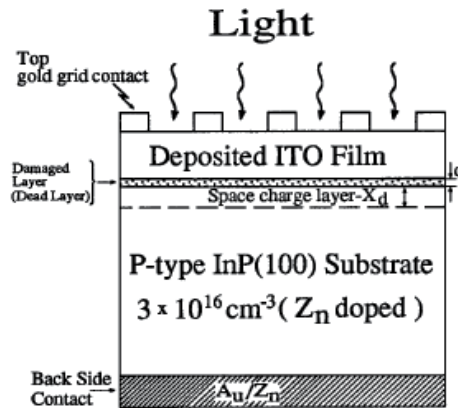
Fig. 7. Schematic diagram of the ITO/InP photovoltaic device obtained by ion bean sputtering.

Accordingly, it forms the "n" side of a homojunction with the "p" type underlying InP. The formation of an n-p junction in InP may be due to tin diffusion from the ITO into the InP, where tin acts as a substitution donor on In sites. The record efficiency of 18.9% was obtained in (Li et al., 1989) for ITO/InP structures, when the ITO layer was deposited by magnetron dispersion on $p^+p$/InP treated preliminary in Ar/O$_2$ plasma.

Using the above-described sputtering process, a small-scale production of 4cm$^2$ ITO/InP photovoltaic solar cells has been organized at Solar Energy Research Institute (now National Renewable Energy Laboratory), Golden, Colorado, the USA (Gessert et al., 1991). Although only a small number of the 4cm$^2$ ITO/InP cells (approximately 10 cells total) were fabricated, the average cell efficiency is determined to be 15.5%, the highest cell performance being 16.1% AM0. Dark I-V data analysis indicates that the cells demonstrate near-ideal characteristics, with a diode ideality factor and reverse saturation current density of 1.02 and 1.1 $\cdot 10^{-12}$mA/cm$^2$, respectively (Gessert et al, 1990).

The second, a simpler, method of ITO/InP photovoltaic devices fabrication consists in spray-pyrolitic deposition of ITO layers onto InP substrates (Andronic et al., 1998; Simashkevich et al., 1999; Gagara et al., 1986; Vasu et al, 1993). ITO layers were deposited on the surface of InP wafers by spraying an alcoholic solution of InCl$_3$ and SnCl$_4$ in different proportions. The following chemical reactions took place on the heated up substrate:

$$4InCl_3 + 3O_2 = 2In_2O_3 + 6Cl_2 \tag{1}$$

$$SnCl_4 + O_2 = SnO_2 + 2Cl_2 \tag{2}$$

ITO thin films with the thickness of 150-250nm were deposited by the above-mentioned spray method in various gaseous environments: O$_2$, Ar, or air atmosphere. When the inert gas was carrier gas, the installation could be completely isolated from the environment that allowed obtaining the structures in the atmosphere without oxygen. A thin insulator layer with the thickness up to 10nm is formed on InP surface due to the oxidation of the substrate during spraying. The oxidation of InP wafers in HNO$_3$ for 20-30s was realized in the case of inert gas atmosphere. In the case of InP crystals, a thin insulator P$_2$O$_5$ layer with the thickness 3-4 nm was formed on InP wafer surface during the ITO layers deposition. Ohmic contacts to pInP were obtained by thermal vacuum evaporation of 95 % Ag and 5 % Zn alloy on the previously polished rear surface of the wafer.

Structures with different crystallographic orientation and holes concentration in the InP substrates were obtained. The optimum concentration of the charge carriers in plnP substrates was $10^{16}$cm$^{-3}$, but the InP wafers with these carrier concentrations and the thickness of 400 nm had a high resistance. For this reason, p/p$^+$InP substrates were used in order to obtain efficient solar cells with a low series resistance. In some cases a plnP layer with the thickness up to 4 μm and concentration p = (3...30) $\cdot 10^{16}$ cm$^{-3}$ was deposited by the gas epitaxy method from the InPCl$_3$ H$_2$ system on the (100) oriented surface of InP heavily doped substrate with the concentrations p$^+$= (1...3) $\cdot 10^{18}$ cm$^{-3}$ for the fabrication of ITO/pInP/p$^+$InP structures. Ag and 5 % Zn alloy evaporated in a vacuum through a special mask were used as an ohmic contact to the ITO and to InP crystal. A schematic diagram of ITO/p/p$^+$InP structure obtained by spray pyrolitic method is presented in Fig. 8.
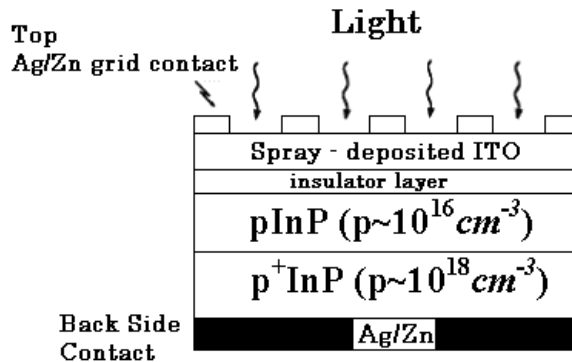


Fig. 8. Schematic diagram of the ITO/InP structure obtained by spray pyrolitic method.

## 2.3.2 Electrical properties of ITO/InP solar cells

The energy band diagram of the ITO/pInP structure proposed in (Botnariuc et al., 1990) is presented in Fig. 9. The current flow mechanism of the ITO/InP structures, obtained in different fabrication conditions, was clarified in (Andronic et al., 1998) on the base of the energy band diagram below.
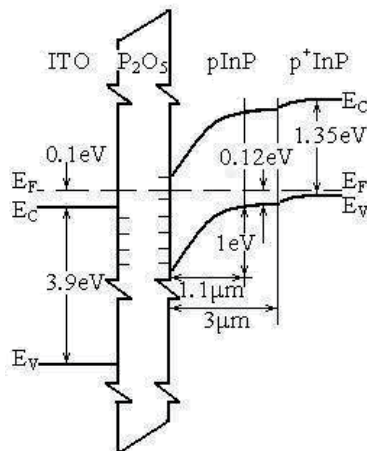


Fig. 9. Energy band diagram of ITO/InP structure obtained in oxygen atmosphere

The I-V characteristics of ITO/pInP structures at different temperatures, obtained in the non- oxide environment are given in Fig. 10a.
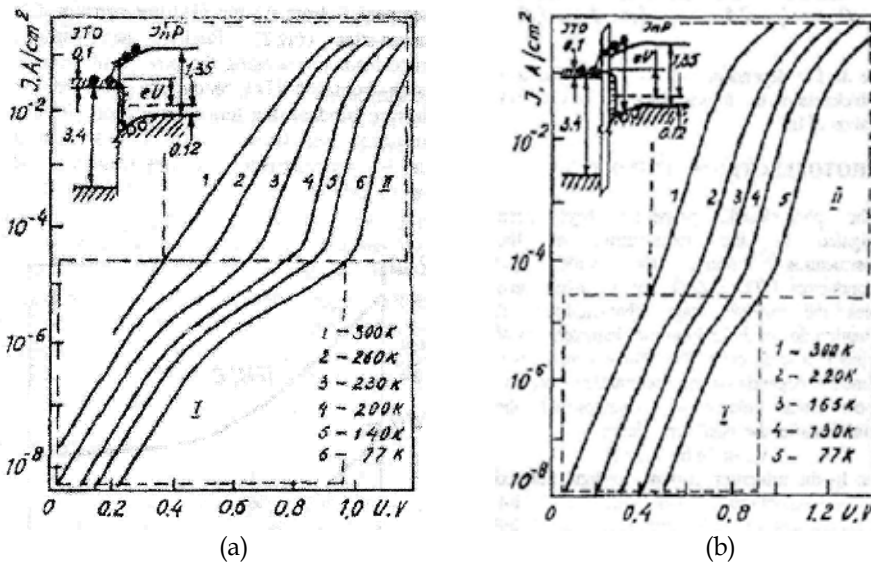


Fig. 10. Dark current-voltage characteristics at direct bias a) obtained in nitrogen atmosphere: b) obtained in oxygen atmosphere

One can suppose the existence of two channels of carriers transport through the structure interface (insertion in Fig. 10a). The first channel is the following: the majority carriers from InP are tunneling through the barrier at the interface and then recombining step by step with electrons from ITO conduction band (Riben & Feucht, 1966). According to this model, the I-V characteristic slope should not depend on temperature. The second channel appears at the direct bias of more than 0.6V and is determined by the emission of electrons from the ITO conduction band to the InP conduction band This emission should occur by changing the I-V curves slope at different temperatures. As one can see from the experimental data, these two channels are displayed by two segments on I-V characteristics.

Fig. 10b shows the I-V characteristics of the ITO/InP structures achieved in an oxygen environment or under substrate oxidation. In this case, the presence of the insulator layer on the interface could be expected. The ITO/InP structures capacity-voltage measurements confirm this supposition. During the fabrication of the ITO/InP structure in oxygen atmosphere, a thin insulator layer on the interface is obtained. Changing the segment II from the ITO/InP structure I-V characteristics shows the presence of a thin insulator layer. The insulator presence leads to changing the process of electron emission from the ITO conduction band to the InP conduction band on the tunneling process through this insulator layer. Thus, the form of segment II on the I-V characteristics becomes similar to the segment I form.

### 2.3.3 Photoelectric properties of ITO/InP solar cells

Photoelectric properties of these SC have been investigated at the illumination of the heterostructures through the wide gap oxide layer. For all investigated samples, the current-voltage characteristics at illumination do not differ from the characteristics of respective

homojunction solar cells. The current short circuit $I_{sc}$ linearly depends on the illumination intensity; the open circuit voltage $U_{oc}$ changes with the illumination after the usual logarithmic dependence:

$$U_{oc} = \frac{kT}{q} \ln \left( \frac{I_{sc}}{I_o} + 1 \right) \tag{3}$$

where $I_L$ - light induced current, $I_s$- the saturation current, T- temperature.

The dependence of ITO/InP cells parameters in AM 0 conditions versus InP substrate orientation and hole concentration was studied. InP wafers with the orientation in (100) and (111) B directions were used to obtain solar cells by the deposition of ITO layers (Table 4).

| Substrate | p, $10^{16}$cm$^{-3}$ | $V_{oc}$, (mV) | $I_{sc}$, (mA/cm$^2$) | $\eta$, (%) |
|---|---|---|---|---|
| pInP (111)B | 2.6 | 674 | 28.3 | 10.4 |
|  | 6.5 | 699 | 23.8 | 9.6 |
|  | 15 | 689 | 25.3 | 9.5 |
| p$^+$/pInP (100) | 10 | 707 | 25.9 | 11.1 |
|  | 30 | 695 | 28.6 | 11.0 |
|  | 2.0 | 707 | 30.8 | 11.6 |
| pInP (111)A | 3.7 | 568 | 22.0 | 5.0 |
|  | 5.7 | 722 | 17.7 | 5.3 |
|  | 37 | 545 | 14.3 | 3.7 |

Table 4. The dependence of ITO/InP cells parameters in AM0 conditions versus InP substrate crystallographic orientation

The photo sensibility spectral distribution of the p$^+$/pInP(100) structure is presented in Fig. 11.
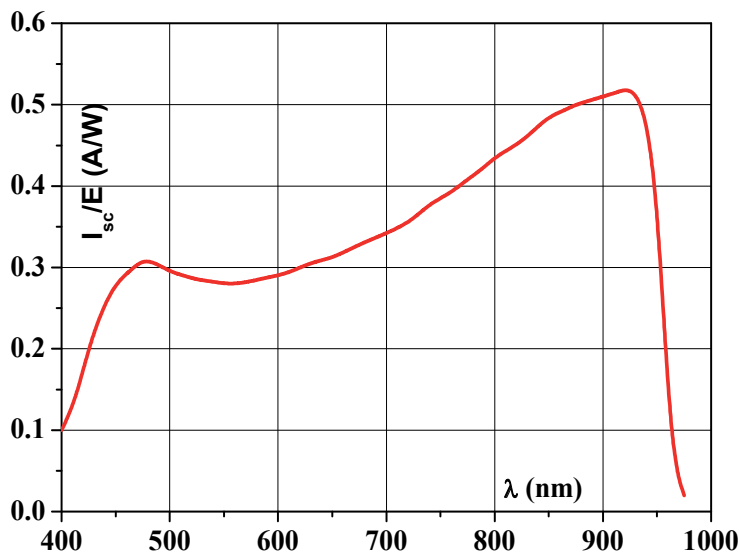


Fig. 11. The photo sensibility spectral characteristic of the p$^+$/pInP (100) SC

The region of the spectral sensibility of Cu/nITO/pInP/Ag:Zn structure is situated between 400 - 50 nm.

The minimum efficiency was observed when solar cells were obtained by deposition of ITO layers onto InP wafers oriented in (111) A direction. To increase the efficiency, those solar cells were thermally treated in $H_2$ atmosphere at the temperature of $350^0C$ during 10 minutes to reduce the series resistance (Bruk et al, 2007).

It was shown that before the thermal treatment the following parameters had been obtained under AM 1.5 illumination conditions: $U_{oc}$= 0.651 V, $I_{sc}$= 18.12 mA/cm², FF = 58 %, Eff. = 6.84 % (Fig. 12, curve 1).
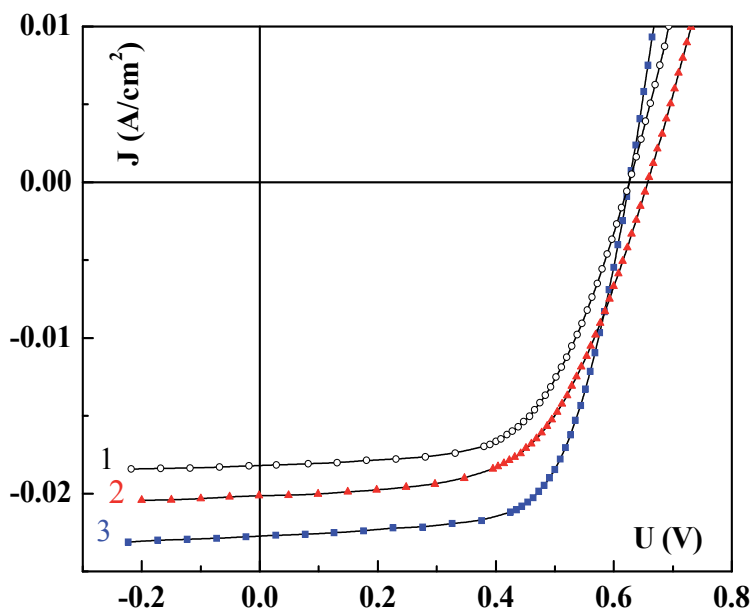


Fig. 12. Load I-V characteristics of Cu/nITO/pInP/Ag:Zn solar cells: 1-before thermal treatment; 2-after thermal treatment in $H_2$; 3-best parameters after thermal treatment in $H_2$

After the thermal treatment the parameters were: $U_{oc}$= 0.658 V, $I_{sc}$= 20.13 mA/cm², FF = 58%, Eff.= 7.68 % (Fig.12, curve 2). The photoelectric parameters of the SC received on InP wafers with the concentration p = $3.10^{17}$cm⁻³ after the thermal treatment were $U_{oc}$=0.626 V, $I_{sc}$= 22.72 mA/cm², FF = 71 %, Eff.= 10.1 % (Fig. 12, curve 3), that is better than for analogous SC without treatment in $H_2$.

The thermal treatment in $H_2$ leads to the undesirable decrease of the photo sensibility in the short wave region of the spectrum (Fig.13).

The highest sensibility is observed at 870nm, which indicates that the maximum contribution in the photo sensibility is due to the absorption in InP.

ITO/InP structures grown by spray pyrolysis were also investigated in Semiconductor Laboratory of the Indian Institute of Technology, Madras (Vasu & Subrahmanyam, 1992; Vasu, et al., 1993). The maximum efficiency of 10.7% was achieved under 100mW/cm² illumination for junctions having 5% by weight of tin in the ITO films. The texturing of the InP crystal surface in ITO/InP SC (Jenkins et al., 1992) reduces the surface reflection. These cells showed improvement in both short circuit current and fill factor, the efficiency can be increased by 6.74%. The texturing reduces the need for an optimum antireflection coating.

SIS structures for SC fabrication were also obtained on the base of other semiconductor materials besides Si and InP. ITO/CdTe (Adeeb et al., 1987) and ITO/GaAs (Simashkevich et al., 1992) structures were obtained by spray pyrolysis of ITO layers on pCdTe and pGaAs crystals. For ITO/CdTe the efficiency was 6%, for ITO/GaAs SC it did not exceed 2.5%.
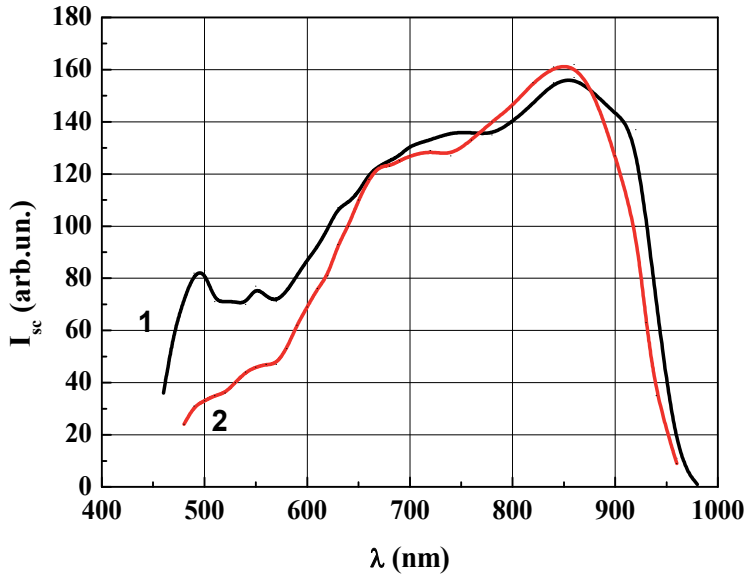


Fig. 13. The spectral photo sensibility of Cu/n+ITO/pInP/Ag:Zn structure: 1- before $H_2$ annealing, 2- after $H_2$ annealing

### 2.3.4 Degradation of photoelectric parameters of ITO/InP solar cells exposed to ionizing radiation

The degradation of photoelectric parameters of ITO/InP solar cells after their irradiation by protons with energies $E_p$=20.6MeV and flux density up to $F_p$=$10^{13}$cm$^{-2}$ and by electrons with $E_c$=1MeV and $F_e$≤$10^{15}$cm$^{-2}$ was investigated (Andronic et al., 1998). The results of the photoelectrical parameter measurements at AM0 conditions after the irradiation are presented in Fig. 14.

Higher efficiency of 11.6% is obtained if the InP substrate is oriented in [100] plane.
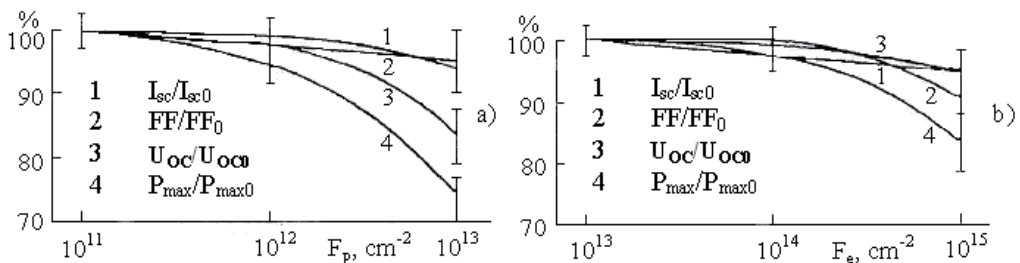


Fig. 14. The degradation of ITO/InP heterostructures photoelectric parameters under protons (a) and (b) electrons irradiation

We notice that after the irradiation of ITO/InP solar cells with an integral proton flux of $10^{13}$cm$^{-2}$, their efficiency decreases by 26%, that is less than in the case of Si and GaAs based solar cells. In the spectral characteristics of ITO/pInP solar cells after proton irradiation a small decrease of the photosensitivity in the long wavelength region of the spectrum was observed due to the decrease of the diffusion length.

Comparing the results of the radiation stability study of ITO/InP SC, fabricated by spray pyrolysis, with the results of similar investigations of other InP based structures, it is possible to conclude that in this case the radiation stability is also determined by the low efficiency of radiation defects generation and, hence, by the low concentration of deep recombination centers, reducing the efficiency of solar energy conversion in electric power.

## 3. Fabrication of ITO/nSi solar cells with enlarged area by spray pyrolisys

From the brief discussion above it can be concluded that the deposition of ITO layers by spray pyrolysis on the surface of different semiconductor materials allows manufacturing SC through a simple and less expensive technology. The most effective are ITO/InP SC but because of a very high cost of the InP crystals they cannot be widely used in terrestrial applications. To this effect ITO/nSi SC with the efficiency higher than 10% may be used, but it is necessary to develop the technology for SC fabrication with the active area enlarged up to 70-80 cm$^2$ as is the case of traditional silicon SC with p-n junction.

### 3.1 Deposition of ITO layers on enlarged silicon wafers

ITO layers are deposited on the nSi crystals surface using the specially designed installation (Simashkevich et al., 2004; Simashkevich et al., 2005) (Fig. 15) that has four main units: the spraying system (7), the system of displacement and rotation of the support on which the substrate is fixed (4, 5), the system of heating the substrate, and the system of the evacuation of the residual products of the pyrolysis (8). The heating system consists of an electric furnace (2) and a device for automatic regulation of the substrate temperature with the thermocouple (3). The rest of the installation parts are: the power unit (1), the cover (10), and the shielding plate (12). Silicon wafers (11) are located on the support (9) and with the displacement mechanism are moved into the deposition zone of the electric furnace (6). The construction of this mechanism provides the rotation of the support with the velocity of 60 rotations per minute, the speed necessary for the obtaining of thin films with uniform thickness on the all wafer surface. The alcoholic solution of the mixture $SnCl_4$ + $InCl_3$ is sprayed with compressed oxygen into the stove on the silicon wafer substrate, where the ITO thin film is formed due to thermal decomposition of the solution and the oxidation reaction. On the heated up substrate there are the chemical reactions describe above in formulas (1) and (2).

The BSF n/n$^+$ junction was fabricated on the rear side of the wafer by a diffusion process starting from $POCl_3$ gas mixture. The junction formation ended with a wet chemical etching of $POCl_3$ residual in a 10% HF bath. A junction depth of 1μm was chosen in order to minimize recombination. To reduce the surface recombination velocity the wafers were thermally oxidized at the temperature of 850°C. The main steps of the fabrication of BSC are schematized in Fig. 16.

### 3.2 Properties of ITO layers

The properties of the thus obtained ITO films depend on the concentration of indium chloride and tin chloride in the solution, the temperature of the substrate, the time of

spraying and the deposition speed. ITO films had a microcrystalline structure that was influenced by the crystal lattice of the support as the X-ray analysis showed. They had cubic structure with the lattice constant 10.14Å (Bruk et al., 2009)). The SEM image of such an ITO film is presented in Fig. 17.
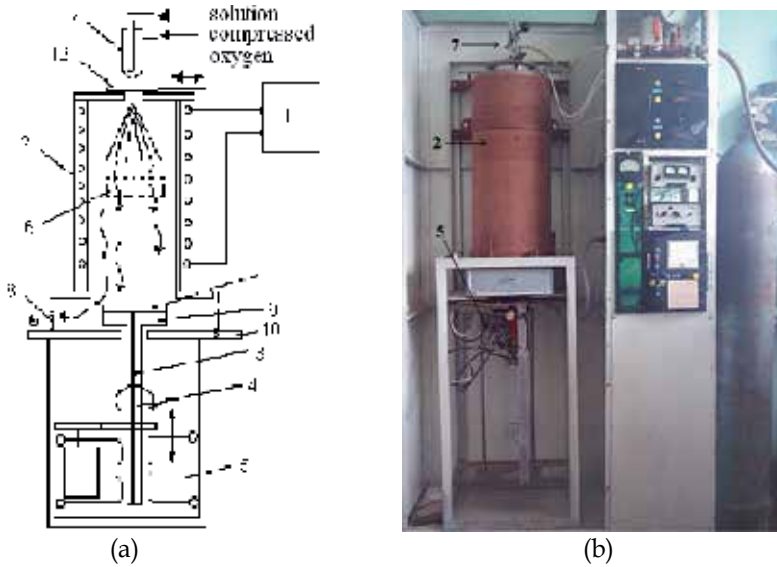


Fig. 15. Schematic a) and real b) view of the installation for ITO thin films deposition

ITO/SiO$_2$/nSi solar cells with the active area of 8.1cm$^2$ and 48.6cm$^2$ were fabricated. In some cases a BSF region was obtained at the rear contact by phosphor diffusion.
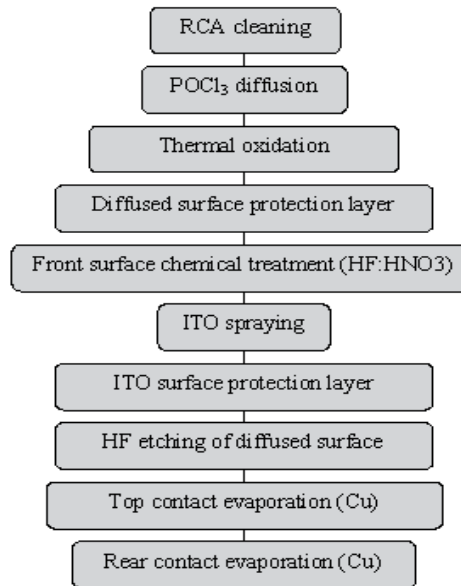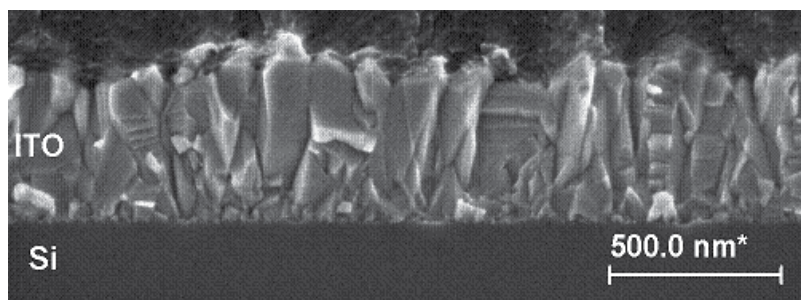


Fig. 16. SC process sequence.

Fig. 17. SEM image of ITO film

From Fig. 17 it is clear that the ITO film with the thickness of 400nm has a columnar structure, the column height being about 300nm and the width 50-100nm.

ITO films with the maximum conductivity $4.7 \cdot 10^3$ Om$^{-1}$cm$^{-1}$, the electron concentration $(3.5 \div 15) \cdot 10^{21}$cm$^{-3}$, the mobility $(15 \div 30)$cm$^2$/(V s). and maximum transmission coefficient in the visible range of the spectrum (87 %) were obtained from solutions containing 90 % InCl$_3$ and 10 % SnCl$_4$ at the substrate temperature 450°C, deposition rate 100 Å/min, spraying time 45 s. ITO layers with the thickness 0.2mm to 0.7mm and uniform properties on the surface up to 75cm$^2$ were obtained.

The dependence of the electrical parameters of ITO layers as a function of their composition is given in Table 5.

| Parameters | Ratio of InCl$_3$:SnCl$_4$:C$_2$H$_5$OH component in the solution | | | | | |
|---|---|---|---|---|---|---|
| | 10:0:10 | 9.5:0.5:10 | 9:1:10 | 8.5:1.5:10 | 8:2:10 | 0:10:10 |
| σ, S·cm$^{-1}$ | $2.6 \cdot 10^2$ | $2.6 \cdot 10^3$ | $4.7 \cdot 10^3$ | $2.6 \cdot 10^3$ | $1.3 \cdot 10^3$ | 42.4 |
| n, cm$^{-3}$ | $1.1 \cdot 10^{20}$ | $5.5 \cdot 10^{20}$ | $1.1 \cdot 10^{21}$ | $6.5 \cdot 10^{20}$ | $5.8 \cdot 10^{20}$ | $5.3 \cdot 10^{19}$ |
| μ, cm$^{-2}$/(V·s) | 15 | 29 | 27 | 25 | 14 | 5 |

Table 5. The dependence of the electrical parameters of ITO layers as a function of their composition

The band gap width determined from the spectral dependence of the transmission coefficient is equal to 3.90eV and changes only for the content of 90-100% of InCl$_3$ in the spraying solution. If the content of InCl$_3$ is less than 90% the band gap remains constant and equal to 3.44eV. The optical transmission and reflectance spectra of the deposited on the glass substrate ITO thin films (Simashkevich et al., 2004) shows that the transparence in the visible range of spectrum is about 80%, 20% of the incident radiation is reflected.

The ITO thin film thickness was varied by changing the quantity of the sprayed solution and it was evaluated from the reflectance spectrum (Simashkevich et al., 2004). The thickness of the layer was determined using the relationship (Moss et al., 1973):

$$d = \lambda_1 \cdot \lambda_2 / \{(\lambda_2 - \lambda_1) \cdot 2n\} \qquad (4)$$

where: n-refraction index equal to 1.8 for ITO (Chopra et al., 1983); λ-the wavelengths for two neighboring maximum and minimum; d-the thickness of the ITO layer. Using this relation the thickness of ITO layers deposited on the nSi wafer surface in dependence on the quantity of the pulverized solution has been determined. This relation is linear and the layer thickness varies from 0.35μm up to 0.5μm.

### 3.3 Obtaining of ITO/nSi structures

The nSi wafers oriented in the (100) plane with resistivity 1.0 Ohm.cm and 4.5 Ohm.cm (concentrations $5 \cdot 10^{15}$ cm$^{-3}$ and $1 \cdot 10^{15}$ cm$^{-3}$) were used for the fabrication of SIS structures. Insulator layers were obtained on the wafers surface by different methods: anodic, thermal or chemical oxidation. The best results have been obtained at the utilization of the two last methods. The chemical oxidation of the silicon surface was realized by immersing the silicon wafer into the concentrated nitric acid for 15 seconds. A tunnel transparent for minority carriers insulator layers at the ITO/Si interface have been obtained thermally, if the deposition occurs in an oxygen containing atmosphere. Ellipsometrical measurement showed that the thickness of the SiO$_2$ insulator layer varies from 30 Å to 60 Å. The frontal grid was obtained by Cu vacuum evaporation. The investigation of the electrical properties of the obtained SIS structures demonstrates that these insulator layers are tunnel transparent for the current carriers. Thereby the obtained ITO/nSi SIS structures represent asymmetrical doped barrier structures in which a wide band gap oxide semiconductor plays the role of the transparent metal.

## 4. Physical properties of n$^+$ITO/SiO$_2$/nSi structures

### 4.1 Electric properties

Current-voltage characteristics in the temperature range 293K–413K were studied. The general behavior of the I-V curves of directly biased devices in Fig. 18 is characterized by the presence of two straight-line regions with different slopes (Simashkevich et al., 2009). Two regions with different behavior could be observed from this figure In the first region, at external voltages lower than 0.3 V, the I-V curves are parallel, i.e., the angle of their inclination is constant.
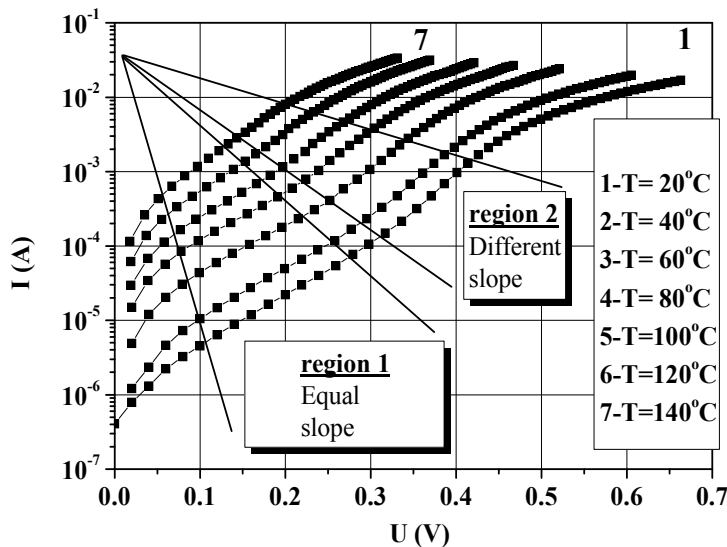


Fig. 18. Temperature dependent direct I-V characteristics in the dark of the n$^+$ITO/SiO$_2$/nSi solar cells

In this case, according to (Riben & Feucht, 1966), the charge carrier transport through the potential barrier is implemented through the tunnel recombination processes in the

space charge region, and the current-voltage dependence could be described by the relation:

$$I = I_o \exp(AV) \exp(BT) \qquad (5)$$

where A and B are constant and do not depend on voltage and temperature, respectively. The numerical value of the constant A, determined from dependences presented in Fig. 18 is equal to 15 $V^{-1}$. The value of the constant B, which is equal to 0.045 $K^{-1}$, was calculated from the same dependences that have been re-plotted as $\ln I = f(T)$. In (Riben & Feucht, 1966) the constant A is expressed by the relation:

$$A = 8\pi/3h \cdot (m^*_e \, \varepsilon_s \, S/N_d)^{1/2} \qquad (6)$$

where $m^*_e$ – is the electron effective mass (in Si in the case considered); $\varepsilon_s$ – the dielectric permeability of the silicon, and S represents the relative change of the electron energy after each step of the tunneling process. Note that 1/S represents the number of tunneling steps.
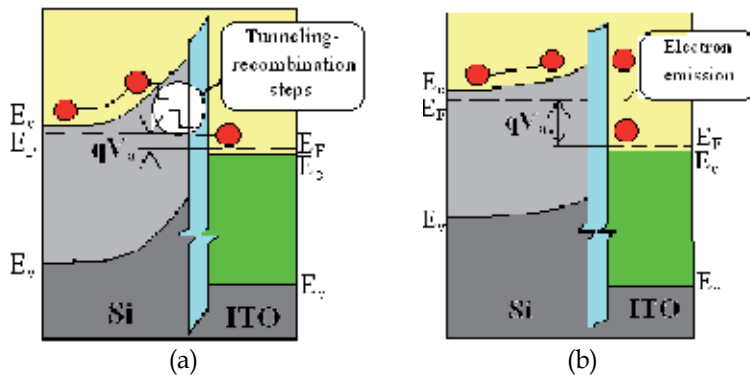


Fig. 19. The energy band diagram for: a) biases lower than 0.3 V (the region 1 in Fig. 18), b) biases higher than 0.3 V (region 2 in Fig. 18)

The numerical value of A is easily calculated, since the other parameters in the respective expression represent fundamental constants or Si physical parameters. Hence, the mechanism of the charge carrier transport at direct biases of less than 0.3 *V* could be interpreted as multi-step tunnel recombination transitions of electrons from the silicon conduction band into the ITO conduction band (see the energy band diagram in Fig.19a), the number of steps being about 100.

At voltages higher than 0.3 V (see different slope region in Fig. 18) the current flow mechanism through the ITO/nSi structure changes. The slopes of the I-V curves become temperature dependent that is confirmed by the constant value n about 1.6 of the parameter n in the relation:

$$I = I_0 \exp(qV_a/nkT) \qquad (7)$$

where

$$I_0 = C\exp(-\varphi_B/kT) \qquad (8)$$

C is a constant depending on the flux current model (emission or diffusion) (Milnes & Feucht, 1972).

Such an I-V dependence expressed by relations (7) and (8) is typical for transport mechanisms involving emission of electrons over potential barriers (Fig. 19b). Thus, at temperatures higher than 20°C, an initial voltage that stimulates the electron emission from Si into ITO over the potential barrier at the Si/ITO interface in $n^+ITO/SiO_2/nSi$ structures is of about 0.3 *V*. From $\ln I = f(1/kT)$ it is possible to determine the height of the potential barrier $\varphi_B$ in ITO/nSi structures because the slope of the above-mentioned dependence is equal to $\varphi_B - qV_a$. The calculated value of $\varphi_B$ is 0.65eV, which is in correlation with the experimental data. A close value of the height of the potential barrier $\varphi_B$ equal to 0.68 eV was determined also from relation (8) (Simashkevich et al., 2009).

To sum up, in $n^+ITO/SiO_2/nSi$ structures two mechanisms of the direct current flow are observed: (i) tunneling recombination at direct voltages of less than 0.3 *V* and (ii) over barrier emission at voltages higher than 0.3 *V*. In the former case, the direct current flow could be interpreted as multi-step tunnel recombination transitions of electrons from the silicon conduction band into the ITO conduction band, the number of steps being of about 100. The reduction of the influence of the former as well as a fine adjustment of the $SiO_2$ thickness in investigated structures will lead to an increased efficiency of converting solar energy into electric energy.

### 4.2 Photoelectric properties

The spectral distribution of the quantum efficiency as well as the photosensitivity of the obtained PV cells have been studied (Simashkevich et al., 2004). The monochromatic light from the spectrograph is falling on a semitransparent mirror and is divided into two equal fluxes. One flux fall on the surface of a calibrated solar cell for the determination of the incident flux energy and the number (N) of incident photons. The second flux falls on the surface of the analyzed sample and the short circuit current Jsc is measured, thus permitting the calculation of the number of charge carriers, generated by the light and separated by the junction, and then the quantum efficiency for each wavelength (Fig. 20).
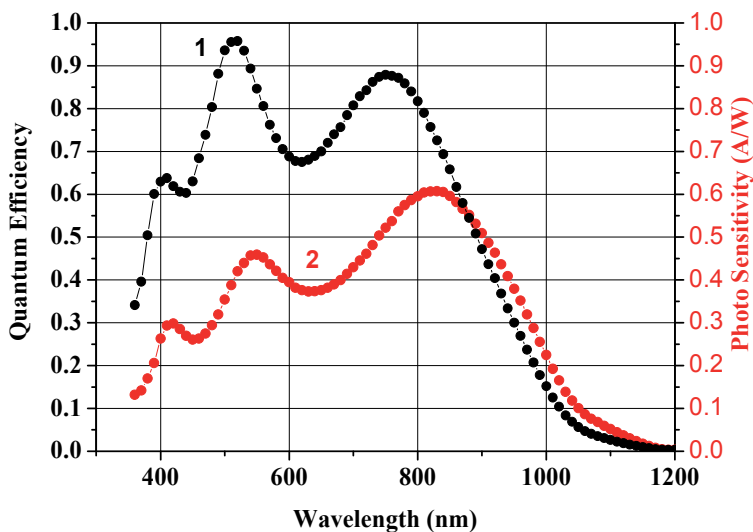


Fig. 20. Spectral distribution of the quantum efficiency (1) and photo sensitivity (2) of the $n^+ITO/SiO_2/nSi$ solar cells

The reproducibility of the process and the performances of the devices during samples realization were checked in each batch of samples as well as batch-to-batch. The enlargement of the area of the solar cells up to 48.6cm² leads to the increasing of the series resistance and to the diminishing of the efficiency down to 7%. Thus, the method of obtaining n⁺ITO/SiO₂/nSi structures based on the thin In₂O₃: Sn layers, which are formed on the surface of Si wafers, traditionally chemically treated, passivated and heated to the temperature of 450°C, by spraying chemical solutions of indium tin chloride was elaborated. Solar cells based on n⁺ITO/SiO₂/nSi structures with an active surface up to 48.6cm² have been fabricated.

Maximum efficiency of 10.52% is obtained in the case of (100) crystallographic orientation of Si wafer with BSF region at the rear surface and active area of 8.1 cm², ITO thickness 0.3mm, SiO₂ thickness - 30Å and the concentration of charge carriers (electrons) in silicon $(1-5)\times10^{15}$cm⁻³ (Fig. 21).
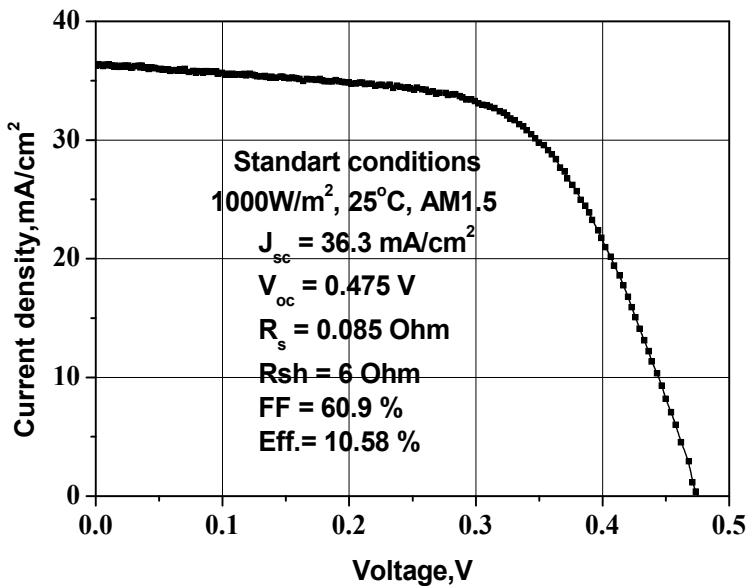


Fig. 21. Load I-V characteristic of the n⁺ITO–SiO₂–nSi cells with active area 8.1cm² and BSF region at rear surface.

The developed technology demonstrates the viability of manufacturing solar cells based on n⁺ITO/SiO₂/nSi junctions by assembling two 15W and two 30W power solar panels (Fig. 22) (Usatii, 2011).

## 5. Bifacial n⁺Si/nSi/SiO₂/n⁺ITO solar cells

For the first time BSC that are able to convert the solar radiation incident of both sides of the cell into electric power have been produced and investigated fifty years ago (Mori, 1960). This type of SC has potential advantages over traditional monofacial SC. First, there is the possibility of producing more electric power due to the absorption of solar energy by the frontal and rear sides of the device, next, they do not have a continuous metallic rear contact, therefore they are transparent to the infrared radiation, which warms

the monofacial SC and reduces their efficiency. As was presented in (Cuevas, 2005), different types of BSC have been fabricated since then, but all those BSC are based on p-n junctions fabricated by impurity diffusion in the silicon wafer. In case of BSF fabrication, these difficulties increase since it is necessary to realize the simultaneous diffusion of different impurities, which have an adverse influence on the silicon properties. Therefore, the problem of protecting the silicon surface from the undesirable impurities appears.
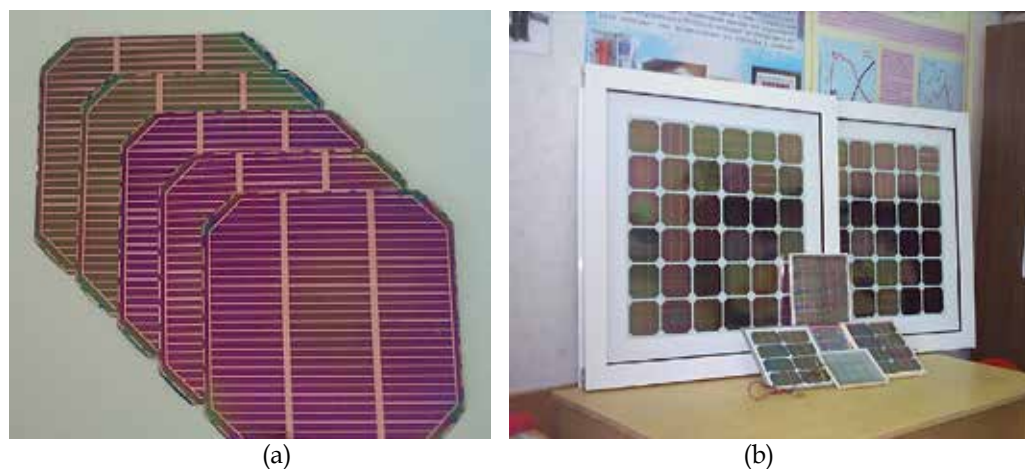


Fig. 22. General view of ITO/nSi photovoltaic converters a) SC with active aria 48.6 cm², b) solar modules with different power

A novel type of BSC formed only by isotype junctions was proposed in (Simashkevich et al., 2007), where the possibility was demonstrated to build BSC on the base of nSi crystals and indium tin oxide mixture (ITO) layers obtained by spraying that contain only homopolar junctions with a $n^+/n/n^+$ structure The utilization of such structures removes a considerable part of the above-mentioned problems of BSC fabrication because a single diffusion process is carried out.

### 5.1 Fabrication and characterization of $n^+ITO/SiO_2/n/n^+Si$ bifacial solar cells

In the work (Simashkevich et al., 2007) the results are presented of producing and investigating the silicon based BSC only on majority carriers. The first frontal junction is a SIS structure formed by an ITO layer deposited on the surface of n-type silicon crystal. The starting material is an n-type doped (0.7–4.5Ohm·cm) single crystalline (100) oriented Cz-Silicon 375µm thick nSi wafer with the diameter of 4 inches. The electron concentrations were $10^{15}$cm$^{-3}$ - $10^{17}$ cm$^{-3}$.

An usual BSF structure consisting of a highly doped nSi layer obtained by phosphorus diffusion was fabricated on the topside of the wafer by a diffusion process starting from $POCl_3$ gas mixture. The rear $n/n^+$ junction formation ends with a wet chemical etching of $POCl_3$ residual in a 10 % HF bath. A junction depth of 1 µm has been chosen in order to minimize recombination.

To reduce the surface recombination velocity the wafers have been thermally oxidized at a temperature of 850ºC. Grids obtained by Cu evaporation in vacuum were deposited on the

frontal and back surfaces for BSC fabrication. The schematic view of the bifacial ITO/nSi solar cell is presented in Fig. 23.



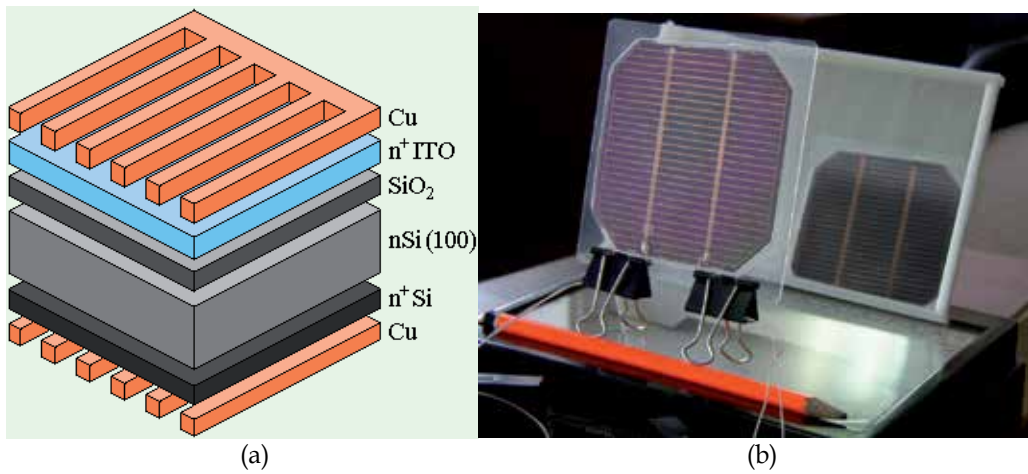(a)                                                                                (b)

Fig. 23. The schematic a) and real b) view of the ITO/nSi BSC

The spectral distribution of the quantum efficiency of BSC, obtained on silicon wafers with different electron concentration, has been studied at frontal and back illumination (Fig.24). With the frontal illumination, in the region of the wavelengths from 400nm to 870nm the value of QY changes in the limits 0.65–0.95. With the back illumination, QY is equal to 0.6–0.8 in the same region of the spectrum (Bruk et al., 2009).
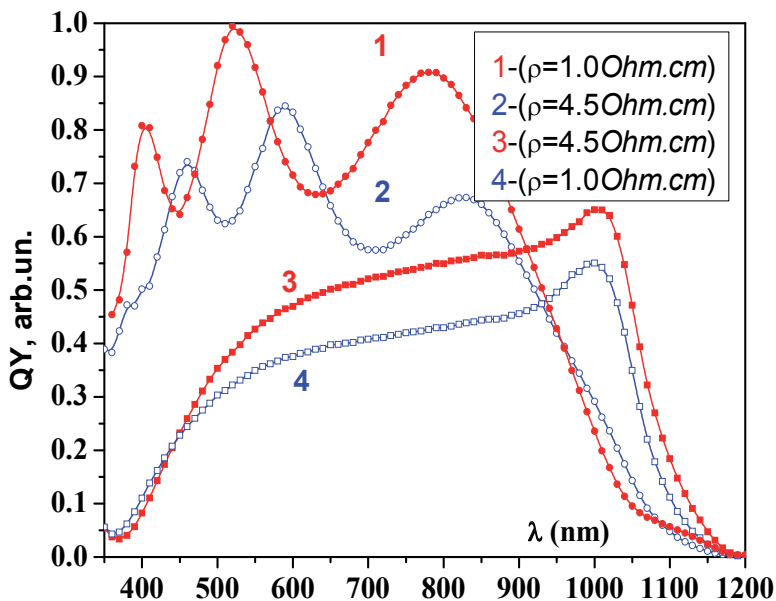


Fig. 24. Spectral distribution of the quantum efficiency 1, 2-frontal illumination; 3, 4-rear illumination

The I-V load characteristics at AM1.5 spectral distribution and 1000W/m² illumination are presented in Fig.25.
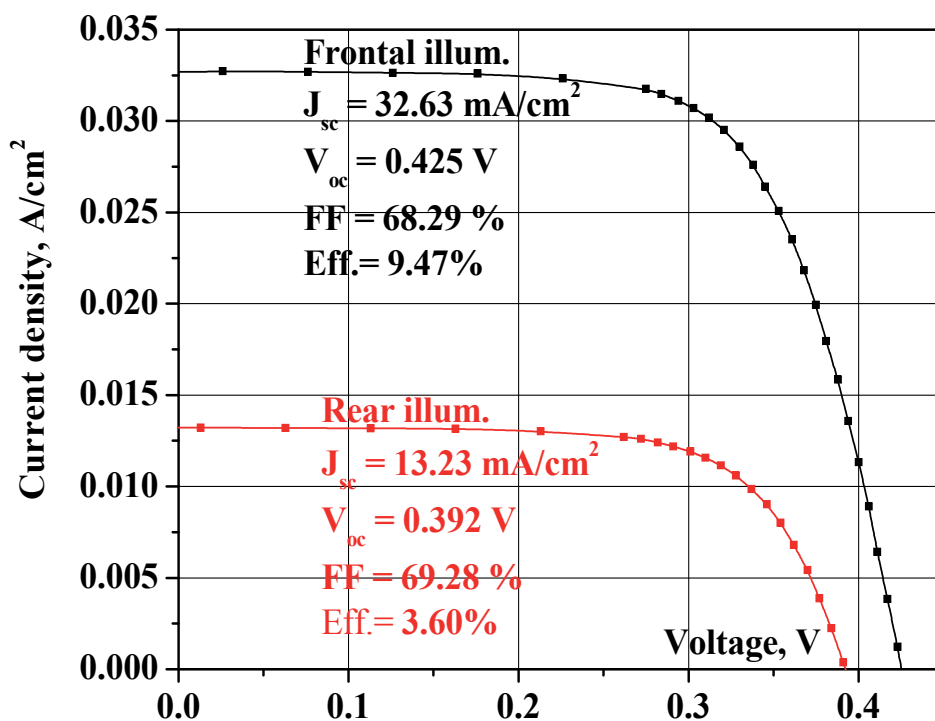


Fig. 25. The I-V load characteristics and the photoelectric parameters of the elaborated BSC at AM1.5 spectral distribution and 1000W/m² illumination

The photoelectric parameters of the elaborated BSC have been determined in standard AM1,5 conditions: for the frontal side $V_{oc}$=0.425V, $J_{sc}$=32.63mA/cm², FF=68.29%, Eff.=9.47%, $R_{ser}$=2.08Ohm, $R_{sh}$=6.7·10³Ohm; for the back side $V_{oc}$=0.392V, $J_{sc}$=13.23mA/cm², FF=69.28%, Eff.=3.6%, $R_{ser}$=3.40Ohm, $R_{sh}$=1.26·10⁴Ohm.
The summary efficiency of the BSC is equal to 13.07%.

### 5.2 n⁺ITO/SiO₂/n/n⁺Si bifacial solar cells with textured surface of Si crystals

Using the method of n⁺ITO/SiO₂/n/n⁺Si bifacial solar cells fabrication described in (Simashkevich et al., 2007) with improved parameters in conformity with p.2 of this communication, in (Simashkevich et al., 2011) two types of bifacial solar cells have been obtained which have different profiles of silicon wafer surface (Fig. 26 and Fig. 27).
It is seen from these data that the effected technology optimization allows to increase of the summary efficiency from 13.07% to 15.73% in the case of irregular etching of the silicon surface and to 20.89% in the case of regular etching. The bifaciality ratio also increases from 0.38 up to 0.75.
On the basis of physical parameters of the silicon wafer, ITO layers and of the results of our experiments, the energy band diagram of the n⁺Si/nSi/SiO₂/n⁺ITO structure was proposed (Simashkevich et al., 2007).

**Frontal illumination**
$J_{SC}$ = 34.6mA/cm$^2$
$U_{OC}$ = 0.478V
FF = 57.4%
Eff. = 9.53%

**Rear illumination**
$J_{SC}$ = 22.5mA/cm$^2$
$U_{OC}$ = 0.461V
FF = 59.4%
Eff. = 6.20%

Voltage, V

Current density, mA/cm$^2$
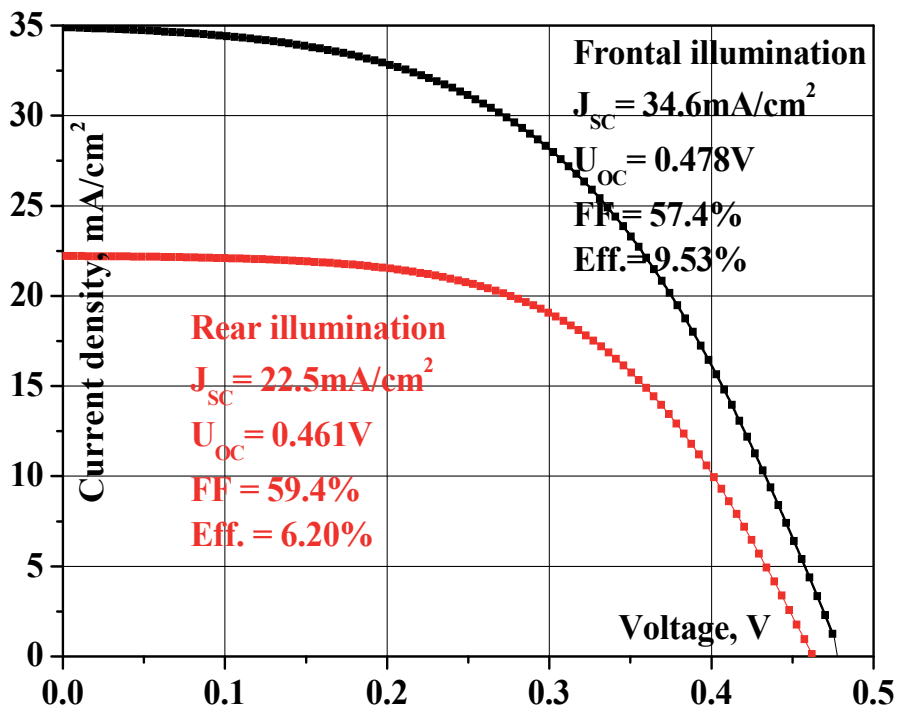
Fig. 26. Load I-V characteristic of n$^+$ITO/SiO$_2$/n/n$^+$Si BSC with irregular Si surface

**Frontal illumination**
$J_{SC}$ = 34.3mA/cm$^2$
$U_{OC}$ = 0.461V
FF = 75.0%
Eff. = 11.91%

**Rear illumination**
$J_{SC}$ = 25.6mA/cm$^2$
$U_{OC}$ = 0.458V
FF = 76.9%
Eff. = 8.98%

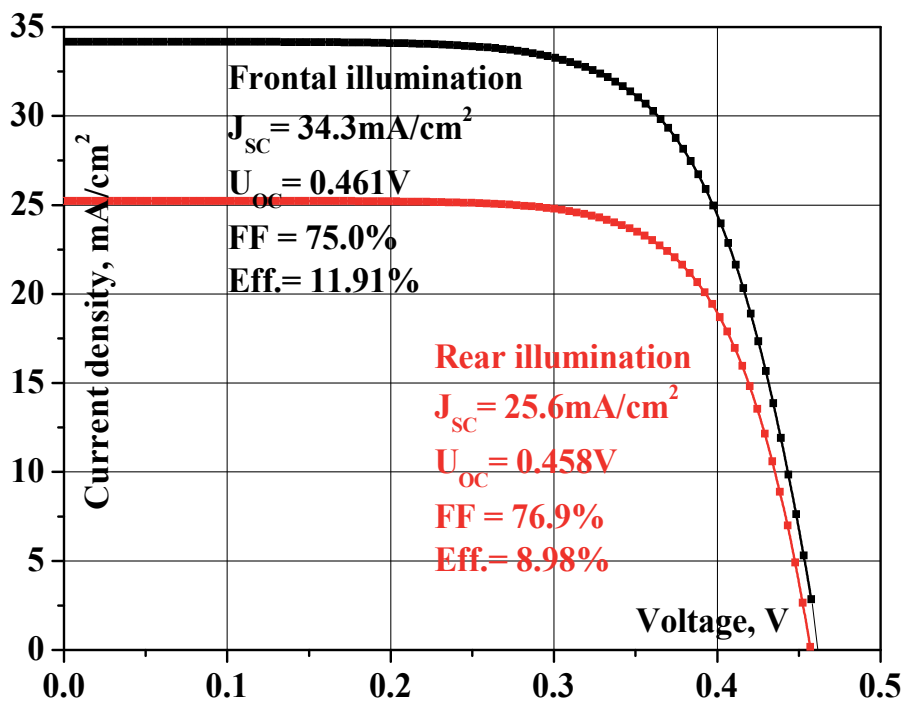Voltage, V

Current density, mA/cm$^2$

Fig. 27. Load I-V characteristic of n$^+$ITO/SiO$_2$/n/n$^+$Si BSC with regular Si surface
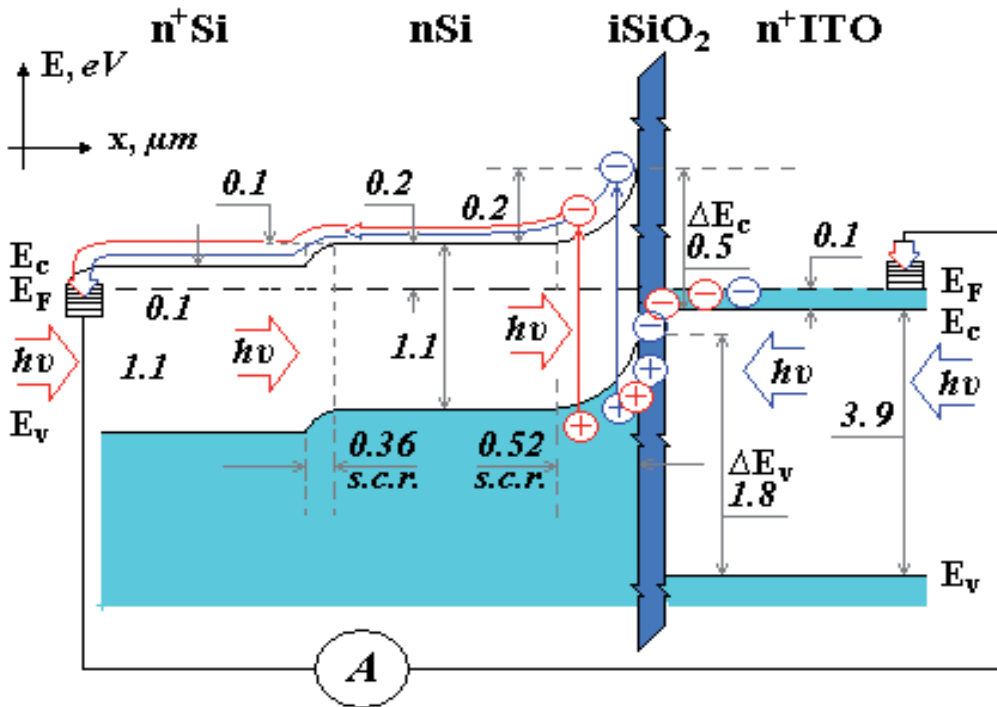
Fig. 28. Energy band diagram of the bifacial Cu/n⁺ITO/SiO₂/nSi/n⁺Si/Cu structure

Fig. 28 shows this energy band diagram at illumination in the short-circuit regime. At the illumination through the frontal contact, the solar radiation is absorbed in the silicon wafer. The light generated carriers are separated by the nSi/SiO₂/ITO junction. The BSF of the n⁺Si/nSi junction facilitate the transport of the carriers to the back contact. The same processes take place at the illumination through the rear contact.

## 6. Conclusion

SC fabricated on the basis of semiconductor-insulator- semiconductor structures, obtained by deposition of TCO films on the surface of different semiconductor solar materials (Si, InP, CdTe etc) are promising devices for solar energy conversion due to the simplicity of their fabrication and relatively low cost. One of the main advantages of SIS based SC is the elimination of the high temperature diffusion process from the technological chain, which is necessary for obtaining p-n junctions, the maximum temperature at the SIS structure fabrication being not higher than 450ºC. The TCO films can be deposited by a variety of techniques among which the spray deposition method is particularly attractive since it is simple, relatively fast and vacuum less. Between different TCO materials, the ITO layers are the most suitable for the fabrication of SIS structures based solar cells.

Silicon remains the most utilized absorbing semiconductor material for fabrication by spray pyrolysis of such type of SC. The maximum efficiency of ITO/nSi SC is 10-12%, but in the case of textured surface of Si crystals the efficiency reaches more than 15%. ITO/nSi SC with enlarged area up to 48 cm² have been obtained by the spray method, the efficiency is 10.58% for cells with area of 8.1cm².

InP based SIS structures fabricated by deposition of ITO layers onto pInP crystal surfaces have high efficiencies, at the same time they are more simple to fabricate in comparison with diffusion junction cells. The efficiency of ITO/InP solar cells obtained by spray pyrolisis depends on the crystallographic orientation of the InP wafers, The maximum efficiency of 11.6% was obtained in the case of fabrication of ITO/pInP/p$^+$InP structures using InP wafers oriented in the (110) plane. ITO/InP SC, obtained by spray pyrolysis demonstrates radiation stability. After the irradiation of ITO/InP solar cells with an integral proton flux of $10^{13}$cm$^{-2}$, their efficiency decreases by 26%, that is less than in the case of Si and GaAs based solar cells.

A new type of bifacial solar cells n$^+$Si/nSi/SiO$_2$/n$^+$ITO based only on isotype junctions was elaborated and fabricated. It was demonstrated that the simultaneous illumination of both frontal and rear surfaces of the structures allow to obtain a summary current. The technological process of manufacturing such solar cells does not require sophisticated equipment. Bifacial solar cells with summary efficiency of 21% and 65% bifaciality coefficient have been obtained using as an absorbent material of single crystalline silicon with a textured surface.

## 7. Acknowledgment

## 8. References

Adeeb, N.; Kretsu, I.; Sherban, D.; Sushkevich, C. & Simashkevich, A. (1987). Spray deposited ITO/CdTe solar cells. *Solar Energy Materials*, Vol. 15, No.1, (January 1987) pp.9-19, ISSN 0927-0248

Aharoni, H.; Coutts, T.J.; Gessert, T.; Dhere, R. & Schilling L. (1986). Ion Beam Sputtered Indium Tin Oxide for InP Solar Cells. *Journal of Vacuum Science and Technology A, Vacuum,Surfaces and Films*. Vol. 4, No.3, pp. 428-431.

Aharoni, H. (1999). ITO/InP Photovoltaic Devices, *Proc. of the International Solar Energy Society (ISES) Solar World Congress*, ISES 1999, SWC Israel. ISBN 008 043 8954, Vol. 1, pp. 95-108, Jerusalem, Israel, (July 1999)

Anderson, R.L. (1975). Photocurrent suppression in heterojunctions solar cells. *Appl.Phys.Lett.* Vol.27, No.12, (December 1975), pp.691-694, ISSN 0003-6951

Andronic, I.; Gagara, L.; Gorceak, L.; Potlog, T.; Sherban, D. & Simashkevich, A. (1998), InP based radiation stable solar cells, *Proc of the 2$^{nd}$ World Conf. on PV Solar Energy Conversion*, Vol.3, pp.3642-3645, ISBN 92-828-5179-6, Vienna, (July 1998)

Ashok, S.; Sharma, P.P. & Fonash, S.J. (1980). Spray-deposited ITO–Silicon SIS heterojuction solar cells. *Electron Devices, IEEE Transactions on,* Vol.27, No.4, 725-730, ISSN 0018-9383

Bobeica, E.; Varsano, F.; Roca, F. & Parretta, A. (2001). Light backscattering properties of textured silicon matirials, *Book of abstracts. INFMMeeting – National Conference on the Physics of Matter*, pp.242-243, Rome, Italy, (June 2001)

Botnariuc, V.M.; Gagara, L.S.; Gorchac, L.V.; Russu, E.V.; Simashkevich, A.V.; Sherban, D.A. & Do Quoc Hung. (1990). ITO/InP surface barrier solar cells obtained by spray method. *Appl.Sol.Energy,* No.3, pp.37-40, ISSN 0003-701X

Bruk, L.; Simashkevich, A.; Sherban, D.; Gorceac, L.; Coval, A. & Usatii, Iu. (2007). The influence of thermal treatment on the parameters of nITO/pInP solar cells obtained by pyrolithic spraying method, *Proc. of the 22th European PV Solar Energy Conf.*, pp.672-674, ISBN: 3-936338-22-1, Milan, Italy, (September 2007)

Bruk, L.; Fedorov, V.; Sherban, D.; Simashkevicha, A.; Usatii, I.; Bobeico, E. & Morvillo P. (2009). Isotype bifacial silicon solar cells obtained by ITO spray pyrolysis. *Materials Science and Engineering B,* Vol.159–160, (March 2009), pp.282–285, ISSN 0921-5107

Calderer, J.; Manifacier, J.C.; Szepessy, L.; Darolles, J.M. & M. Perotin. (1979). Caractérisation des cellules solaires silicium (n)-In2O3 (dope Sn) préparées par une méthode de vaporisation. *Revue de Physique Appliquée.* Vol.14, No.3, page 485-490, HAL: jpa-00244619, version 1

Chang, N.S. & Sites, R. (1978). Electronic characterization of indium tin oxide/silicon photodiodes. *J.Appl.Phys,* Vol.49, No.9, (September 1978), pp.4833 -4837, ISSN 0021-8979

Chapin, D.M.; Fuller, C.S. & Pearson, G.I. (1954). A New Silicon p-n Junction Photocell for Converting Solar Radiation into Electrical Power, *J. Appl. Phys.*, Vol. 25, No.5, (May 1954), pp.676-677, ISSN 0021-8979

Chopra, K.L.; Major S. & Pandya D.K. (1983). Transparent conductors. A status review. *Thin Solid Films,* Vol.102, No.1, (April 1983), pp.1-46, ISSN 0040-6090

Cuevas, A. (2005). The early history of bifacial solar cells, *Proc. of the 20th European Photovoltaic Solar Energy Conference*, pp.801-805, ISBN 3-936338-19-1, Barcelona, Spain, (June 2005)

Dikusar, A.I.; Bruk, L.I.; Monaico, E.V.; Sherban, D.A.; Simashkevich, A.V. & Tiginyanu, I.M. (2008). Photoelectric structures based on nanoporous p-InP. *Surface Engineering and Applied Electrochemistry*, Vol.44, No.1, (February 2008), pp.1-5, ISSN 1068-3755

DuBow, J.; Burk, D. & Sites, J. (1976). Efficient photovoltaic heterojunctions of indium tin oxides on silicon. *Appl.Phys.Lett.*, Vol.29, No.8, (October 1976), pp.494-496, ISSN 0003-6951

Feng, T.; Ghosh A.K. & Fishman C. (1979). Efficient electron-beam deposited ITO/nSi solar cells. *J.Appl. Phys.*, Vol.50, No.7, (June 1979), pp.4972-4974, ISSN 0021-8979

Gagara, L.; Gorcheac, L.; Radu, C.; Radu S.; Sherban, D. & Simaschkevici, A. (1996). Photovoltaic converters of Solar Energy on the base of SIS structures, *Proc. of the Int. Conf. "Euro Sun 96"*, Vol.2, pp.665-669, Munchen, (August 1996)

Garcia, F.J.; Muci, J. & Tomar M.S. (1982). Preparation of (thin film SnO₂)/(textured n-Si) solar cells by spray pyrolysis. *Thin Solid Films*, Vol.97, No.1 (November 1982), pp.47-51, ISSN 0040-6090

Gessert, T.A.; Li, X.; Wanlass, M.W. & Coutts, T.J. (1990). Progress in the ITO/InP Solar Cell, *Proc. of the second Int. Conf. "Indium Phosphide and related materials"*, pp.260-264, Denver, CO, USA, (April 1990)

Gessert, T.A.; Li, X.; Coutts, T.J.; Phelps, P. & Tsafaras, W.N. (1991). Small-scale production of 4cm² ITO/InP photovoltaic solar cells, *Proc. of the third Int. Conf." Indium Phosphide and related materials"*, pp.32-35, ISBN 0-87942-626-8, Cardiff, UK, (April 1991)

Horvath, Zs.J.; Subrahmanyam, A.; Manivannan, P. & Blasubramanian N. (1998). Electrical and photovoltaic study of ITO/GaAs and ITO/InP heterojunctions, *Proc of the 2ⁿᵈ World Conf. on PV Solar Energy Conversion*, Vol.3, pp.3711-3714, ISBN 92-828-5179-6, Vienna, (July 1998)

Jenkins, P.; Landis, G.A.; Fatemi, N.; Li,X.; Scheiman, D. & Bailey, S. (1992). Increased efficiency with surface texturing in ITO/InP solar cells, *Proc. of the fourth Int. Conf. "Indium Phosphide and related materials"*, pp.186-189, ISBN 0-87942-626-8, Newport,, RI, USA, (April 1992)

Kobayashi, H.; Ishida,T.; Nakato, Y. & Tsubomura, H. (1991). Mechanism of carrier transport in highly efficient solar sells having indium tin oxide/Si junction. *J.Appl.Phys.* Vol.69, No.3, (February 1991), pp.1736-1743, ISSN 0021-8979

Li, X.; Wanlass M.W.; Gessert T.A.; Emery, K.A. & Coutts, T.J. (1989). High-efficiency indium tin oxide/indium phosphide solar cells. *Appl. Phys. Lett.*, Vol.54, No.26, (June 1989), pp.2674-2676, ISSN 0003-6951

Malik, A.; Baranyuk, V. & Manasson, V. (1979). Solar cells based on the SnO₂-SiO₂-Si heterojunction. *Appl.Sol.Energy,* No.2, pp.83-84, ISSN 0003-701X

Malik, A.; Baranyuk, V. & Manasson, V. (1980). Improved model of solar cells based on the In₂O₃/SnO₂/SiO₂/nSi structure. *Appl. Sol. Energy,* No.1, pp.1-2, ISSN 0003-701X

Malik, O.; De la Hidalga-W, F.J.; Zuniga –I, C. & Ruiz-T, G. (2008). Efficient ITO/Si solar cells fabricatd with a low temperature technology. Results and perspectives. *Journal of Non -Crystalline Solids*, Vol.354, No.19-25, pp.2472-2477, ISSN 0022-3093

Malik, O. & F.Javier De La Hidalga-W. (2009). Efficient Silicon Solar Cells Fabricated with a Low Cost Spray Technique. In: *Solar Energy*, Radu D. Rugescu, pp. (81-104), In theh, ISBN 978-953-307-052-0, Vukovar, Croatia

Manifacier, J.C. & Szepessy, L. (1977). Efficient sprayed In₂O₃:Sn n-type silicon heterojunction solar cell. *Appl. Phys. Lett.*, Vol.31, No.7, (October 1977), pp.459-462, ISSN 0003-6951

Marques, F. & Chambouleyron, I. (1986). Surface barrier SnO₂/SiOₓ/cSi(n) solar cells: optimization of the fabrication process. *Solar Cells*, Vol.17, No.2-3 (April-May 1986), pp.167-181, ISSN 0927-0248

Milnes, A.G. & Feucht, D.L. (1972). *Heterojunctions and metal-semiconductor junctions*, Academic Press Inc (October 1972), ISBN-10 0124980503, ISBN-13 978-0124980501, New-York and London, 408 p.

Mizrah, T. & Adler, D. (1976). Operation of ITO-Si heterojunction solar cells. *Appl.Phys.Lett.*, Vol.29, No.8, (November 1976*)*, pp.682-684, ISSN 0003-6951

Moss, T.S.; Burrell, G.J. & Ellis B. (1973). *Semiconductor Opto-Electronics*, Butterworths, London

Nagatomo, T.; Endo, M. & Omoto, O. (1979). Fabrication and characterization of $SnO_2$/n-Si solar cells. *Jpn. J. Appl. Phys.*, Vol.18, No.6, (June 1979) pp.1103-1109, ISSN 0021-4922

Nagatomo, T.; Inagaki, Y.; Amano, Y. & Omoto, O. (1982). A comparison of spray deposited ITO/n-Si and $SnO_2$/n-Si solar cells. *Jpn. J. Appl. Phys.*, Vol.21, Suppl.21-2, pp.121-124, ISSN 0021-4922

Riben, A.R. & Feucht, D.L. (1966). Electrical transport in nGe-pGaAs heterojunctions. *International Journal of Electronics,* Vol.20, No.6, (June 1966), pp.583-599, ISSN 0020-7217

Saim H.B. & Campbell D.S. (1987). Properties of indium-tin-oxide (ITO)/silicon heterojunction solar cells by thick-film techniques. *Solar Energy Materials,* Vol.15 No.4, (May-June 1987), pp. 249-260, ISSN 0927-0248

Shewchun, J.; Dubow, G.; Myszhkowsky, A. & Singh, R. (1978). The operation of semiconductor-insulator-semiconductor (SIS) solar cells: Theory. *J. Appl. Phys.*, Vol.49, No.2, (February 1978*)*, pp.855-864, ISSN 0022-3727

Shewchun, J.; Burk, D.; Singh, R.; Spitzer, M. & Dubow, G. (1979). The semiconductor-insulator-semiconductor (indium tin oxide on silicon) solar cells: characteristics and loss mechanisms. *J.Appl.Phys.* Vol.50, No.10, (October 1979*)*, pp.6524-6533, ISSN 0021-8979

Shewchun, J.; Dubow, G.; Wilmsen, C.; Singh, R.; Burk, D. & Wagner J. (1979). The operation of semiconductor-insulator-semiconductor (SIS) solar cells: Experiment. *J.Appl.Phys.*, Vol.50, No.4, (April 1979*)*, pp.2832-2839, ISSN 0021-8979

Shewchun, J.; Burc, D. & Spitzer, M.B. (1980). MIS and SIS solar cells. *Electron Devices, IEEE Transactions on*. Vol.27, No.4, pp.705-716, ISSN 0018-9383

Simashkevich, A.; Toyi, J-M.; Sherban, D. & Yakubu, H. (1992). Investigation of ITO-GaAs structures. *Bull. of ASM, Phys.& Tech.*, No.3, pp.26-29

Simashkevich, A.; Do Quoc Hung; Bobeico, E.; Gorcheac, L. & Sherban, D. (1999). Solar cells based on SIS structures, *Proc. of the 3rd Int. Workshop on Material Science*, Part.1, pp.56-59, ISBN 90-5776-033-9, Hanoi, Vietnam, (November 1999)

Simashkevich, A.; Sherban, D.; Bruc, L.; Coval, A.; Fedorov, V.; Bobeico, E. & Usatii., Iu. (2004). I. Spray-deposited ITO/nSi solar cells with enlarged area. *Moldavian Journal of Physical Sciences*, Vol.3, No.3-4, (December 2004), pp.334-339, ISSN 1810-648X

Simashkevich, A.; Serban, D.; Bruc, L.; Coval, A.; Fedorov, V.; Bobeico, E. & Usatii. Iu. (2005). Spray deposited ITO/nSi solar cells with enlarged area, *Proc. of the 20th European Photovoltaic Solar Energy Conference*, pp.980-982, ISBN 3-936338-19-1, Barcelona, Spain, (June 2005)

Simashkevich, A.; Sherban, D.; Morvillo, P.; Bobeico, E.; Bruk, L. & Usatii, Iu. (2007). Bifacial solar cells based on isotype junctions, *Proc. of the 22th European PV Solar Energy Conf.*, ISBN: 3-936338-22-1, Milan, Italy, (September 2007), pp.484-486

Simashkevich, A.; Sherban, D.; Rusu, M.; Bruk, L. & Usatii. Iu. (2009). ITO/nSi solar cells: voltage dependent charge transport mechanisms, *Proc. of the 24th European Photovoltaic Solar Energy Conference,* pp.2230-2232, ISBN: 3-936338-24-1, Hamburg, Germany, (September 2009)

Simashkevich, A.; Serban, D.; Bruc, L.; Fyodorov, V.; Coval, A. & Usatii. Iu. (2010). Features of the mechanism of a current flowing through an ITO/nSi isotype structure. *Surface engineering and applied electrochemistry*, Vol.46, No.1, (February 2010), pp.40-42, ISSN 1068-3755

Simashkevich, A.V.; Sherban, D.A.; Bruk, L.I.; Usatii, Iu.V. & Fedorov V.M. (2010). Transparent Conductive Oxide Layers and Their Application in Solar Energetic. *Physics and Chemistry of Solid State*, Vol.11, No.4, (October 2010), pp. 950-956

Simashkevich, A.V.; Sherban, D.A.; Bruk, L.I., Harea, E.E. & Usatii, Iu. (2011). Efficient ITO/nSi solar cells with silicon textured surface. *Elektronnaya Obrabotka Materialov*, Vol.47, No.3, ( May-June 2011), pp.79-84, ISSN 0013-5739

Tarr, N. & Pulfrey, D. (1979). New experimental evidence for minority-carrier. *Appl. Phys. Lett.*, V.34, No.4, (February 1979), pp.295-297, ISSN 0003-6951

Untila, G.G.; Chebotareva, A.V.; Osipov, A.S. & Samborsky, D.V. (1998). Series resistance of solar cell with antireflection coating of transparent conducting oxide, *Proc of the 2nd World Conf. on PV Solar Energy Conversion*, Vol.1, pp.300-302, ISBN 92-828-5179-6, Vienna, (July 1998)

Usatii, Iu. (2011). Preparation of ITO-Si solar cells with enlarged area and the study of their properties. (in Romanian). *Ph.D. Thesis*, Chisinau, (February 2011)

Vasu, V. & Aubrahmanyam. A. (1992) Photovoltaic properties of indium tin oxide (ITO)/silicon junctions prepared by spray pyrolysis - dependence on oxidation time. *Semicond. Sci. and Tech.*, Vol.7, No.3, (March 1992), pp.320-323, ISSN 0268-1242

Vasu, V.; Subrahmanyam, A.; Kumar, J. & Ramasamy, P. (1993). Spray-pyrolytic-grown ITO/InP junctions: effect of tin doping. *Semicond. Sci. Technol.*, Vol.8, No.3 (March 1993) pp.437-440, ISSN 0268-1242

Wishwakarma, S., Rahmatullah R. & Prasad, H.C. (1993). Low cost $SnO_2$:P/$SiO_2$/n-Si (textured) heterojunction solar cells. *J.Phys.D:Appl.Phys.*, v.26, No.6, (June 1993), pp.959-962, ISSN 0022-3727

Yamamoto, A.; Yamaguchi, M. & Uemura. C. (1984). High conversion efficiency and high radiation resistance InP homojunction solar cells. *Appl. Phys. Lett.*, Vol.44, No.6, (March 1984), pp.611-614, ISSN 0003-6951

# Maturity of Photovoltaic Solar-Energy Conversion

Michael Y. Levy
*Hartsdale, New York*
*U.S.A.*

## 1. Introduction

In this chapter, the author explains the present technological and scientific maturity of the field of solar-energy conversion. The author builds on scientific foundations to generalize several upper limits of solar-energy conversion as a function of the geometric-concentration factor. These limits are used to define a high-efficiency regime for the terrestrial conversion of solar-energy. The current world-record efficiency is measured in solar cells composed of three junctions operating in tandem under a geometric-concentration factor of 454 Suns. By illustrating that the current world-record efficiency is clearly within the high-efficiency regime, the author argues that the field of photovoltaic solar-energy conversion is far removed from its infancy. Inasmuch that the world-record efficiency is less than half of the theoretical terrestrial limit, the author argues that there is significant space for scientific innovation. In addition, by noting that the world-record efficiency, which is measured with a tandem solar cell with three junctions operating at 454 Suns, is 9% less than the physical limit of a tandem solar cells with two junctions operating under the same number of Suns, the author makes apparent the potential for improvement to the present technological paradigm. The author concludes that solar-energy science and technology has significantly more challenges to address and innovations to realize before it may be considered a fully mature field.

The remainder of this chapter is organized as follows. In Section 2, the author describes an ideal *p-n* junction solar cell and distinguishes the solar cell's absorber, its function, and its relation to the other essential components of the solar cell. In Section 3, the author reviews three important approaches that establish upper-limiting efficiencies of solar-energy conversion: the radiation-in-radiation-out approach of Landsberg and Tonge, the omni-colour approach of DeVos, Grosjean, and Pauwels, and the detailed-balance approach of Shockley and Queisser. The detailed-balance approach establishes the maximum-power conversion-efficiency of a single *p-n* junction solar cell in the terrestrial environment as 40.7%. Yet, the omni-colour approach establishes the maximum-power conversion-efficiency of solar energy in the terrestrial environment as 86.8%. In Section 4, the author reviews four approaches for realizing a global efficiency enhancement with respect to the maximum-power conversion-efficiency of a single *p-n* junction solar cell. The current technological paradigm experimentally demonstrates high-efficiencies by using stacks of *p-n* junction solar cells operating in tandem. Other next-generation approaches propose the incorporation of one or more physical phenomena (*e.g.*, multiple transitions, multiple electron-hole pair generation, and hot carriers) to reach high-efficiencies. In Section 5, the author offers concluding remarks.

## 2. Ideal *p-n* junction solar cell

In Figure 1, the present author illustrates the ideal electronic structure of a photovoltaic solar cell (Würfel, 2002; Würfel, 2004), a device that converts the energy of radiation into electrical energy. The ideal structure of the solar cell is comprised of several components: an absorber, two emitters and two contacts. The absorber enables photo-chemical conversion, the emitters enable electro-chemical conversion, and the contacts enable useful work to be performed by an external load. In the following paragraphs, the present author describes an ideal solar cell in more detail.
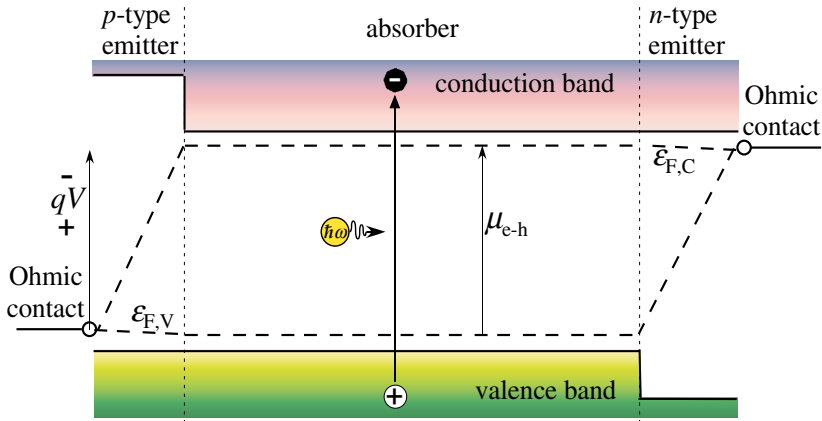


Fig. 1. Ideal structure of a solar cell. Shown is the absorber, which is sandwiched between an *n*-type emitter and a *p*-type emitter. An Ohmic contact is made to each of the emitters. A voltage, *V*, exists between the contacts of the solar cell.

An absorber is in the center of the solar cell. The absorber is a medium whose electronic states form a conduction band and a valence band. The conduction and valence bands are separated by an energetic gap that is characterized by the absence of electronic states. The occupancy of the electronic states of the conduction band and valence band are described by the quasi-Fermi energies $\varepsilon_{F,C}$ and $\varepsilon_{F,V}$, respectively. The absorber is the region of the solar cell where the absorption of photons occurs and where the subsequent photogeneration of electrons and holes takes place. Ideally, each photon with energy greater than that of the energetic gap may generate a single electron-hole pair. In such case, the energy of each photon with energy greater than the bandgap is converted to the chemical energy of an electron-hole pair, $\mu_{e-h}$, where $\mu_{e-h} = \varepsilon_{F,C} - \varepsilon_{F,V}$ (Würfel, 2002; Würfel, 2004).

The absorber is sandwiched between two semi-permeable emitters (Würfel, 2002; Würfel, 2004). The emitters are selected to produce an asymmetry in the band structure. The electronegativity and bandgap of the emitter on the right (*i.e.,* the *n*-type emitter) are selected so that the (*i*) electrons largely or completely permeate through and (*ii*) holes largely or completely do not (Würfel, 2002; Würfel, 2004). A small gradient drives the majority carriers (*i.e.,* holes) to the right so that a beneficial current is produced. A large gradient drives minority carriers (*i.e.,* electrons) to the right so that a detrimental current is produced. The latter current is very small, resulting from the relative impermeability of the rightmost emitter to electrons. The emitter on the left is similarly selected, except that it is the holes that permeate through and yield a beneficial current.

On the external surface of both emitters is a metallic contact. The carriers in the contacts are in equilibrium with one another, so where the contact interfaces with the emitter the occupancy of holes and electrons are described by the same Fermi energy. The absolute value of the Fermi energy at the contact of the $n$-type emitter is roughly equal to the absolute value of the quasi-Fermi energy of majority carriers at the interface between the absorber interfaces with the $n$-type emitter. An analog of this statement holds for the contact to the $p$-type emitter. Thus, between the two contacts there is a voltage, $V$, that is proportional to the potential difference $\varepsilon_{F,C} - \varepsilon_{F,V}$ as $V = (\varepsilon_{F,C} - \varepsilon_{F,V})/q$, where $q$ is the elementary charge. Therefore, the chemical energy of each electron-hole pair, $\mu_{e-h}$, is converted to electrical energy by a unit pulse of charge current, $q$, at the voltage $V$. In the following subsection, the present author reviews various limits describing the efficiency of solar-energy conversion.

## 3. Limits to ideal solar-energy conversion

In this section, the present author reviews three distinct approaches to upper-bound the efficiency of solar-energy conversion. In Section 3.1, the present author offers a schematic of a generalized converter and uses the schematic to define the conversion efficiency. In sections 3.2, 3.3, and 3.4, the present author reviews the Landsberg-Tonge limit, the Shockley-Queisser limit, and the omni-colour limit, respectively. In Section 3.5, the present author compares and contrasts these three approaches. Finally, in Section 3.6, the present author draws conclusions regarding the upper-theoretical efficiency of converting solar energy to electricity in the terrestrial environment. The present author concludes that though the efficiency limit of a single $p$-$n$ junction solar cell is large, a significant efficiency enhancement is possible. This is because, in the first approximation, the terrestrial limits of a single $p$-$n$ junction solar cell are 40.7% and 24.0%, whereas those of an omni-colour converter are 86.8% and 52.9% for fully-concentrated and non-concentrated sunlight, respectively.

### 3.1 Generalized energy converter

Figure 2 is a schematic of a generalized energy converter (*c.f.* the converter in Landsberg & Tonge (1980)). The converter is pumped with a power flow, $\dot{E}_p$, and a rate of entropy flow, $\dot{S}_p$. Analogously, the converter, which maintains a temperature $T_c$, sinks a power flow, $\dot{E}_s$, and a rate of entropy flow, $\dot{S}_s$. Meanwhile, a rate of useable work, $\dot{W}$, is delivered and a rate of heat flow, $\dot{Q}$, is transmitted to the ambient. Internally, the converter experiences a rate change of energy, $\dot{E}$, and a rate change of entropy, $\dot{S}$. In addition, the converter, by its own internal processes, generates a rate of entropy, $\dot{S}_g$.

The first-law conversion efficiency, $\eta$, is defined as the ratio of the useable power over the energy flow pumped into the converter, so that (Landsberg & Tonge, 1980)

$$\eta \doteq \frac{\dot{W}}{\dot{E}_p}. \tag{1}$$

Typically, in the science of solar-energy conversion, no more than two radiation flows pump the converter (see Figure 3). Always present is a direct source of radiation from the sun, which is assumed a black body with a surface temperature $T_S$, yielding an energy flux, $\dot{U}_{p,S}$. Sometimes present, depending on the geometric-concentration factor, $C$, is a diffuse source of radiation scattered from the Earth's atmosphere, which is assumed to be a black body with a surface temperature $T_E$, yielding an energy flux, $\dot{U}_{p,E}$. Considering the dilution factor of solar radiation, $D \left[2.16 \times 10^{-5}\right]$, which is linearly related to the solid angle subtended by the sun on
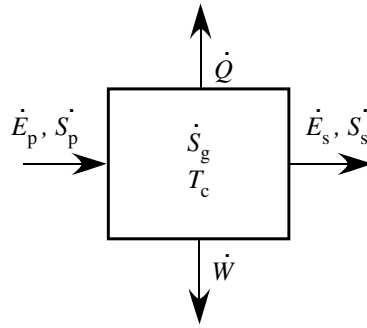
Fig. 2. Generalized schematic diagram of an energy converter. In the radiative limit, the energy flows pumped to and sunk by the converter (*i.e.* $\dot{E}_p$ and $\dot{E}_s$) are limited to the radiant energy flux [J m$^{-2}$ s$^{-1}$] pumped to and sunk by the converter: $\dot{E}_p$ and $\dot{E}_s$, respectively.

the earth (Shockley & Queisser, 1961), and a geometric-concentration factor of solar energy, $C$, which may range between unity and $1/D$ (De Vos, 1992), the total energy flux impinging upon the converter, $\dot{E}_p$, is written with the Stefan-Boltzmann constant, $\sigma$ $\left[5.67 \times 10^{-8} \text{ W/m}^2/\text{K}^4\right]$, as

$$\dot{E}_p = \sigma \left[ C D T_S^4 + (1 - C D) T_E^4 \right]. \tag{2}$$

Meanwhile, the quantification of the power density generated by the converter depends on the specific details of the converter. As this section only discusses a generalized converter, no further mathematical form of the power density is specified.

Calculating the performance measure by substituting the right-hand side of Equation (1) into the denominator of Equation (2) is different from the manner of calculating the performance measure as done in the detailed-balance work of many references (Bremner et al., n.d.; Brown & Green, 2002a;b; De Vos, 1980; 1992; De Vos & Desoete, 1998; Levy & Honsberg, 2006; Luque & Martí, 2001; Martí & Araújo, 1996; Shockley & Queisser, 1961; Werner, Brendel & Oueisser, 1994). In the latter references, though the particle flux impinging upon the solar cell is given in terms of the dual source, the performance measure is calculated with respect to the energy flux from the sun, $\dot{U}_{p,S}$. This distorts the performance measure of the device, resulting in efficiencies $\left[ 1 + \frac{1 - C D}{C D} \left( \frac{T_E}{T_S} \right)^4 \right]$ times those obtained using the first-law efficiency (Levy & Honsberg, 2008a). . In the following subsection, the present author reviews an approach to upper bound the efficiency limit of converting solar energy to useful work.

### 3.2 Landsberg-Tonge limit

Landsberg and Tonge present thermodynamic efficiencies for the conversion of solar radiation into work (Landsberg & Tonge, 1980). The converter is pumped with all the radiation emitted from a black body, which maintains a surface temperature $T_p$. The converter is also given as a black body, however its temperature is maintained at $T_c$. The converter, therefore, sinks black-body radiation associated with this temperature. With the use of two balance equations, for energy and for entropy, Landsberg and Tonge derive the following inequality for the
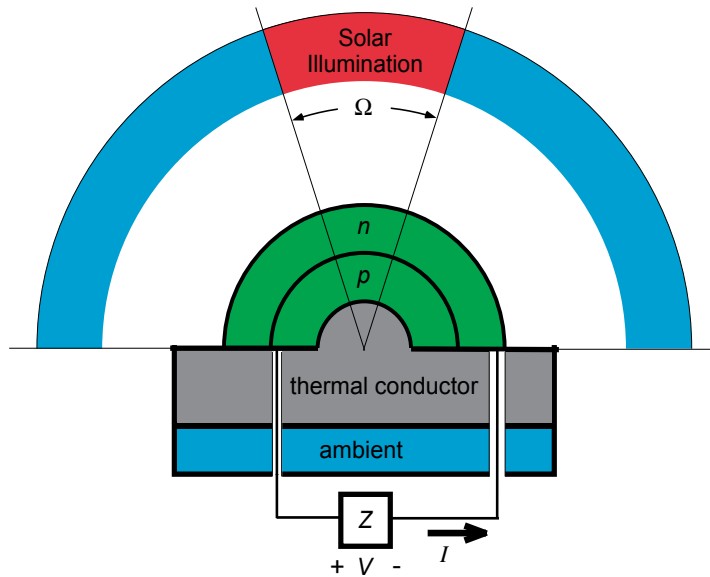
Fig. 3. Cross section of an abstracted *p-n* junction solar cell with spherical symmetry. The exaggerated physical symmetry reinforces the solar geometry, where a solid angle of the solar cell's surface, $\Omega$, is subtended by direct insolation from the sun and the remainder of the hemisphere is subtended by diffuse radiation from the atmosphere. The solid angle may be adjusted by geometrical concentration of the sun's light. The solar cell is maintained at the ambient temperature, the surface terrestrial temperature, by a thermal conductor.

first-law efficiency:

$$\eta \leq 1 - \frac{4}{3}\frac{T_c}{T_P} + \frac{1}{3}\left(\frac{T_c}{T_P}\right)^4. \tag{3}$$

In arriving at the above inequality, Landsberg and Tonge assume steady-state conditions. Equality holds for the special case where there is no internal entropy generation (*i.e.* $\dot{S}_g = 0$). The resulting equality is first derived by Patela by considering the exergy of heat radiation (Petela, 1964). The Landsberg-Tonge limit may be extended so as to model the dual sources of the solar geometry (Würfel, 2002). In the case of two black-body sources simultaneously pumping the converter, a derivation similar to that of Landsberg and Tonge yields a first-law efficiency given as

$$\eta \leq \frac{(CD)\left(T_S^4 - \frac{4}{3}T_c T_S^3 + \frac{1}{3}T_c^4\right) + (1-CD)\left(T_E^4 - \frac{4}{3}T_c T_E^3 + \frac{1}{3}T_c^4\right)}{(CD)\, T_S^4 + (1-CD)\, T_E^4}. \tag{4}$$

Figure 4 illustrates the Landsberg-Tonge efficiency limit. In Section 3.3, the detailed-balance method of Shockley and Queisser is presented and applied to a single *p-n* junction solar cell.

### 3.3 Shockley-Queisser limit
Shockley and Queisser present a framework to analyze the efficiency limit of solar-energy conversion by a single *p-n* junction (Shockley & Queisser, 1961). They name this limit the detailed-balance limit for it is derived from the notion that, in principle, all recombination
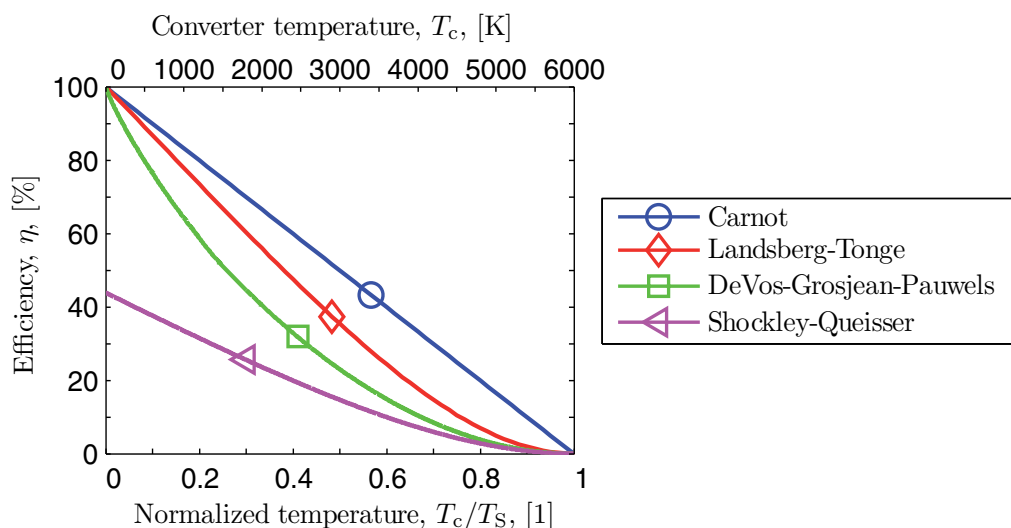
Fig. 4. Efficiency limits of ideal solar-energy converters as a function of the ratio of the converter's temperature, $T_c$, to the pump's temperature, $T_S$. Shown are the Landsberg-Tonge closed-form efficiencies of the radiation-in-radiation-out converter, the DeVos-Grosjean-Pauwels analytic efficiencies of the omni-colour converter, and the Shockley-Queisser numerical efficiencies of the *p-n* junction converter. All efficiencies are for fully-concentrated solar irradiance. As a visual aid, the Carnot efficiencies are presented.

processes may be limited to photo-induced processes and balanced by photo-induced generation processes. Their *ab initio* limit – as opposed to a semi-empirical limit based on factors such as measured carrier lifetimes – represents an upper-theoretical limit above which a single *p-n* junction solar cell may not perform. In addition, it is a reference for experimental measurements of single-junction solar cells in terms of future potential.

In their framework, Shockley and Queisser identify several factors that may degrade the efficiency of energy conversion and ideally allow that the degrading factors are perfectly mitigated. Therefore, in the detailed balance limit it is permissible that:

- the fractions of recombination and generation events that are coupled to radiative processes are both unity,

- the probability that incident photons with energy greater than or equal to the semiconductors band-gap are transmitted into the solar cell is unity,

- the probability with which a transmitted photon creates an electron-hole pair is unity,

- the probability that an electron-hole pair yields a charge current pulse through an external load is unity, and,

- the fraction of solid angle subtended by the sun may be unity- *i.e.*, the sun's radiation is completely concentrated onto the solar cell (see Figure 3 on page 5).

Figure 4 illustrates the upper-efficiency limit of solar-energy conversion by a single *p-n* solar cell. The Shockley-Queisser model predicts that the the upper limiting efficiency of a *p-n* junction solar cell is 44%. This efficiency limit is valid only when the solar cell's temperature is held to absolute zero. In Section 3.4, the omni-colour limit is presented.

### 3.4 Omni-colour limit

In principle, the detailed-balance method may be applied to omni-colour converters (De Vos, 1980; 1992; De Vos et al., 1982). The omni-colour limit may be derived in terms of either photovoltaic processes (Araújo & Martí, 1994; De Vos, 1980; 1992; De Vos et al., 1982; Würfel, 2004), photothermal processes (De Vos, 1992), or hybrids thereof (De Vos, 1992; Luque & Martí, 1999). In either case, as the number of layers in a stack of photovoltaic converters (Alvi et al., 1976; De Vos, 1992; Jackson, 1955; Loferski, 1976; Wolf, 1960) or in a stack of photothermal converters (De Vos, 1992; De Vos & Vyncke, 1984) approach infinity, the solar-energy conversion efficiencies approach the same limit (De Vos, 1980; 1992; De Vos & Vyncke, 1984) – the omni-colour limit. Figure 4 illustrates the upper-efficiency limit of omni-colour solar-energy conversion. In Section 3.5, the present author compares and contrasts the efficiency limits that are heretofore reviewed.

### 3.5 Comparative analysis

In Section 3.2 through Section 3.4, the present author reviews several approaches that quantify the efficiency limits of solar-energy conversion. The aforementioned limits are now compared and contrasted.

All of the limits reviewed in this Section 3 have in common an efficiency limit of zero when the converter's temperature is that of the pump. In addition, several of the limits approach the Carnot limit for the special case where the converter's temperature is absolute zero. These include the Landsberg-Tonge limit and the De Vos-Grosjean-Pauwels limit. At absolute zero the Shockley-Queisser limit is substantially lower (44%) than the Carnot limit. It is interesting to note that the Landsberg-Tonge limit (see Equation 4 on page 5) and the omni-colour limit (De Vos, 1980) both approach unity for regardless of the geometric-concentration factor of solar irradiance.

The large differences between the Shockley-Queisser limit and the other limits are attributed to the relationship between the energetic gap of the semiconductor comprising the *p-n* junction and the range of photon energies comprising the broadband spectrum of black-body radiation. Sub-bandgap photons do not yield a photovoltaic effect and so do not participate in generating charge current. Meanwhile, the conversion of each supra-bandgap photon uniformly generates a single electron-hole pair at a voltage limited by the bandgap. Therefore, the portion of each supra-bandgap photon's energy in excess of the bandgap does not contribute to useful work. By using an omni-colour converter, the efficiency degradation caused by the relationship between the energetic gap of the semiconductors comprising the tandem stack and the broadband nature of the solar spectrum are eliminated. Therefore, the difference between the De Vos-Grosjean-Pauwels limit and the Landsberg-Tonge limit is attributed to the generation of internal irreversible entropy. Except for the two temperature extremes aforementioned, each layer of the omni-colour converter generates a rate of irreversible entropy resulting from its internal processes. This is so even though each layer of the omni-colour converter operates at its maximum-power point and converts monochromatic light (Würfel, 2004).

As illustrated by the present author in Figure 4, the efficiency limits reviewed heretofore may be given in descending order as Carnot, Landsberg-Tonge, De Vos-Grosjean-Pauwels, and Shockley-Queisser. Photovoltaic converters may not exceed the De Vos-Grosjean-Pauwels limit for their internal processes are associated with a rate of irreversible internal entropy generation (Markvart, 2007; Würfel, 1982). In Section 3.6, the present author concludes these findings by describing limits to the conversion of solar energy in the terrestrial environment.

### 3.6 Terrestrial conversion limits

Table 1 lists the upper-efficiency limits of the terrestrial conversion of solar energy.  As is convention in the science of solar-energy conversion, all efficiencies are calculated for a surface solar temperature of 6000 K, a surface terrestrial temperature of 300 K, and a converter maintained at the surface terrestrial temperature. In addition, the geometric dilution factor is taken as $2.16 \times 10^{-5}$ (De Vos, 1992). For each type of converter listed, the upper- efficiency limit is given for fully-concentrated sunlight and, in some cases, for non-concentrated sunlight. The values listed depend only on the sun's surface temperature, the earth's surface temperature, and the geometric-concentration factor, as opposed to consideration regarding the air mass of the Earth and other secondary phenomena.  The present author concludes that though the upper-efficiency limit of a single *p-n* junction solar cell is large, a significant efficiency enhancement is possible. This is true because the terrestrial limits of a single *p-n* junction solar cell is 40.7% and 24.0%, whereas the terrestrial limits of an omni-colour converter is 86.8% and 52.9% for fully-concentrated and non-concentrated sunlight, respectively.  In Section 4, the present author defines the notion of high-efficiency approaches to solar-energy conversion and briefly reviews various proposed high-efficiency approaches.

## 4. High-efficiency approaches

In this section, Section 4, the present author reviews several distinct approaches for high-efficiency solar cells.  In Section 4.1, the present author defines "high-efficiency" in terms of the upper-conversion efficiencies of the Shockley-Queisser model and the De Vos-Grosjean-Pauwels model.  In Section 4.2, the present author reviews the current technological paradigm to realize high-efficiency solar cells: stacks of single *p-n* junction solar cells operating in tandem. In sections 4.3,  4.4, and  4.5, the present author reviews three next-generation approaches to realize high-efficiency solar cells: the carrier-multiplication solar cell, the hot-carrier solar cell, and the multiple-transition solar cell, respectively. Finally, in Section 4.6, the present author draws conclusions regarding the justification for researching and developing next-generation approaches. Though stacks of single *p-n* junction solar cells operating in tandem are the only high-efficiency approach with demonstrated high-efficiency performance, the present author concludes that development on a next-generation solar cell is justified in that a (*i*) next-generation solar cells offer a global-efficiency enhancement in themselves and (*i*) also per layer if incorporated in a stack of solar cells operating in tandem. Immediately below in Section 4.1, the present author defines what is meant by high-efficiency performance.

### 4.1 Global efficiency enhancement

There are several proposals for high-efficiency solar cells. In this chapter, similar to Anderson in his discussion of the efficiency enhancements in quantum-well solar cells (Anderson, 2002), the present author defines high-efficiency in terms of a global efficiency enhancement. Shown in Figure 5 are the upper-efficiency conversion limits of the single-junction solar cell and the omni-colour solar cell. In Figure 5, the upper-efficiency conversion limits are given as a function of the geometric-concentration factor, *C*. The present author defines "high efficiency" in terms of the numerical data given in Figure 5.  The present author asserts that, for any and all geometric concentration factor, a proposal for high-efficiency solar cell must, when optimized, offer an efficiency greater than that of an optimized Shockley-Queisser solar cell at that same geometric-concentration factor. For example, according to the present author's definition, under non-concentrated sunlight a high-efficiency proposal, when optimized,

| Converter | $\eta|_{\text{Ter}}$, [%] | |
|---|---|---|
| | $C = 1/D$ | $C = 1$ [†] |
| Carnot | 95.0 | 95.0 |
| Landsberg-Tonge | 93.3 [a] | 72.4 [b] |
| De Vos-Grosjean-Pauwels | 86.8 [c] | 52.9 [d] |
| Shockley-Queisser | 40.7 [e] | 24.0 [f] |

[†] Listed values are first-law efficiencies that are calculated by including the energy flow absorbed due to direct solar radiation and the energy flow due to diffuse atmospheric radiation. The listed values are likely to be less than what are previously recorded in the literature. See Section 3.1 on page 3 for a more comprehensive discussion.

[a] Calculated from Equation (3) on page 5.

[b] Calculated from Equation (4) on page 5.

[c] Obtained from reference (De Vos, 1980) and reference (Würfel, 2004).

[d] Adjusted from the value 68.2% recorded in reference (De Vos, 1980) and independently calculated by the present author.

[e] Obtained from reference (Bremner et al., n.d.).

[f] Adjusted from the value 31.0% recorded in reference (Martí & Araújo, 1996).

Table 1. Upper-efficiency limits of the terrestrial conversion of solar energy, $\eta|_{\text{Ter}}$. All efficiencies calculated for a surface solar temperature of 6000 K, a surface terrestrial temperature of 300 K, a solar cell maintained at the surface terrestrial temperature, a geometric dilution factor, $D$, of $2.16 \times 10^{-5}$, and a geometric-concentration factor, $C$, that is either 1 (non-concentrated sunlight) or $1/D$ (fully-concentrated sunlight).

must have an upper-efficiency limit greater than 24.0.%. Clearly, for physical consistency, the optimized theoretical performance of the high-efficiency proposal must be less than that of the omni-colour solar cell at that geometric concentration factor. Furthermore, the present author asserts that any fabricated solar cell that claims to be a high-efficiency solar cell must demonstrate a global efficiency enhancement with respect to an optimized Shockley-Queisser solar cell. For example, to substantiate a claim of high-efficiency, a solar cell maintained at the terrestrial surface temperature and under a geometric concentration of 240 suns must demonstrate an efficiency greater than 35.7% – the efficiency of an optimized Shockley-Queisser solar cell operating under those conditions. Before moving on to Section 4.2, where the present author reviews the tandem solar cell, the reader is encouraged to view the high-efficiency regime as illustrated in Figure 5. The reader will note that there is a significant efficiency enhancement that is scientifically plausible.
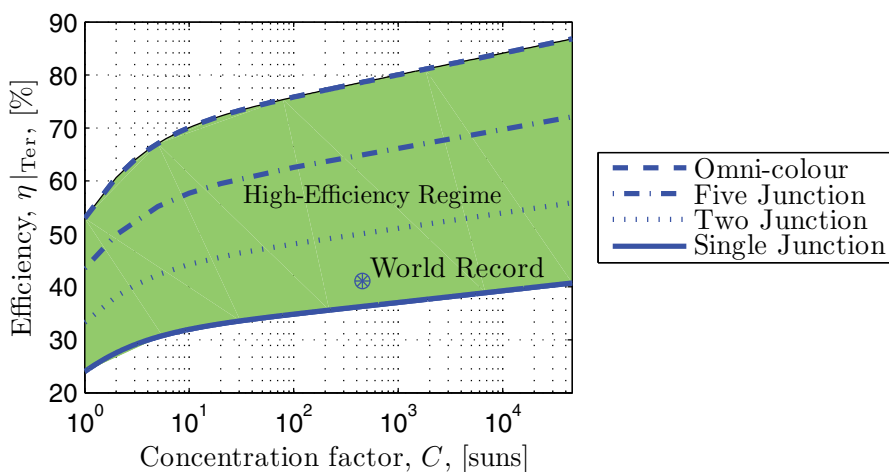
Fig. 5. The region of high-efficiency solar-energy conversion as a function of the geometric-concentration factor. The high-efficiency region (shaded) is defined as that region offering a global-efficiency enhancement with respect to the maximum single-junction efficiencies (lower edge) and the maximum omni-colour efficiencies (upper edge). The efficiency required to demonstrate a global efficiency enhancement varies as a function of the geometric-concentration factor. For illustrative purposes, the terrestrial efficiencies (see Table 2) of a two-stack tandem solar cell and a five-stack tandem solar cell are given . Finally, for illustrative purposes, the present world-record solar cell efficiency is given (*i.e.*, 41.1% under a concentration of 454 suns (Guter et al., 2009)).

### 4.2 Tandem solar cell

The utilization of a stack of *p-n* junction solar cells operating in tandem is proposed to exceed the performance of one *p-n* junction solar cell operating alone (Jackson, 1955). The upper-efficiency limits for *N*-stack tandems ($1 \leq N \leq 8$) are recorded in Table 2 on page 11 . As the number of solar cells operating in a tandem stack increases to infinity, the upper-limiting efficiency of the stack increases to the upper-limiting efficiency of the omni-colour solar cell (De Vos, 1980; 1992; De Vos & Vyncke, 1984). This is explained in Section 3.4 on page 7. In practice, solar cells may be integrated into a tandem stack via a vertical architecture or a lateral architecture. An example of a vertical architecture is a monolithic solar cell. Until now, the largest demonstrated efficiency of a monolithic solar cell – or for any solar cell – is the metamorphic solar-cell fabricated by Fraunhofer Institute for Solar Energy Systems (Guter et al., 2009). This tandem is a three-junction metamorphic solar cell and operates with a conversion efficiency of 41.1% under a concentration of 454 suns (Guter et al., 2009). An example of horizontal architectures are the solar cells of references (Barnett et al., 2006; Green & Ho-Baillie, 2010), which utilize spectral-beam splitters (Imenes & Mills, 2004) that direct the light onto their constituent solar cells. The present author now reviews the carrier-multiplication solar cell, the first of three next-generation proposals to be reviewed in this chapter.

### 4.3 Carrier-multiplication solar cell

Carrier-multiplication solar cells are theorized to exceed the Shockley-Queisser limit (De Vos & Desoete, 1998; Landsberg et al., 1993; Werner, Brendel & Queisser,

| Converter | $\eta|_{\mathrm{Ter}}$, [%] | |
|---|---|---|
| | $C = 1/D$ | $C = 1$ [†] |
| Infinite-Stack Tandem [*] | 86.8 [a] | 52.9 [b] |
| Eight-Stack Photovoltaic Tandem | 77.63 [c] | 46.12 [e] |
| Seven-Stack Photovoltaic Tandem | 76.22 [c] | 46.12 [e] |
| Six-Stack Photovoltaic Tandem | 74.40 [c] | 44.96 [e] |
| Five-Stack Photovoltaic Tandem | 72.00 [c] | 43.43 [e] |
| Four-Stack Photovoltaic Tandem | 68.66 [c] | 41.31 [e] |
| Three-Stack Photovoltaic Tandem | 63.747 [c] | 38.21 [e] |
| Two-Stack Photovoltaic Tandem | 55.80 [c] | 33.24 [e] |
| One-Stack Photovoltaic Solar Cell [**] | 40.74 [c] | 24.01 [e] |

[†] Listed values are first-law efficiencies that are calculated by including the energy flow absorbed due to direct solar radiation and the energy flow due to diffuse atmospheric radiation. The listed values are likely to be less than what are previously recorded in the literature. See Section 3.1 on page 3 for a more comprehensive discussion.

[*] Recorded values are identical to those of the omni-colour converter of Table 1 on page 9.

[**] Recorded values are identical to those of the Shockley-Queisser converter of Table 1 on page 9.

[a] Obtained from reference (De Vos, 1980) and independently calculated by the present author.

[b] Adjusted from the value 68.2% recorded in reference (De Vos, 1980) and independently calculated by the present author.

[c] Obtained from reference (Bremner et al., n.d.) and independently calculated by the present author.

[d] Adjusted from the values recorded in reference (Martí & Araújo, 1996) and independently calculated by the present author.

[e] Calculated independently by the present author. Values are not previously published in the literature.

Table 2. Upper-efficiency limits, $\eta|_{\mathrm{Ter}}$, of the terrestrial conversion of stacks of single-transition single *p-n* junction solar cells operating in tandem. All efficiencies calculated for a surface solar temperature of 6000 K, a surface terrestrial temperature of 300 K, a solar cell maintained at the surface terrestrial temperature, a geometric dilution factor, $D$, of $2.16 \times 10^{-5}$, and a geometric-concentration factor, $C$, that is either 1 (non-concentrated sunlight) or $1/D$ (fully-concentrated sunlight).

1994; Werner, Kolodinski & Queisser, 1994), thus they may be correctly viewed as a high-efficiency approach. These solar cells produce an efficiency enhancement by generating more than one electron-hole pair per absorbed photon via

inverse-Auger processes (Werner, Kolodinski & Queisser, 1994) or via impact-ionization processes (Kolodinski et al., 1993; Landsberg et al., 1993). The efficiency enhancement is calculated by several authors (Landsberg et al., 1993; Werner, Brendel & Oueisser, 1994; Werner, Kolodinski & Queisser, 1994). Depending on the assumptions, the upper limit to terrestrial conversion of solar energy using the carrier-multiple solar cell is 85.4% (Werner, Brendel & Oueisser, 1994) or 85.9% (De Vos & Desoete, 1998). Though the carrier-multiple solar cell is close to the upper-efficiency limit of the De Vos-Grosjean-Pauwels solar cell, the latter is larger than the former because the former is a two-terminal device. The present author now reviews the hot-carrier solar cell, the second of three next-generation proposals to be reviewed in this chapter.

## 4.4 Hot-carrier solar cell

Hot-carrier solar cells are theorized to exceed the Shockley-Queisser limit (Markvart, 2007; Ross, 1982; Würfel et al., 2005), thus they may be correctly viewed as a high-efficiency approach. These solar cells generate one electron-hole pair per photon absorbed. In describing this solar cell, it is assumed that carriers in the conduction band may interact with themselves and thus equilibrate to the same chemical potential and same temperature (Markvart, 2007; Ross, 1982; Würfel et al., 2005). The same may be said about the carriers in the valence band (Markvart, 2007; Ross, 1982; Würfel et al., 2005). However, the carriers do not interact with phonons and thus are thermally insulated from the absorber. Resulting from a mono-energetic contact to the conduction band and a mono-energetic contact to the valence band, it may be shown that (*i*), the output voltage may be greater than the conduction-to-valence bandgap and that (*ii*) the temperature of the carriers in the absorber may be elevated with respect to the absorber. The efficiency enhancement is calculated by several authors (Markvart, 2007; Ross, 1982; Würfel et al., 2005). Depending on the assumptions, the upper-conversion efficiency of any hot-carrier solar cell is asserted to be 85% (Würfel, 2004) or 86% (Würfel et al., 2005). The present author now reviews the multiple-transition solar cell, the third of three next-generation proposals to be reviewed in this chapter.

## 4.5 Multiple-transition solar cell

The multi-transition solar cell is an approach that may offer an improvement to solar-energy conversion as compared to a single *p-n* junction, single-transition solar cell (Wolf, 1960). The multi-transition solar cell utilizes energy levels that are situated at energies below the conduction band edge and above the valence band edge. The energy levels allow the absorption of a photon with energy less than that of the conduction-to-valence band gap. Wolf uses a semi-empirical approach to quantify the solar-energy conversion efficiency of a three-transition solar cell and a four-transition solar cell (Wolf, 1960). Wolf calculates an upper-efficiency limit of 51% for the three-transition solar cell and 65% four-transition solar cell (Wolf, 1960).

Subsequently, as opposed to the semi-empirical approach of Wolf, the detailed-balance approach is applied to multi-transition solar cells (Luque & Martí, 1997). The upper-efficiency limit of the three-transition solar cell is now established at 63.2 (Brown et al., 2002; Levy & Honsberg, 2008b; Luque & Martí, 1997). In addition, the upper-conversion efficiency limits of *N*-transition solar cells are examined (Brown & Green, 2002b; 2003). Depending on the assumptions, the upper-conversion efficiency of any multi-transition solar cell is asserted to be 77.2% (Brown & Green, 2002b) or 85.0% (Brown & Green, 2003). These upper-limits

justify the claim that the multiple-transition solar cell is a high-efficiency approach. Resulting from internal current constraints and voltage constraints, the upper-efficiency limit of the multi-transition solar cell is asserted to be less than that of the De Vos-Grosjean-Pauwels converter (Brown & Green, 2002b; 2003). That said, it has been shown (Levy & Honsberg, 2009) that the absorption characteristic of multiple-transition solar cells may lead to both incomplete absorption and absorption overlap (Cuadra et al., 2004). Either of these phenomena would significantly diminish the efficiencies of these solar cells.

### 4.6 Comparative analysis

In Section 4.1, the present author defined the high-efficiency regime of a solar cell. In Sections 4.2-4.5, the present author reviewed several approaches that are proposed to exceed the Shockley-Queisser limit and reach towards De Vos-Grosjean-Pauwels limit. Of all the approaches, only a stack of *p-n* junctions operating in tandem has experimentally demonstrated an efficiency greater than the Shockley-Queisser limit. The current world-record efficiency is 41.1% for a tandem solar cell operating at 454 suns (Guter et al., 2009). The significance of this is now more deeply explored.

The fact that the experimental efficiency of solar-energy conversion by a photovoltaic solar cell has surpassed Shockley-Queisser limit is a major scientific and technological accomplishment. This accomplishment demonstrates that the field of solar energy science and technology is no longer in its infancy. However, as may be seen from Figure 5 on page 10 there is still significant space for further maturation of this field. Foremost, the present world record is less than half of the terrestrial limit (86.8%). Reaching closer to the terrestrial limit will require designing solar cells that operate under significantly larger geometric concentration factors and designing tandem solar cells with more junctions. That said, there is significant room for improvement even with respect to the present technologic paradigm used to obtain the world record. The world-record experimental conversion efficiency of 41.1% is recorded for a solar cell composed of three-junctions operating in tandem under 454 suns. Yet, this experimental efficiency is fully 9 percentage points and 16 percentage points less than the theoretical upper limit of a solar cell composed of a two-junction tandem and three-junction tandem (i.e., 50.1%), respectively, operating in tandem at 454 suns (i.e., 50.1%) and 16 percentage points less than the theoretical upper limit of a solar cell composed of three-junctions (i.e., 57.2%) operating at 454 suns. The author now offers concluding remarks.

## 5. Conclusions

The author begins this chapter by reviewing the operation of an idealized single-transition, single *p-n* junction solar cell. The present author concludes that though the upper-efficiency limit of a single *p-n* junction solar cell is large, a significant efficiency enhancement is possible. This is so because the terrestrial limits of a single *p-n* junction solar cell is 40.7% and 24.0%, whereas the terrestrial limits of an omni-colour converter is 86.8% and 52.9% for fully-concentrated and non-concentrated sunlight, respectively. There are several high-efficiency approaches proposed to bridge the gap between the single-junction limit and the omni-colour limit. Only the current technological paradigm of stacks of single *p-n* junctions operating in tandem experimentally demonstrates efficiencies with a global efficiency enhancement. The fact that any solar cells operates with an efficiency greater than the Shockley-Queisser limit is a major scientific and technological accomplishment, which demonstrates that the field of solar energy science and technology is no longer in its infancy. That being said, the differences between the present technological record (41.1%) and

sound physical models indicates significant room to continue to enhance the performance of solar-energy conversion.

## 6. Acknowledgments

## 7. References

Alvi, N. S., Backus, C. E. & Masden, G. W. (1976). The potential for increasing the efficiency of photovoltaic systems by using multiple cell concepts, *Twelfth IEEE Photovoltaic Specialists Conference 1976*, Baton Rouge, LA, USA, pp. 948–56.

Anderson, N. G. (2002). On quantum well solar cell efficiencies, *Physica E* 14(1-2): 126–31.

Araújo, G. & Martí, A. (1994). Absolute limiting efficiencies for photovoltaic energy conversion, *Solar Energy Materials and Solar Cells* 33(2): 213 – 40.

Barnett, A., Honsberg, C., Kirkpatrick, D., Kurtz, S., Moore, D., Salzman, D., Schwartz, R., Gray, J., Bowden, S., Goossen, K., Haney, M., Aiken, D., Wanlass, M. & Emery, K. (2006). 50% efficient solar cell architectures and designs, *Conference Record of the 2006 IEEE 4th World Conference on Photovoltaic Energy Conversion (IEEE Cat. No. 06CH37747)*, Waikoloa, HI, USA, pp. 2560–4.

Bremner, S. P., Levy, M. Y. & Honsberg, C. B. (2008). Analysis of tandem solar cell efficiencies under Am1.5G spectrum using a rapid flux calculation method, *Progress in Photovoltaics* .

Brown, A. S. & Green, M. A. (2002a). Detailed balance limit for the series constrained two terminal tandem solar cell, *Physica E* 14: 96–100.

Brown, A. S. & Green, M. A. (2002b). Impurity photovoltaic effect: Fundamental energy conversion efficiency limits, *Journal of Applied Physics* 92(3): 1329–36.

Brown, A. S. & Green, M. A. (2003). Intermediate band solar cell with many bands: Ideal performance, *Journal of Applied Physics* 94: 6150–8.

Brown, A. S., Green, M. A. & Corkish, R. P. (2002). Limiting efficiency for a multi-band solar cell containing three and four bands, *Physica E* 14: 121–5.

Cuadra, L., Martí, A. & Luque, A. (2004). Influence of the overlap between the absorption coefficients on the efficiency of the intermediate band solar cell, *IEEE Transactions on Electron Devices* 51(6): 1002–7.

De Vos, A. (1980). Detailed balance limit of the efficiency of tandem solar cells., *Journal of Physics D* 13(5): 839–46.

De Vos, A. (1992). *Endoreversible Thermodynamics of Solar Energy Conversion*, Oxford University Press, Oxford, pp. 4, 7, 18, 77, 94–6, 120–123, 124–125,125–129.

De Vos, A. & Desoete, B. (1998). On the ideal performance of solar cells with larger-than-unity quantum efficiency, *Solar Energy Materials and Solar Cells* 51(3-4): 413 – 24.

De Vos, A., Grosjean, C. C. & Pauwels, H. (1982). On the formula for the upper limit of photovoltaic solar energy conversion efficiency, *Journal of Physics D* 15(10): 2003–15.

De Vos, A. & Vyncke, D. (1984). Solar energy conversion: Photovoltaic versus photothermal conversion., *Fifth E. C. Photovoltaic Solar Energy Conference, Proceedings of the International Conference*, Athens, Greece, pp. 186–90.

Green, M. A. & Ho-Baillie, A. (2010). Forty three per cent composite split-spectrum concentrator solar cell efficiency, *Progress in Photovoltaics: Research and Applications* 18(1): 42–7.

Guter, W., Schöne, J., Philipps, S. P., Steiner, M., Siefer, G., Wekkeli, A., Welser, E., Oliva, E., Bett, A. W. & Dimroth, F. (2009). Current-matched triple-junction solar cell reaching 41.1% conversion efficiency under concentrated sunlight, *Applied Physics Letters* 94(22): 223504.

Imenes, A. G. & Mills, D. R. (2004). Spectral beam splitting technology for increased conversion efficiency in solar concentrating systems: a review, *Solar Energy Materials and Solar Cells* 84(1-4): 19–69.

Jackson, E. D. (1955). Areas for improvement of the semiconductor solar energy converter, *Proceedings of the Conference on the Use of Solar Energy*, Tucson, Arizona, pp. 122–6.

Kolodinski, S., Werner, J. H., Wittchen, T. & Queisser, H. J. (1993). Quantum efficiencies exceeding unity due to impact ionization in silicon solar cells, *Applied Physics Letters* 63(17): 2405–7.

Landsberg, P. T., Nussbaumer, H. & Willeke, G. (1993). Band-band impact ionization and solar cell efficiency, *Journal of Applied Physics* 74(2): 1451.

Landsberg, P. T. & Tonge, G. (1980). Thermodynamic energy conversion efficiencies, *Journal of Applied Physics* 51: R1.

Levy, M. Y. & Honsberg, C. (2006). Minimum effect of non-infinitesmal intermediate band width on the detailed balance efficiency of an intermediate band solar cell, *4th World Conference on Photovoltaic Energy Conversion*, Waikoloa, HI, USA, pp. 71–74.

Levy, M. Y. & Honsberg, C. (2008a). Intraband absorption in solar cells with an intermediate band, *Journal of Applied Physics* 104: 113103.

Levy, M. Y. & Honsberg, C. (2008b). Solar cell with an intermediate band of finite width, *Physical Review B* .

Levy, M. Y. & Honsberg, C. (2009). Absorption coefficients of an intermediate-band absorbing media, *Journal of Applied Physics* 106: 073103.

Loferski, J. J. (1976). Tandem photovoltaic solar cells and increased solar energy conversion efficiency, *Twelfth IEEE Photovoltaic Specialists Conference 1976*, Baton Rouge, LA, USA, pp. 957–61.

Luque, A. & Martí, A. (1997). Increasing the efficiency of ideal solar cells by photon induced transitions at intermediate levels, *Physical Review Letters* 78: 5014.

Luque, A. & Martí, A. (1999). Limiting efficiency of coupled thermal and photovoltaic converters, *Solar Energy Materials and Solar Cells* 58(2): 147 – 65.

Luque, A. & Martí, A. (2001). A metallic intermediate band high efficiency solar cell, *Progress in Photovoltaics* 9(2): 73–86.

Markvart, T. (2007). Thermodynamics of losses in photovoltaic conversion, *Applied Physics Letters* 91(6): 064102 –.

Martí, A. & Araújo, G. L. (1996). Limiting efficiencies for photovoltaic energy conversion in multigap system, *Solar Energy Materials and Solar Cells* 43: 203–222.

Petela, R. (1964). Exergy of heat radiation, *ASME Journal of Heat Transfer* 86: 187–92.

Ross, R. T. (1982). Efficiency of hot-carrier solar energy converters, *Journal of Applied Physics* 53(5): 3813–8.

Shockley, W. & Queisser, H. J. (1961). Efficiency of *p-n* junction solar cells, *Journal of Applied Physics* 32: 510.

Werner, J. H., Brendel, R. & Oueisser, H. J. (1994). New upper efficiency limits for semiconductor solar cells, *1994 IEEE First World Conference on Photovoltaic Energy Conversion. Conference Record of the Twenty Fourth IEEE Photovoltaic Specialists Conference-1994 (Cat.No.94CH3365-4)*, Vol. vol.2, Waikoloa, HI, USA, pp. 1742–5.

Werner, J. H., Kolodinski, S. & Queisser, H. (1994). Novel optimization principles and efficiency limits for semiconductor solar cells, *Physical Review Letters* 72(24): 3851–4.

Wolf, M. (1960). Limitations and possibilities for improvement of photovoltaic solar energy converters. Part I: Considerations for Earth's surface operation, *Proceedings of the Institute of Radio Engineers*, Vol. 48, pp. 1246–63.

Würfel, P. (1982). The chemical potential of radiation, *Journal of Physics C* 15: 3867–85.

Würfel, P. (2002). Thermodynamic limitations to solar energy conversion, *Physica E* 14(1-2): 18–26.

Würfel, P. (2004). Thermodynamics of solar energy converters, *in* A. Martí & A. Luque (eds), *Next Generations Photovoltaics*, Institute of Physics Publishing, Bristol and Philadelphia, chapter 3, p. 57.

Würfel, P., Brown, A. S., Humphrey, T. E. & Green, M. A. (2005). Particle conservation in the hot-carrier solar cell, *Progress in Photovoltaics* 13(4): 277–85.

# Application of the Genetic Algorithms for Identifying the Electrical Parameters of PV Solar Generators

Anis Sellami[1] and Mongi Bouaïcha[2]
*[1]Laboratoire C3S, Ecole Supérieure des Sciences et Techniques de Tunis,*
*[2]Laboratoire de Photovoltaïque, Centre de Recherches et des Technologies de l'Energie,*
*Technopole de Borj-Cédria,*
*Tunisia*

## 1. Introduction

The determination of model parameters plays an important role in solar cell design and fabrication, especially if these parameters are well correlated to known physical phenomena. A detailed knowledge of the cell parameters can be an important way for the control of the solar cell manufacturing process, and may be a mean of pinpointing causes of degradation of the performances of panels and photovoltaic systems being produced. For this reason, the model parameters identification provides a powerful tool in the optimization of solar cell performance.

The algorithms for determining model parameters in solar cells, are of two types: those that make use of selected parts of the characteristic (Chan et al., 1987; Charles et al., 1981; Charles et al., 1985; Dufo-Lopez and Bernal-Agustin, 2005; Enrique et al., 2007) and those that employ the whole characteristic (Haupt and Haupt, 1998; Bahgat et al., 2004; Easwarakhanthan et al., 1986). The first group of algorithms involves the solution of five equations derived from considering select points of an current-voltage (I-V) characteristic, e.g. the open-circuit and short-circuit coordinates, the maximum power points and the slopes at strategic portions of the characteristic for different level of illumination and temperature. This method is often much faster and simpler in comparison to curve fitting. However, the disadvantage of this approach is that only selected parts of the characteristic are used to determine the cell parameters. The curve fitting methods offer the advantage of taking all the experimental data in consideration. Conversely it has the disadvantage of artificial solutions. The nonlinear fitting procedure is based on the minimisation of a not convex criterion, and using traditional deterministic optimization algorithms leads to local minima solutions. To overcome this problem, the nonlinear least square minimization technique can be computed with global search approaches such Genetic Algorithms (GAs) (Haupt and Haupt, 1998; Sellami et al., 2007; Zagrouba et al., 2010) strategy, increasing the probability of obtaining the best minimum value of the cost function in very reasonable time.

In this chapter, we propose a numerical technique based on GAs to identify the electrical parameters of photovoltaic (PV) solar cells, modules and arrays. These parameters are, respectively, the photocurrent ($I_{ph}$), the saturation current ($I_s$), the series resistance ($R_s$), the

shunt resistance ($R_{sh}$) and the ideality factor (n). The manipulated data are provided from experimental I-V acquisition process. The one diode type approach is used to model the AM1.5 I-V characteristic of the solar cell. To extract electrical parameters, the approach is formulated as a non convex optimization problem. The GAs approach was used as a numerical technique in order to overcome problems involved in the local minima in the case of non convex optimization criteria.

This chapter is organized as follows: Firstly, we present the classical one-diode equivalent circuit and discuss its validity to model solar modules and arrays. Then, we expose the limitations of the classical optimization algorithms for parameters extraction. Next, we describe the detailed steps to be followed in the application of GAs for determining solar PV generators parameters. Finally, we show the procedure of extracting the coordinates (Vm,Im) of the maximum power point (MPP) from the identified parameters.

## 2. The one diode model

The I-V characteristic of a solar cell under illumination can be derived from the Schottky diffusion model in a PN junction. In Fig. 1, we give the scheme of the equivalent electrical circuit of a solar cell under illumination for both cases; the double diode model and the one diode model.
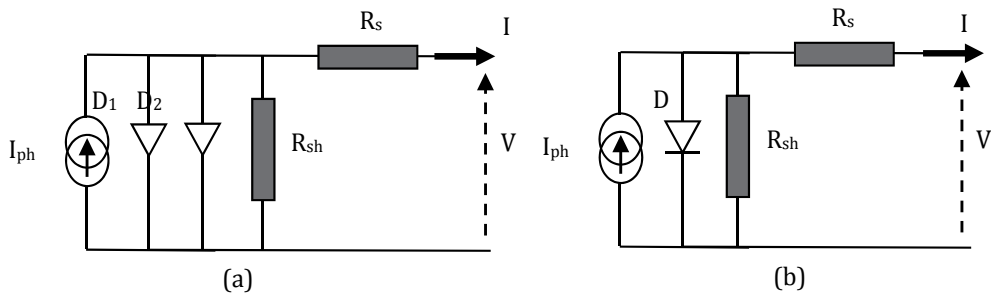


Fig. 1. Scheme of the equivalent electrical circuit of an illuminated solar cell: (a) the double diode model, and (b) the one diode model.

A rigorous and complete expression of the I-V characteristic of an illuminated solar cell that describes the complete transport phenomena is given by: (Sze, 1982)

$$I = I_{ph} - I_{s1}\left[e^{\frac{V+R_sI}{V_{th}}} - 1\right] - I_{s2}\left[e^{\frac{V+R_sI}{2V_{th}}} - 1\right] - \frac{V+R_sI}{R_{sh}} \tag{1}$$

Where $I_{ph}$ is the photocurrent, $I_{s1}$ and $I_{s2}$ are the saturation currents of diodes $D_1$ and $D_2$, respectively. $R_s$ is the series resistance, $R_{sh}$ is the shunt resistance and $V_{th}$ is the thermal voltage. However, it is well established that value of $I_{s2}$ is generally $10^{-6}$ times lesser than that one of $I_{s1}$. For this reason, it is well suitable to restrict ourselves to the one diode model.

In addition, despite the fact that the double diode model can take into account all the conduction modes, which is likely for physical interpretation, it may generate many difficulties. Hence, in this case, the accuracy of the fitting related to the value of the ending cost of the objective function, which corresponds to the admitted absolute minimum can be improved (Ketter et al., 1975). However, the physical meaning of the solution is lost, since

the number of parameters is augmented by 2 for the second diode. Consequently, the unicity of the solution is affected. However, precise experiments taking into account different physical phenomena contributing to the electronic transport are suitable to identify all the conduction modes. The single one diode model used here is rather simple, efficient and sufficiently accurate for process optimization and system design tasks. In photovoltaic, the output power of a solar module and a solar array is generally dependant of the electrical characteristics of the poor cell in the module, and the electrical characteristics of the poor module in an array. To skip this difficulty, electrical parameters of all cells forming a photovoltaic module should be very close each one to the other. For a photovoltaic array, all solar modules forming it should also have similar electrical characteristics. Consequently, the one diode model can also be applied to fit solar modules and arrays if we ensure that the cell to cell and the module to module variations are not important (Easwarakhanthan et al., 1986). It should be noted, however, that the parameters determined by the one diode model will lose somewhat their physical meaning in the case of solar modules and arrays. Consequently, the precision of each fitting approach will be certainly better in the case of solar cells than that of solar modules, which itself, should be more accurate than that of solar arrays.

Under these assumptions, results could be very acceptable with a good accuracy, and in replacement of expression (1), we will use the I-V relation given by expression (2), where n is the ideality factor. (Charles et al., 1985)

$$I = I_{ph} - I_s \left[ e^{\frac{V + R_s I}{n V_{th}}} - 1 \right] - \frac{V + R_s I}{R_{sh}} \tag{2}$$

Using expression (2) and the GAs, we can determine values of the electrical parameters $R_s$, $G_{sh} = 1/R_{sh}$, $I_{ph}$, n and $I_s$.

## 3. Classical optimization algorithms

The error criterion which used in classical curve fitting is based on the sum of the squared distances separating experimental Ii and predicted data $I(V_i, \theta)$:

$$S(\theta) = \sum_{i=1}^{m} \left[ I_i - I(V_i, \theta) \right]^2 \tag{3}$$

Where $\theta = (I_{ph}, I_s, n, R_s, G_{sh})$, $I_i$ and $V_i$ are respectively the measured current and voltage at the $i^{th}$ point among m data points.

The equation (3) is implicit in I and one way of simplifying the computation of $I(V_i, \theta)$ is to substitute $I_i$ and $V_i$ in equation (3). Hence, we obtain the following equation:

$$I(V_i, \theta) = I_{ph} - I_s \left[ Exp \left( \frac{(V_i + R_s I_i)}{n V_{th}} \right) - 1 \right] - G_{sh} (V_i + R_s I_i) \tag{4}$$

The equation (4) is nonlinear. Hence, the resulting set of normal equations $F(\theta) = 0$, derived from multivariate calculus will be non linear and no exact solution can be found. To obtain

an approximation of the exact solution, we use Newton's method. The Newton functional iteration procedure evolves from:

$$[\theta_k] = [\theta_{k-1}] - [J(\theta_{k-1})]^{-1}[F(\theta_{k-1})] \qquad (5)$$

Where J[θ] is the Jacobean matrix

Although, using Newton's Method, the initializing step of the five parameters plays a prominent part in the identification and determines drastically the convergence. There is a net difficulty in initializing the fitting parameters, which can be overcome by performing a procedure based on a reduced non-linear least-squares technique in which only two parameters have to be initialized. The electrical parameters are grouped in two classes: the series resistance $R_s$ and the diode quality factor n for the first one and the shunt resistance $R_{sh}$, the photocurrent $I_{ph}$ and the saturation current is for the second one.

The model is highly non-linear for the first class, if n and $R_s$ were fixed, the model would have a linear behaviour in regard to the second class. So that theses parameters are estimated by linear regression (Chan et al., 1987). Keeping theses three parameters constant, the model will be non-linear in regard to the first class of parameters. The objective function S(θ) will be minimized with respect to n and $R_s$. The two non-linear equations resulting from multivariate calculus are solved also by Newton's method, the iterations for n and $R_s$ are continued till the relative accuracy for each of them becomes less then 0,1%. The steps are then repeated with the new determined values of n and $R_s$, till the relative difference between two consecutive values of S computed soon after each linear regression, becomes smaller than a relative error which depends on the accuracy of the measured data.

The intention of the initializing procedure is to reduce from five to two the number of parameters that have to be initialized; a result of this first step is to have five starting values of the parameters within the domain of convergence. The feature of this set of values obtained from the first step is:

- The two parameters responsible on the non linearity are almost near the final result.
- The three parameters of the second class which are responsible on the supra linearity are sufficiently accurate.

To overcome the undesired oscillations and an eventual overflow which results from the Newton step choice, the algorithm uses a step adjustment procedure at each iteration. The modified Newton functional iteration procedure evolves from:

$$[\theta_k] = [\theta_{k-1}] - \lambda [J(\theta_{k-1})]^{-1}[F(\theta_{k-1})] \qquad (6)$$

The Newton steps are continued until the successively computed parameters are found to change by less than 0.0001%. At this end, Dichotomies method is used to solve the implicit equation (3).

This algorithm is tested for a number of samples of solar cells and for many configurations of initial values, it has been demonstrated that it converges in few seconds. The number of bugs resulting from overflows is scarce. Dead lock events do not exceed 3% for all the cells that are performed. The results of the fitted curve and experimental data for a 57 mm diameter silicon solar cell are presented in Fig. 2, Fig. 3 and Fig. 4.

The results show that for Fig. 4, the algorithm finds the absolute minimum with the desired accuracy (less than 0.3%). However, the initialized parameters in Fig. 2 and Fig. 3 allow the algorithm to converge to local minimums.
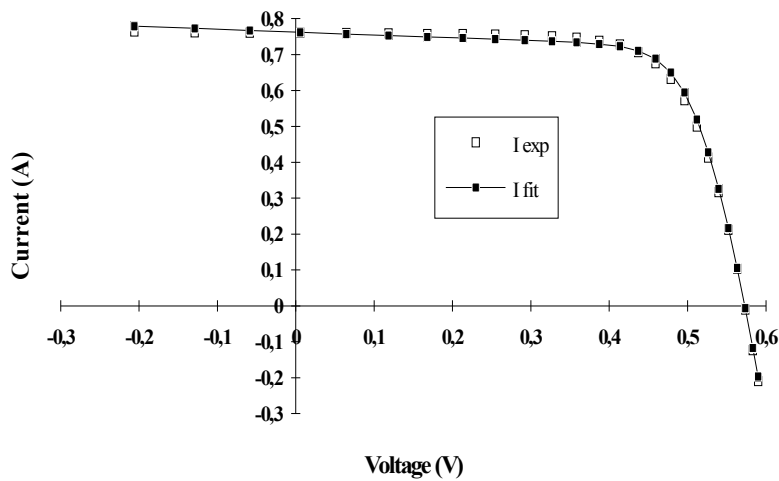
Fig. 2. Comparison between the experimental I-V characteristic and the fitted curve for a 57 mm diameter solar cell. The initial value of n and $R_s$ are: n=1; $R_s$=0Ω
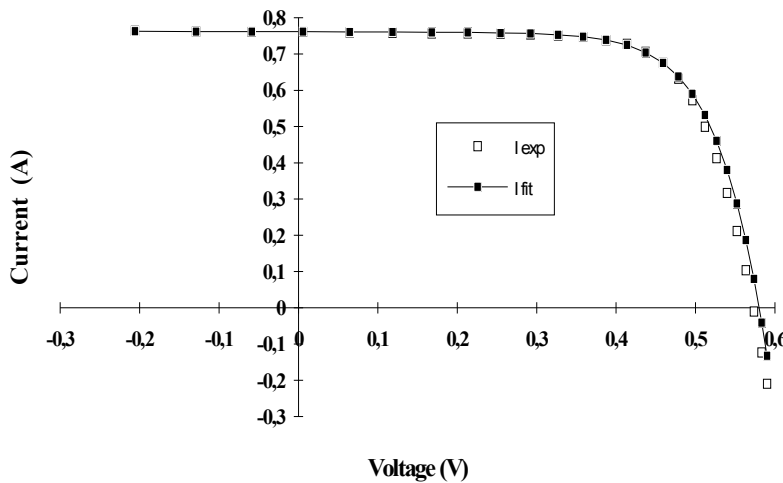


Fig. 3. Comparison between the experimental I-V characteristic and the fitted curve for a 57 mm diameter solar cell. The initial value of n and $R_s$ are: n=2; $R_s$=0Ω

In order to analyse the effect of the initialized parameters n and $R_s$ on the minimization of the error criterion, we have fixed one of them and we have varied the other.

Fig. 5 depicts the evolution of the objective function in regard to the initial value of N parameters (N varies from 1 up to 2). The initial value of Rs is fixed, and the minima are represented by dots joined just more clearness. We remark that the initial value of N parameters decides on the type of minimum whether it is absolute (case $N_{init}$=1.5) or relative (the other cases). We note that the search trajectory is a set of parabolic arcs confirming the fact that:

-      the minimum is the absolute and hence it represents the real solution, and

- the objective function is almost quadratic near the absolute minimum.

Fig. 6 gives the evolution of the objective function with the initial value of $R_s$ (the initial value of $R_s$ varies from $10^{-6}$ to 0.1 $\Omega$); the initial value of n is fixed. We deduce that the starting value of $R_s$, has, practically no influence on the minimum in comparison with the effect of the initial
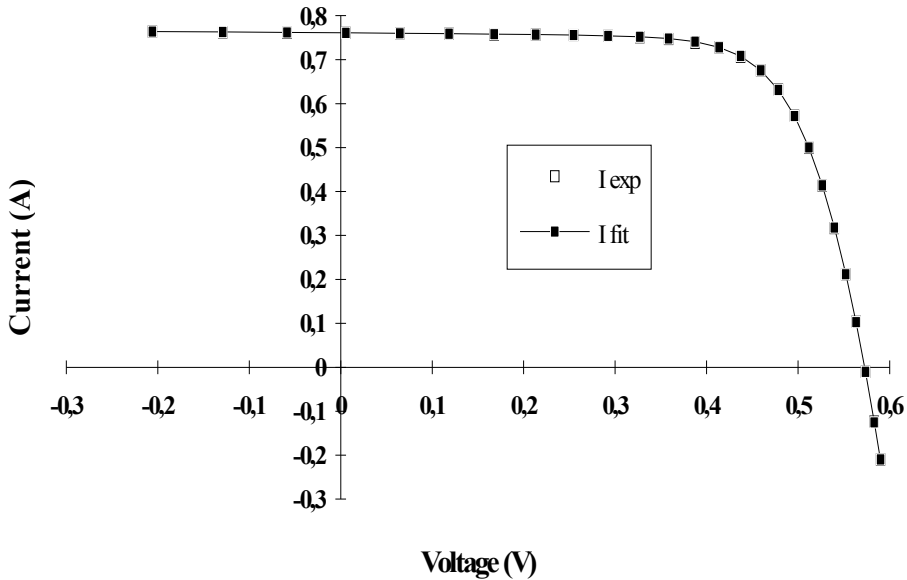


Fig. 4. Comparison between the experimental I-V characteristic and the fitted curve for a 57 mm diameter solar cell. The initial value of n and $R_s$ are: n=1,5; $R_s$=0,001$\Omega$
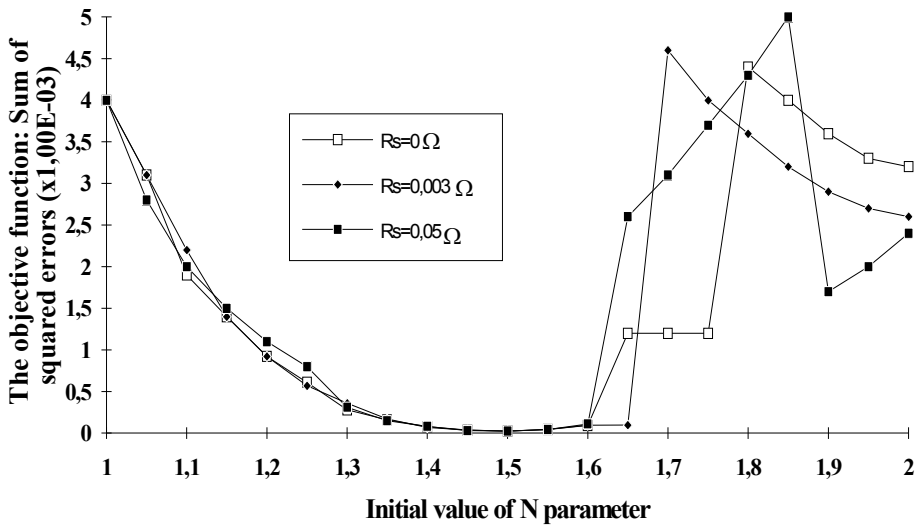


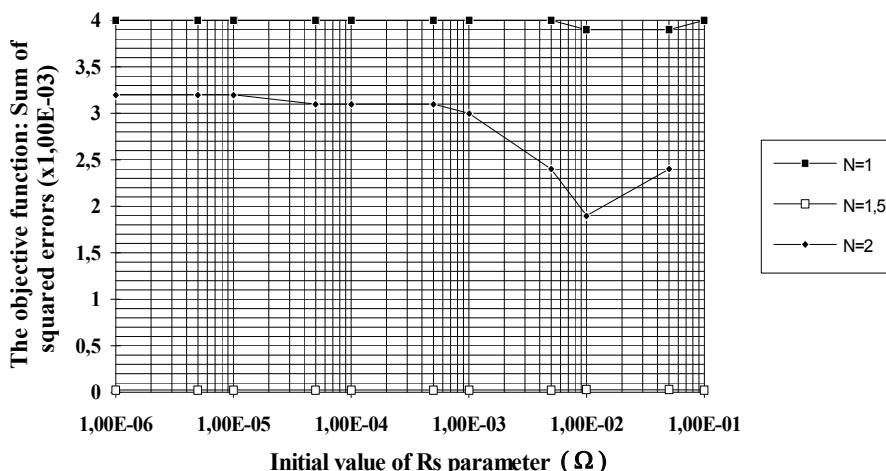Fig. 5. Search path of the absolute minimum in $R_s$ plans.

Fig. 6. Search path of the absolute minimum in n plans.

value of n parameter. Therefore, the initial value of $R_s$ is tacked to be arbitrary within an interval witch take into consideration the physical proprieties of this parameter.

For each combination of ($R_s$ initial, n initial), the algorithm converges to a minimum which can be relative or absolute. We stress on the fact that theoretically there is no way to predict the nature of the minimum (absolute or relative) for non linear models when we use Newton method. When the initial value of the n parameter is sampled linearly in the interval of its natural variation from 1 to 2 (Fig. 5), we have excluded, in such manner, the influence of the initial conditions. We obtain a set of minima; we deduce the absolute minimum which is the lowest and the real solution.

## 4. Application of the genetic algorithms

To numerically carry out the electrical parameters of the solar generators (cell and module), from the measured I-V curves, we fit the theoretical expression given in equation (2) to the experimental one. The fitting procedure is based on the use of the genetic algorithms (GAs). The error criterion in the nonlinear fitting procedure is based on the sum of the squared difference between the theoretical and experimental current values. As a consequence, the cost function to be minimized is given by (Easwarakhanthan et al., 1986; Phang et al., 1986):

$$\chi = \sum_{i=1}^{m}[I_i^{\exp} - I(V_i, \theta)]^2 \tag{7}$$

Where $I_i^{\exp}$ is the measured current at the $V_i$ bias, $\theta = (I_{ph}, I_s, R_s, G_{sh}, n)$ is the set of parameters to carry out, m the number of considered data points and $I(V_i, \theta)$ is the predicted current.

Eq. (2) is implicit in I; one way of simplifying the computation of $I(V_i, \theta)$ is to substitute $I_i$ and $V_i$ in Eq. (2). Hence, we obtain Eq. (8).

$$I(V_i, \theta) = I_{ph} - I_s\left[\exp\left(\frac{q(V_i + R_s I)}{nKT}\right) - 1\right] - G_{sh} (V_i + R_s I) \tag{8}$$
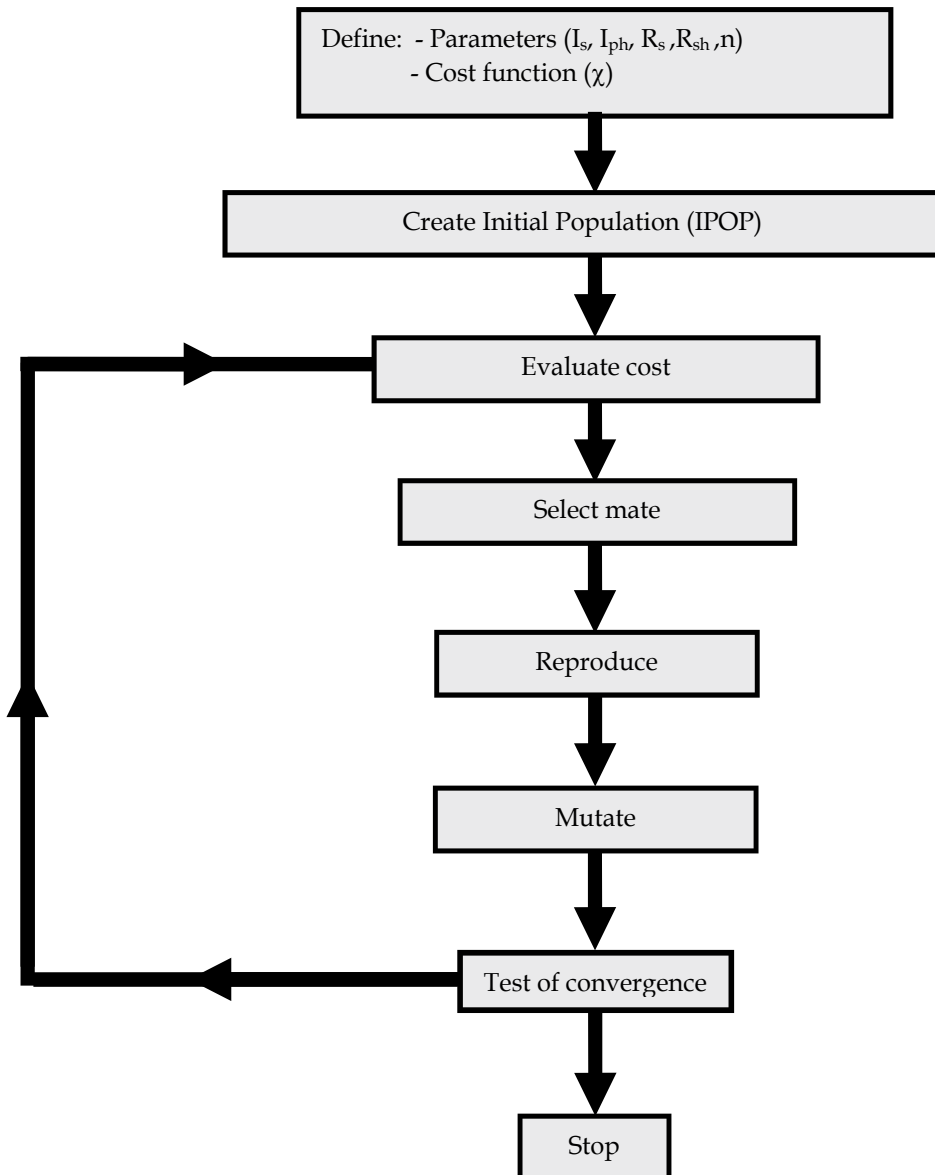
Fig. 7. Flow chart of the genetic algorithms.

Where:

$N_{ipop}$ is the initial number of chromosomes in IPOP,

$N_{par}$ is the number of parameters in the chromosome ($N_{par}$ = 5 in our case),

$l_o$ and $h_i$ are respectively the lowest and the highest values of parameters $I_s$, $I_{ph}$, $R_s$, $R_{sh}$ and n.

In Fig. 7, we give the flow chart of the GAs. The chromosome here is the vector θ containing the five parameters $I_{ph}$, $I_s$, $R_s$, $G_{sh}$, and n. The initial population (IPOP) of chromosomes is a matrix given by Eq. (9): (Easwarakhanthan et al., 1986)

$$IPOP = (h_i - l_o).random[N_{ipop}, N_{par}] + l_o \qquad (9)$$

The very common operators used in GAs are selection, reproduction and mutation (Haupt and Haupt, 1998; Sellami et al., 2007; Zagrouba et al., 2010), which are described as follows:

1. *Selection:* This procedure is applied to select chromosomes that participate in the reproduction process to give birth to the next generation. Only the best chromosomes are retained for the next generation of the algorithm, while the bad ones are discarded. There are several methods of this process, including the elitist model, the ranking model, the roulette wheel procedure, etc.

2. *Reproduction/pairing*: This procedure takes two selected chromosomes from a current generation (parents) and crosses them to obtain two individuals for the new generation (offspring's). There are several types of crossing, but the simplest methods choose arbitrary one or more points (parameters) in the chromosome of each parent to mark as crossover points. Then the parameters between these points are merely swapped between the two parents.

   In our case, each parent is represented by a chromosome containing five parameters. The paring is performed by crossing one, two, three, four and five parameters between the two parents, leading to obtain from these two parents a new generation of $2^5$ individuals (chromosomes).

3. *Mutation*: It consists of introducing changes in some genes (parameters) of a chromosome in a population. This procedure is performed by GAs to explore new solutions. Random mutations alter a small percentage of the population (mutation rate) except for the best chromosomes. A mutation rate between 1% and 20% often works well. If the mutation rate is above 20%, too many good parameters can be mutated, and then the algorithm stalls. In our case, mutation was applied to all parameters of 4% of chromosomes number. Note that the new value of each parameter should be in the $[l_o, h_i]$ corresponding interval. Consequently, after paring, mutated parameters are engaged to ensure that the parameters space is explored in new regions.

The used GA program is a homemade. We developed it on Matlab environment, for both PV cell, module and array. For flexibility, we choose to develop this program instead of using Genetic Algorithms and Direct Search Toolbox of Matlab.

## 4.1 Identification of the electrical parameters of the solar cell

Current-Voltage characteristic under AM1.5 illumination was performed using the cell tester CT 801 from Pasan (Pasan, 2004). This cell tester includes in the same compact architecture a single-flash xenon light source, an automatic sliding contact frame, a test chuck with interchangeable plates to fit any cell configuration, a calibrated reference cell, and a Panel-PC type computer. To become a fully featured cell testing unit, it needs to be connected to an external electronic load and flash generator, itself included in a 19" 6U rack. Its single-flash technology gives a negligible heating of the cell, in the tenths of a degree range, much lower than continuous-light testers, so an accurate I-V curve determination can be achieved (Pasan, 2004). In Fig. 8, we give the plot of the I-V curve of a multicrystalline silicon solar cell having a surface area of 4 cm².

To determine the cell parameters, we use equation (2) and the I-V curve of Fig. 8. Obtained results are compared to those obtained by the Pasan cell tester software version V3.0.

In general, the time-convergence of the algorithm is influenced by the choice of the IPOP. If coordinates of the absolute minimum of the cost function in the parameter's space are unknown, initial invidious (IPOP) were generated randomly. The latter were chosen
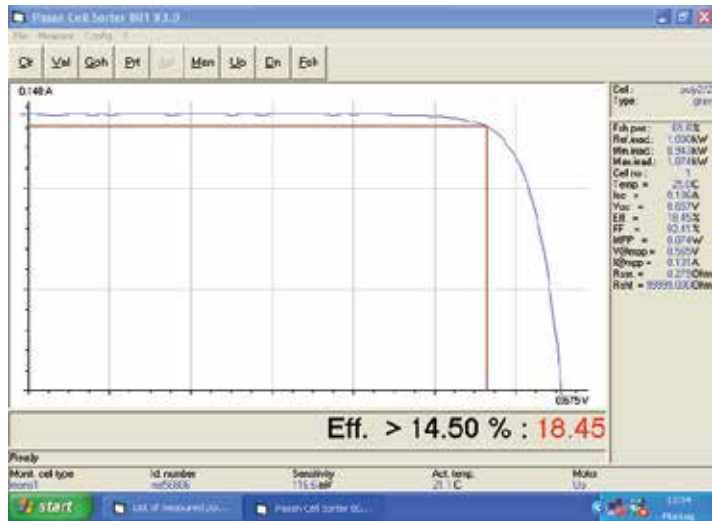
Fig. 8. Experimental I-V curve of the solar cell performed with the Pasan machine.

uniformly between the highest and the lowest value of each parameter. In this work, the first generation was started with $14^5$ (537824) chromosomes as the initial population (IPOP), where 5 is the number of parameters to be identified. Each parameter in a chromosome has a lowest ($l_o$) and a highest ($h_i$) value. Since the interval between $l_o$ and $h_i$ contains an infinite number of values, we started in the simulation with different values such as 200, 100, 50, 25, 15, 10 and 5. We remark that simulation results are similar for all values 200, 100, 50, 25, 15 and 14. For values less than 14, the algorithm leads to a relatively high value of the cost function.

After determining the cost function for each chromosome, we apply a selection in IPOP (Select mate): only a family of good chromosomes that corresponds to good values of the cost was kept for the pairing (reproduce) and the others (bad) were killed. To ensure that the parameters space is suitably explored, a mutation of 4% in the chromosomes was operated (mutate). At the end of the algorithm, the convergence was tested. If the result (last value of $\chi$) does not give satisfaction compared to a predefined cost minimum ($\chi=0.000270$ A$^2$), all below steps are repeated in the second generation and so on. The fitting result is plot in Fig. 9. As we can see, theoretical curve fits very well experimental results.

In Fig. 10, we plot the mean and the minimum values of the cost function with respect to the generation number. One can notice that beyond the third generation, the cost function becomes stable in a relative good minimum. The minimum value of the cost function was found to be equal to 0.000256 A$^2$ and was reached after five generations. According to this relatively good value, one can assume that the GAs are very suitable for the estimation of the electrical parameters via the fitting method. In table 1, we compare the electrical parameters resulting from the use of the GAs-based fitting procedure, with those given by the Pasan cell tester software. Hence, the minimization problem is of five parameters ($I_{ph}$, $I_s$, $R_s$, $R_{sh}$, n), which is a hard problem in fitting procedures. As presented in table 1, the Pasan software gives only estimations of three parameters ($I_{ph}$, $R_s$, $R_{sh}$) from the five unknown ones. The saturation current $I_s$ and the ideality factor n are not performed. In contrast, using the GAs method, we can estimate values of $I_s$ and n in addition to the other three parameters ($I_{ph}$, $R_s$, $R_{sh}$). Obtained values' using the Pasan software and GAs method are identical for $I_{ph}$ and

Application of the Genetic Algorithms
for Identifying the Electrical Parameters of PV Solar Generators
359

differs of 1% for $R_{sh}$. However, value of $R_s$ obtained with the Pasan software is 7.5 times that one obtained with GAs. Regarding the good fitting result in Fig. 9, and taking into account that the $R_s$ effect on the I-V curve is in general observed for voltages near the $V_{oc}$ value, one can argue that the output value of $R_s$ obtained with GAs is reasonable, but no conclusion can be done on the $R_s$ value given by the Pasan software since no fitting is presented.
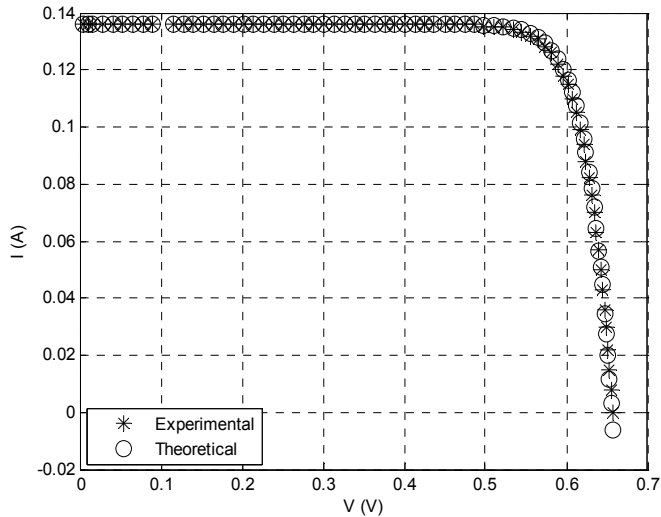


Fig. 9. Adjustment of the theoretical I-V curve of the solar cell's to the experimental one using GAs method.
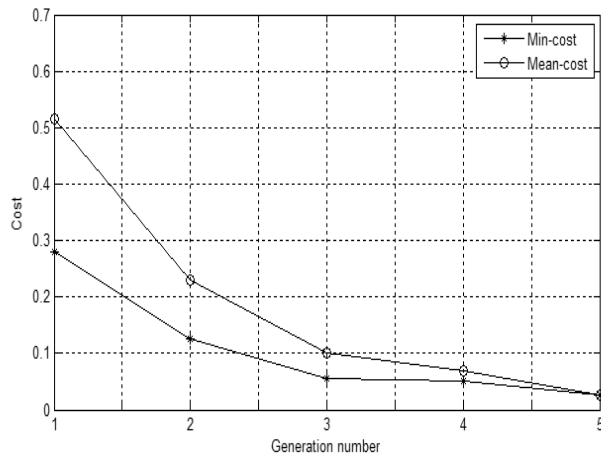


Fig. 10. Mean and minimum values of the $\chi$ function versus generation number of the solar cell.

| Electrical parameters | Pasan CT 801 | Genetic Algorithms |
|:---:|:---:|:---:|
| $I_s$ (A) | Not performed | $1.2170\ 10^{-2}$ |
| $I_{ph}$ (A) | 0.1360 | 0.1360 |
| $R_s$ (Ω) | 0.2790 | 0.0363 |
| $R_{sh}$ (Ω) | 99999 | 99050 |
| $n$ | Not performed | 1.0196 |

Table 1. Comparison between the electrical parameters determined using GAs and those given by the Pasan CT 801 software in the case of the used solar cell.

### 4.2 Determination of the PV module parameters

For the module characterization, we use a homemade solar module tester. The system takes advantage of the quick response time of PV devices by illuminating and characterising the samples within a few milliseconds. The tester measures the complete I-V curve of the PV module by using a capacitor load (Sellami et al., 1998). In the meantime, it measures the illumination level, the temperature, the voltage and its corresponding current in order to minimize the quantification errors coming from ADC and DAC conversion. Data are then transferred to the computer that calculates the efficiency, the short circuit current, the open circuit voltage and the fill factor. The bloc diagram of the PV module tester is given in Fig. 11. We used a commercial 50 Wp PV module manufactured by ANIT-Italy. Testing was performed at 44°C and 873 W/m² illuminations.
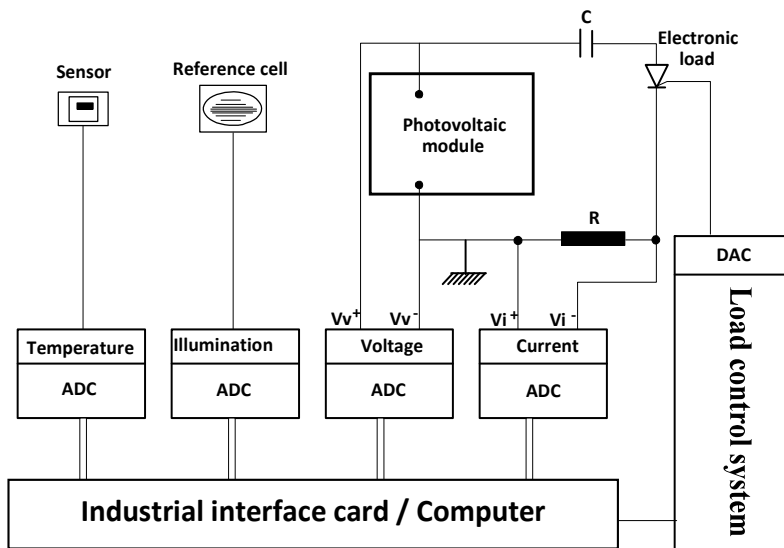


Fig. 11. Block diagram of the PV module tester.

The adjustment of the theoretical I-V curve of the PV module to the experimental one using GAs, and the mean and the minimum values of the cost function χ versus generation number are given in Fig. 12 and 13, respectively. In this simulation (PV module), we choose $12^5$ chromosomes as IPOP and the predefined cost minimum is χ=0.0700 A².

In the case of the used PV module, the GAs-based fitting procedure of the theoretical I-V curve to the experimental one (achieved using the PV module tester shown in Fig. 11) gives a minimum value around 0.0676 A$^2$ and was reached after only seven generations. The results of this minimization are shown in Table 2.
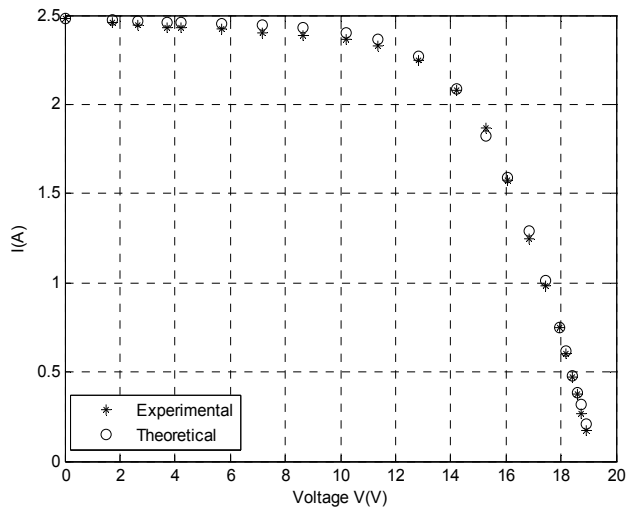


Fig. 12. Adjustment of the theoretical I-V curve of the PV solar module to the experimental one, using Gas.
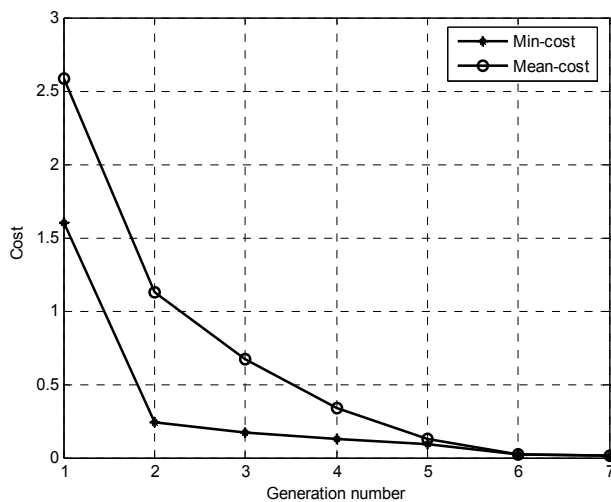


Fig. 13. The mean and the minimum values of the standard deviation χ versus generation number (case of PV solar modules).

| Electrical parameters | Values (GAs) |
|---|---|
| $I_s$ (A) | 8.1511 10⁻⁶ |
| $I_{ph}$ (A) | 2.4901 |
| $R_s$ (Ω) | 0.9539 |
| $R_{sh}$ (Ω) | 196.4081 |
| $n$ | 60.4182 |

Table 2. Electrical parameters of the PV module obtained with GAs.

## 4.3 Determination of the Maximum Power Point

In order to extract the maximum available power from a PV cell, it is necessary to use it (the cell) at its maximum power point (MPP). Several MPP methods, such as perturbation, fuzzy control, power–voltage differentiation and on-line method have been reported (Dufo-Lopez and Bernal-Agustin, 2005; Bahgat et al., 2004; Yu et al., 2004). These control methods have drawbacks in stability and response time in the case when solar illumination changes abruptly. A direct MPP method using PV model parameters was introduced in (Yu et al., 2004). However, the validity of obtained result depends on the accuracy of the model parameters; i.e. the criterion for parameters extraction is not convex, and the traditional deterministic optimization algorithm used in (Yu et al., 2004) leads to local minima solutions. Indeed, in our case, we use the GAs, which belongs to heuristic solutions that represent a trade-off between solution quality and time. The GAs have a stochastic search procedure in nature, they usually outperform gradient based techniques in getting close to the global minima and hence avoid being trapped in local ones.

A derivative of the output power P with respect to the output voltage V is equal to zero at MPP.

$$\frac{dP}{dV} = I - V \left[ \frac{\frac{q}{nkT}\left(I_{ph} + I_s - I - \frac{V + R_s I}{R_{sh}}\right) + \frac{1}{R_{sh}}}{1 + \frac{qR_s}{nkT}\left(I_{ph} + I_s - I - \frac{V + R_s I}{R_{sh}}\right) + \frac{R_s}{R_{sh}}} \right] = 0 \qquad (10)$$

If the parameters of the equivalent circuit model are given, MPP is obtained by solving Eq. (10) using standard numerical non-linear method. This can be easily achieved with the optimisation Toolbox of MATLAB software.

In table 3, we give the current and voltage values corresponding to the Maximum Power Points (MPP) obtained using Eq. (10) and the electrical parameters given in tables 1 and 2 identified by the GAs. The output results in the case of the solar cell are compared to those provided by the Pasan software. In the case of the cell (table 3), one can notice that our GAs simulations results differ at least by 5.3% from those given by the Pasan software. In general, the well used procedure to estimate the MPP in cell and module testers is based on the selection of the maximum power from an experimental set of current-voltage multiplication. The accuracy of this statistical approach depends on the precision of the experimental data, which should surround the real value of the MPP. However, our approach presents two advantages; first, it is based on Eq. (10), which is free of these experimental constrains. Secondly, Eq. (10) itself, uses the identified electrical parameters extracted by the GAs that belong to a sophisticated global search method.

Obtained results in the case of the PV cell using the Pasan software and the GAs are nearly identical. However, in the case of the PV module, our homemade system is able to measure I-V characteristics, but it is not equipped with sophisticated software to give the electrical characteristics of the module. Consequently, the measured I-V curve of the module is analysed only with the GAs method, and no comparison is performed as shown in table 3. The credibility of obtained results with the PV module is extrapolated from that one of the PV solar cell, where obtained results with the GAs technique are compared to those obtained using a professional machine (Pasan CT 801).

| | $I_{opt}$ (A) | $U_{opt}$ (V) | MPP (W) |
|---|---|---|---|
| **Cell** (using GAs) | 0.137 | 0.571 | 0.078 |
| **Cell** (using Pasan software V 3.0) | 0.131 | 0.565 | 0.074 |
| *Module (using GAs)* | 2.120 | 14.200 | 30.104 |

Table 3. MPP's coordinates of the solar cell and the solar module and their corresponding powers.

## 5. Conclusion

This chapter has studied the extraction of solar generators' (cell and module) parameters from the I-V characteristics under illumination. The main problem that has been addressed is the accuracy of the determined parameters with curve fitting by using optimisation algorithms.

In this work, we proposed the genetic algorithms to extract PV solar cells electrical parameters. The determination of these parameters using experimental data was formulated in the form of a non convex optimization problem. The curve fitting by the Newton algorithm, conducts to less satisfactory results, which depend on the initial conditions leading to local minima solutions. We thus used the genetic algorithms (GAs) as an optimization tool in order to increase the probability to reach the global minima solutions.

The algorithm for the identification of solar modules electrical parameters can be extended to multi-diode model. Furthermore, we can use a minimisation criterion based on the area difference between the experimental and theoretical characteristics. Moreover, hybrid algorithms which combine heuristic solutions as GAs and PSO (Particle Swarm Optimisation) with deterministic methods can be a powerful tool in the future.

## 6. References

Bahgat, A. B. G., Helwa, N.H., Ahamd, G.E., El Shenawy, E.T., 2004. Estimation of the maximum power and normal operating power of a photovoltaic module by neural networks. Ren. Energy 29 (3), 443–457.

Chan, Daniel S. H,. Phang, Jacob C. H., 1987, Analytical Methods for the extraction of Solar-Cell Single- and Double-Diode Model Parameters from I-V Characteristics, IEEE Transactions on Electron Devices, Vol. ED-34, N°2, p. 286-293.

Charles, J. P., Abdelkrim, M., Muoy, Y. H., Mialhe, P., 1981. A practical method of analysis of the current voltage characteristics of solar cells. Solar cells, 4, p.169-178.

Charles, J. P., Ismail, M.A., Bordure, G., 1985, A critical study of the effectiveness of the single and double exponential models for I-V characterization of solar cells. Solid-State Electronics, Vol. 28, N°8, p. 807-820.

Dufo-Lopez, Rodolfo, Bernal-Agustin, José L., 2005, Design and control strategies of PV-Diesel systems using genetic algorithms. Sol. Energy, 79, 33–46.

Easwarakhanthan, T., Bottin, J., Bouhouch, I., Boutrit, C., 1986. Non linear minimization algorithm for determining the solar cell parameters with microcomputers. Int. J. Solar Energy, Vol.4, p.1-12.

Enrique, J.M., Durán, E., Sidrach-de-Cardona, M., Andújar, J.M., 2007. Theoretical assessment of the maximum power point tracking efficiency of photovoltaic facilities with different converter topologies. Solar Energy, Volume 81, Issue 1, Pages 31-38.

Haupt, R. L., Haupt, S. E., 1998. Practical Genetic Algorithms (New York: Wiley).

Ikegami, T., Maezono, T., Nakanishi, F., Yamagata, Y., Ebihara, K., 2001. Estimation of equivalent circuit parameters of PV module and its application to optimal operation of PV system.  Solar Energy Materials & Solar Cells, 67, 389-395.

Ketter, Robert L., Prawel, Sherwood P., 1975. "Modern methods of engineering computation"; Mac Graw-Hill book company.

Pasan Cell Tester CT 801 operating manual., 2004, (www. pasan.ch).

Phang, Jacob C.H., Chan, S.H. Daniel., 1986. A review of curve fitting error criteria for solar cell I-V characteristics. Solar cells, 18, p.1-12.

Sellami, A., Ghodbane, F., Andoulsi, R., Ezzaouia, H., 1998. An electrical performance tester for PV modules. Proc. WREC (Florence, Italy) vol 3, pp 1717–1720.

Sellami, A., Zagrouba, M., Bouaïcha, M., Bessaïs, B., Meas. Sci. Technol. 18 (2007) 1472–1476.

Sze, S. M., ''Physics of Semiconductors Devices'', 2nd edition (1982).

Yu, G.J., Jung, Y.S., Choi, J.Y., Kim, G.S., 2004. A novel two-mode MPPT control algorithm based on comparative study of existing algorithms. Sol. Energy 76, 455–463.

Zagrouba, M., Sellami, A., Bouaïcha, M., Solar Energy Solar Energy 84 (2010) 860–866.

*Edited by Leonid A. Kosyachenko*

The third book of four-volume edition of 'Solar Cells' is devoted to solar cells based on silicon wafers, i.e., the main material used in today's photovoltaics. The volume includes the chapters that present new results of research aimed to improve efficiency, to reduce consumption of materials and to lower cost of wafer-based silicon solar cells as well as new methods of research and testing of the devices. Light trapping design in c-Si and mc-Si solar cells, solar-energy conversion as a function of the geometric-concentration factor, design criteria for spacecraft solar arrays are considered in several chapters. A system for the micrometric characterization of solar cells, for identifying the electrical parameters of PV solar generators, a new model for extracting the physical parameters of solar cells, LBIC method for characterization of solar cells, non-idealities in the I-V characteristic of the PV generators are discussed in other chapters of the volume.